Anion-Templated Self-Assembly – From Anion Complexes to the Formation of Supramolecular 2D Networks

Anna Aletti

September 2018

University of Dublin

Trinity College

Based on research carried out under the direction of
Prof. Thorfinnur Gunnlaugsson

A thesis submitted to the School of Chemistry,
University of Dublin, Trinity College for the degree of
Doctor of Philosophy

Declaration

I declare that this thesis has not been submitted as an exercise for a degree at this or any other university and it is entirely my own work, except where duly acknowledged. I agree to deposit this thesis in the University's open access institutional repository or allow the Library to do so on my behalf, subject to Irish Copyright Legislation and Trinity College Library conditions of use and acknowledgement.

I consent to the examiner retaining a copy of the thesis beyond the examining period, should they so wish (EU GDPR May 2018).

Anna Aletti

“…cercai di spiegargli alcune delle idee che a quel tempo confusamente coltivavo. Che la nobiltà dell’Uomo, acquisita in cento secoli di prove e di errori, era consistita nel farsi signore della materia, e che io mi ero iscritto a Chimica perché a questa nobiltà mi volevo mantenere fedele. Che vincere la materia è comprenderla, e comprendere la materia è necessario per comprendere l’universo e noi stessi: e che quindi il Sistema Periodico di Mendeleev, che proprio in quelle settimane imparavamo laboriosamente a dipanare, era una poesia, più alta e più solenne di tutte le poesie digerite in liceo: a pensarci bene, aveva perfino le rime! Che, se cercava il ponte, l’anello mancante, fra il mondo delle carte e il mondo delle cose, non lo doveva cercare lontano: era lì, nell’Autenrieth, in quei nostri laboratori fumosi, e nel nostro futuro mestiere.”

Primo Levi, Ferro, Il Sistema periodico

“...I tried to explain to him some of the ideas that at the time I was confusedly cultivating. That the nobility of Man, acquired in a hundred centuries of trial and error, lay in making himself the conqueror of matter, and that I had enrolled in chemistry because I wanted to remain faithful to this nobility. That conquering matter is to understand it, and understanding matter is necessary to understanding the universe and ourselves: and that therefore Mendeleev’s Periodic Table, which just during those weeks we were laboriously learning to unravel, was poetry, loftier and more solemn than all the poetry we had swallowed down in school; and come to think of it, it even rhymed! That if one looked for the bridge, the missing link, between the world of words and the world of things, one did not have to look far: it was there, in our Autenrieth, in our smoke-filled labs, and in our future trade.”

Primo Levi, Iron, The periodic system

Abstract

This thesis, entitled “Anion Templated Self-Assembly – From Anion Complexes to the Formation of Supramolecular 2D Networks” covers the anion complexation and ATSA abilities of different sets of ligands. The work will be divided into five chapters, gathering the work on each different sets of ligands separately.

Chapter 1 will introduce the most recent advances in anion complexation and anion-templated self-assembly, from the formation of 1:1 (Ligand:Anion) complexes to the formation of higher order bundles. Particular focus will be given to the use hydrogen bonding as the main interaction for the formation of anion-templated self-assemblies.

Chapter 2, will discuss the synthesis and anion binding studies of tripodal tris(urea) ligands with Cl^-, CH_3COO^-, $H_2PO_4^-$ and SO_4^{2-}. The anion binding studies carried out in solution on these ligands indicated that ATSA was occurring which lead us to investigate also the self-assembly behaviour in solution and in the solid state, which will also be discussed in detail.

Chapter 3 will focus on the synthetic challenges engaged to obtain ‘dipodal’ ligand, not simply as a side product. Solution binding studies on a dipodal thiourea analogue with tetrahedral anions (*i.e.* $H_2PO_4^-$ and SO_4^{2-}) will be included in this chapter.

In chapter 4 the formation of anionic complexes with a family of macrocycles and [2]catenanes, combining the 2,6-bis(triazolo)pyridine (BTP) moiety and amide groups as binding units, will be presented. The discussion will cover the differences given by the different substitution pattern and the higher preorganisation of hydrogen bond donors within the [2]catenanes structures.

Chapter 5 will include the studies on halide encapsulation within bis(tren) cage with imidazolate binding units, which were carried out in collaboration with Prof. Amendola, from Università degli studi di Pavia. Detailed NMR characterisation of the anionic complexes will be presented, which will show the conformational changes caused by the encapsulation of the halide anions.

Chapter 6 will provide detailed experimental procedures. References are provided in Chapter 7 and supplementary data and spectra are presented in the Appendices A2-A5.

Acknowledgements

My first thanks must go to my supervisor Prof. Thorfinnur Gunnlaugsson for giving me the opportunity and honour to be part of his team, and for always believing in my abilities more than I do in myself. I will never be grateful enough for the chances I was given, for the inspiration and trust, for the understanding and the help. Most of all, thank you for bringing together such an amazing group of researchers, which I surely will not forget for the rest of my life.

I would like to thank Prof. Valeria Amendola for involving me into an interesting project, valuing my skills and knowledge.

A massive thank you to all the people that have offered their knowledge and technical skills to support my research, with patience and dedication over the past four years. In particular, I would like to thank Dr. Savyasachi Aramballi Jyanth, Ms Amy Lines and Mr Jason Delente for sharing their time and skills at the SEM, as well as to Dr Samuel Bradberry for the preliminary studies with polymers and to Dr Bjørn la Cour Poulsen for the molecular modelling. Thank you also to the crystallographers who spent their early mornings and weekends at the diffractometer for my crystals: Dr Miguel Martinez Calvo, Dr Salvador Blasco, Dr Chris S. Hawes, Dr Eoin McCarney, as well as Ms Hannah Dalton and Ms June Lovitt. I am very grateful to Dr Manuel Reuther for the patience and help with DOSY NMR and to Dr John O'Brien for his enthusiasm when teaching me everything about NMR and for showing me what it looks like when one really loves his job. Thank you also to the precious work of Drs Gary Hessman and Martin Feeny with the mass spec.

These years have been full of joy and difficulties and I must thank all the TG group fellows who accompanied me into this journey: thank you all for your patience and for the cakes and crisps and chocolate and jellies and donuts. Thank you to those who were here when I started and have left for new adventures: Joe for making every conversation interesting, Fergus never being able to say no, Helen for your stories and Raju for your knowledge. Thank you Sachi for showing me that patience can take you a long way, Dawn for your incredible talent for doing twice as many things in half the time and also finding time to proofread my drafts and to Adam for "being able to sneeze in seven different ways" (cit. Jacobo). I would also like to thank the people who have been in the PhD journey with me wishing them the best for their future: Amy, thank you for introducing me to the best coffee (and donuts) around; Sandra, thank you for always being such a good scientist and never being satisfied for nothing than the best; Elena, thanks for your knowledge and hard work; Dermot, thank you

for being such a fun company with all your knowledge of plants, birds, sophisticated food and all the rest. Thanks to Isabel, Hannah and June for your kind help with proofreading. Thank you also to Oxana, for being so much more than a colleague, an example to look up to, for sustaining me through the years, being supportive and understanding but also firm and honest when needed: a very good friend. Thank you, Viola, for your smile and positivity: life in TBSI would have been more difficult without our evenings at the swimming pool and our cokes and coffees, I have missed you in the last year.

My gratitude also goes to Rita, Megghy, Alice and Mariavi: arriving in Dublin to start a new life would have been so different without you. Every night in Finsbury was the best night and every weekend was full of surprises and laughs, and I could not have been more blessed. I cannot believe how much we have grown together and after. Thank you for your friendship and may life continue to surprise us the way it has done in these years. I would like to thank also all the friends in Dublin who have shown their support in many ways, in particular to Fr Terence and Fr Philip, Maria, Aileen, Chiara, Claudia and Pietro, Anna and Jim, Kathryn, Elena and Roberto.

Thank you to my new family who have welcomed me in such an amazing way: Sue and Geoff for our precious times together in both Ireland and UK, Rachel, Steve, Dan and Hannah for being such welcoming hosts every time we want to visit. You will always be most welcome in our home. And thanks to Ethan, Alice and Izzy, for bringing me a smile when is most needed.

Grazie a mamma e papà per avermi lasciato libera di venire così lontano per seguire la mia strada. La lontananza è stata difficile, ma presto sarò di ritorno arricchita in modi che mai avrei potuto immaginare. Grazie nonna per il tuo affetto e il tuo sostegno costanti.

Grazie ai miei fratelli Luca, che ogni giorno mi rende sempre più orgogliosa e Fabio, che da lassù si prende cura di me e mi ispira sempre a dare il massimo.

Last, but surely not least, thank you to the most incredible person I met in Dublin, and has blessed my life by sharing it all with me. Sam, thank you for being the amazing person you are every day, thank you for being with me through all of this journey, in good and bad times, and for putting up with me. Thank you for being there every time I need you, no matter what. Thank you for making me feel the luckiest person in the world every day.

List of Abbreviations

ATP	adenosine-5’-triphosphate
bip	bis-imidazolium pyridine
Boc_2O	di-*tert*-butyl dicarbonate (Boc_2O) or
Boc-Osu	*N*-(*tert*-butoxycarbonyloxy)succinimide
br.	broad
BTA	benzene 1,3,5-tricarboxamide
btp	bis-triazolyl pyridine
btph	bis-triazolyl phenylene
Cbz	carboxybenzyl
CFC	chloro-fluoro-carbons
COSY	correlation spectroscopy
CuAAC	copper(I)-catalyzed alkyne-azide cycloaddition
d	doublet
dd	doublet of doublets
DNA	deoxyribonucleic acid
DPPA	diphenylphosphoryl azide
dt	doublet of triplets
EDG	electron donating group
eq.	equivalents
EWG	electron withdrawing group
FT-IR	Fourier-transform infra-red spectroscopy
HMBC	heteronuclear multiple bond correlation
HPLC	high performance liquid chromatography
HRMS	high resolution mass spectrometry
HSQC	heteronuclear single quantum correlation
IR	infra-red
J	coupling constant (Hz)
M	molar (mol dm^{-3})

m	multiplet
m/z	mass to charge ratio
MALDI	matrix-assisted laser desorption/ionisation
MLCT	metal-to-ligand charge transfer
NMR	nuclear magnetic resonance
PEG	poly(ethylene glycol)
ppm	parts per million
RCM	ring closing metathesis
RNA	ribonucleic acid
ROESY	rotating frame Overhauser effect spectroscopy
RT	room temperature
s	singlet
SC-XRD	Single crystal X-ray diffraction
SEM	scanning electron microscopy
t	triplet
TBA	tetrabutylammonium
TEA	triethylamine
tmBTA	N^1,N^3,N^5-trimethylbenzene-1,3,5-tricarboxamide
TOF	time of flight
tren	tris(2-aminoethyl)amine
UV-vis	ultraviolet-visible
λ_{max}	wavelength of absorbance maximum (nm)
ν_{max}	frequency of molecular vibrations (cm^{-1})

Note on publications

Sections of this work have been published in peer-reviewed journals prior to submission of the thesis, or included in manuscripts submitted for review.

Chapter 4 contains work that has been published in the communication "Formation of Self-Templated 2,6-Bis(1,2,3-triazol-4-yl)pyridine [2]Catenanes by Triazolyl Hydrogen Bonding: Selective Anion Hosts for Phosphate" co-authored with Dr Joseph P. Byrne, Dr Salvador Blasco, Dr Gary Hessman, and Prof. Thorfinnur Gunnlaugsson in Angewandte Chemie, (*Angew. Chem. Int. Ed.* **2016**, 55, 8938 –8943).

Work carried out during the preparation of this thesis has also contributed to the publication of the review "Luminescent/colorimetric probes and (chemo-) sensors for detecting anions based on transition and lanthanide ion receptor/binding complexes" co-authored with Mr Dermot M. Gillen and Prof. Thorfinnur Gunnlaugsson in Coordination Chemistry Reviews (Coord. Chem. Rev. **2018**, 354, 98–120) and the article "Supramolecular Anion Recognition Mediates One-Pot Synthesis of 3‑Amino-[1,2,4]-triazolo Pyridines from Thiosemicarbazides" co-authored with Dr Komala Pandurangan, Mr Devis Montroni, Dr Jonathan. A. Kitchen, Dr Miguel Martínez-Calvo, Dr Salvador Blasco, Prof. Thorfinnur Gunnlaugsson and Prof. Eoin M. Scanlan in Organic Letters (Org. Lett. **2017**, 19, 1068−1071).

Table of Contents

1. Introduction

1.1. Anion coordination

While the coordination of metal ions has a history, which dates back the late 19th century, with Alfred Werner understanding the role of coordinative bonds, the history of anion coordination is a more recent. The first examples of bicyclic cages by Park and Simmons in 1968 led the way towards the development of a field of anion coordination chemistry using designed ligands.[1] Anion and metal-coordination can be compared with complementary definitions and rules, which are well known within the vocabulary of supramolecular chemistry. A “ligand” for metal-coordination is considered a Lewis-base, which donates a pair of electron to the metal centre through a coordinative bond. In the case of anion coordination, a ligand is rather a Lewis acid, which can “accept” a lone pair of electrons from an anion.[2]

Anions have a larger charge to radius ratio than their isoelectronic cations.[3] As a result, the interaction between an anion and a ligand can be less effective, and the binding less strong. A more effective interaction between a target anion guest and a host molecule can be achieved by increasing the number of interacting sites, giving rise to a “chelate effect”. Similarly to that observed for metal ligands, pre-organisation of the binding sites within an enclosed space, like a macrocycle or a cryptand, can favour the binding, thanks to the “macrocyclic effect” or “cryptand effect”.[4] To create efficient and selective binding it is essential for the ligand binding-site to be preorganised to reflect the geometry of the targeted guest. Efficient binding comes as a result of the correct balance of entropic and enthalpic factors. The preorganisation of the ligand (*e.g.* a macrocycle or a cage) enhances the binding as the molecules do not need to rearrange to a less entropically favoured conformations. That is to say, the energy input needed to bring the ligand into the optimal conformation for recognition is avoided thanks to the pre-existing organisation. The preorganisation and complementarity are key features to consider during ligand design. The creation of preorganised binding pockets with a combination of a number of highly directional hydrogen bonds donors makes it possible to bind anions with highly symmetric features.[5-8]

In solution, the polarity as well as the hydrogen bond donor/acceptor ability of the solvent affects the binding as any interaction with the binding site creates competition with the anion. This makes the recognition less effective, as it will require desolvation of the binding motif prior to anion association. Similarly, the interaction of the solvent with the anion has to be considered. In protic solvents hydrogen bonds can help in stabilising both the host and the guest in solution, making them heavily solvated. Effective host-guest interaction will be affected by both the energetic penalty of the desolvation process and the

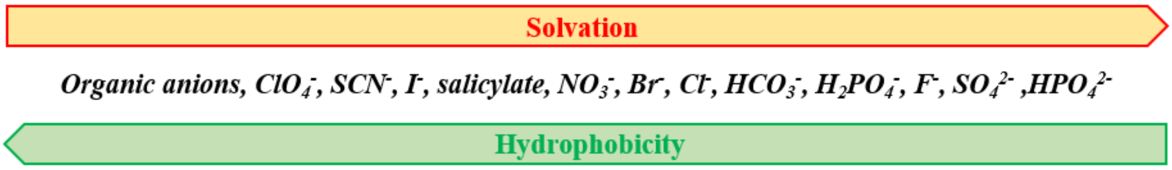

Figure 1.1. Hofmeister series.

solvophobic effect.[9] On the other hand in less polar solvents, with poorer solvation strength, it is likely to find charged species strongly paired with counter ions that can compete for the target host-guest interaction.[10] All of these features must be considered when creating a new anion receptor. Balancing these for each application to achieve appropriate selectivity, specificity and reversibility is a great challenge in anion recognition.

In aqueous solutions, most anions are sensitive to the effect of pH which may reduce their negative charge at lower pH due to protonation, or *vice versa* in strongly basic conditions. This can also change the number of hydrogen-bond donor/acceptors available, affecting the non-electrostatic supramolecular interactions.

The solvation of the anions has been related to their hydrophobicity by the Hofmeister series, which orders anions by their decreasing hydrophobicity, or increasing degree of aqueous solvation, Figure 1.1.[11] This sequence was originally established according to the studies on the effects of salts on the solubility of proteins and has become widely used to understand anion recognition as their tendency to associate to proteins in water is directly comparable to their affinity to the hosts.[12] The binding of oxyanions in highly polar and hydrogen bonding donating solvents has thus proved to be challenging because of their great solvation energies, particularly so for polyanions, such as SO_4^{2-} or $H_2PO_4^-$. The specific and selective interaction between an anion and an ‘ideal’ receptor can ‘interfere’ with the series, binding preferentially with less interacting anions (more solvated or less basic), generating an ‘anti-Hofmeister’ behaviour.

Within the past 30 years, the field of anion coordination chemistry has gained increased interest and many various examples of anion complexes have been reported, with various uses and for different purposes.[13-18] In the next sections characteristics of some key anions will be presented and the most important binding interactions in anion coordination and supramolecular chemistry will be discussed.

1.2. Coordinative interactions for anion binding

Anionic molecules can come in a variety of charges as well as shapes, meaning that each one will have different coordination requirements, Figure 1.1. The geometric requirements of metal coordination are more or less strictly dependent on the crystalline field of the orbitals around the spherical metal ion, with restricted coordination number. Anion coordination is not as strictly controlled by the same rules, making their coordination more various in terms of geometries, coordination numbers and possible receptors.[13]

One of the most convenient ways of classifying existing anion receptors, is considering the way they interact with their targets. The anion receptors reported to date may be divided in two classes: i) positively-charged and ii) neutral receptors. One or more positive charges on a ligand can favour the anion binding process thanks to electrostatic interaction, which can be strong, but at the same time non-selective. The presence within a host, of one or more coordinatively unsaturated metal centres,[19,20] or positively charged moieties, such as polyammonium, quaternary ammonium, guanidinium,[21] triazolium, imidazolium and benzimidazolium[11] can also favour such interactions. In a number of cases, these cationic receptors can also act as hydrogen bond donors, combining electrostatic interactions and directionality using charged-assisted H-bonds leading to efficient binding properties. Neutral receptors, on the other hand, use polarised groups that can act as H-bond donors or acceptors, which give more directionality to the binding compared to a localised formal charge. The anion binding ligands discussed in this thesis use hydrogen bonding donor groups as binding sites. Therefore, in the introduction, more attention will be given to hydrogen bonding interactions over the others.

Many functional groups can participate in hydrogen bonding, such as amines,[22] amides[23] or pyrroles[24] and corresponding derivatives. Ditopic groups such as ureas[25] and thioureas,[26] or even selenoureas[27,28] and increasingly popular squaramide[29] derivatives have also be used.[30] Modifications of the squaramide motif to give deltamides and croconamides[31,32] or thiosquaramide[29] can offer improved anion binding properties (compared to urea-based receptors), thanks to increased acidity of the NH residues, Figure 1.2. All the mentioned examples employ the highly polarised N–H bond as hydrogen bond donor. While the polarisation of aromatic C–H bonds is generally less strong, if combined with appropriate vicinal atoms or functional group, they can be activated and be involved into hydrogen bonds. Examples of ligands including aromatic C–H from phenyl, pyridine or triazoles have been reported.[33]

The acidity of the proton is the key feature for H-bond donors, as a lower pK_a will result in a stronger H-bond with the anion, but at the same time will increase the

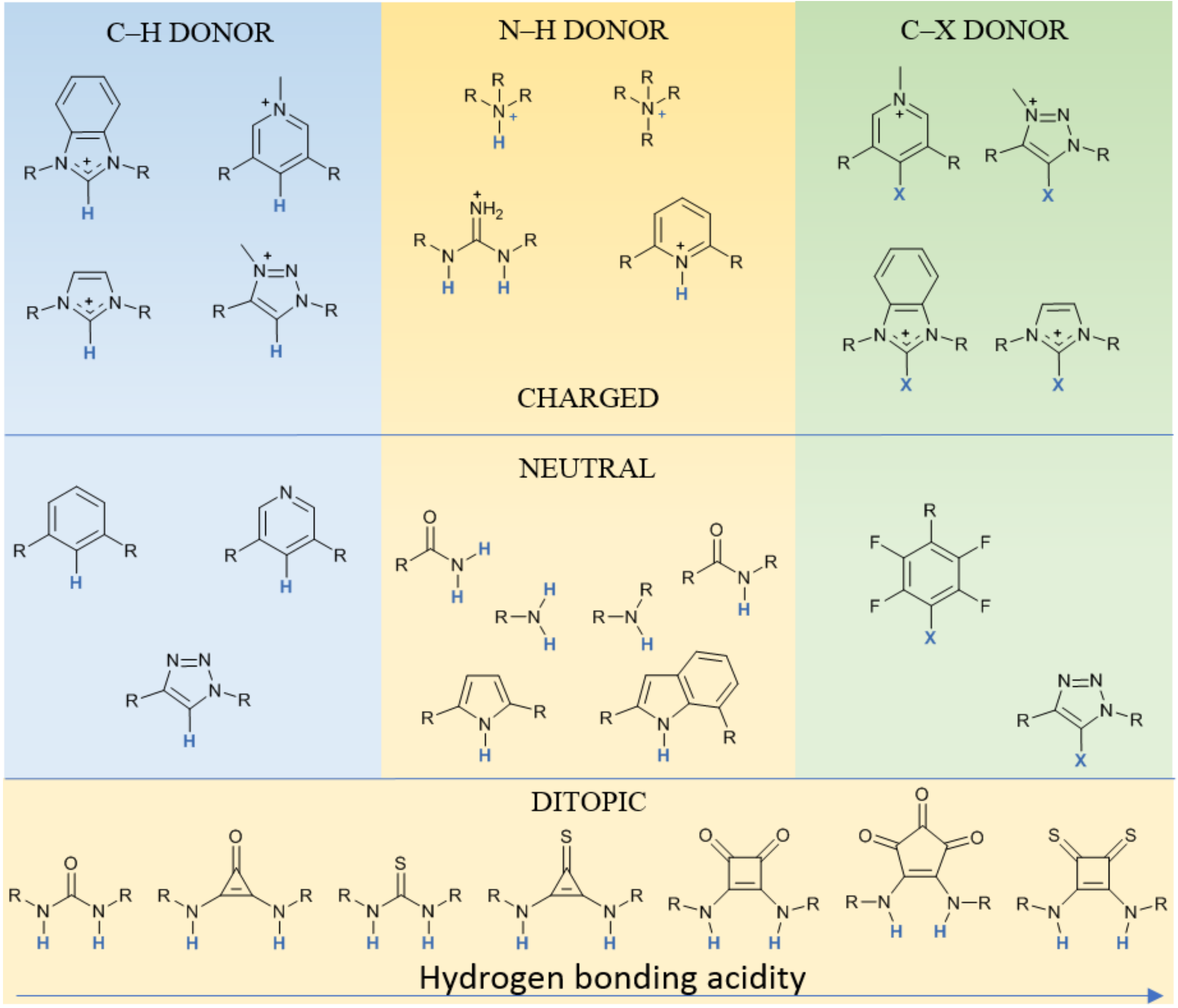

Figure 1.2. Scheme of most commonly used hydrogen (C–H and N–H) and halogen bond (C–X) donor groups in anion recognition and binding. Each section is divided into charged and neutral compounds, with a subsection of the neutral N-H donor compounds showing ditopic urea-like groups arranged according their acidity. Refs. 22-32.

susceptibility to deprotonation by a range of basic anions,[34] which again highlights the challenge of balancing these properties effectively.

The use of halogen bonds have also increased in popularity and many examples of anion-templated self-assembly have been reported.[35] Halogen bonds can occur between two halogen atoms within two molecules or as monoatomic species. The anisotropic distribution of the charge causes on one of the atoms the formation of electrophilic region which interacts with the nucleophilic region of the other.[35,36] This interaction is less affected by protic solvents, compared to hydrogen bonds, as well as due to the hydrophobic nature of halogenated molecules.

The urea, the 2,6-bis(triazole)pyridine (**btp**) and the imidazolium binding motifs will be explored as part of this thesis. The first two rely on multiple hydrogen bonds in a preorganised arrangement for chelate binding, while the imidazolium unit can donate a charged assisted hydrogen bond.

The selection of donor type, from those discussed above, as well as ligand geometry allows for complementary receptors to be designed that balance the specific characteristics of a given anion type. For example, halides carry one negative charge, are monoatomic and have a spherical shape. Their ionic radii increase with their atomic numbers, making the charge of larger halides more delocalised and less densely charged.[3] Consequently, they are generally challenging to bind using neutral ligands with poor preorganisation of the hydrogen bond donors.[37] The ideal binding pocket for each of the halide has complementary size and geometry and contains a high number of binding sites (*e.g.* H-donor) directed towards the centre of the binding pocket.[37] The coordination of Cl^-, Br^- and I^- is largely similar, and selectivity amongst them is based on size-exclusion.[38] In the case of F^-, however, the anion posseses some peculiar characteristics: with an ionic radius of 1.19 Å (Table 1.1) it is the smallest of the group and of the entire periodic table. Consequently, it is very charge dense, basic and strongly solvated. As a result, in most scenarios F^- will cause the deprotonation of the most acidic group in a receptor, and form the HF_2^- species.[39] However, examples of complexes with F^- have been reported, for example through encapsulation within small cages, rich of hydrogen bond donors within their cavities.[38,40,41]

The carboxylate moiety has a trigonal shape and can conveniently receive double hydrogen bonding in a chelated fashion. For example, it has high geometrical complementarity with ditopic binding sites, *e.g.* urea and guanidinium motifs, with which it can create strong hydrogen bonding interactions in a “Y-shaped” arrangement. Molecules containing multiple carboxylate moieties can be the ideal guests for molecules containing a number of binding moieties strategically positioned to give geometrical complementarity.[42]

The urea group can also offer interactions with tetrahedral *e.g.* $H_2PO_4^-$, SO_4^{2-}, SeO_4^{2-}, ReO_4^-, CrO_4^{2-} or other oxyanions through bifurcation which can assist in fulfilling the

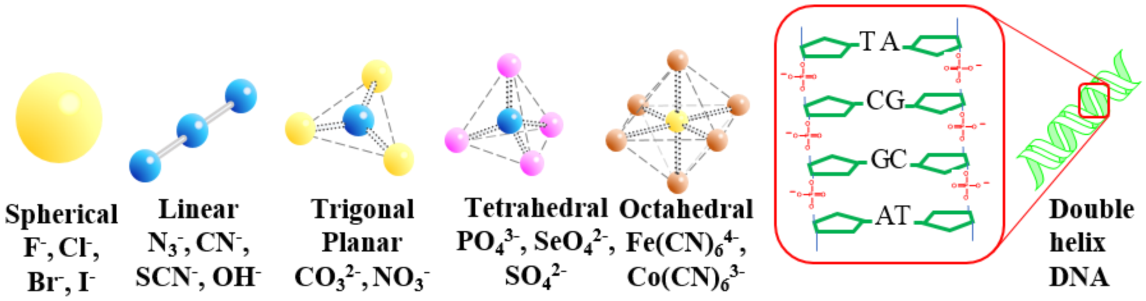

Figure 1.3. Examples of anion shapes.

Table 1.1. Comparison of the ionic radii size of halides (taken from ref. 3)

Anion	*Ionic radius/Å*
F-	1.19
Cl^-	1.67
Br^-	1.82
I^-	2.06

saturation requirement of these anions. These anions have comparable size, but significantly different charges and solvation energies. SO_4^{2-} is generally highly solvated, therefore a ligand needs to overcome the desolvation energy for efficient complexation. The protonation state of phosphate anions is highly affected by the pH in aqueous solution, with $H_2PO_4^-$ being the major species at $2.14 < pH < 7.20$ and HPO_4^- at $7.20 < pH < 12.37$. In organic solvents the presence of water can also affect the protonation state of the anions, which can be challenging to control. Consequently, the charge or the availability to receive hydrogen bonding can be affected by the medium.

When all these challenges are overcome, anion complexation can form a great multitude of complexes, which differ by number and type of Host:Guest interactions, as well as giving rise to the self-assembly of two or more ligands.[14] This anion-templated self-assembly (ATSA) process has been employed by supramolecular chemists for the synthesis of macrocycles and interlocked structures, for the transport or extraction of anions, and even the formation or disruption of soft materials. After a general review of the most common interactions employed, a collection of relevant and recent ATSA will be presented.

A general review of the state of the art of anion-coordination and anion templated self-assembly will be discussed next, with the most relevant examples being discussed in each chapter.

1.3. Anion coordination and anion-templated self-assembly: a review

The following section will present some recent examples of anion coordination. This will include some relevant examples of highly preorganised hosts (*e.g.* multipodal, macrocycles, cages, foldamers) which can coordinate anions with high selectivity in a 1:1 (Ligand:Anion) stoichiometry. Moreover, examples of anion-coordination driving the self-assembly of two equivalent or diverse ligands will be discussed, including the formation of macrocyclic “sandwiches”, dimeric capsules and the anion-templated synthesis of interlocked molecules. Higher order anion-templated self-assembly will then be described, including some recent examples of anion-templated cages and helicates, as well as anion templated networks, with examples of anion-directed formation of soft materials.

1.3.1. Anion coordination with one ligand

As stated above, the coordination of anions by one single ligand generally requires the development of highly preorganised molecules, with the binding sites strategically positioned in order to respond to geometrical demand of the target anion. In some cases, however, molecules with apparently low preorganisation, can undergo conformational changes to accommodate one or more anions within a suitable binding pocket.[43] This is the case for anion-driven foldamers, which possess a linear structure, but can rearrange into helices thanks to the coordinating effect of anions through well positioned binding sites.[44] Many examples of polyphenylene derivatives by Wu[45,46] showed complexation abilities with halides, while Gale and Caltagirone showed their use for transmembrane anion transport.[47] Jeong and co-workers recently reported the multi-step synthesis of ligands **1** and **2**, containing three indolocarbazole-pyridine moieties as binding units, Figure 1.4.[48] The complexity of ligand **1** allowed for the formation of a SO_4^{2-} complex with the ligand folded in single helicate donating a total of eight hydrogen bonds to the anion, as shown in Figure 1.4. Moreover, the interaction would selectively enhance the fluorescence emission of the foldamer in water-saturated CH_2Cl_2, which was 'turned off' in the absence of the anion. Another interesting example by Beer and co-workers showed how linear ligand bearing iodo-triazole groups, **3**, could be folded around spherical halides, with highest affinity for I^- because of size complementarity.[49] In the crystal structure, the triethylene glycol chain showed ability to also fold around the Na^+ counterion generating an ion-pair receptor, Figure 1.5. From the development of hydrogen-bonding halide-templated foldamers developed by

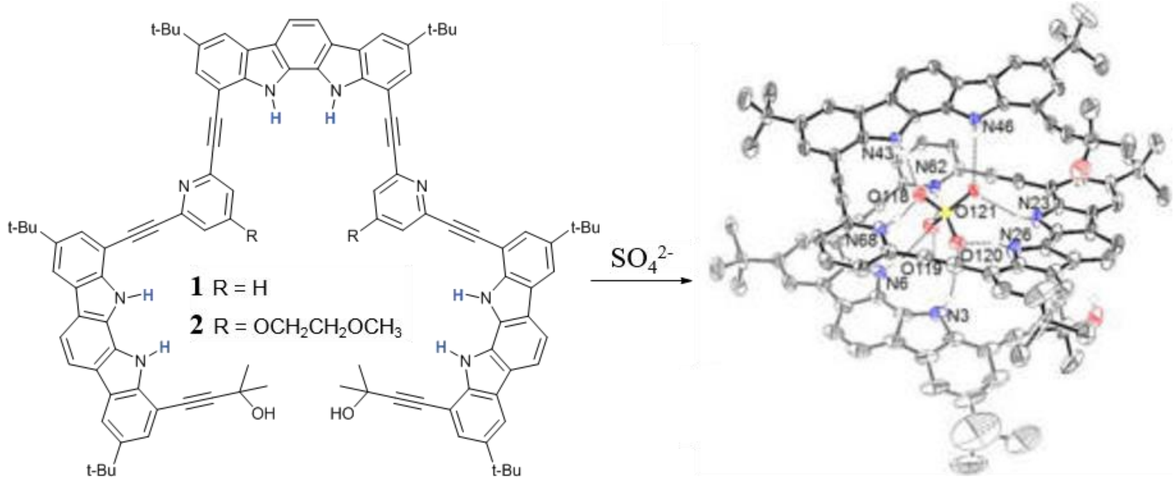

Figure 1.4. Example of SO_4^{2-} templated foldamer by Jeong. (Crystal structure reproduced from ref. 48)

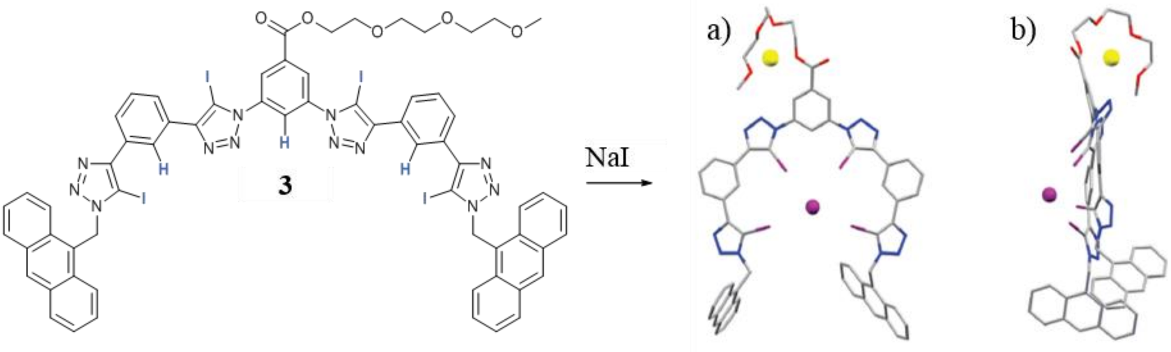

Figure 1.5. Example of halide$^-$ templated foldamer by Beer; a-b) crystal structure of **3**·NaI reproduced from ref. 49.

Craig[50] and Hecht[51], Flood also developed the synthesis of a series of triazole based macrocycle, which will be discussed further in Chapter 4.

Multi-podal ligands have been used successfully in many cases for the binding and transport of anions. These are characterised by the presence of binding sites on multiple "arms" appended onto a central core, which can favour the chelation effect[52] in the anion recognition process. The flexibility of the arm can also favour the rearrangement of the arms to accommodate molecules of various shapes. One example of this was given by Pfeffer and co-workers,[53] who used a [3]polynorbornene molecule, **4** with two side arms carrying phenylthiourea moieties, which showed complexation abilities towards different dicarboxylate isomers, like terephthalate and isophtalate, Figure 1.6. Similarly conceived

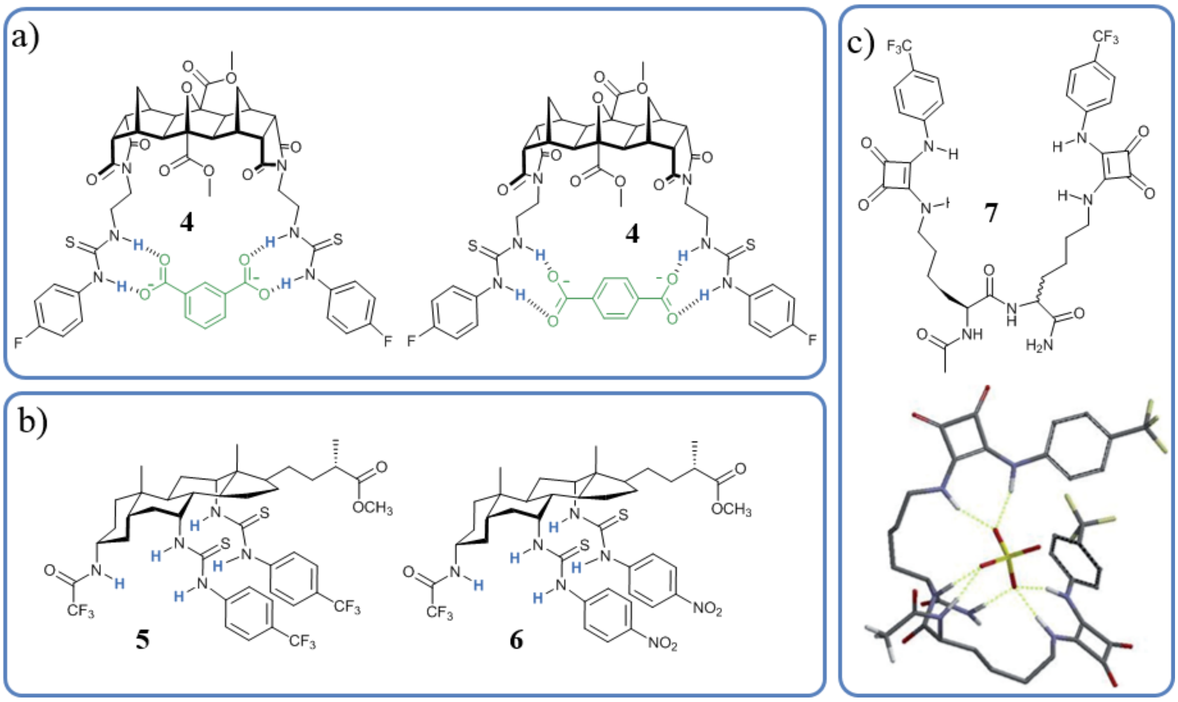

Figure 1.6. Examples of dipodal based structures a) norbornene bis(urea) for binding of dicarboxylate anions, b) cholapod bis(urea) for Cl$^-$ transport and c) peptide bis(squaramide) for oxyanions binding with modelled structure (DFT) of its SO_4^{2-} complexes. Reproduced from refs. 53-55.

molecules **5**-**6** were developed by Davis and Sheppard, Figure 1.6, with two phenylthiourea arms attached to a steroid-based 'cholapod' scaffold, donating five hydrogen bondings.[54] These proved to be efficient transmembrane anion transport with no cytotoxicity and, as such, suitable candidates for therapeutic applications.

Elmes, Jolliffe and co-workers proposed the use of peptide-based dipodal structures with squaramide binding units, **7**, which showed very strong affinity for SO_4^{2-} ($K_{1:1} > 10^4$) in 5:95 H_2O:DMSO-d_6 solution.[55] The formation of multiple hydrogen bonds between the ligand and the anion was supported by DFT calculations, as shown in Figure 1.6.

Tripodal molecules have also shown great anion complexation abilities, thanks to the combined interaction of three arms. Anion complexes with tripodal molecules can be used for anion transport,[56] as well as for separation of tetrahedral anions from aqueous solutions.[57,58] Tris-imidazolium ligand **8**, was reported by Amendola *et al.* and showed the formation of complexes with Cl^- in CD_3CN solution and in the solid state, Figure 1.7.[59] The imidazolium hydrogen bonds were accompanied by the presence of four fluorine substituents on the phenyl rings, which increased the acidity of the remaining aryl C–Hs and allowed them to participate in the complex formation with additional hydrogen bonds. Interestingly, additional stabilisation of the complex was given by the formation of C–H hydrogen bonds donated by the ligand from the CH_2 groups connecting the imidazolium and the phenyl units.

Tris-urea ligand **9**, developed by Davis and Valkenier,[60] according to *ab initio* calculations was able to donate six hydrogen bonds to a Cl^- ion from the three urea-appended

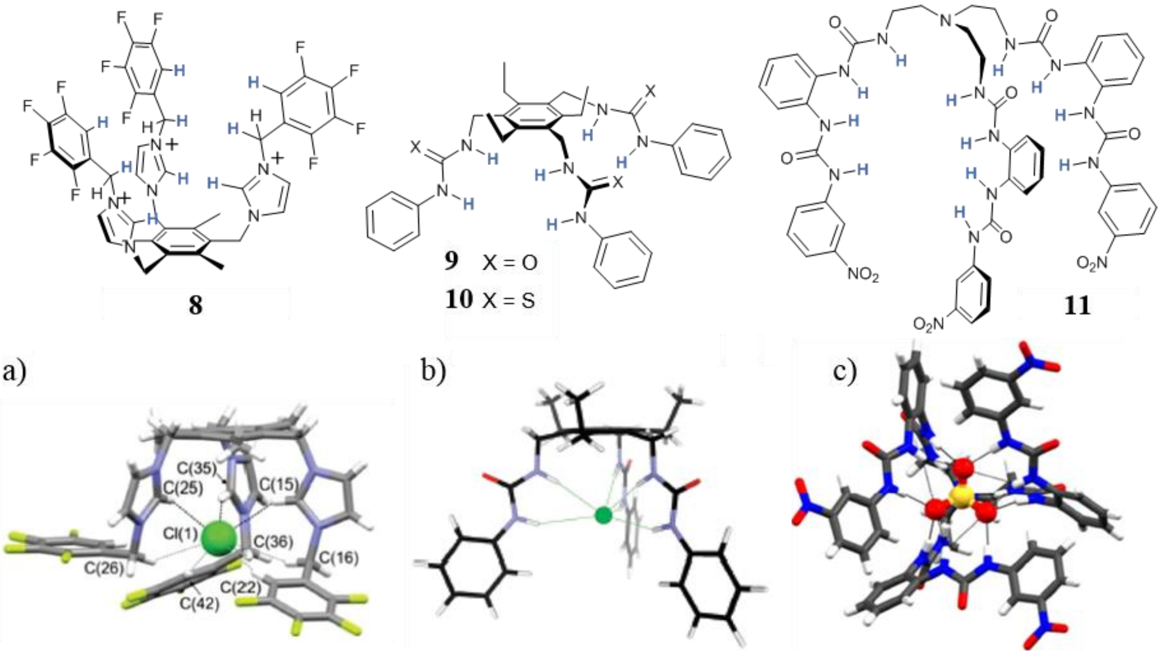

Figure 1.7. Examples of tripodal based structures. a) Crystal structure of **8** with Cl^-, b) molecular model of **9** with Cl^-, c) crystal structure of **11** with SO_4^{2-}. Reproduced from refs. 59-61.

arms. The thiourea analogue, **10**, showed relatively good transmembrane Cl$^-$/NO$_3^-$ exchange abilities, compared to other analogues. When compared to the cholapod structures, **5** and **6** above, the transport was not as efficient, but the much higher synthetic accessibility of these compounds, which could be made in one step, balances the potential.

The C_{3v} symmetry of tripodal molecules have shown remarkable geometrical complementarity with tetrahedral anions, such as SO$_4^{2-}$ or H$_2$PO$_4^-$. While in many examples the "saturation" of the coordination sphere of the anions is reached by the self-assembly of two ligands around one or more anions (see Section 1.3.2), the fulfilment of the coordination sphere by one single tripodal molecule can be achieved. One remarkable example of sulfate coordination was reported by Hossain and Leszczynski with hexaurea ligand **11**,[61] which showed the formation of 1:1 complexes with SO$_4^{2-}$, both in DMSO solution ($K_{1:1} > 10^5$) and in the solid state, Figure 1.7. The crystal structures showed the six urea moieties organised around the SO$_4^{2-}$ anion and donating 12 hydrogen bonding to saturate its coordination sphere.

A more preorganised arrangement can be provided by macrocyclic ligands which should favour the 'macrocyclic effect', similarly to the one observed for metal complexes.[62] As an example of this, Flood has shown that macrocyclic [3$_4$]triazolophanes were able to bind Cl$^-$ and other halides with binding constant up to six orders of magnitude larger than the corresponding non-cyclic ligand.[63] Similarly, Jolliffe and co-workers reported a family of new squaramide based macrocycles, **13** and **14**, which showed high affinity for tetrahedral oxyanions over other anions, Figure 1.8.[64]

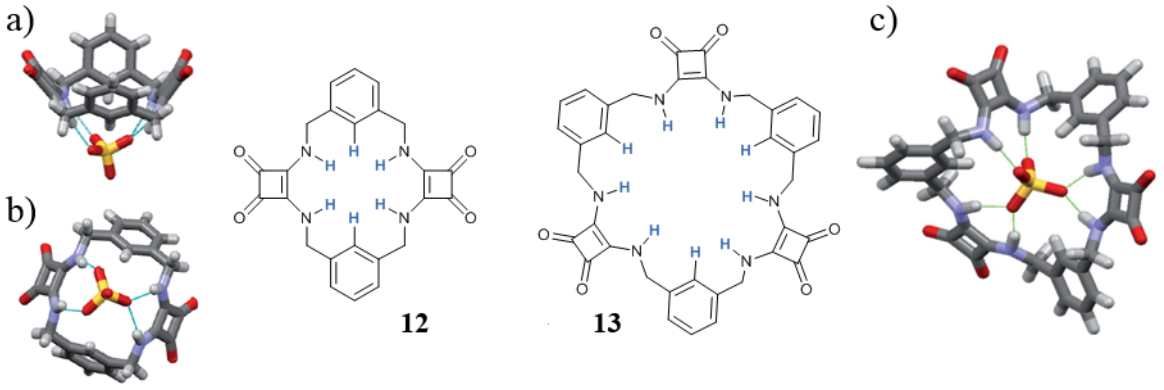

Figure 1.8. Examples of macrocycles with squaramide units ideal for SO$_4^{2-}$ complexation. a-b) Crystal structure of complex **13**·SO$_4^{2-}$ and c) molecular model of complex **14** SO$_4^{2-}$. Reproduced from ref. 64.

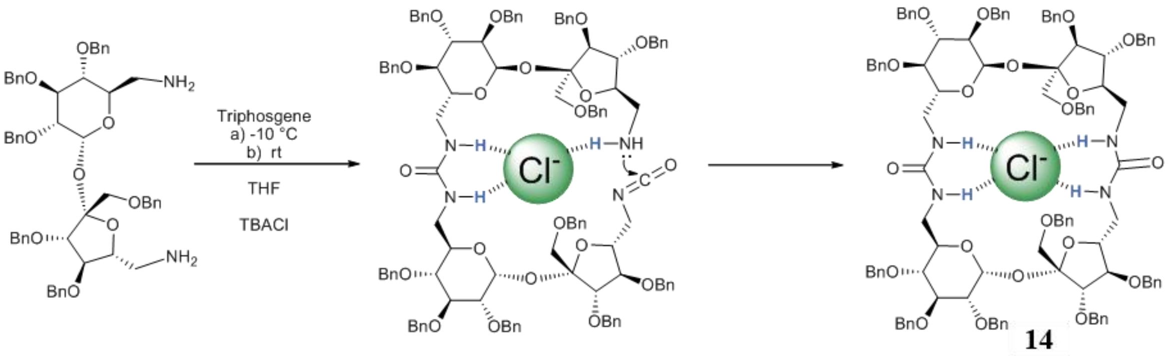

Scheme 1.1. Cl$^-$-templated synthesis of a sucrose-based macrocycle **12** by Jarosz *et al.* Ref. 65.

Jarosz and Łęczycka-Wilk recently showed the use of anion templation for the synthesis of sucrose-based macrocycle **12**, Scheme 1.1.[65] The macrocycle was obtained in 90% yield by reacting the amino-sucrose with triphosgene to give the isocyanates groups which reacted with another unreacted amino-sucrose to give a first urea intermediate. In the absence of the anion only 40% yield had been observed, indicating a clear template effect of Cl$^-$. The intermediate then exploited the urea and amide affinity for chloride and favoured the ring closing reaction, *via* the formation of a second urea moiety from the isocyanate and amine groups. The macrocycle obtained after displacement of the Cl$^-$ template, displayed the ability of forming complexes in CD_3CN solution with $H_2PO_4^-$, Cl$^-$, CH_3COO^- and PhCOO$^-$. The benzoate anion showed the highest constant calculated for the formation of 1:1 complex ($K_{1:1}$ = 3772 M^{-1}), compared to Cl$^-$ ($K_{1:1}$ = 259 M^{-1}) or $H_2PO_4^-$ ($K_{1:1}$ = 126 M^{-1}).

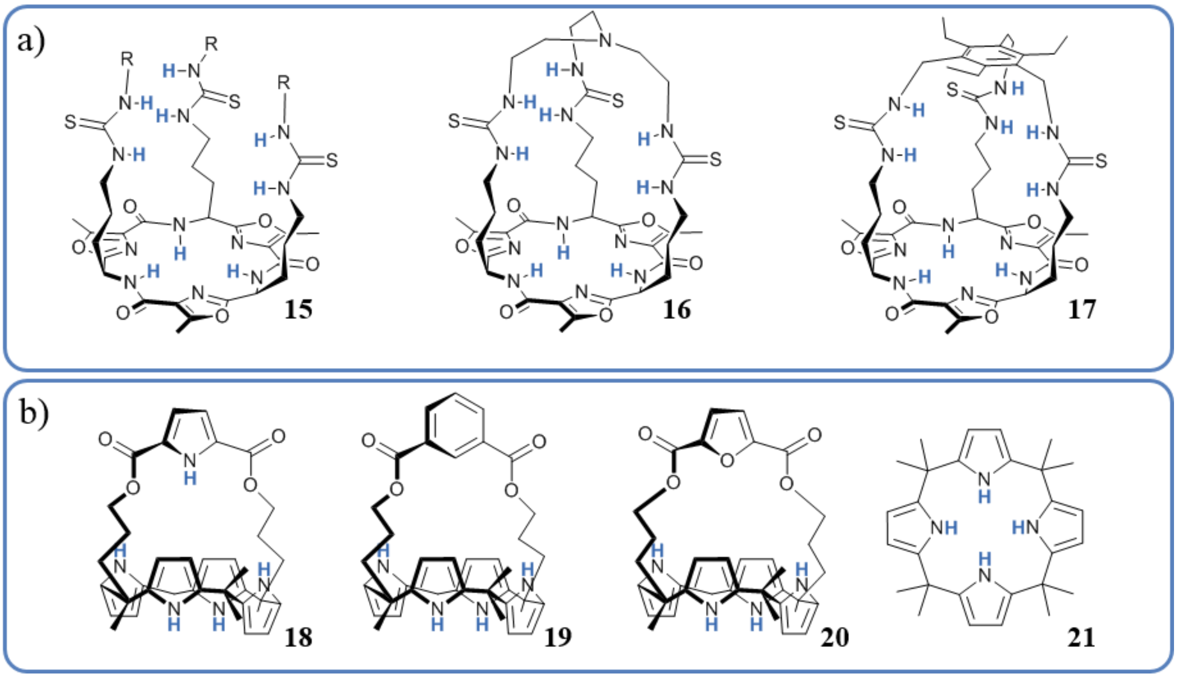

Figure 1.9. Examples of a) cyclopeptide-based and b) calix[4]pyrroles- based cryptands for anion binding. Refs. 71-72.

Cyclic oligopeptides have good affinity with anions thanks to the presence of multiple amide groups for hydrogen bonding.[30] Jolliffe's group has produced many examples of functionalisation of the side chain with anion binding groups, such as (thio)urea groups[66,67] or metal complexes[68-70], which can increase the binding affinity thanks to the possibility of 3D organisation of binding sites and, consequently, to the chelate effect. By 'capping' the appended arms of **15** with a ***tren*** or 1,3,5-triethylbenzene moieties, Jolliffe and co-workers synthesised cryptand molecules **16** and **17**, which showed improved halide binding abilities compared to the open **15** in a more competitive environment (99.5:0.5 DMSO-d_6:H_2O for cages **16-17**, $CDCl_3$ for **15**).[71]

Sessler, Hay and Lee reported the efficient use of the strapped calix[4]pyrroles macrocycles, **18**, **19** and **20**, which showed improved Cl^- binding properties compared to the non-strapped analogue, **21**. Ligand **18**, thanks to the presence of an additional hydrogen-bonding from the pyrrole group, showed the strongest interaction with Cl^- in CH_3CN, measured by isothermal titration calorimetry (ITC), with $K_{1:1} = 1.8 \times 10^7$ M^{-1}.[72]

Leigh and co-workers have demonstrated the strong and selective binding of a molecular pentafoil knot (**22**) as well as doubly (**23**) and triply (**24**) entwined [2]catenanes based on circular Fe(II) double-helicates scaffolds, Figure 1.10.[73] The cavities of these interlocked molecules (obtained *via* anion-templated synthesis as discussed in Section 1.3.3) were of different diameters and were able to accommodate spherical halide anions, bound through a combination of C–H···X^- hydrogen bonds and long-range Fe(II)···X^- electrostatic interactions. The formation of these high order self-assemblies was known, as reported by Hasenknopf *et al.* previously.[74] The binding involved the exchange of one of the PF_6^-

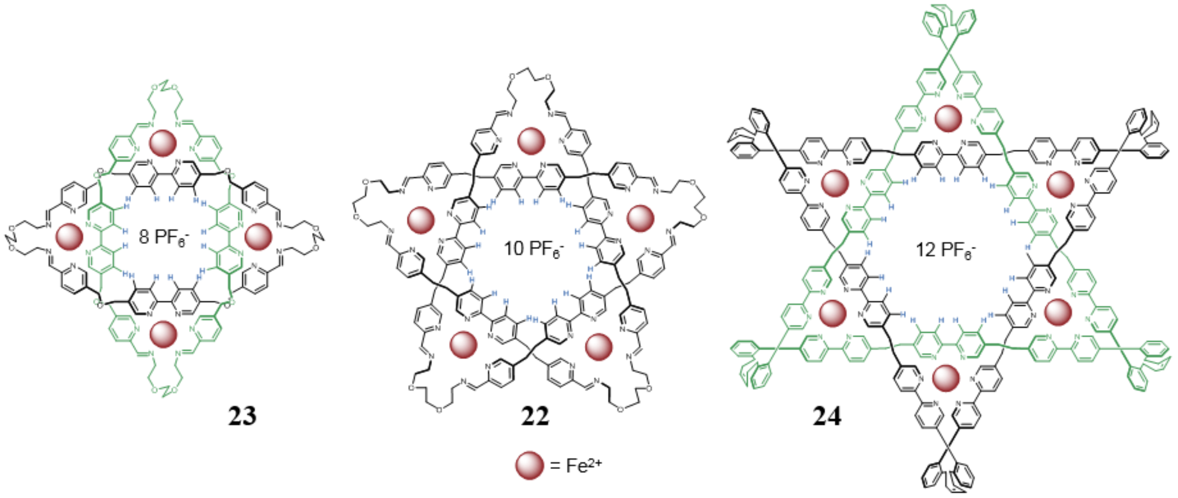

Figure 1.10. Structures of molecular pentafoil knot (**22**) as well as doubly (**23**) and triply (**24**) entwined [2]catenanes based on circular Fe(II) double helicate scaffolds by Leigh *et al.* Ref. 73.

counterions with the halide and showed very large equilibrium constants in CD_3CN ($K > 10^4$ M^{-1}), with highest values for the pentafoil knot **22** with Cl^- ($K_{1:1} = 3.6 \times 10^{10}$ M^{-1}) and Br^- ($K_{1:1} = 1.7 \times 10^{10}$ M^{-1}). Having reviewed the anion coordination from a single molecule, the next section will focus on the anion coordination of two molecules, giving rise to anion-templated self-assembly.

1.3.2. Coordination and Anion-Templated Self-Assembly of two ligands

The coordination properties of anions can give rise to anion-templated self-assemblies (ATSA) with a variety of different ligands. The high level of preorganisation of the binding sites needed for successful anion complexation might suggest that large and complicated ligands are always required. While this can be true in many cases, it is also possible to find ligands of low molecular weight and simple design, which can give rise to interesting architectures and functionalities. It is the case of ligand **25**, part of a class of indole-based perenosins designed and studied by Gale *et al.* for H^+/Cl^- transmembrane co-transport.[75] This family of ligands were found to form both 1:1 and 1:2 (L:A) complexes, and modelling of the 2:1 Cl^- complex **26** indicated the formation of a complex with the two ligands surrounding the Cl^- like the seam in a tennis ball,[11] Figure 1.11a. Chmielewski and Bąk reported the pH-dependent self-assembly of diamidocarbazole ligands **27** and **28** in the presence of SO_4^{2-}, Figure 1.11b.[76] The self-assembly of **27** was also in a tennis ball

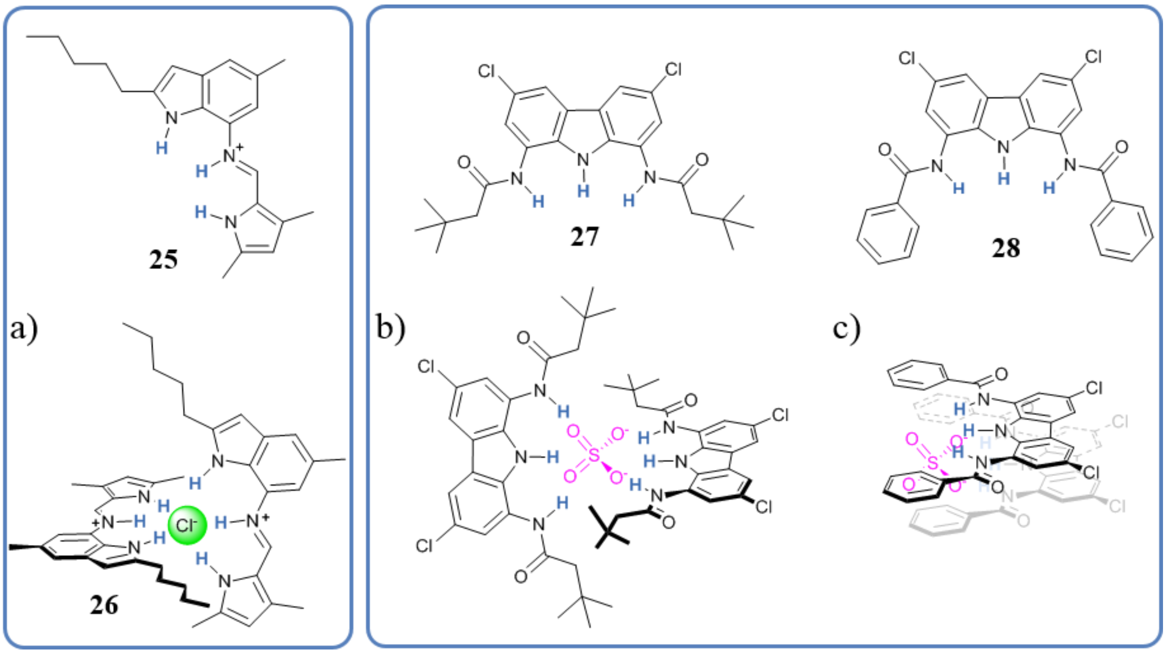

Figure 1.11. Structures of linear molecules which give rise to 2:1 (L:A) ATSA. Representation of a) ligand **25** forming a 'tennis ball' complex with Cl^-. In the same ways b) ligand **27** with SO_4^{2-} , c) **28** with SO_4^{2-} assembles in a superimposed arrangement. Refs. 75-76.

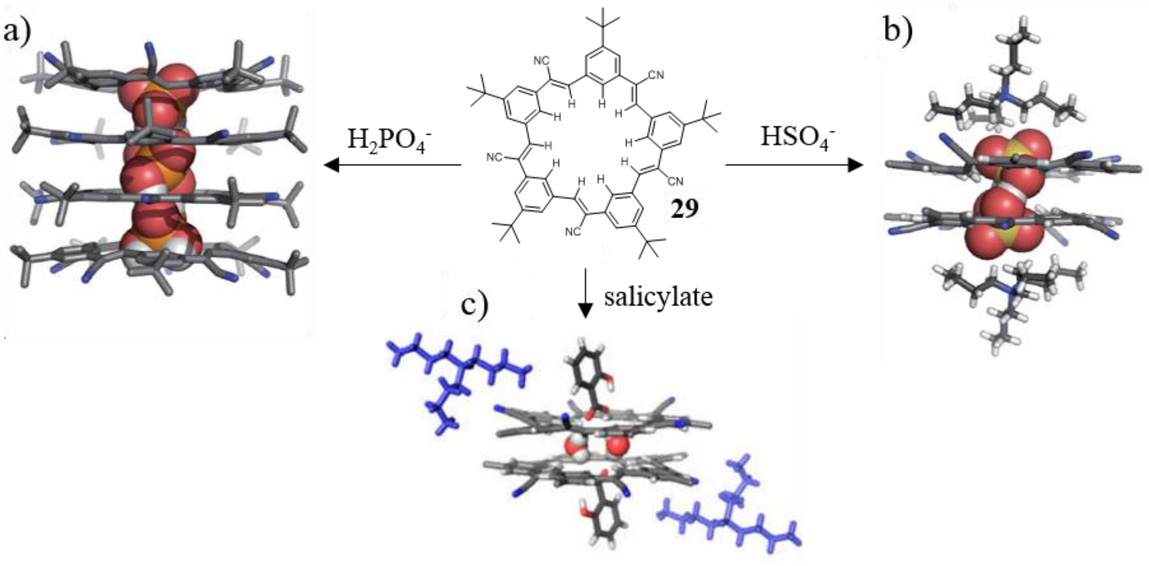

Figure 1.12. Formation of ATSA sandwich complexes from macrocycle cyanostar **29**. Crystal structure of ‘macrocyclic sandwiches’ of **29** with a) $H_2PO_4^-$ b) HSO_4^- and c) salicylate. Reproduced from refs. 77-80.

arrangement (2:1, L:A stoichiometry), while **28** was more in a superimposed arrangement, where the anion bridges the hydrogen bonding pockets of the two ligands.

When the ATSA process involves two macrocyclic molecules and one or more anions, the complex can be referred as a “sandwich” complex. Examples of such bundles have been studied by Flood and co-workers, demonstrating the self-assembly behaviour of cyanostar macrocycle ligand **29** in the presence and absence of anions, Figure 1.12.[77-80] While simple 2:1 (L:A) sandwiches were formed with **29** and ClO_4^-, in the presence of salicylate and HSO_4^- the sandwiches were formed around dimers of the anions, in a 2:2 arrangement. With $H_2PO_4^-$ **29** showed the formation of multiply-stacked structures in a tubular arrangement with the $H_2PO_4^-$ molecules forming hydrogen bonding ribbons in the cavity of the self-assembled tube. The self-assembly of the cyanostar with $H_2PO_4^-$ was also used by Flood to form ATSA rotaxanes which will be discussed in section 1.3.3. Another

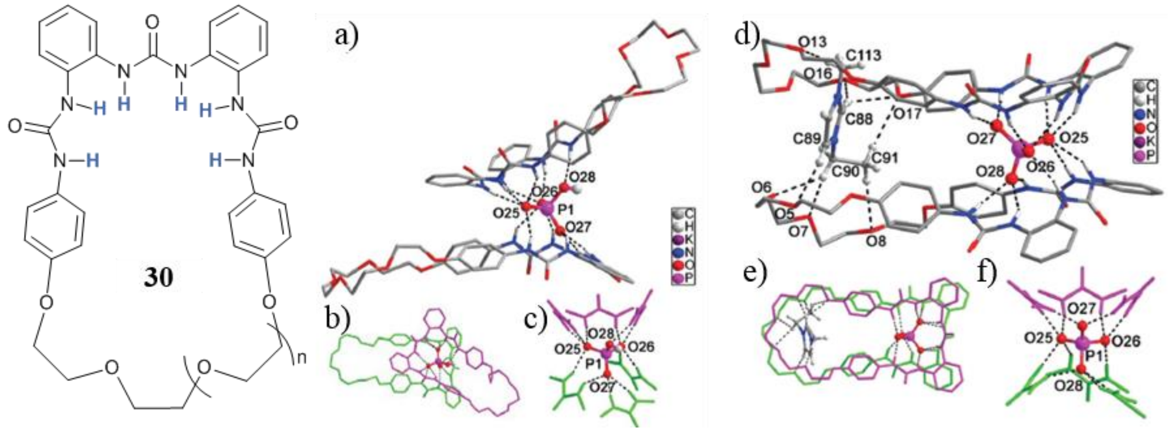

Figure 1.13. Examples ATSA sandwich from macrocycle **30**. Crystals with $H_2PO_4^-$ in a-c) alternate arrangement and d-f) a superimposed arrangement. Reproduced from ref. 81.

example was recently reported by Wu and co-workers, **30**, based on the bis-phenylene tris(urea) binding site, Figure 1.13a.[81] In the presence of tetrahedral oxyanion such as $H_2PO_4^-$ and SO_4^{2-} would form 2:1 (L:A) sandwich complexes in different arrangements, Figure 1.13.

The formation of 2:1 (L:A) capsules from tripodal molecules has been observed in examples with oxyanions.[82] The design of such molecules from the ***tren*** scaffold has successfully given rise to the self-assembly of dimeric capsules.[83] Examples of ATSA of ***tren***-based tripodal molecules into dimers are shown in Figure 1.14. Thiourea-containing **31** in the presence of PO_4^- gave rise to capsules, Figure 1.14a, [84] similarly to urea-containing **32** which also self-assembled in the presence of with SO_4^{2-}, Figure 1.14b, as well as with other oxyanions such as CO_3^{2-} and CrO_4^{2-}.[85] Ligand **33**, in DMSO, encapsulates the hexafluorosilicate anion within a dimeric capsular assembly while with the hexafluorosilicate anion *via* side cleft binding, Figure 1.14c.[86] The SO_4^{2-} dimer of **34**, obtained *via* crystallisation from aqueous alkaline solutions, showed potential for use of anion removal from radioactive waste, Figure 1.14d.[58,87,88] The successful use of the ***tren*** scaffold combined with the urea binding moiety for the complexation of tetrahedral anion can be attributed to the preorganised, yet flexible, structure, which can arrange around the anion with a combination of up to 12 hydrogen bonds, Figure 1.14e.[84]

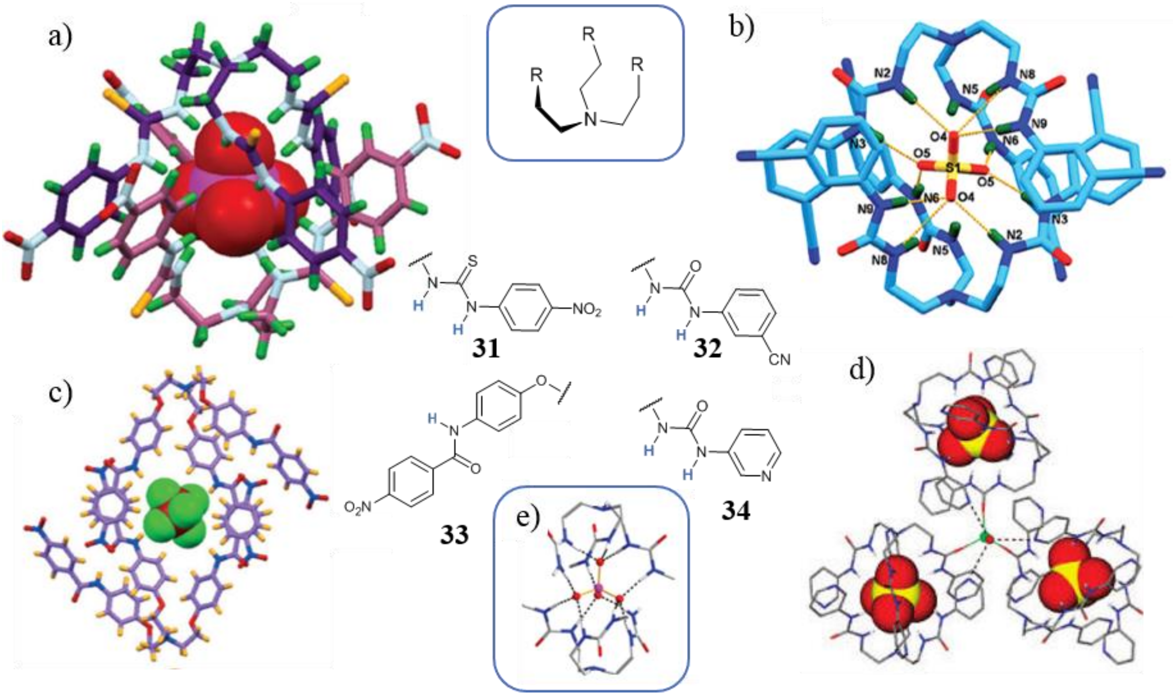

Figure 1.14. Examples of ATSA capsules of tripodal ***tren***-based ligands with tetrahedral oxyanions. Crystal structure of a) **31** with PO_4^{2-}, b) **32** with SO_4^{2-}, c) **33** with SiF_6^{2-}, d) **34** with SO_4^{2-}, e) arrangement of hydrogen bonds from urea moieties to the anion in a capsule of **31** with PO_4^{2-}. Crystals reproduced from refs. 84-88.

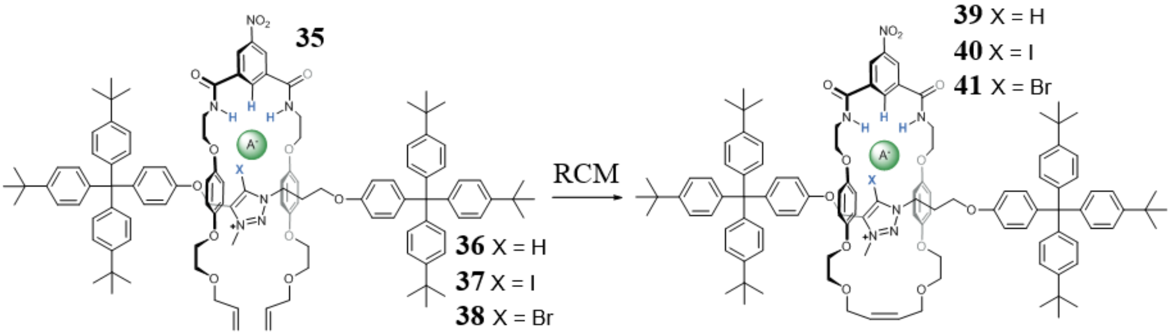

Figure 1.15. Examples of ATSA synthesis of rotaxanes by Beer, from refs. 90-92.

Beer and co-workers have been exploring ATSA in the synthesis of interlocked systems.[89] The combination of hydrogen and halogen bonds has successfully been used for the synthesis of many catenanes and rotaxanes, with the use of different strategies of clipping or threading. The formation of a complex of **35** with Cl^-, through a combination of amide and activated C–H hydrogen bonds, induced the additional self-assembly of **36**, **37** or **38** through the formation of hydrogen (**36**) or halogen bonds (**37** and **38**). Ring closing metathesis (RCM) of **35** led to the synthesis of rotaxanes with higher yields for **39** (21%), rather than the halogen bonding **40** (13%), *via* the clipping method, Figure 1.15.[90-92]

The threading of compound **42** with **43** was used by Beer, allowing the Cl^- templated synthesis of **44**.[93,94] Also in this example a combination of halogen, amide, and C–H bonds were employed for the Cl^- templated self-assembly, yielding a catenane in a remarkable 45% yield. The NO_3^- anion was, instead, used to thread **42** with the polyamide olefin **45**, as shown in Figure 1.16. RCM yielded **46**, the first reported NO_3^--templated catenane, in 20% yield.[95] With large molecules with multiple binding sites the self-assembly between two molecules can happen in separate positions in the same molecules, to form multiple rotaxanes[96] and catenanes.[97]

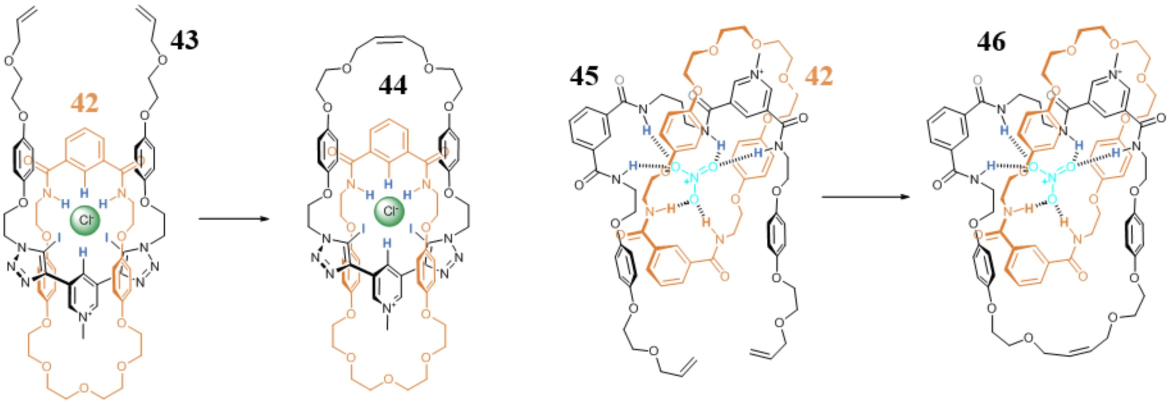

Figure 1.16. Examples of ATSA synthesis of [2]catenanes by Beer, from refs. 93-95.

1.3.3. Higher order coordination and ATSA

The self-assembly of three ligands in the presence of one or more anions can give rise to ATSA triple helicates. Examples have been reported by Das with phenylene bis(urea) ligands **47**, **49** and **48**, Figure 1.17.[98,99] The first one, **47**, formed triple helicates structures around an assembly of two SO_4^{2-} and three H_2O molecules, while **48** assembled into a triple helicate around an assembly of three Cl^- around a DMSO molecule. Tetrameric assemblies of **49** with SO_4^{2-}, were also obtained by Das, Figure 1.17c-d.[100] By linking two phenylene bis(urea) binding groups through a *m*-xylylene spacer forming ligand **50**, Wu and co-workers obtained a triple helicate assembly templated by two SO_4^{2-} anions, Figure 1.18.[101] The self-assembly of these structures is one elegant example of how the combination of urea binding sites, with their hydrogen bonds, can create a suitable binding pocket even for highly solvated anions like SO_4^{2-}.

The formation of anion complexes can give rise to higher order assemblies, which include discrete assemblies, as well as extended 2D and 3D networks. The formation of discrete bundles around clusters of anions has been recently reviewed, by Sessler.[102]

The tripodal tris(urea) ***tren***-based **51**, developed by Das, formed not only dimeric capsules, similar to those described above, but also tetrameric assemblies with H_3PO_4 or $H_2PO_4^-$ in a 4:4 stoichiometry, Figure 1.19.[103] The two assemblies differed in their shape, with H_3PO_4 **51** self-assembled by side-cleft bonds with tetrameric square anion-acid clusters. $H_2PO_4^-$, on the other hand, formed tetrahedral molecular cage by encapsulation of a tetrameric tetrahedral mixed phosphate cluster. In such structures the formation of the self-assembly complex, is favoured by the assembly of the anion cluster. These clusters of anions,

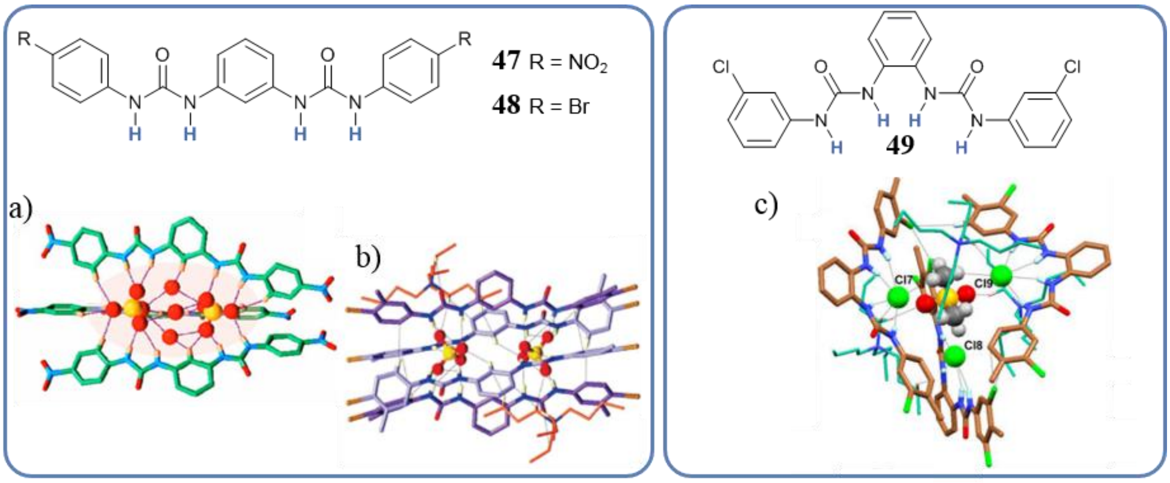

Figure 1.17. Examples of ATSA helicates by Das. a) Triple helicates of **47** with SO_4^{2-} and b) tetrameric assemblies of **49** with SO_4^{2-}. c) Triple helicates of **48** with Cl^-. Reproduced from refs. 98-100.

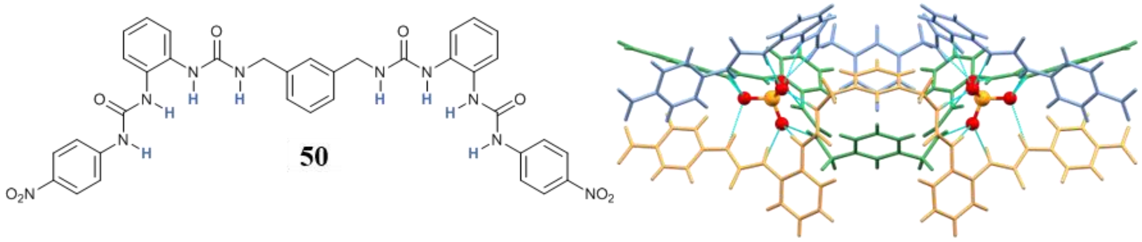

Figure 1.18. Example of ATSA triple helicate by Wu, Reproduced from ref. 101.

are stabilised by hydrogen bonds among the anions and/or solvent molecules, as well as by the complexation with the ligand, which help to overcome the electrostatic repulsion. Therefore, these clusters are more likely to form with amphoteric anions, like phosphate, which can both donate and receive hydrogen bonding, favouring the self-association. Basarić and co-workers reported the formation of tetrahedral 4:4 bundles around $H_2PO_4^-$ tetrameric clusters with adamantane bisurea ligands **52** and **53**, Figure 1.20.[104]

Nitschke has successfully employed tetrahedral oxyanions as templates for Fe^{II} metallo-organic cages.[105,106] While the anion complex acts as a geometrical template, the stability of the cages is attributable to the Fe^{II} complexes, and the anion lies in the cavity as "guest". Inspired by the structure of **50**, Wu obtained the self-assembly of cages using exclusively anionic complexes. This was done using tripodal ligand **54** with a triphenylamine core, ligand **55**, with a 2,4,6-triphenyl-1,3,5-triazine core, and **56** with a 1,3,5-triphenylbenzene core, Figure 1.21.[107-110]

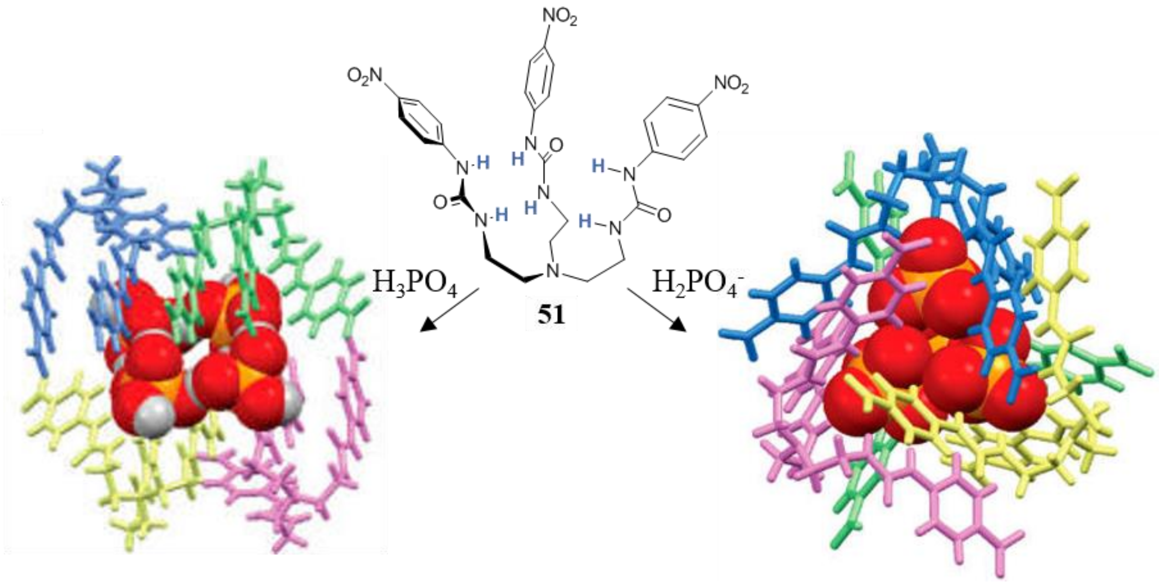

Figure 1.19. Bundles (4:4) of **51** with H_3PO_4 and $H_2PO_4^-$. Anions shown in spacefill while the ligands in capped stick representation. Reproduced from ref. 103.

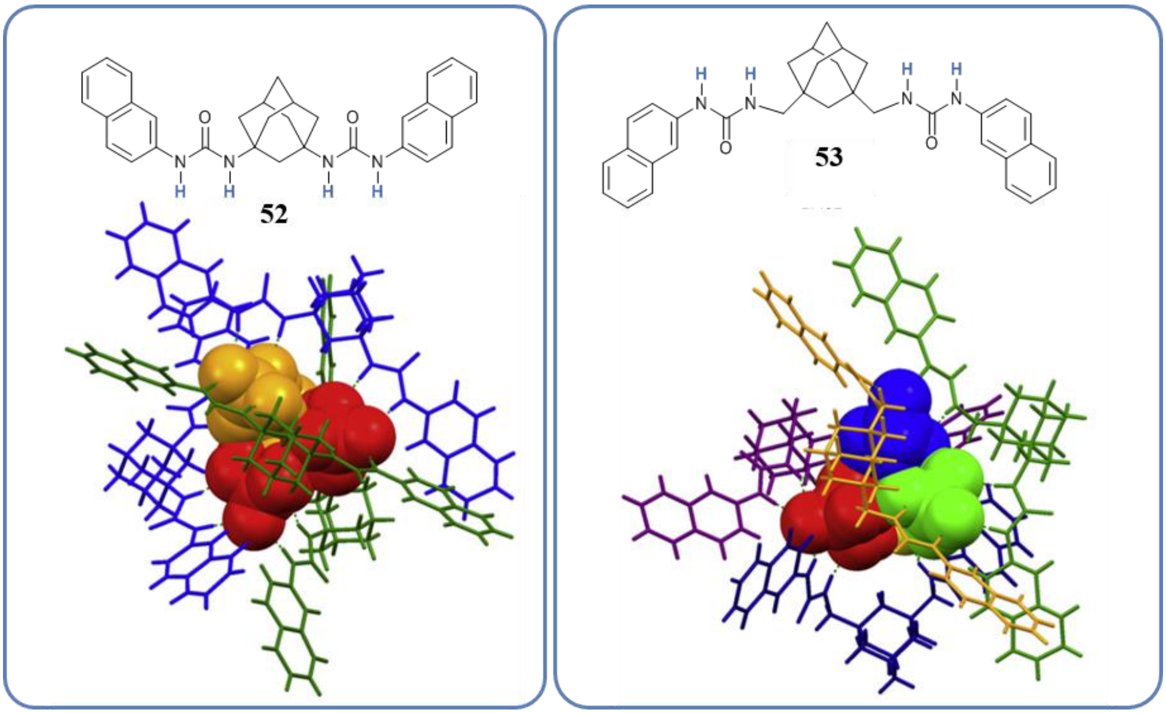

Figure 1.20. 4:4 bundles of **52** and **53** with $H_2PO_4^-$. Anions shown in spacefill while the ligands in capped stick representation. Reproduced from ref. 104.

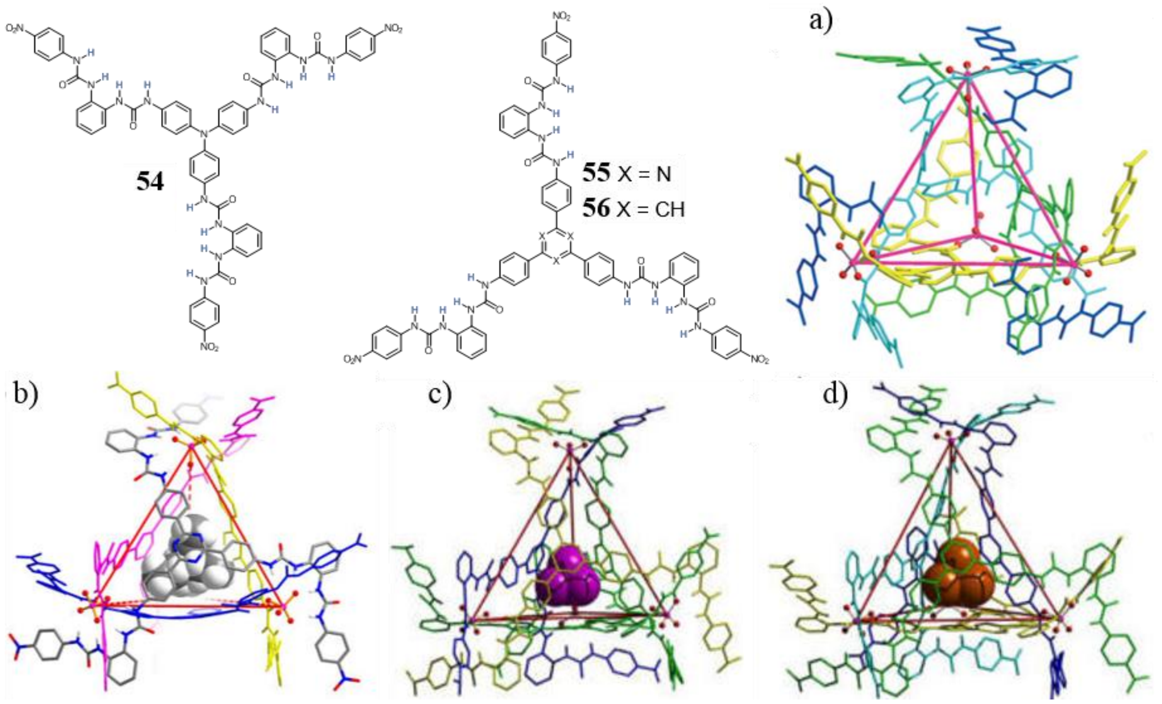

Figure 1.21. 4:4 cages of **54**, **55** and **56** through H-bond coordination of PO_4^{3-}. a) **54** with PO_4^{3-}; b) **55** with PO_4^{2-} hosting a tetraethylammonium (TEA) molecule within its cavity; c-d) **56** with PO_4^{3-} encapsulating c) P_4 and d) As_4 within their cavity. Reproduced from refs. 107-110.

One first cage containing only solvent molecules, was obtained with four **54** ligands coordinating four PO_4^{3-} molecules through urea NH hydrogen bonds, Figure 1.21a. A similar ligand, **55**, with a triazine core, also formed tetrahedral cages, with four PO_4^{3-} complexes positioned on the vertices of the structure, which could also host a TEA molecule within its cavity, Figure 1.21b. Encapsulation of P_4 and As_4 was obtained within the 4:4 cage built from **56** and PO_4^{3-}, Figure 1.21c-d.

The combination of $[Fe(bipy)_3]^{2+}$ complexes and anion templation is the key behind the development of pentafoil knot and other interlocked molecules developed by Leigh and co-workers.[111-114] One recent example presented in Figure 1.22, and shows the remarkable action of Cl^- ion, together with five Fe^{II} ions to arrange five molecules of **57**, into a large complex, **58**, so that they could be connected through RCM into one single knotted macrocyclic molecule, **59**.

In slightly less complex structures, Flood has reported the synthesis of a [3]rotaxane, based on the self-assembly properties of the macrocyclic cyanostar **29**, presented earlier in section 1.3.2, with a phosphonate thread, **60**. By stoppering the formed pseudo-rotaxane by Copper(I)-catalysed Alkyne-Azide Cycloaddition (CuAAC) with **61** the [3]rotaxane **62** was obtained in 50% yield, as the first example of phosphonate templated rotaxane.[115,116] Improved yields of 70% were obtained with a shorter phosphonate thread, thanks to stronger

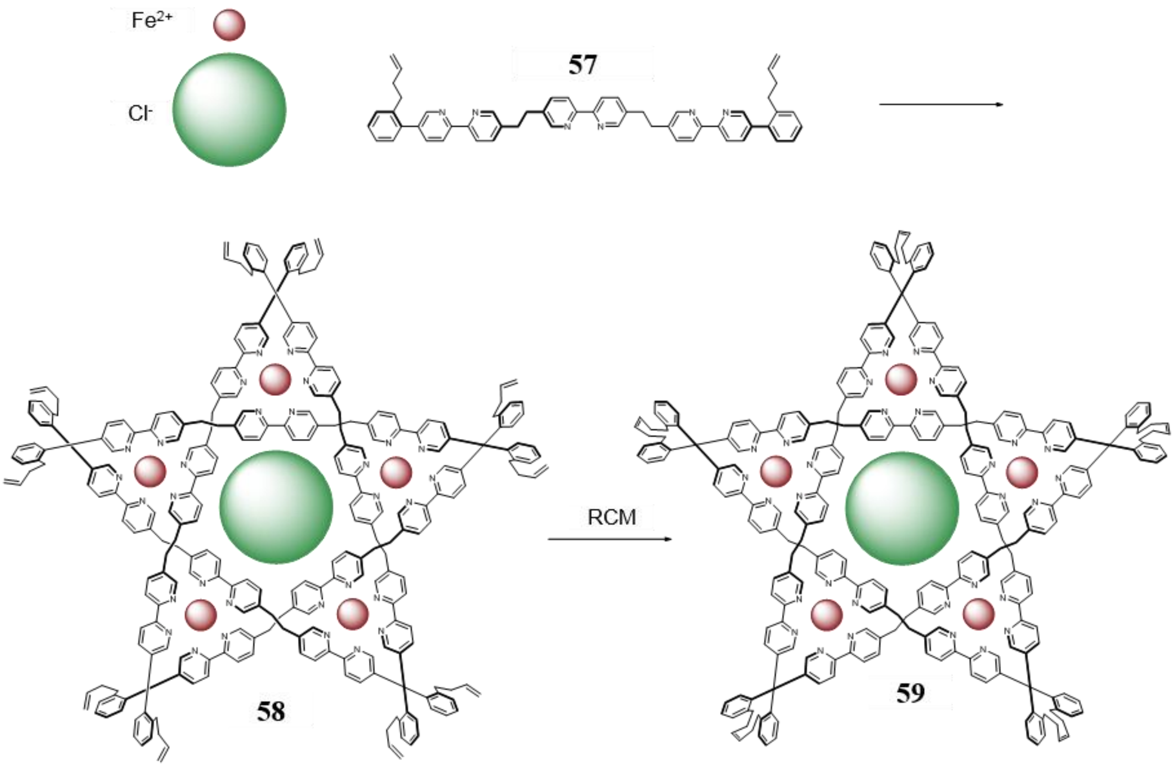

Figure 1.22. Example of $Fe^{II}Cl_2$-templated synthesis of pentafoil knot **59** from the ATSA of **57** into complex **58**, from ref. 111-114.

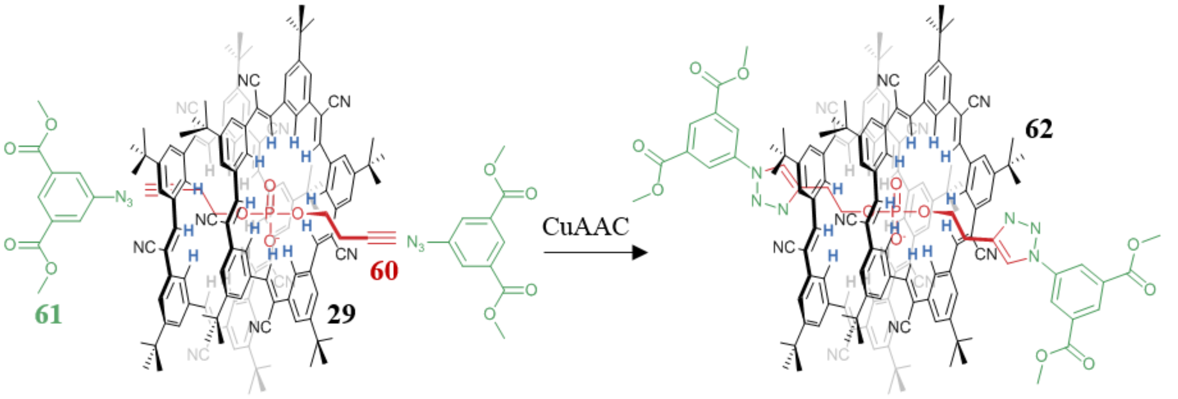

Figure 1.23. Example of ATSA synthesis of [3]rotaxane **62** from ligands **29** and **61** with a phosphonate thread, **60**, from ref. 115-116.

binding with the macrocycle **29**.[95] Through crystal structure analysis and solution studies Flood showed interaction of the phophonate group with the CH groups of the macrocycles (Figure 1.23, highlighted in blue). Addition of triflic acid to a solution of **62** in CD_2Cl_2:CD_3CN (2:1) caused the protonation of the phosphonate thread, resulting in a significant upfield shift of the CH resonances of the cyanostar involved in the binding, indicating that the hydrogen bonding interaction was not occurring anymore. The interaction could be reestablished by addition of base, confirming that the protonation was not causing dethreading of the rotaxane.

1.3.4. ATSA networks for the development of soft materials

As described above, different binding sites within a single molecule can participate together into the complexation of one anion or a cluster. This occurs when the binding sites converge towards the same centre. The presence of diverging binding sites, on the other hand, can favour the formation of extended networks, giving rise to anion-templated supramolecular polymers. While the use of metal coordination in this direction is very well established,[117,118] few examples can be found in the literature of ATSA of extended supramolecular polymers and soft-materials. Examples of ATSA networks with small ditopic linear molecules have been reported by Wang and Huang[119,120] as well as MacLachlan who also showed the formation of 3D nanotubes templated by Br^- anion.[121-123] Custealcean reported the use of bis(guanidinium) ligand **63** which formed hydrogen bonded layers with oxyanions such as NO_3^- and ClO_4^-, shown in Figure 1.24, and even more challenging anions, such as Cl^- and SO_4^{2-}.[124] In particular the crystals formed with SO_4^{2-} showed a lower solubility than the others, such that crystallisation of **63** with SO_4^{2-} would occur selectively, even in the presence of the other anions. This selectivity has shown potential use into the separation of sulfate from aqueous environments, even in the case of radioactive waste.[58]

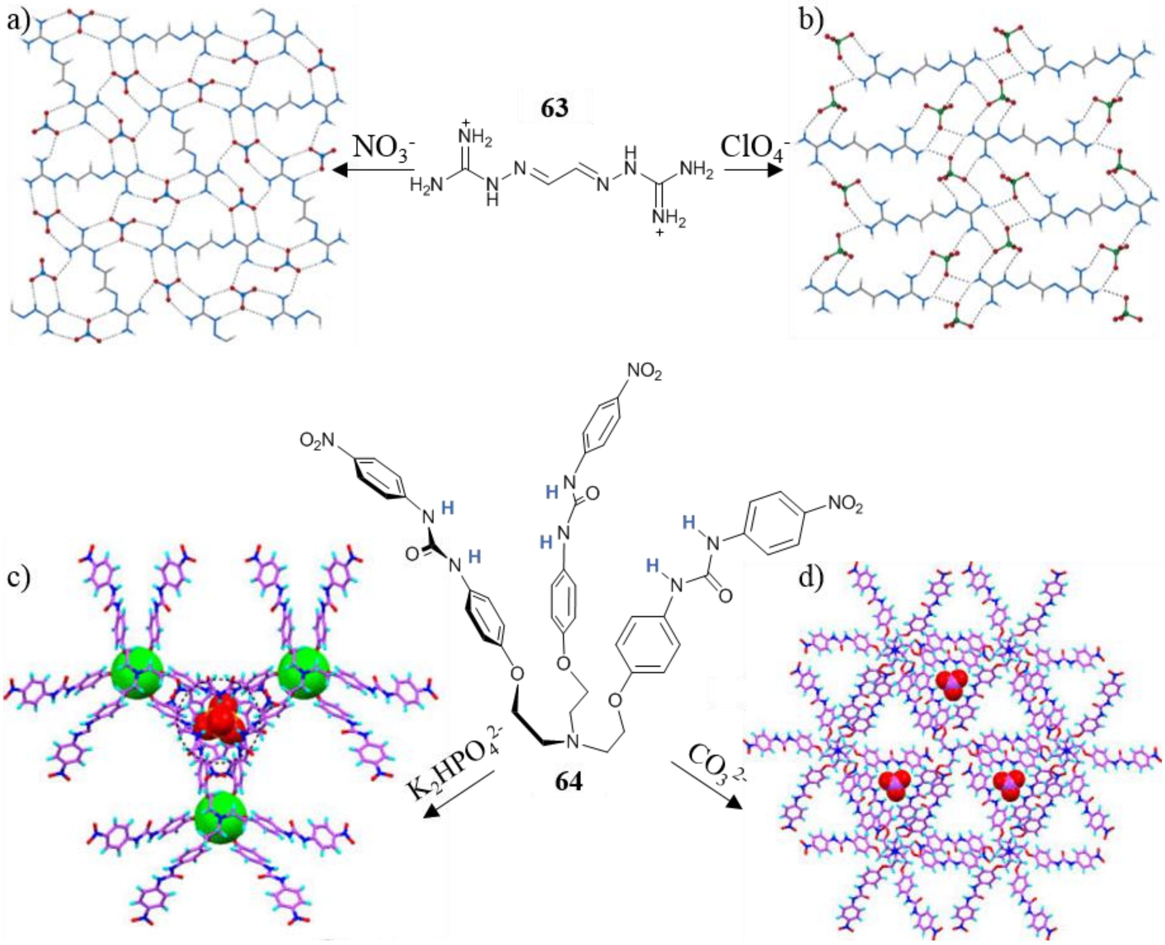

Figure 1.24. Structure of **63** and **64**. X-ray crystal structures of the hydrogen-bonded network of **63** with a) NO_3^- and b) ClO_4^-. X-ray crystal structures of the hydrogen-bonded network of **64** with c) $K_2HPO_4^{2-}$ -K^+ ions (green) and HPO_4^{2-}(red) both interacting with the ligands- and d) CO_3^{2-} deprotonated from $TEAHCO_3$. Reproduced from ref. 124-125.

Tripodal tris(urea) ligand **64**[125] can crystallise into extended 2D networks with K_2HPO_4, as shown in Figure 1.24c, generating a polymeric ion pair complex. The crystallisation with HCO_3^- gave rise to the formation of complexes of **64** with fully deprotonated CO_3^{2-} ion receiving six hydrogen bonds from three urea moieties of three separate molecules, Figure 1.24d. In this case, a pseudo capsular association of two molecules of **64** was observed, with a 'cleft-side' binding of the CO_3^{2-} anion, which gave rise to the network by connecting different pseudo-capsular assemblies.

The influence of anions in the formation of networks is primarily observed within a crystal structure which can clearly show the formation of connections and supramolecular interactions. However, the development of such systems in the presence of anions can lead to morphological changes on the microscale which can be observed through scanning electron microscopy (SEM). One example of this was shown by Caballero and Molina employing ligand **65**,[126] which features both hydrogen and halogen bonding donors groups

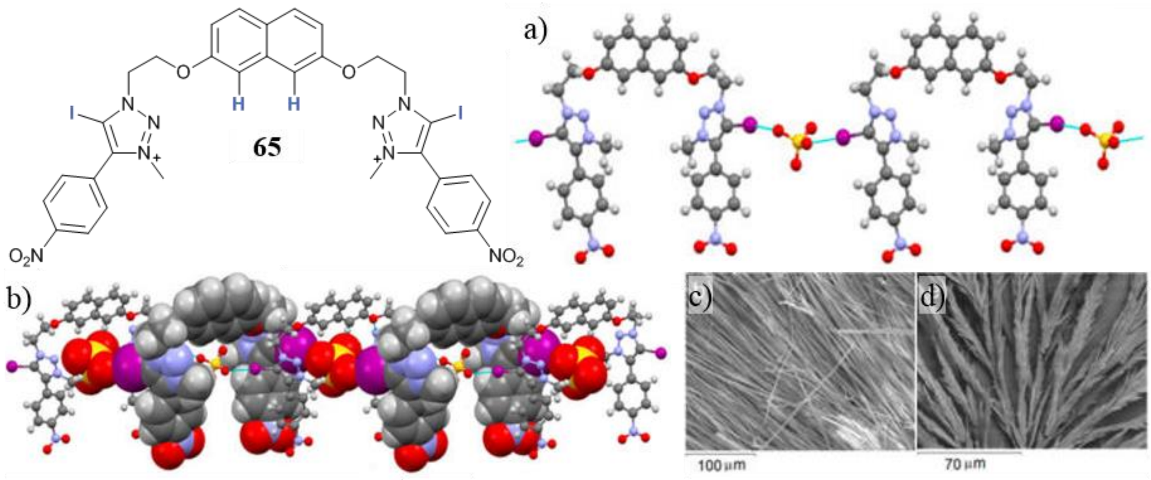

Figure 1.25.Structure of **65**. a) X-ray crystal structure in which one chain has been omitted for clarity SEM images of the self-assembled compounds, b) X-ray crystal structure of the supramolecular polymer **65**·SO_4^{2-}, in which one chain is represented in ball-and-stick and the other in space-filling. SEM images of the self-assembled compounds c) **65**·$2H_2PO_4^-$ and d) **65**·SO_4^{2-}. Reproduced from ref. 126.

as binding sites. Ligand **65** would form interconnected ATSA complexes with SO_4^{2-} and $H_2PO_4^-$ propagating in a single dimension, which would be maintained in the macroscale, Figure 1.25.

Steed has shown on many occasions,[127,128] the addition of anions to low weight gelators can disrupt the hydrogen bonding network. Yamanaka has also showed the interfering effect of anions of tripodal tris(urea) molecules.[129] to the gelation effect However, the interaction with anions can, in fact, give rise to ATSA soft-materials, such as gels which can take part into the network and modify or even induce the formation of new materials.[130,131]

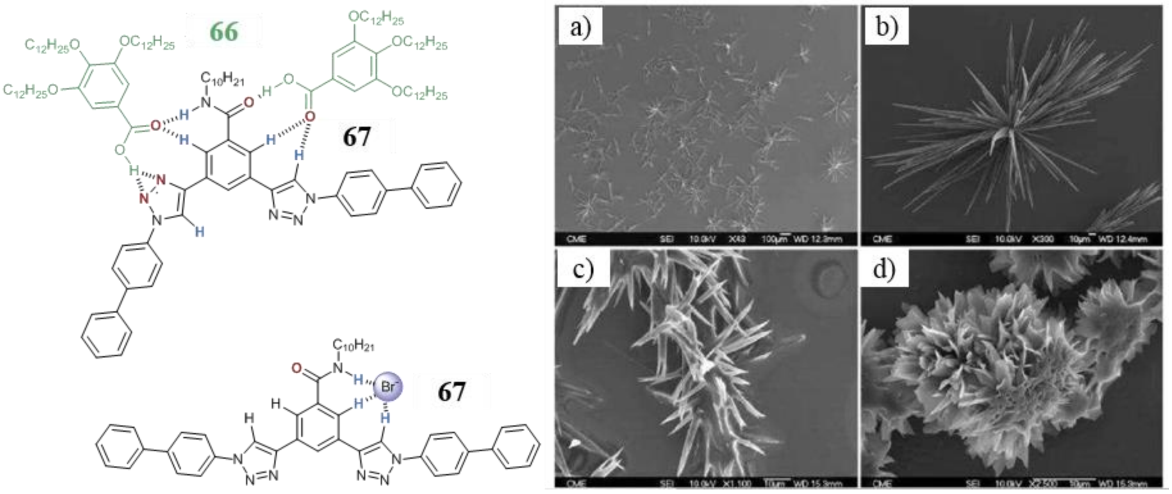

Figure 1.26. Structure of **67** showing hydrogen bonding to **66** or Br^-. SEM images of the aggregates formed by the self-assembly of a-b) free **67** and aggregation of receptor **67** in the presence of c) Br^- or d) the gallic acid derivative **66**, showing the formation of aggregates of different morphologies. Reproduced from ref. 133.

Sánchez studied in detail the conformational changes on aryl bis(triazole) receptors, showing how the planarity of the molecule could affect the morphology of the self-assembly.[132] He then showed through DFT calculations and ^{1}H NMR titration experiments that the interactions with Br^- and **66** would cause conformational changes in ligand **67**, by rotation of the bonds between the triazoles and the central aryl unit, Figure 1.26.[133] The morphology of the self-assembly of receptor **67** would reflect these conformational changes, with bulkier and less thin structures.

Haridas and co-workers showed that the self-assembly of asymmetrical tripodal-like peptide **68** in $CH_3OH/CHCl_3$ (1:1) generated non-uniform spherical aggregates, as displayed in Figure 1.27a, with different morphologies observed with other similar oligopeptides.[134] After evaluating the binding affinity of a group of oligopeptides with different anions, **68** was found to form 1:1 complexes with $H_2PO_4^-$ selectively in $CHCl_3$, with a lower constant than other analogue molecules in the family ($K_{1:1}$ = 22 M^{-1}). This lower interaction, allowed for a gradual disruption of the self-assembled spheres of **68** with increasing amounts of $H_2PO_4^-$, generating holes in the surface of the spheres, Figure 1.27. The authors attributed the disruption of the self-assemblies to the preferential interaction of **68** with the anion.

Ghosh has recently shown that the self-assembly of **69** would generate gels with helical fibres in DMSO:H_2O (8:2) at low concentration (0.9 wt%), Figure 1.28a.[135] Self-assembly abilities of **69** were due to the presence of benzene,1,3,5-carboxyamide (BTA) moiety, which can engage into hydrogen bonds, as well as by the presence of quinoline residues, which provided additional π-π stacking. BTA-based tripodal molecules can also interact with anions through hydrogen bonds from the amide NH groups. Binding studies revealed that **69** was able to interact with anions. It was seen through absorption and emission

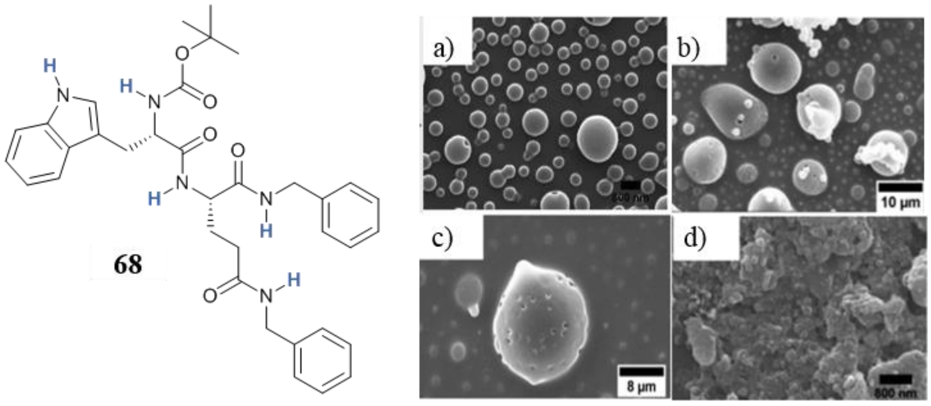

Figure 1.27. Structure of tripodal molecular gelator **68**. SEM images of a) **68** (3.4 mM) in 1:1 $CH_3OH/CHCl_3$ and in the presence of b) 0.5 equiv (c) 1.0 equiv (d) 2.0 equiv of $TBAHPO_4$. Reproduced from ref. 134.

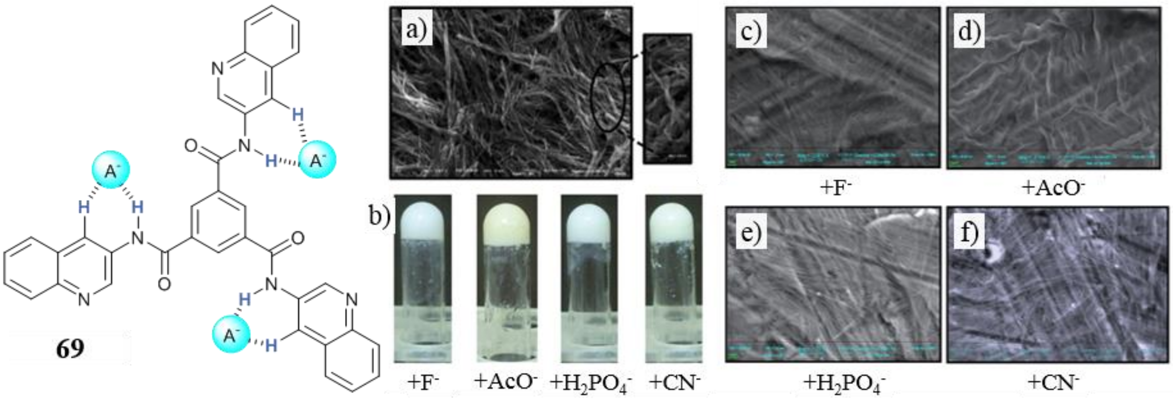

Figure 1.28. Structure of tripodal molecular gelator **69**. a) Representative SEM micrographs of **69** displaying entangled fibers having both handednesses; inset depicts the right-handedly twisted fibers; b) Photographs of test tubes showing gelation of compound **69** in the presence of different anions. c-f) Representative SEM micrographs of the gel formed by **69** in in the presence of different anions. (DMSO:H_2O 8:2, 0.9 wt%). Reproduced from ref. 135.

studies, that the binding would induce a divergence of the chromophore, rather than bringing them close together.

This indicated that the binding did not occur through the three arms simultaneously to the same anion. Furthermore, through ^{1}H NMR studies it was shown that the anion binding did not induce de-symmetrisation of the arms, indicating that the binding occurred on the three arms in the same way. Considering that the luminescence studies excluded the 1:1 stoichiometry, a 1:3 (L:A) one was assumed, as shown in Figure 1.28, with a combination of hydrogen bonding from the amide NH and a quinoline CH. Upon addition of excess (10 equiv.) of F^-, CH_3COO^-, $H_2PO_4^-$ or CN^- (as TBA salts) the gelation properties of **69** were retained, showing that either the anions would bind to multiple ligands into a network, or the ligand self-assembly would be mainly due to π-π stacking rather than hydrogen bonding, for which the anions would compete. Changes in the morphology were observed, Figure 1.28b-f, as the presence of the anions would generate in all cases a less fibrous material and more uniform film, potentially due to the additional interconnections between the molecules. While the authors did not attempt to explain how the anions would affect the self-assembly interaction at a molecular level, given their studies on the binding properties, the formation of interconnected networks seems plausible.

1.4. Recent advances in anion-templated self-assembly from Gunnlaugsson

The Gunnlaugsson research group has been involved into the development of many different anion-templated self-assembly systems. Early examples focussed on the fluorescent detection of anions in organic and aqueous environments, by connecting the receptor unit to lanthanide complexes[136] or a naphthalimide units.[137] More recently the interest has widened

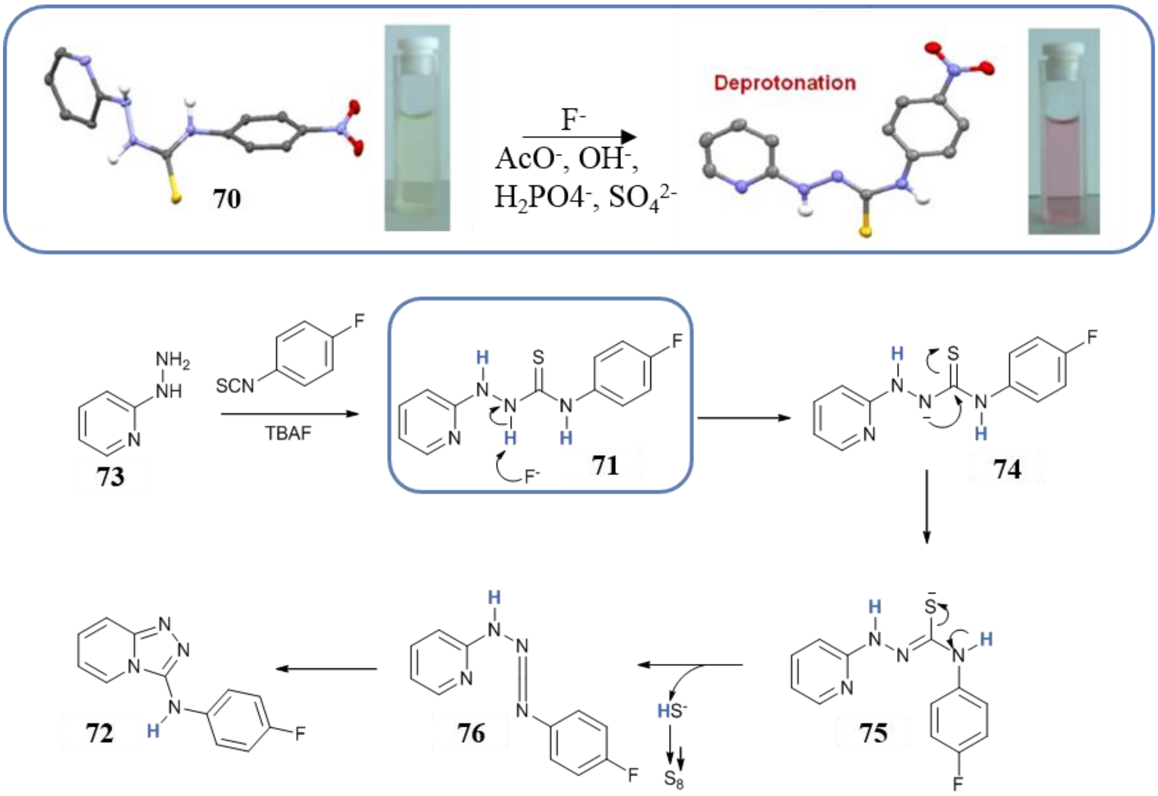

Figure 1.29. Mechanism of the one-pot synthesis of heterocycle **72** from **73** and 4-fluorophenyl isothiocyanate. The synthesis is catalysed by F^- which promotes the deprotonation of the thiosemicarbazide compound **71**, in the same way observed previously for the analogous compound **70**. From ref. 138.

to include anion-catalysed reactions and anion complexation for the development of ATSA networks, capsules or helicates.

Binding studies on pyridine thiosemicarbazide compound **70** and **71** revealed that interaction with anions (*e.g.* F^-, CH_3COO^-, OH-, $H_2PO_4^-$ or SO_4^{2-}) induced significant changes in the UV-vis absorption spectrum of the ligands.[34] The changes were caused to by deprotonation of the thiourea moiety, as observed from X-ray diffraction crystal structures of **70**, Figure 1.29. Deprotonation would also cause significant colour changes, making **70** a colorimetric 'naked eye' anion sensor. Interestingly, the deprotonation of the thiosemicarbazide could also induce a series of reactions, which would lead to the formation of 3‑amino-[1,2,4]-triazolo pyridines.[138] The mechanism of the synthesis of heterocycle **72** is shown in Figure 1.29 as an example, starting from 2-hydrazino pyridine, **73**, and 4-fluorophenyl isothiocyanate, which react to form thiosemicarbazide **71**. The F^- ion in solution can deprotonate **71**, at the thiourea, and the presence of an electron withdrawing group on the phenyl group can favour the elimination of HS^-. The carbodiimide intermediate **76** then can undergo intramolecular attack and generate the fused heterocyclic compound **72**. This was a first example of anion-templated and catalysed synthesis of biologically

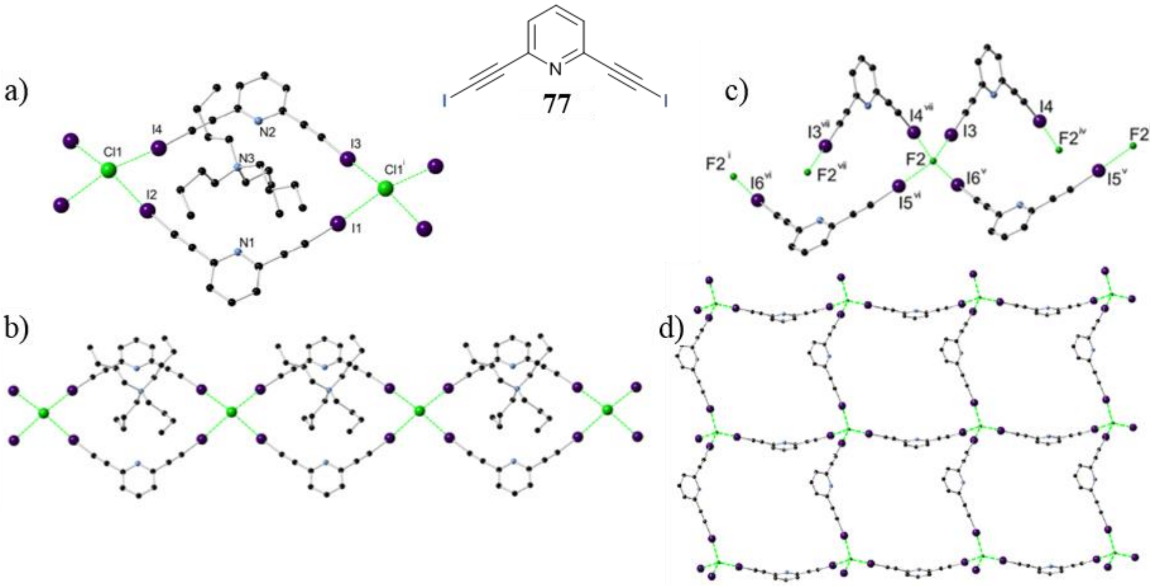

Figure 1.30. Structure of pyridine 2,6-bis(iodoethynyl)pyridine **77**. a) Halogen bond interaction of **77** with Cl^- and b) corresponding extended 2D network. c) Halogen bond interaction of **77** with F^- and d) corresponding extended 2D network. Reproduced from ref. 142.

relevant 3-amino-[1,2,4]-triazolo[4,3-*a*]pyridines, through the formation, in a metal-free one-pot reaction, of an anion receptor which becomes a reagent.

Together with the formation of metallo-organic frameworks (MOF) and supramolecular polymers[139-141] one example of ATSA into extended networks was reported with 2,6-bis(iodoethynyl)pyridine ligand **77**, Figure 1.30.[142] Halogen bond interactions from the iodine atoms of **77** to Cl^- gave rise to 1D network with each Cl^- ion receiving four halogen bonds from four different molecules into an approximately square-planar geometry, Figure 1.30a-b. With F^- a halogen bonded 2D network was formed, with the anion also receiving four bonds from four different molecules, but this time in a trigonal pyramidal arrangement,

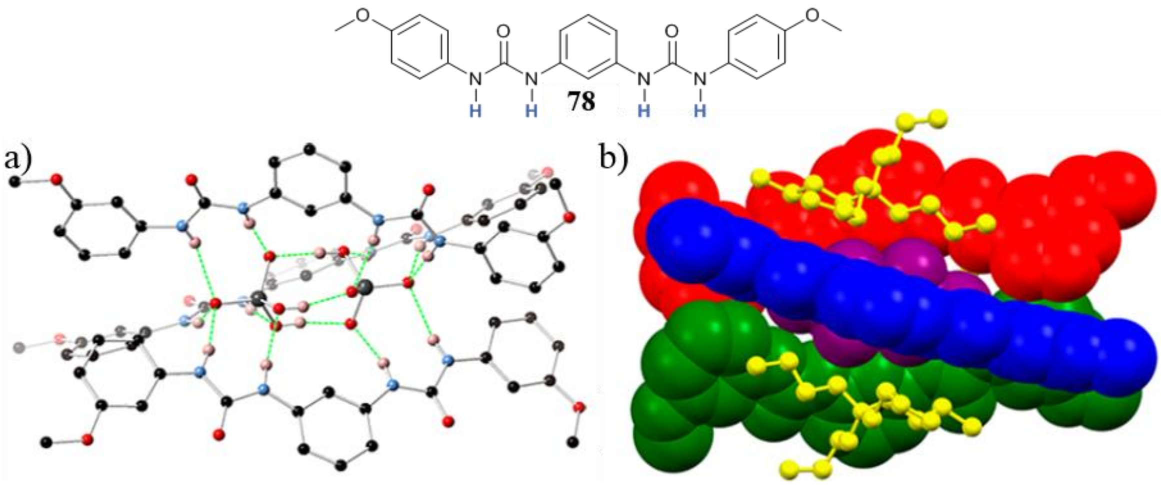

Figure 1.31. Structure of **78** and crystal structure of the ATSA with two $H_2PO_4^-$ molecules in a) ball and stick or b) spacefill representation. Reproduced from ref. 143.

Figure 1.30c-d. Other crystal structures of **77** donating halogen bonding to Br^- and I^- were reported, which showed discrete assemblies rather than extended networks.

Another recent example of ATSA developed in the Gunnlaugsson group includes triple helicates of *meta*-phenylene bis(phenylurea) compound **78**, Figure 1.31.[143] ^1H NMR solution studies on a family of analogues of **78** showed strong interactions in DMSO-d_6 with $H_2PO_4^-$ CH_3COO^- and $PhCOO^-$ and a lower interaction with Cl^-, HSO_4^- and SO_4^{2-}. The crystal structure of **78** with anions in the solid state showed the formation of triple helicate structures, as well as the formation of 1:2 (L:A) clusters with CH_3COO^- including a water molecule bridging the two anions.

The Gunnlaugsson group has also focussed a lot of effort in the development of tripodal structures with a benzene-tricarboxyamide (**BTA**) core, not only for the development of smart soft materials with sensing or self-healing properties,[139,144-150] but also for the development of ATSA.[151,152] One first generation set of tripodal tris(diphenylurea) derivatives was designed about 10 years ago, integrating previously developed diphenylurea-amide[153] derivatives to a central **BTA** moiety through a secondary amide bond, Figure 1.32.[151] According to the initial intuition, this design was intended to create bowl-shaped structures with a C_{3v} symmetry which, similarly to the examples discussed above (Section 1.3), could allow for high binding affinity with tetrahedral anions, both as 1:1 complex and as an ATSA of dimeric capsules. The first generation of tripodal ligands, Figure 1.32, was predicted to employ both the urea protons and the amide NH groups as donors in the formation of hydrogen bonds, in a concerted fashion. This would potentially offer the ideal binding site for tetrahedral oxyanions within the cavity of a bowl-shaped ligand. A

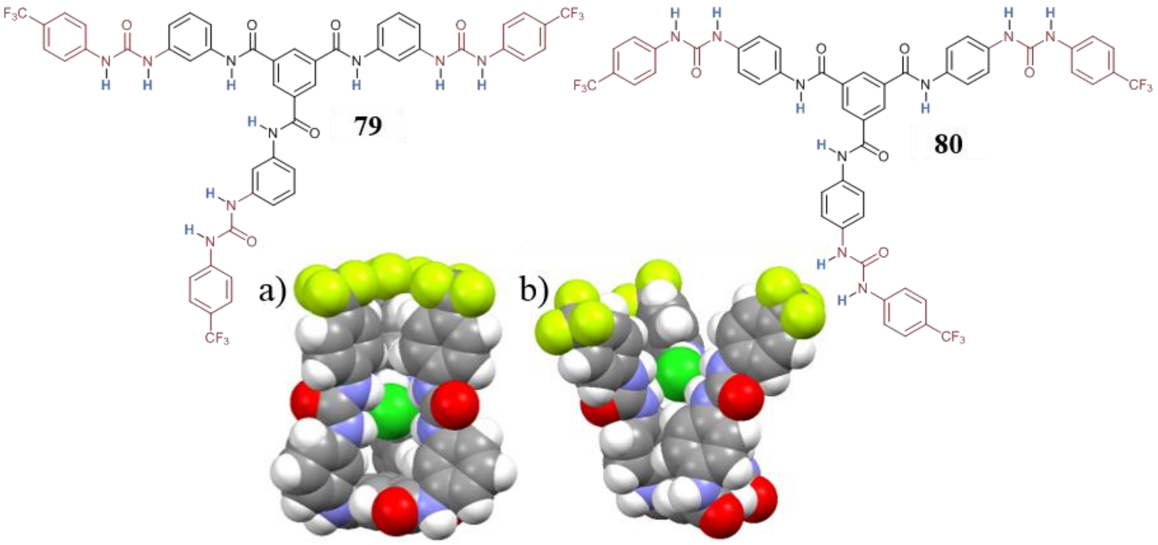

Figure 1.32. Chemical structures of first generation tripodal ligands, **79** and **80**, and their MM2 host-guest calculations with Cl^-. Reproduced from ref. 151.

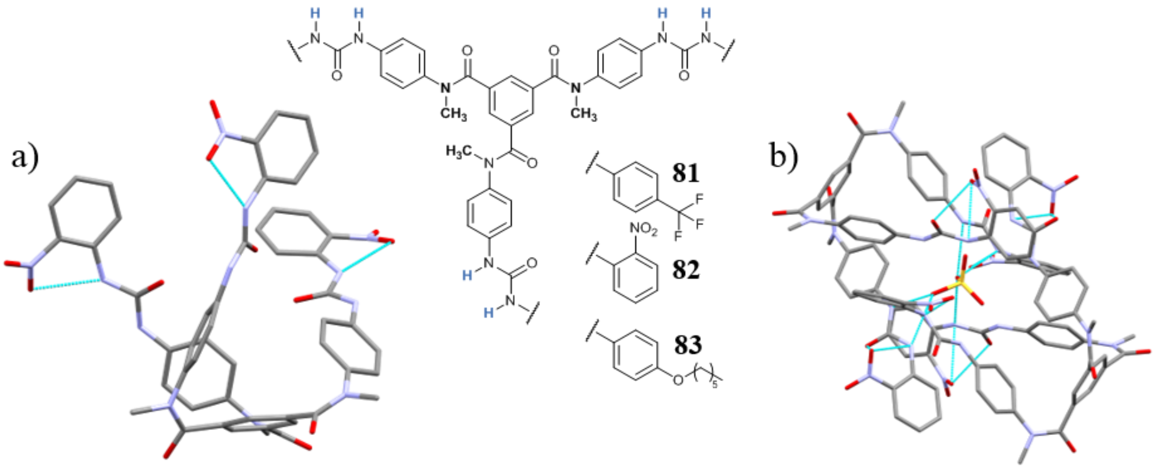

Figure 1.33. Structures of **81**, **82** and **83** and a) crystal structure of free ligand **82**, b) crystal structure of capsule **82**$_2$·SO_4^{2-}. Hydrogens, solvent molecules and TBA$^+$ counterions omitted for clarity, from ref. 152.

combination of ^{1}H NMR experiments and MM2 calculations demonstrated that the binding occurred only from the urea moieties, while the amide protons, orientated towards the outside of the ‘cavity’, were not taking part into the binding process, Figure 1.32. The modelling of the host-guest interaction of the two compounds **79** and **80** with Cl$^-$, Figure 1.32, shows the bowl-shaped conformation with a tighter arrangement of the arms of the *meta*-phenylurea compound **79**, if compared to its *para*-phenylurea analogue, **80**. The binding abilities of the first generation of compounds, evaluated through the non-linear regression fitting of the changes in the proton resonances during ^{1}H NMR titrations in DMSO-*d*$_6$, showed one example of sulfate-binding ligand.[151]

A second generation of tripodal ligands was then developed, introducing a methyl group on the amide, which would force the three amides in a *cis* conformation[154] and would stabilise the cavity formation, ensuring a stronger binding. This was the case for the *para*-phenylurea ligands, **81**,**82** and **83**, which were studied through single crystal X-ray diffraction, as shown in Figure 1.33a for ligand **82**.[152] The crystal structure of the free ligand

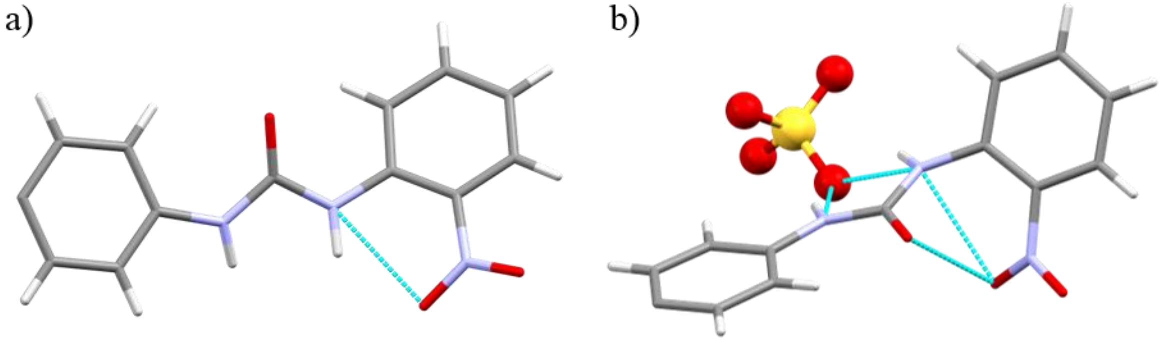

Figure 1.34. Zoomed region of the one arm of **82** from the crystal structures showing the reciprocal positions of the urea and the *o*-NO$_2$ phenyl groups a) in the free ligand and b) in the complex with SO_4^{2-}, from ref. 152.

82 is an example of how these ligands can organise the arms closer together in a bowl-shaped arrangement, thanks to the *cis* conformation of the amide carbonyl and N–CH_3 groups. With such a conformation, this set of ligands showed significant anion binding abilities and formation of 2:1 (L:A) capsules enclosing tetrahedral anions such as $H_2PO_4^-$ and SO_4^{2-}, as displayed in Figure 1.33b for $\mathbf{82}_2{\cdot}SO_4^{2-}$. The crystal structure of **82** also showed that the *o*-NO_2 of the peripheral phenyl ring group can engage into an internal hydrogen bond with the adjacent urea NH. This interaction, in the free ligand, Figure 1.34a, brought the *o*-NO_2 group closer to the urea NH group, so that the nitrophenyl group lay approximately on the same plane as the urea moiety. The interaction of **82** with the anion, Figure 1.34b, caused a rotation of the nitrophenyl moiety about the bond with the urea.

In the synthesis of ligand **83**, performed by reacting the tripodal amine ligand **84** with 4-hexiloxyphenyl isocyanate, the formation of the ‘dipodal’ analogue **85** as a side product

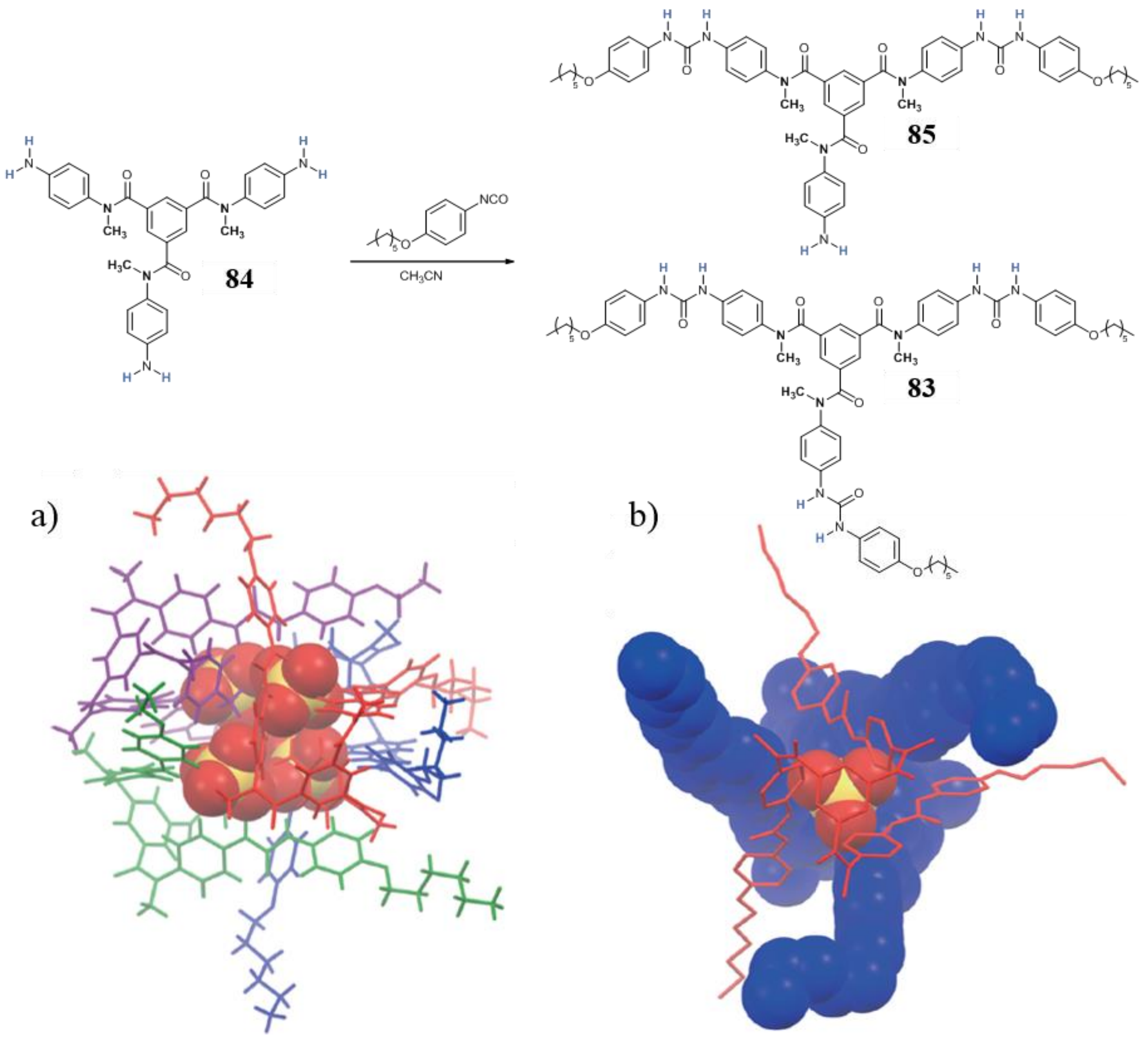

Figure 1.35. Synthesis scheme of **83** from **84**, giving **85** as a side product. Self-assorted crystallisation with SO_4^{2-} would lead to different ATSA: a) 4:4 (L:A) of **85** and b) 2:1 (L:A) dimeric capsular assemblies of **83**. Reproduced from ref. 152.

was observed. Separation of the two molecules could be only acheved by crystallisation in the presence of SO_4^{2-}. The 'dipodal' ligand **85** formed 4:4 (L:A) ATSA, as shown in Figure 1.35a, while the tripodal ligand **83**, formed 2:1 (L:A) dimeric capsular assemblies, as observed for the other ligands in the family, Figure 1.35b. As discussed earlier, the formation of high order bundles around clusters of multiple anions can be more commonly observed with amphoteric anions, such as $H_2PO_4^-$ which can both receive and donate hydrogen bonds. The formation of the ATSA of the neutral ligand **85** with four SO_4^{2-} anions disposed in a tetrahedral arrangement, is unusual in its own nature, as SO_4^{2-} can only receive hydrogen bonds and it is also highly charged. The formation of this bundle can be attributed to a combination of the formation of a favourable binding pocket rich in hydrogen bonds within the internal cavity of the bundle and the formation of a solvophobic layer on the outside.

Having discussed the state of the art in the field of ATSA I will now present the work I carried out in the same field during my postgraduate studies.

1.5. Aims and objectives

The overall aim of this PhD research was to understand further the anion complexation and ATSA abilities of various ligand scaffolds that form the basis of molecular and materials designs by Gunnlaugsson. Our initial objectives were to study substitution patterns in tripodal systems based on the BTA core and diphenylurea anion binding group and how these affected the ligands behaviour and properties in solution and in the solid state. The proposed study of these systems was through a combination of spectroscopic (UV-vis, NMR) and crystallographic measurements, with the support of electron microscopy to study morphological features as well as other characterisation techniques, such as MS or DLS.

The secondary aim was then to further functionalise BTA-based tris(urea) and bis(urea) receptors to improve their physical and chemical properties (such as solubility, responsive nature) that could potentially lead towards more realistic applications and address the demands required for particular working environments. It was intended to achieve this by developing an efficient synthesis of a BTA-based dipodal bis(urea) ligand which contained a handle for broad functionalisation with the purpose of being able to achieve functional derivatives.

Beyond the BTA core, a focus on further understanding the anion binding properties of BTP was also a key objective. The BTP motif has been extensively used for the anion binding within macrocyclic hosts, while its direct involvement in the binding of anionic guests within interlocked systems is less explored. Therefore, it was intended to evaluate the binding abilities of available sets of BTP-based [2]catenanes (synthesised within the Gunnlaugsson group as part of an independent project) and compare them with those of the corresponding macrocycles. The combination of different NMR techniques (^{1}H NMR, DOSY) was intended to elucidate and compare the nature and consequences of the interactions of the ligands with anions of different chemical nature and geometry.

Finally, it was aimed to understand, in a similar fashion, the binding properties of a cage system, which had been developed by Amendola and co-workers. Similarly to interlocked systems, a cage molecule contains an internal cavity, which has the potential to accommodate guests. Given crystallographic observations of structure modifications upon binding with Cl^- there was interest to understand the cage behaviour in solution, which was the goal of the final experiments undertaken as part of this research, in collaboration with Amendola. The discussion of these objectives will be divided into four chapters, gathering the work on the different sets of ligands, as shown in Figure 1.36, separately.

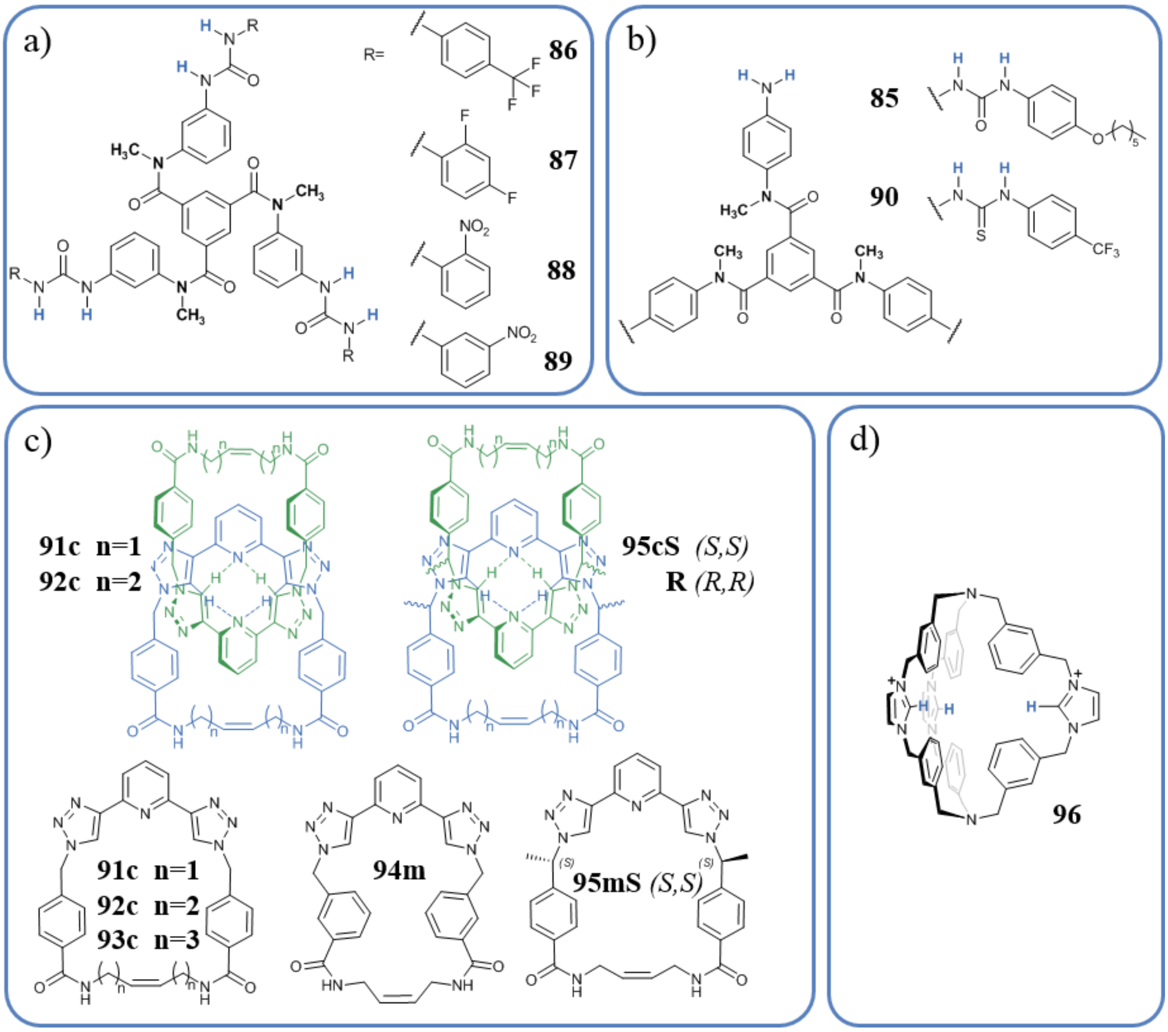

Figure 1.36. Structures of ligands presented in these thesis, divided by chapter: a) chapter 2, b) chapter 3, c) chapter 4 and d) chapter 5.

Chapter 2, will discuss the synthesis and anion binding studies of tripodal tris(urea) ligands **86**, **87**, **88** and **89** with Cl^-, CH_3COO^-, $H_2PO_4^-$ and SO_4^{2-}. The anion binding studies carried out in solution on these ligands indicated that ATSA was occurring which lead us to investigate also the self-assembly behaviour in solution and in the solid state, which will also be discussed in detail.

Chapter 3 will focus on the synthetic challenges engaged to obtain ‘dipodal’ ligand **85**, not simply as a side product. Solution binding studies on a dipodal thiourea analogue **90** with tetrahedral anions (*i.e.* $H_2PO_4^-$ and SO_4^{2-}) will be included in this chapter.

In chapter 4 the formation of anionic complexes with a family of macrocycles and [2]catenanes, combining the 2,6-bis(triazolo)pyridine (BTP) moiety and amide groups as binding units, will be presented. The discussion will cover the differences given by the different substitution pattern and the higher preorganisation of hydrogen bond donors within the [2]catenanes structures. Some of the studies included in this chapter were published as a communication.[155]

Chapter 5 will include the studies on halide encapsulation within bis(***tren***) cage with imidazolate binding units, **96**, which were carried out in collaboration with Prof. Amendola, from Università degli studi di Pavia. Detailed NMR characterisation of the anionic complexes will be presented, which will show the conformational changes caused by the encapsulation of the halide anions.

2. Tripodal tris(urea) ligands for anion-templated self-assembled structures

2.1. Introduction

In this chapter, the anion-binding properties of novel tripodal tris(urea) ligands based on the *N*^{1},*N*^{3},*N*^{5}-trimethylbenzene-1,3,5-tricarboxamide (**tmBTA**) scaffold will be discussed, as well as their involvement into the formation of self-assembled structures in the presence and in the absence of anions. The aim of this project was to evaluate the binding abilities of these **tmBTA** systems and to investigate the formation of new ATSA architectures.

The **tmBTA** tripodal building block is directly derived from the benzene-1,3,5-tricarboxamide (**BTA**) moiety, and it differs from it by the simple methylation of the amides. As discussed in Chapter 1, this change impedes the formation of hydrogen bonding network through the amide protons, as well as locking their conformation with the methyl group in *cis* conformation to the amide carbonyl bond,[154] allowing for the formation of a cavity, as demonstrated for compounds **81**, **82** and **83**. Ligands **86**, **87**, **88** and **89**, Figure 2.1, are such tripodal molecules, with a **tmBTA** core and three bis-phenylurea arms attached to the core through the amide bond. Each arm has a first phenyl group, defined as “vicinal”, which connects the amide and the urea, in the *meta* position to each other. Each of the urea moieties is then further connected to a second “distal” phenyl ring. The four ligands differ from each other by the substituent groups on the distal phenyl ring. Their design was inspired by previous tripodal molecules **81**, **82** and **83** developed within the Gunnlaugsson research group and presented in Chapter 1. Ligands **86-89** will be referred in this chapter as the “*meta*-substituted”, as opposed to the “*para*-substituted”, which will refer to the **tmBTA** ligands **81**, **82** and **83**, Figure 1.33. This identification will be used throughout the chapter and refers to the relationship between the substituents on the phenyl ring vicinal to the core, and not to the substituents on the distal one. The tripodal structure and the presence of hydrogen-bonding urea groups, was designed to interact with various anions, with special attention to

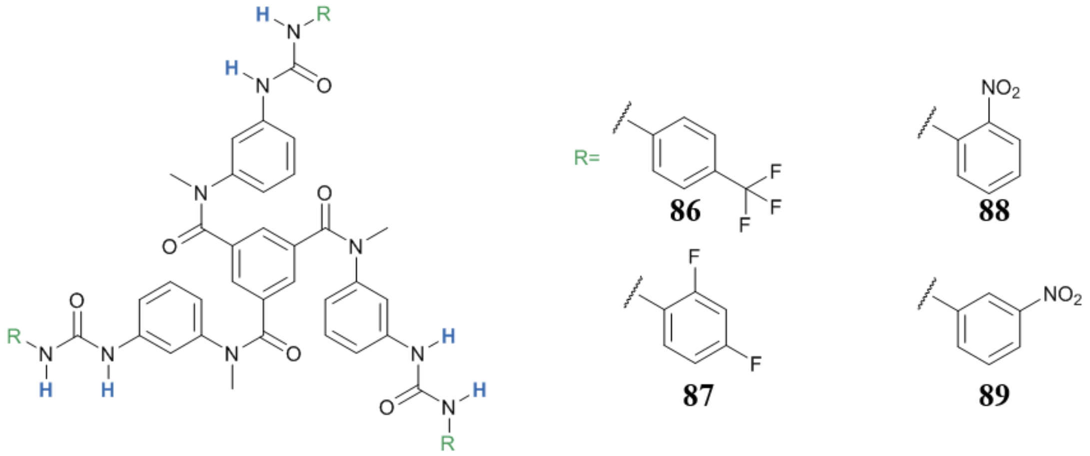

Figure 2.1 Chemical structure of compounds **86**, **87**, **88** and **89**

tetrahedral oxyanions. The choice of electron withdrawing substituents on the distal phenyl rings was made considering their ability to increase the acidity of the urea protons, by either inductive or mesomeric effects. This modification will increase the availability of these protons to engage in hydrogen bonding to anions. In addition to this, the groups were also chosen to be the analogues of the pre-existing families, to allow direct comparisons with them.

2.2. Synthesis and characterisation

The synthesis of **86-89** was achieved in three steps, as showed in Scheme 2.1, starting from the commercially available benzene tricarbonyl trichloride **97**, and *N*-methyl-3-nitroaniline **98**, and by adapting the synthesis of pre-existing family of tripodal ligands. Starting materials **97** and **98** were reacted together under reflux for 48 hrs in CH_3CN, giving the desired intermediate **99** in excellent yield. Upon completion of the reaction, which was monitored by TLC, the solvent was removed *in vacuo* and the obtained oil dissolved in $CHCl_3$. The addition of Et_2O caused the precipitation of the crude product, which was filtered and further purified by trituration under CH_3OH. This gave the intermediate as a pale-yellow powder, consistent with the introduction of the nitro group. The nitro groups of **99** were then reduced to the corresponding aniline using $N_2H_4{\cdot}H_2O$ in EtOH under microwave irradiation for one hour in the presence of 10% Pd/C as a catalyst. The resulting suspension was filtered through

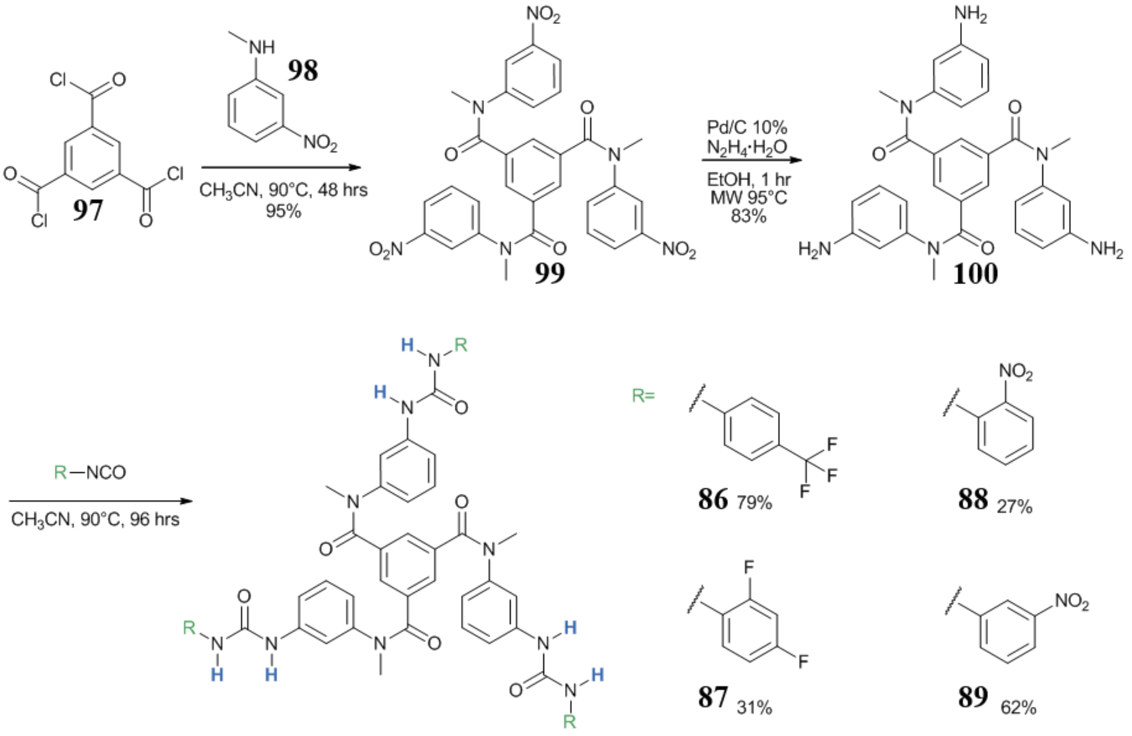

Scheme 2.1 Synthesis of tripodal urea ligands **86-89**.

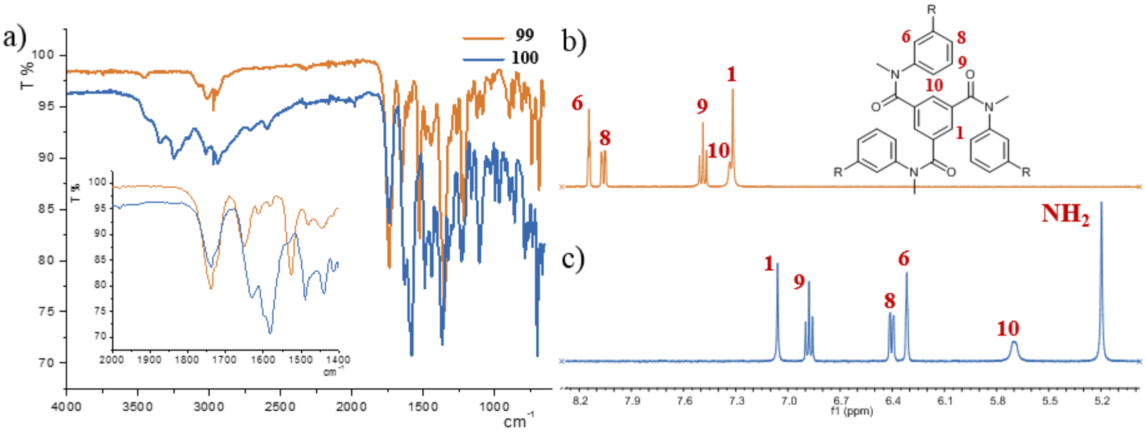

Figure 2.2 Comparison of a) IR spectra of **99** and **100**with expansion (inset). b-c) Comparison of ^{1}H NMR spectra of b) **99** and c) **100**.

celite and washed with a hot mixture of CH_3OH:CH_3CN (1:1). The oil obtained after the removal of solvent under reduced pressure, was dissolved in a 1:1 mixture of $CHCl_3$:CH_3OH and the subsequent addition of Et_2O gave a precipitate, which was further purified by trituration under CH_3OH to give **100** in high purity and in 95% yield. The successful formation of **100** was confirmed by IR, Figure 2.2a, with the disappearance of the bands typical of the NO_2 symmetric and asymmetric stretching (1349, 1525 cm^{-1}) and the appearance at 3348 and 3251 cm^{-1} of two bands corresponding to the NH_2 stretching. The reduction of the nitro group was also evident in the ^{1}H NMR spectrum with the appearance of a sharp singlet at 5.2 ppm, corresponding to the amine group. The changes in the electronics of the aromatic rings from the EWG to EDG, caused a significant shielding in the aromatic protons, Figure 2.2,b. Further confirmation was given by HRMS analysis which showed a peak at m/z = 523.2465 corresponding to the $[M+H]^+$ ion.

The tripodal aniline was next reacted with the relevant phenyl-isocyanates to give the desired tripodal ligands, in moderate to good yields. In all cases, the formation of the phenyl-urea moieties was established by ^{1}H NMR, as is evident in Figure 2.3, with the presence of two sharp resonances characteristic of the urea N–H protons. In addition to this, the presence of new resonances in the aromatic regions, which were absent in the spectrum of **100**, indicated the presence of the new phenyl rings. In all cases, HRMS and ^{13}C NMR spectra confirmed, together with 2D ^{1}H-^{13}C Heteronuclear Single-Quantum Correlation (HSQC), ^{1}H-^{13}C Heteronuclear Multiple Bond Correlation (HMBC), ^{1}H-^{13}C Heteronuclear Single-Quantum Correlation (HSQC) and ^{1}H-^{15}N Heteronuclear Multiple-Quantum Correlation (HMQC) NMR experiments the successful formation of the desired ligands.

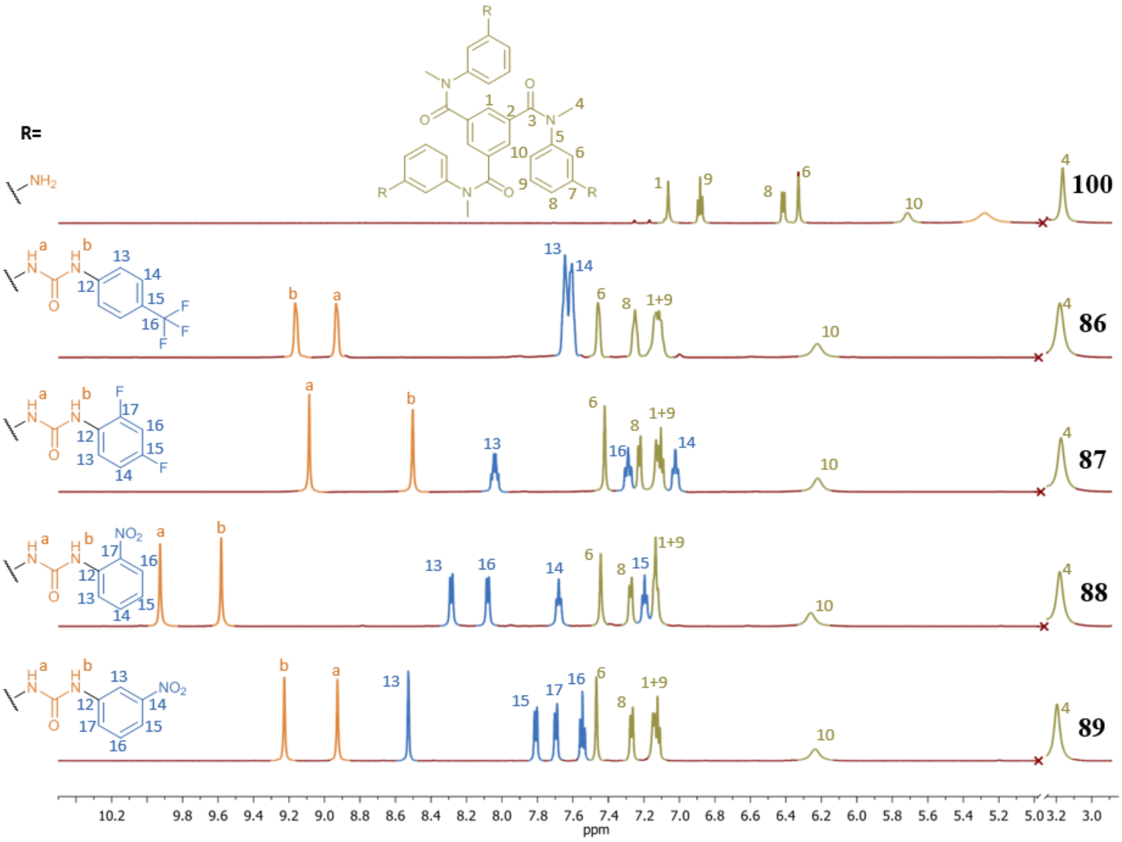

Figure 2.3. Stacked ^{1}H NMR spectra (400-600 MHz, DMSO-d_6, 298 K) of tripodal ligands **86**, **87**, **88** and **89** compared to starting tripodal amine **100**. Featureless regions omitted for clarity.

From the comparison of the ^{1}H NMR spectra, Figure 2.3, it was evident that for all the ligands, the resonances relative to the common central aromatic core (khaki colour) were more deshielded than in **100**, due to the delocalisation of the amine nitrogen lone pair. Upon reaction of the amine to form the urea, this delocalisation was decreased, causing the deshielding of the protons and, consequently, the downfield shifts of these resonances. In all the spectra, one broad resonance was observed at 6.2 ppm in the ^{1}H and at 5.7 ppm for the precursor **100**, unusually shielded for aromatic protons. This resonance, was assigned through 2D NMR (Appendix A2), to the aromatic proton H10, which is in the *para* position to the urea moieties. The reason for this strong shielding was attributed to the conformational arrangement of the **tmBTA** core, which brings those protons close to the central benzene ring. This conformation, was also consistently displayed by different ligands in the solid state and will be discussed in the following section. When compared to the *para*-substituted analogues, previously developed within the Gunnlaugsson Group,[152] marginally higher solubility was observed for ligands **86-89**, which allowed easier purification of these compounds by column chromatography for ligands **86** and **87**. Purification of ligand **88** was obtained by crystallisation from CH_3CN, while **89** was obtained pure by filtration of the reaction mixture, from which it precipitated. The higher solubility, especially for **86**, prevented the growth of crystals suitable for SC-XRD for this ligand, which were otherwise obtained for the *para*-substituted analogue. However, crystals were obtained, by slow evaporation, for ligands **87** and **88** as well as for the intermediate aniline **100** and these results will be discussed in the following section.

2.2.1. Solid-state characterisation of of 100, 87 and 88

Crystalline materials of **100**, **87** and **88** were obtained that were suitable for single crystal X-ray diffraction experiments. These studies provided useful insights into the conformation of these molecules and allowed useful comparisons with the solution studies (*vide infra*). Moreover, from the packing interaction it was possible to obtaine information about the potential self-assembly interactions of the ligands. The X-ray diffraction data in this chapter were collected and refined by Dr Salvador Blasco, Dr Chris Hawes and Dr Miguel Martinez-Calvo, who were all members of the Gunnlaugsson Group at the time. In the following

Table 2.1. Selected dihedral angles of **100**, expressed as the angle between the planes defined by atoms ABC and BCD. For numbering refer to Figure 2.4.

A	B	C	D	θ°
O3	C27	N3	C29	4.3(4)
O2	C14	N5	C28	0.7(4)
O1	C7	N1	C30	1.9(4)
C1	C6	C27	O3	47.0(3)
C5	C4	C14	O2	44.2(4)
C3	C2	C7	O1	34.9(4)
C29	N3	C21	C22	61.1(3)
C28	N5	C15	C20	61.2(3)
C30	N1	C8	C13	66.0(3)

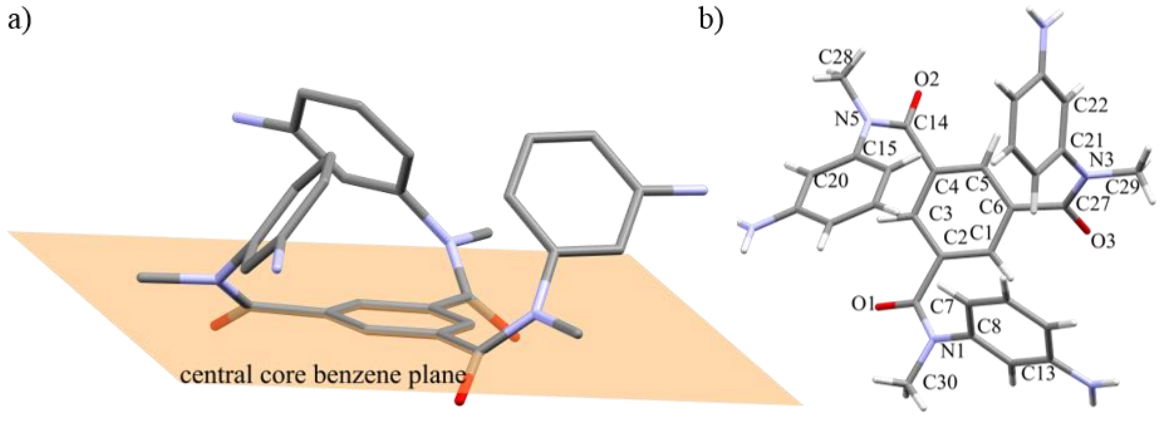

Figure 2.4. a) Crystal structure of **100**. The plane of the central core benzene ring is shown, which highlights the different directions of the amide carbonyls and the arms. Hydrogen atoms are hidden for clarity. b) Capped stick representation of **100** showing hydrogen atoms.

section, these crystal structures are described and discussed, with particular focus to the molecule conformation and the hydrogen bonding interactions.

Single crystals of the aniline precursor **100** were obtained by slow evaporation from a CH_3CN solution.[156] The data were solved and refined in the Monoclinic space group $P2_1/c$ with the asymmetric unit containing one molecule of the ligand. The crystal structure, as shown in Figure 2.4, displayed a *cis* conformation between the carbonyl and the methyl group of the amide with dihedral angles between the *N*-methyl group and the carbonyl of 0.7(4)°, 1.9(4)°and 4.3(4)°, respectively, Table 2.1. This was consistent with previous observation in the *para*-substituted family of ligands, as well as other literature examples.[151,154] In this conformation, the carbonyl groups were twisted out of the plane of the central benzene ring, with angles equal to 34.9(4)°, 44.2(4)° and 47.0(3)°, Table 2.1, while the rest of the arms extend on the opposite side of that plane, Figure 2.4a. The *meta*-amino groups of the phenyl-amide moiety were diverging from the centre of the molecule, Figure 2.4b, with angles between the *N*-methyl groups and the aniline ring between 61.1 – 66.0°, Table 2.1, with the aromatic protons H10, in *para* position to the amine, were lying above the central benzene ring. This conformation, was consistent with the strong shielding of the H10 protons in the ^{1}H NMR discussed above. A similar arrangement of the central core was observed for the crystals of ligands **87** and **88**.

Ligand **87** crystallised by slow evaporation from both solutions of DMSO and CH_3OH and the two sets of crystals showed slightly different conformation of the ligands. While they both displayed similar conformation of the central **tmBTA** to the previously discussed crystal structures, the disposition of the arms presented some different arrangements and hydrogen bonding. Crystals of ligand **87** were obtained by slow evaporation from hot CH_3OH solution. The data were solved and refined formed in the triclinic space group $P\bar{1}$, with two solvent molecules and one of ligand in the asymmetric

Table 2.2. Hydrogen bond lengths [Å] and angles [°] for the structure of **87** obtained from CH_3OH.

D–H···A	**d(D–H)**	**d(H···A)**	**d(D···A)**	**∠(DHA)**
O8–H8D···O6	0.84	1.95	2.746(5)	158.3
N2–H2A···O8	0.88	2.04	2.868(4)	156.4
N3–H3···O8	0.88	2.13	2.941(5)	153.7
N9–H9···O3	0.88	2.08	2.869(5)	148.8
N8–H8···O3	0.88	1.95	2.782(5)	158.2
O7–H7···O1	0.84	1.80	2.623(5)	168.2
N6–H6A···O7	0.88	2.03	2.888(6)	164.6

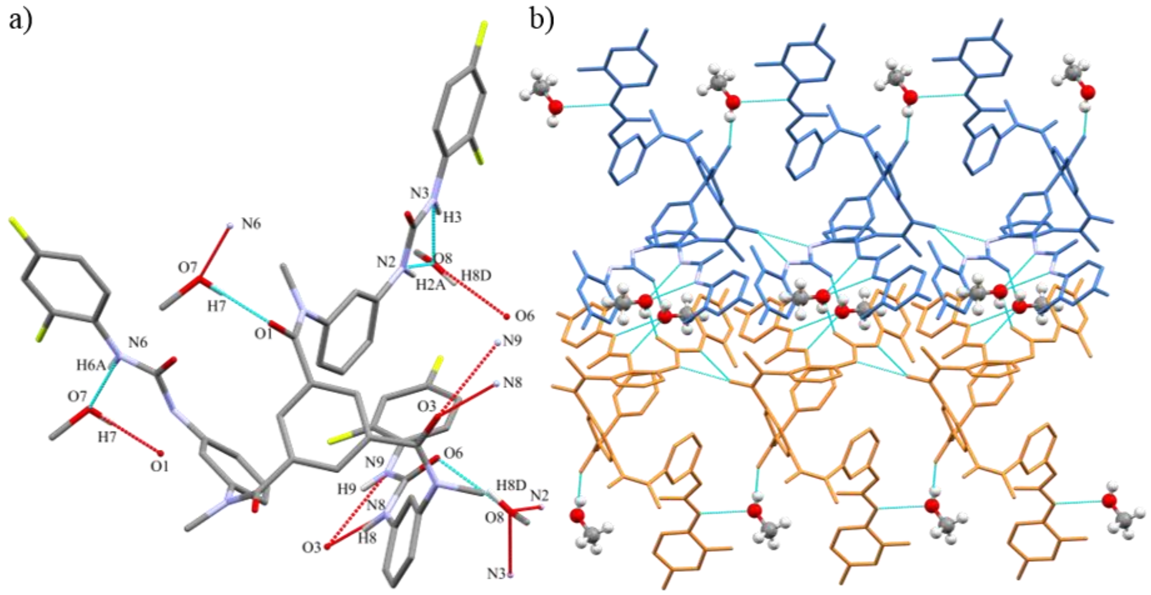

Figure 2.5. Crystal structure of **87** obtained from MeOH. a) Capped stick representation showing intermolecular hydrogen bonding; solvent molecules and hydrogen atoms involved into H-bonds are shown. b) Capped stick representation showing intermolecular hydrogen bonding network including solvent molecules, hydrogen atoms on ligands removed for clarity.

unit. The solvent molecules, in this case, showed hydrogen bonding to ligand **87**, Figure 2.5, in two distinct modes. One CH_3OH molecule was bridged between ligands by accepting a hydrogen bond on the oxygen atom O7 from a single urea NH donor, with a donor-acceptor distance N6···O7 measuring 2.888(6) Å. The same solvent molecule donated a hydrogen bond form O7 to the carbonyl oxygen O1 on the adjacent ligand, with O7–H7···O1 = 2.623(5) Å. A second solvent molecule was bound directly to another urea *via* a bifurcated hydrogen bond from N2 and N3 to the O8 of the CH_3OH. The same solvent molecule also bridged adjacent ligands through a H-bond donation from the hydroxyl group O8–H8D to the urea oxygen O6 of the third urea moiety, which was not directly donating to solvent (O8–H8D···O6 = 2.746(5) Å). This urea group was further engaged in a bifurcated intermolecular bridging interaction with an amide carbonyl on the neighbouring ligand with bonds N9–H9···O3= 2.869(5) Å and N8–H8···O3= 2.782(5) Å. These strong interactions with the solvent affected the packing and the conformation of the molecule, which displayed the three arms in three different twist arrangements. The arm which formed the bifurcated bond with CH_3OH showed the two rings of diphenylurea moiety to be essentially coplanar, with the urea (*ca*.12° offset from the phenyl rings plane). The urea of the second arm donates one NH proton to CH_3OH, and in this case only the distal phenyl ring was coplanar (8.8° torsion angle) with the urea carbonyl, while the vicinal phenyl ring was offset by 45.4°. The third arm is the most twisted, showing a torsion angle of 25.9° between the distal phenyl ring and the urea carbonyl, and 26.9° between the urea carbonyl and the central phenyl ring.

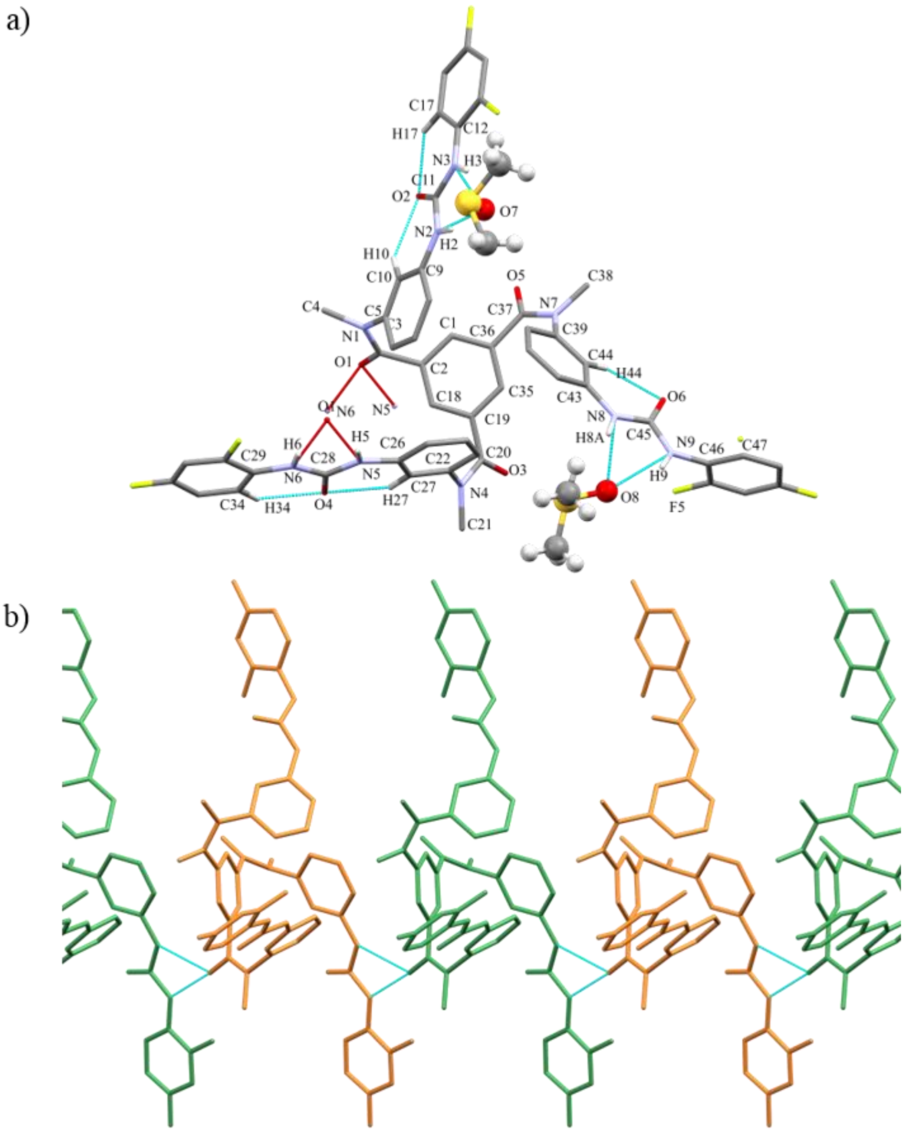

Figure 2.6. Crystal structure of **87** obtained from DMSO. Capped stick representation showing a) intermolecular hydrogen bonding (solvent molecules and hydrogens involved into H-bonds are shown); b) intermolecular hydrogen bonding network, hydrogen atoms removed for clarity.

A slightly more symmetric arrangement of the ligand was observed when it crystallised from DMSO solution at RT. In this case, the data were solved and refined in the triclinic $P\bar{1}$ space group, with an asymmetric unit containing one molecule of the ligand and two disordered solvent molecules. It was possible to observe, Figure 2.6a, a conformation of the central core like the one observed for the starting amine **100** with the amide groups and carbonyl on one side of the central benzene plane (dihedral angles between 42.3(7)° and 61.5(6)°, Table 2.3), and the methylamino group, in *cis* orientation with the carbonyl pushed on the opposite side of the plane (torsion angles of 3.1(8)° and 9.0(7)°, Table 2.3). The vicinal ring of the bis-phenylurea displayed similar conformation as seen for **100**, such that the aromatic proton, *para* to the urea, was found on top of the core benzene ring. Also in this

Table 2.3. Selected dihedral angles of **87** (DMSO), expressed as the angle between the planes defined by atoms ABC and BCD. For numbering refer to Figure 2.6.

A	B	C	D	θ
C1	C36	C37	O5	-42.3(7)
C35	C19	C20	O3	-44.4(7)
C18	C2	C3	O1	-61.5(6)
O5	C37	N7	C38	-3.1(8)
O3	C20	N4	C21	-9.0(7)
O1	C3	N1	C4	-3.6(7)
C38	N7	C39	C44	-69.1(6)
C44	C43	C45	O6	18.0(6)
O6	C45	C46	C47	84.0(7)
C21	N4	C22	C27	-69.7(5)
C27	C26	C28	O4	5.9(4)
O4	C28	C29	C34	-3.5(4)
C4	N1	C5	C10	-70.4(6)
C10	C9	C11	O2	-2.4(5)
O2	C11	C12	C17	5.1(5)

case, it can be speculated that a similar conformation is maintained in solution, as the H10 proton was very shielded appearing at 6.2 ppm. The receptor showed an open propeller-like conformation, shown in Figure 2.6, with diverging arms, unlike in the closed capsule formed by the *para*-substituted analogues. The carbonyl group with the largest torsion angle to the central unit was also partaking in a bifurcated hydrogen bondings to the oxygen atom O1, donated by the urea N5–H5 and N6–H6 of a neighbouring **87** molecule. This intermolecular interaction between the urea and the carbonyl groups, which was consistently observed among all of the crystal structures of this set of ligands, formed a 1D network, as clearly visible in Figure 2.6. The other two urea moieties are engaged in interactions with two DMSO molecules through bifurcated N–H···O hydrogen bonds, Table 2.4, reflecting solvation of the potential binding cavity of the receptor. The three distal phenyl rings showed diverse behaviour, with the two arms involved in the intramolecular hydrogen bonding showing a flat conformation, and the phenyl rings almost coplanar with the respective urea carbonyls with dihedral angles smaller than 6°, Table 2.3. The third arm showed a more twisted arrangement, with a smaller torsion angle of 18.0(6)°, between the vicinal ring and the urea carbonyl, and a larger one between the urea and the distal phenyl ring of 84.0(7)°. The coplanar conformation of two of the arms was stabilised by low angle (*ca*. 120º, see Table 2.4) hydrogen bonds between the aromatic CH donors and the oxygen acceptor of the ureas C17–H17 and C10–H10 to O2 on one arm, and C27–H27 and C34–H34 to O4 on the other arm. These interactions stabilised the conformation of 2,4-difluorophenyl moiety which, in principle, could freely rotate. However, only in this conformation the hydrogen in *ortho* position can participate in hydrogen bonding with the urea oxygen.

Table 2.4. Hydrogen bond lengths [Å] and angles [°] for the crystal structure of **87** obtained from DMSO.

D–H···A	d(D–H)	d(H···A)	d(D···A)	∠(DHA)
N6–H6···O1	0.88	2.096	2.933(6)	158.6
N5–H5···O1	0.88	2.168	2.991(6)	155.5
N8–H8A···O8	0.88	2.109	2.928(9)	154.4
N9–H9···O8	0.88	2.264	3.02(1)	144.1
N3–H3···O7	0.88	2.168	2.977(7)	152.6
N2–H2···O7	0.88	1.956	2.811(6)	163.5
C10–H10···O2	0.95	2.256	2.867(7)	121.3
C17–H17···O2	0.95	2.251	2.859(7)	121.0
C27–H27···O4	0.95	2.341	2.934(7)	120.0
C34–H34···O4	0.95	2.317	2.924(7)	121.1
C44–H44···O6	0.95	2.314	2.884(8)	117.9

In the case of the arm with the rotated conformation of the urea, fewer hydrogen bonding interactions than expected between distal phenyl CH and the urea were observed. The best model of the electron density showed that the fluorine and the hydrogen atoms occupy both positions, with 36% of the molecules displaying the rotamer which forms the hydrogen bonding. The non-planar conformation of the third arm is stabilized by intermolecular π-π interactions of the distal phenyl ring, while the vicinal phenyl moiety is directed hydrogen bonding with the urea group. The rotated phenyl ring has a π-π stacking interaction, over a distance of 3.4 Å, which is a face-to-face interaction with a 2,4-difluorophenyl moiety of the distal phenyl ring of a neighbouring molecule of **87**. This 'co-planar' phenyl ring then π-stacks with an equivalent moiety of another neighbouring molecule, by an inversion centre, with a shorter stacking distance of 3.23 Å. The crystal structure of **87** demonstrated clearly the balance of π-π and hydrogen bonding interactions in the behaviour of receptor, indicating and reflecting key interactions of binding site solvation and competition (from self-association) which were investigated for the ligand structures in the solution state (*vide infra*).

In general, in the solid structures of these ligands some general features were observed, which could give some interesting information about the possible behaviour of the ligand in solution. The first was that the conformation of the central benzene of the **tmBTA** core, which was consistent with that described in the literature,[152,154] displaying a *cis* conformation of the methyl group and the amide carbonyl. This conformation of the amide favoured all the proximal phenyl group of the arm to lie on one side of the plane of the core benzene ring, such that the urea groups (or amine in the case of **100**) are diverging from the centre of the molecule and the proton in *para* position to the urea are lying on top of the core

Table 2.5. Selected dihedral angles of **88**, expressed as the angle between the planes defined by atoms ABC and BCD. For numbering refer to Figure 2.7.

A	B	C	D	θ°
O1	C3	N1	C4	4.2(5)
O5	C20	N5	C21	0.4(5)
O9	C38	N9	C39	4.7(5)
C18	C2	C3	O1	59.4(5)
C36	C19	C20	O5	64.2(5)
C1	C37	C38	O9	40.8(5)
O6	C28	C29	C35	-19.9(4)
O10	C46	C47	C52	-25.6(3)
O2	C11	C12	C17	13.8(4)

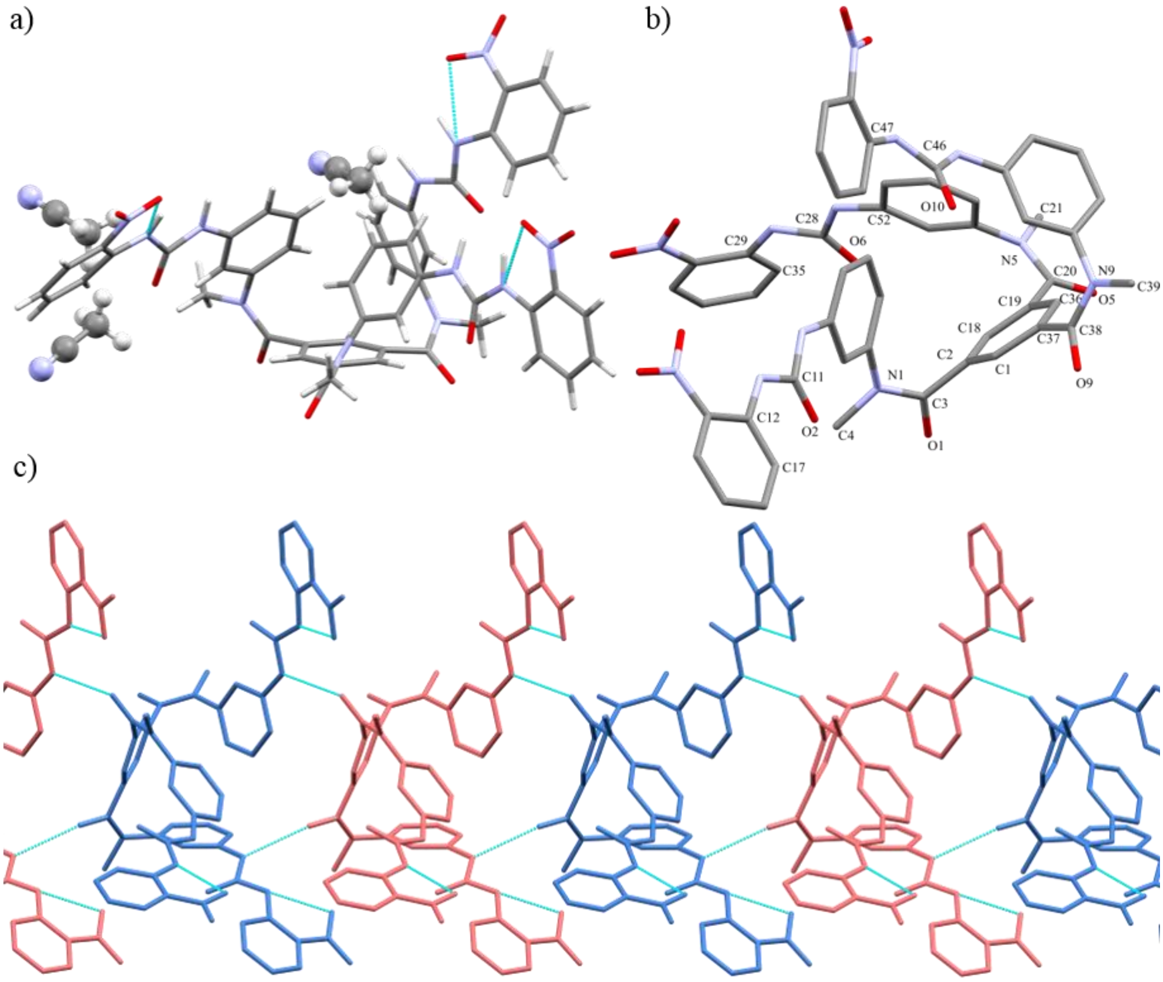

Figure 2.7. Crystal structure of **88**. a) Capped stick representation showing internal hydrogen bonding between the urea and the nitro groups. b) Capped stick representation of a single molecule of **88**, hydrogen atoms and solvent molecules are hidden for clarity. c) Capped stick representation showing intramolecular and intermolecular hydrogen bonding network, hydrogen atoms removed for clarity.

benzene ring. If this conformation was retained in solution, this could explain the strong shielding of this proton which was observed in the ^{1}H NMR for all the ligands and the starting material.

Also, the divergent urea groups might suggest that to act as a tripodal chelating ligand (surrounding one anion with all three arms) would require a conformational rearrangement. Such an additional process would add a thermodynamic penalty to binding in 1:1 and 2:1 (L:A) stoichiometries. The overall binding energy is perhaps maximised in the 'open' conformation, which favours other stoichiometries such as 1:3 (L:A), with three binding events being preferable to a single chelation.

In the solid-state structure of **88** the solvent molecules were not interacting with the binding moiety. While for **87** the solvent was hydrogen bonded to the urea or amide groups, as would be expected for protic and polar solvents, such as CH_3OH and DMSO. This indicated that these interactions with the solvents were likely to happen also in solution, creating additional competition for the binding site by adding desolvation energy to the binding process, which, again, could affect negatively the binding process.[157,158] In all ligands crystal structures, the urea moieties showed hydrogen bonding interactions with amide carbonyls of neighbouring molecules. For **BTA** ligands it is common, in the solid state to observe hydrogen bonding interactions between the amide groups of neighbouring molecules, with the amides functioning, at the same time, as donor and acceptors. This interaction is often responsible for classical **BTA** self-assembly properties in solutions and in the formation of soft materials. In this set of **tmBTA** ligands, while the amide could not function as hydrogen donor, the presence of urea moieties allowed the formation of this alternative hydrogen bonding interaction. This interaction, could also potentially give rise to the self-assembly of the ligands in solution, which could create even additional competition with anions to the binding site, which will be discussed in the next sections.

A crystal structure of **88** was also obtained, Figure 2.7, by slow evaporation from a CH_3CN solution. The data were solved and refined in the triclinic space group $P\overline{1}$, with an asymmetric unit containing one ligand molecule and three solvent molecules. The crystal packing was directed by a range of different interactions: π-π stacking, intermolecular hydrogen bonds and CH-π bonds being the major interactions. The central **tmBTA** moiety was again in a conformation with all three amidic carbonyl units tilted out-of-plane of the central ring with dihedral angles of 59.4(5)°, 64.2(5)°, and 40.8(5)°, Table 2.5. The torsion angles between the carbonyl and the *N*-methyl groups in this case were equal to 4.2°, 0.4°

and 4.7°, Table 2.5, showing a *cis* conformation, consistent with the structure of the precursor **100**. Similarly to what was observed for similar *ortho*-nitrophenyl urea structures,[152,159,160] there were intramolecular hydrogen bonds between the NO_2-substituted distal phenyl ring and urea NHs, Figure 2.7c. These interactions left only one of the urea hydrogens available for the formation of intermolecular hydrogen bonding, between N6–H6···O1 and N10–H10···O9, to the amide groups of neighbouring molecules. Concomitantly, two of the three amide oxygen atoms were receiving one hydrogen bond from neighbouring molecules, Figure 2.7c. In each molecule, therefore, one amide oxygen and one urea, from different arms, did not strongly interact. This feature ultimately forms a twisted 1D network, which propagates along the crystallographic *a* axis, Figure 2.7c. The conformation of the distal nitro-phenyl urea moieties was slightly rotated from the plane of the urea carbonyl, with the phenyl ring rotated by 13.8°, 19.9° and 25.6°, Table 2.5. This twist in urea conformation was smaller than the one observed in the crystal structure of its *para*-substituted analogue **82**. Additional π-stacking interactions were observed, with each individual molecule relating with two neighbouring molecules through two different π-stacking interactions involving two of the three nitro-phenyl moieties. This stacking was related through an inversion centre with two stacking distances of 3.28 Å and 3.40 Å, Appendix Figure A2.74.

From the above analysis it was clear that the ligands could interact with anions through a different overall mode / mechanism to that observed for the *para*-susbstituted family and therefore it was worth investigating. The ‘open’ conformation of the ligand with diverging binding sites could provide an interesting platform for different types of ATSA. In particular, the formation of interconnected networks templated by anions was investigated. Prior to this, the anion binding abilities of these **tmBTA** ligands were tested and the results will be presented and discussed in the next section.

2.3. Anion binding studies

The anion binding abilities of ligands **86-89** were probed by using UV-vis and ^1H NMR spectroscopy. The UV-vis absorption spectroscopy was carried out in CH_3CN solution for ligands **86**, **87** and **88**, while for **89** they were carried out in a CH_3CN:DMSO (99.7:0.03) mixture because of the poor solubility of the ligand in CH_3CN. In order to screen a diverse range of anion geometries, sizes and desolvation energies, titrations were carried out with four different anions: Cl^-, CH_3COO^-, $H_2PO_4^-$ and SO_4^{2-}, all as tetrabutylammonium (TBA) salts. Attempts to study the binding process in a more competitive solvent like DMSO were not successful due to the UV cut-off of this solvent (268 nm) which would exclude most part of the aromatic absorption band and prevented the collection of meaningful spectra. Preliminary solubility studies also excluded the possibility of studies being carried out in mixed aqueous solvent, as precipitation of the ligands would occur. UV-vis absorption spectroscopy studies were carried out at a concentration between 5-7 × 10^{-6} M, after verification of linearity according with the Beer-Lambert law. Binding studies of the ligands were also carried out by ^{1}H NMR titrations, with the same anions, in DMSO-d_6 solution. Due to the poor solubility of ligands **87**, **88** and **89** at higher concentrations (1-7 × 10^{-3} M), ^{1}H NMR titrations could not be carried out in CD_3CN, while for **86**, it was possible to study the binding in CD_3CN. This allowed for a direct comparison to the UV-vis absorption titration results. The outcomes of all these binding studies will be presented in the following sections.

2.3.1. UV-vis absorption binding studies

Anion binding studies with ligands **86-88** were carried out and reported previously [156] and, therefore, will only be briefly discussed alongside the recent studies on ligand **4**. The absorption spectra of ligands **86-88** were collected in CH_3CN solutions and are shown in Figure 2.8, while in Table 2.6 the main features are summarised.

The UV-vis absorption spectrum of ligand **86** displayed a main band with a λ_{max} = 263 nm (ε = 78 × 10^3 cm^{-1} M^{-1}) assigned to the $\pi\rightarrow\pi^*$ transition of the central core, while the urea $n\rightarrow\pi^*$ transition appeared at higher energy and only the shoulder was visible at λ > 200 nm. Similarly, ligand **87** showed a band relative to the $\pi\rightarrow\pi^*$ transition with λ_{max} =

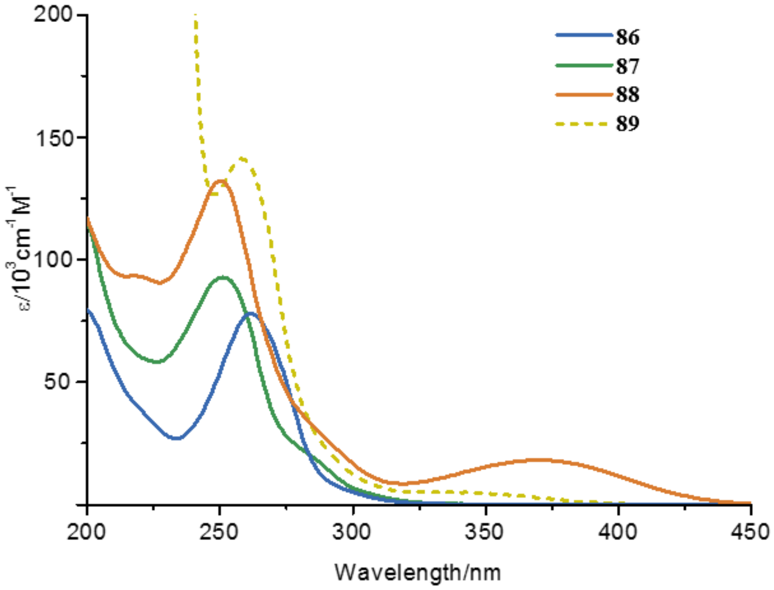

Figure 2.8. UV-vis absorbance spectra of ligands **86**, **87** and **88** (solid lines) were collected in CH_3CN, while spectrum of ligand **89** (dashed line) was collected in CH_3CN:DMSO (99.97:0.03) mixture.

Table 2.6. UV-vis absorption photophysical paramenters for ligands **86**-**89**.

Ligand	Solvent	Substituent phenylurea	λ_{max} (nm)	ε ($10^3 cm^{-1} M^{-1}$)	Transition
86	*CH_3CN*	*p*-CF_3	263	78	$\pi \rightarrow \pi^*$
87	*CH_3CN*	*o*-F, *p*-F	251	93	$\pi \rightarrow \pi^*$
88	*CH_3CN*	*o*-NO_2	218	90	$\pi \rightarrow \pi^*$
			251	130	$\pi \rightarrow \pi^*$
			372	18	$n \rightarrow \pi^*$
89	*CH_3CN:DMSO (99.7:0.03)*	*m*-NO_2	258	145	$\pi \rightarrow \pi^*$
			347	5	$n \rightarrow \pi^*$

251 nm (ε = 93 × 10^3 cm^{-1} M^{-1}) and a second band at higher wavelength. The UV-vis absorption spectrum of ligand **88**, was characterised by three main bands, two in the UV region of the spectrum, with λ_{max} = 218 nm and λ_{max} = 251 nm (ε = 90 × 10^3 cm^{-1} M^{-1} and ε = 130 × 10^3 cm^{-1} M^{-1}, respectively) and one in the visible region, corresponding to the n→ π* transition of the nitro group, with λ_{max} = 372 nm (ε = 18 × 10^3 cm^{-1} M^{-1}). However, in general, for these ligands only, small changes were observed upon addition of the anions and the presence of different isosbestic points indicated the existence of multiple pairs of correlated species in solution, an indication of a complicated binding equilibrium.[161] A representative titration profile and binding isotherm for **86** with $H_2PO_4^-$ is shown in Figure 2.9a, along with the corresponding fitted isotherm plot (Figure 2.9b) and speciation distribution diagram (Figure 2.9b, inset) obtained from the global non-linear regression analysis. Despite the small changes in the absorption, the reproducible data obtained were fitted using a non-linear regression analysis software (SPECFIT)[162], to elucidate the binding modes. This software employs global analysis, which fits each isotherm simultaneously, reflecting, therefore the overall changes in the spectrum. The fitting process requires the input of some hypothetic formation constants, estimating the concentration profiles. The fitting process then refines these values providing the closest model (*i.e.* a weighted average of model components with the smallest overall residual error) that reflects the data. Different binding modes, were used to try and obtain a good fitting of the data. First of all, it was tested whether a simple model of a 1:1 binding would suit, but in all cases, despite the convergence of the data, the fitted curve would not reflect the changes in the data. Therefore, the addition of other species to the model was attempted, beginning from the binding model of the *para*-substituted family (including 1:1 and 1:2) to test its suitability, however with negative results, due to the non-convergence of the calculation. The best fitting, which could be also

chemically rationalised, was obtained using 1:1 and 1:3 model in most of the anion interactions. In most cases, the fitting of the three-species model (*i.e.* 1:1, 1:2 and 1:3) would not allow the convergence of the data. In some exceptions, however, the 1:2 calculated constant would be significantly smaller than the other two. Considering that the fitting program is applying a mathematical tool to the changes and is not directly observing the binding process, adding species to the model, could easily lead to overfitting of the data, without necessarily describing the process correctly. Moreover, it is important to note that the changes observed in the absorbance only reflect the presence of persistent species in solution. Having said this, it would be unreasonable to think that the 1:2 species does not form at all in solution, but it could simply be a transient, non-persistent species, or a persistent complex of negligible mole fraction. The stoichiometry 1:1 and 1:3 was chemically rationalised as a chelating effect of the three urea arms in the 1:1 complex and independent interaction of each urea with a single anion for 1:3 complex. This would be consistent with an obvious driving force of a chelating effect, favouring the formation of a 1:1 complex over 1:2 in the presence of lower stoichiometric equivalents of the anions. In contrast, at higher equivalents of the anions, it is possible that the receptors favour saturation of the urea binding sites if there are favourable enthalpic contributions from three-fold binding in balance with conformational rearrangement with entropic losses. While not available during this study, these thermodynamic parameters could potentially be elucidated by calorimetry (*e.g.* isothermal titration calorimetry). The experimental binding constants obtained (shown in Table 2.8) were quite high in comparison with other similar ligands[151,152] and this was in contrast with the small changes observed, in particular for SO_4^{2-}.

However, the values observed were comparable to those obtained for the linear single arm analogues of the tripodal molecule studied in the past that were used as models for comparison, Table 2.7.[153] In contrast, the tripodal analogues only showed binding of a single anion for each urea moiety, likely due to both electrostatic repulsion and steric exclusion, which prevented multiple guests to bind to the ligand. The binding model considered took into account the possibility of conformational changes between the binding with one anion

Table 2.7. Binding constants for ligands **81**-**83** obtained from NMR titrations. in DMSO (M^{-1}). From ref 152.

Ligand	**Cl^-**		**CH_3COO^-**		**$H_2PO_4^-$**		**SO_4^{2-}**	
	$K_{1:1}$	**$K_{2:1}$**	**$K_{1:1}$**	**$K_{2:1}$**	**$K_{1:1}$**	**$K_{2:1}$**	**$K_{1:1}$**	**$K_{2:1}$**
81	5.0×10^1	-	6.3×10^2	2.0×10^3	-	-	6.3×10^1	1.0×10^3
82	3.0×10^1	6.3×10^2	2.5×10^2	4.0×10^3	-	-	1.0×10^2	1.0×10^3
83	1.0×10^3	1×10^3	5.0×10^2	1.2×10^3	-	-	1.0×10^2	1.0×10^3

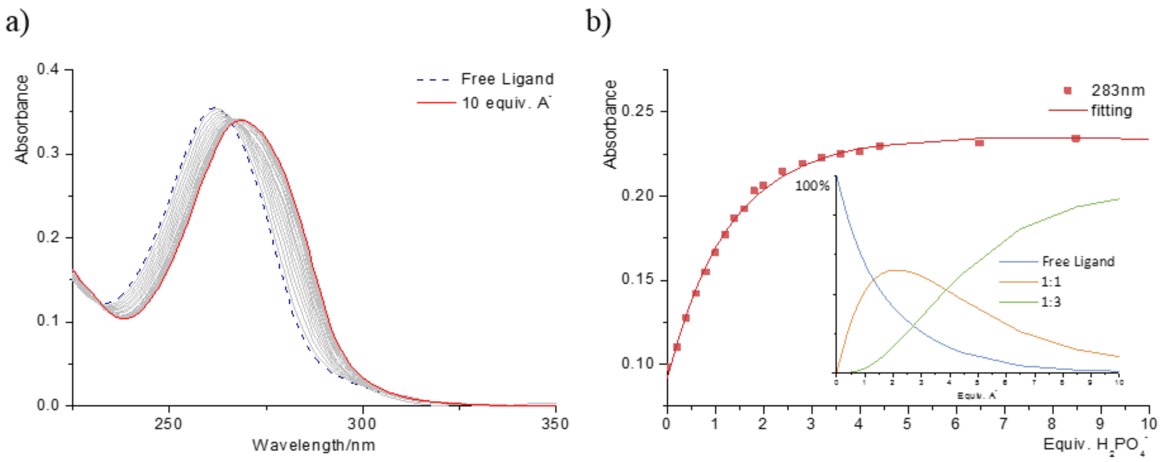

Figure 2.9. a) Changes in the absorption spectra of ligand **86** during the titration up to addition of 10 equiv. of $H_2PO_4^-$; b) binding isotherm of the UV-vis titration of **86** with $H_2PO_4^-$ showing data (points) and fitted model (line); (inset) speciation distribution diagram obtained through global non-linear regression analysis of the data.

and three, from a closed, bowl-shaped conformation, to the open propeller-like one. The fact that different ligands with different substituents showed very similar binding constants, could indicate a common conformational rearrangement between the two species, which would affect the hydrogen bonding differently.

After this analysis the development of ligand **89** was carried out to understand whether the different substitution of the nitro group, compared to **88**, would affect the ligand binding abilities. In fact, the internal hydrogen bonding observed in the solid state, was likely to exist also in solution, and could affect negatively its binding abilities. The change in the substitution pattern, from *ortho* to *meta* could avoid this from happening, while retaining the nitro group EWD effect. The absorption spectrum of the free ligand **89**, in CH_3CN:DMSO solution (99.7:0.03) at $c = 5 \times 10^{-6}$ M displayed a broad band at high energy (λ_{max} = 258 nm,

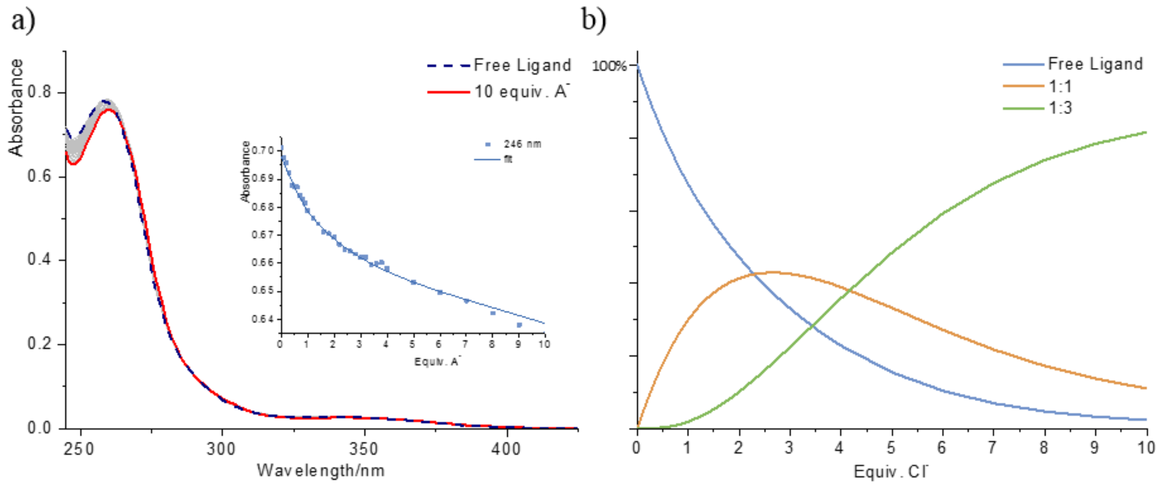

Figure 2.10. a) Changes in the absorption spectra of ligand **89** during the titration with Cl^- (CH_3CN:DMSO, 99.7:0.03) up to addition of 10 equiv. of Cl^-; inset) binding isotherm at 246 nm from the UV-vis titration of **89** with Cl^- showing data (points) and fitted model (line); b) speciation distribution diagram obtained through global non-linear regression analysis of the data. This titration is representative of reproducible trends.

ε ≈ 145 × 10^3 $cm^{-1}M^{-1}$) for the BTA core and a weaker band at λ_{max} = 347 nm (ε ≈ 5 × 10^3 $cm^{-1}M^{-1}$) due to the internal charge transfer to the nitro group, Figure 2.10a. This was consistent with the spectra of ligands **86-88**, whose profiles and main features are collected in Figure 2.8. The overall changes observed in the absorption spectrum of **89**, upon titration with Cl^-, can be observed in Figure 2.10a, and showed a small redshift in the main absorption band, while almost no change could be detected in the nitro band at 350 nm.

The non-linear regression fitting of the changes in the UV-vis spectrum agreed to the same binding model as the other ligands, showing the formation of two main species, 1:1 and 1:3 (L:A), Figure 2.10b, with constants of $K_{1:1} = 1.3 \times 10^5$ M^{-1} and $K_{1:3} = 6.3 \times 10^9$ M^{-1}. This showed that, also for this ligand, an apparent discordance between the small changes and the high binding constant was obtained, with values consistent to the other ligands for this anion.

The titration of ligand **89** with CH_3COO^- also resulted in a redshift of the 264 nm band, after addition of 10 equivalents of anion, as well as a smaller redshift of the long wavelength band to 351 nm (Figure 2.11a). The same binding equilibrium as before was employed when fitting the data, with similar binding constants being observed as for **86-88**, $K_{1:1} = 7.9 \times 10^5$ M^{-1} and $K_{1:3} = 2.5 \times 10^5$ M^{-1}. From the speciation distribution diagram, Figure 2.11b, it can be seen that the 1:1 species was only formed in a very low yield, with the 1:3 species being the main component after the addition of 4 equivalents of anion. This behaviour could be justified by the interaction of one anion with each of the urea moieties. A geometrical complementarity favours the arrangement of the CH_3COO^- anion as a

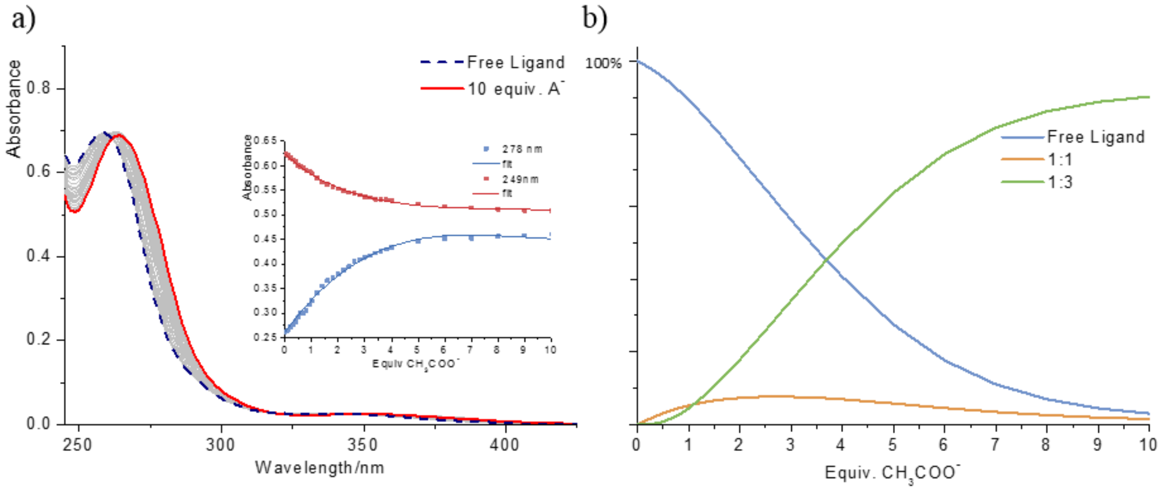

Figure 2.11. a) Changes in the absorption spectra of ligand **89** during the titration with CH_3COO^- (CH_3CN:DMSO, 99.7:0.03) up to addition of 10 equiv. of CH_3COO^-; inset) binding isotherms at 249 nm and 278 nm from the UV-vis titration of **89** with CH_3COO^- showing data (points) and fitted model (line); b) speciation distribution diagram obtained through global non-linear regression analysis of the data. This titration is representative of reproducible trends.

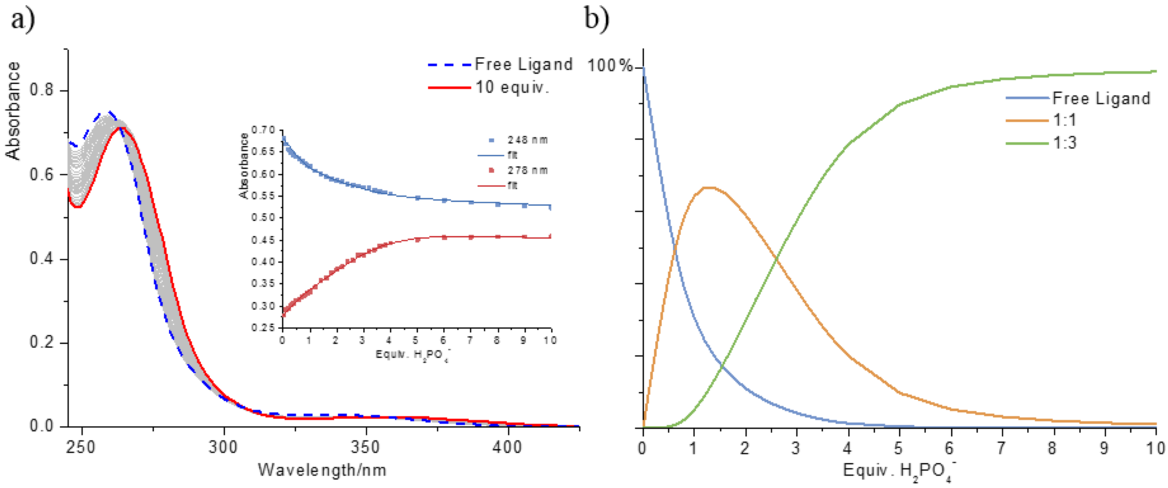

Figure 2.12. a) Changes in the absorption **89** during the titration with $H_2PO_4^-$ (CH_3CN:DMSO, 99.7:0.03) up to addition of 10 equiv. of $H_2PO_4^-$; inset) binding isotherms at 248 nm and 278 nm from the UV-vis titration of **89** with $H_2PO_4^-$ showing data (points) and fitted model (line); b) speciation distribution diagram obtained through global non-linear regression analysis of the data. This titration is representative of reproducible trends.

bidentate hydrogen bond acceptor through the carboxylate moiety.[163] This could favour the binding of three anions with the three arms of the ligand, over the chelation with the three arms of the ligand on the same anion.

In contrast to these results, the addition of $H_2PO_4^-$ caused a significant redshift in the main absorption band, which was accompanied by a hypochromic shift, Figure 2.12a. The changes reached a plateau after the addition of 3 equivalents of anion (Figure 2.12a, inset). As above, it was possible to fit the experimental data to the same binding model. In this case, the 1:1 species was found to be the major component between 1→3 equivalents of $H_2PO_4^-$, showing a strong interaction with the ligand, probably due to their geometrical complementarity. On the contrary to what was seen for CH_3COO^-, $H_2PO_4^-$ partakes in multiple hydrogen bondings interactions. However, at higher concentrations of anion, a potential rearrangement of its arms into a more open conformation, seemed to favour the formation of 1:3 adducts, with one anion bound per urea moiety of the ligand. However, the formation of the 1:3 complex would not be favoured by electrostatic repulsion of the anions and through this study alone the formation of such complex could not be confirmed.

The titration of ligand **89** with SO_4^{2-} also similar trends as above, Figure 2.13a. However, the shape of the binding isotherm, was different from the others, with a rapid change being seen up to the addition of 0.5 equivalents of SO_4^{2-}. Therefore, a slower change between 0.5→10 equivalents, Figure 2.13b. This behaviour suggested the formation of 2:1 (L:A) bundles, similar to the capsule formed by the *para*-phenylurea substituted analogues, **82** and **81**. Unfortunately, a reliable fitting with this or any other binding models could not be obtained, and, consequently, it was not possible to confirm this hypothesis.

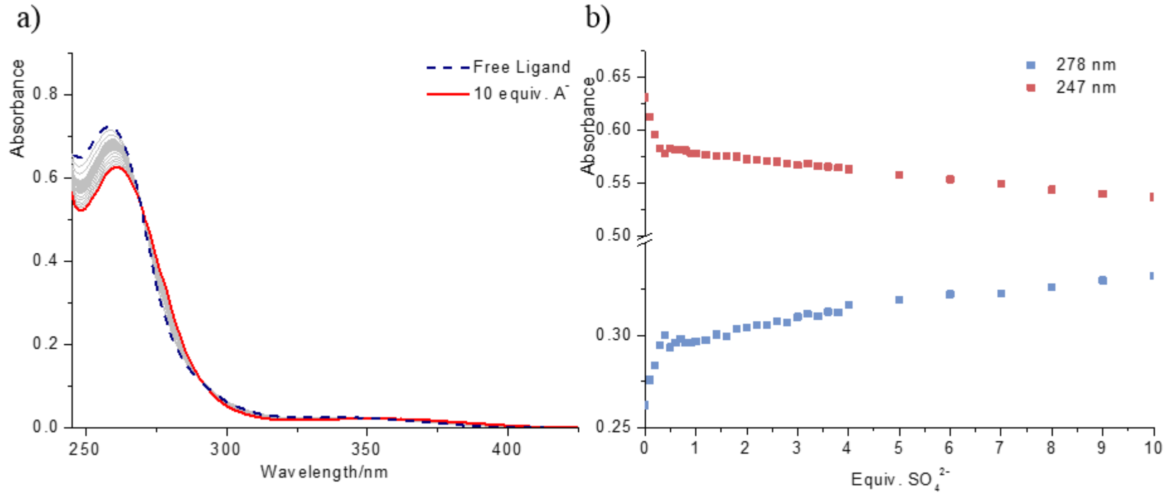

Figure 2.13. a) Changes in the absorption spectra of ligand **89** during the titration with SO_4^{2-} (CH_3CN:DMSO, 99.7:0.03) up to addition of 10 equiv. of SO_4^{2-}; b) binding isotherm at 247 nm and 278 nm from of the UV-vis titration of **89** with SO_4^{2-}. This titration is representative of reproducible trends.

Ligand **89** displayed a binding behaviour consistent with the other analogue ligands, **86-87**, with the exception of the interaction with SO_4^{2-}, which showed the possibility of the formation of 2:1 (L:A) capsule. The binding constants obtained from the UV-vis titrations of ligands **86**, **88**, **87** and **89** are collected in Table 2.8. The calculated binding constants were derived from the fitting of the reproducible behaviour of each receptor, assuming that the change in UV-vis spectrum accounted for the binding due to the urea site, but if conformational changes caused modifications of the electronic environment of the chromophore, the constants would reflect both H-bonding and conformational change. This could account for the high binding constants obtained. However, the changes observed in the UV-vis absorption spectra were very small, in contrast with the large values obtained for the binding constants. Therefore, the binding constants obtained from UV-vis titrations could not alone reliably describe the ligand-anion binding at the urea moiety. To study the interactions of the anion with the urea protons, ^{1}H NMR titrations studies were carried out and will be presented in the next section.

Table 2.8. Stability constants for ligands **86-89** obtained from UV-vis absorption titrations [M^{-1}]. ^{a}Titration in CH_3CN; ^{b}Titration in CH_3CN:DMSO; ^{c} data could not be fitted to any of the chosen binding models. Errors are estimated within 10%.

Ligand	**Cl^-**		**CH_3COO^-**		**$H_2PO_4^-$**		**SO_4^{2-}**	
	$K_{1:1}$	**$K_{1:3}$**	**$K_{1:1}$**	**$K_{1:3}$**	**$K_{1:1}$**	**$K_{1:3}$**	**$K_{1:1}$**	**$K_{1:3}$**
86^{a}	1.6×10^{5}	7.9×10^{6}	4.0×10^{5}	6.3×10^{6}	4.0×10^{5}	2.0×10^{6}	2.0×10^{6}	2.0×10^{9}
87^{a}	3.1×10^{4}	5.0×10^{5}	3.1×10^{5}	6.3×10^{8}	–^{c}	–^{c}	5.0×10^{3}	3.2×10^{5}
88^{a}	2.0×10^{4}	1.0×10^{7}	1.3×10^{5}	2.5×10^{6}	–^{c}	–^{c}	5.0×10^{4}	1.6×10^{8}
89^{b}	1.3×10^{5}	6.3×10^{9}	7.9×10^{5}	2.5×10^{5}	2.0×10^{6}	7.9×10^{10}	–^{c}	–^{c}

2.3.2. ^{1}H NMR anion binding studies

The UV-vis spectroscopy studies highlighted the formation of strong interactions between ligands **86-89** with anions of different geometries and size, with no particular selection trends. In most cases, with few exceptions, the ligands showed the ability to form a 1:1 (L:A) complex at lower concentrations of added anion, while, at higher concentrations, a 1:3 (L:A) stoichiometry was favoured, with the ligand binding three anions, one per binding unit. Binding studies using ^{1}H NMR spectroscopy were carried out to verify that this interaction between the ligand and the anions was due to the formation of direct hydrogen bonding, and to determine the binding constant, using a different technique, to compare with the results obtained from UV-vis absorption measurements. The ^{1}H NMR studies were carried out for all ligands in DMSO-*d*$_6$, which is a highly polar competitive solvent. The same solvent could not be used for UV-vis absorption titrations due to high solvent cut-off, while the use of CD_3CN for ^{1}H NMR titration was prevented by low solubility of compounds **87**-**89**, making the comparison between the two techniques complicated. For ligand **86**, instead, titrations were also carried out in CD_3CN, thanks to the higher solubility of the ligand, which allowed a more direct comparison with the results of the UV-vis absorption titrations. However, the different working concentrations of the two techniques, *ca.* 5×10^{-6} M for UV-vis and *ca.* 5×10^{-3} M for ^{1}H NMR titrations, caused some dissimilarities in the values of the binding constants, due to the self-assembly properties of the ligands. This self-assembly behaviour will be thoroughly discussed between this section and Section 2.4. Full 2D NMR characterisation was carried out on the ligands, in order to identify the individual resonances unambiguously, and to be able to follow them during the titrations. Identification of the resonances is reported in Figure 2.3. Titrations of ligands **86-89**, with Cl^-, CH_3COO^-, $H_2PO_4^-$ and SO_4^{2-}, are reported in the next few sections.

2.3.2.1. Binding properties of ligands 86-89 with Cl^- in DMSO-*d*$_6$

The first anion tested was Cl^-. The UV-vis absorption analysis showed the formation two species of Cl^- complexes, 1:1 and 1:3, in CH_3CN or CH_3CN:DMSO (99.7:0.03). In the case of ligands **86**-**89**, we envisaged that a ‘closed-cup’ conformation would have been necessary to form 1:1 binding with the ligands, with convergent urea protons, in contrast with the ‘open propeller-like’ conformation of the ligands. To investigate the possibility of forming this 1:1 complex, a DFT calculation of the binding of **87** with Cl^- in DMSO was carried out in collaboration with Dr Bjørn La cour Poulsen, based on the crystal structure of the ligand, Figure 2.14. This was stabilised in a 1:1 bundle with the ligand arranged in a ‘closed-cup’ conformation, Figure 2.14a, with the three urea moieties converging and binding to the

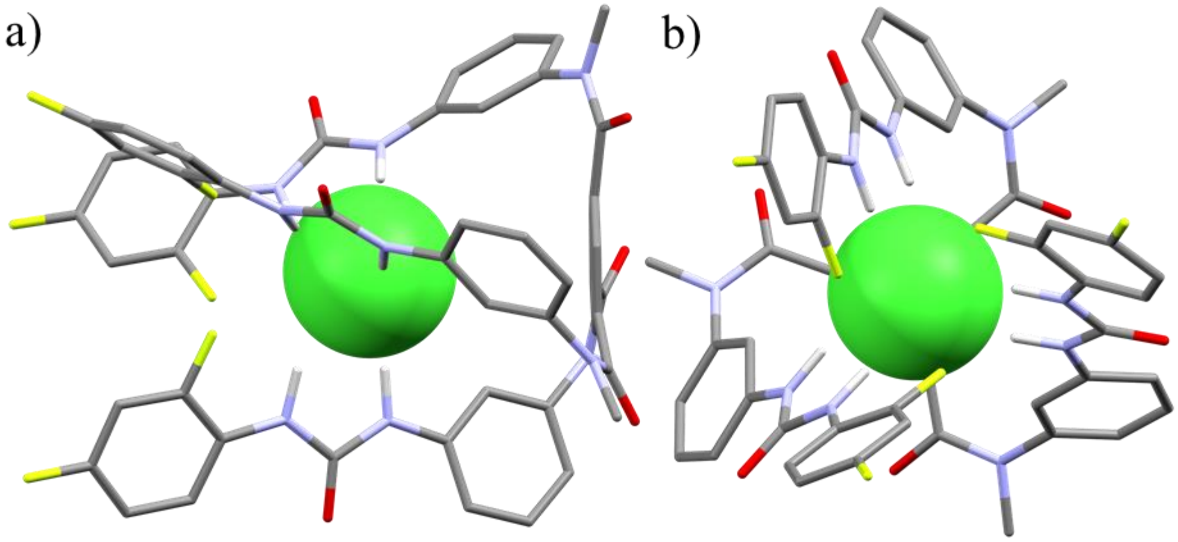

Figure 2.14. DFT calculated structures of 1:1 bundles of **87**·Cl$^-$ in DMSO. The complex **87**·Cl$^-$ wa modelled using the structural data of the crystal structure of **87** by Dr Bjørn la Cour Poulsen. Non-urea protons not shown for clarity.

anion, Figure 2.14b. This initial theoretical result showed the potential ability of this set of ligands of rearranging the free ‘open propeller-like’ conformation into a ‘closed-cup’ upon binding with Cl$^-$. In addition to this, it showed geometrical complementarity of the ligand, hinting to potential effective binding of the anion in a classical 1:1 capsule formation.

Increasing additions of Cl$^-$ to a solution of the *para*-CF_3 substituted ligand **86** caused deshielding of the urea protons Ha and Hb of up to 0.58 ppm and 0.61 ppm, respectively, in the presence of 5 equivalents of Cl$^-$, Figure 2.15, which was indicative of hydrogen bond formation. The gradual shift of the resonances showed that the interaction was occurring in fast exchange for the NMR timescale. Only very small shifts ($\Delta\delta$ =0.01ppm) were observed for the aromatic protons, in particular for H1 and H14, which were weakly shielded, while H13 was deshielded. The resonance shifts were fitted by non-linear regression, and a binding constant for a 1:1 binding mode was obtained as $K_{1:1}$ = 32 M^{-1}. Furthermore, using MALDI-HRMS analysis this binding stoichiometry was confirmed, showing the presence of [M + Cl]$^-$ species corresponding to *m/z* = 1118.2808 with an isotopic distribution pattern matching that of the calculated one, Figure 2.16a-b.

Similarly, the titration of the 2,4-difluoro substituted ligand **87** with Cl$^-$ is shown in Figure 2.17. Here, the titration resulted in the deshielding of the urea protons and only minor changes in the aromatic resonances were observed. In this case, a different interaction was observed between the two urea protons, as Ha became deshielded by 0.56 ppm, while Hb was shifted only by 0.27 ppm. This could be due to the presence of a fluoro substituent *ortho*

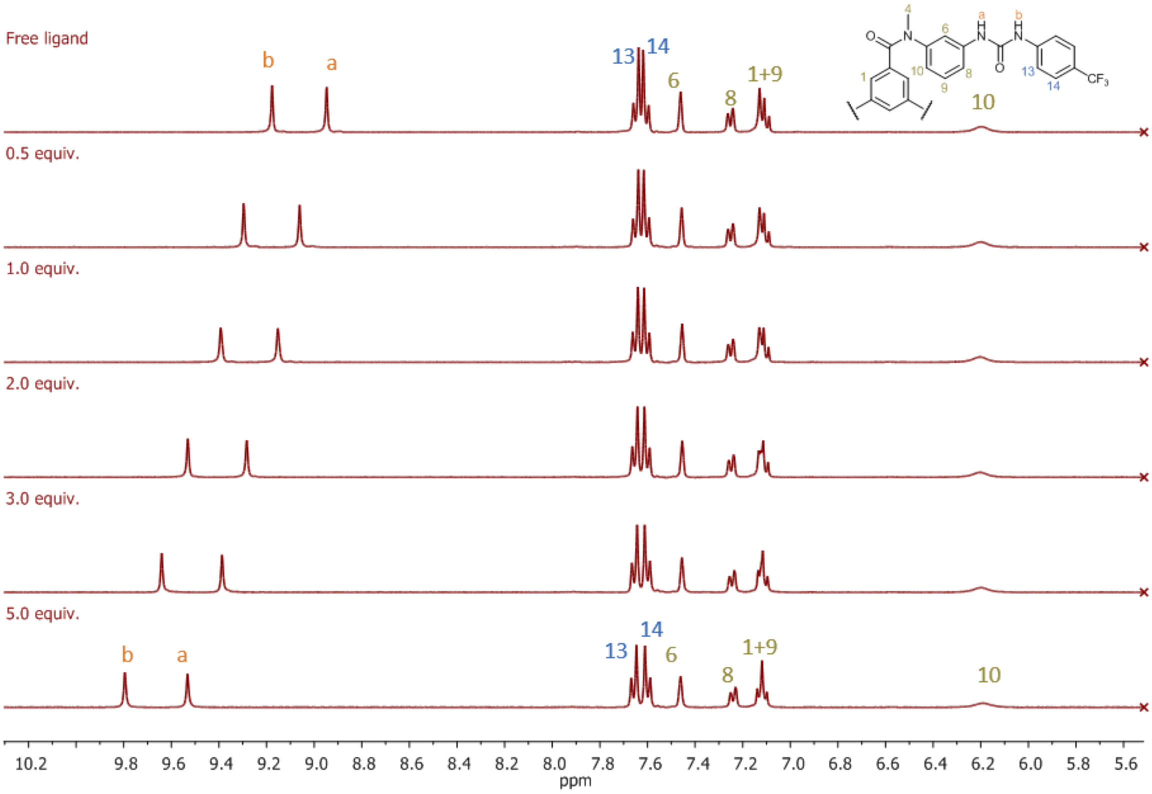

Figure 2.15. ^{1}H NMR titration profile of **86** with Cl$^-$, in DMSO-d_6. [**86**] = 7 mM. Only aromatic and urea protons region shown for clarity. Isotherm plot displayed in Figure A2.53a. This titration is representative of reproducible trends.

to the urea, which creates steric hindrance and reduces the binding ability of the adjacent urea proton Hb. Furthermore, analysis of this interaction showed a small binding constant was obtained by non-linear regression fitting of the shifts, of $K_{1:1}$ = 25 M^{-1}. HRMS MALDI-analysis also confirmed the presence of [M + Cl]$^-$ species, with a *m/z* = 1022.2443 and an isotopic distribution pattern matching the calculated one, Appendix Figure A2.48b.

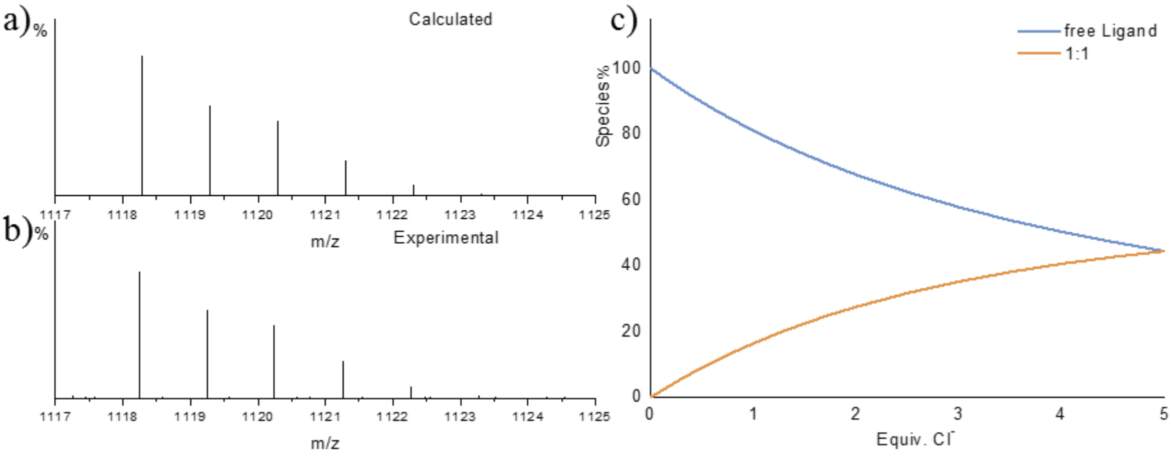

Figure 2.16.a) Calculated and b) experimental HRMS isotopic distribution pattern from experiments carried out at the end of the titration of **86**·Cl$^-$ by HRMS–MALDI-TOF (*m/z*): [M + Cl]$^-$ calcd for $C_{54}H_{42}N_9O_6F_9Cl$, 1118.2808; found, 1118.2367. c) Speciation diagram obtained from the fit of the NMR titration of **86** with Cl$^-$

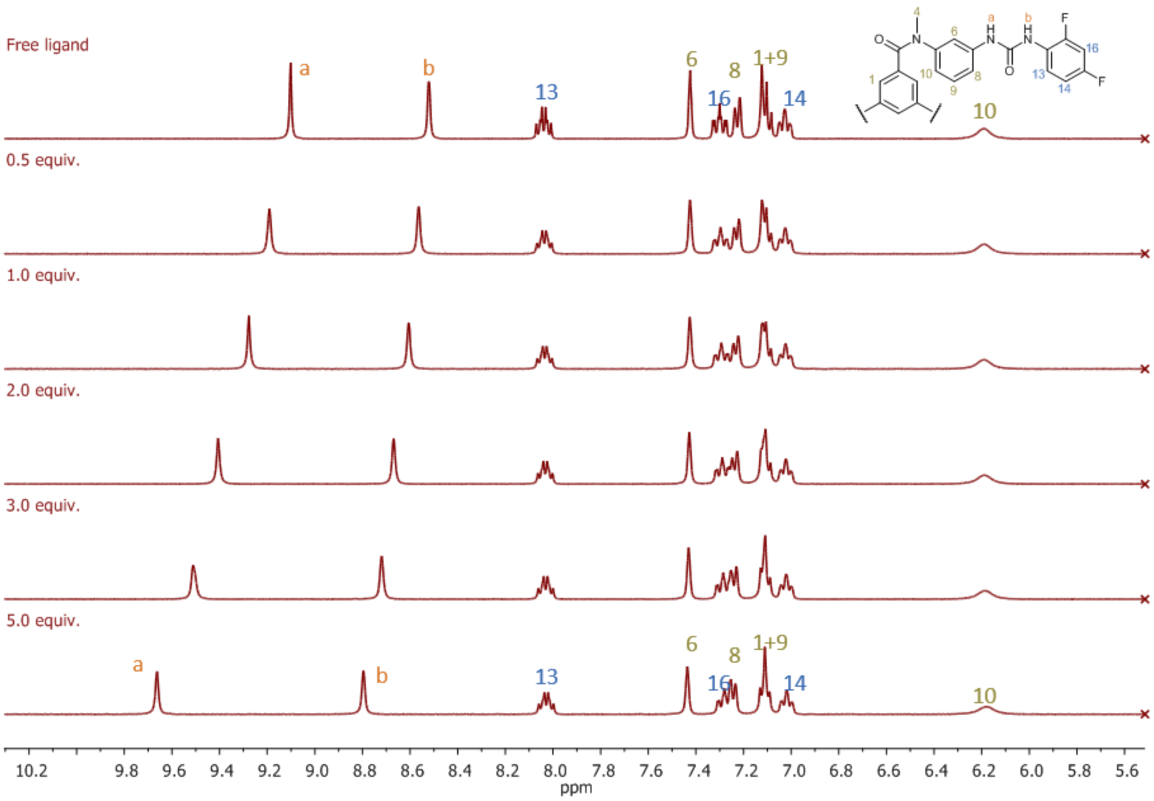

Figure 2.17. ^1H NMR titration profile of **87** with Cl$^-$, in DMSO-d_6. [**87**] = 7 mM. Only aromatic and urea protons region shown for clarity. Isotherm plot displayed in Figure A2.53b.This titration is representative of reproducible trends.

Ligand **88**, having a nitro substituent on the distal phenyl ring, which is *ortho* to the urea and can form intramolecular hydrogen bonding interaction, as seen from the crystal structure in Figure 2.7. The titration of ligand **88** with Cl$^-$, Figure 2.18, also displayed a mild deshielding of the urea protons (0.09 ppm Ha and 0.05 Hb), which could indicate weak hydrogen bond interaction, while no shift was observed in the aromatic protons. For ligand **88**, a small binding constant of $K_{1:1}$ = 32 M^{-1} was calculated through non-linear regression fitting of the data, which was comparable with the binding between Cl$^-$ and the other ligands above. HRMS MALDI- analysis at the end of the titration showed the presence of [M + Cl]$^-$ species corresponding to *m/z* = 1049.2670 with an isotopic distribution pattern matching the calculated one, Appendix Figure A2.50b. While the binding constant is similar to that of the other ligands, the shift was smaller than for the other ligands, in this case only 0.10 ppm for Ha and 0.05 ppm for Hb. This is probably because the titration was carried out at a lower concentration (2 mM instead of 7 mM), reducing the changes observed upon binding.[164]

The last ligand, **89**, which carries a *meta*-nitro group on the distal phenyl ring, was also titrated with Cl$^-$ and showed a behaviour consistent with the other analogues. In the ^1H NMR spectrum, Figure 2.19, there was an evident downfield shift in the urea protons upon addition of increasing equivalents of TBACl. Both protons Ha and Hb were shifted by 0.63

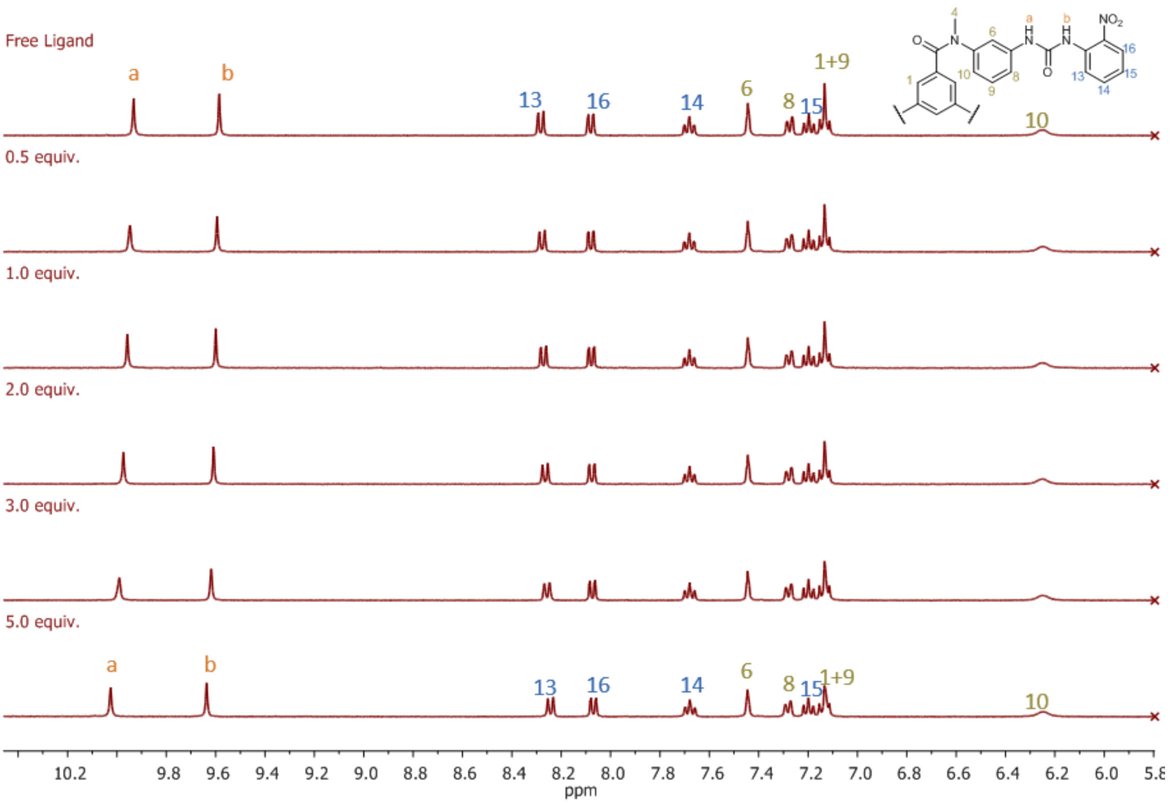

Figure 2.18. ^{1}H NMR titration profile of **88** with Cl$^-$, in DMSO-*d*$_6$. [**88**] = 2 mM. Only aromatic and urea protons region shown for clarity. Isotherm plot displayed in Figure A2.53c.This titration is representative of reproducible trends.

ppm after the addition of 5 equivalents of Cl$^-$, while only minor shifts for H15 and H17 were observed, which were consistent with the changes in the electronic of the distal ring upon hydrogen bond donation of the urea to Cl$^-$. Also in this case, the binding constant obtained by non-linear regression fitting was for a 1:1 binding mode, with a value of $K_{1:1}$ = 16 M^{-1}, was a smaller absolute constant but of comparable strength.

In general, titrations of this family of ligands with Cl$^-$ showed the deshielding of urea protons, with only minor shifts of the aromatic protons. This urea proton deshielding could be caused by the formation of hydrogen bonding between the ligand and the anion and the non-linear regression fitting of the changes indicated the formation of 1:1 complexes with $K_{1:1}$ values between 16-32 M^{-1}, Table 2.9. It is possible that the formation of these 1:1 bundles were arranged as suggested by the DFT calculations in Figure 2.14, with the ureas converging towards the anion. However, it would have been expected that some changes occurred in the electronic environment of proton H10 as, from what was discussed in Section 2.2.1, the free ligand in solution was believed to be in the ‘open propeller-like’ conformation, and the binding according to the DFT calculation, would cause the rotation of the arms. In this rotated position, H10 would not be any more in the shielding cone of the central benzene

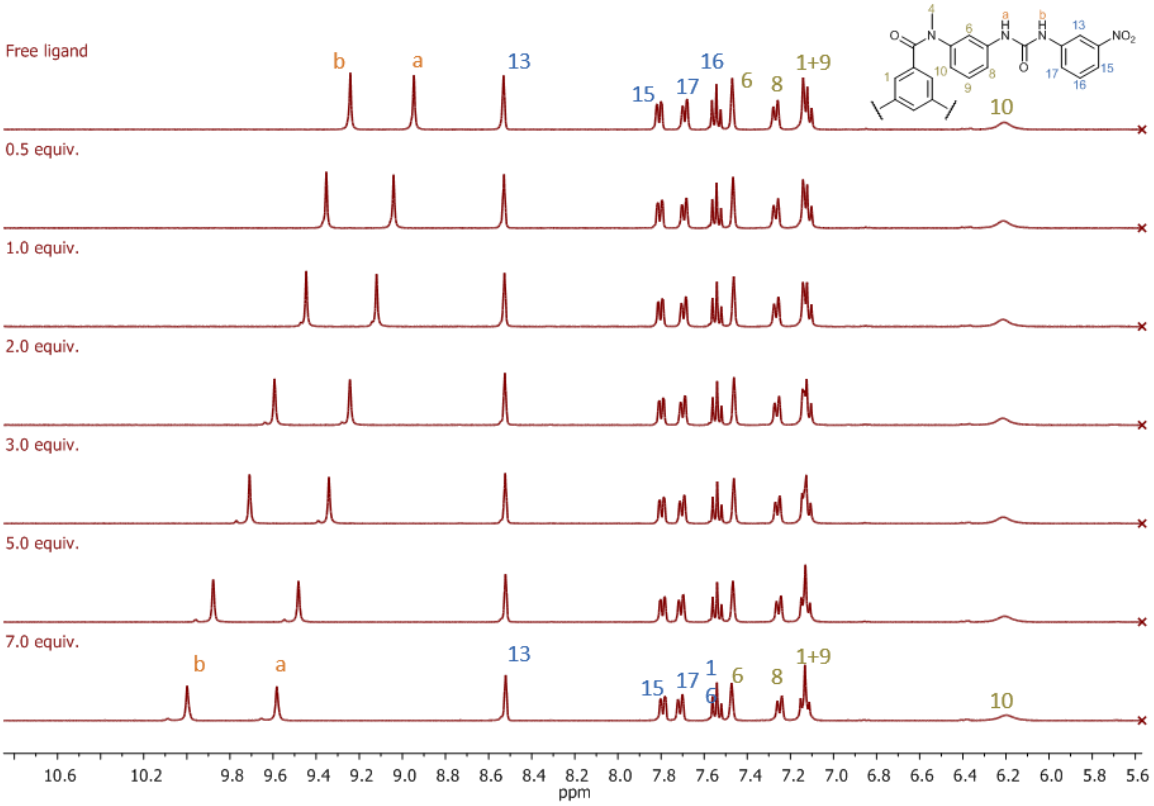

Figure 2.19. ^{1}H NMR titration profile of **89** with Cl$^-$, in DMSO-d_6. [**89**] = 7 mM. Only aromatic and urea protons region shown for clarity. Isotherm plot displayed in Figure A2.53d.This titration is representative of reproducible trends.

ring, therefore such rotation would cause the deshielding of H10. Since no shift on the H10 protons was detected, it was envisaged that either the binding with Cl$^-$ in the competitive environment of DMSO-d_6 is not strong enough to produce changes, unless at much higher equivalents, or it is possible that the 1:1 binding is occurring through a different self-assembly mode than that depicted by the DFT calculations. Additional studies on the self-assembly processes which could account for this will be discussed further in Section 2.4.

Following the studies of ligands **86-89** with Cl$^-$, which showed the formation of self-assembled 1:1 bundles, the binding abilities of ligands **86-89** were next investigated with CH_3COO^-. The CH_3COO^- anion is geometrically different from Cl$^-$, and possesses the ability to form directional hydrogen bondings and so will be discussed in the next section.

Table 2.9. Binding constants for ligands **86-89** obtained from ^{1}H NMR titrations with Cl$^-$ (DMSO-d_6, 400 MHz, 298K), [M^{-1}].

Ligand	**Cl$^-$** **$K_{1:1}$**
86	32(3)
87	25(2)
88	32(3)
89	16(1)

2.3.2.2. Binding properties of ligands 86-89 with CH_3COO^- in DMSO-d_6

CH_3COO^- is known to create strong hydrogen bonding interactions in a "Y-shaped" arrangement with urea hosts, as was discussed in section 1.1.1 of Chapter 1. Therefore, it was anticipated that, unlike that seen for Cl^-, the preferential binding would be observed between one anion and one urea moiety.

The titration of ligand **86** with CH_3COO^- showed some interesting features, which are shown in Figure 2.20. The urea protons showed a very strong deshielding of 3.3 ppm, with a gentle plateau reached after the addition of three equivalents of CH_3COO^- (Appendix, Figure A2.54a). Different to what was observed for Cl^-, some relevant shifts of the aromatic protons were seen. Protons H13 and H14, of the distal phenyl ring, separated into distinct resonances moving towards higher and lower chemical shifts, respectively. In contrast, protons H6 and H8 were deshielded, but only after the addition of more than 1 equivalent of anion. Also, proton H10 was shielded by 0.24 ppm between 1→3 equivalents, which, together with H6 and H8, could indicate a possible rearrangement towards a more 'open propeller-like' conformation for the binding of three anions, as was suggested by the UV-vis absorption titrations results above. The broadening of the urea signals between 1→3 equivalents, with clear splitting in intermediate equivalents (see Appendix, Figure A2.57 for

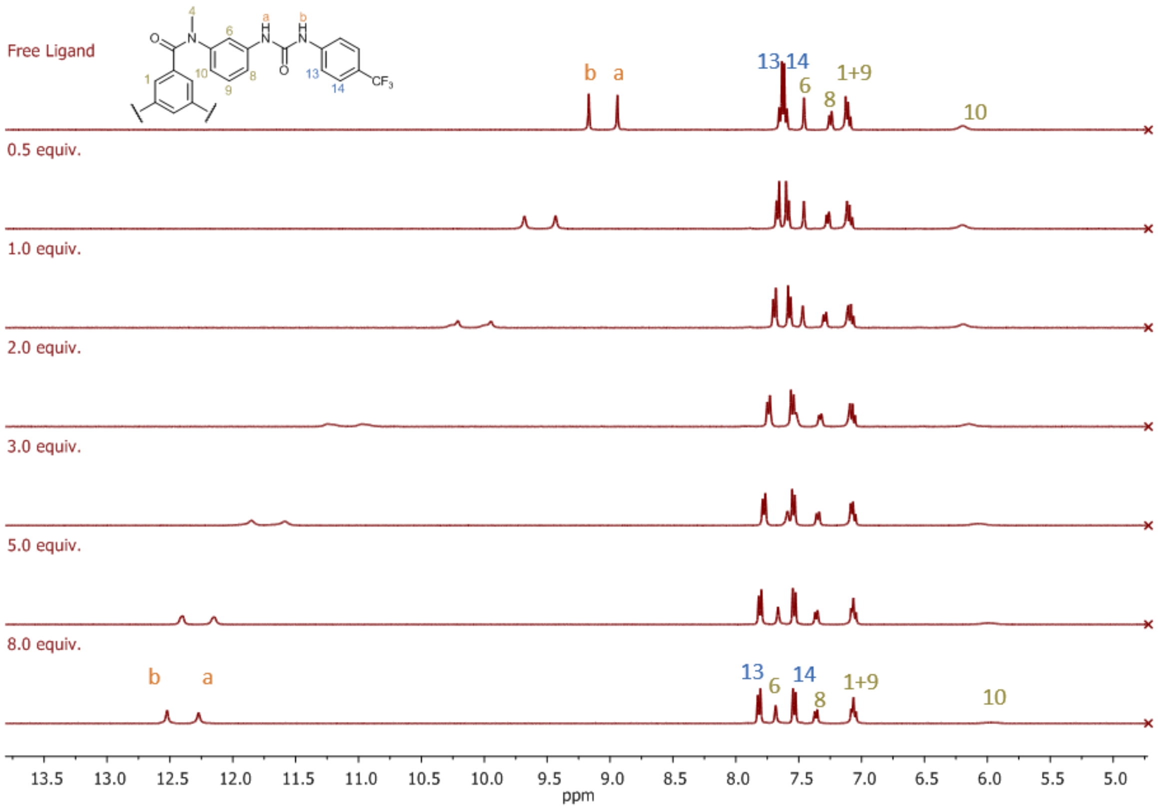

Figure 2.20. ^{1}H NMR titration profile of **86** with CH_3COO^-, in DMSO-d_6. [**86**] = 7 mM. Only aromatic and urea protons region shown for clarity. Isotherm plot displayed in Figure A2.54a.This titration is representative of reproducible trends.

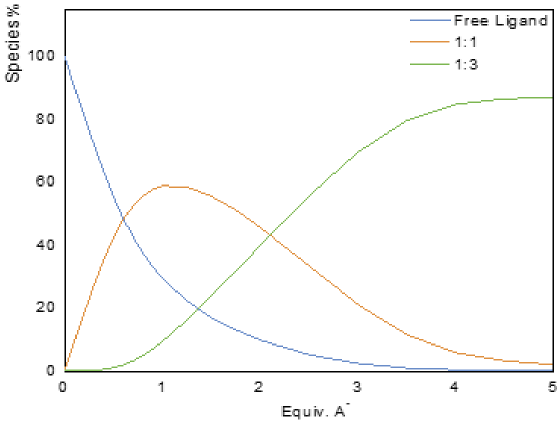

Figure 2.21. Speciation diagram obtained from the fitting of the NMR titration of **86** with CH_3COO^-.

full spectrum) could be also a sign of dynamic binding of one anion to one urea which breaks the symmetry of the ligand and consequently splits the signals.

The changes in shifts were also best fit to a 1:1 and 1:3 (L:A) binding model, with relatively large constants calculated as $K_{1:1} = 2.5 \times 10^3\ M^{-1}$ and $K_{1:3} = 3.1 \times 10^5\ M^{-1}$, respectively. The speciation diagram showed, in the presence of 1 equivalent of CH_3COO^-, the formation of the 1:1 species as the major component, being formed in *ca*. 60% yield, with the 1:3 species present as less than 10%. The remaining 30% was assumed to be free ligand. However, after the addition of 3 equivalents of anion, the 1:3 species formed as the major component, with the free ligand and the 1:1 species accounting for less than 10% after the addition of 4 equivalents, Figure 2.21.

A similar behaviour was observed in the titration of **89** with CH_3COO^-, Figure 2.22. Here, the addition of excess CH_3COO^- (7 equivalents) caused an significant shift of the urea resonances Ha and Hb of 3.35 ppm and 3.51 ppm, respectively. A deshielding of 0.15 ppm for protons H13 and H8, and of 0.20 ppm for protons H17 and H6 was also evident. In this case, proton H10 was shifted from 6.21 ppm to 5.99 ppm between the addition of 1 equivalent and 7 equivalents of anion, suggesting a rearrangement of the arms to accommodate the binding of 3 anions. Similarly, to the studies on ligand **86**, the Δδ were best fit to a 1:1 and 1:3 binding model, with binding constants of $K_{1:1} = 8 \times 10^2\ M^{-1}$ and $K_{1:3} = 2.0 \times 10^5\ M^{-1}$ (which were comparable to the constants obtained for ligand **86**). Here, after the addition of one equivalent of CH_3COO^-, about 10% of 1:3 species was already formed, with the free ligand and the 1:1 species present in equal parts. Similarly to **86**, after 3 equivalents the 1:3 species became the major component, with it being present in more than 80% after 4 equivalents, Figure 2.23. In both titrations, for **86** and **89**, the shifting of H10 upon binding with the anion is concomitant to an additional broadening of the resonance

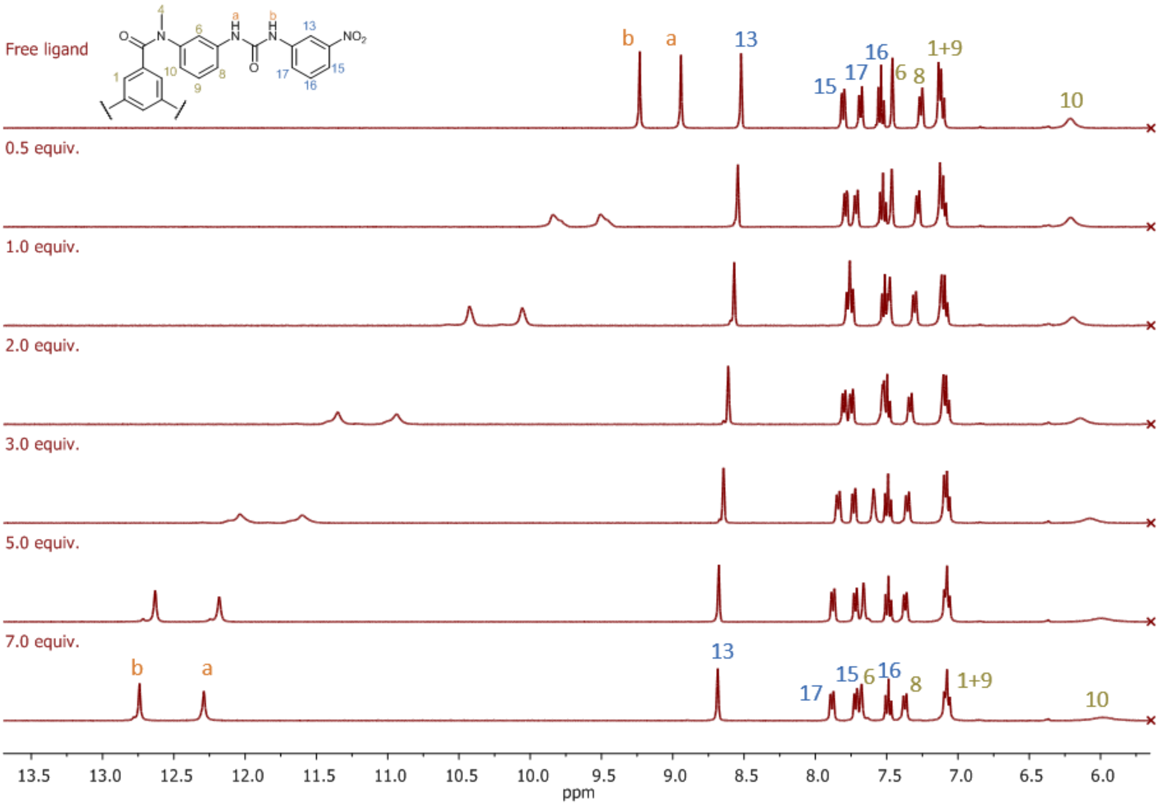

Figure 2.22. ^{1}H NMR titration profile of **89** with CH_3COO^-, in DMSO-d_6. [**89**] = 7 mM. Only aromatic and urea protons region shown for clarity. Isotherm plot displayed in Figure A2.54d. This titration is representative of reproducible trends.

peak. In the free ligand the H10 peak is, in fact, already quite broad and shielded, suggesting that the position of that proton is not fixed, but rather fluctuating between the two conformational forms. Additional broadening and shift in the urea H10 could be due to both a change in the conformation to favour the simultaneous binding of three anions, as well as the electronic effect that the urea hydrogen bonding on the proton H10 which is *para* to the urea and, therefore, is affected by the partial delocalisation of the charge.

The titration of ligand **87** with CH_3COO^-, Figure 2.24, while displaying some common features with that seen for **86** and **89**, showed some differences as well. Here, **87** showed a strong deshielding of 2.68 ppm for the urea peaks after the addition of 4 equivalents of CH_3COO^- added. However, these changes were more pronounced between 0→1 equivalents than was observed previously. A gradual change was evident for protons H13, H16 and H8, while H1, H6 and H10 were shifted only after the addition of 3 equivalents. This indicated a different behaviour, compared to ligands **86** and **89**, and the best fitting obtained implied the formation of 1:1 species as the major product, with a constant of $K_{1:1}$ = 79 M^{-1}. However, it was also possible that the solvent competition for the binding site of this

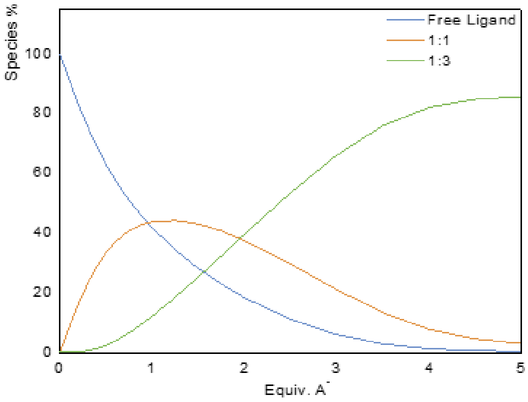

Figure 2.23. Speciation diagram obtained from the fitting of the NMR titration of **89** with CH_3COO^-.

ligand is too strong and prevents the association of **87** with three anion molecules, which was observed in UV-vis absorption studies above with less competitive CH_3CN solvent.

The titration of **88** with CH_3COO^-, Figure 2.25, displayed features more similar to the titration of CH_3COO^- with **87**, than **86** and **89**. The shifts of these resonances were gradual and did not show a neat change of behaviour before and after the addition of 1 equivalent of anion. Most of the aromatic protons, H10, H13, H14 and H16, became shielded, which caused their resonances to move to lower chemical shifts. The only aromatic proton which was weakly deshielded was H8, which was shifted by 0.06 ppm. This is likely

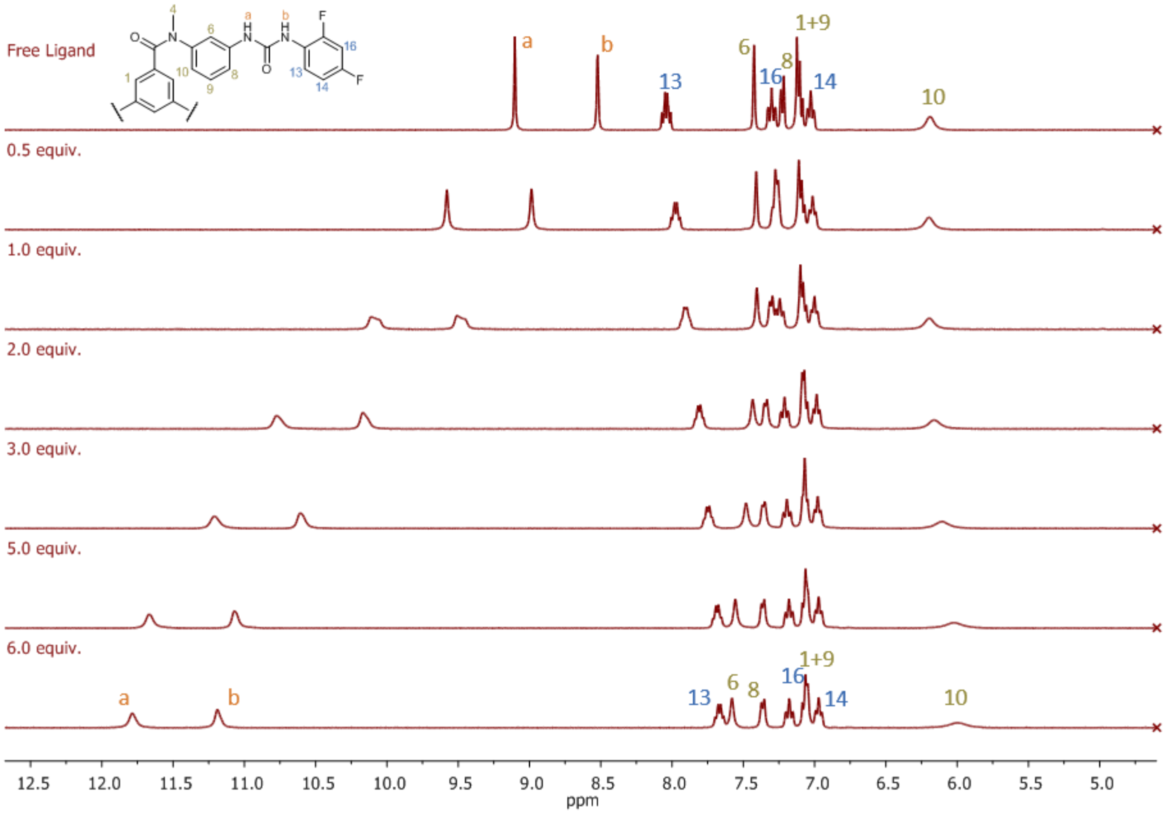

Figure 2.24. ^{1}H NMR titration profile of **87** with CH_3COO^-, in DMSO-d_6. [**87**] = 7 mM. Only aromatic and urea protons region shown for clarity. Isotherm plot displayed in Figure A2.54b. This titration is representative of reproducible trends.

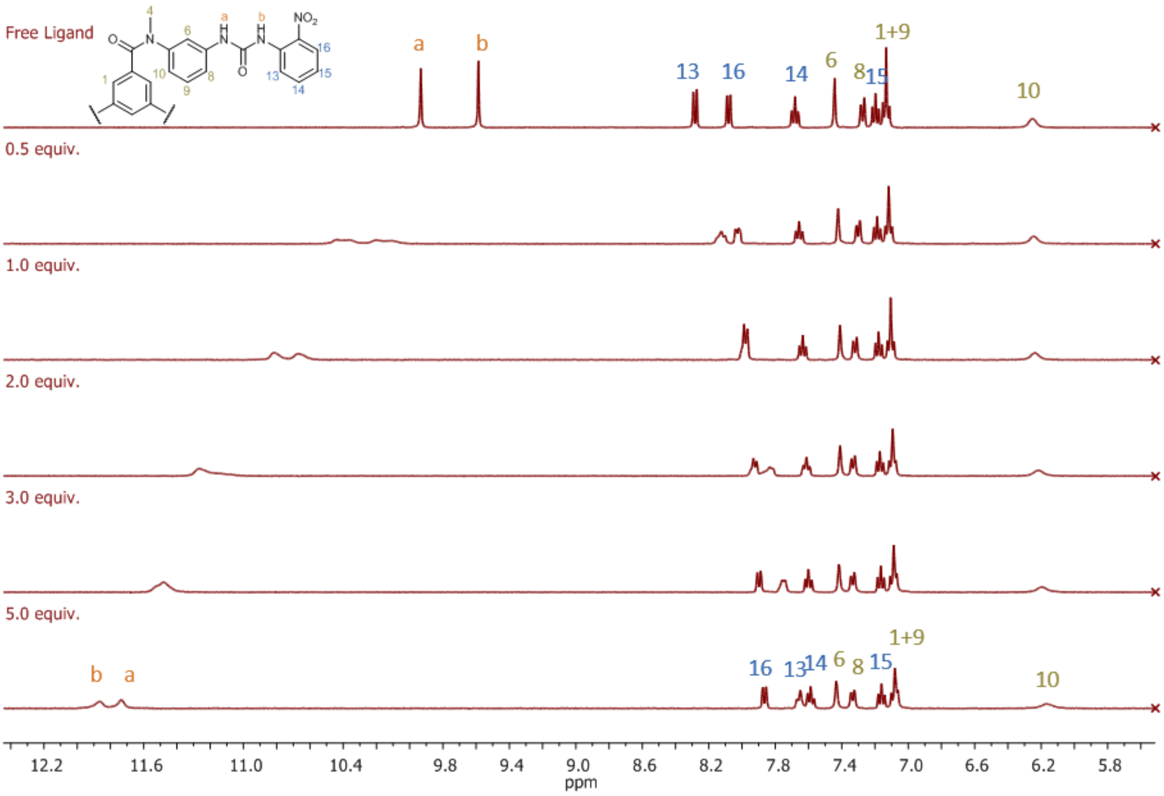

Figure 2.25. ^{1}H NMR titration profile of **88** with CH_3COO^-, in DMSO-d_6. [**88**] = 2 mM. Only aromatic and urea protons region shown for clarity. Isotherm plot displayed in Figure A2.54c. This titration is representative of reproducible trends.

due to the ‘twisting’ of the arm upon binding, which results in the shielding of H10. The urea protons also got deshielded by 2.27 ppm for Hb and 1.8 ppm for Ha, with a crossover of the two resonances between the addition of 2 and 3 equivalents of the anion. Proton Hb, which in the free ligand was likely to form intramolecular hydrogen bonding, underwent a strong change in the electronic environment, which caused a $\Delta\delta$ larger than Ha. This was probably due to a 180° rotation of the bond between the urea and the nitrophenyl moiety, which brought the nitro group in proximity to the carbonyl group. This reduced steric hindrance at the urea NH which hydrogen bonded to the carboxylic group of CH_3COO^-. The change in chemical shift by 0.6 ppm for H13, further confirmed this, as the rotation moves it further from the anisotropic currents of the urea carbonyl group, causing an enhanced shielding and thus shifting in the N–H resonances. The non-linear regression fitting was best obtained with a 1:1 binding model, with a binding constant of $K_{1:1} = 5.0 \times 10^2$ M^{-1}.

Ligands **86-89** showed strong interactions with CH_3COO^- in the ^{1}H NMR. The interactions caused the deshielding of the urea resonances to occur, accompanied by a broadening and splitting of the signals. This indicates that possibly the interaction of a single anion caused the de-symmetrisation of the signals, which would account for resulting in the

Table 2.10. Binding constants for ligands **86**-**89** obtained from ^{1}H NMR titrations with CH_3COO^- in (DMSO-*d*$_6$, 400 MHz, 298K), [M^{-1}].[a] Only one type of species were possible to propose from non-linear regression fitting.

Ligand	**CH_3COO^-**	
	$K_{1:1}$	**$K_{1:3}$**
86	$2.5(2)\times10^3$	$3.2(3)\times10^5$
87	$7.9(8)\times10^1$	–[a]
88	$5.0(5)\times10^2$	–[a]
89	$8.0(8)\times10^2$	$2.0(3)\times10^5$

broadening and splitting of the ^{1}H NMR signals at various points of the titrations. For ligands **86** and **89**, the self-assembly of the ligand with the anion was characterised by the formation of two main species, 1:1 and 1:3 (L:A), consistent with the results obtained from the UV-vis absorption titrations.

Relatively high binding constants were estimated[164] for these species by non-linear regression fitting, which denote a strong interaction of the ligand with the anion. However, the fitting of ^{1}H NMR titration data still allowed elucidation of the binding model and speciation in solution. On the other hand, ligands **87** and **88**, showed a more gradual change in the resonances shifts, upon addition of CH_3COO^-, displaying a less strong binding interaction and the sole formation of the 1:1 species. It is interesting to note that these two ligands have a substituent in the *ortho* position of the distal phenyl ring, which could create steric hindrance and an additional energetic barrier to overcome for the binding. This, in addition to the more polar nature of the solvent, which is competitive for the urea binding site, could be the main reasons for the weaker binding of ligands **87** and **88**, compared to ligands **86** and **89**, and the resulting stoichiometries.

The strong geometrical complementarity of the carboxylic moiety to the urea, proved to be the main driving force of the binding of ligands **86-89** to CH_3COO^-, without taking advantage of the tripodal nature of the ligand. However, the tripodal nature of the ligand could be favourable, in the case of ligands **86** and **89**, in an anion extraction context, as one molecule, would be able to bind 3 anions, even in a competitive solvent.

Tripodal ligands **86-89**, were next investigated for their binding ability with of tetrahedral anions. It was anticipated that these anions would be geometrically favoured for accepting hydrogen bonds simultaneously from the three arms of the ligands. Initially, ligands **86** and **89** were titrated with $H_2PO_4^-$ and the studies will be presented in the following section.

2.3.2.3. Binding properties of ligands 86-89 with $H_2PO_4^-$ in DMSO-d_6

The first tetrahedral anion which was used to test the anion binding abilities of ligands **86-89** was $H_2PO_4^-$.

Key points from the titration of ligand **86** with $H_2PO_4^-$ are shown in Figure 2.26, and these are indicative of both anion binding and self-assembly formation. The urea resonances were strongly deshielded, and at the same time significantly broadened, with complete loss of the signal being observed upon the addition of 5 equivalents of phosphate. Also, some resonances assigned to the aromatic protons were lost (specifically H1, H6 and H8), while the remaining resonances underwent a significant broadening. This could be due to the shielding effect of the electronic delocalisation of the negative charge gained by the ligand upon deprotonation. The fitting of the differences in the chemical shifts, by non-linear regression, suggested the formation of 1:1 (L:A) self-assemblies, with a calculated binding constant of $K_{1:1} = 2.0 \times 10^2\ M^{-1}$. MALDI- HRMS analysis confirmed this, showing the presence of [M + $H_2PO_4^-$] species corresponding to *m/z* = 1118.2808 with an isotopic distribution pattern matching the calculated one, Figure 2.27a-b.

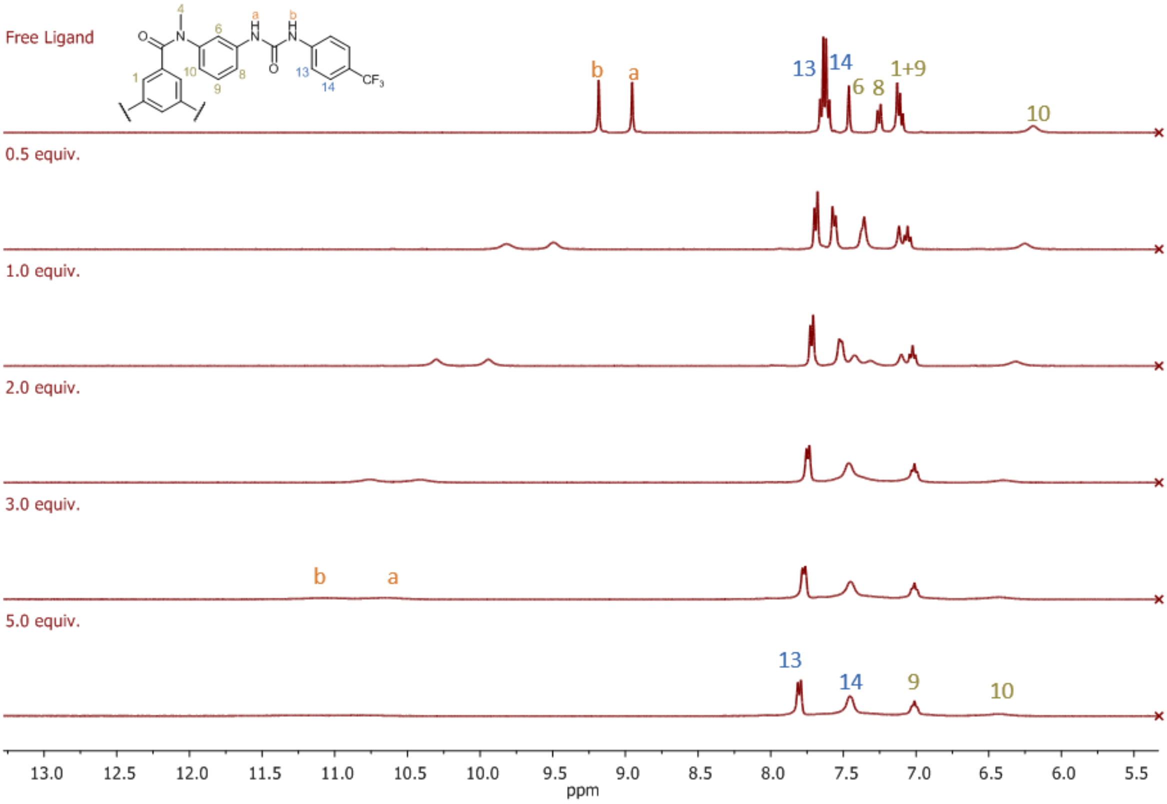

Figure 2.26. ^1H NMR titration profile of **86** with $H_2PO_4^-$, in DMSO-d_6. [**86**] = 7 mM. Only aromatic and urea protons region shown for clarity. Isotherm plot displayed in Figure A2.55a. This titration is representative of reproducible trends.

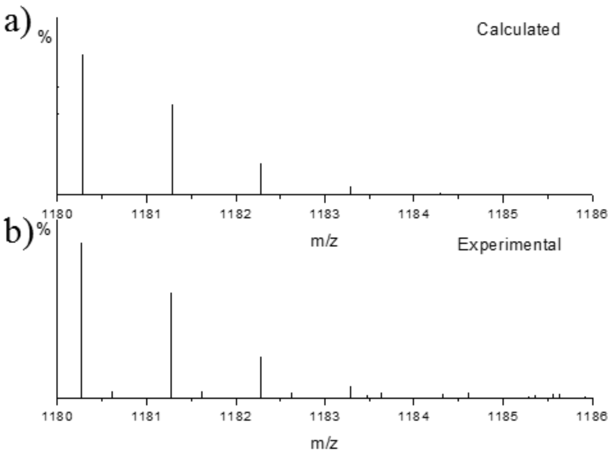

Figure 2.27. a) Calculated and b) experimental HRMS isotopic distribution pattern carried out at the end of the titration of **86**.$H_2PO_4^-$ by HRMS–MALDI-TOF (*m/z*): [M + $H_2PO_4^-$]$^-$ calcd. for $C_{54}H_{42}N_9O_6F_9{\cdot}H_2PO_4$, 1180.2811; found, 1180.2640.

Upon titrating ligand **89** with $H_2PO_4^-$, a similar behaviour with regards to the two urea protons was observed, with both Ha and Hb being shifted and broadened simultaneously, Figure 2.28. Upon anion recognition, similar to **86**, the aromatic protons H1, H6 and H8 became broadened and then disappeared. A binding constant of $K_{1:1} = 2.0 \times 10^2$

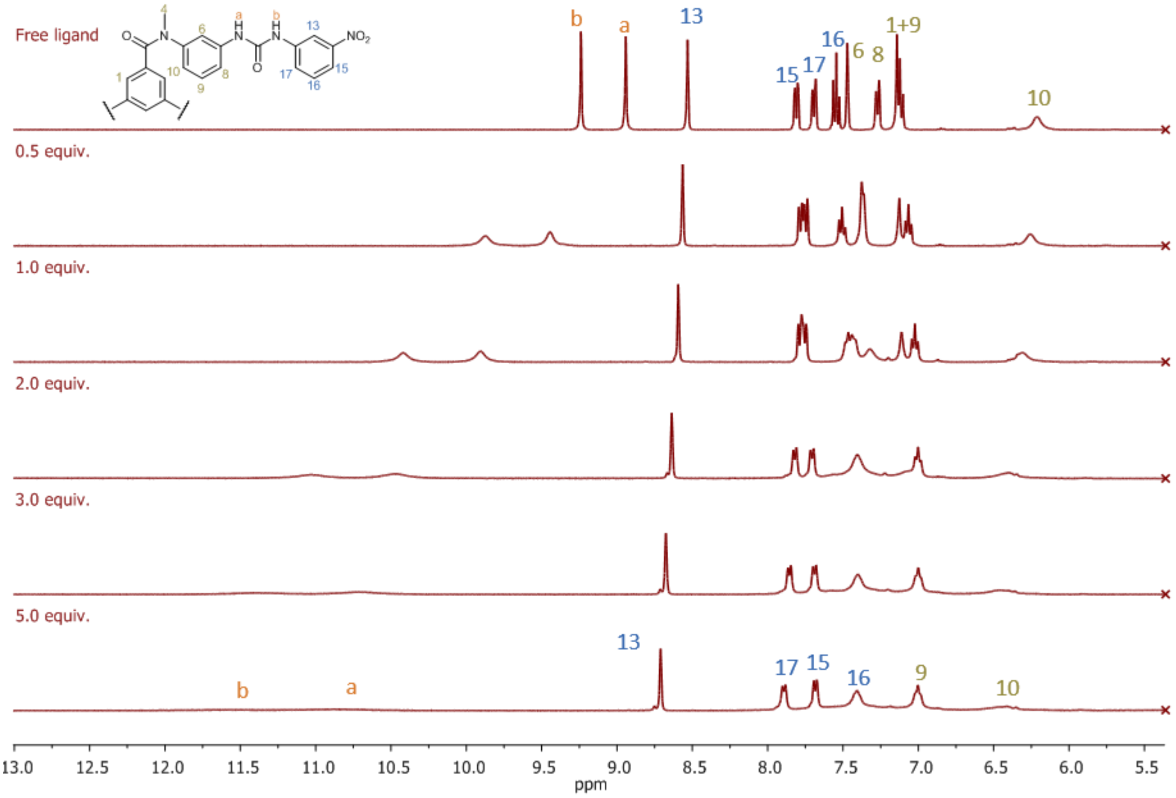

Figure 2.28. ^1H NMR titration profile of **89** with $H_2PO_4^-$, in DMSO-d_6. [**89**] = 7 mM. Only aromatic and urea protons region shown for clarity. Isotherm plot displayed in Figure A2.55d. This titration is representative of reproducible trends.

M^{-1} was obtained from the non-linear regression fitting to a 1:1 model, similar that obtained for **86**. It is possible that, the preorganisation of the tripodal urea moieties allows for the binding to occur with the three urea moieties simultaneously, similarly to what was previously hypothesised for Cl^-.

In the same way as was seen previously with CH_3COO^-, the behaviour of **87** and **88** was mildly different from **86** and **89**, while still indicating the formation of hydrogen bonding with the anion. Gradual addition of $H_2PO_4^-$ to a solution of **87**, Figure 2.29, caused deshielding in the urea protons, along with significant broadening, indicating the formation of hydrogen bonding and possibly deprotonation. Interestingly, for **87** the broadening occurred earlier for Hb than Ha. This could possibly be due to a further de-symmetrisation in the two urea protons in the binding process, where Hb appeared to contribute in a greater manner to the hydrogen bonding. A significant broadening of the aromatic peaks occurred for **87** with $H_2PO_4^-$ indicating a strong magnetic perturbation close to the ligand, which could be caused by the self-assembly with the anion. The binding constant obtained by using non-linear regression fitting of the data was $K_{1:1} = 3.1 \times 10^2$ M^{-1}.

In a similar way, the titration of **88** with $H_2PO_4^-$, shown in Figure 2.30, displayed shifts to higher chemical shifts of the urea resonances, as well as a significant broadening,

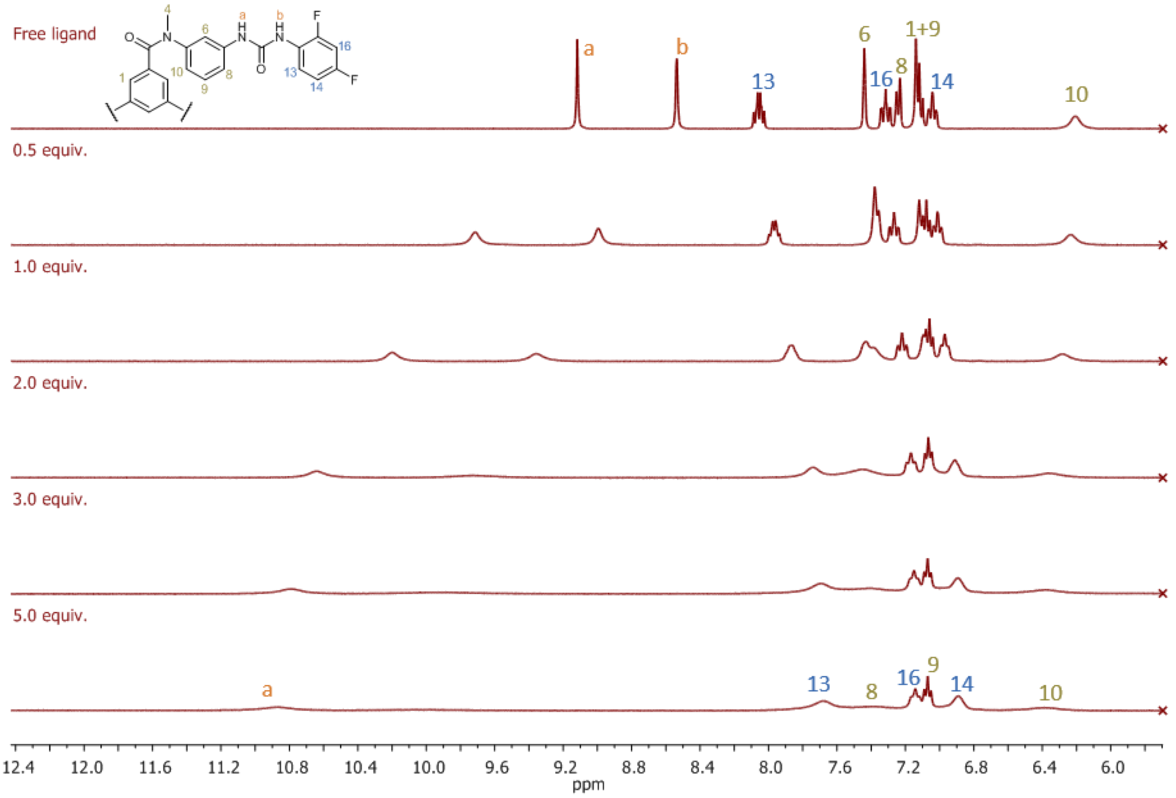

Figure 2.29. ^1H NMR titration profile of **87** with $H_2PO_4^-$, in DMSO-d_6. [**87**] = 7 mM. Only aromatic and urea protons region shown for clarity. Isotherm plot displayed in Figure A2.55b. This titration is representative of reproducible trends.

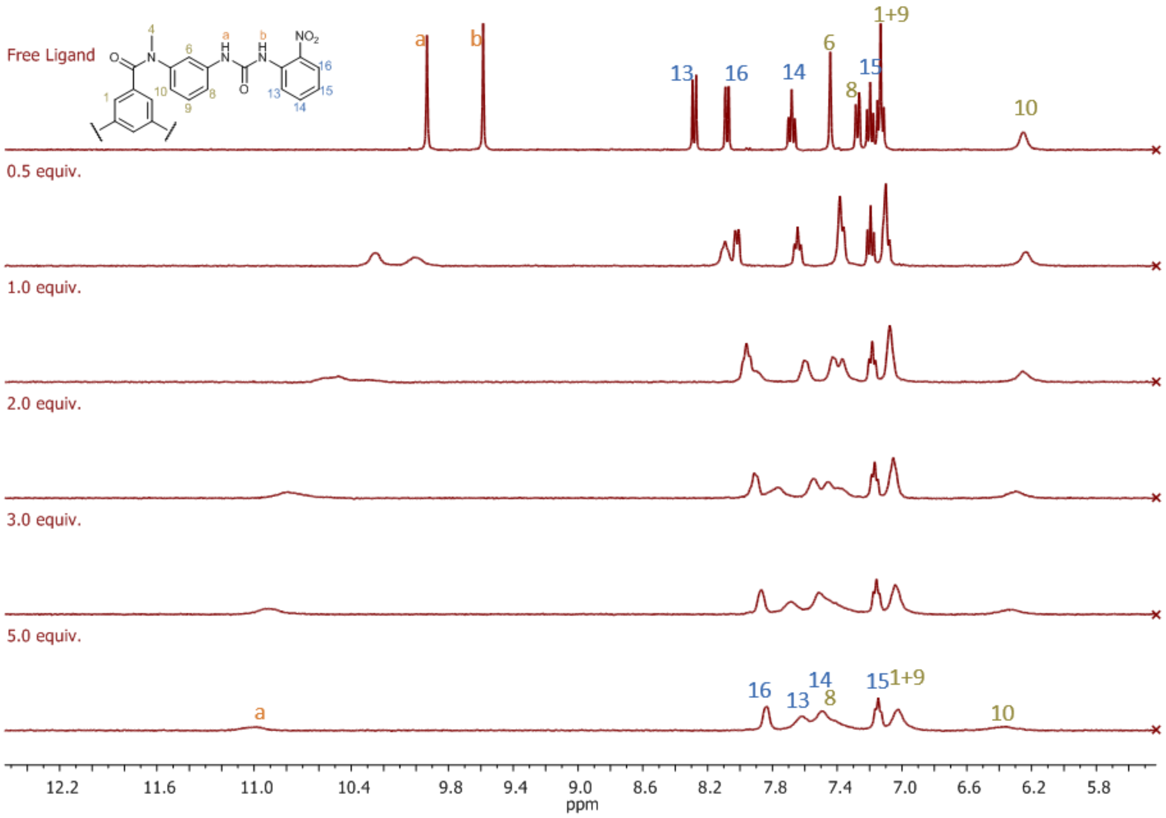

Figure 2.30. ^{1}H NMR titration profile of **88** with $H_2PO_4^-$, in DMSO-d_6. [**88**] = 2 mM. Only aromatic and urea protons region shown for clarity. Isotherm plot displayed in Figure A2.55c. This titration is representative of reproducible trends.

faster for Hb than Ha, resulting, eventually, in the disappearance of these resonances. A binding constant of $K_{1:1} = 7.9 \times 10^2$ M^{-1} was determined by the non-linear regression fitting, which was slightly higher than the ones of the other ligands but still in the same order of magnitude.

One common feature to all of the ligands interactions with $H_2PO_4^-$ was the deshielding of the aromatic core proton H10, along with its broadening. This behaviour was opposite to that observed during the titrations with CH_3COO^-, in which the ‘open propeller’ structure was favoured for the binding of multiple anions, causing the shielding of the H10 protons. In contrast, in the case of $H_2PO_4^-$, a deshielding of this proton suggested that the binding was instead favouring a ‘closed-cup’ arrangement with a 1:1 binding mode for the self-assembly between the ligands and the anion. Because of this arrangement, the important broadening and shifts which occurred for all the ligands upon addition of $H_2PO_4^-$, could be caused by the proximity of the anion to the ligand, combining binding interactions and the effects of the local magnetic field of the anion. The highly organised and geometrically favoured interaction, could also cause the self-assembled bundle to interact so strongly by

Table 2.11. Binding constants for ligands **86-89** obtained from ^{1}H NMR titrations with $H_2PO_4^-$ (DMSO-*d*$_6$, 400 MHz, 298K), [M^{-1}].

Ligand	**$H_2PO_4^-$** **$K_{1:1}$**
86	$2.0(2)\times10^2$
87	$3.1(3)\times10^2$
88	$7.9(8)\times10^2$
89	$2.0(2)\times10^2$

hydrogen bonding, influencing the $H_2PO_4^-$ effective pK_a and favour the deprotonation of the ligand.

The ^{1}H NMR titrations of ligands **86-89** with $H_2PO_4^-$ in DMSO-*d*$_6$ supported the formation of self-assembled ligand:anion 1:1 bundles, favoured by the preorganised arrangement of the urea protons in the ligands. A slightly stronger interaction of $H_2PO_4^-$ seemed to occur with **88**, rather than the other ligands, probably due to the strong withdrawing effect of the nitro substituent in the *ortho* position. Having tested the ability of binding of $H_2PO_4^-$, the interactions of ligands **86-89** with another tetrahedral anion, SO_4^{2-}, were studied and will be presented in the next section.

2.3.2.4. Binding properties of ligands 86-89 with SO_4^{2-} in DMSO-*d*$_6$

The next anion studied was SO_4^{2-}: another tetrahedral anion, which is highly solvated in comparison to phosphate, which makes anion recognition more difficult. To address this, commonly, ligands are designed with a high geometrical complementarity. Additionally, a rigidity in such a ligand can favour the binding process by reducing the loss of entropy upon binding that would arise from reorganisation, thus limiting the thermodynamic penalty associated with the binding.[58]

Adding increasing equivalents of a TBA_2SO_4 solution to a DMSO-*d*$_6$ solution of **86** caused the shift of the urea protons of the ^{1}H NMR from 8.95 ppm to 9.45 ppm (Ha) and 9.18 ppm to 9.70 ppm (Hb) after 5 equivalents of SO_4^{2-}, Figure 2.32. A concomitant broadening of the same resonances indicated the formation of hydrogen bonding between the receptor and the anion. A deshielding of protons H13, H6 and H8 together with a shielding of protons H14, H1 and H9 was consistent with the interaction happening on the urea binding site. Consistent with the behaviour of **86** with other anions, a weak shift of 0.02 ppm was observed for H10. From these data a weak binding constant of $K_{1:1}$ = 8 M^{-1} was obtained by the fitting of the data to a 1:1 binding model, consistent with a competitive media.

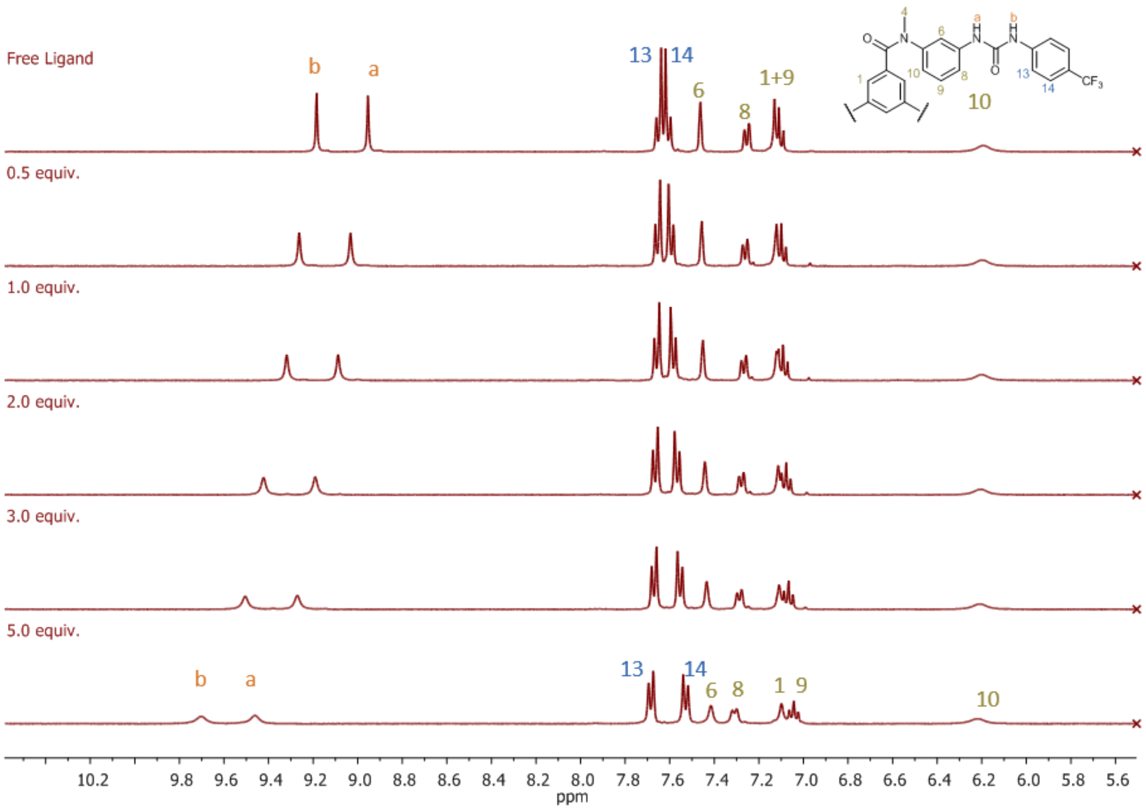

Figure 2.32. ^{1}H NMR titration profile of **86** with SO_4^{2-}, in DMSO-d_6. [**86**] = 7 mM. Only aromatic and urea protons region shown for clarity. Isotherm plot displayed in Figure A2.56a. This titration is representative of reproducible trends.

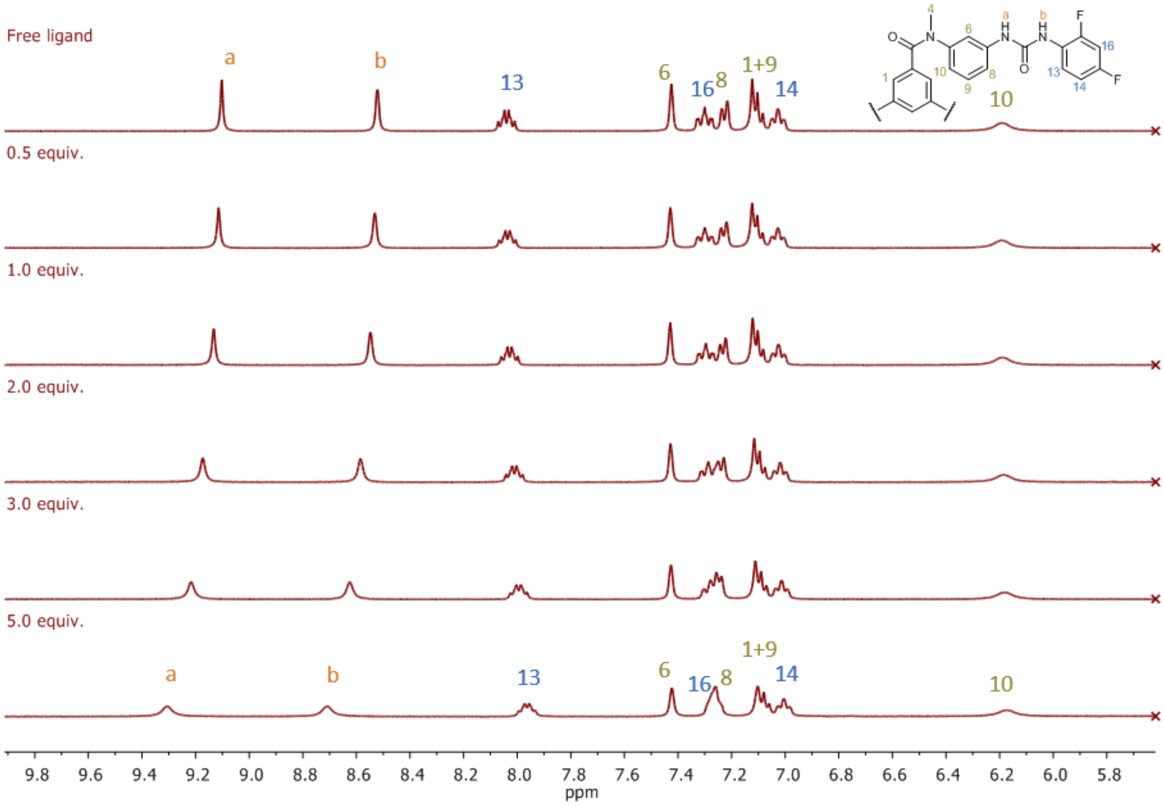

Figure 2.31. ^{1}H NMR titration profile of **87** with SO_4^{2-}, in DMSO-d_6. [**87**] = 7 mM. Only aromatic and urea protons region shown for clarity. Isotherm plot displayed in Figure A2.56b. This titration is representative of reproduceible trends.

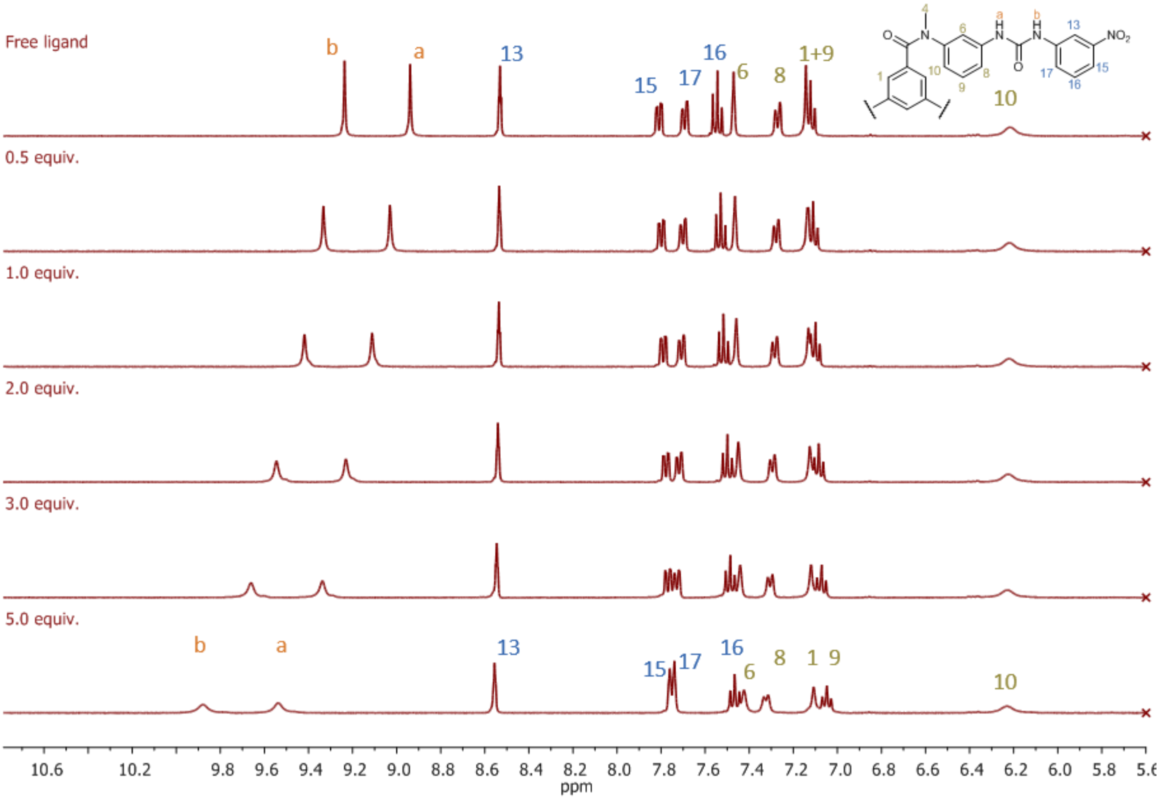

Figure 2.33. ^{1}H NMR titration profile of **89** with SO_4^{2-} , in DMSO-*d*$_6$. [**89**] = 7 mM. Only aromatic and urea protons region shown for clarity. Isotherm plot displayed in Figure A2.56d. This titration is representative of reproducible trends.

An even weaker effect was observed in the titration of ligand **87** with SO_4^{2-}, Figure 2.31. While a deshielding of the urea protons was also observed, in this case the fitting of the data could not be obtained, as the changes were too small. Slight broadening of the urea and aromatic resonances was also visible, indicating the interaction of the ligand with SO_4^{2-}. However, while a binding constant could not be determined, a MALDI-TOF analysis showed the presence, in the titration solution, of the $[M+H+SO_4^{2-}]^-$ ion with *m/z* = 1084.2198 (calculated *m/z* = 1084.2534) and a matching isotopic distribution pattern which supported the assignment of this species (see Appendix Figure A2.49b).

The titration of ligand **89** with SO_4^{2-}, Figure 2.33, also suggested a hydrogen-bonding formation, as the urea protons became deshielded by 0.60 ppm for Ha and 0.64 ppm for Hb after the addition of 5 equivalents of the anion. Deshielding of proton H17 and shielding of proton H15 also occurred, which brought the two resonances to overlap at 7.75 ppm, after 5 equivalents of anions were added. The binding constant obtained by the non-linear regression fitting to a 1:1 model of $K_{1:1}$ = 40 M^{-1} showed a binding in line with the other ligands.

The titration of ligand **88** with SO_4^{2-} showed only very small shifts of the resonances, suggesting weak interaction of the ligand with the anion. However, with the non-linear

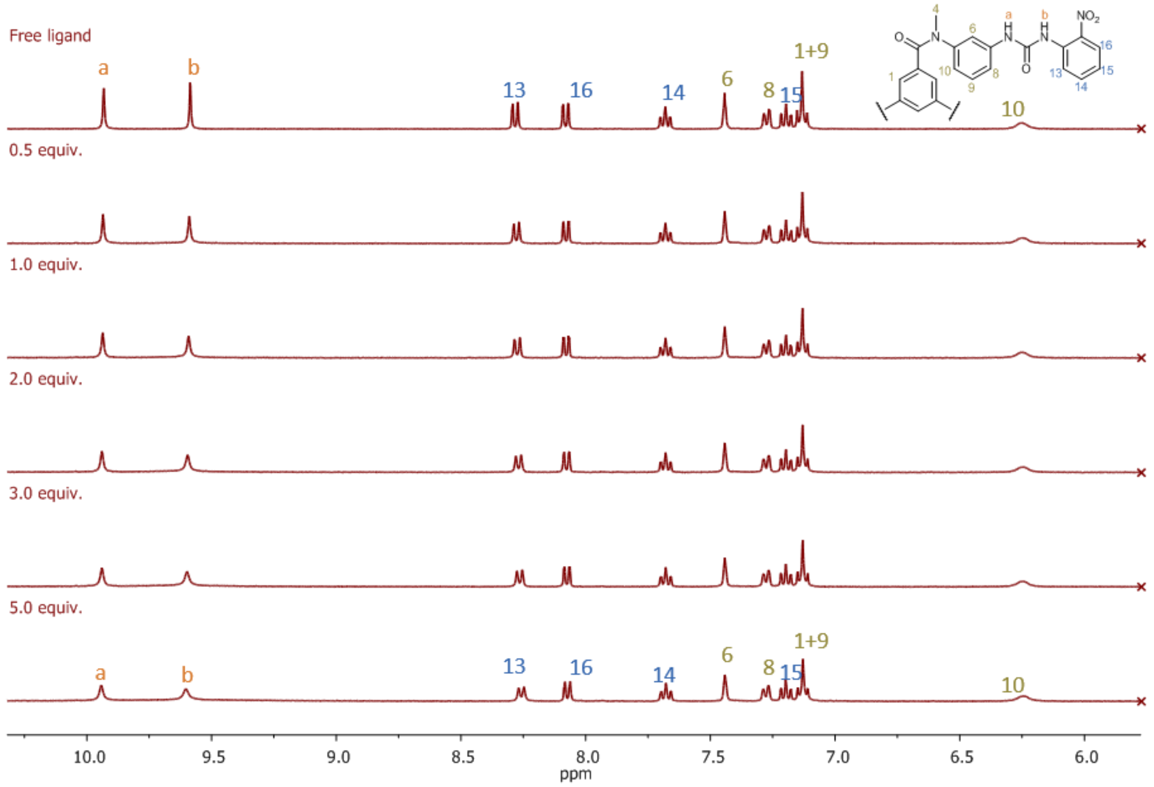

Figure 2.34. ^{1}H NMR titration profile of **88** with SO_4^{2-}, in DMSO-d_6. [**88**] = 2 mM. Only aromatic and urea protons region shown for clarity. Isotherm plot displayed in Figure A2.56c. This titration is representative of reproducible trends.

regression fitting a binding constant of $K_{1:1} = 1.3 \times 10^2\ M^{-1}$ was calculated. As for the other anions, titrations of **88** were carried out at a lower concentration. Considering the possibility of self-aggregation of the ligand, at higher concentration, such behaviour could be expected to explain the smaller shifts observed.

The studies of ligands **86-89** with SO_4^{2-} showed, in general, only relatively small shifts of the urea protons resonances, and even smaller shifts of the aromatic protons resonances. The deshielding of H10, while very small (0.01 ppm), would be consistent with simultaneous binding of the three arms of one ligand to SO_4^{2-}, as was the case with $H_2PO_4^-$ and Cl^-.

Table 2.12. Binding constants for ligands **86-89** obtained from ^{1}H NMR titrations with SO_4^{2-} (DMSO-d_6, 400 MHz, 298K), [M^{-1}]. ^{a} Data could not be fitted to the model.

Ligand	**SO_4^{2-}** **$K_{1:1}$**
86	8(1)
87	–^{a}
88	120(10)
89	40(4)

Table 2.13. Binding constants for ligands **86**-**89** obtained from ^{1}H NMR titrations (DMSO-*d*$_6$, 400 MHz, 298K), [M^{-1}].[a]Data were fitted to a single species model; [b]data could not be fitted to the model.

Ligand	**Cl^-**	**CH_3COO^-**		**$H_2PO_4^-$**	**SO_4^{2-}**
	$K_{1:1}$	**$K_{1:1}$**	**$K_{1:3}$**	**$K_{1:1}$**	**$K_{1:1}$**
86	$3.2(3)\times10^{1}$	$2.5(2)\times10^{3}$	$3.2(3)\times10^{5}$	$2.0(2)\times10^{2}$	$8(1)\times10^{0}$
87	$2.5(2)\times10^{1}$	$7.9(8)\times10^{1}$	–[a]	$3.1(3)\times10^{2}$	–[b]
88	$3.2(3)\times10^{1}$	$5.0(5)\times10^{2}$	–[a]	$7.9(8)\times10^{2}$	$1.2(1)\times10^{2}$
89	$1.6(1)\times10^{1}$	$8.0(8)\times10^{2}$	$2.0(2)\times10^{5}$	$2.0(2)\times10^{2}$	$4.0(4)\times10^{1}$

The ^{1}H NMR studies of ligands **86-89** with four different anions in DMSO-*d*$_6$ have evidenced the interaction and the formation of self-assembled anion complexes. With Cl^-, $H_2PO_4^-$ and SO_4^{2-} the shifts in the ^{1}H NMR suggested that the interaction occurred as symmetrical hydrogen bonding from the three urea moieties of the ligand and the data was, in general, best fitted to a 1:1 binding model. A slightly different behaviour was noticed for CH_3COO^-: with **86** and **89**, as the formation of both 1:1 and 1:3 (L:A) stoichiometries was seen. The higher order species formed as the main component in the presence of more than 3 equivalents of the respective anion. Similar results were observed in the UV-vis absorbance titrations above. On the other hand, ligands **87** and **88** only showed the formation of the 1:1 species. This was probably due to a major interaction of these ligands with the highly polar solvent, which prevented the formation of higher order species. These studies demonstrated different binding behaviour between the *para*-substituted **tmBTA** family (see Table 2.7) and that of the *meta*-substituted ligands. In fact, the ^{1}H NMR binding studies with the *para*-substituted **tmBTA** ligands **82** and **81** showed, in the presence of Cl^-, SO_4^{2-} and CH_3COO^-, the formation of two species, 1:1 and 2:1 (L:A). On the other hand, in the binding of **82** and **81** with $H_2PO_4^-$ species were in slow exchange. Despite the different binding stoichiometry, the binding constants for the 1:1 species in the two families were of comparable magnitude.

When comparing, as an example, the results obtained for ligands **86** by ^{1}H NMR and UV-vis absorption spectroscopy, Table 2.14, two main differences were evident. The first one was in the binding model, which showed the formation of two main species (1:1 and 1:3, L:A) by absorption and only the 1:1 species was observed in the ^{1}H NMR titration; the only exception was that of CH_3COO^- with ligands **86**. Secondly, the binding constants determined were few orders of magnitude smaller by ^{1}H NMR than in the UV-vis. However, these differences in the binding between the two techniques could be understood by two main factors considering the hypothesis of aggregation: i) the difference in the media; and ii) the difference in working concentrations. Titrations with **86** in DMSO-*d*$_6$ were carried out, with the help of Dr Dawn Barry at a lower concentration of 2×10^{-3} M, to test for changes in the binding. These studies, as shown in Table 2.14, showed similar shifts in the protons resonances as had been previously seen. In general, however, the changes were larger and resulted in larger binding constants. This pointed towards the aggregation of the ligand, at higher concentration, resulting in a smaller anion affinity (likely due to lower binding sites availability and de-aggregation penalty) and a general difficulty in determining clear binding constants. Similar effects on the binding constants were observed by Basarić *et al.* when studying the anion binding properties of a series of bis(naphthylurea) receptors.[165]

The difference in the solvent media also needed to be examined. While the anion binding studies were initially carried out in CH_3CN (low polarity, meaning less interaction with anion and binding site) and then in DMSO-*d*$_6$, to facilitate ^{1}H NMR studies (high polarity, meaning more interaction with anion and binding site), lower binding constants and lower-order species could be expected to be observed in the ^{1}H NMR studies. Unfortunately, as discussed above, the absorption studies in DMSO were inconclusive, due to the absorption bands of the ligands having low energy and being outside of the cut-off range of the solvent (see test in Appendix A2 Figure A2.76). The ^{1}H NMR anion titration studies could not be carried out in CD_3CN, due to low solubility at the required experimental concentration, for ligands **87-89**. However, in the case of **86**, the solubility of the ligand was higher, and these titrations were carried out and will be discussed in the next section.

While the binding constants are, by their own nature, independent from the concentration, self-aggregation of the ligand at high concentrations could cause interference in the binding and, consequently, affect negatively the binding constant. Considering, the well-known self-assembly properties of BTA based tripodal ligands, the possibility of self-

Table 2.14. Binding constants for ligands **86** obtained from ^{1}H NMR titrations and UV-vis absorption titrations, [M^{-1}]. ^{a} Titration carried out in DMSO, ^{b} titration carried out in CH_3CN; ^{c} the only species obtained was 1:1.

		Cl^-		**AcO^-**		**$H_2PO_4^-$**		**SO_4^{2-}**	
	conc/M	**$K_{1:1}$**	**$K_{1:3}$**	**$K_{1:1}$**	**$K_{1:3}$**	**$K_{1:1}$**	**$K_{1:3}$**	**$K_{1:1}$**	**$K_{1:3}$**
^{1}H NMR^a	7×10^{-3}	3.2×10^1	-^{c}	2.5×10^3	3.2×10^5	2.0×10^2	-^{c}	8.0×10^0	-^{c}
^{1}H NMR^a	2×10^{-3}	3.1×10^2	-^{c}	2.0×10^4	2.0×10^6	1.0×10^3	-^{c}	2.5×10^2	-^{c}
UV-vis^b	8×10^{-6}	1.6×10^5	7.9×10^6	4.0×10^5	6.3×10^6	4.0×10^5	2.0×10^6	2.0×10^6	2.0×10^9

aggregation of the **tmBTA** ligands at higher concentrations needed to be considered. For these reasons, aggregation studies were carried out, and will be discussed in detail in section 2.4.

2.3.2.5. Anion binding properties of ligand 86 in CD_3CN *vs.* DMSO-d_6

To compare the results obtained from ^1H NMR and UV-vis absorption, titrations of ligand **86** in CD_3CN were carried out with Cl^-, CH_3COO^-, $H_2PO_4^-$ and SO_4^{2-}. The same titration could not be carried out with the other ligands, due to solubility issues.

Key equivalents of ligand **86** with Cl^- in CD_3CN are shown in Figure 2.35. The changes in the chemical shifts indicated that hydrogen bonding was occurring between the ureas and these anions. Furthermore, strong deshielding of the urea protons resulted in the shift of the urea protons from 7.93 ppm to 10.00 ppm for Ha and from 8.05 ppm to 10.33 ppm for Hb. Among the aromatic protons, four different behaviours were evident: firstly, the resonance assigned to H14 was the only one unchanged; a second trend was noted in the resonance of proton H13, which was deshielded up to the addition of 1 equivalents. Resonances of protons H9 and H10 did not undergo shifts in the presence of less than 1 equivalent of anion. However, at higher concentration of the anion H9 became deshielded, while H10 was shielded. The resonance for H10 in the free ligand (in CD_3CN) was split due

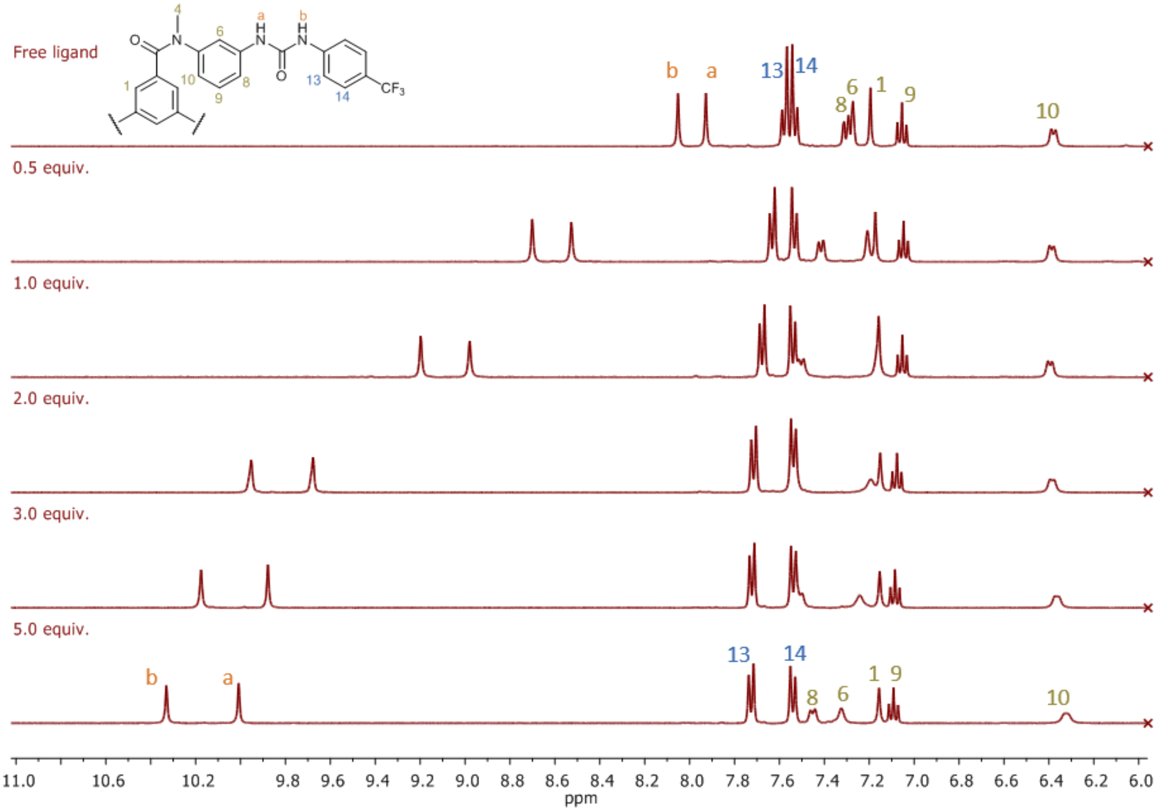

Figure 2.35. ^1H NMR titration profile of **86** with Cl^-, in CD_3CN. [**86**] = 7 mM. Only aromatic and urea protons region shown for clarity. This titration is representative of reproducible trends.

to spin coupling to H9, which was not visible in the ^{1}H NMR of the ligand in DMSO-d_6 due to broadening of the resonance. The addition of Cl^- caused the resonance of H10 to become broadened along with strong shielding. This indicated the rearrangement into a more ‘open propeller’ conformation, consistent with the previous titrations, to bind multiple anions, in the presence of excess Cl^-. The trend of other aromatic protons, over the titration, indicated the same behaviour: the Δδ of protons H1, H6 and H8 displayed a sharp inversion after the addition of 1 equivalent, suggesting two different arrangements in the two conditions (<1 equivalent and >1 equivalent of Cl^-). These changes were best fitted using non-linear regression analysis and a model containing two binding stoichiometries, namely 1:1 and 1:3 (L:A). This gave binding constants of $K_{1:1} = 2.5 \times 10^3\ M^{-1}$ and $K_{1:3} = 3.1 \times 10^5\ M^{-1}$. The binding model resembled that observed in the absorption titration, demonstrating that a significant solvent effect existed. The values of the binding constants determined were lower than the ones calculated from UV-vis titrations. However, the same factors discussed above also have to be considered here. Specifically, that the fitting of ^{1}H NMR titration data is not reliable with constants higher that $K_{1:1} = 10^6\ M^{-1}$ and, also, the higher ligand concentration of the ^{1}H NMR titrations could cause self-aggregation of the ligand to occur, which would result in a weaker anion binding.

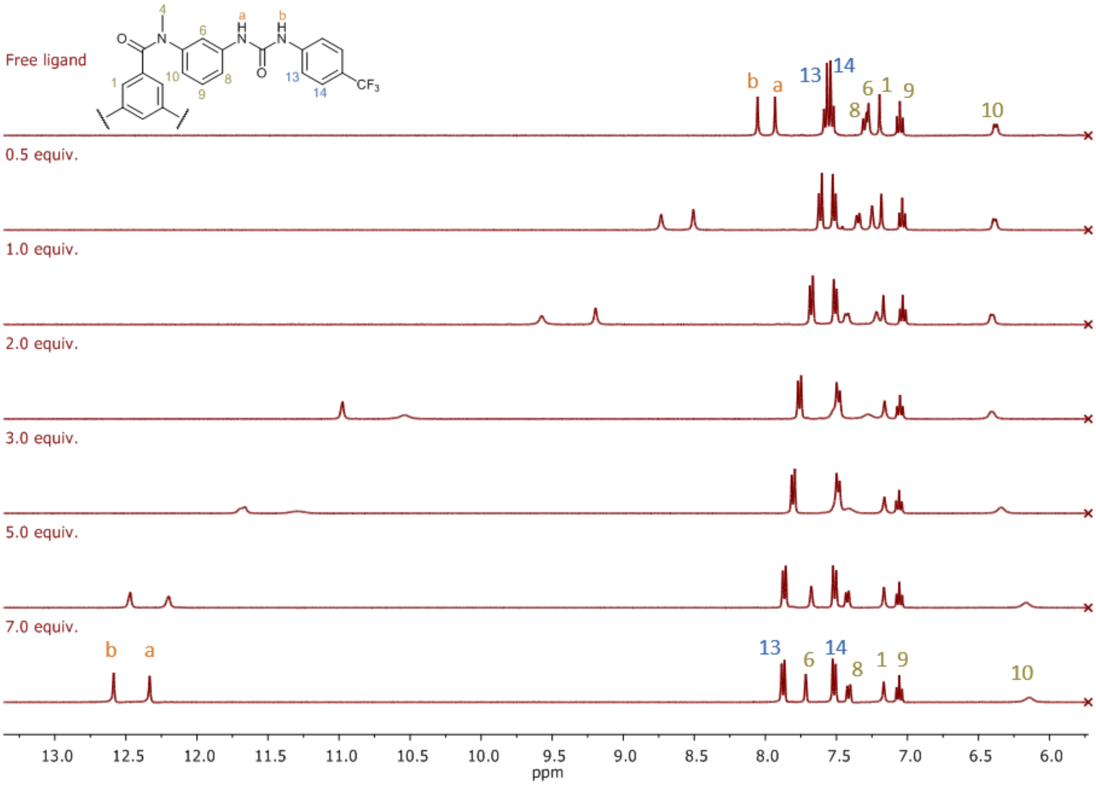

Figure 2.36. ^{1}H NMR titration profile of **86** with CH_3COO^-, in CD_3CN. [**86**] = 7 mM. Only aromatic and urea protons region shown for clarity. This titration is representative of reproducible trends.

When titrating **86** in CD_3CN with CH_3COO^- a similar trend was observed. Although, here larger downfield shifts were seen for the urea protons. As shown in Figure 2.36, urea protons Ha and Hb were shifted by 4.40 ppm and 4.54 ppm, respectively, suggesting the formation of hydrogen bonding interactions with the anion. The aromatic protons were also shifted in a manner consistent with the titration with Cl^-. However, a more pronounced shift of protons H6 and H10 was observed, Figure 2.39b. Also in this case, a return of the shifts towards their original positions was noted after 1 equivalent of CH_3COO^-. The opposite behaviour was observed for H10, which returned close to its original chemical shift and in fact became shielded after the addition of 2 equivalents. The best fit was obtained with the same two species binding model, giving $K_{1:1} = 6.3\times 10^6$ M^{-1} and $K_{1:3} = 1.6 \times 10^5$ M^{-1} . This model confirmed a similar behaviour of this ligand observed in the absorption titrations. However, as these binding constants are large, the absolute values should be considered with caution due to the limitation of the ^1H NMR titration.[164]

The same trend was observed in the titration of ligand **86** with SO_4^{2-}, Figure 2.37, showing that their binding was weaker than the binding with CH_3COO^-, Figure 2.39a-c. However, a strong interaction was observed with a different binding model and with binding constants ($K_{1:1} = 1.0 \times 10^3$ M^{-1} and $K_{1:3} = 1.3 \times 10^3$ M^{-1}) larger than those observed for **86** in DMSO-d_6. From the shifts in the aromatic proton resonances during the titration with $H_2PO_4^-$

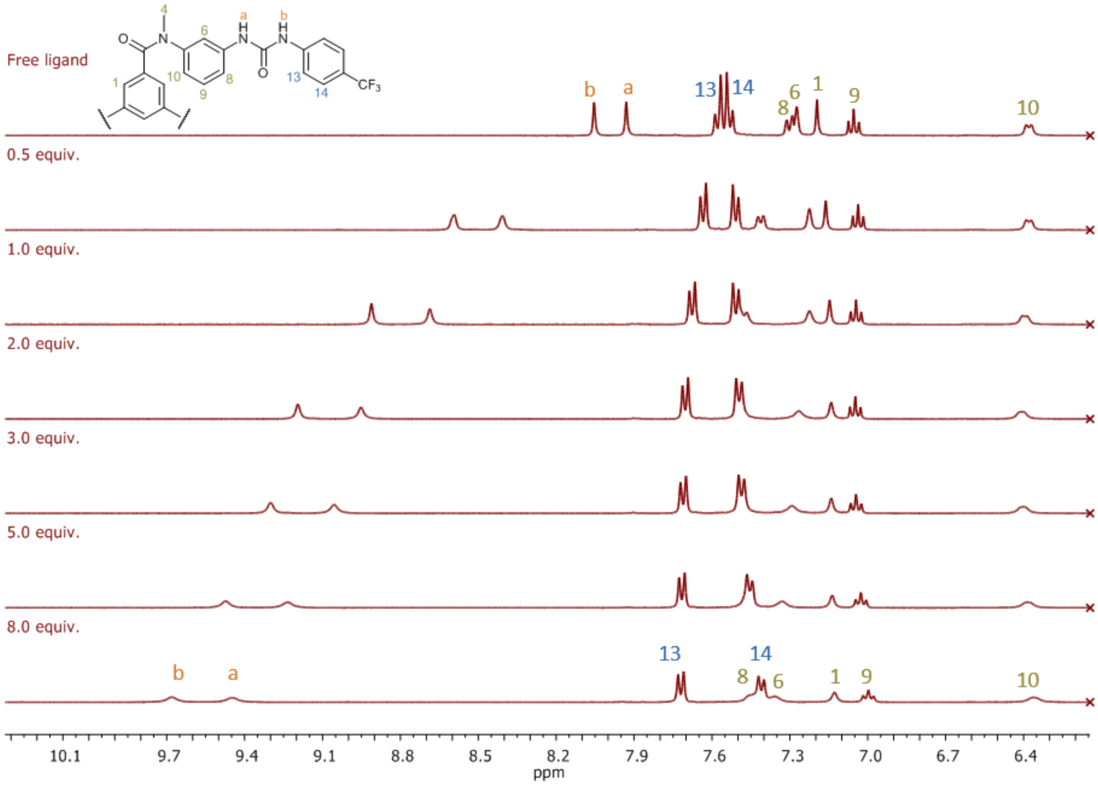

Figure 2.37. ^1H NMR titration profile of **86** with SO_4^{2-}, in CD_3CN. [**86**] = 7 mM. Only aromatic and urea protons region shown for clarity. This titration is representative of reproducible trends.

, Figure 2.38, it could be seen that the binding with this anion did not follow the same behaviour. In fact, here it was evident that a deprotonation was occurring, which was consistent with the behaviour observed in DMSO-*d*$_6$. The data were best fitted to the same binding models and large binding constants were obtained, $K_{1:1} = 4.0 \times 10^6$ M^{-1} and $K_{1:3} = 2.5 \times 10^5$ M^{-1}, showing a strong interaction with the anion (similar to Cl$^-$) in this media. The changes in the chemical shifts of the ligand also agreed with the two-species binding model as they changed direction after one equivalent, reaching a plateau after the addition of 3 equivalents, Figure 2.39d.

As expected, the ^{1}H NMR titrations of **86** in CD_3CN showed stronger interactions of the ligand with the anions than the titration in DMSO-*d*$_6$, with a two-species (1:1 and 1:3) binding mode consistent to the UV-vis absorption titrations in the same solvent, Figure 2.40. Similarly, the changes of the proton resonances throughout the course of the titrations would support that conformational changes occur. The binding constants calculated by the fitting of the data to the model were relatively large, Table 2.15, and, hence, more challenging to calculate reliably. In DMSO-*d*$_6$ there was discrimination between the various anions, with $H_2PO_4^-$ and CH_3COO^- displaying significantly larger changes in chemical shift than Cl$^-$ and SO_4^{2-}. In CD_3CN, a larger interaction of the ligand with all the anions was observed compared to in DMSO-*d*$_6$, however, the differences between the four anions in CD_3CN were

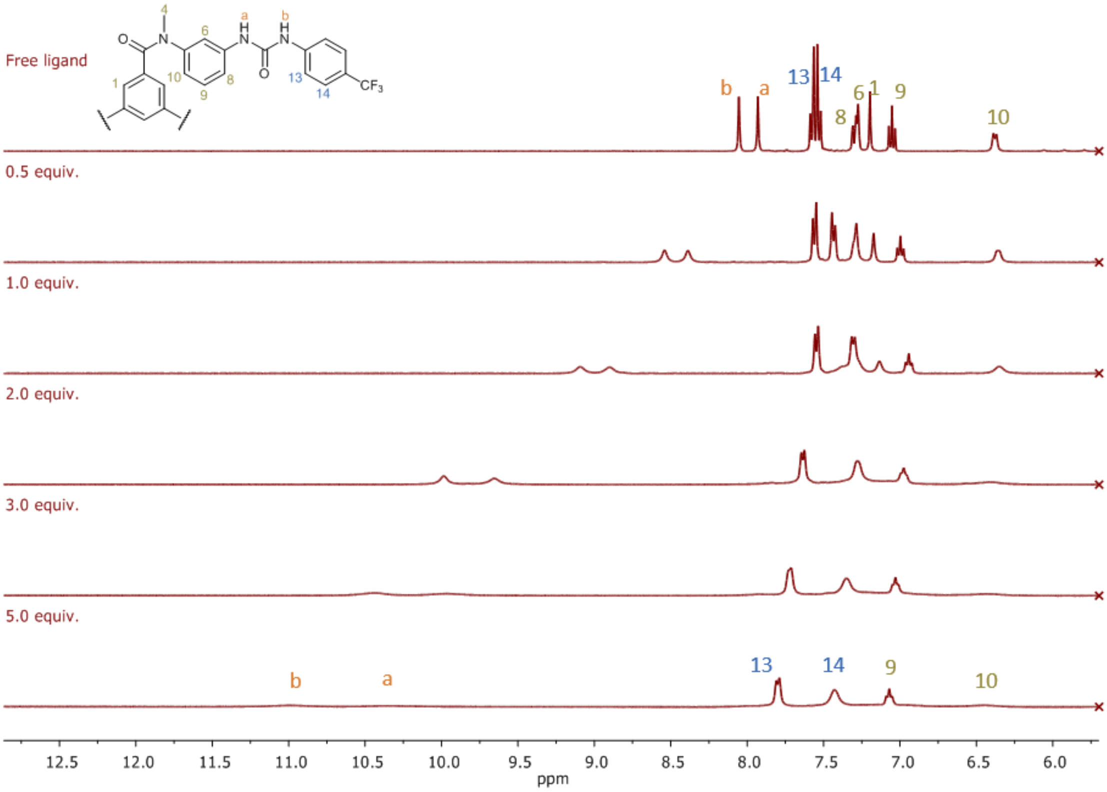

Figure 2.38. ^{1}H NMR titration profile of **86** with $H_2PO_4^-$, in CD_3CN. [**86**] = 7 mM. Only aromatic and urea protons region shown for clarity. This titration is representative of reproducible trends.

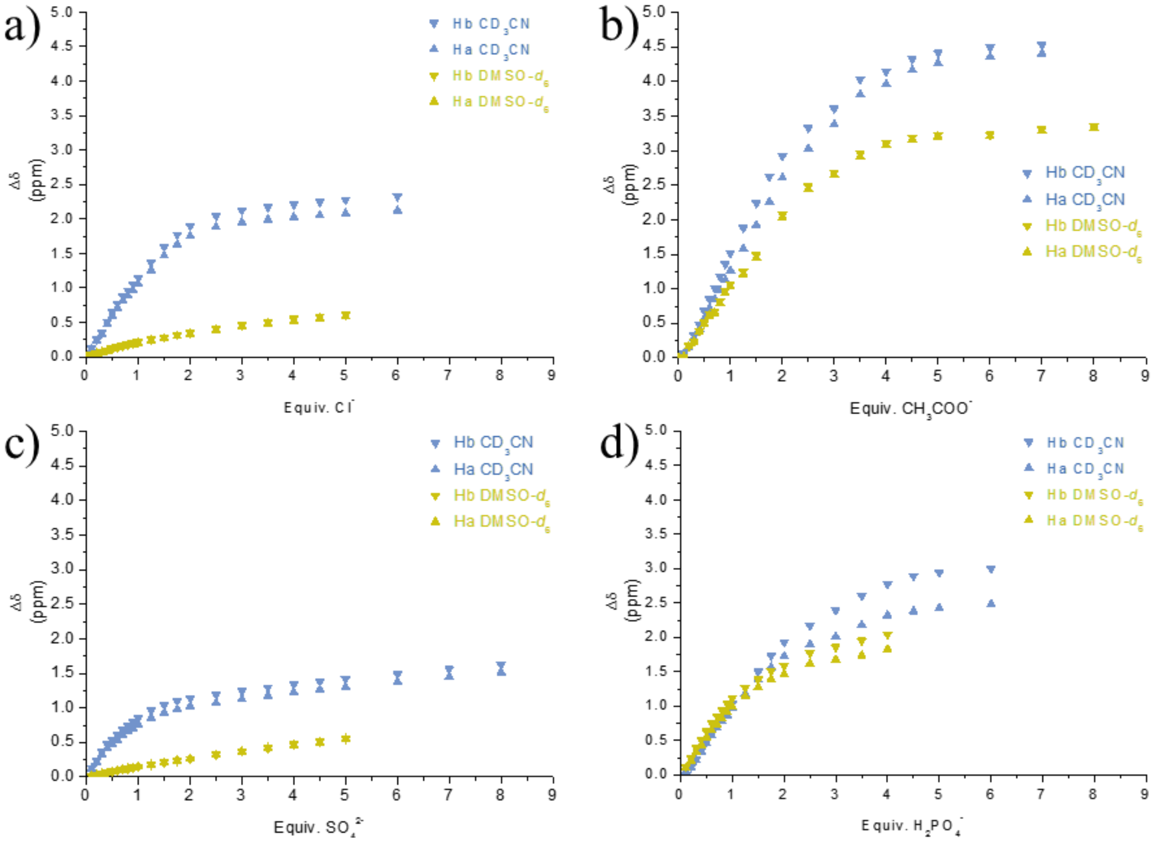

Figure 2.40. Selected binding isotherms of urea protons in CD_3CN (blue) and DMSO-d_6 (green) titration of **86** with a) Cl^-, b) CH_3COO^-, c) SO_4^{2-}, d) $H_2PO_4^-$.

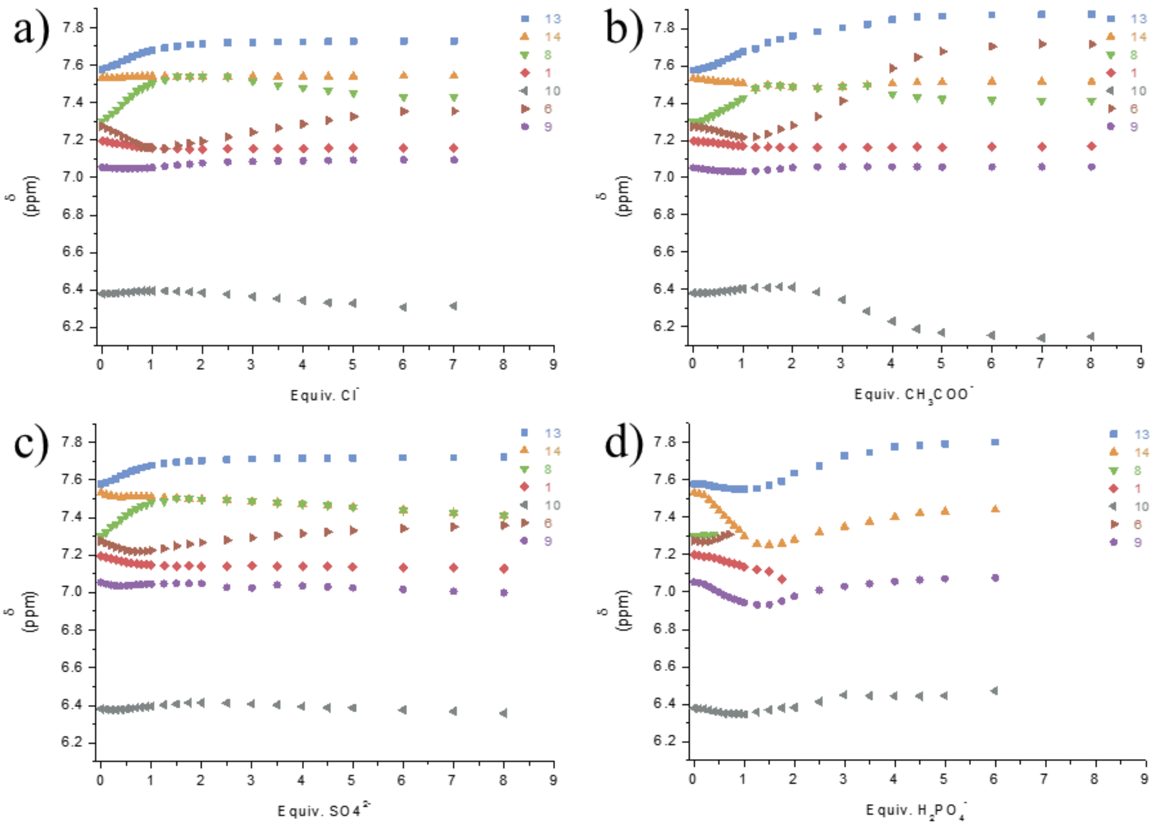

Figure 2.39. Selected binding isotherms of aromatic protons in CD_3CN titration of **86** with a) Cl^-, b) CH_3COO^-, c) SO_4^{2-}, d) $H_2PO_4^-$.

Table 2.15. Binding constants for ligands **86** obtained from ^1H NMR titrations and UV-vis absorption titrations, [M^{-1}]; errors are estimated within 10%. [a] Titration carried out in DMSO, [b] titration carried out in CH_3CN; [c] the only species obtained was 1:1.

		Cl^-		**AcO^-**		**$H_2PO_4^-$**		**SO_4^{2-}**	
	conc/M	**$K_{1:1}$**	**$K_{1:3}$**	**$K_{1:1}$**	**$K_{1:3}$**	**$K_{1:1}$**	**$K_{1:3}$**	**$K_{1:1}$**	**$K_{1:3}$**
^1H NMR[a]	7×10^{-3}	3.2×10^{1}	-[c]	2.5×10^{3}	3.2×10^{5}	2.0×10^{2}	-[c]	8.0×10^{0}	-[c]
^1H NMR[a]	2×10^{-3}	3.1×10^{2}	-[c]	2.0×10^{4}	2.0×10^{6}	1.0×10^{3}	-[c]	2.5×10^{2}	-[c]
^1H NMR[b]	7×10^{-3}	2.0×10^{3}	5.0×10^{5}	6.3×10^{6}	1.6×10^{5}	4.0×10^{6}	2.5×10^{5}	1.0×10^{3}	1.3×10^{3}
UV-vis[b]	8×10^{-6}	1.6×10^{5}	7.9×10^{6}	4.0×10^{5}	6.3×10^{6}	4.0×10^{5}	2.0×10^{6}	2.0×10^{6}	2.0×10^{9}

smaller, thus reducing the discrimination among the anions. This was also consistent with the observation in the UV-vis studies of non-specific behaviour between the ligand and the anions.

These studies demonstrated the strong influence of the solvent in the self-assembly process between anionic guests and **86**, and it is reasonable to consider that analogous interactions being involved in the binding processes of the other ligands. This strong influence of the solvent was also significant in the solid state, as discussed in section 2.2.1 for the free ligands. Indeed, the importance of solvent was also noted in the solid-state binding of ligand **87** with SO_4^{2-}, which will be discussed in the next section.

2.3.3. Solid state binding studies

To further characterise the anion binding properties of the ligands discussed above, attempts to grow crystals of anion complexes of **86-89** from different solvents were carried out. However, crystals were obtained only from solutions of **87**. These provided insight into the solid-state structural properties of the compounds and their packing interactions, as well as giving information about the binding geometry around the anion. The general crystallographic data and structure refinements are provided in **Errore. L'origine riferimento non è stata trovata.**. Identical single crystals, **87**·SO_4^{2-}(DMSO) and **87**·SO_4^{2-}(CH_3CN), were obtained by slow evaporation of both DMSO and CH_3CN solutions, respectively, in the presence of excess of TBA sulfate. The same solutions of the ligand with other anions (CH_3COO^-, $H_2PO_4^-$, Cl^-) resulted in the crystallization of the free ligand alone, showing preference of **87** for SO_4^{2-} in the solid state. Only one of the two identical structures will be discussed, **87**·SO_4^{2-}(DMSO), but tables will include the data of both for comparison.

The crystallographic data of **2** with SO_4^{2-} (**87**·SO_4^{2-}) were solved and refined by Dr Salvador Blasco in the trigonal space group R_{-3}, with each of the SO_4^{2-} anion positioned on a hexagonal axis, within a tight hydrogen binding pocket. The asymmetric unit contains 1/3 of a molecule of **87**, 1/6 of a SO_4^{2-} anion. Solvent molecules and the counterions were present, however, these were disordered and not interacting with their host receptor or guest anion. Within the crystal structure of **87**·SO_4^{2-}, each ligand binds to three different SO_4^{2-} ions, Figure 2.42. In contrast to the structure of **87** (*cf*. Figure 2.5 and Figure 2.6), in **87**·SO_4^{2-} , all the three 2,4-difluorophenyl moieties are now equally rotated at 77.07° with respect to the urea groups; the amide carbonyls and the *N*-methyl groups pointing away from the central C_3 axis, and it is clear that the preorganisation observed in **87** is to greater extent maintained in **87**·SO_4^{2-}, where **87** upholds its 'propeller-like' conformation.

The combined hydrogen bonding interactions gave rise to a supramolecular self-assembled polymeric structure, Figure 2.42b. Instead of behaving like the *para*-phenylurea analogues in creating capsules,[152] the open "propeller-like" structure of this ligand offered a better arrangement for SO_4^{2-} in this 2D network. Each SO_4^{2-} ion is surrounded by six urea

Table 2.16. Hydrogen bond lengths [Å] and angles [°] for the structure of **87**·SO_4^{2-} obtained from DMSO.

Structure	D–H···A	d(D–H)	d(H···A)	d(D···A)	∠(DHA)
87·SO_4^{2-} (DMSO)	N2–H2···O4[1]	0.88	2.29	3.111(7)	155.5
	N2–H2···O4[2]	0.88	2.24	3.095(8)	163.6
	N3–H3···O3[2]	0.88	1.92	2.740(6)	153.9
	N3–H3···O3[3]	0.88	2.19	2.975(8)	147.9

[1] 1-Y,1+X-Y,+Z; [2] 2/3-X,4/3-Y,1/3-Z; [3] 2/3-Y+X,1/3+X,1/3-Z

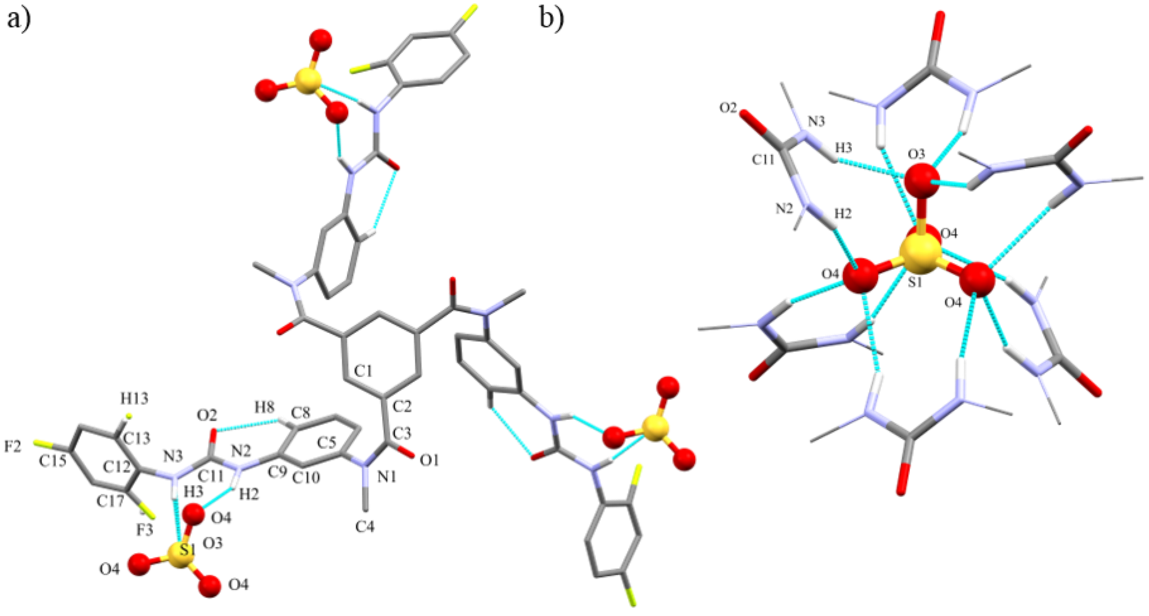

Figure 2.41. SC-XRD crystal structure of **87·SO_4^{2-}**: a) capped stick representation showing one ligand hydrogen bonding to three SO_4^{2-} molecules. b) Perspective and detail of the sulfate hydrogen bonding. The sulfate anion has two possible orientations; only one is shown for clarity, together with non-H-bonding hydrogens.

groups, from six different molecules of **87**, Figure 2.42c, with a total of 12 hydrogen bonds, with N-H···O(S) bond lengths ranging from 1.933-2.290 Å, Table 2.1. This demonstrated that the high-coordination preference of the anion was fulfilled within this binding arrangement.[23] In fact, the formation of 12 hydrogen bonds towards SO_4^{2-} is not commonly observed, because of its high solvation energy and the highly symmetrical geometric requirements. The anion templation effect resulted in an overall C_3 symmetry of the ligand within the crystal, tessellating around the SO_4^{2-} anion and resulting in the formation of the extended 2D layers along the *ab* plane. These layers were stacked along the *c* axis, each one rotated +/- 120° with respect to the surrounding planes. This network was stabilised further by inter-ligand π-π stacking and additional hydrogen bonding interactions. For example, an

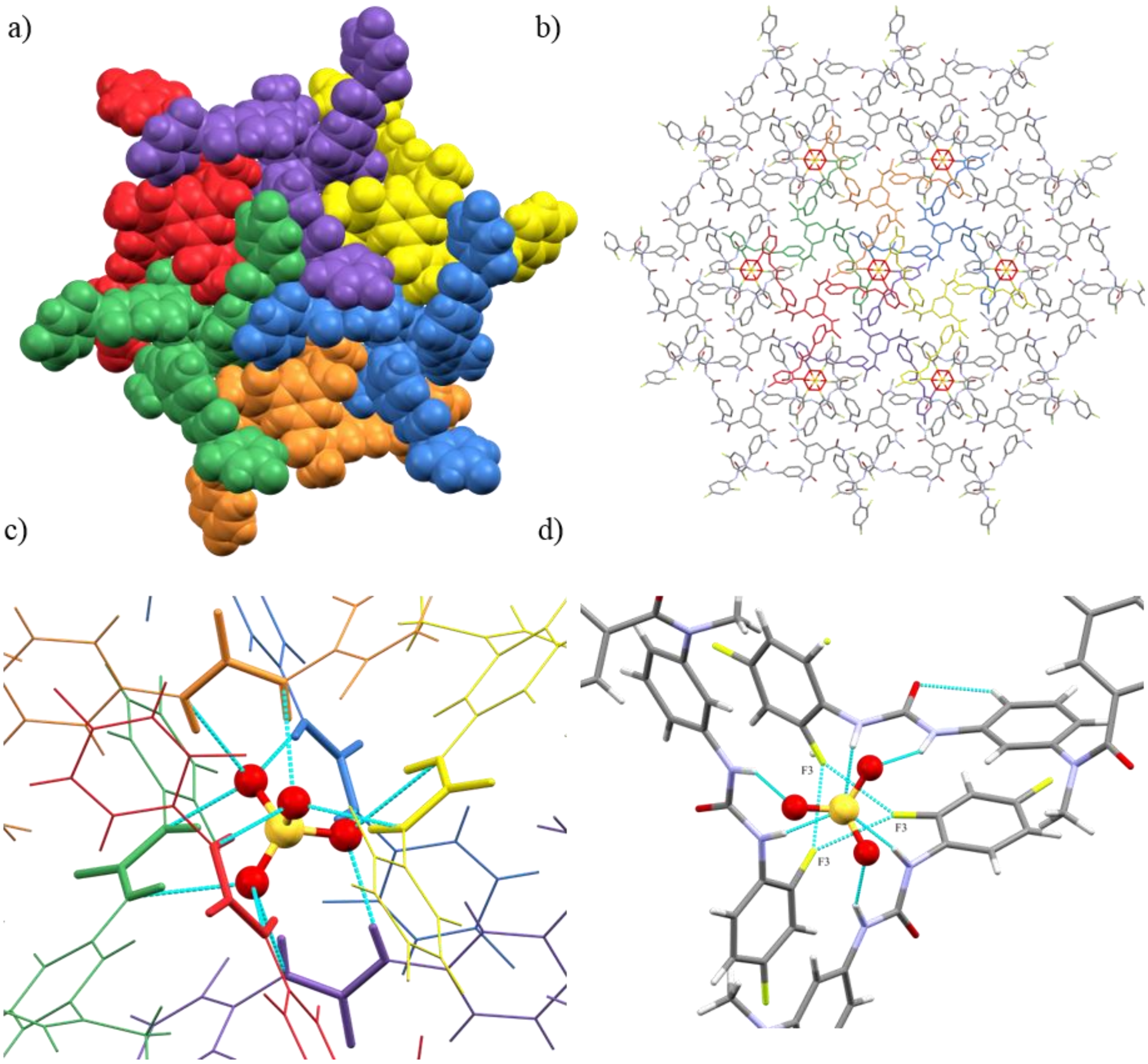

Figure 2.42. Crystal structure of **87**·$\mathbf{SO_4^{2-}}$: a) cluster formed by 6 molecules of **87** around 1 sulfate; b) packing details viewed down *c* axis (only one layer shown): every sulfate interacts with 6 different molecules of **87** and every molecule of **87** interacts with three different SO_4^{2-} molecules; c) hydrogen bonding detail: ligands depicted in different colours with urea moiety highlighted with capped sticks over the wireframe representation. The sulfate anion has two possible orientations; one of them has been omitted for clarity. d) Perspective and detail of the sulfate hydrogen bonding and F-F interaction.

internal hydrogen bonding between the urea carbonyl and the hydrogen atom H8 which planarize the moiety, Figure 2.41, and an interaction from the “activated” proton H14 to the carbonyl of the central core in a neighbouring molecule. The π-stacking interactions differs from the ligand crystal where face-to-face interaction were seen between distal phenyl rings from the neighbouring molecules. This places the *ortho*-fluorine in one of two sites within the bulk crystal structure, with a similar occupancy distribution to the ligand crystal, where 32% has a potential aromatic CH···O(amide) hydrogen bond in place and 68% in the alternate conformation. The SO_4^{2-} anion was found in two different orientations along the *c* axis, producing two crystallographically different oxygens in axial (O3) or equatorial (O4) orientations (see Appendix A2, figure A2.70). One of the *ortho*-fluorine atoms is situated very close to this axis, so has two symmetry generated fluorine atoms at 2.59(4) Å, suggesting the possibility of F-F bond, Figure 2.42d, as Gunnlaugsson and co workers[153] have also observed in other self-assembly structures. While a recent example by Das showed the trigonal CO_3^{2-} templating a tripodal ligand in a similar fashion,[125] structures of anions templating the self-assembly of 2D networks have rarely been reported (Section 1.3.4) ; particularly so for sulfate. The network formed by **87**·SO_4^{2-} represents the first example of the use of SO_4^{2-} anion as a template to generate such a higher order 2D self-assembly from tripodal ligands, instead of the more commonly seen capsule formation.[166]

It was interesting to notice that while hydrogen bonding was observed for **87** with SO_4^{2-} in the solid state, the same interaction was not detected by ^{1}H NMR in DMSO-d_6. This, again, indicated that a strong interaction between the solvent and the binding site as well as between the solvent and the anion, was preventing the interaction to occur in solution. However, the crystallisation process, which, by evaporation of the solvent, naturally reduces those interactions, opening the possibility for new ones. Having obtained the same structure by evaporation of the **87**·SO_4^{2-} complex from two different solvents, also indicates the independence of the 2D network formation from the solution interaction.

Aggregation studies of the ligand in the solvent media used for the anion binding studies will be presented in the next section, and will give more insight into their interactions.

2.4. Self-assembly studies on ligands 86-89

Molecules with the BTA motifs have been extensively used in recent years for the development of self-assembled gels, and materials, because of its natural ability to stack and aggregate.[117] The stacking properties of the BTA’s core generally take advantage from a combination of π-π stacking and intermolecular hydrogen bonding between the amide

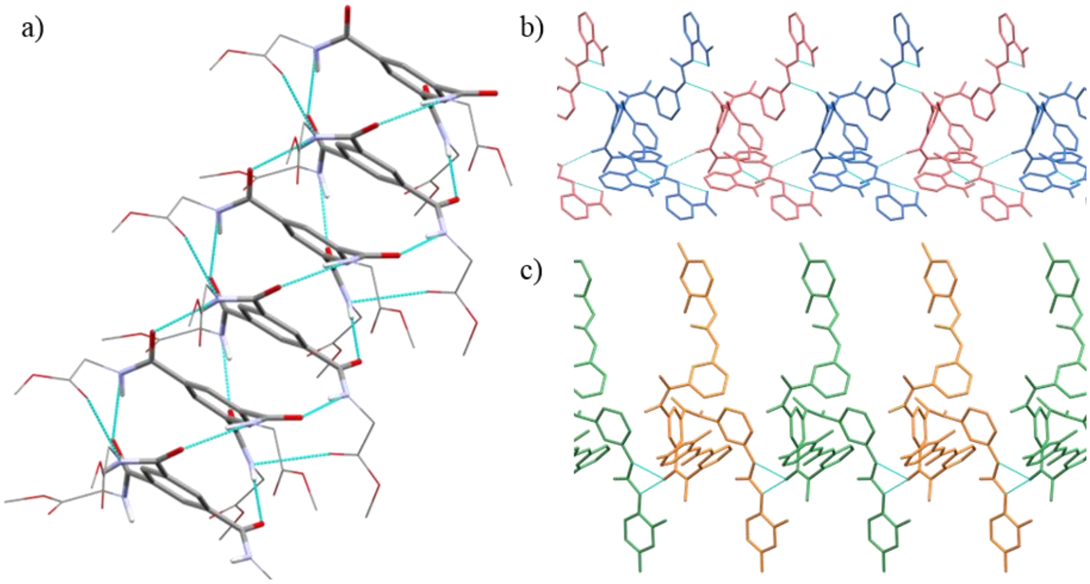

Figure 2.43. Crystal structures showing the self-assembly of a) general tripodal **BTA** structures (from ref 146) with hydrogen bonding between amide groups of the central core; b) **tmBTA** ligand **88** and c) ligand **87** showing hydrogen bonding connection between the amide carbonyl and urea groups of the arms of neighbouring molecules.

groups of adjacent molecules, as demonstrated in Figure 2.43a[146]. In the case of ligands **86-89**, the same hydrogen bonding between the amides was prevented due to the methyl substituent on the amide nitrogen. However, the presence of urea groups on the arms of these ligands could still interact with the carbonyl groups of the amides, as seen in the crystal structure of the ligands **87** and **88**, in Figure 2.43b-c, giving rise to self-assembled hierarchical structures.

The anion binding studies suggested that at higher concentration the self-assembly of the ligand in solution could occur and compete, together with the solvent, for the binding site, lowering its availability for the anions. Hydrogen bonding interactions observed in the solid state, suggested the possibility that these would occur also in solution. Therefore, aggregation studies were carried out which will be discussed in the next section. Aggregation studies were performed using different techniques such as UV-vis absorption spectroscopy, ^{1}H NMR spectroscopy, Scanning Electron microscopy (SEM) and DLS analysis, depending on the case and the solubility of the ligands. The studies were carried out in organic solvents such as CH_3CN, DMSO, CH_3OH, and their aqueous mixtures, to understand the effects of the polarity of the solvent medium. Sample preparation and imaging by SEM was carried out by Dr Savyasachi A.J.

2.4.1. Self-assembly studies in CH_3CN

To evaluate the aggregation properties in CH_3CN initially the ligands solubilities were tested. From preliminary investigations, ligands **87** and **88** were found to be soluble in

CH_3CN at a concentration lower than *ca*. 1 × 10^{-4} M, **89** showed a very poor solubility in this solvent, as mentioned in section 2.3.1, while **86** displayed good solubility even at concentrations of *ca*. 1 × 10^{-2} M. For **86-88** the linearity of the Beer-Lambert plot in CH_3CN, within the range of the UV-vis studies, excluded the aggregation of the ligands in this range of concentration. For **86** the linearity of the Beer-Lambert plot was confirmed up to 3 ×10^{-4} M, Figure 2.44; at higher concentrations saturation effects prevented the collection of data. By ^{1}H NMR a wider range of concentrations, 5×10^{-5}- 1×10^{-2} M, could be analysed, Figure 2.46. At concentrations higher than 5×10^{-4} M some shifts of the proton resonances were evident, suggesting that aggregation could be occurring at higher concentrations. Most evidently, the shift of the urea proton resonances Ha and Hb by *ca*. 0.03 ppm towards higher frequencies suggested their involvement in hydrogen bonding interactions. Meanwhile, the resonances of the aromatic protons H8 were shifted upfield by 0.12 ppm, as well as H13 and H14, which were also shifted downfield by 0.06 and 0.04 ppm, respectively. Similarly, H9 and H10 were shifted by 0.04 and 0.02 ppm, displaying a shielding effect. In contrast, upon increasing the concentration of the ligand in solution, both protons H1 and H6 displayed a shift of 0.04 ppm towards higher resonances. These studies indicated that during the titrations of **86** at the concentration of 7×10^{-3} M, aggregation of the ligand could have been occurring and, as a result, interfering with the anion binding process. This behaviour could justify the differences observed in the binding constants between the UV-vis absorption and ^{1}H NMR studies, in CH_3CN.

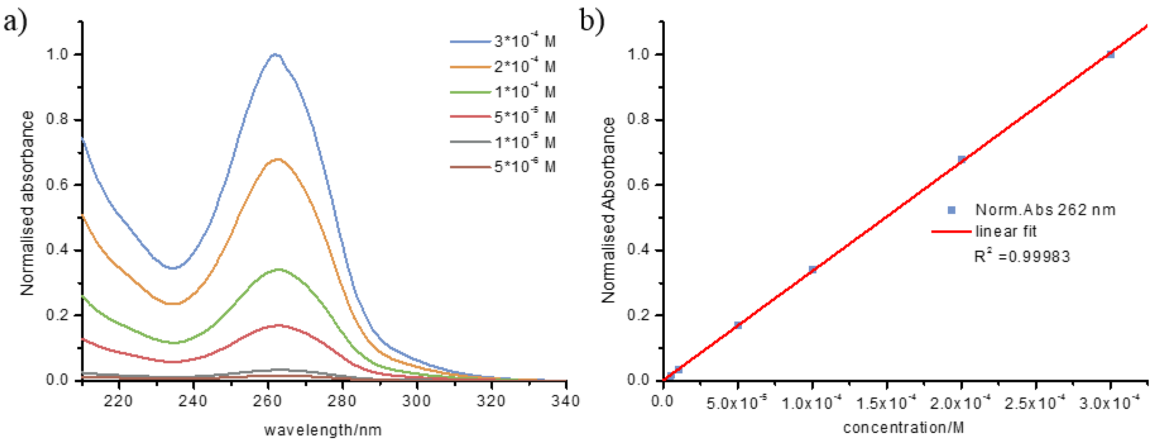

Figure 2.44. UV-vis aggregation studies for **86** in CH_3CN: a) UV-vis plot, run with 0.2 cm path quartz cell, with normalised absorbance; b) Beer-Lambert plot at 262nm displaying good linearity.

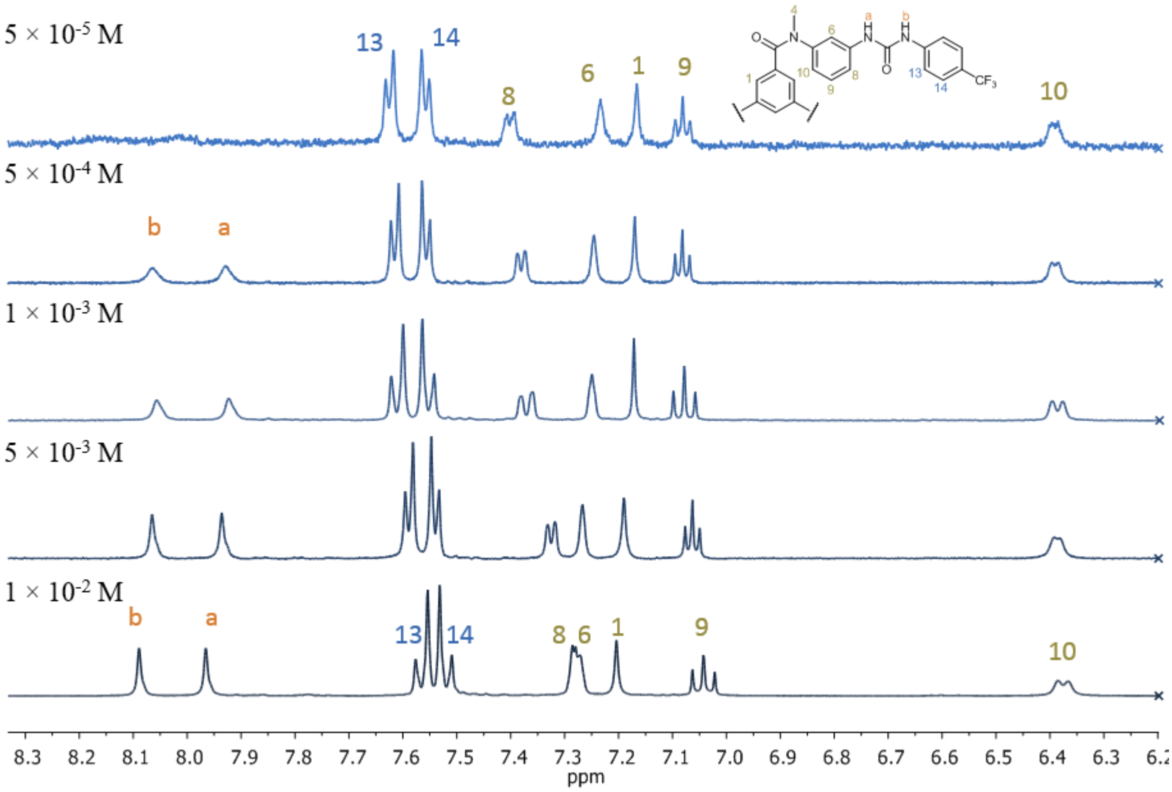

Figure 2.46. Stacked ^{1}H NMR (600MHz) spectra of **86** in CD_3CN showing the shift in the proton resonances upon increase of the concentrations from $5×10^{-5}$ to $1×10^{-2}$ M.

In an attempt to visualise the morphology of the self-assembly process, solutions of **86** in CH_3CN were drop-cast onto silica plates and dried in the air overnight and for 2 hrs in high vacuum. Following this, the samples were plated with a layer of gold. SEM imaging of the samples revealed the aggregation into a 'film-like' morphology, Figure 2.45 (analyses of the remaining ligands were prevented because of their low solubility, see Appendix A2, FigureA2.64). This 'film-like' morphology was characterised by the presence of holes and cracks, depending on the concentration of the deposited solution. From a solution at the concentration of 1 × 10^{-2} M the sample showed a denser morphology with long cracks and

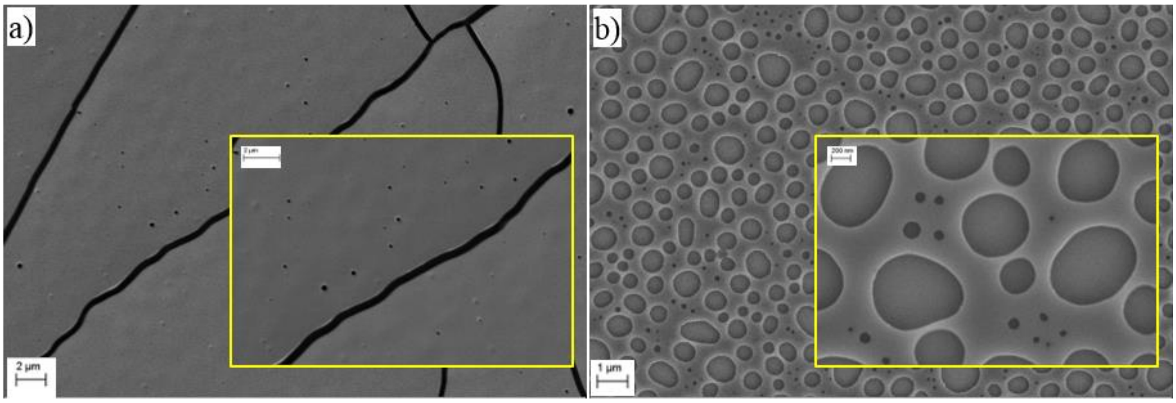

Figure 2.45. SEM images of dried deposited solution of **86** in CH_3CN at different concentrations at time of deposition: a) $1×10^{-2}$M (bar = 2μm); b) $1×10^{-3}$M (bar = 1μm, inset = 200 nm). Inset: magnified image of the same sample.

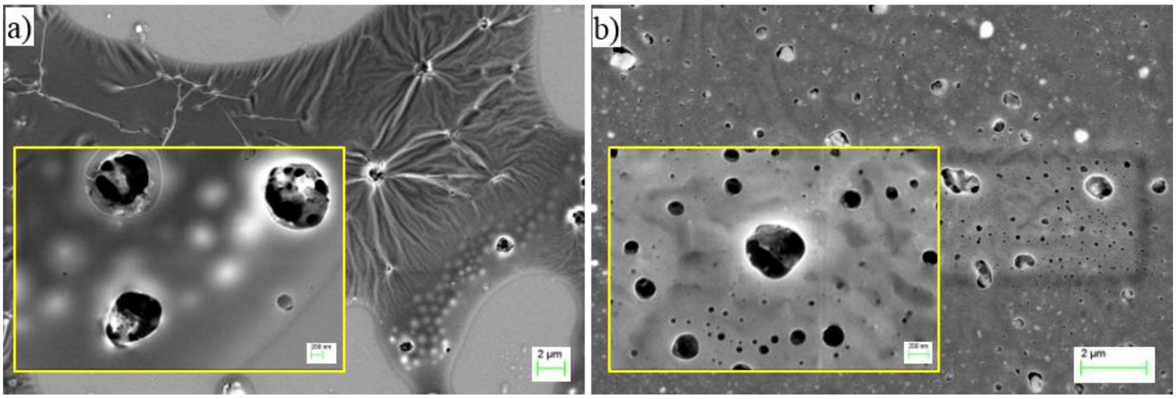

Figure 2.47. SEM images of dried deposited solution of **86** in CH_3CN:H_2O, 1:1. Concentration of sample at time of deposition 1×10^{-3} M. a) free ligand **86** (bar = 2µm, inset = 200 nm); b) ligand **86** with 1 equivalent of TBA_2SO_4 (bar = 2µm, inset = 200 nm). Inset: magnified image of the same sample.

smaller holes, Figure 2.45a, while imaging of samples deposited from a solution of 1×10^{-3} M did not present the same cracks, but larger holes that were more uniformly distributed, Figure 2.45b. Similar morphologies are normally observed in the study of polymeric materials, suggesting that the aggregation event could occur by the formation of supramolecular polymer.[167] The formation of the holes within the film was likely due to the evaporation of the solvent and the aggregation of the ligand, however this could not be experimentally confirmed. To understand the effect of the solvent polarity and the solubility of the ligand on the morphology, samples were prepared in CH_3CN:H_2O (1:1) at the concentration of 1×10^{-3} M, in the presence and absence of 1 equivalent of TBA_2SO_4. In both cases the aggregation showed again the formation of films, but the holes seemed to display a thicker layer covering a more porous structure, Figure 2.47. From these SEM images it was clear that the ligand was creating some supramolecular-polymeric structures, likely due to hydrogen bonding interaction from the urea moieties, intensified by the evaporation of the solvent. However, it was not possible to draw definitive conclusions on the aggregation process.

2.4.2. Self-assembly studies in DMSO

Aggregation properties of ligands **86-89** in DMSO were next analysed through a combination of ^1H NMR experiments and SEM imaging. In this case all the ligands could be analysed, thanks to their higher solubility in DMSO.

The ^1H NMR spectra of the ligands at different concentrations did not indicate any significant aggregation effect (see Appendix, Figure A2.59-61). For example, the self-assembly study for **87**, performed by ^1H NMR showed no shift of the resonances, Figure 2.48. However, in the presence of excess of TBA_2SO_4, the urea and some of the aromatic resonances showed changes which could have been caused by the formation and aggregation

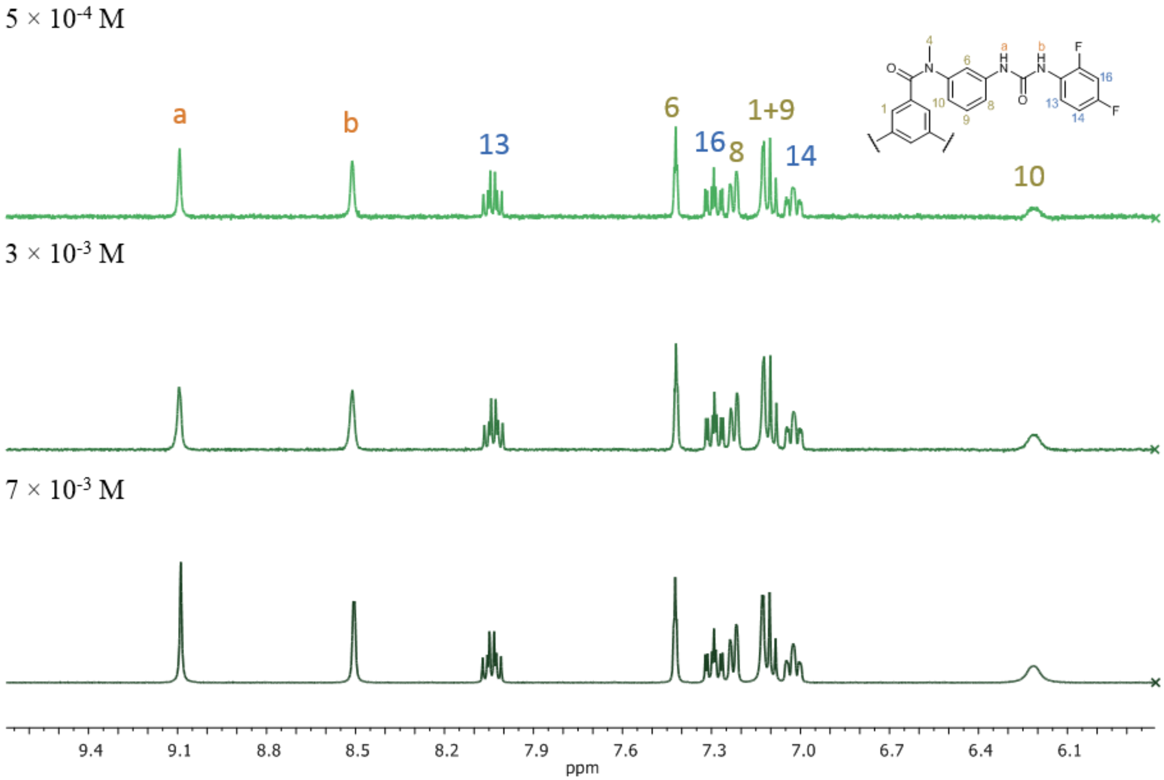

Figure 2.48. Stacked ^{1}H NMR spectra of **87** in DMSO at increasing concentrations between 5×10^{-4}-7×10^{-3}M.

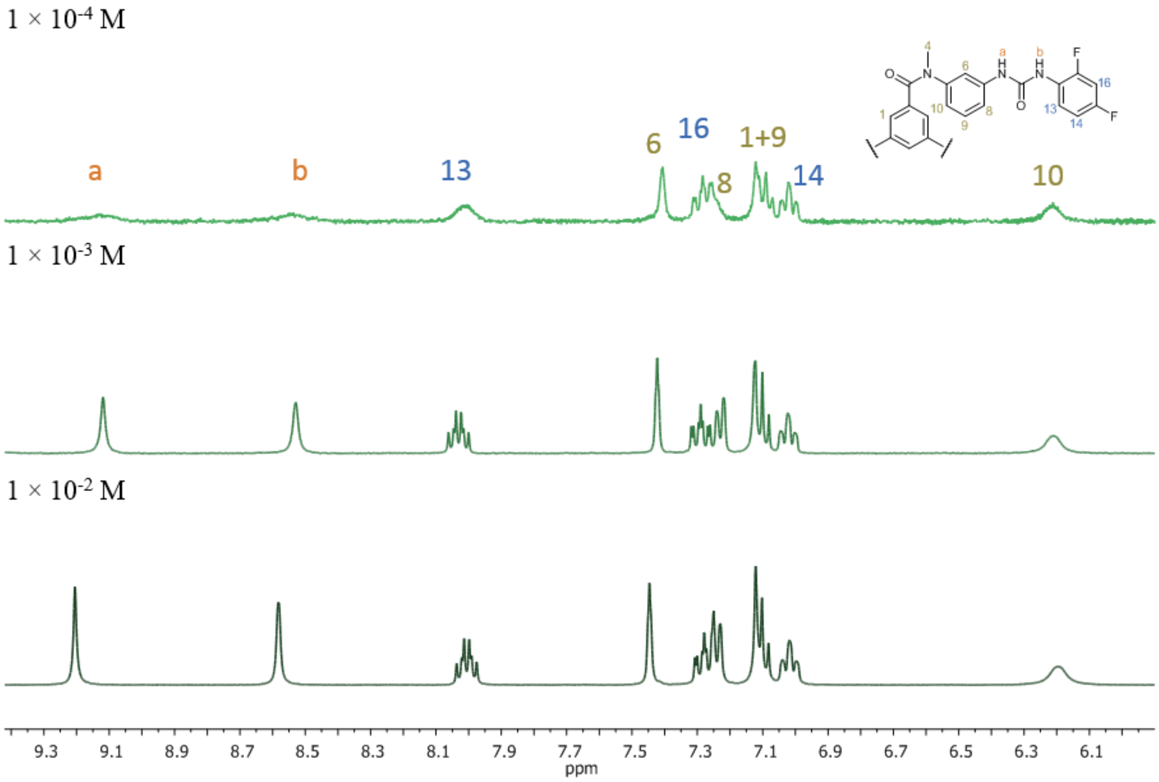

Figure 2.49. Stacked ^{1}H NMR spectra of **87**.SO_4^{2-} in DMSO-d_6 at increasing concentrations between 5×10^{-4}-7×10^{-3}M.

of the SO_4^{2-} complex, Figure 2.49. As it was seen in Section 2.3.3, where ligand **87**, in the presence of SO_4^{2-}, gave rise to a 2D hydrogen bonded crystalline network, the aggregation observed in the ^1H NMR experiments could represent the initial stages of this process.

To visualise the micro-morphology of the self-assembly process, solutions of the ligands in DMSO were deposited and imaged using SEM. In this case, the solutions were deposited on the silica plates and dried in the air over a week and then for 12 hrs in the vacuum prior to imaging, to make sure the high boiling DMSO was completely dried. The SEM images of the dried solutions of free ligands displayed in the formation of films, Figure 2.50, with the exception of ligand **89**, which formed droplet-shaped aggregates, within the film, probably due to its lower solubility, Figure 2.50g. In the presence of 1 equivalent of TBA_2SO_4 the ligand showed the formation of pseudo-spherical self-assemblies within a film-like arrangement, for ligands **86, 88** and **89**, Figure 2.50. In contrast, for ligand **87**, the same pseudo-spherical structures were not formed, instead some semi-crystalline aggregates were visible within the film structure. This behaviour suggested that the interaction of the ligand with SO_4^{2-} was giving rise to ATSA structures, which in the case of **87** could organise themselves into 2D crystalline networks, Section 2.3.3. For the other ligands **86**, **88** and **89**, the same high-ordered structure could not give rise to crystalline networks. However, it was possible that the ligand-anion adducts self-assembled into pseudo-spheres in a similar manner as the one observed in the crystal.

The formation of more defined micro-spherical aggregates in the presence of TBA_2SO_4 was likely due to a combination of the interaction of the anion to the ligand and the highly hygroscopic nature of the SO_4^{2-} salt (which likely became partially hydrated during the air drying process). To further investigate the effect of water in the formation of the spherical aggregates, water was added to a solution in DMSO of the ligands in the presence of 1 equivalent of SO_4^{2-}, to obtain a 1:1 DMSO:H_2O mixture. SEM images of the solutions of **86**, **87** and **88** deposited onto silica wafer are showed in Figure 2.51a-d. These displayed more defined smooth spherical structure, for **86**$\cdot SO_4^{2-}$ and **88**$\cdot SO_4^{2-}$ complexes, while the **87**$\cdot SO_4^{2-}$ complex showed a pseudo-crystalline structure, Figure 2.51d. It was not clear from these analyses whether the aggregate would form with this morphology immediately in the solution, or if it crystallised during the drying process. By using cryo-SEM this question could be addressed, giving us more insight in the solution behaviour. However, this was beyond the immediate scope of the current investigation and access to the technique. The aggregation studies in DMSO highlighted that the free ligands would not aggregate in

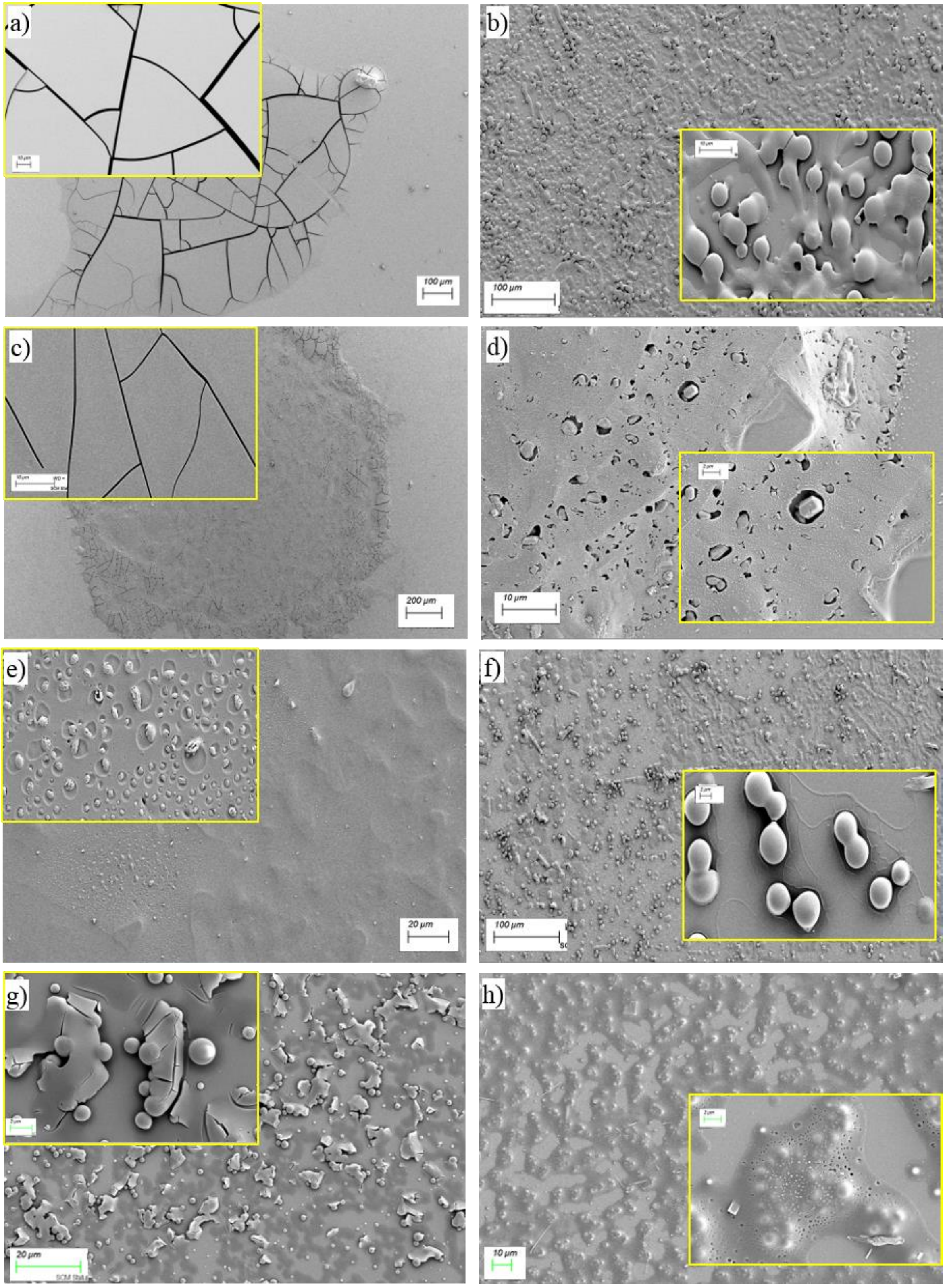

Figure 2.50. SEM images of dried deposited DMSO solutions of a) **86** (bar = 100µm, inset = 10 µm); b) **86**·SO_4^{2-} (bar = 100µm, inset = 10 µm); c) **87** (bar = 200µm, inset = 10 µm); d) **87**·SO_4^{2-} (bar = 10µm, inset = 2 µm); e) **88** (bar = 20 µm, inset = 2 µm); f) **88**·SO_4^{2-} (bar = 100µm, inset = 2 µm); g) **89** (bar = 20µm, inset = 2 µm); h) **89**·SO_4^{2-} (bar = 10µm, inset = 2 µm). Concentration of samples at time of deposition 1×10^{-3}M. Zoomed region inset.

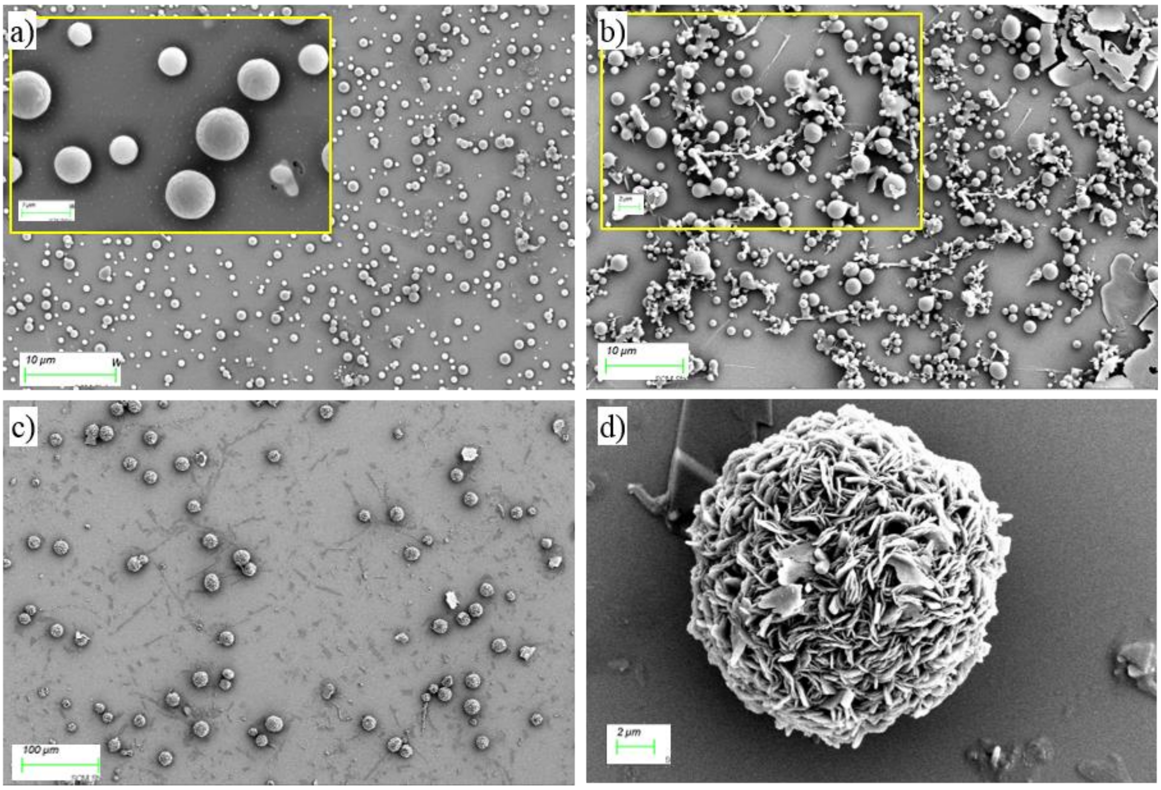

Figure 2.51. SEM images of dried deposited DMSO:H_2O solutions of a) **86**·SO_4^{2-} (bar = 10µm, inset = 1 µm); b) **88**·SO_4^{2-} (bar = 10 µm, inset = 2 µm); c-d) **87**·SO_4^{2-} (bar = 100 µm, expansion = 2 µm).

solutions at concentrations lower than 7 × 10^{-3} M, at which the anion titrations were carried out. However, aggregation effects were observed in the same concentration range in the presence of SO_4^{2-} by ^1H NMR indicating that the binding process would affect the ligand self-assembly or, rather, that it directs the self-assembly through a templation effect. SEM images of these solutions deposited and dried evidenced a similar behaviour, with the free ligand forming a solid film. On the other hand, in the presence of 1 equivalent of SO_4^{2-}, the complexes combined into droplet-like particles. This behaviour was enhanced by addition of water to the anion complexes solutions, which resulted in the formation of more defined spheres. This clearly demonstrated the hydrophobic effect on their formation in solution *i.e.* Figure 2.51a. As the aggregation studies performed in DMSO were aimed mainly to verify the potential aggregation in the anion binding processes, aggregation in this medium was not investigated further. A more detailed study in aqueous mixtures was carried out in CH_3OH and will be discussed in the next section.

2.4.3. Self-assembly studies in CH_3OH

Having studied the self-assembly behaviour in the media used for the anion binding, other solvents were also tested for the ligands solubility to understand which could be used for further self-assembly studies. The ligands proved to be insoluble in most organic solvents,

Table 2.17. Solubility of ligands **86**-**89** at 25 °C in a range of various solvents. P’ is the polarity index.

Solvent	*P’*	***86***	***87***	***88***	***89***
Et_2O	2.8	insoluble	insoluble	insoluble	insoluble
CH_2Cl_2	3.1	insoluble	insoluble	insoluble	insoluble
THF	4.0	insoluble	insoluble	insoluble	insoluble
$CHCl_3$	4.1	insoluble	insoluble	insoluble	insoluble
CH_3OH	5.1	soluble	insoluble	insoluble	insoluble
CH_3CN	5.8	soluble	weakly soluble	weakly soluble	weakly soluble
DMSO	7.2	soluble	soluble	soluble	soluble
H_2O	10.2	insoluble	insoluble	insoluble	insoluble

as reported in Table 2.17, with the exception of ligand **86** which displayed good solubility in CH_3OH, allowing the study of self-assembly properties in another highly polar solvent.

In a similar way as was done in CH_3CN, UV-vis absorption spectra of ligand **86** were collected in CH_3OH, at concentrations between 2.0 × 10^{-5} M and 2.6 × 10^{-6} M, Figure 2.52a. As before, at higher concentrations saturation effects prevented collection of the spectrum. Within this range, the linearity of the Beer-Lambert plot showed that aggregation was not occurring in CH_3OH. Studies within a wider range of concentrations could be carried out by ^{1}H NMR experiments, which showed that, over 1.0 × 10^{-3} M aromatic resonance H8 and H9 were weakly shifted, Figure 2.53. This effect indicated a larger potential aggregation of the ligand in CH_3OH than in DMSO. Considering that this self-assembly could have more effect

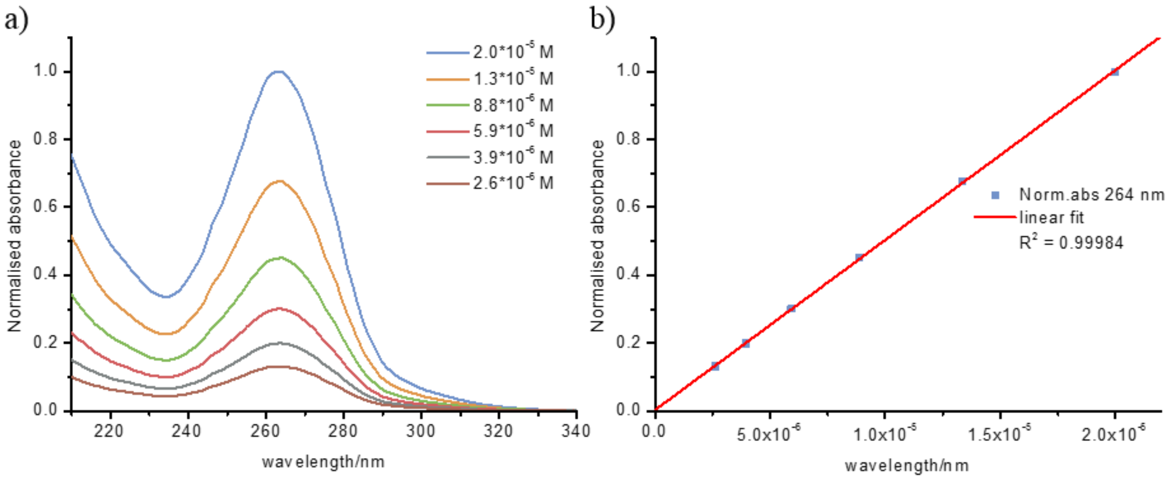

Figure 2.52. UV-vis absorption aggregation studies for **86** in CH_3OH: a) overlaid spectra at various concentrations, 0.2 cm path quartz cell, with normalised absorbance; b) Beer-Lambert plot at 264 nm displaying good linearity.

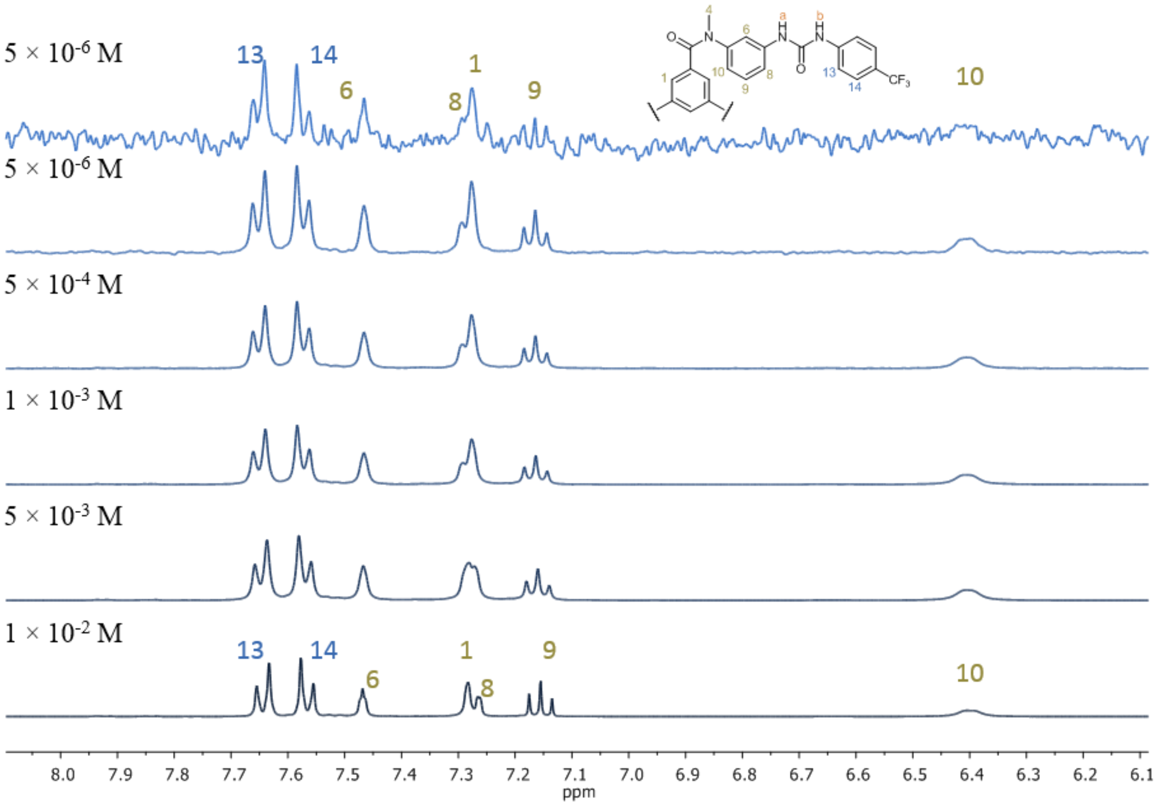

Figure 2.53. Stacked ^{1}H NMR (600MHz) spectra of aromatic region of **86** in CD_3OD at varying concentrations between 5×10^{-6} and 1×10^{-2} M.

at higher concentrations and upon complete evaporation of the solvent, solutions of **86** in CH_3OH, at the borderline concentration of 1.0×10^{-3} M were deposited onto silica wafer, dried in air and under vacuum and then observed using SEM. Upon evaporation of the solvent, the concentration would increase, giving rise to the self-assembly. SEM images of these samples showed the formation of spherical aggregates of *ca.* 1μm diameter, Figure 2.55a. However, images of the same sample 1 week after being deposited and stored at room temperature in air, showed that these self-assembled structures had collapsed, possibly indicating their poor stability. The formation of these spherical structures was due to the decreased solubility of the ligand in the solvent, and in solution seemed to begin to occur at concentrations higher than 1×10^{-3} M, as seen in the ^{1}H NMR experiments. By adding deionised H_2O to the CH_3OH solution (decreasing the ligand solubility) it was expected that bulk precipitation of the ligand would occur. However, upon addition of H_2O, the solution became cloudy and gained a white iridescent colour, and the particles that formed did not completely precipitate, remaining suspended. This behaviour indicated the formation of colloidal aggregates of the ligand, and this phenomenon was thus investigated further. Colloidal solutions were prepared at 1:1 and 3:1 ratios of $CH_3OH:H_2O$, deposited onto silica plates and then stored at room temperature overnight to facilitate the solvent evaporation.

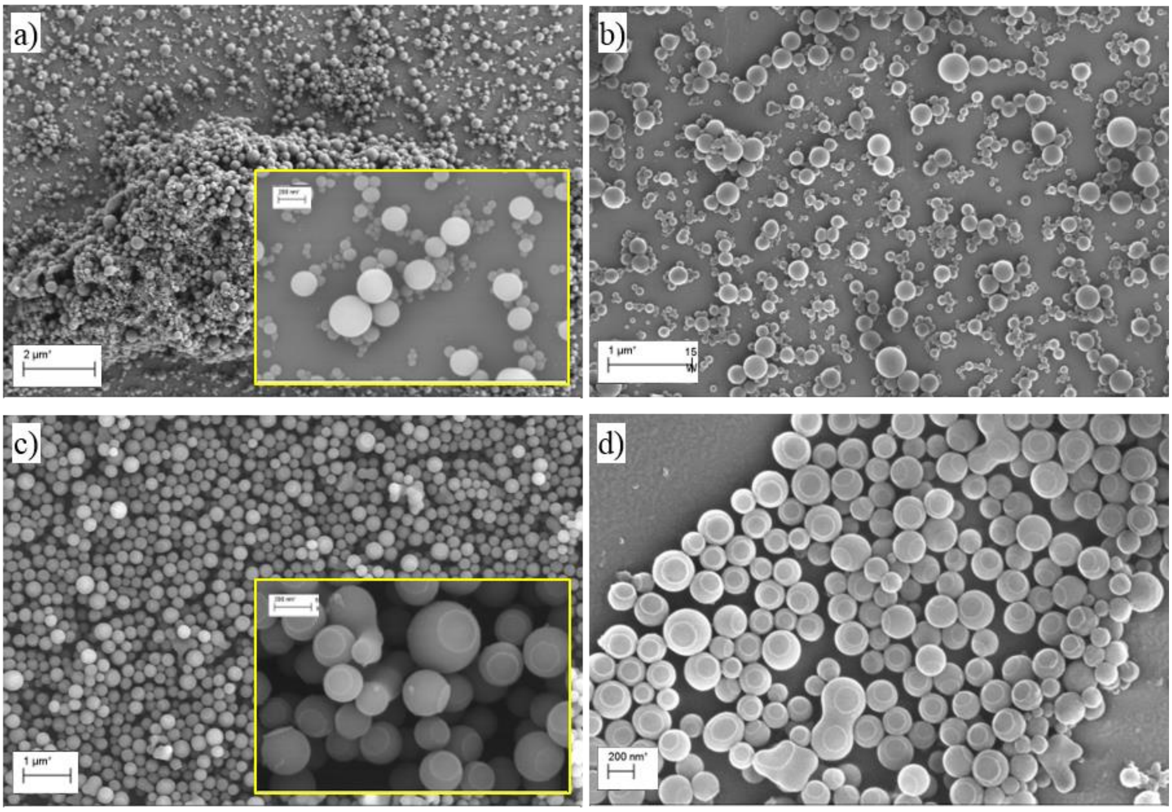

Figure 2.54. SEM images of dried deposited $CH_3OH:H_2O$ suspensions of **86**. Concentration of samples at time of deposition 1×10^{-3} M. Zoomed region inset. a-b) $CH_3OH:H_2O$ ratio 3:1 Image taken a) 24 hr after deposition (bar = 2 µm, expansion = 200 nm); b) 1 week after deposition (bar = 1 µm). c-d) $CH_3OH:H_2O$ ratio 1:1 Image taken: c) 24 hr after deposition (bar = 1 µm, expansion = 100 nm); d) 1 week after deposition (bar = 200 nm).

Complete dryness was ensured by placing the samples *in vacuo* for 2 hrs prior to imaging, they were then gold plated and images were taken by SEM. Images of these samples showed the formation of spherical self-assembly, Figure 2.54a-c, with more uniform and monodispersed particles formed in the 1:1 mixture of $CH_3OH:H_2O$. Unlike from CH_3OH, these samples showed good stability, after deposition, over one week, Figure 2.54b-d. While the self-assembly process in CH_3OH was occurring only at higher concentrations, the

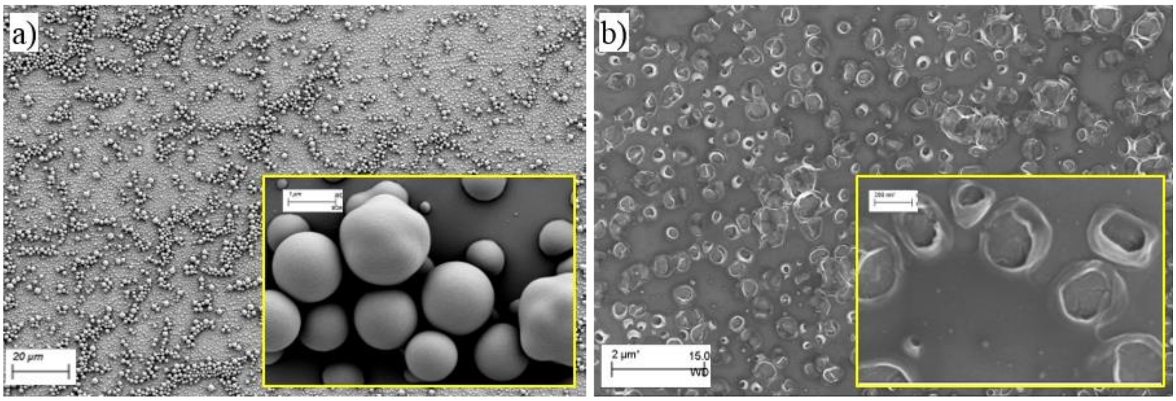

Figure 2.55. SEM images of dried deposited CH_3OH solutions of **86**. Concentration of samples at time of deposition 1×10^{-3} M. Zoomed region inset. Image taken a) 24 hr after deposition (bar = 20 µm, expansion = 1 µm); b) 1 week after deposition (bar = 2 µm, expansion = 200 nm).

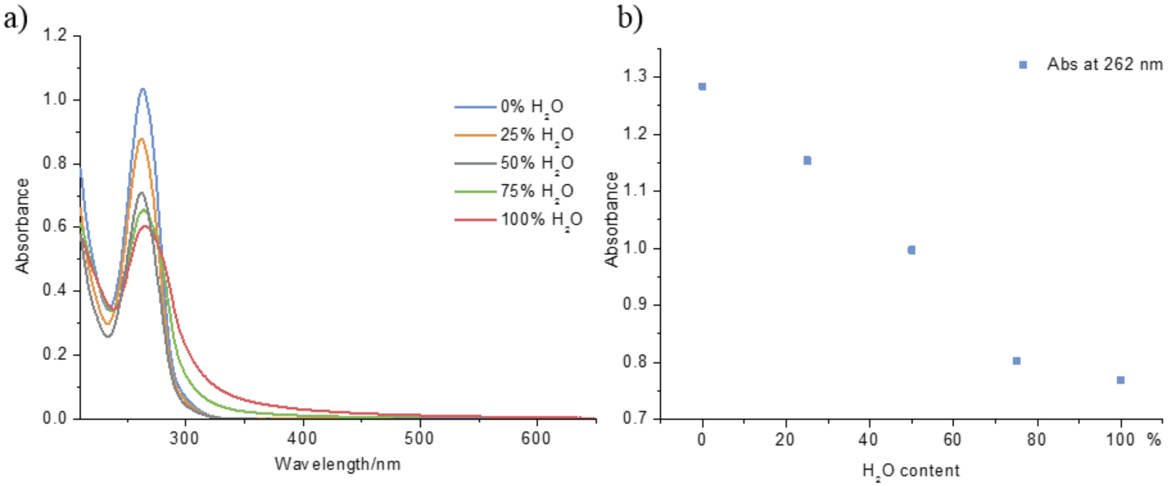

Figure 2.56. UV-vis aggregation studies for **86** in CH_3OH:H_2O: a) UV-vis plot; b) plot of absorbance at 262 nm against H_2O content in solution, displaying good linearity up to 50 % H_2O in CH_3OH. Ligand concentration 8×10^{-6} M.

addition of H_2O, by lowering the solubility of the ligand, caused the same self-assembly process to occur at lower concentrations. To verify this possibility, UV-vis absorption spectra of **86**, at different ratio of CH_3OH:H_2O were taken, keeping the concentration of the sample constant, Figure 2.56. The absorption spectra of ligand **86** showed a decreasing in the extinction coefficient with the increase of H_2O content in solution, with no shift of the λ_{max}, which showed a linearity up to 50% H_2O in CH_3OH. However, in the presence of higher H_2O content a redshift was observed for the λ_{max}, accompanied by a broadening and the appearance of a shoulder around 300 nm. This indicated that while the solubility of the ligand decreased, the ligand was self-assembling while being still absorbing and dispersed in solution. The appearance of a shoulder band was due to the scattering of the particles, which caused the white-iridescent colouring of the suspension, also visible to the naked eye.

As the SEM images showed that the particles were of similar size, and fairly monodispersed, the same solutions were analysed by dynamic light scattering (DLS) to evaluate the stability of the particles and their size within this concentration range. To ensure the reproducibility of the particles formation, the controlled addition of water water to the CH_3OH solution of **86** for the DLS measurement was made by means of a syringe pump optimised to the speed of 120 ml h^{-1}. These measurements evidenced that, in pure CH_3OH, aggregates were not present at 8×10^{-6} M, while they would form in 1:1 CH_3OH:H_2O mixtures at the same concentration. Homogeneous monodisperse aggregates were observed for all samples, with the exception of the solution in 1:99, CH_3OH:H_2O, which demonstrated the presence of different sized particles. In all other cases samples did not show sedimentation, allowing the light scattering measurement, and they displayed a low

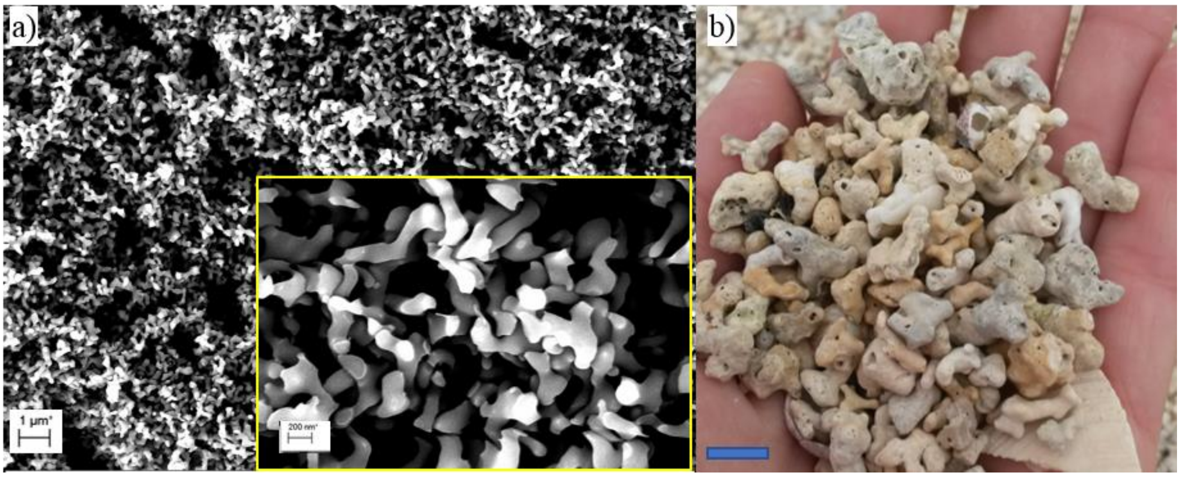

Figure 2.57. a) SEM images of dried deposited MeOH:H_2O suspensions of **86** to which 1 equivalent of $TBAH_2PO_4$ was added. Concentration of samples at time of deposition 1×10^{-3}M. Zoomed region inset (bar = 1 µm, expansion = 200 nm). b) Picture of coral sand from Carraroe beach, (*Trá an Dóilín*), Connemara, Ireland (bar ≈ 1 cm).

polydispersion of PdI < 0.13 for the particles sizes, Figure 2.58. Various tests were carried out to understand the different parameters which could affect the particles size, including the initial concentration of ligand **86** in the CH_3OH solution, the final concentration after the addition of H_2O, the speed of H_2O addition and the CH_3OH:H_2O ratio (summary in Appendix A2 Table A2.3). The size distribution of the aggregates from ligand **86** in solutions of CH_3OH:H_2O, at 25°C, proved to be affected by all those factors, with a general average hydrodynamic diameters the range of 150-400 nm. These results were consistent with the particles sizes observed by SEM.

Considering the ability of the ligand of binding to anions, changes in the aggregates morphology could be caused upon addition of anions. The addition of TBA salts of Cl^-, CH_3COO^-, $H_2PO_4^-$ and SO_4^{2-} to the preformed microspheres in CH_3OH:H_2O, 1:1 ([**86**] = 1

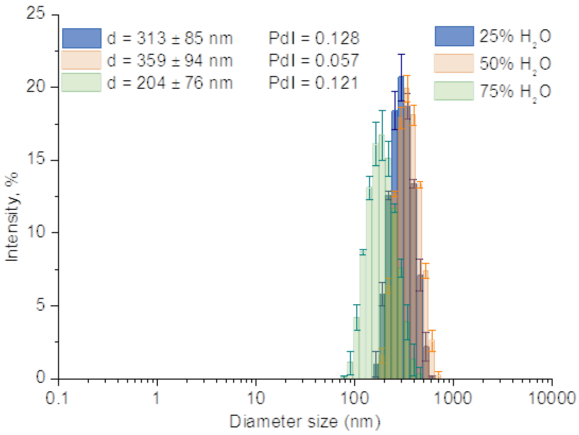

Figure 2.58. Average particle size distribution determined using DLS technique from suspensions of ligand **86**, prepared in CH_3OH:H_2O in different ratios (c = 8 × 10^{-6} M, at 25 °C).

× 10^{-3} M) in 1 equivalent caused an instantaneous flocculation caused by further aggregation of the spheres. Such observation was similar for the four anions. This flocculation caused the precipitation of the colloidal suspension giving a clear solution. SEM images of the flocculates were collected after evaporation of the solution and, as an example, in Figure 2.57a is the result of the interaction of $TBAH_2PO_4$ with preformed spheres of **86**. The flocculates displayed a micro coral-like morphology, which, on a different size scale, resembled the coralline sand of Carraroe beach (*Trá an Dóilín*), in Connemara, Ireland, Figure 2.57b. This morphology was only obtained through the addition of the anion to the preformed colloidal spheres, while the addition of anion to the CH_3OH solution of **86**, prior to the sphere formation, did not cause discrete aggregates to form, but only the formation of a film, Appendix A2, Figure A2.65. This self-assembly behaviour of ligand **86** was attributed to a combination of the hydrogen bonding interactions and the hydrophobicity due to the presence of a fluorinated moiety at the edges of the arms. Similar fluorinated segments are used in the formation of colloidal solutions for pharmaceutical applications, due to their double hydrophobic and lipophilic nature, which allows the formation and stabilisation of colloidal solutions in aqueous media and can also favour the transport through the cellular phospholipidic bilayer.[168] However, the *para*-substituted analogue **81**, did not generate the same morphology under the same conditions (CH_3OH and CH_3OH:H_2O solutions at 10^{-3} M), Appendix A2, Figure A2.63. The reason for this could be found in the SC-XRD of these set of ligands, Figure 1.34, which showed a more closed structure than the *meta*-substituted **tmBTA** family, with the arms arranged in a converging fashion. In this conformation those same hydrogen bonding interactions between the amides and the ureas, observed in Figure 2.43b-c for the *meta*-substituted family, were less favoured.

The self-aggregation properties of **86** were tested by UV-vis absorption and ^{1}H NMR spectroscopy and showed that at concentrations higher than 1 × 10^{-3} M in CH_3OH, the ligand would start to self-assemble into aggregates. The addition of H_2O to CH_3OH solution of **86** caused the formation of microspheres to occur even at lower concentrations, a direct effect of the medium polarity. The formation of the spheres at low concentration was observed, in the aqueous solvent by UV-vis absorption titrations, DLS studies and SEM imaging. The additional interaction of these self-assembled spheres with anions modified the morphology of the aggregates from spherical to a less symmetric coral-like shape.

2.5. Conclusions and future perspective

In this chapter, four novel tripodal tris(urea) ligands **86-89** based on the **tmBTA** scaffold were designed, synthesised and characterised. Their abilities for use in anion recognition and binding were explored by studying their behaviour using UV-vis absorption and ^{1}H NMR spectroscopic techniques. The ligands showed the ability to bind to anions in a two species mechanism, 1:1 and 1:3 (L:A) in CH_3CN. When more competitive solvents such as DMSO were used, which can interact with the ligand binding sites through hydrogen bonding, the binding mechanism presented the formation of the 1:1 self-assembly alone. Among the synthesised ligands, **86** and **89** showed the ability to bind CH_3COO^- by a two-species mechanism even in DMSO. This could be due to the high geometrical complementarity of the urea binding moieties with the carboxylate, which allowed the hydrogen bonding of one anion per urea moiety in each ligand, forming the 1:3 (L:A) species. The ligands discussed in this chapter showed a higher solubility then their *para*-substituted analogues previously developed by Gunnlaugsson and presented comparable binding abilities in DMSO, but with different binding modes. The *para*-substituted analogues showed the formation of 2:1 (L:A) capsules with tetrahedral anions, both in solution and in the solid state,[152] which were not observed for ligands **86**-**89**. While in CH_3CN solution ligands **86**-**89** were able to bind one anion per arm (*i.e.* 1:3 binding), yet only one anion in the more competitive DMSO solution (*i.e.* 1:1 binding). In the solid-state, ligand **87** in the presence of SO_4^{2-}, showed the formation of extended 2D networks. While examples of anion templated 2D networks have been reported before, as discussed in Section 1.3.4, this was the first example of bi-dimensional network templated by SO_4^{2-} through the formation of 12 hydrogen bondings from six different ligands. A common bi-dimensional self-assembly was formed through the hydrogen bonding between the ligand and SO_4^{2-} by evaporation of either DMSO or CH_3CN solutions. Upon removal of the two different solvents (*i.e.* evaporation of the solvent in the crystallisation process), the same interaction of the ligand with the anion occurred. This highlights the specific influences of solvents on the binding processes in solution.

The anion binding process was affected by the nature of the solvent media and its ability to interact with the binding site, as well as the concentration of the ligand. This prevented the confident calculation of the binding constants, which, by their nature, should be independent from the concentration. This led to the study of the self-aggregation process of the ligands in the solvents in which the binding studies could be carried out. These studies highlighted the formation of amorphous films or pseudo-spherical aggregates at concentrations higher than 10^{-3} M. The formation of these aggregates was confirmed by SEM imaging, while UV-vis absorption studies confirmed the absence of self-assembly structures at concentrations lower than 10^{-4} M. Additional studies for ligand **86** in CH_3OH and

CH_3OH:H_2O mixture, showed the formation of similar spherical aggregates and gave rise to colloidal solutions

While the self-aggregation properties of ligands **86-89** proved to lower their anion binding abilities, the self-assembly studies highlighted additional interesting properties, characteristic of the *meta*-substituted **tmBTA** family of ligands. The formation of colloidal spheres in CH_3OH:H_2O mixtures was observed and could further aggregate and flocculate upon addition of anions. Such behaviour opens the possibility of using such molecules for the use in water treatments for anion purification.[58,169,170] Further development could be needed to try and tune the selectivity for environmentally relevant anions,[58] such as SO_4^{2-} or $H_2PO_4^-$, and also SeO_4^{2-} or TcO_4^-. In this way the colloidal solution could be used in batch processes of water purification the addition of which to the contaminated water binds to the anions and causes flocculation of the particles, which could be then removed by decanting or filtering. The further development would need to consider the formation of colloidal particles using least amount of CH_3OH possible to avoid further water contamination. In addition to this, it would be necessary to understand the purification yields, in terms of anion extraction from the solution, and establish the complete removal of the ligands. In order to make the process efficient, the recovery of the starting material would also be important, which could allow its reuse in multiple cycles. To give additional stability to the particles, one suggestion could be to load them onto polymeric supports. Some preliminary studies were undertaken in this direction, using the "dipodal equivalent" of these **tmBTA** tripodal ligands, in which only two of the three anilines of the starting material reacted to form the urea. This third unreacted arm was functionalised with a methacrylate monomer to create polymeric beads. This work will be discussed in the next chapter together with the study and development of the dipodal ligands.

3. Development of dipodal bis(urea) ligands based on the tmBTA platform for anion-templated self-assembly

3.1. Introduction

Given the strict dependence of life on clean and uncontaminated water, the purification of water has always been a topical issue. In recent years, particular attention has been put into the analysis and purification of water from environmentally harmful anions, and this has generated a surge of research in this direction.[171] While examples of removal of anions from aqueous solutions by crystallisation[124] or liquid-liquid extraction has showed good potential,[172] with many examples of sulfate removal from nuclear waste[58] or even $^{99}TcO_4^-$ from water,[22,173] the use of functionalised materials has provided a number of advantages. Among others, it can overcome the obstacle of lower solubility of some ligands in water and can limit the risk of contamination with different pollutants, which can occur with liquid-liquid extraction. Among some examples of functionalised materials for the removal of anions, Biesuz *et al.* reported the functionalisation of both mesoporous silica MCM-41 and Amberlite CG50 with cage **101**, for the sensing and extraction of ReO_4^- and TcO_4^- from aqueous solutions, Figure 3.1.[22,174] While the amberlite-based material **102** was more readily synthesisable, **103** showed higher concentration of active sites, while **104** displayed higher affinity and faster kinetics.

In 2015 Romański and Zdanowski[175] reported the use of L-tyrosine-based receptors **105** and **106** possessing 4-nitrophenyl-(thio)urea anion binding site and a 1-aza-18-crown-6 moiety, Figure 3.2, selective for Na^+. the dual receptor was then attached to a polymeric support (poly(butyl methacrylate)) for the extraction of ion pairs from aqueous solutions. However, a low extraction efficiency was observed, which was only 21% in the case of $NaNO_3$ (at 15.2 M, effective receptor concentration). The authors claimed that the presence of a second anion binding unit, within the receptor could have positive effects on the extraction efficiency.[176] More recently Sessler and co-workers showed how macrocyclic molecule **107** could be grafted onto a poly(vinyl alcohol) (PVA) polymer *via* esterification, giving the polymeric material **108**.[169]

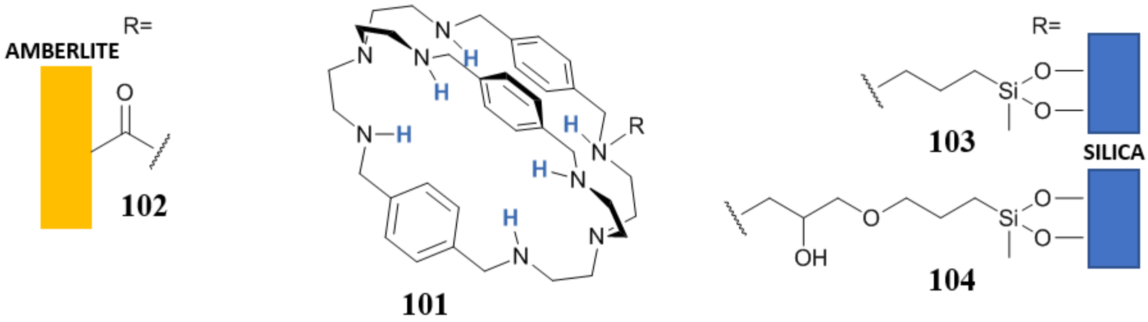

Figure 3.1. Schematic representation of mesoporous silica and amberlite materials functionlaised with **101**, developed by Biesuz *et al.*

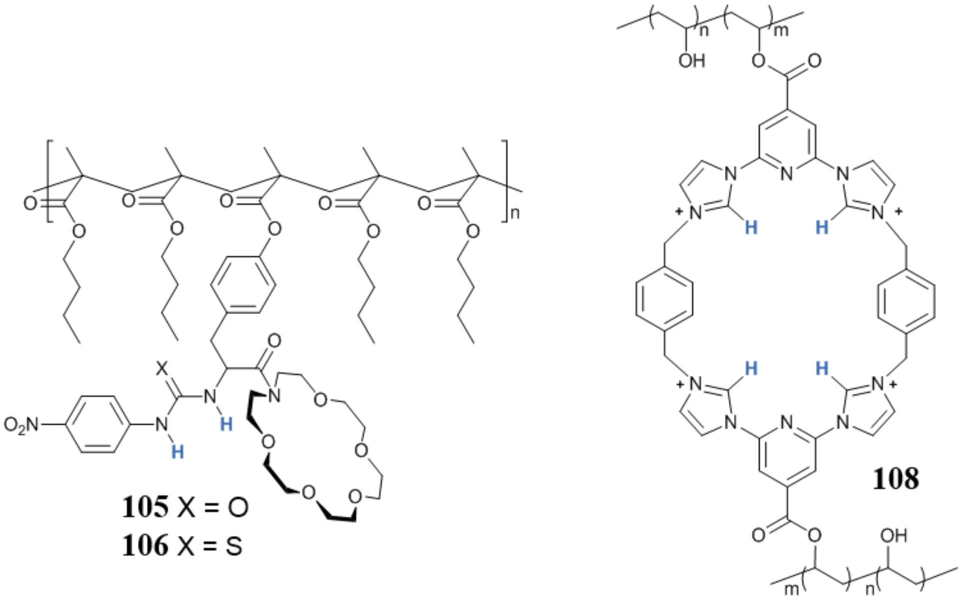

105 X = O
106 X = S
108

Figure 3.2. Examples of anion receptors supported onto polymeric scaffolds developed by Romański (**105** and **106**) and by Sessler (**108**).

In this case, removal of NaNO$_3$ was the most efficient (68%) while the least effective, with only 47% was NaF, with the efficiency of extraction being measured through the changes in the solution conductivity.

This chapter will focus on the synthetic challenges confronted in attempts to obtain the "dipodal" ligand **85**, Figure 3.3. This ligand was originally formed as a side product of the synthesis of ligand **83** and so the initial goal of this project was to reproduce the SO$_4^{2-}$ cluster observed in the crystal structure of **85**·SO$_4^{2-}$, as well as exploring its binding properties with other anions.[152] In addition to this, having considered both the anion binding and the self-assembly properties of similar structures (see Chapter 2), the presence of one unsubstituted arm opens up the possibility of supporting the dipodal structure onto a polymeric scaffold. This functionalised polymer could be potentially used for the capture and removal of anions from organic or even aqueous solutions in a manner similar to those examples described above.

With the aim of developing a functional material inspired by the previous examples, the initial challenge[152] posed the separation of the two products, **83** and **85**. This separation could not be achieved by column chromatography, due to the similar elution profiles of the two compounds in various conditions and could only be obtained by self-sorted crystallisation of the two molecules with SO$_4^{2-}$. As presented in Chapter 1, ligand **83** formed 2:1 (L:A) capsules around the tetrahedral SO$_4^{2-}$, while ligand **85** formed 4:4 (L:A) bundles, with four ligands enclosing four molecules of SO$_4^{2-}$. This kind of 4:4 assembly was

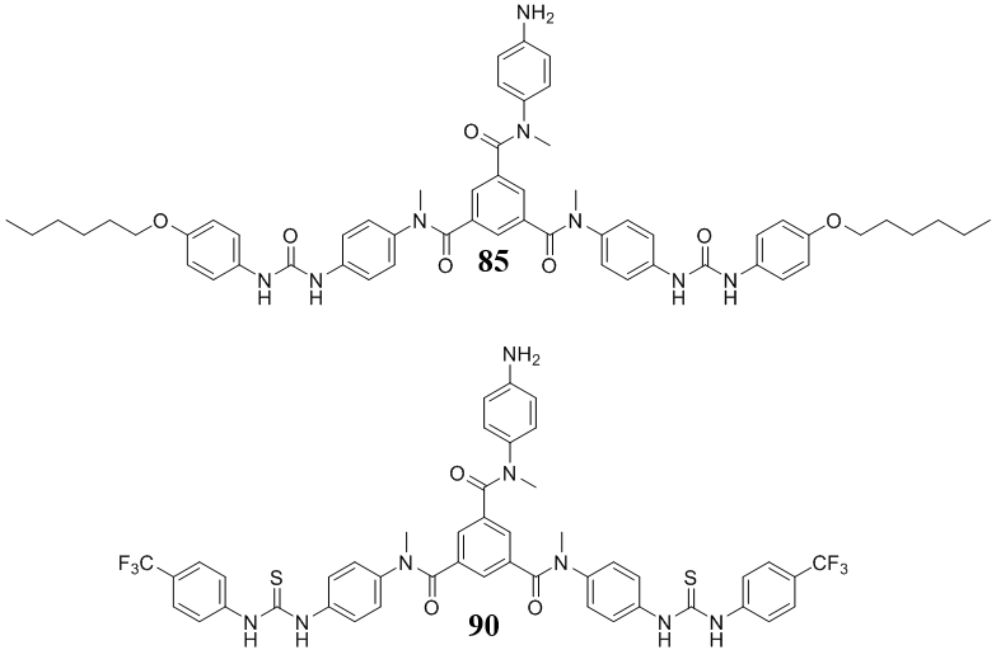

Figure 3.3. Chemical structure of ligands **85** and **90**.

interesting due to the proximity of highly charged molecules, which would be expected to naturally repel each other. However, the self-assembly of ligand **85** would arrange a combination of hydrogen bonding interactions which managed to stabilise the anionic tetramer in a local arrangement.

Two approaches to the synthesis of **85** will be presented and discussed: i) a linear synthesis based on the modification of the tripodal **83** synthesis; ii) a modular route, which eventually led to the desired product albeit in poor yield.

Due to ligand **85** being obtained in negligible yields, functionalisation studies on this dipodal molecule could not be carried out. However, while investigating the formation of the thiourea analogues of the *para*-substituted tripodal family, the formation of the partially substituted molecule was observed, similar to that observed in the synthesis of tripodal **83**. In particular, the synthesis of “dipodal” molecule **90** will be discussed in later sections. Higher yields in this case, allowed the investigation of binding properties of **90** with $H_2PO_4^-$ and SO_4^{2-} in CD_3CN:DMSO-d_6 (5:1) solution. Preliminary studies on the functionalisation of polymeric materials with **90** will be discussed in the final part of this chapter.

3.2. Design and Synthesis strategies for Dipodal ligands

The synthetic challenge to obtain ligand **85** was pursued in light of the SO_4^{2-}-templated self-assembly properties that this ligand had previously shown[152], which lead to the formation of 4:4 (L:A) “complexes”, by self-sorting from a mixture with the tripodal molecule. The possibility of obtaining similar anion-templated structures was the main goal of this project, which encouraged us to overcome the difficulties encountered.

Many synthetic approaches were investigated, however only two of them will be discussed herein. The initial method involved a five-step synthetic procedure. After the two-step synthesis of **84**, Scheme 3.2, the third step involved the mono-protection of the aniline precursor **84** prior to the urea formation on the two remaining arms. The final deprotection step of **112** would have resulted in the synthesis of **85**, Scheme 3.1. The second method involved a modular approach: in this way the selective protection of one arm over the other would be performed on the starting material **97**, which was more easily manageable, the results of which are discussed below in Section 3.2.2. With this second method a negligible amount of compound was isolated pure, however it did not yield a sufficient amount for the desired studies.

3.2.1. Linear approach

The first attempts to synthesise ligand **85** started from the synthesis of the precursor **84** according to a literature procedure,[152] Scheme 3.2. The first step was to react commercially available *N*-methyl-4-nitroaniline, **109**, with benzene-1,3,5-tricarbonyl trichloride, **97**, in

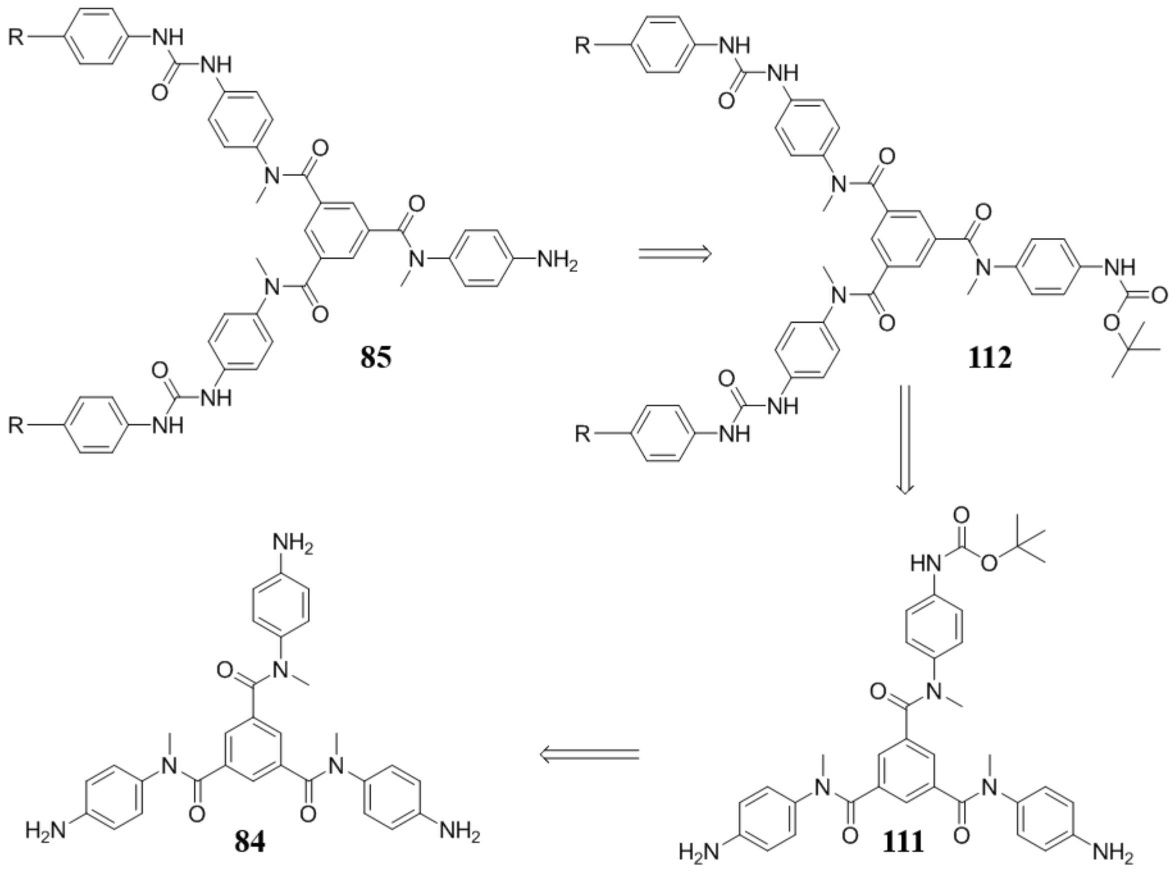

Scheme 3.1. Retrosynthetic scheme for the linear synthesis of **85** from **84** using Boc as a protective group.

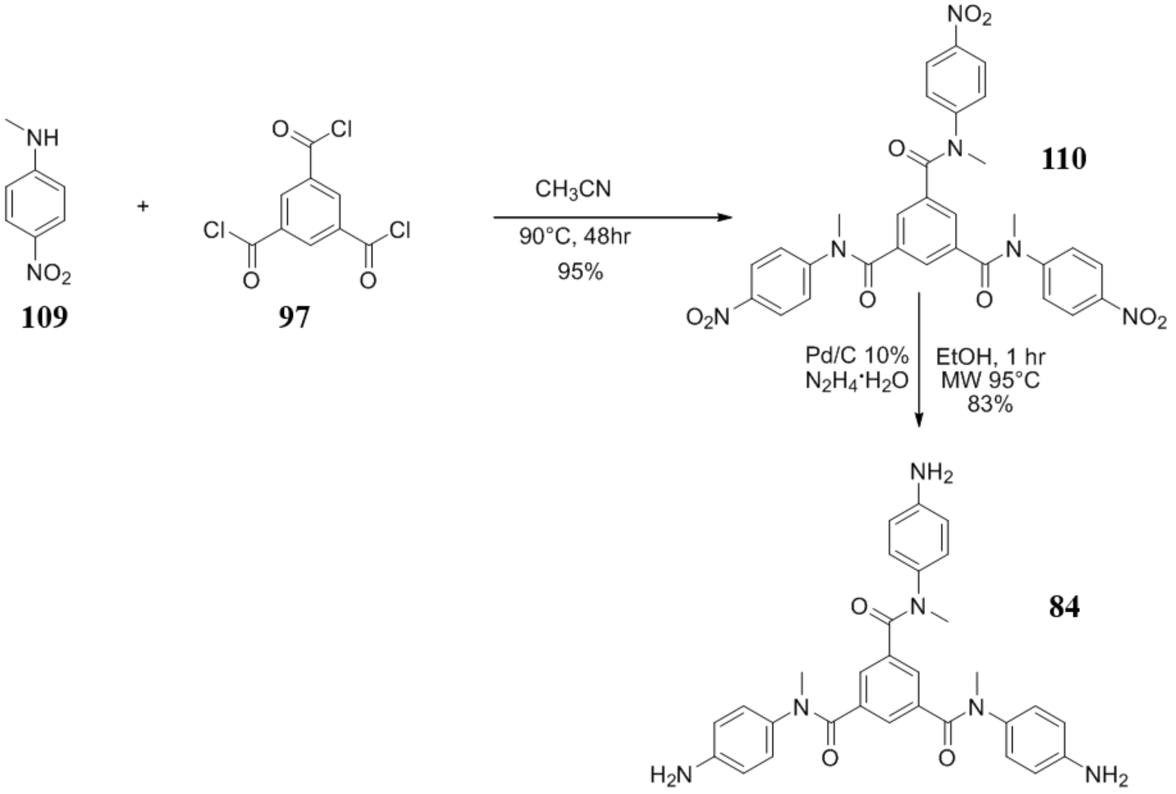

Scheme 3.2 Synthesis of precursors **110** and **84**.

CH_3CN solution at 90° C for 48 hrs. At completion of the reaction (TLC), the solvent was removed *in vacuo* and compound **110** was obtained in 95% yield, by triturating the crude compound with a mixture of $CHCl_3$:Et_2O (1:10). The nitro groups of compound **110** were reduced by suspending the compound in EtOH, followed by the addition of 10% Pd/C and hydrazine monohydrate and heating at 90° C under microwave irradiation for 120 minutes. After filtration through a celite plug, and washing with a hot mixture of CH_3OH:CH_3CN (1:1), ligand **84** was obtained crude, and further purified by trituration in a mixture of $CHCl_3$:CH_3OH:Et_2O (2:1:10), yielding the pure ligand in 83% yield.

To synthesise **85** starting from **84** the first step involved the selective mono-protection of only one of the three NH_2 groups, to give **111**. This was reacted with 4-hexiloxyphenyl isocyanate in a 2:1 ratio to yield **112**, as shown in Scheme 3.1. The *tert*-

Table 3.1. Methods attempted for formation of **111**. [a] Boc group added as Boc-OSu.

Solvent	Temperature	Ratio 84:**Boc$_2$O**	Result
THF	-78	3:1	Starting material recovered
THF:DMF	20	3:1	Starting material recovered
DMF	20	3:1	Starting material recovered
DCM:CH_3OH	20	3:1	Starting material recovered
DCM:CH_3OH	20	3:1[a]	Starting material recovered

butoxycarbonyl (Boc) group was chosen as a protecting group, due to its wide availability and reactivity. The selective protection of one functional group, in the presence of other equivalent groups could be achieved by using excess substrate, or by slowing the reaction enough to limit multi substitution. Different conditions were tested to obtain **111**, listed in Table 3.1, using either di-*tert*-butyl dicarbonate (Boc_2O) or *N*-(*tert*-butoxycarbonyloxy)succinimide (Boc-OSu). However, under all the reaction conditions ligand **84** did not convert to give the Boc-protected **111**, and starting material was recovered. This was attributed to the low solubility of **84**, which would need high temperatures for the reaction to occur. These high temperatures, however, are not compatible with the selective protection of only one NH_2 group. Following the unsuccessful attempts to synthesise **111**, a new approach was required to obtain the desired molecule.

3.2.2. Modular approach

The new modular approach for the synthesis of **85** was developed with two main issues in mind. The first was the poor solubility of the precursor **84** and the second was the unavailability of the 4-hexyloxyphenyl isocyanate as a commercial reagent, which had previously been used for the synthesis of **83**.

The synthesis of the diphenylurea “arm” **113** is described in Scheme 3.3. In this procedure, 4-(tert-butoxycarbonyl(methyl)amino)benzoic acid, **114**, is first obtained by protecting the amine group of **115** with a Boc group. The urea group was synthesised by reacting **114** with diphenyl phosphoryl azide (DPPA), in the presence of TEA, forming *tert*-

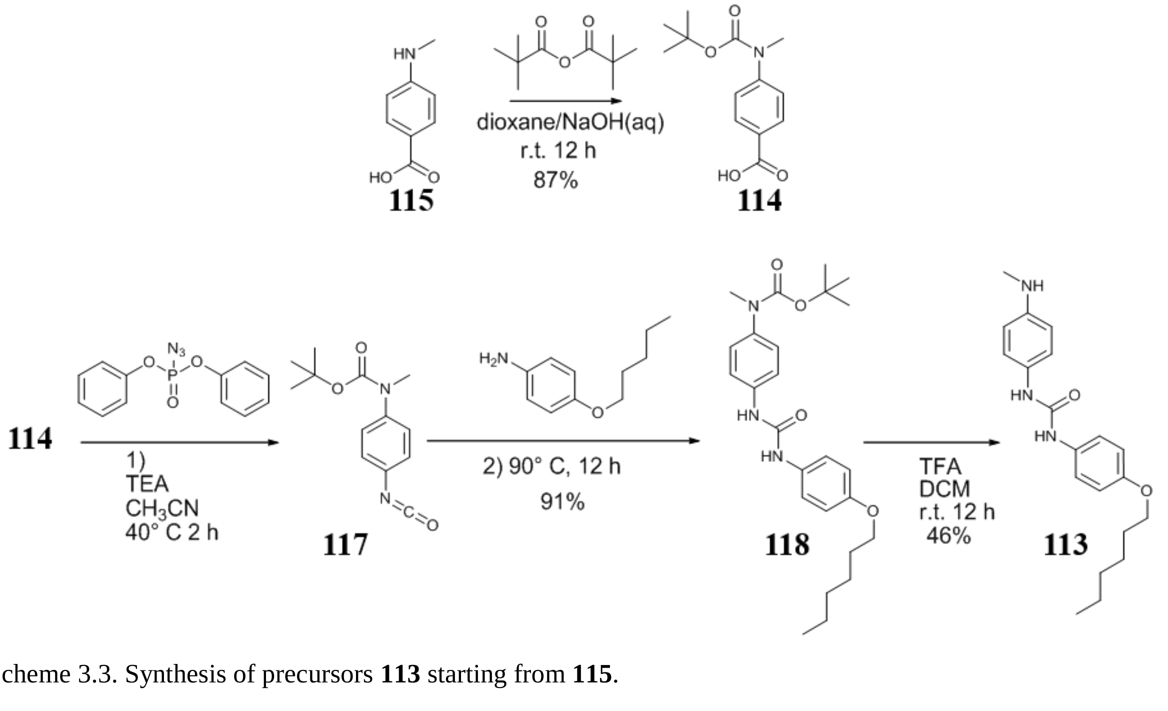

Scheme 3.3. Synthesis of precursors **113** starting from **115**.

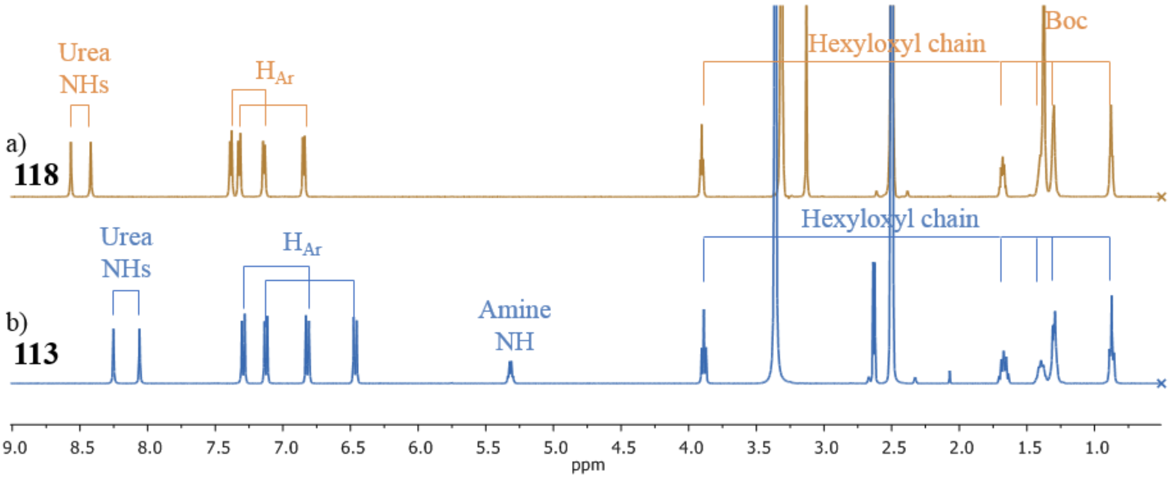

Figure 3.4. Compared ^{1}H NMR spectra (600MHz, DMSO-d_6, 298 K) of compounds a) **118** and b) **113**.

butyl 4-isocyanatophenyl(methyl)carbamate, **117**, *via* Curtius rearrangement. This was then reacted *in situ* with commercially available 4-hexyloxy aniline, **116**, to give the Boc-protected precursor **118**. In this way the hazardous use of phosgene, normally used for synthesis of isocyanates, was avoided by using DPPA as an azide transfer reagent. Purification of the precursor **118** was achieved by flash column chromatography (gradient of CH_3OH:EtOAc) and recrystallisation from CH_3CN gave **118** in 91% yield. ^{1}H NMR spectra showed the formation of the diphenylurea moiety, clearly showing the presence of urea characteristic NHs resonances at 8.57 ppm and 8.42 ppm, as well as the presence of two pairs of coupling doublets, corresponding to the phenyl aromatic protons H_{ar}, Figure 3.4a. HRMS analysis (by ESI+) also confirmed the presence of a **118** peak at m/z = 464.2523, corresponding to $[M+Na]^+$ (calcd m/z = 464.2525). The deprotected "arm" **113** was obtained in a good yield (46%) by stirring a CH_2Cl_2 solution of **118** in the presence of excess of TFA for 24 hrs. The successful deprotection was confirmed by the disappearance of the resonance at 1.38 ppm, corresponding to the Boc group, and the appearance of a new quartet at 5.32 ppm, corresponding to the *N*-methyl substituted amine, Figure 3.4b.

For additional characterisation, both **118** and **113** were crystallised from CH_3CN and yielded SC-XRD quality crystals: their diffraction data were collected and solved by Dr. Chris Hawes (TCD). The general crystallographic data and structure refinements are provided in appendix A3. Crystals of precursor **118** were obtained in the orthorombic space group *Pbca*, with the asymmetric unit containing a single molecule of **118**. The molecule displayed a conformation with the two urea NHs in *anti* conformation and the two phenyl rings in a non-planar arrangement, Figure 3.6a, with torsion angles between the urea carbonyl and the rings of 38.2(4)° and 52.7(4)°.

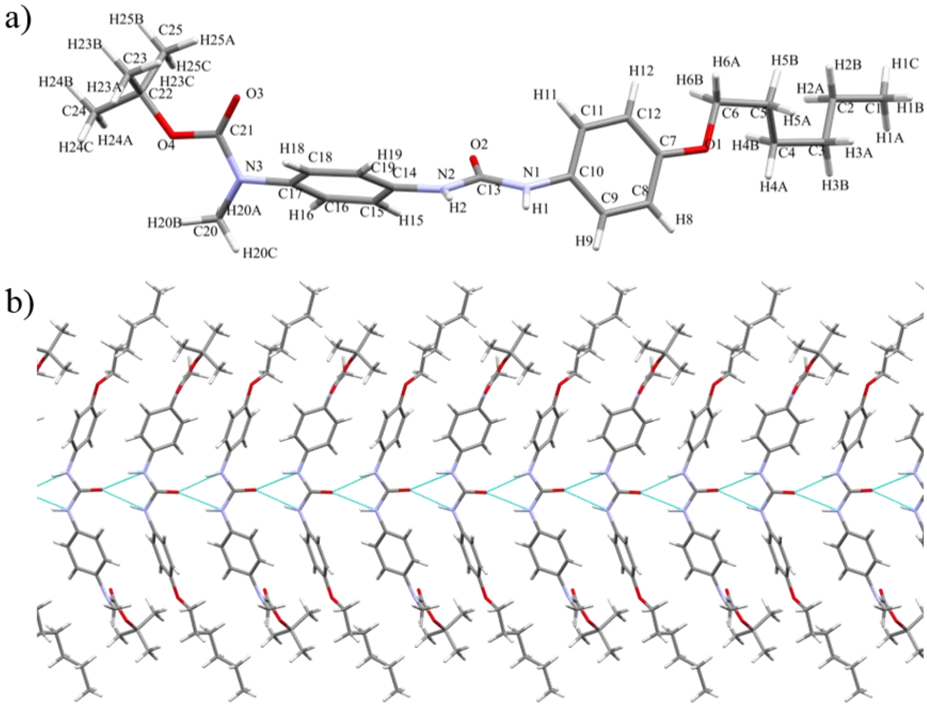

Figure 3.6. SC-XRD structure of **118**. A) capped stick representation showing the twisted arrangement of the diphenyl urea moiety; b) hydrogen bonding network displaying characteristic “urea tape”.

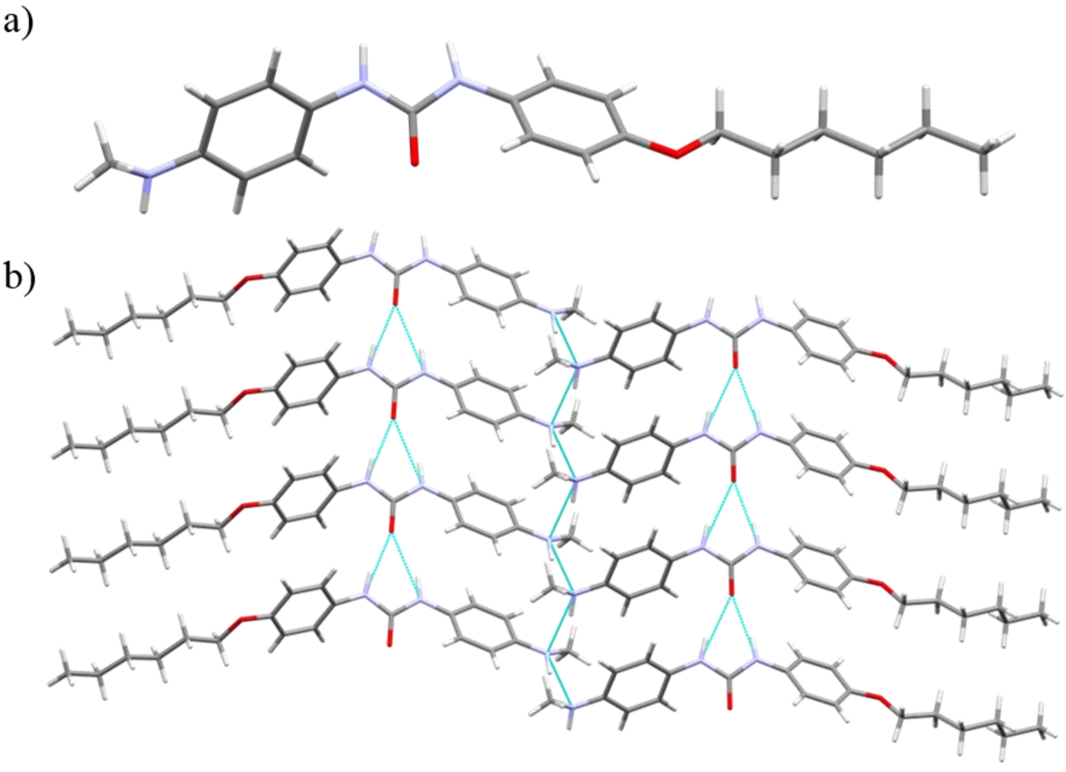

Figure 3.5. SC-XRD structure of **113**. A) capped stick representation showing the twisted arrangement of the diphenyl urea moiety; b) hydrogen bonding network displaying characteristic “urea tape”.

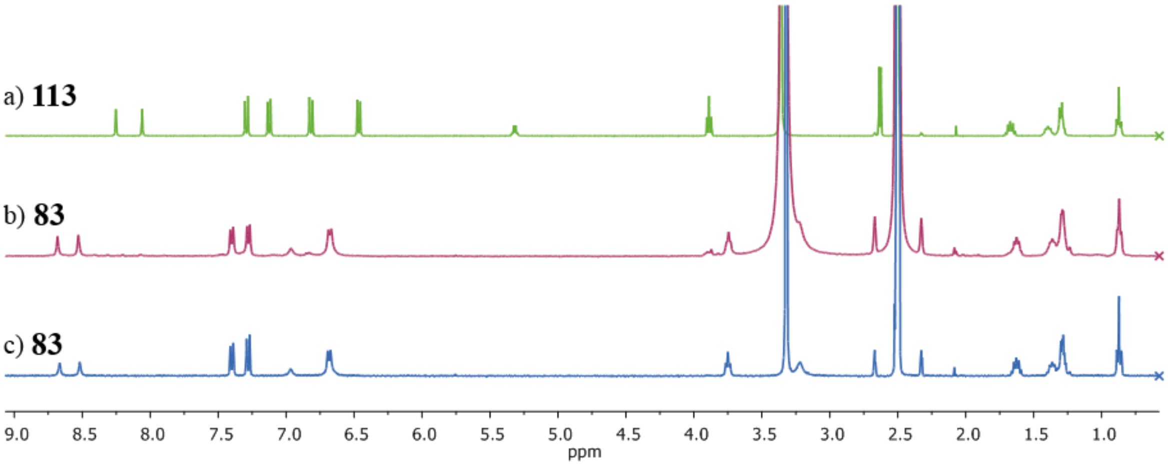

Figure 3.7. Comparison of ^{1}H NMR spectra (400MHz, DMSO-d_6, 298 K) obtained from synthesis shown in Scheme 3.4. a) starting material **113**, b) **83** obtained from **119**, and c) **83** obtained from **120**. Residual solvent resonances: DMSO-d_6 2.5 ppm and H_2O 3.33 ppm.

The crystal structure displayed the typical "urea tape" formation of intramolecular hydrogen bonding, Figure 3.6b. Within the urea tape, the molecules were arranged in an alternated fashion, such that the N-Boc group of one molecule would be close to the hexyloxyl groups of the adjacent molecules, Figure 3.6b.

The deprotected arm **113**, crystallised in the monoclinic space group *C*2, with the asymmetric unit containing 5 molecules of **113**. Similarly to **118**, the conformation of the diphenyl urea moiety was elongated and twisted, Figure 3.5a, with torsion angles between the urea carbonyl and the rings, between 38.0(6)° and 45.6(6)°. Also for **113,** the urea NHs would donate a bifurcate hydrogen bond to the urea carbonyl oxygen of a neighbouring molecule, giving rise at the characteristic "urea tape" network, Figure 3.5b. In the crystal of **113** and additional hydrogen bonding was observed between the deprotected amine NHs of neighbouring molecules, Figure 3.5b.

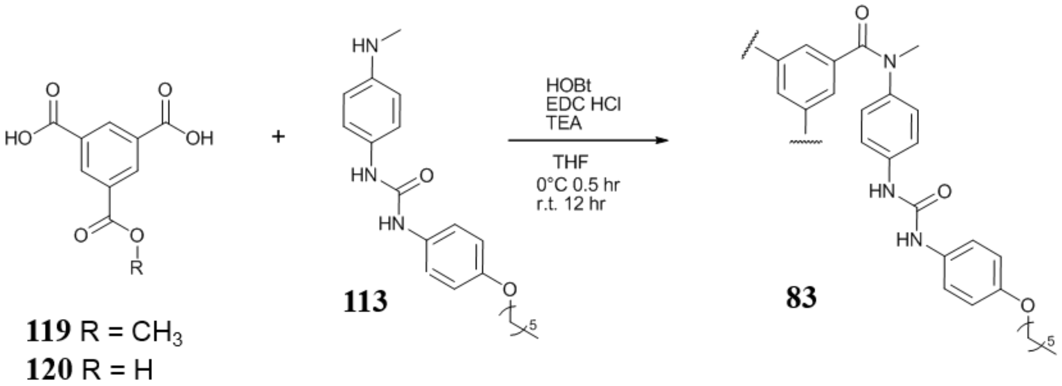

Scheme 3.4. Synthesis of the tripodal ligand **83**. The tripodal ligand was also obtained in the attempt of synthesising a precursor for dipodal starting from **119**, as transesterification of the methyl ester occurred.

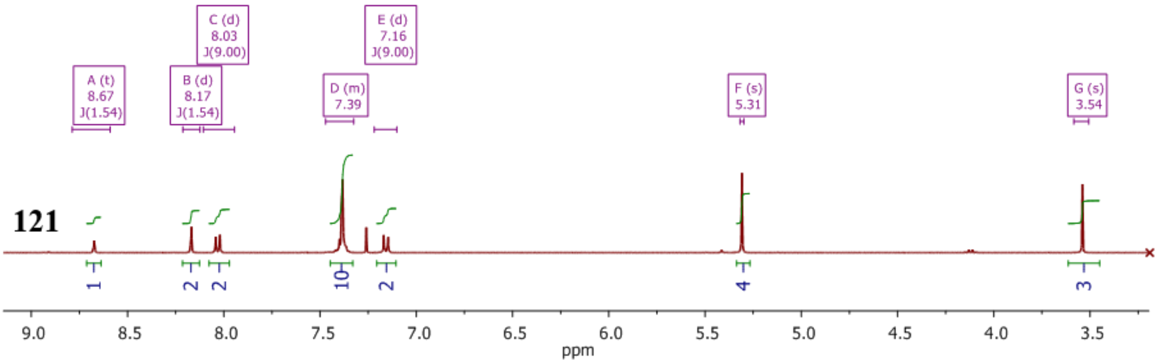

Figure 3.8. ^{1}H NMR spectra (400MHz, $CDCl_3$, 294 K) of **121**, proton assignment given in Scheme 3.5.

To address the solubility issue of the tripodal synthesis precursor **84**, the more soluble central core **BTA** was used for mono-protection. In the literature some examples of **BTA** tripodal structures with three diversely-substituted arms were reported starting from 5-(methoxycarbonyl)isophthalic acid, **119**, prepared from **120**.[177,178] However, the same approach was unsuccessful when attempting to functionalise with compound **113** because, together with the reaction on the two carboxylic moieties, transesterification of the methyl ester was observed when coupling **119** to **113**, yielding the full tripodal ligand **83**, Scheme 3.4 and Figure 3.7.

Among other alternatives, the use of the benzyl ester group as a protecting group instead of the methyl ester was investigated. While the synthesis of **119** was well established within the literature (by selective deprotection of the fully esterificated BTA substrate) the mono-benzylester equivalent, proved to be more challenging. The protection of two of the three carboxylic acid groups had been previously obtained by Salamończyk,[179] therefore by adapting the same procedure, compound **121** was synthesised, Scheme 3.5. By means of a syringe pump, a solution containing 2 equivalents of benzylalcohol and TEA in a dry mixture of THF/CH_2Cl_2 (8:1) was slowly added, over one hour at -20° C, to a solution of **97** in the same THF/CH_2Cl_2 mixture, giving **122** as an intermediate. *N*-Methyl-4-nitroaniline, **109**, was then added to the reaction mixture and stirred at -20° C for another hour, after which the

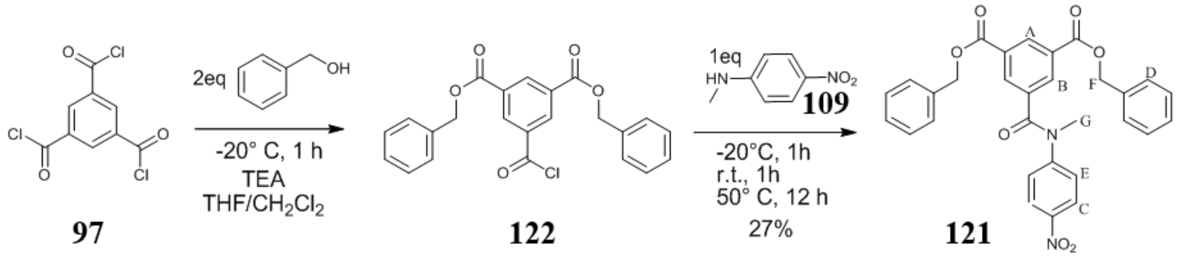

Scheme 3.5. Synthesis of precursors **121** starting from **97**, by forming intermediate **122**.

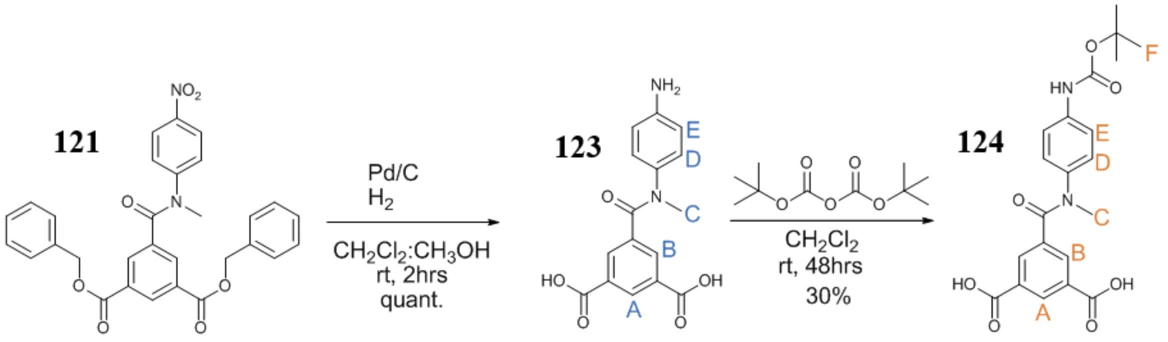

Scheme 3.6. Synthesis of intermediate compounds **123** and **124**.

solution was heated to 50° C and stirred overnight. The solution was then cooled down and a white crystalline solid was separated and filtered. Precursor **121** was obtained pure after purification by flash chromatography on silica in a gradient of EtOAc/Hexane. The ^1H NMR spectrum, Figure 3.8, showed two separate peaks for H_A and H_B, at 8.67 ppm and 8.17 ppm, respectively, with a matching *J* = 1.5 Hz, as well as a multiplet resonance at 7.39 ppm integrating for 10 protons, corresponding to the benzyl rings. The resonances corresponding

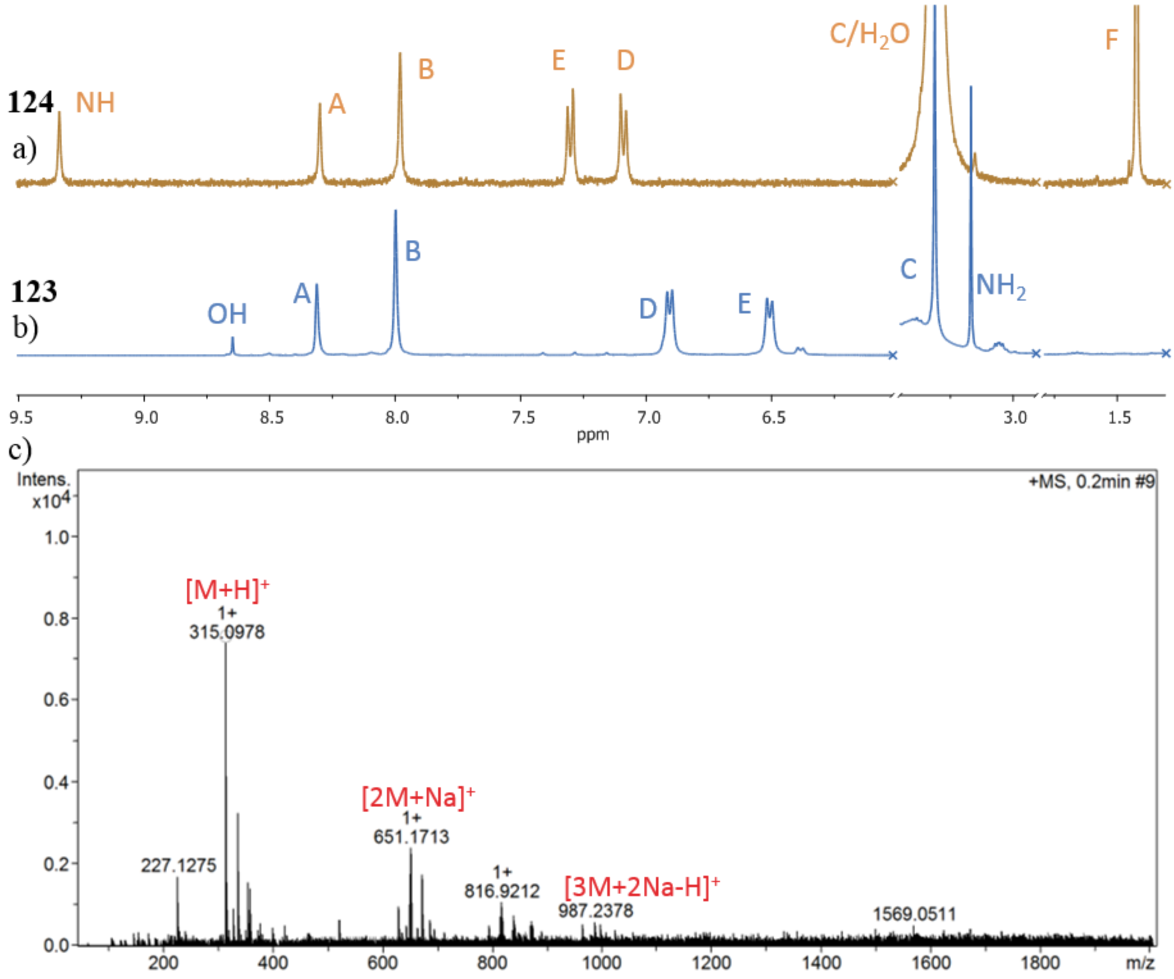

Figure 3.9. ^1H NMR spectra (400MHz, DMSO-d_6, 294 K) of a) **124**, b) **123**; for resonance identification refer to Scheme 3.6. c) HRMS-ESI+ of **123**, showing the presence of $[M+H]^+$, $[2M+Na]^+$ and $[3M+2Na-H]^+$ adducts.

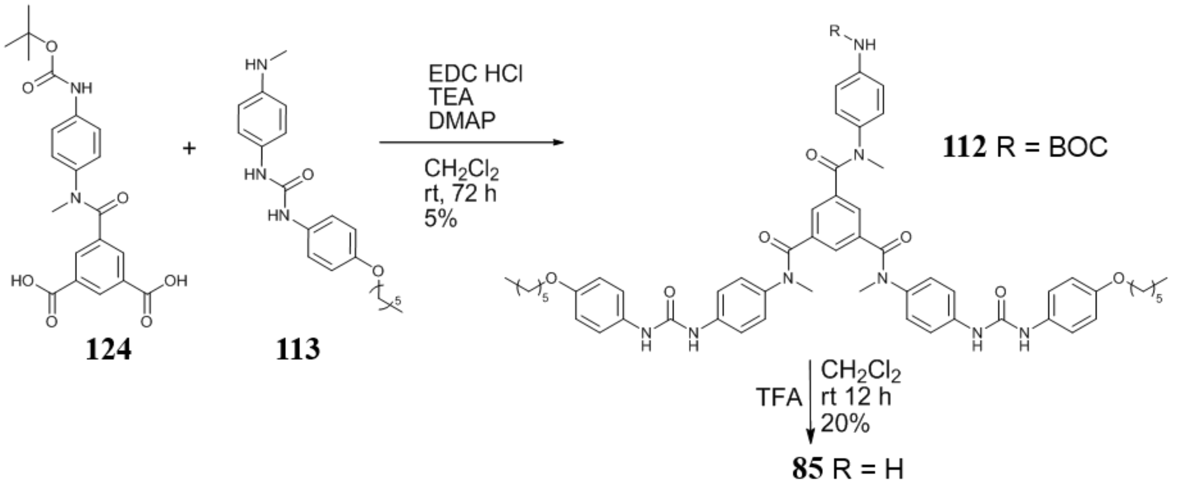

Scheme 3.7. Synthesis of dipodal **85**, by coupling of **124** and **113** and following cleaving the N-Boc group of the intermediate **112**.

to the *N*-methyl 4-nitroamide moiety were also identified in the pair of doublets at 8.03 ppm and 7.16 ppm, coupling with a *J* = 9.0 Hz, together with the *N*-methyl group protons, resonating as a singlet at 3.54 ppm. Cleavage of the benzyl ester groups and reduction of the nitro group of **121** to amine were obtained simultaneously by hydrogenation over Pd/C (20% w/w) in a CH_2Cl_2:CH_3OH (1:1) mixture at room temperature, in 2 hours, Scheme 3.6. After filtration over a pad of celite, the solvent was evaporated and **123** was obtained quantitatively. HRMS-ESI+analysis showed a peak at *m*/*z* = 315.0978 corresponding to $[M+H]^+$ (calcd for $C_{16}H_{15}N_2O_5$, 315.0975), Figure 3.9. The amine group was reacted with Boc_2O, in order to protect the amine for the following coupling step, as shown in Scheme 3.6, giving **124** in moderate yields.

At this point, by coupling **124** with the arm **113**, and one last Boc-deprotection step could give the desired dipodal ligand **85**, Scheme 3.7. However, the coupling between **124** and **113** also proved to be challenging and different conditions were tested, which are listed in Table 3.2. As can be seen from Table 3.2, only a combined use of EDC·HCl, TEA and DMAP in CH_2Cl_2 managed to successfully coupling **124** and **113**. However, the yield of the compound was extremely low (5%). In all the other conditions only the starting material **113** was recovered, while degradation of **124** occurred. The reasons for the difficulties for the reaction success were attributed to the deactivation of both the amine arm and the carboxylic acids in **124**. However, in the same conditions as entry **1**, Table 3.2, the successful coupling of arm **113** was obtained with trimesic acid **120**. Considering the deactivation of the carboxylic acids in **124** the transformation of the carboxylic acids into acyl chlorides was also considered. However, the direct treatment of **124** with $SOCl_2$ or $COCl_2$ was avoided, as

Table 3.2. Methods attempted for coupling reaction between **124** and **113** to synthesise **112**.

#	Coupling agents	Solvent	T (°C)	Time (hrs)	Result
1	EDC·HCl, TEA, HOBt	THF	0-20	72	Starting material recovered
2	EDCI, TEA	CH_2Cl_2	0-20	72	Starting material recovered
3	EDCI, TEA	$CHCl_3$	0-50	72	Starting material recovered
4	EDC·HCl, DMAP	CH_2Cl_2	0-20	72	Starting material recovered
5	EDC·HCl, DMAP, TEA	CH_2Cl_2	0-20	72	5% yield

the HCl produced as a side product from those reagents could have cleaved the N-Boc protecting group. The use of 1-chloro-*N*,*N*,2-trimethyl-1-propenylamine (Ghosez's reagent), which can covert carboxylic acids into acyl chloride in neutral conditions,[180] was attempted, however with unsuccessful outcomes. Similarly, the alternative protection of the amine of the intermediate **123** with carboxybenzyl (Cbz) group was pursued, with unsuccessful result.

Therefore, despite the very poor yield, **112** was identified by mass spec MALDI-TOF+ with a peak at *m/z* = 1083.5336, as $[M+Na]^+$, Figure 3.11, for which the best synthetic conditions were those presented in Scheme 3.7. Compound **112** was largely purified from the unreacted starting materials by flash chromatography on silica, in a gradient of CH_3OH:CH_2Cl_2, as demonstrated by ^1H NMR, Figure 3.10a. Without further purification, to minimise loss of product, deprotection of the Boc group with TFA in CH_2Cl_2 solution was performed, to obtain the target ligand **85**. The compound was purified by column chromatography in a gradient of CH_3OH:CH_2Cl_2. However, it was not possible to fully remove the impurities of **113**, which were still present, Figure 3.10b. Characterisation by mass spectroscopy by MALDI-TOF+ showed a peak at m/z = 983.4801 which was confidently identified as being

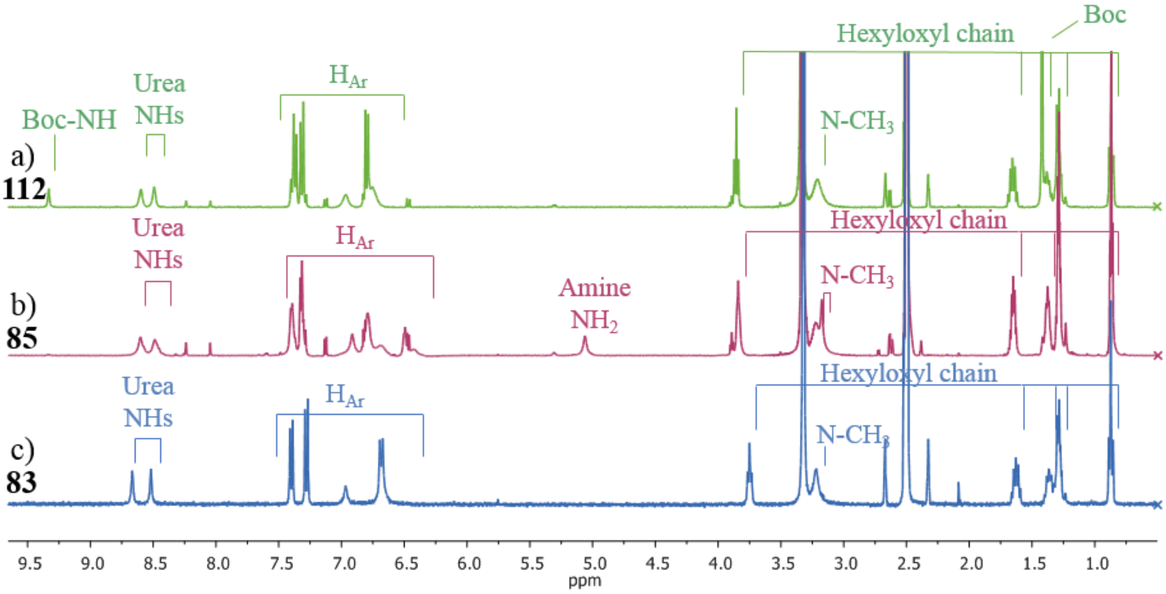

Figure 3.10. Comparison of ^1H NMR spectra (400MHz, DMSO-d_6, 298 K) of a) Boc-protected dipodal precursor **112**, b) final dipodal ligand **85** and c) equivalent tripodal ligand **83** for comparison.

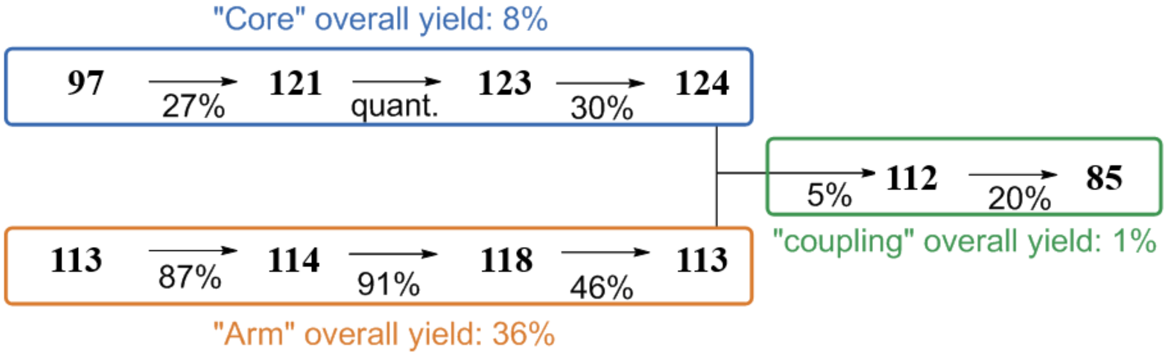

Scheme 3.8. Full synthesis of **85** using the modular approach, indicating the yields of each step and the overall yields of the two components **124** and **113**, and of the final coupling step.

$[M+Na]^+$, Figure 3.11. The ^1H NMR spectrum of **85**, Figure 3.10b, was partially comparable to the spectrum of the tripodal **83**, with urea NH protons resonating between 8.4 ppm and 8.8 ppm, and similar resonances for the hexyloxyl chain. The loss of the C_3 symmetry in the dipodal ligand **85**, resulted in the presence of a greater number of resonances, compared to the ^1H NMR spectrum of **83**, in the aromatic region and a broadening of the signals, possibly due to increased flexibility and movement of the arms. The key characteristics of **85** were the presence of a broad singlet at 5.6 ppm, corresponding to the NH_2 resonance, and the splitting of the *N*-methyl group on the amide, because of two non-equivalent sets of protons were present in the dipodal **85**. By ^1H-^{15}N HSQC, the resonances corresponding to the amine and urea protons were confirmed, while identification of the aromatic protons was prevented, due to their broadness. Due to the very small amount of compound obtained (3 mg), it was not possible to further characterise the obtained dipodal ligand. Attempts to crystallise **85**, in the presence of SO_4^{2-} were unsuccessful, most likely due to the contamination with **113**.

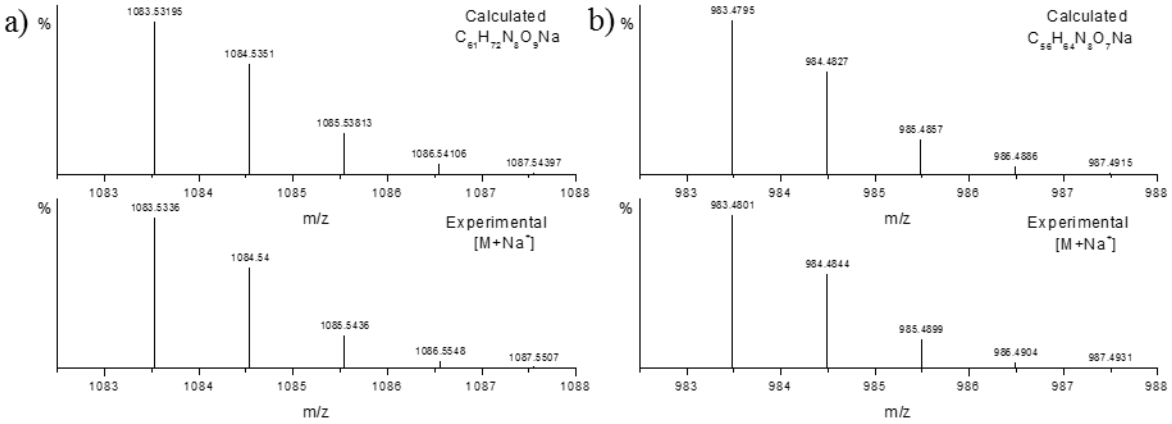

Figure 3.11. HRMS-MALDI-TOF+ of a) of **112** showing the species $[M+Na]^+$ and b) **85** showing the species $[M+Na]^+$.

The target ligand **85** was synthesised by a modular approach with a total of eight steps: three steps for the synthesis of the "core" with an overall yield of 8%, three for the synthesis of the "arm" with an overall yield of 36%, and two final steps for the coupling of the two parts, with a very poor overall yield of 1% after the deprotection step. The moderate to low yields on the two modular components were balanced by a relatively low cost and large availability of the starting materials, which allowed the isolation of reasonable amounts (0.050 – 0.200 g). However, the negligible yields obtained from the subsequent coupling step, did not allow isolation of the quantities necessary for the desired anion binding analyses. Attempts to improve the efficiency of the coupling step were unsuccessful, and this was attributed to a low reactivity of the carboxylic groups on the "core" structure, **124**. In all of the tested reactions, the compound **124** could not be recovered, which indicated that initial reaction with the coupling agents could have occurred, but the obtained "activated" esters would not react with the already deactivated and sterically hindered secondary amine **113**.Some crystals were obtained from DMSO for **112** and **85**, however they did not show diffraction properties and their crystal structures could not be identified or characterised further.

Despite the difficulties of the synthesis of **85**, a similar dipodal molecule, **90**, was successfully obtained by reaction of **84** with 4-(trifluoromethyl)phenyl isothiocyanate. The synthesis and anion binding properties of this ligand will be discussed in the next section.

3.2.3. Thiourea

The synthesis of **90**, was initially achieved by Dr Komala Pandurangan, in the attempt of synthesising **125**, the thiourea analogue of **125**, Figure 3.12, by reacting **84** with 3 equivalents of 4-(trifluoromethyl)phenyl isothiocyanate in CH_3CN at reflux overnight (following the same procedure that was used to synthesise **81**).

Initially, it was thought, from ^1H NMR analysis of the solid obtained after evaporation of the solvent, Figure 3.14, that a mixture of the desired tripodal and the starting material had been recovered. However, HRMS did not show any peak related to the tripodal ligand. After reviewing more carefully the ^1H NMR of **90** and the starting material, Figure 3.14, it was later evident that the aromatic resonances of **84** were not all present. In addition to this it was noted that, the integral ratio between the NH_2 resonance and the broad aromatic resonance at 6.85 ppm, corresponding to the central benzene proton resonance, was 1. In the ^1H NMR spectrum of starting material **84**, this integral ratio corresponded to 2, because for each NH_2 there was one aromatic proton in the central core. The integral ratio of 1 was

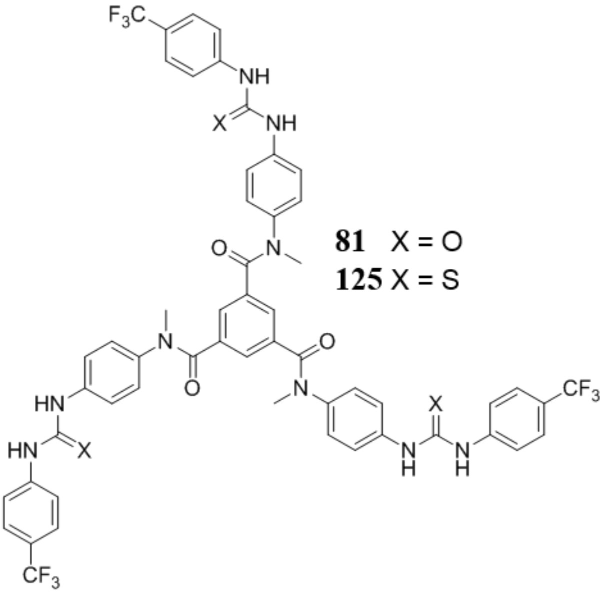

Figure 3.12. Structure of **81** and **125**.

consistent with the formation of a dipodal **84**, with only one NH_2 group on one arm, and only 2 equivalent aromatic protons in the central core. The presence of two separate resonances at 3.21 ppm and 3.18 ppm, corresponding to the N-CH_3 protons and integrating for a total of 9 protons, suggested that two non-equivalent sets of N-CH_3 protons were present. These two main features suggested that the ^{1}H NMR was not, in fact, of a mixture of **125** and **84**, but indeed of the sole dipodal compound **90**. Confirmation of the formation of the dipodal molecule was found by HRMS, using MALDI-TOF+ where the peak corresponding to $[M+Na]^+$ (calcd. *m/z* = 951.2310) was found at *m/z* = 951.2295. ^{13}C NMR showed the correct number of resonances for **90**, as well as two very close resonances at 37.6 ppm and 37.8 ppm for the two N-CH_3 non-equivalent sets of carbons. By ^{1}H-^{15}N HMQC NMR it was also confirmed that the resonances at 10.00 ppm, 10.09 ppm and 5.08 ppm are protons bonded to a nitrogen atom, corresponding to urea protons and the aniline respectively. The presence of

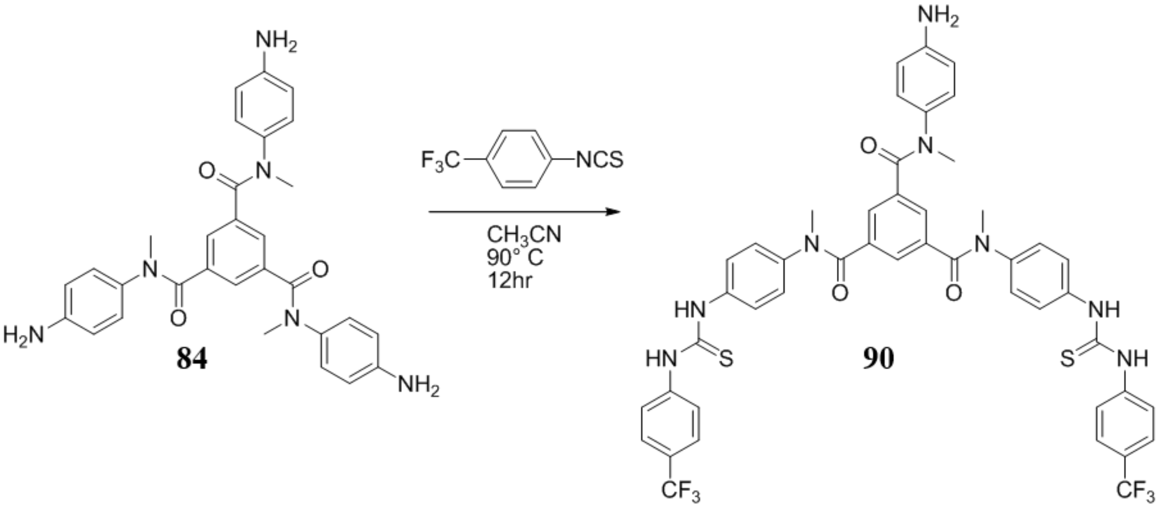

Figure 3.13. Synthesis of dipodal compound **90**.

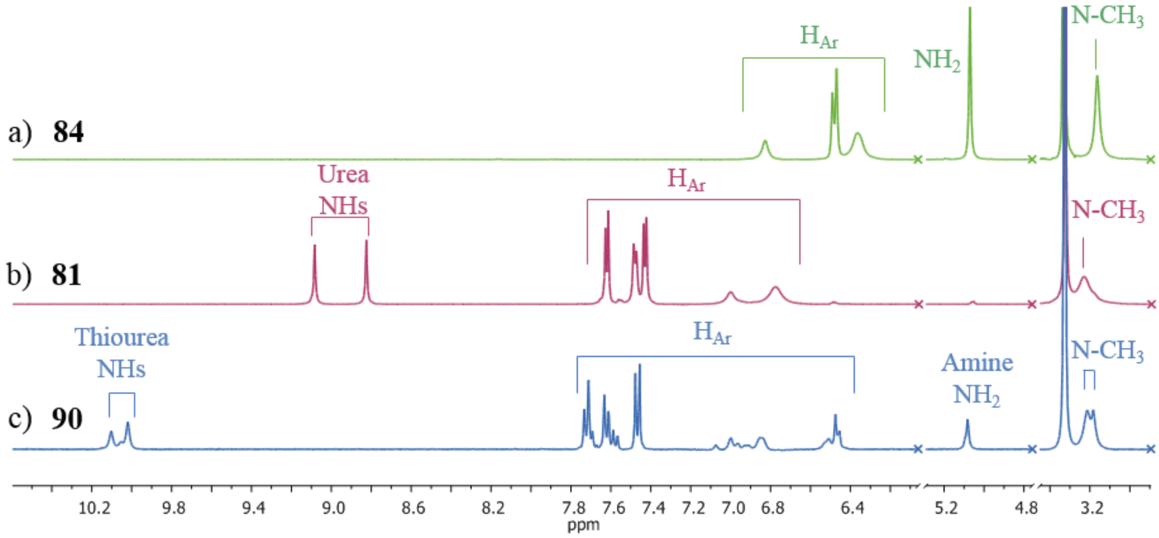

Figure 3.14. Stacked ^{1}H NMR spectra (400 MHz, DMSO-d_6, 298 K) of compound: a) **84**, b) **81**, c) **90**.

broad signals, like in the case of the other dipodal molecule, **85**, did not allow the full identification of the resonances by HSQC and HMBC. In the ^{1}H NMR analysis, a small impurity was also identified, which could not be separated by chromatography, due to the low solubility, or by trituration. Despite this, to test the response of these ligands with tetrahedral anions, titrations with $H_2PO_4^-$ and SO_4^{2-} were carried out and will be discussed in the next section.

3.3. Anion binding studies on thiourea dipodal molecule 90.

Binding studies with tetrahedral anions $H_2PO_4^-$ and SO_4^{2-} were carried out for ligand **90** to study its self-assembly behaviour in the presence of these anions, and compare it to the binding abilities of the dipodal **85** and the other tripodal ligands of the *para*-substituted family.

To obtain a more resolved spectrum, the studies were carried out in a CD_3CN:DMSO-d_6 (5:1) mixture. This allowed the full characterisation and resonance identification at the beginning and at the end of each titration, which was not possible for DMSO-d_6 due to the broadness of some resonances.

The titration of **90** with $H_2PO_4^-$, Figure 3.17, displayed some important changes in both the aromatic and the urea resonances. The resonance corresponding to the NH_2 disappeared upon the initial addition of $H_2PO_4^-$, due to deprotonation. A significant downfield shift of the urea resonances was accompanied by broadening, and disappearance of the resonances, corresponding to 1 equivalent of anion added. The aromatic resonances underwent shielding, apart from protons H7, H7' and H12 which were deshielded and moved downfield. The binding isotherms, Figure 3.16a, showed a faster change before 1 equivalent

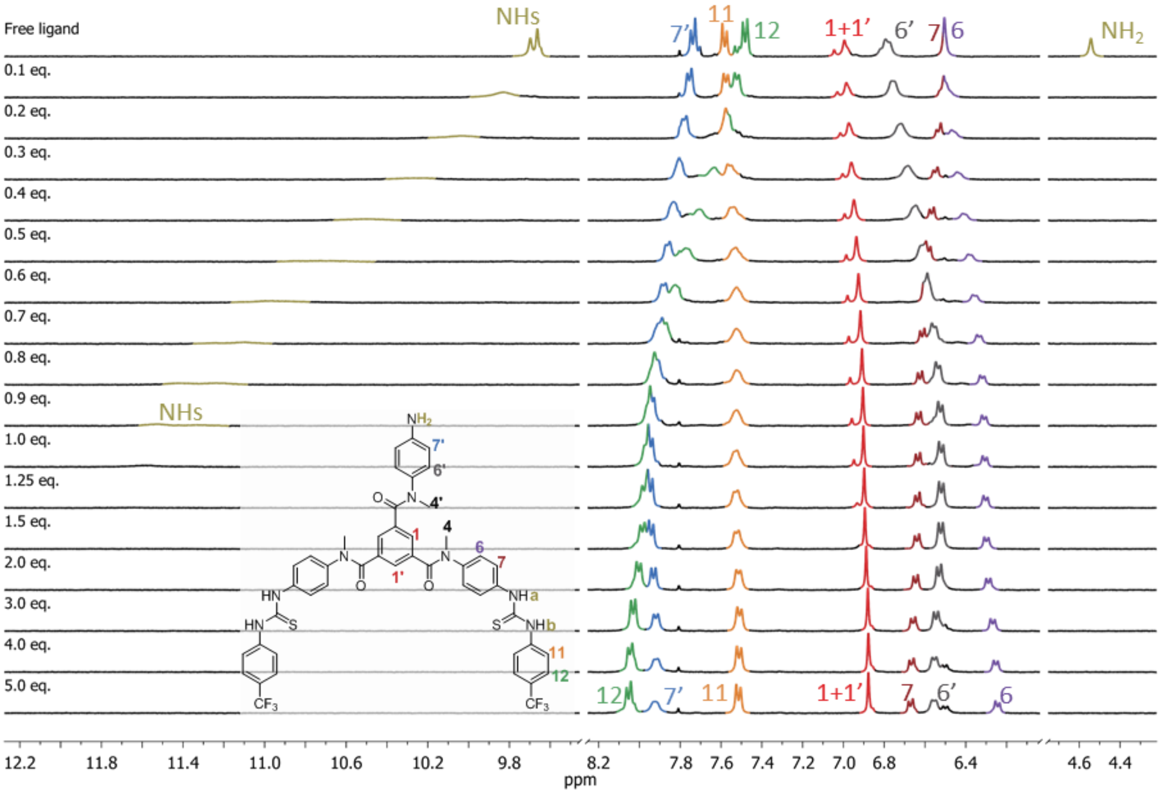

Figure 3.15. ^{1}H NMR titration profile of **90** with $H_2PO_4^-$, in CD_3CN:DMSO-d_6 (5:1). [**90**] = 2 mM. Only aromatic and urea protons region shown for clarity. This titration is representative of reproducible trends.

of $H_2PO_4^-$, and a slower one at higher equivalents. The fitting by non-linear regression of the changes revealed the formation of two species, 1:1 and 1:2 (L:A), with constants equal to $K_{1:1} > 10^4$ M^{-1} and $K_{1:2} = 500$ M^{-1}. The large values indicated the effective formation of hydrogen bonding. As shown in the speciation diagram in Figure 3.16b, the 1:1 species was the major species at 1 equivalent, with the 1:2 complex becoming the main component after the addition of 2.5 equivalents of $H_2PO_4^-$. The tripodal urea analogue **81**, reported by Gunnlaugsson and coworkers,[152] reacts in slow exchange with $H_2PO_4^-$, therefore the

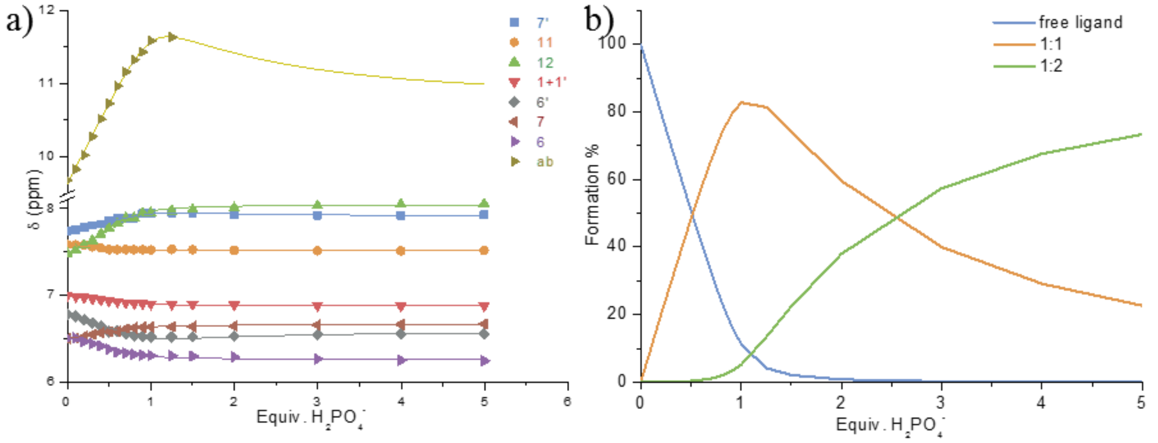

Figure 3.16. a) Plots of binding isotherms with the relative fitting curve of ^{1}H NMR titration of **90** with $H_2PO_4^-$ b) Speciation diagram obtained from the fitting showing the formation of two species, 1:1 and 1:2 (L:A).

identification of the association in solution could not be obtained. However, in the solid-state formation of capsules with two molecules of **81** and two $H_2PO_4^-$ was observed.

Titration of **90** with SO_4^{2-} also showed important changes to the ^{1}H NMR spectrum of the ligand, Figure 3.15, which indicated the formation of hydrogen bonding between the anion and the ligand. In this case, the downfield shift of the urea resonances was not accompanied by broadening, and they could be followed throughout the entire titration. The shielding and deshielding of the aromatic protons were similar to the titration with $H_2PO_4^-$. However in this case the isotherms showed a less sharp change. The best model, Figure 3.18a, was obtained with the formation of only the 2:1 (L:A) species as the only one being formed, as shown in the speciation diagram in Figure 3.18b, with a $K_{2:1} > 10^6$ M^{-1}. Also in this case, the calculated constant was relatively large, and was larger than the constant calculated upon titrating the tris(urea) tripodal analogue **81** with SO_4^{2-}, (which formed two species, 1:1 and 2:1, with $K_{1:1} = 60$ M^{-1} $K_{2:1} = 1000$ M^{-1}, in DMSO-*d*$_6$. This was likely due to a combination of factors, mainly the less competitive media used and the more effective hydrogen bonding formation of the thiourea group over the urea one. For a direct comparison of the thiourea effect the tripodal thiourea **125** would be a more appropriate analogue to

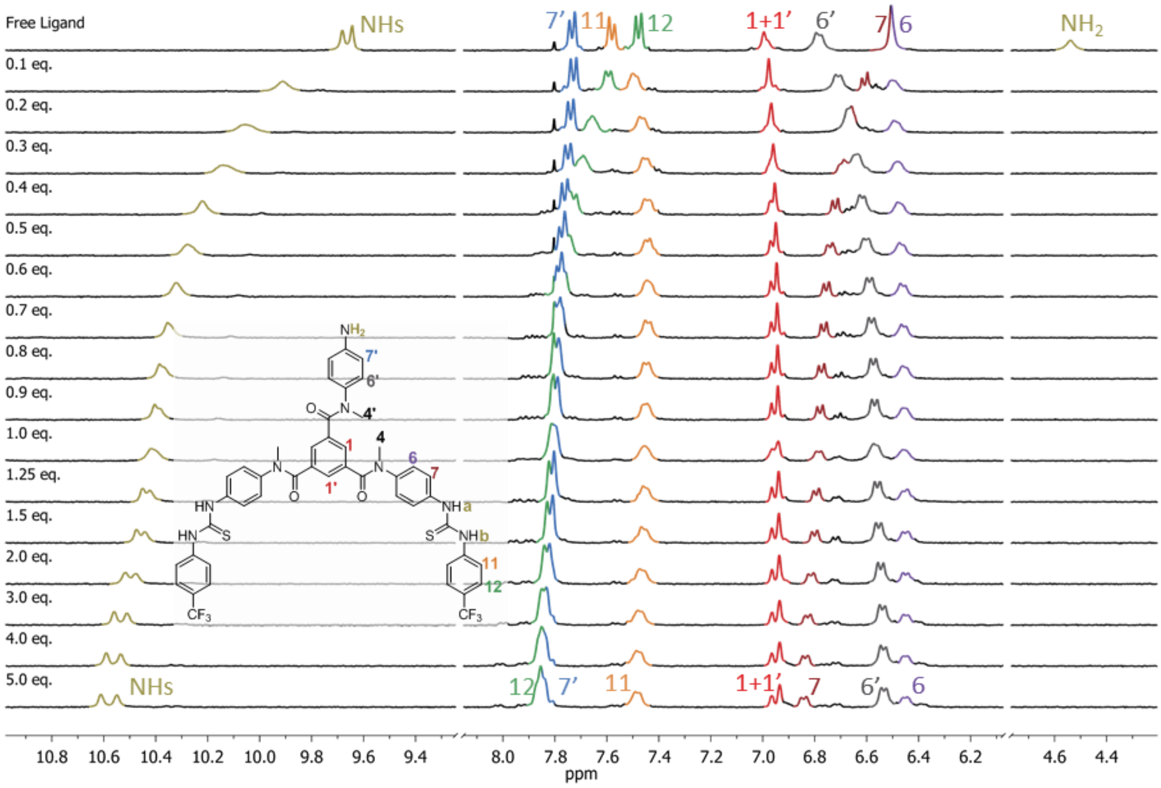

Figure 3.17. ^{1}H NMR titration profile of **90** with SO_4^{2-}, in CD_3CN:DMSO-*d*$_6$ (5:1). [**90**] = 2 mM. Only aromatic and urea protons region shown for clarity. This titration is representative of reproducible trends.

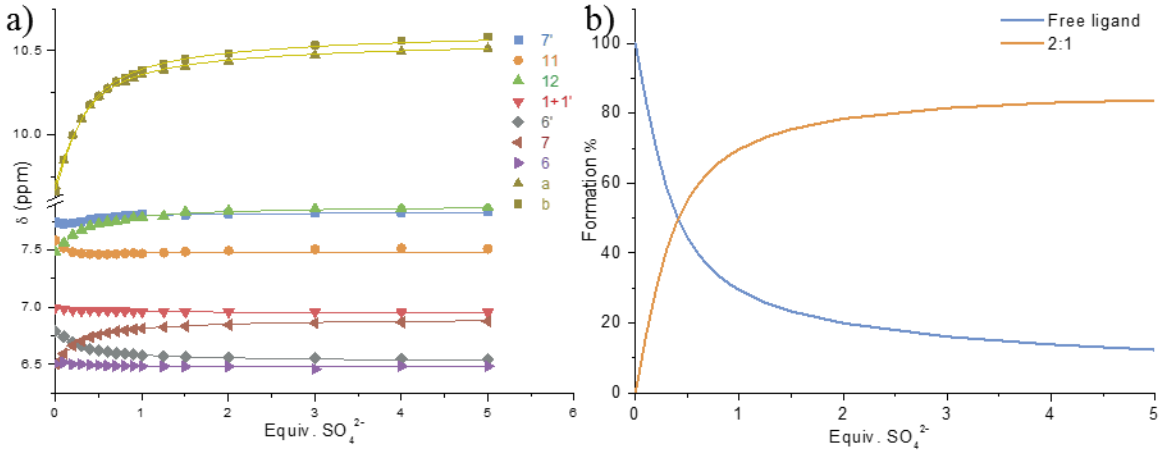

Figure 3.18. a) Plots of binding isotherms with the relative fitting curve of ^{1}H NMR titration of **90** with SO_4^{2-} b) Speciation diagram obtained from the fitting showing the formation of the 2:1 (L:A) species.

consider, however the molecule could not be synthesised, as the poorly soluble dipodal ligand **90** would precipitate and, in fact, prevent further reaction.

The binding abilities of **90** with the tetrahedral anions $H_2PO_4^-$ and SO_4^{2-} were evaluated and the formation of self-assemblies of the ligand with the anion were observed. With $H_2PO_4^-$ ligand **90** would form 1:1 and 1:2 (L:A) species, while with SO_4^{2-} two ligands would associate to one anion to form a 2:1 “complex”. These associations are different from the 4:4 observed for the dipodal **85** with SO_4^{2-} in the solid-state, however higher order association of the formed assemblies could potentially occur and give rise to similar structures. Attempts to grow crystals from solutions of **90** with the anions were carried out; however, the crystal obtained were not suitable for XRD analysis.

Considering the good binding abilities of the dipodal ligand **90**, which showed the highest binding with tetrahedral anions observed among the families of analogue structures, it was thought that functionalisation of the third unreacted arm with a different moiety could be pursued. Among other interests, the functionalisation with a polymerizable unit was motivating, for the potential use in the formation of anion capturing materials. Preliminary studies on this work will be briefly presented in the next section.

3.4. Polymeric functionalisation: preliminary studies of potential precursors and future approach

The anion binding of the tripodal ligands presented in this and the previous chapter could not be tested in water due to their insolubility. Being able to include these ligands within a solid support could allow us to overcome the insolubility problem and test the anion capturing properties of these ligands from an aqueous environment. It was proposed that including the ligand within a polymeric support could be used, similarly to the examples presented earlier.

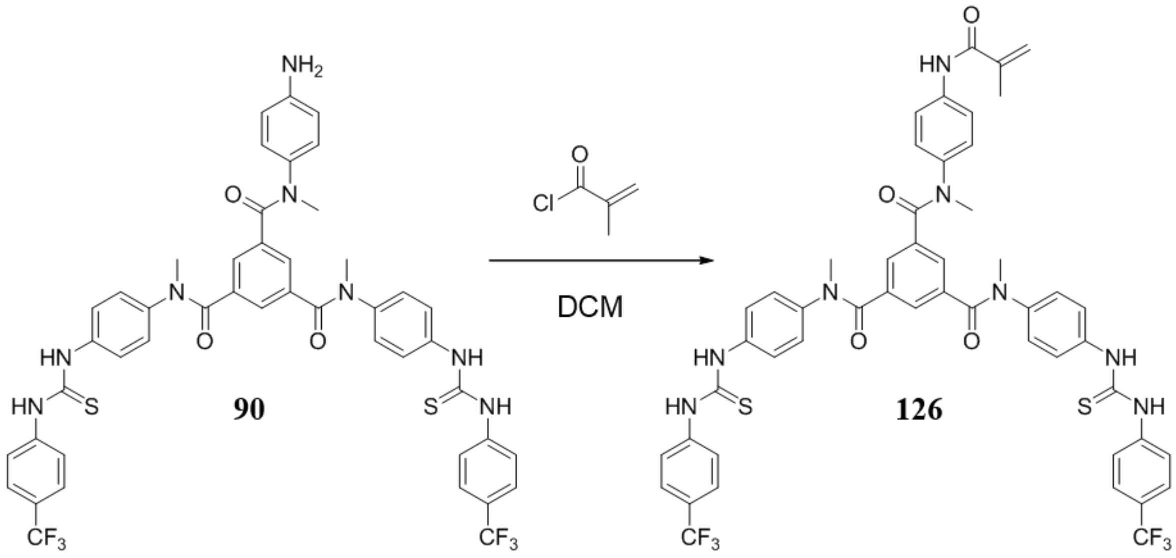

Scheme 3.9. Synthesis of **126** from **90**.

Preliminary studies in this direction were carried out in collaboration with Dr. Samuel Bradberry and aimed at studying the binding abilities of a p(HEMA) material functionalised with **90**. The properties of such polymer, including hydrophilicity,[181] can be easily modulated by the combination of the two components prior to the polymerisation and allow access of larger compounds to the aqueous environment. To include the structure of

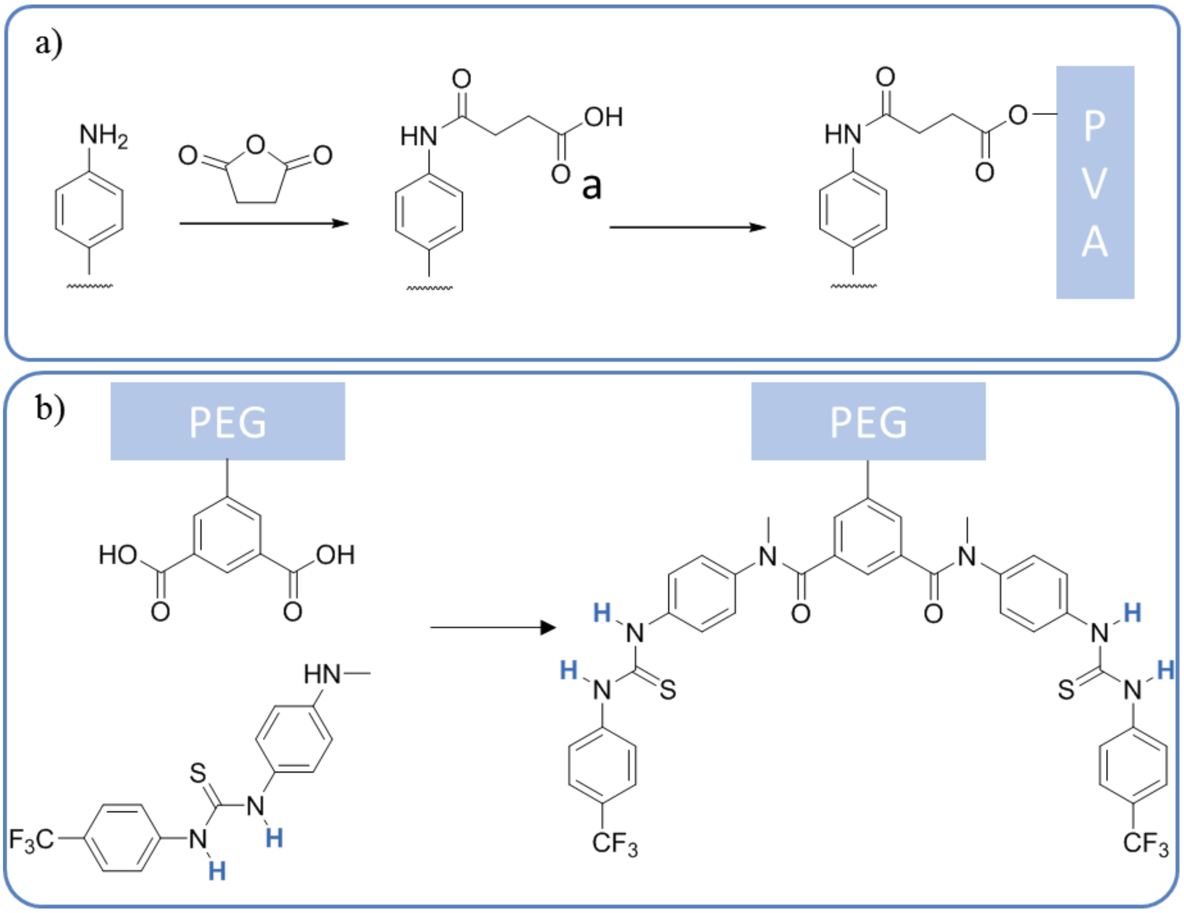

Figure 3.19. Example of future developments of a) PVA with dipodal ligands and b) PEG with dipodal ligands..

90 in the material it was considered to react it with methacryloyl chloride, to obtain **126**, Scheme 3.9. Copolymerisation of **126** with HEMA and EGDMA would yield the desired material p(HEMA-*co*-EGDMA). While ^{1}H NMR analysis of the crude material proved the formation of **126** (Appendix A3, Figure A3.45), upon purification by column chromatography the degradation of the methacrylate portion of the molecule was observed by oligomerisation. The cause of this is likely due to the interaction of this group with the *p*-trifluoromethylphenyl thiourea moieties of **90**, which are known and widely used as catalytic activators.[182] Polymer functionalisation with **90** following this approach could not be performed due to the mentioned issues, however interest in the success of this project motivated to find suitable alternatives to the methods used for the development of anion-capturing materials.

Inspired by the material developed by Sessler,[169] alternative functionalisation could be attempted with PVA, which is a highly hydrophilic gelating matrix. In order to couple **90** to the hydroxyl groups of PVA, a linker would need to be attached. For example, by reacting **90** with succinic anhydride, Figure 3.19a. The obtained ligand could then be ‘appended’ onto the polymeric matrix, and after optimisation, anion binding tests could be carried out. However, the low solubility of such ‘dipodal’ structures could still pose an obstacle for the successful and efficient functionalisation. Alternatively, an approach which does not involve the synthesis of the actual dipodal molecule, but only of the urea-functionalised ‘arm’ can be considered. A polymer (*e.g.* PEG co-polymers) with isophthalic residues could be coupled with the amine of pre-synthesised bis(phenyl)-urea ‘arms’. This would result in a polymer carrying a slightly modified of dipodal **90**, Figure 3.19b, would avoid a number of synthetic challenges associated with the synthesis of a discrete dipodal, as well as using a polymer synthesis which is cheaper and more easily handled.

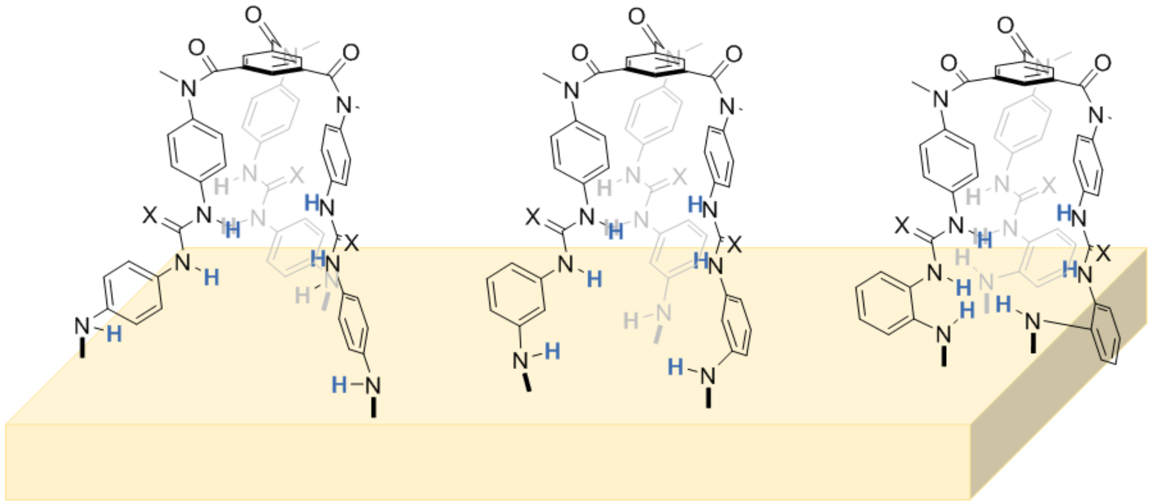

Figure 3.20. Example of future developments of tripodal ligands for surface functionalisation.

Retaining the tripodal design, a similar approach could be considered. The reduction to amines of the of NO_2 moieties of *para*-substituted **tmBTA** tripodal structures (*e.g.* **82**) would lead to the formation of tripodal tris(amine) molecules which could be used to linked to various materials (*e.g.* polymers, glass, gold), with diverse methods.

3.5. Conclusions and future perspective

The synthesis of 'dipodal' ligand **85** was achieved through a modular synthesis, however low yields were obtained which did not allow to carry put the desired binding studies. Binding studies with $H_2PO_4^-$ and SO_4^{2-} were carried out with an analogue bis(thiourea) molecule **90**. This dipodal formed 1:1 and 1:2 complexes with $H_2PO_4^-$($K_{1:1} > 10^4$ M^{-1} and $K_{1:2} = 500$ M^{-1}), while with SO_4^{2-} 2:1 complexes ($K_{2:1} > 10^6$ M^{-1}) in CD_3CN:DMSO-d_6 (5:1).

Due to the low solubility of the ligand, attempts to synthesise polymeric materials functionalised with ligand **90** were not successful. However, some modification to the structure could improve the overall yield and solubility. Optimisation of the synthesis of the ligand as well as the functionalised material is needed, and the strong binding abilities of these structures are a promise for the future development of such structures.

4. Anion binding properties of a set of BTP based catenanes and macrocycles

4.1. Introduction

This chapter will focus on the anion complexation studies of a set of [2]catenanes and macrocycles containing the 2,6-bis(1,2,3-triazol-4-yl)pyridine (**btp**) moiety. The structures of the ligands discussed in this chapter are shown in Figure 4.1. This project was carried out in collaboration with Dr Joseph Byrne, Dr Eoin McCarney and William McCarthy, who synthesised the ligands. Part of the results presented in this chapter have been published in a communication paper,[155] and revealed the anion binding properties of the first set of [2]catenanes and macrocycles. The **btp** motif is a versatile building block that has been used for many different purposes in supramolecular chemistry.[133,183-188] The synthesis of **btp** is achieved *via* copper(I)-catalysed alkyne-azide cycloaddition (CuAAC) on a substituted pyridine. The possibility of forming any desired azide-substituted molecule (with respect to safety), allows the easy functionalisation of the **btp** motif, with an infinite number of substituents, for different scopes.[186] As recently reviewed by Byrne,[188] the coordinative abilities of **btp** have been studied with both d- and f-metals. Byrne and Gunnlaugsson have explored the use of **btp** for metal coordination and have studied the behaviour of 2,6-bis(1-(4-(carboxy)benzyl)-1,2,3-triazol-4-yl)pyridine (**127** and **128**), Figure 4.2a, with d^6 metal ions Ru(II) and Ir(III) and d^8 metal ions Ni(II) and Pt(II). The complexes formed displayed characteristic photophysical behaviour as well as forming metallo-supramolecular gels.[189] The addition of chiral centres to the structure, *i.e.* ligand **152**, Figure 4.2b, allowed the study

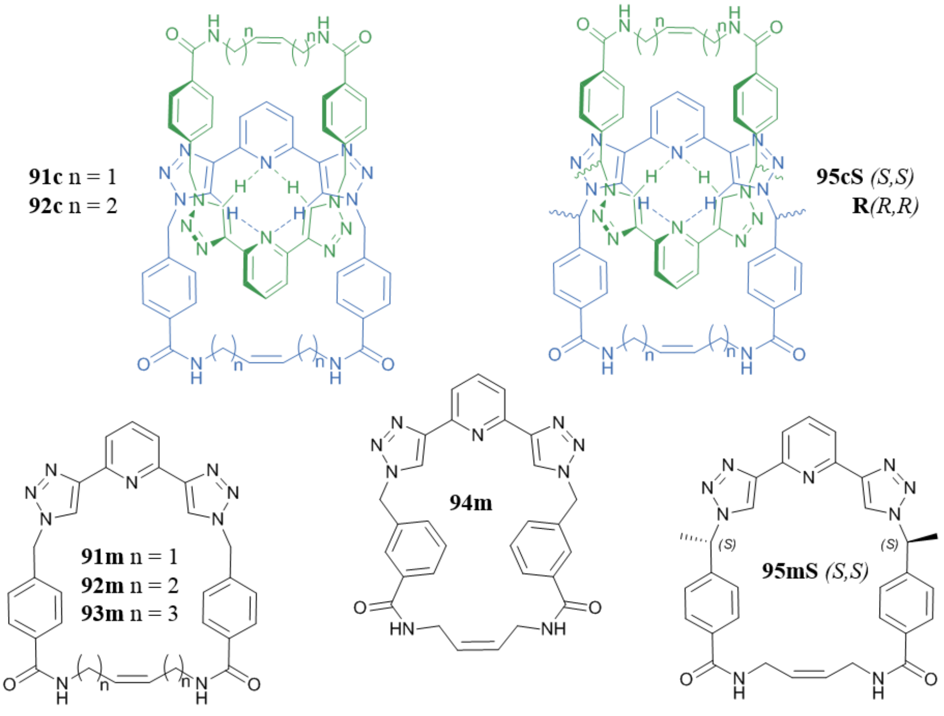

Figure 4.1. Structures of [2] catenanes **91c**, **92c**, **95cR/S** and macrocycles **91m**, **92m**, **93m**, **94m**and **95mS**.

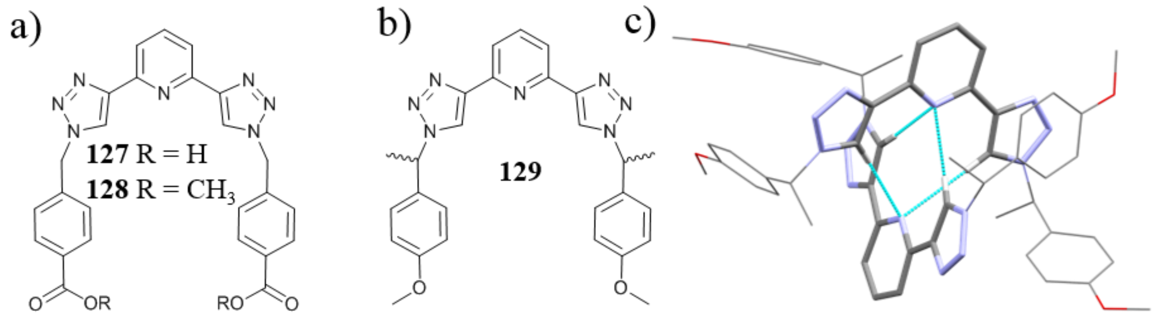

Figure 4.2. Chemical structure of ligand **127**, **128** and **152**, developed by Dr Joseph Byrne for metal coordination.

of metal coordination through chiral spectroscopy (*i.e.* CD, CPL) and showed the transfer of the chiral nature of the ligand to the metal centre luminescence properties.[190] In both cases, Byrne and co-workers observed in the solid-state that the triazolyl group would be available to form hydrogen bonds with a guest species, through the donation of the C-H proton. In particular, the crystal structures of the three complexes [Ru·**127**$_2$](PF$_6$)Cl, [Ni·**128**$_2$](PF$_6$)Cl and [Ir·**128**·Cl$_3$] displayed the formation of hydrogen bonding interactions between the triazole CH and chloride counterions present in the crystal structures. More interestingly, both enantiomers of ligand **152** were shown to self-assemble into dimers with hydrogen bonding bridges between the triazolyl CHs and the pyridine nitrogen atom in the solid-state, Figure 4.2c. This self-assembly interaction was exploited by Byrne and McCarney for the self-templated synthesis of the [2] catenanes as will be described in this chapter.

The free rotation of the triazole ring about the bond with the central pyridine unit of the **btp** motif creates an ideal binding site for anion complexation, Figure 4.3. Examples of anion complexation from ligands containing the triazole or **btp** unit were presented in Chapter 1. However, it is essential, prior to this discussion, to give a brief overview of the state of the art developments strictly relevant to our systems.

As stated above, the **btp** unit has played an important role in the past years in anion binding and self-assembly, together with other isostructural groups, such as bis-triazolyl

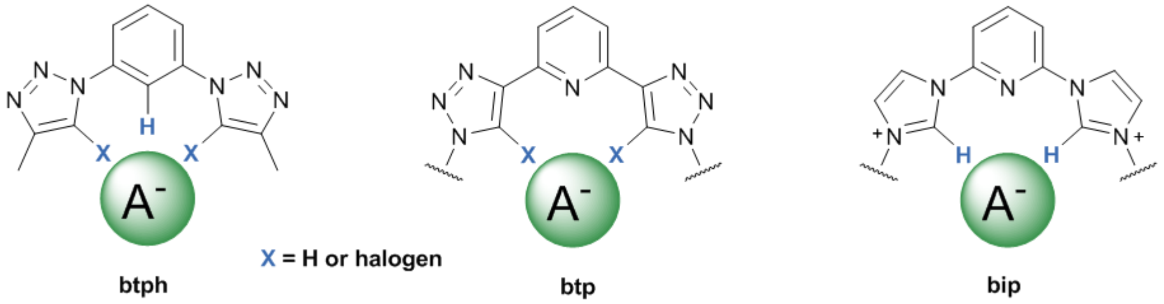

Figure 4.3. Schematic structures of bis-triazolyl phenylene (**btph**), bis-triazolyl pyridine (**btp**) and bis-imidazolium pyridine (**bip**).

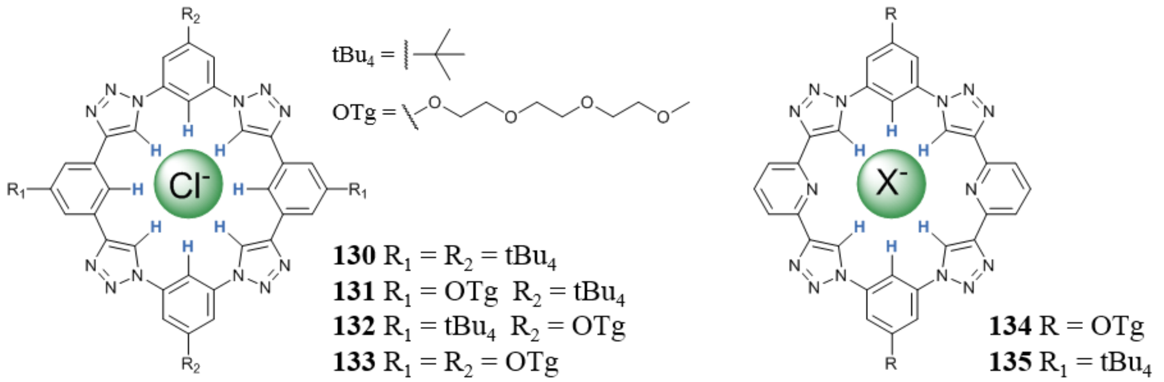

130 $R_1 = R_2 = tBu_4$
131 $R_1 = OTg$ $R_2 = tBu_4$
132 $R_1 = tBu_4$ $R_2 = OTg$
133 $R_1 = R_2 = OTg$

134 R = OTg
135 $R_1 = tBu_4$

Figure 4.4. Structures of **btp**/**btph** based macrocycles **130-135**, developed by Flood *et al.*

phenylene (**btph**) and bis-imidazolium pyridine (**bip**), Figure 4.3.[133,183-188] The bis-triazolyl phenylene (**btph**) group can avail of an additional hydrogen bond donor from the phenylene proton in the 2 position of the phenyl ring, which can be additionally activated by modulating the group *para* to it. In the bis-imidazolium pyridine (**bip**) motif, an increased binding interaction is brought about by the positive charges on the imidazolium rings. Varying combinations of these groups with other hydrogen/halogen bonding groups have been recently exploited for the study of anion binding and complexation within macrocyclic rings[63,191-193] and interlocked systems,[194] such as catenanes and rotaxanes, and some relevant examples will be highlighted in this section.

Flood developed a series of macrocyclic ligands containing the **btph** and **btp** moieties, **130-133**, Figure 4.4,[63,191-193] at the same time as Hecht[51] and Craig[50] developed halide-directed self-assembly helical foldamers with similar structures. These ligands showed good binding abilities towards halides in CH_2Cl_2 (a low competitive solvent) with a preference for Cl^-. In all cases, the strongest binding was seen for the 1:1 complex of **130** with Cl^- ($K = 11(2) \times 10^6$ M^{-1}).[63] The binding with Cl^- for the open foldamer analogue of **130** displayed a much lower constant of $K = 6.9(3)$ M^{-1}, clearly demostrating the significance of the macrocyclic effect. The **btp**/**btph** compounds**134** and **135** also displayed good anion binding with higher affinity for Cl^- over other halides. In all cases, the formation of the 1:1 (L:A) complex followed by the 2:1 (L:A) sandwich complexes were observed, with the exception of I^- which showed only the formation of the 2:1 complex.[192] These examples by Flood confirm the good affinity of macrocycles with hydrogen bond donor groups converging towards the cavity for spherical halides, with size being the main discriminant.

Sessler *et al.* showed the use of the **bip-**based macrocycle **136**,[195] inspired by the renowned cyclobis(paraquat-*p*-phenylene) system previously developed by Stoddart.[194,196,197]

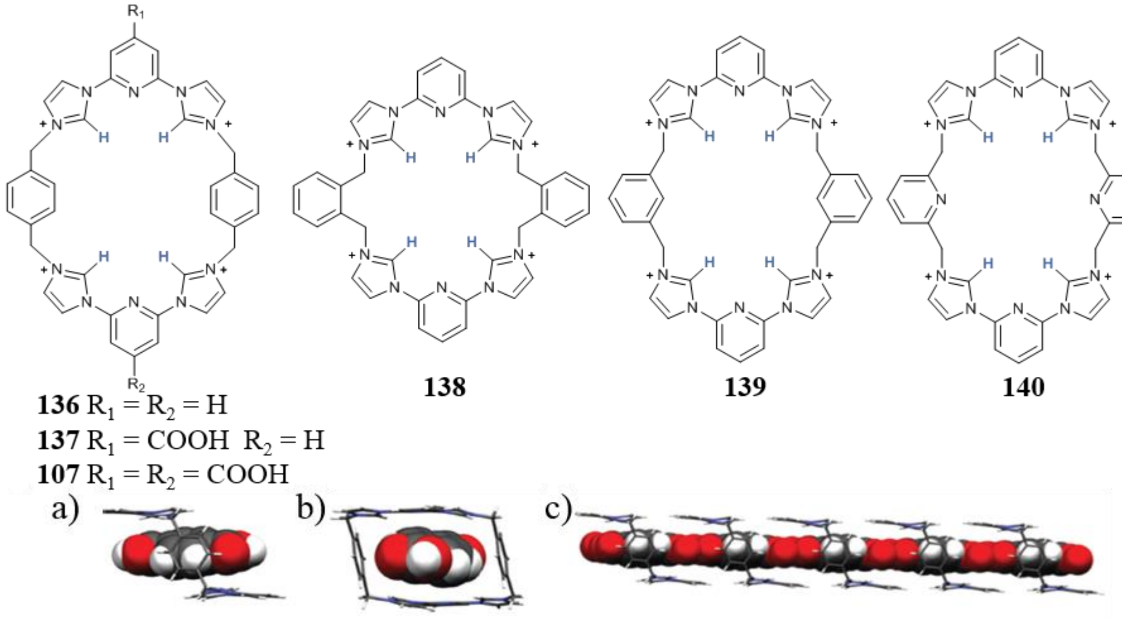

136 $R_1 = R_2 = H$

137 $R_1 = COOH$ $R_2 = H$

107 $R_1 = R_2 = COOH$

138

139

140

Figure 4.5. Structures of **bip**-based macrocyles **107**, **136**-**139**, developed by Sessler *et al.* Crystal structure of **136** with mono-terephtalate showing a-b) the pseudorotaxane structure and c) the self assembled pseudo-polyrotaxane structure. Reproduced from ref 199.

Macrocycle **136** displayed pseudo-polyrotaxanes formations with terephthalic acid, Figure 4.5b, which were stabilised by C–H···π hydrogen bond, electrostatic and hydrogen-bonding interactions. In more recent years, macrocycles **137**-**140** were developed,[198] showing interactions with various carboxylate anions, in a similar manner to that observed for **136** with terephthalic acid.[199] As discussed in Chapter 3, covalent linkage of macrocycle **107** within a poly(vinyl alcohol) (PVA) network displayed the ability to remove a number of environmentally relevant anions such as NO^{3-}, NO^{2-}, $SO_4^{2-}$and F^-, from aqueous solutions.[169] Sessler *et al.* also developed the **btph**-based macrocycle **141**, containing pyrrole moieties in order to provide additional hydrogen-bonding donors in the cavity. This modification gave rise to stronger binding for pyrophosphate ($K_{1:1} = 2.3(4) \times 10^6$ M^{-1}) over other anions, such as tetrahedral $H_2SO_4^-$ ($K_{1:1} = 4.9(4) \times 10^5$ M^{-1}), $H_2PO_4^-$ ($K_{1:1} = 2.4(3) \times 10^5$ M^{-1}) or spherical Cl^- ($K_{1:1} = 1.2(1) \times 10^4$ M^{-1}) and Br^- ($K_{1:1} = 2.6(1) \times 10^3$ M^{-1}), in low competitive $CDCl_3$ solution.[200]

The family of macrocycles and catenanes presented in this chapter include, along with the **btp** binding site, amide groups, which can also contribute to the overall hydrogen-bonding ability of the system. Examples of macrocycles which coordinate anions through both triazoles and amides were recently reported by Kubik and co-workers.[201,202] Changes in the ^1H NMR spectrum of pseudo-cyclopeptide **142**, Figure 4.6, were observed upon titrating against different anions in competitive media.[202] In DMSO-*d₆*:acetone-*d₆* (95:5), Cl^- showed the strongest interaction among the halides, and even larger changes were observed

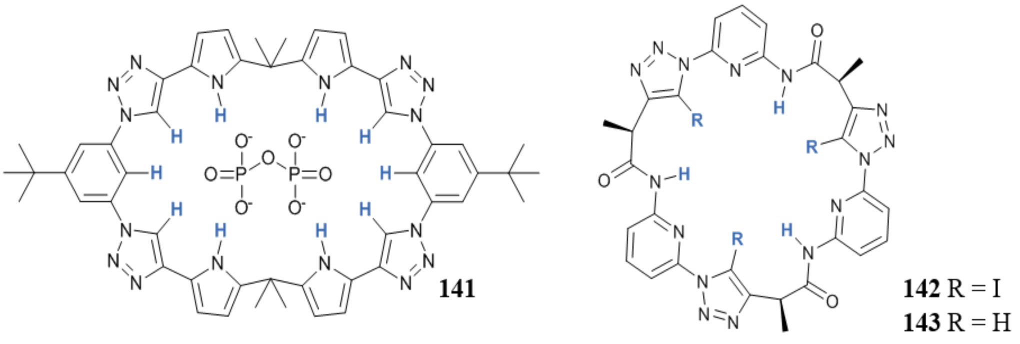
141

142 R = I
143 R = H

Figure 4.6. Structures of **btph**-based macrocyles **141**, developed by Sessler *et al.* and cyclic peptide containing triazoles and amides **142-143**, developed by Kubik *et al.*

for tetrahedral oxyanions SO_4^{2-} and $H_2PO_4^-$. Changes involved with downfield shifts of the triazole C–H, the amide N–H and even aliphatic chiral CH_2 protons, while the disappearance of the amide resonance was also observed upon the addition of oxyanions, due to proton exchange. Binding studies in more competitive DMSO-*d*$_6$/D_2O media showed no interaction with halides, while interaction with SO_4^{2-}, $H_2PO_4^-$ and $HP_2O_8^{3-}$ was evaluated and the formation of 1:1 and 2:1 (L:A) sandwich complexes was established by means of ITC and ^{1}H NMR titrations, as well as X-ray diffraction. Interaction with halides in the DMSO-*d*$_6$/D_2O mixture was reported for ligand **143**, thanks to halogen bonding interactions.[201]

The uses of triazoles and modified **btp** analogues have been extensively explored by Beer and co-workers in the past few years, in the formation of anion-templated self-assembled interlocked molecules, as discussed in Chapter 1. Many of these structures, have also shown anion binding abilities, through the same hydrogen/halogen bonding groups employed for the anion-templated synthesis.[90,92-94,96,203,204] Examples of anion complexation with interlocked systems using halogen bonding were discussed in Chapter 1. Some recent examples of hydrogen bonding interlocked molecules containing triazole and triazolium units developed by Beer are shown in Figure 4.7.

[2]Catenane **144** possesses amide and triazole binding units, and showed the formation of complexes with Cl^-, Br^-, I^- and $H_2PO_4^-$ in competitive $CDCl_3$:CD_3OD (1:1), with the largest constant calculated for Cl^- ($K_{1:1}$ = 680(20) M^{-1}) and the smallest for $H_2PO_4^-$ ($K_{1:1}$ = 49(4) M^{-1}).[93] The presence of the 3,5-substituted *N*-methyl pyridinium moiety provides additional electrostatic interaction with the anion and the PEG chain of the other macrocycle.[205] [2]Rotaxane **145** is a member of a series of rotaxanes of similar structure which have been developed by Beer, Figure 4.7.[91,92,206] The series of rotaxanes differed in axle length and macrocycle size, with **145** being the one with the shortest axle. [2]Rotaxane

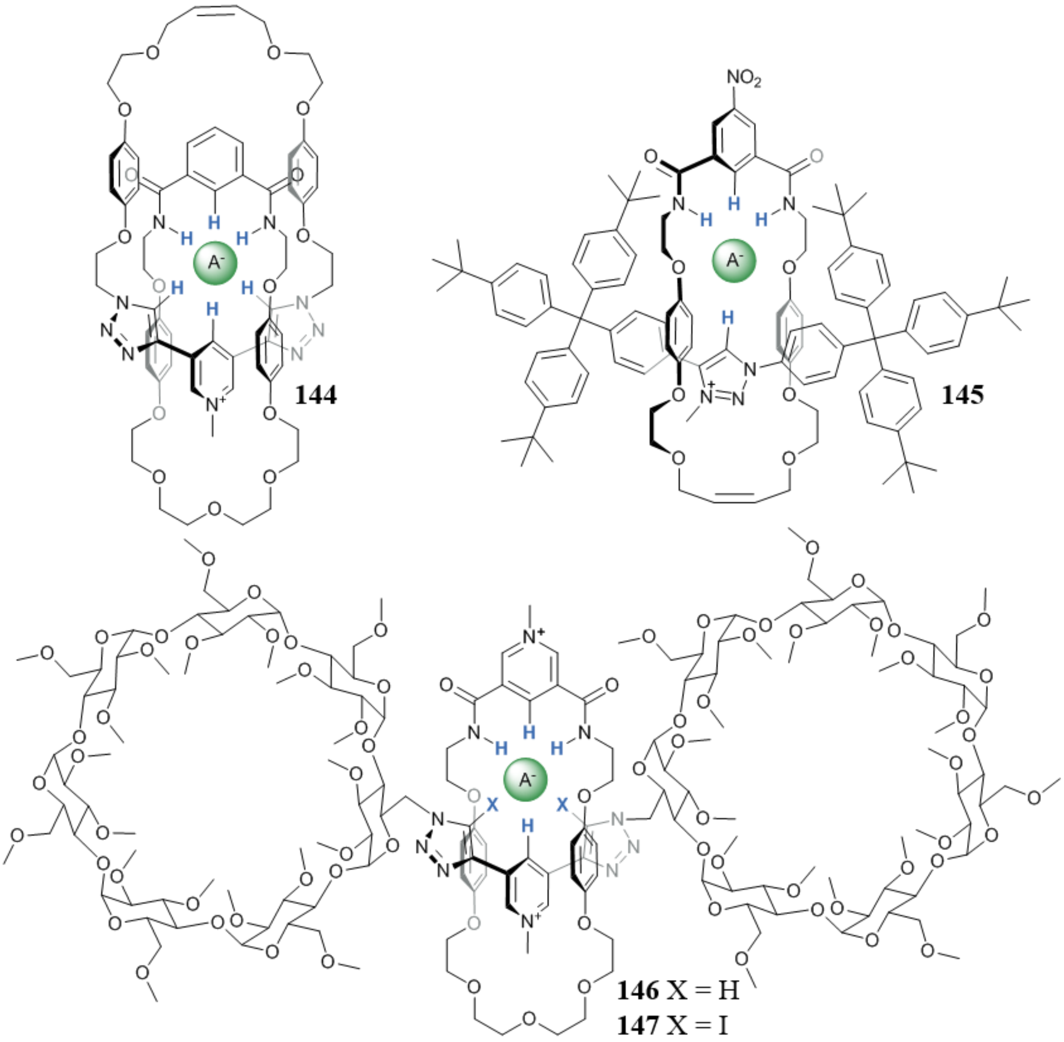

144

145

146 X = H
147 X = I

Figure 4.7. Examples by Beer and co-workers of hydrogen bonding interlocked molecules containing triazole and triazolium units and possessing anion binding abilities.

145, displayed the greatest interactions with anions, which were evaluated by ^{1}H NMR in $CDCl_3$:CD_3OD (1:1), with the highest constants obtained for Cl^- ($K_{1:1}$ = 1287(50) M^{-1}) and Br^- ($K_{1:1}$ = 1455(76) M^{-1}). Control experiments proved that the binding within the rotaxane was significantly higher than the binding with the sole axle (Cl^-: $K_{1:1}$ = 552(33) M^{-1}; Br^-: $K_{1:1}$ = 688(20) M^{-1}), showing the positive effect of preorganisation of the binding cavity. The same effect was proven for [2]rotaxanes **146** and **147**, Figure 4.7, which showed binding ability with halides in water, which was significantly higher in the rotaxane compared to the respective axles. The strongest interaction was shown for the iodotriazolyl-based rotaxane **147**, as a result of minor interference from the solvent in the formation of halogen bonding interactions.[204]

A recent collaboration by Jolliffe and Goldup led to the development of fluorescent rotaxane **148** containing both a triazolyl and a urea moiety, Figure 4.8, which also showed

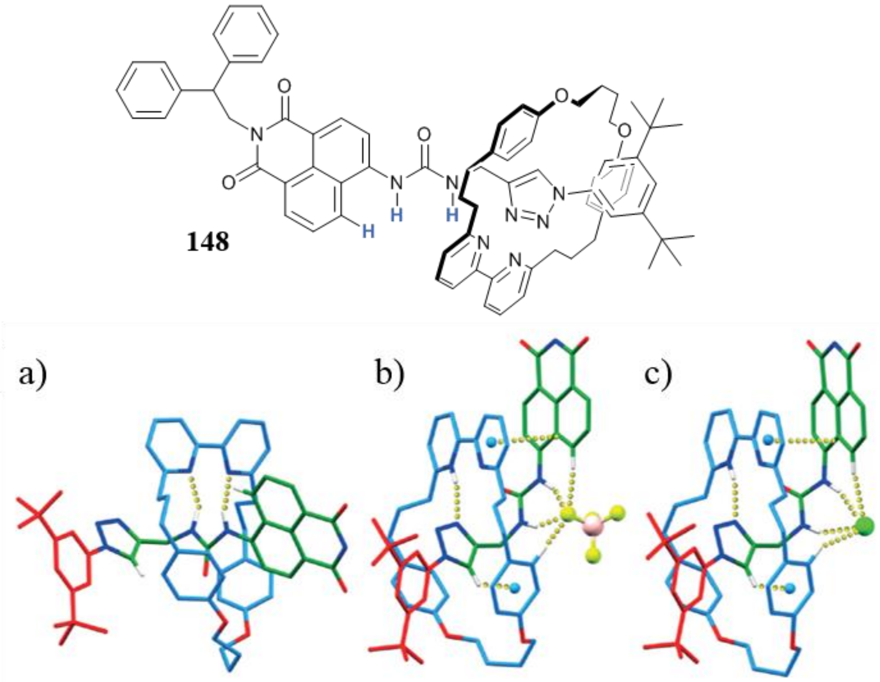

Figure 4.8. Fluorescent rotaxane with anion binding properties developed by Jolliffe and Goldup. Crystal structures of a) free ligand **148**, complex of **148** with b) HBF_4 and c) HCl; reproduced from ref. 207.

anion binding abilities.[207] In this case, the synthetic approach did not involve the use of anions as a template, and the interlocked structure does not offer a higher organised binding pocket. Instead, the presence of the mechanically bonded macrocycle restricts the urea binding site accessibility and generates selectivity with respect of the host size, with a high affinity for F^- and Cl^- over other halides, in $CDCl_3$:CD_3CN (1:1).

Considering the proven anion-binding abilities of macrocycles and interlocked systems containing triazoles and/or amide groups, the binding studies carried out on four [2]catenanes and five macrocycles will be presented in this chapter. Thanks to this combination of hydrogen-bond donor groups the macrocyclic ligands could potentially offer a good binding pocket for anions (*e.g.* Cl^-, $H_2PO_4^-$). The presence of the same binding units within the [2]catenanes structures hinted at their potential ability to encapsulate the same anions within a tighter binding pocket, therefore with potentially stronger interactions. In the next section the synthetic procedures for the synthesis of the [2]catenanes and equivalent macrocycles will be presented.

4.2. Synthetic strategies for Catenanes and Macrocycles

The synthesis of the [2]catenanes was based on the self-assembly properties of the **btp** moiety, by performing a RCM reaction on the relevant "open" macrocyclic ligand shown in Figure 4.9, at a concentration high enough to ensure the self-association of two molecules.

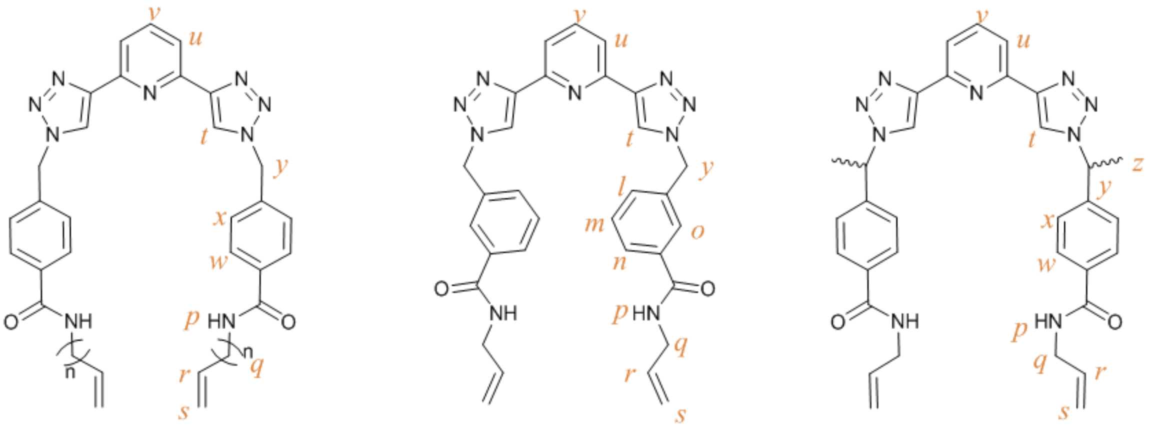

149 n = 1
150 n = 2
151 n = 3

152

153S *(S,S)*
153R*(R,R)*

Figure 4.9. "Open" macrocyclic precusors used for the syntheses of [2]catenanes and macrocycles in this chapter.

The RCM reaction would yield both the [2]catenanes and the corresponding macrocycles as products in different ratios, which were separated by column chromatography.

The synthesis of the first set of ligands was carried out by Byrne starting from three olefins, **149**, **150** and **151**, each with side chains longer than the previous by 1 carbon. By treating each "open" ligand at room temperature with 2nd generation Hoveyda-Grubbs catalyst in a degassed solution of CH_2Cl_2 for 4 to 7 days the desired ligands were obtained,

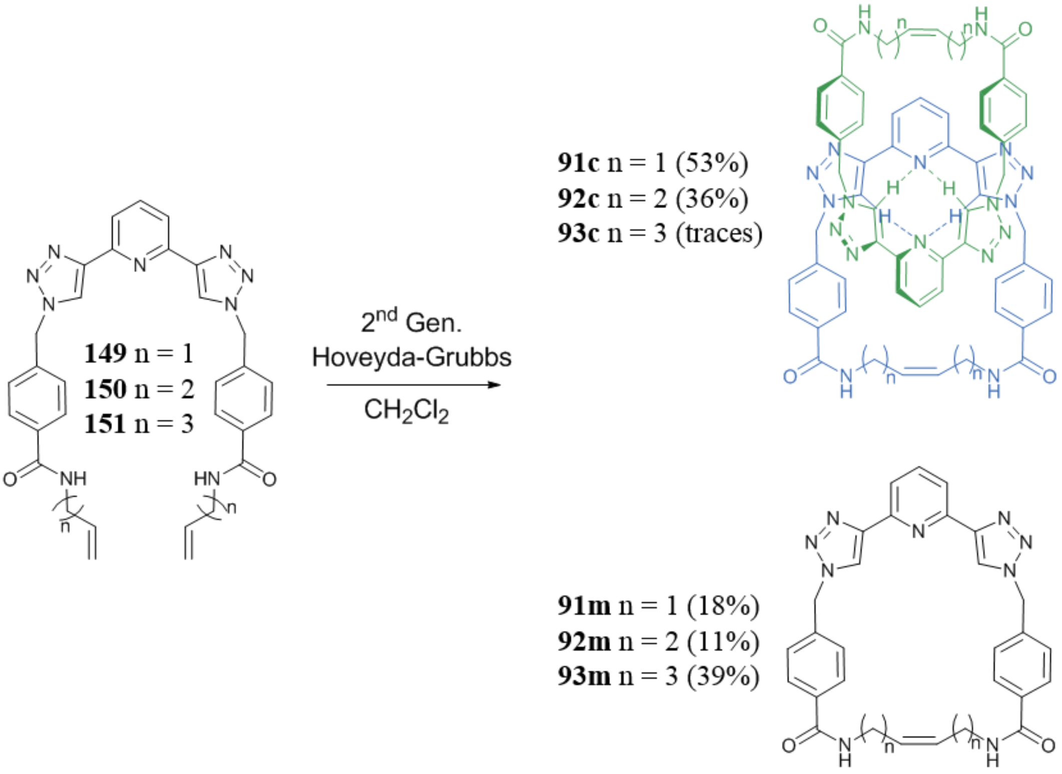

149 n = 1
150 n = 2
151 n = 3

91c n = 1 (53%)
92c n = 2 (36%)
93c n = 3 (traces)

91m n = 1 (18%)
92m n = 2 (11%)
93m n = 3 (39%)

Scheme 4.1. Synthesis of macrocycles **91m**, **92m**, **93m** and [2]catenanes **91c** and **92c**.

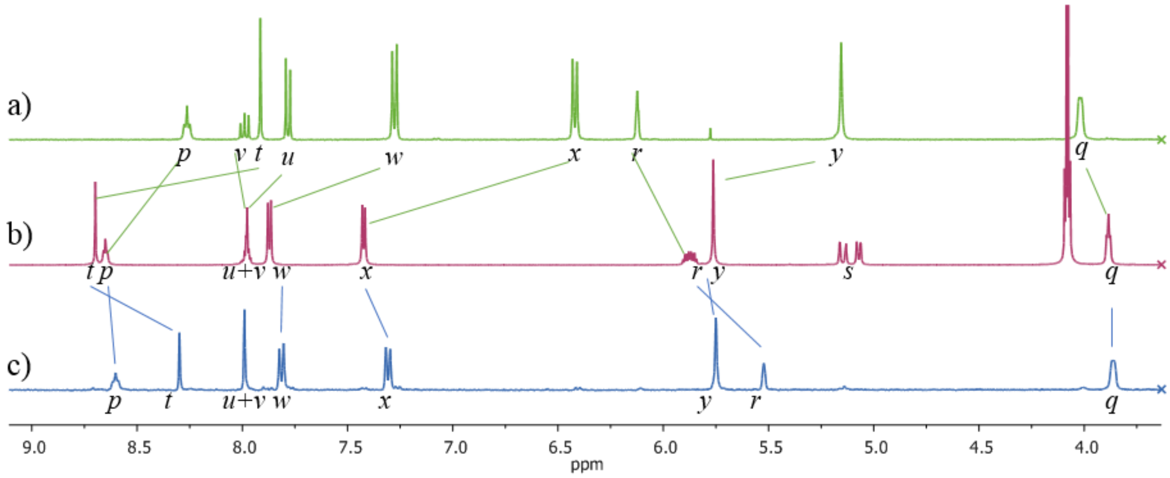

Figure 4.10. ^{1}H NMR spectra (400MHz, DMSO-d_6, 293K) of a) [2]catenane **91c**, b) open ligand **149** and c) macrocycle **91m**.

as shown in Scheme 4.1. In all three cases, the reaction yielded both the macrocycles and catenanes, with larger catenane yield obtained for the short chain **91c** (53%), and increasingly smaller yields for the longer chains, with **92c** forming in 36% yield and the longest **93c** forming only in trace amounts. This was attributed to the higher flexibility of the longer arms which did not favour the RCM. The two macrocycles **91m** and **92m** formed in lower yields compared to the relative [2]catenanes, with 18% and 11% yield, respectively, while **93m** was isolated as the major product in 39% yield from the reaction of **151**. The catenanes and respective macrocycles were separated by flash column chromatography on silica, in a gradient of CH_3OH in EtOAc, or by simple trituration in cold CH_3OH.

The ^{1}H NMR spectra of both **91c** and **91m** showed the successful RCM, by displaying the absence of the characteristic terminal olefin proton resonances, which were otherwise present in the spectrum of starting material at 5.15 and 5.06 ppm marked as ***s***, Figure 4.10. Moreover, the resonances of protons ***r*** appeared as a singlet, consistent with successful closure of the ring. It was interesting to notice how the aromatic protons (***x*** and ***w***) as well as the methylenic proton (***y***) of the [2]catenane **91c**, Figure 4.10a, were significantly shielded in comparison to the corresponding protons in the macrocycle **91m**, Figure 4.10c, which showed, instead, resonances similar to the open ligand **149**, Figure 4.10b. This behaviour was attributed to the close interaction between the phenyl ring and the **btp** motif, within the [2]catenane, consistent with previous observations in other interlocked species.[208,209]

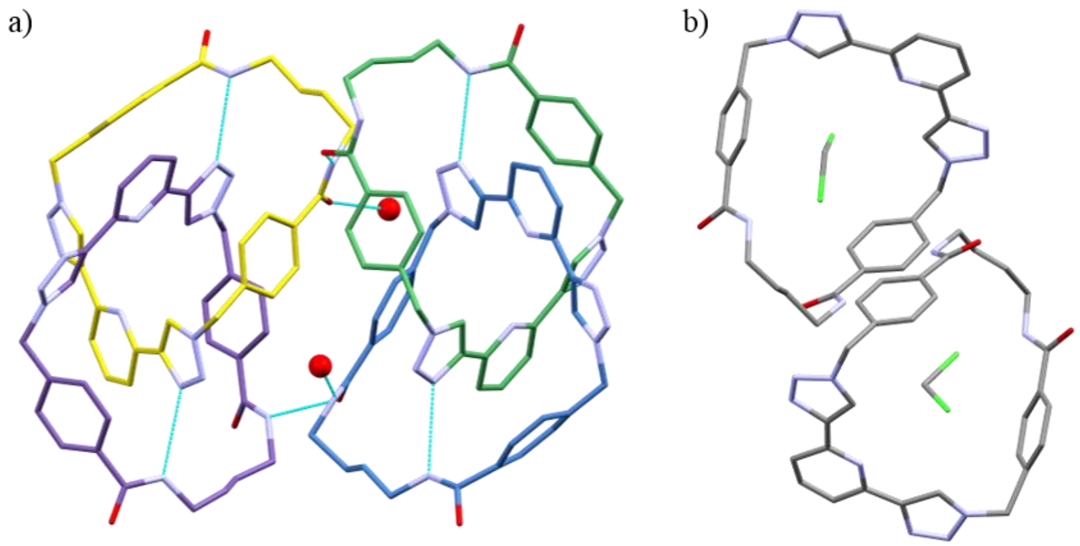

Figure 4.11. Crystal structure of a) [2]catenane **91c** and b) macrocycle **91m**.

Additional confirmation of the successful RCM was given by X-ray diffraction studies which have been reported fully by Byrne and Blasco,[155] and a representation of the two structures of **91c** and **91m** is shown in Figure 4.11. By HRMS two peaks identified the catenane at *m/z* = 1063.4346 and *m/z* = 1085.4147, which were assigned to the $[M+H]^+$ and $[M+Na]^+$ species, respectively. In the same way, **92c** and **92m** were isolated and their ^1H NMR displayed very similar features in the aromatic region to the ones of the smaller ring **91c** and **91m**. Macrocycle **93m** was the main product isolated from the RCM reaction of **151**, while the corresponding [2]catenane was identified by HRMS (MALDI+) with a peak at *m/z* = 1197.5438 corresponding to the $[M+Na]^+$ adduct, but obtained only as a trace product. The three macrocycles and two [2]catenanes obtained were first investigated for their anion binding properties, which will be presented and discussed in Section 4.3. Considering the results obtained for the first set of ligands, the RCM reaction was performed

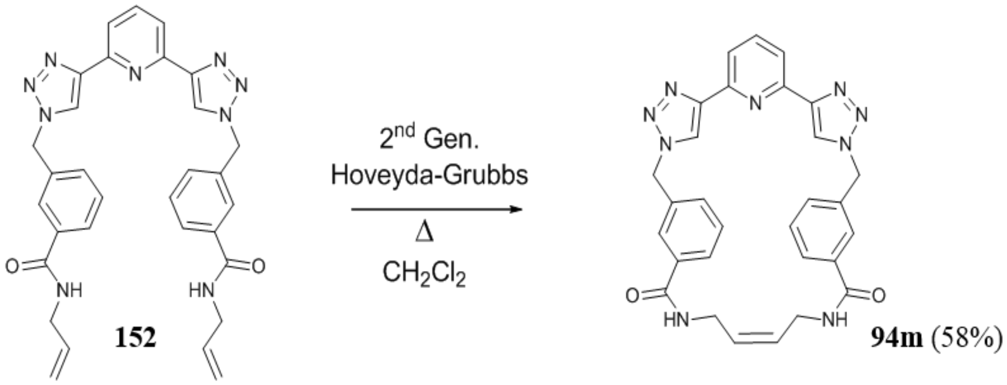

Scheme 4.2. Synthesis of macrocycle **94m**.

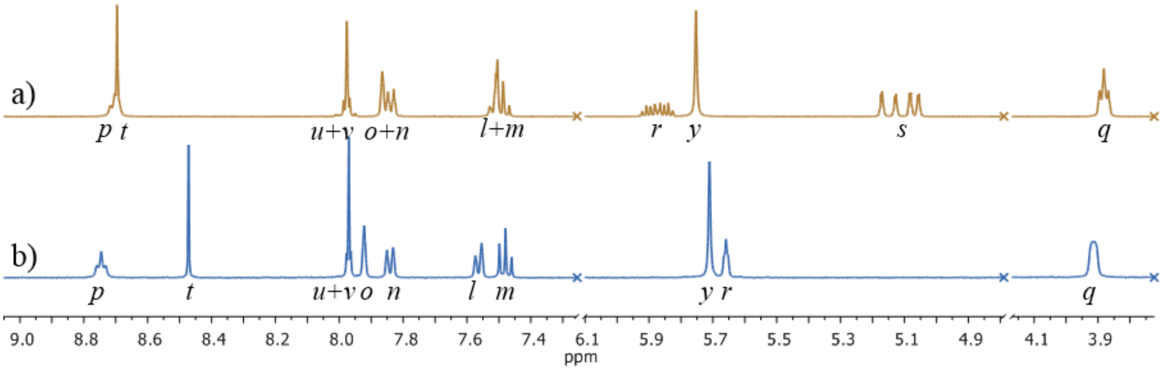

Figure 4.12. ^{1}H NMR spectra (400MHz, DMSO-d_6, 293K) of a) open ligand **152** b) macrocycle **94m**.

by McCarthy on the *meta*-substituted isomer of **152**. However, under the same conditions as for the catenanes above, RCM was unsuccessful. By heating the reaction at 60 °C for 24 hours and an additional 4 days of stirring **152** with the catalyst in the dark at RT was the RCM was effective. Only the macrocycle **94m** was isolated, in good yields, giving 58% conversion, Scheme 4.2. By HRMS (MALDI+), a peak corresponding to $[M+H]^+$ was found at m/z = 532.2236, while the absence of the terminal olefinic protons (*s*) in the ^{1}H NMR spectrum of **94m** confirmed the formation of the macrocycle from the open ligand **152**, Figure 4.12. The ^{1}H NMR spectrum of **94m** resembled the spectrum of **91m**, with the main differences being the resonances of the benzyl ring (due to the different substitution pattern),

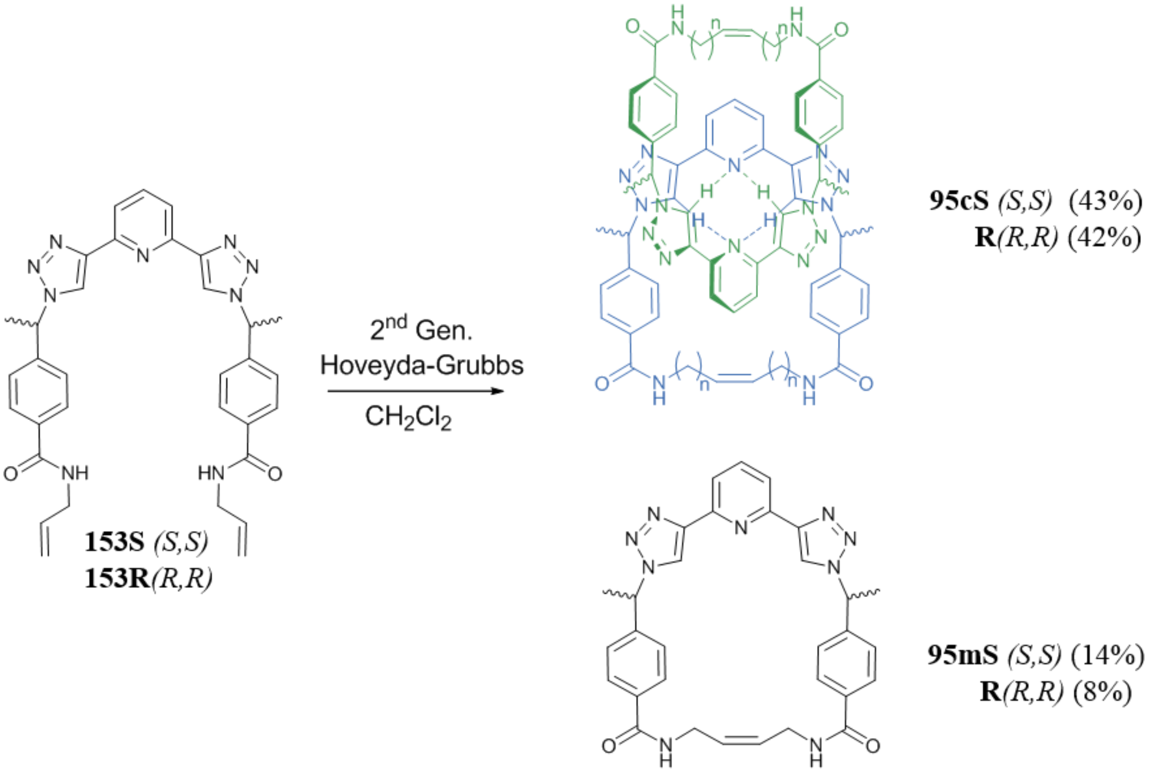

Scheme 4.3. Synthesis of [2]catenanes **95cR** and **95cS** and macrocycles **95mR** and **95mS**.

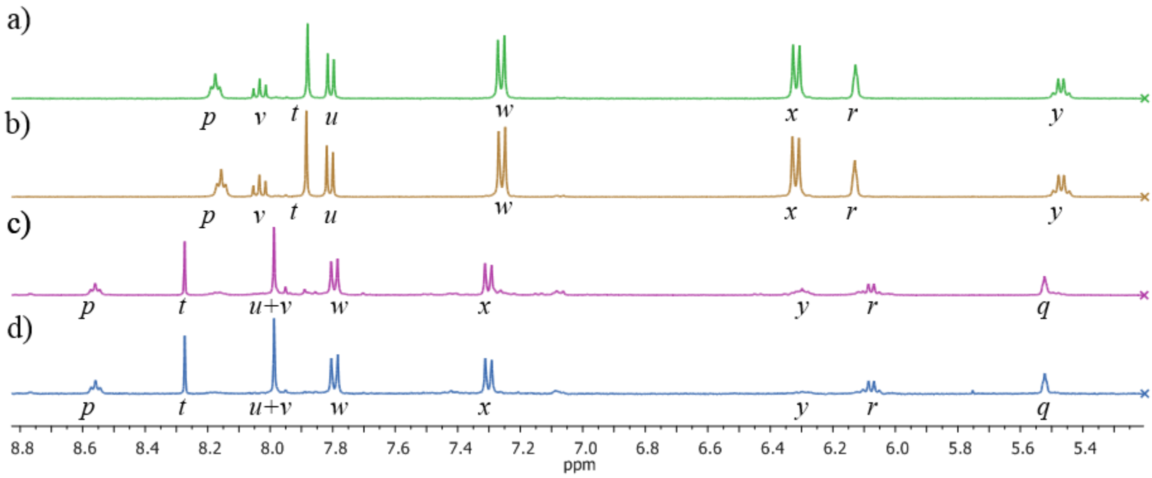

Figure 4.13. ^{1}H NMR spectra (400MHz, DMSO-d_6) of a) **95cR**, b) **95cS**, c) **95mR** and d) **95mS**.

the triazolyl singlet (***t***) and the amide triplet (***p***) (being more deshielded by 0.17 ppm and 0.15 ppm, respectively). This behaviour suggested that the triazole and amide groups, within this macrocycle, were closer together and potentially interacting with each other through hydrogen-bonding.

The design of the last set of [2]catenanes and macrocycles was also inspired by **91c** and **91m**, however, the addition of a methyl group on the methylene carbons generated a new chiral centre and thus the enantiomeric pairs **95cR/S** and **95mR/S**. The synthesis was carried out by McCarney,[210] Scheme 4.3, after which a set of two enantiomerically pure [2]catenanes (**95cR** in 42%, **95cS** in 43% yield) and two enantiomerically pure macrocycles (**95mR** in 8%, **95mS** in 14 % yield) were obtained. Ligands **95cR/S** and **95mR/S** were fully characterised and displayed identical chemical properties with the only differences observed in the chiral CD spectroscopy.[210] In Figure 4.13, the ^{1}H NMR spectra of the four molecules are shown. Similarly to what was observed for the achiral molecules **91m** and **91c** above (Figure 4.10), the resonances of all protons were more shielded for the catenane than for the corresponding macrocycle with a significant difference observed for the amide and triazole protons (***p*** and ***t***) as well as the protons of the phenyl rings (***x*** and ***w***).

The combined anion binding properties of amides and **btp** discussed above and the presence within our set of macrocycles and [2]catenanes of two amides and two triazole rings, all within a preorganised macrocyclic arrangement, were a motivation to investigate the anion binding ability of these ligands, which will be discussed in the next section.

4.3. Anion binding studies

The ability of this set of catenanes and macrocycles to bind, and potentially encapsulate, anions was investigated. These properties were initially studied on [2]catenane **91c** due to the presence within its structure of four amide groups and four triazole groups, which in combination had the potential for 8-fold hydrogen bond donor ability. A preliminary screening of **91c** with anions of different sizes and shapes showed by ^{1}H NMR in DMSO-d_6 that hydrogen bonding occurred with $H_2PO_4^-$, while in the presence of other anions such as Cl^-, CH_3COO^-, NO_3^- and SO_4^{2-} no detectable change occurred, Figure 4.14. Therefore, the binding with $H_2PO_4^-$ was also investigated with the other analogue ligands in order to compare the effects of different substitution patterns on their anion binding properties. As a comparison, the binding with Cl^- was studied for all of the ligands. It was considered a good candidate for the binding with the macrocycles, thanks to its spherical shape and, considering that other macrocycles, containing triazoles and/or amide groups have been reported in the literature by Flood[8-11] and Kubik[20,21] that have showed good affinity for Cl^-. Anion titrations were carried out in highly competitive DMSO-d_6, solution at a concentration of 1×10^{-3} M and the anions were added as TBA salts. Non-linear regression fitting was performed by using the software HypNMR on reproducible titrations, by fitting repetition of the same titration in the same process.[211,212]

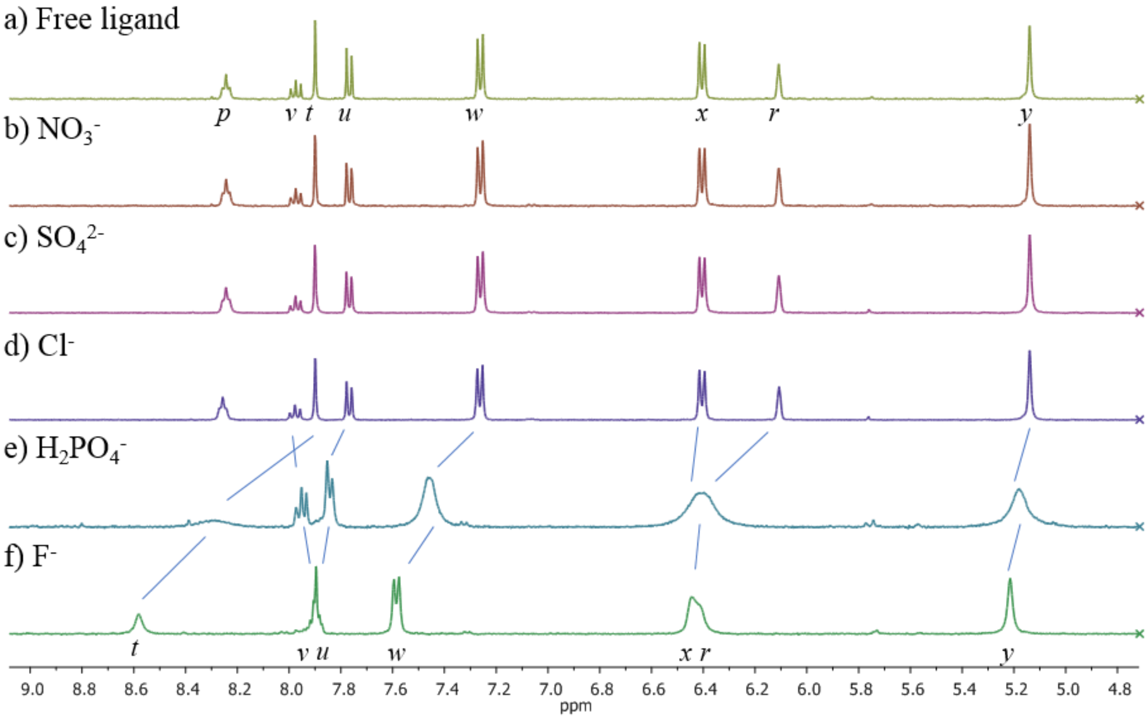

Figure 4.14. ^{1}H NMR spectra of [2]catenane **91c** in the presence of anions (10 equivalents) in DMSO-d_6.

4.3.1. ^{1}H NMR anion binding studies of [2]catenane 91c and macrocycle 91m

The first interlocked molecule from the set that was investigated was **91c**, as from the preliminary studies it showed anion binding abilities with $H_2PO_4^-$. Upon successive increasing additions of $H_2PO_4^-$ to a solution of **91c** in DMSO-d_6 changes in the resonance shifts were observed, consistent with what had been observed in the preliminary studies. Moreover, the interactions were in fast exchange, compared to the NMR timescale, causing gradual changes in the resonances shifts. As shown in Figure 4.15, after the addition of the first equivalent of $H_2PO_4^-$ anion the amide proton (***p***) deshielded and the relative resonance shifted and broadened before disappearing, indicating that exchange of this proton was occurring and possibly even deprotonation. The resonance of the triazolyl proton (***t***) was also deshielded by 0.36 ppm. It also displayed an important broadening, a sign of hydrogen bonding. The interaction with $H_2PO_4^-$ also caused the deshielding and broadening of all the other protons, except for the pyridine proton ***v*** which was weakly shielded by 0.03 ppm after the addition of 10 equivalents of the anion. These changes were similar to what observed by Kubik *et al.*[201] in their studies on the cyclic pseudopeptide **143**, and these were attributed to the binding of the anion to the [2]catenane through hydrogen bonding. In particular, the affinity of **91c** for $H_2PO_4^-$ over the other anions, as observed from the preliminary tests, was

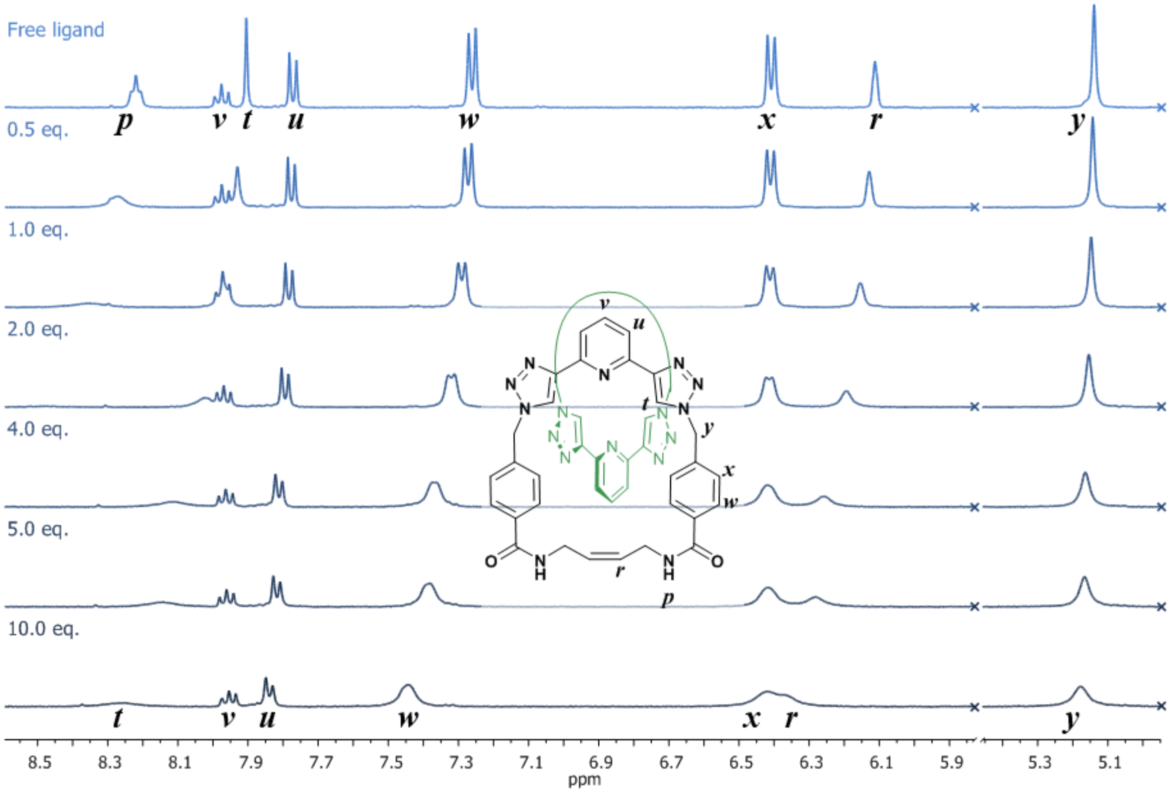

Figure 4.15. ^{1}H NMR titration profile of **91c** with $H_2PO_4^-$, in DMSO-d_6. [**91c**] = 1 mM. Featureless regions of spectrum are not shown. This titration is representative of reproducible trends.

attributed to the geometrical directionality of the triazolyl CHs within the ligand. The changes in the ^{1}H NMR spectra were fit to a 1:1 binding model and a $K_{1:1}$ = 54 M^{-1} was calculated. As discussed above, the self-assembled synthesis of the [2]catenane was based on the dimerization of the **btp** moieties, and in this arrangement, the triazole protons are found in a tetrahedral arrangement.

To verify the effect of this arrangement on the binding, a control study was carried out on the analogous macrocycle **91m**, shown in Figure 4.16. Addition of $H_2PO_4^-$ to a solution of the macrocycle caused a downfield shift of the amide resonance (***p***) by 0.30 ppm after the addition of 10 equivalents of anion, which increased to 0.44 ppm after the addition of 20 equivalents. In this case, there was no evidence of amide deprotonation, and the triazole (***t***) resonance was deshielded by only 0.07 ppm in the presence of 10 equivalents of anion, while maintaining a sharp profile. Minor deshielding was also observed for the aromatic protons ***w*** and ***x***. The changes in the chemical shifts of **91m** indicated the formation of a hydrogen bonding interaction between the macrocycle and the anion. However, the effects on the ^{1}H NMR were less significant than seen for the [2]catenane analogue. The fitting of the data to a 1:1 binding model gave a result of $K_{1:1}$ = 33 M^{-1}. This value was not too dissimilar to the value calculated for the binding of **91c**, however it should be noted that, in

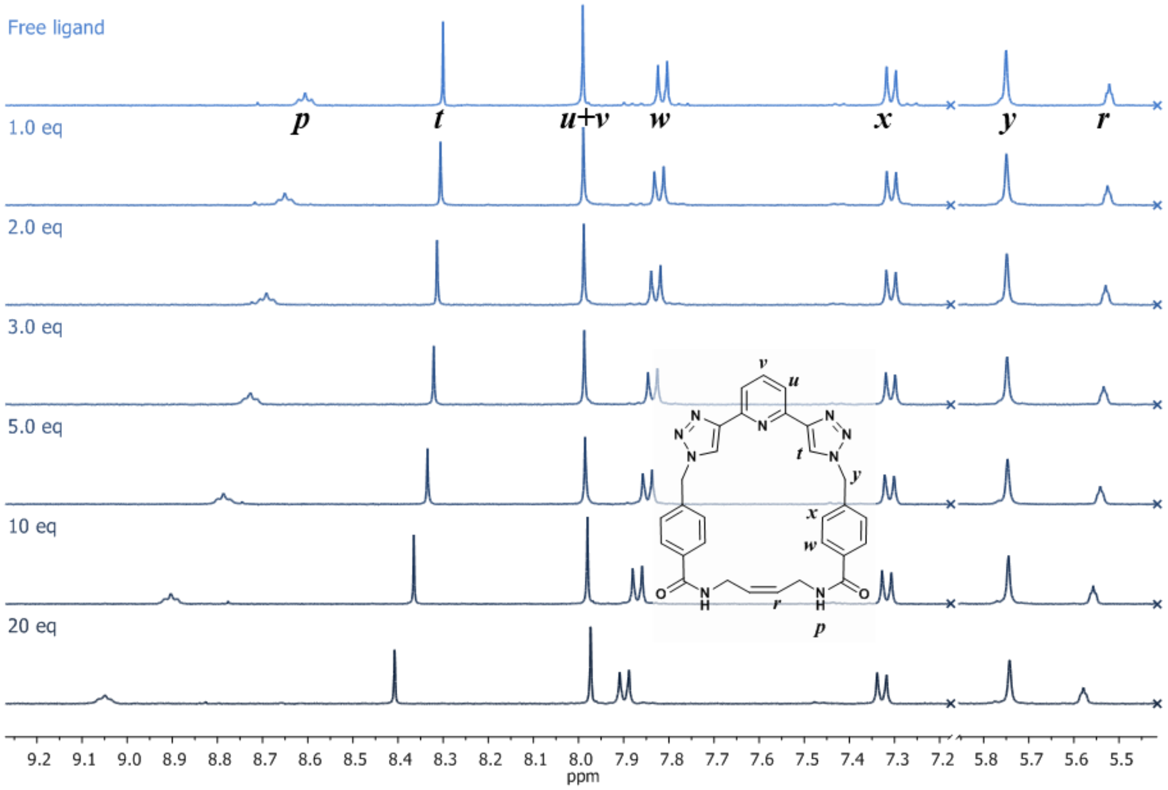

Figure 4.16. ^{1}H NMR titration profile of **91m** with $H_2PO_4^-$, in DMSO-d_6. [**91m**] = 1 mM. Featureless regions of spectrum are not shown. This titration is representative of reproducible trends.

contrast to **91m**, the amide proton resonance (***p***) broadened significant which prevented the use of this signal in the fitting of the macrocycle binding. It was clear, however, in both cases that the amide proton played a major role in the binding process, while the triazole was less affected; this was consistent with the geometrical complementarity discussed previously. From the comparison of the binding of the two molecules with $H_2PO_4^-$, both showed the formation of hydrogen bonding. In the catenane, the formation of hydrogen bonding between the anion and the triazole was evident and was likely favoured by the tetrahedral arrangement of the H-bond donors. The hydrogen bonding between the macrocycle and $H_2PO_4^-$ occurred mainly from the amide protons, with a minor effect on the triazole. The broadening and eventual disappearance of the amide resonances of the catenane **91c** suggested that proton exchange was occurring between the catenane and the anion when constrained into the cavity. The absence of the same effect within the macrocycles indicated that within macrocycle **91m** the hydrogen bonding donors were too far apart to effectively contribute concomitantly to the binding event.

The binding between the $H_2PO_4^-$ anion and **91c** suggested that the anion, when bound to the triazole rings of the **btp**, would be "encapsulated" within the catenane rings, similarly to what happens with cryptands. Therefore, the difference of the binding within the [2]catenane and the macrocycle could be considered a case of the "cryptate-effect". A definitive way to confirm this would be from a crystal structure, which, however, could not be obtained, despite numerous attempts of crystallisation from different solvent and different conditions. To understand whether encapsulation was occurring, without confirmation from the solid-state, DOSY NMR experiments on the free ligand and on the complex **91c**$\cdot H_2PO_4^-$ were carried out in order to calculate the diffusion coefficient of the two species. The diffusion coefficient D of a spherical particle is inversely proportioned to the hydrodynamic radius of the particle in solution, according to the Stokes-Einstein equation (Equation 4.1)

Equation 4.1
$$\boldsymbol{D = \frac{kT}{6\eta\pi r}}$$

where ***k*** is Boltzmann constant, ***T*** the temperature, $\boldsymbol{\eta}$ the viscosity of the liquid and ***r*** the hydrodynamic radius of the molecule. The fitting of the data obtained from the DOSY experiment of the free catenane **91c** gave a result of $\boldsymbol{D} = 1.5 \times 10^{-10}$ m^2s^{-1} for the diffusion coefficient, while for the "complex" **91c·**$H_2PO_4^-$ a value of $\boldsymbol{D} = 2.2 \times 10^{-10}$ $m^2s^{-1}$was obtained (Appendix A4, Figure A4.1). With these values, from Equation 4.1 it was possible to calculate the hydrodynamic radii ***r*** of the two species in solution, assuming a perfectly spherical particle. The hydrodynamic radius of the free catenane **91c** in DMSO-d_6 was calculated as $r = 7.2$ Å, while the radius of **91c**·$H_2PO_4^-$ was calculated to be $r = 4.9$ Å. The binding with $H_2PO_4^-$ caused a change in the hydrodynamic radius which was sufficient to increase the diffusion coefficient. While it might be expected that the hydrodynamic radius increased upon encapsulation of the anion, the formation of hydrogen bonding could have caused the donor moieties to move closer to the anion and, thus, towards the centre of the cavity. A similar behaviour was observed also while studying the anion binding properties of a tris-imidazolate cage, which will be discussed later, in Chapter 5. Therefore, this result was consistent with the encapsulation of phosphate within the catenane, rather than binding on the outer surface.

Preliminary anion binding studies the catenane **91c** had already shown that the addition of Cl^- did not cause changes in the ^1H NMR spectrum of the catenane, indicating that binding was not occurring, or was negligible. Titration of a solution of **91c** with a TBACl solution confirmed this result, as shown in Figure 4.17. Interestingly, no effect on the amide or the triazole was detected, indicating that hydrogen bonding was not occurring. Also in this case, a comparative experiment with the analogous macrocycle **91m** was carried out, to

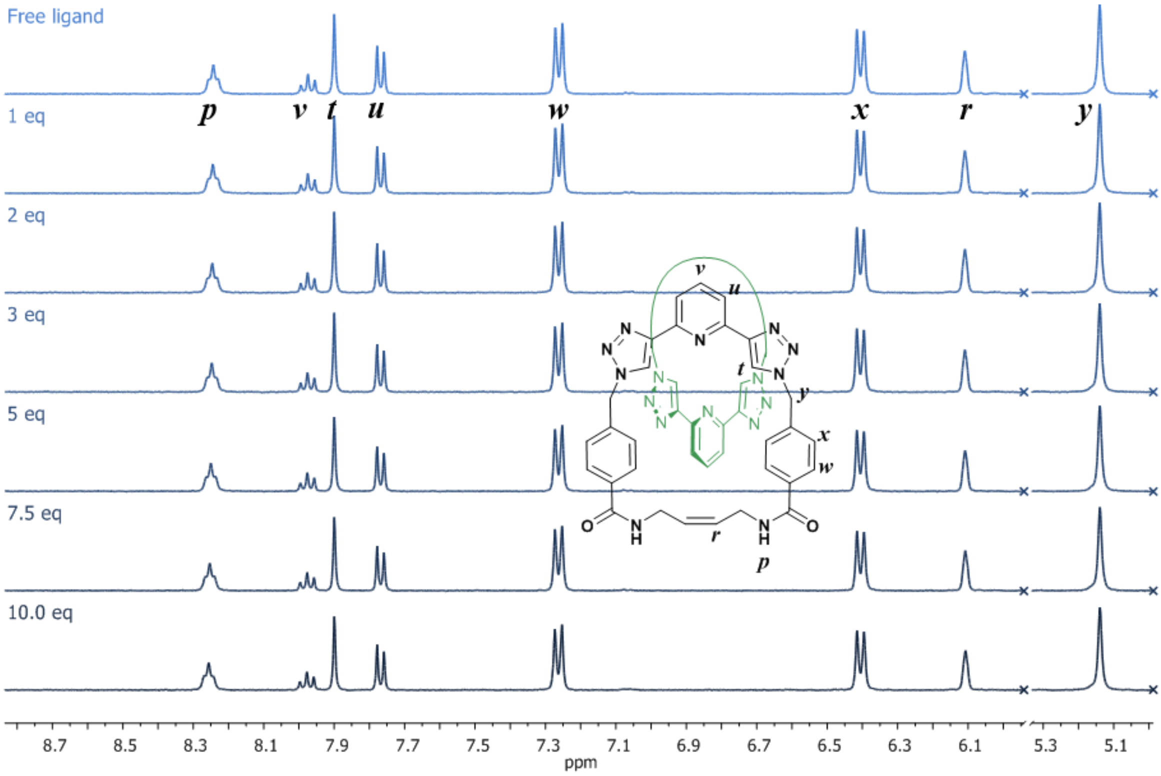

Figure 4.17. ^1H NMR titration profile of **91c** with Cl^-, in DMSO-d_6. [**91c**] = 1 mM. Featureless regions of spectrum are not shown. This titration is representative of reproducible trends.

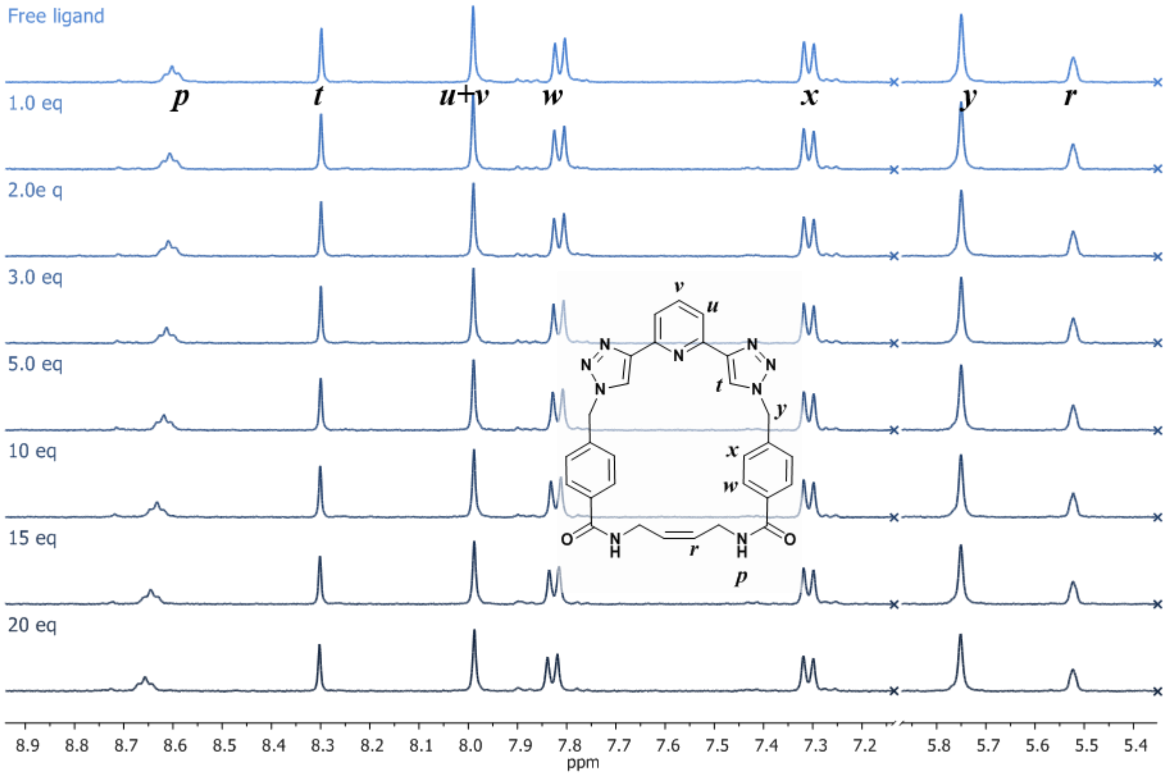

Figure 4.18. ^{1}H NMR titration profile of **91m** with Cl^-, in DMSO-d_6. [**91m**] = 1 mM. Featureless regions of spectrum are not shown. This titration is representative of reproducible trends.

investigate its affinity for Cl^-. In Figure 4.18 key points of the titration of **91m** with Cl^- are shown, where a slight deshielding of the amide protons (***p***) by 0.06 ppm was visible, while the resonance of the triazole proton (***t***) did not change. A small deshielding of 0.02 ppm was also observed for the aromatic proton (***w***) resonance, while no detectable change was observed for the other protons. By fitting the changes to a 1:1 binding model a binding constant of $K_{1:1} = 3\ M^{-1}$ was calculated. This constant reflected a weaker binding, compared to the binding of **91m** with $H_2PO_4^-$. However, it was larger than the binding observed for the analogous catenane **91c** with Cl^-. The hydrogen bond from the ligand to the anion was donated only through the amide group, while the triazole did not appear to be involved in the binding. This, like in the case of $H_2PO_4^-$, was probably due to the distance between the hydrogen bond donors within the macrocycle, which allowed the binding to occur only at the amide side, which was the most acidic site within this structure.

[2]Catenane **91c** and its analogue macrocycle **91m** were tested for their binding ability with Cl^- and $H_2PO_4^-$. For the spherical Cl^-, binding with the [2]catenane was not detected, while a weak interaction with the corresponding macrocycle through the amide was measured, showing more affinity for this anion. In the case of $H_2PO_4^-$, higher affinity

was observed for the [2]catenane than for the macrocycle, with larger changes in chemical shifts and a larger binding constant calculated, Table 4.1.

A similar behaviour was observed for catenane **92c** and corresponding macrocycle **92m**, which feature two additional carbon atoms in the back chain, and analysis of these structures will be discussed in the following section.

4.3.2. ^{1}H NMR anion binding studies of [2]catenane 92c and macrocycle 92m

Macrocycle **92m** differed from **91m** by the presence of two additional carbon atoms in the chain between the amide groups, generating a slightly larger macrocycle. Similarly, the [2]catenane **92c** was characterised by a larger cavity than **91c**. These ligands were also tested for their binding abilities with $H_2PO_4^-$ and Cl^-.

When titrated with increasing equivalents of $H_2PO_4^-$, [2]catenane **92c** showed changes in the ^{1}H NMR spectrum which resembled those of the smaller catenane **91c**, Figure 4.19. Again, the addition of $H_2PO_4^-$ caused the deshielding and broadening of the amide proton (***p***) resonance, and it disappeared in the presence of over one equivalent of $H_2PO_4^-$. The triazole proton (***t***) was strongly deshielded, with the corresponding resonance being shifted by 0.5 ppm after 12.5 equivalents of anion. Aromatic resonances ***w*** and ***x*** also moved towards higher chemical shifts, by 0.2 ppm and 0.05 ppm, respectively. Other resonances

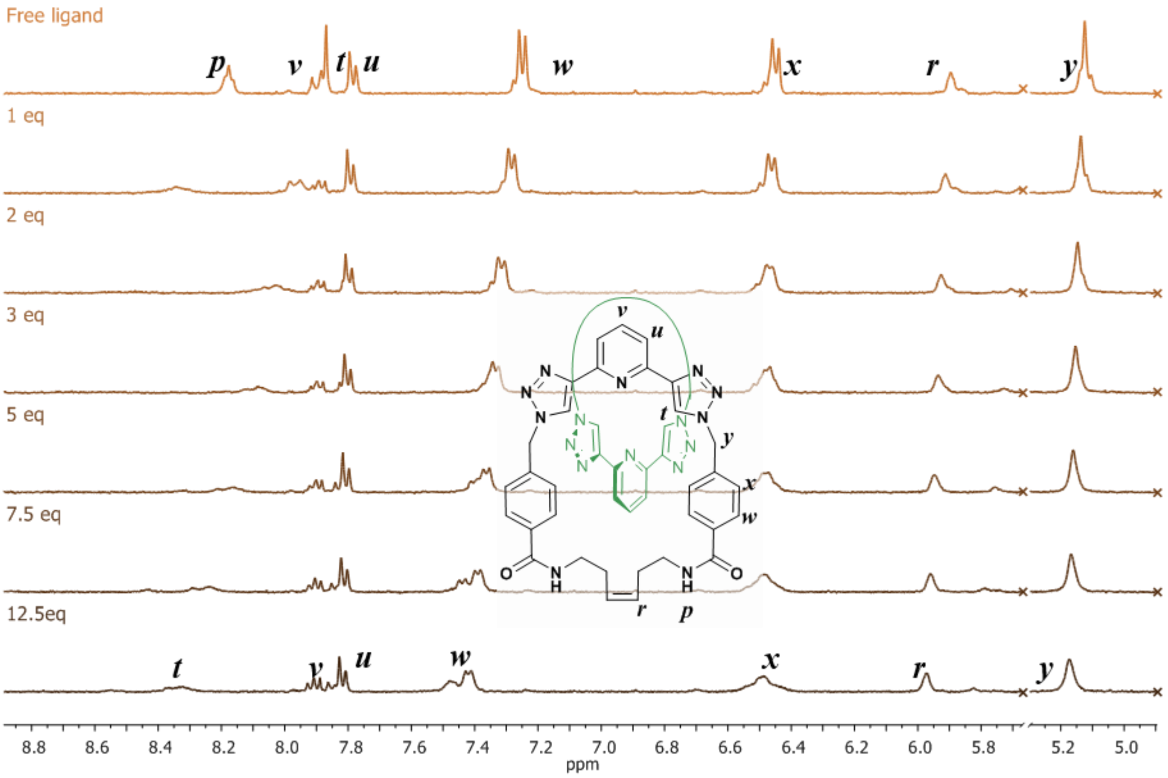

Figure 4.19. ^{1}H NMR titration profile of **92c** with $H_2PO_4^-$, in DMSO-d_6. [**92c**] = 1 mM. Featureless regions of spectrum are not shown. This titration is representative of reproducible trends.

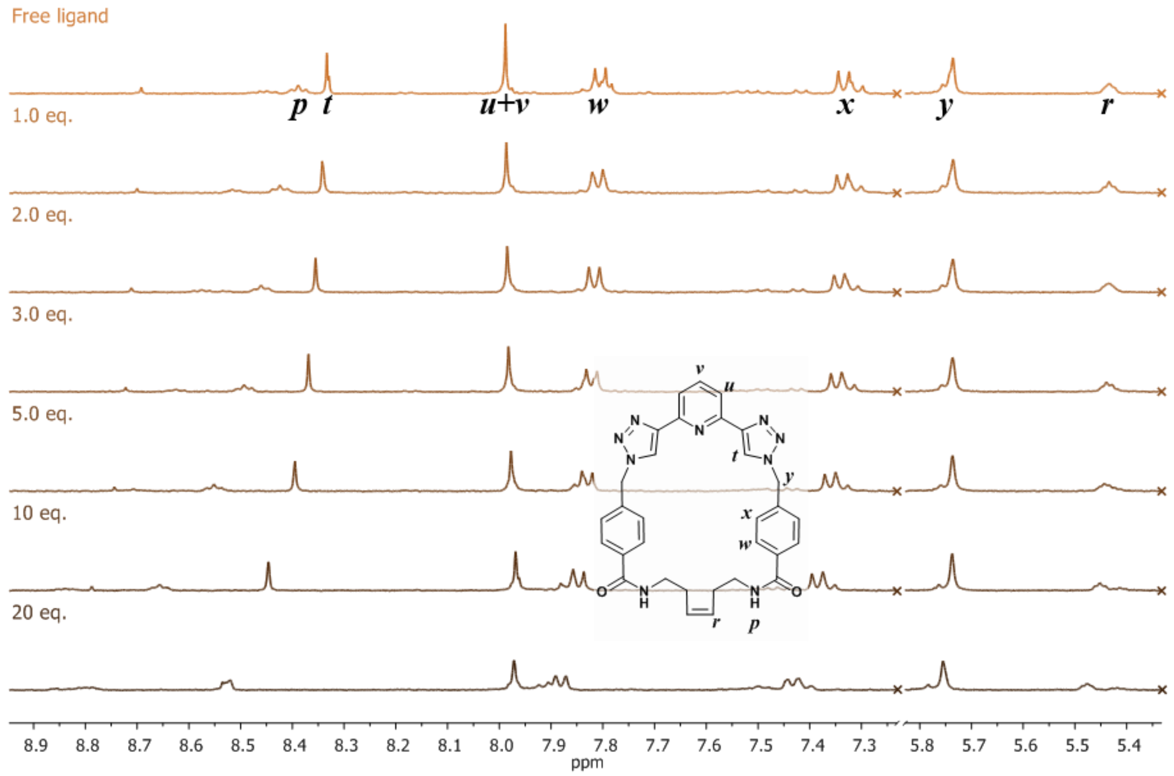

Figure 4.20. ^{1}H NMR titration profile of **92m** with $H_2PO_4^-$, in DMSO-d_6. [**92m**] = 1 mM. Featureless regions of spectrum are not shown. This titration is representative of reproducible trends.

were shifted by less than 0.1 ppm and all displayed broadening, with the exception for the pyridine resonances ***u*** and ***v***. The changes were best fit to a 1:1 binding model with a binding constant of $K_{1:1}$ = 112 M^{-1} being obtained, which was larger than the binding constant obtained for the smaller catenane **91c** (by *ca*. 15%). The larger cavity of [2]catenane and a greater flexibility of **92c** was more suited to accommodate the anion within the hydrogen bonding rich binding site. To study whether the preorganisation of the cavity was a key factor, the binding with $H_2PO_4^-$ was also investigated with the corresponding macrocycle **92m**.

Upon addition of $H_2PO_4^-$ to macrocycle **92m** the amide proton (***p***) was deshielded by 0.4 ppm and its resonance broadened, indicating that a hydrogen bonding interaction with the anion was occurring. A downfield shift was observed for the resonance of the triazole CH proton (***t***) by 0.2 ppm, along with similar, yet smaller, shifts, for the resonances of protons ***w***, ***x***, ***y*** and ***r***. From the non-linear regression fitting of these changes to a 1:1 model the binding constant was calculated to be $K_{1:1}$ = 15 M^{-1}. This value indicated that the binding of the macrocycle was weaker than for the corresponding [2]catenane, as well as being less strong if compared to the smaller macrocycle **91m**.

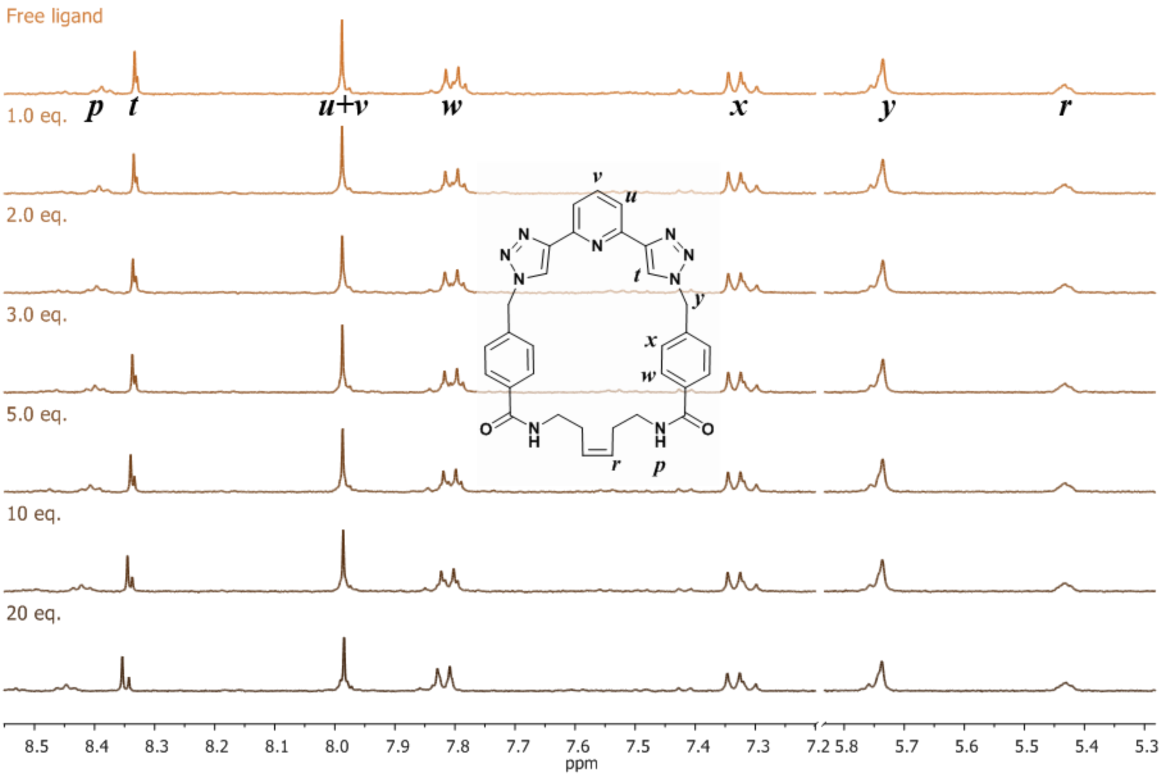

Figure 4.21. ^{1}H NMR titration profile of **92m** with Cl^-, in DMSO-d_6. [**92m**] = 1 mM. Featureless regions of spectrum are not shown. This titration is representative of reproducible trends.

While for the catenane **92c** the longer carbon chain in the macrocyclic ring helped to increase the binding affinity for $H_2PO_4^-$ within the catenane structure. In contrast, for the single macrocycle **92m** the binding was reduced. Again, this was probably due to the presence of a larger cavity, which for the catenane meant less constraint for the encapsulated $H_2PO_4^-$ anion, but within the macrocycle the hydrogen bond donors were situated further apart.

The binding of the [2]catenane **92c** with Cl^- was also investigated. The addition of Cl^- did not cause changes in the ^{1}H NMR spectrum, as had been observed for **91c**, a sign that binding was not occurring or was negligible (Appendix A4, Figure A4.2). On the other hand, the single macrocycle **92m**, Figure 4.21, showed shifts in the resonances which indicated a weak binding to Cl^-. The largest changes were observed for the amide proton (***p***) by 0.05 ppm and of the triazole proton (***t***) by 0.02 ppm after the addition of 20 equivalents of ligand. The fitting of the changes in the chemical shifts was obtained with a 1:1 model and a binding constant of $K_{1:1} = 9\ M^{-1}$. This binding constant was mildly larger than that of **91m** with Cl^-, but still very small. The spherical shape of the Cl^- ion allows it to accept hydrogen bonding from every direction, while binding of $H_2PO_4^-$ necessitates higher directionality. Therefore, it is reasonable to assume that rearrangement of the larger macrocycle **92m**, when compared to **91m**, favours the binding of Cl^- and not that of $H_2PO_4^-$,Table 4.1.

The binding for $H_2PO_4^-$ was stronger for the [2]catenane **92c** than the macrocycle **92m**, while interaction with Cl^- was only observed with the macrocycle. Comparing the larger chain catenane **92c** with the smaller one, **91c**, a higher affinity was observed for the former in the interactions between the catenane **92c** with $H_2PO_4^-$. Having found some interesting differences in the binding between the two different-sized sets of macrocycle/catenane, the studies on the largest macrocycle obtained, **93m**, were carried out next and will be presented in the following section.

4.3.3. ^{1}H NMR anion binding studies of macrocycle 93m

The largest macrocycle **93m** was investigated for its binding abilities towards $H_2PO_4^-$ and Cl^- in an analogous manner to that described above. The low yielding analogue [2]catenane **93c** was only obtained in trace amounts, and hence, the anion binding ability of this host was not investigated as part of this study.

Key points of the titration of **93m** with $H_2PO_4^-$ are shown in Figure 4.22. Upon addition of $H_2PO_4^-$ to a solution of the macrocycle, the resonance of the amide proton (***p***) was shifted downfield by 0.25 ppm and that of the triazole proton (***t***) by 0.11 ppm, in the

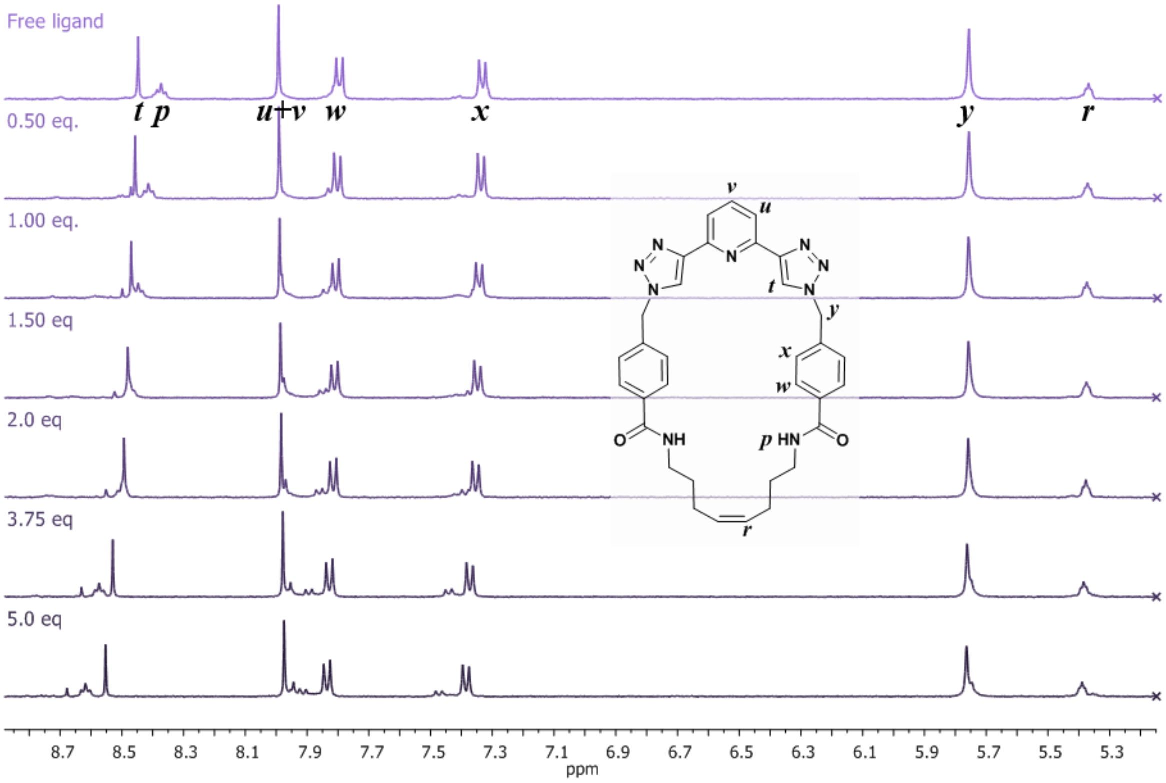

Figure 4.22. ^{1}H NMR titration profile of **93m** with $H_2PO_4^-$, in DMSO-d_6. [**93m**] = 1 mM. Featureless regions of spectrum are not shown. This titration is representative of reproducible trends.

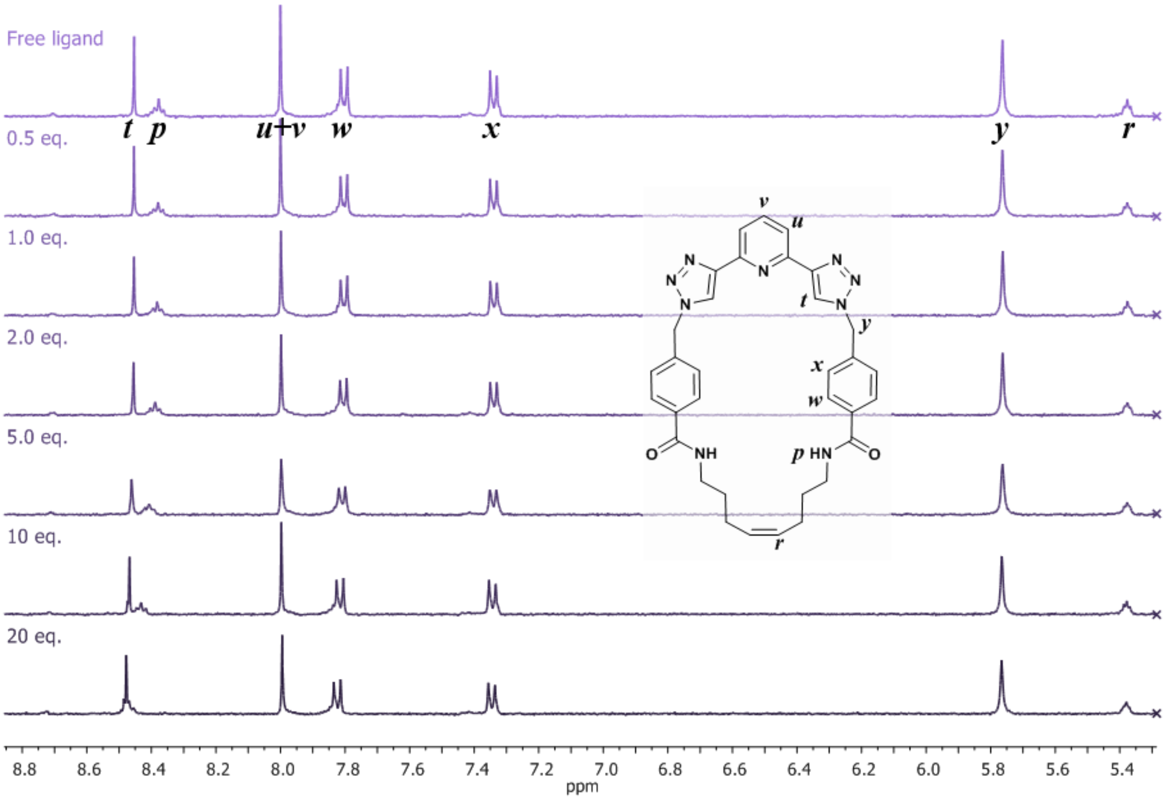

Figure 4.23. ^{1}H NMR titration profile of **93m** with Cl^-, in DMSO-d_6. [**93m**] = 1 mM. Featureless regions of spectrum are not shown. This titration is representative of reproducible trends.

presence of 5 equivalents of $H_2PO_4^-$. Also for this ligand, weak deshielding was also observed for the aromatic protons ***x*** and ***w***, indicating a relatively small interaction. The data were best fit to a 1:1 binding model with a binding constant of $K_{1:1}$ = 31 M^{-1}, which was comparable to that of the short chain macrocycle **91m**. When titrating a solution of the macrocycle with a solution of Cl^-, a deshielding of the amide proton (***p***) and triazole (***t***) was observed, by 0.06 ppm and 0.01 ppm, respectively, indicating a weak hydrogen bonding interaction with the anion. A binding constant of $K_{1:1}$ = 11 was calculated from the non-linear regression fitting of the changes in the chemical shifts.

The affinity with Cl^- appeared to increase with the size of the macrocycle, probably due to the increased flexibility which allowed rearrangement of the hydrogen bonding donors, in a more favourable conformation, Table 4.1. In this case the increased flexibility was sufficient to favour also the binding of $H_2PO_4^-$ which was reflected in a constant similar to that of the smallest macrocycle **91m**.

When considering the binding abilities of [2]catenanes **91c** and **92c**, it is important to notice that the anion-binding abilities were not employed during the synthesis of the mechanical bond, like in the many examples by Beer and co-workers discussed previously. Instead, like for the example of Goldup and Jolliffe with **148**,[207] the anion binding ability of the interlocked system did not generate from the self-assembly formation of the mechanical bond. Attempts to synthesise of the [2]catenane **91c** in the presence of $H_2PO_4^-$ were carried out by Byrne, but were unsuccessful. The open ligands **149** did not show interaction with the anion in solution by ^{1}H NMR spectroscopy, indicating that the dimerization and self-templation was the preferential route for the catenane formation.

After studying this first group of ligands the chiral ligands **95cR/S** and **95mR/S** were investigated for their anion binding properties, and the results will be discussed in the next section.

4.3.4. ^{1}H NMR anion binding studies of [2]catenanes 95cR/S and macrocycles 95cR/S

Encouraged by the results obtained from the first set of macrocycles and catenanes, the chiral analogues of **91c** and **91m**, carrying a methyl substituent on the two methylene carbons were investigated for their anion binding abilities. The presence of the chiral centres was interesting due the potential selectivity through conformational restriction. Two enantiomeric [2]catenanes, **95cR**(*R*,*R*) and **95cS**(*S*,*S*), were titrated with $H_2PO_4^-$ and Cl^-, under the same condition as the achiral analogues. Due to low compound availability, only one enantiomer of the corresponding macrocycles **95mS**(*S*,*S*) could be studied. Interestingly, in all cases, the chiral catenanes and the macrocycle systems did not show any interaction

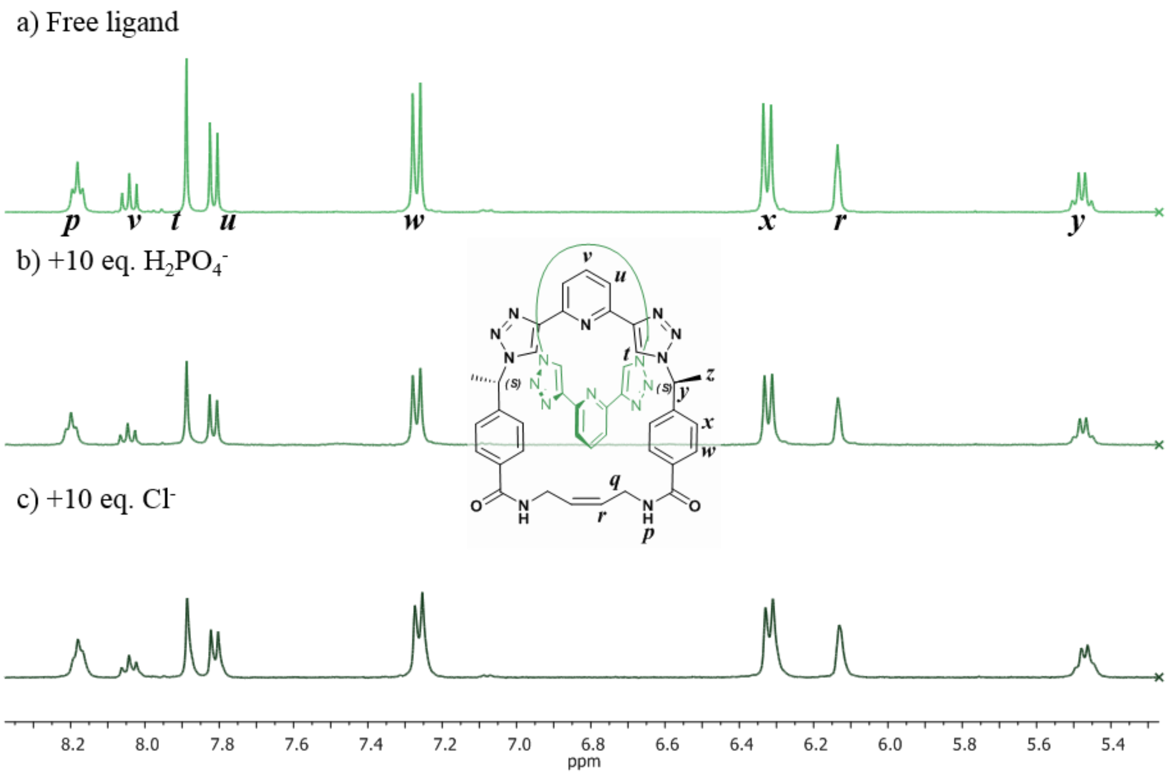

Figure 4.24. Stacked ^{1}H NMR spectra of **95cS** a) free catenane and with the addition of 10 equivalent of b) $H_2PO_4^-$ and c) Cl^-, in DMSO-d_6. [**95cS**] = 1 mM. Featureless regions of spectrum are not shown. This titration is representative of reproducible trends.

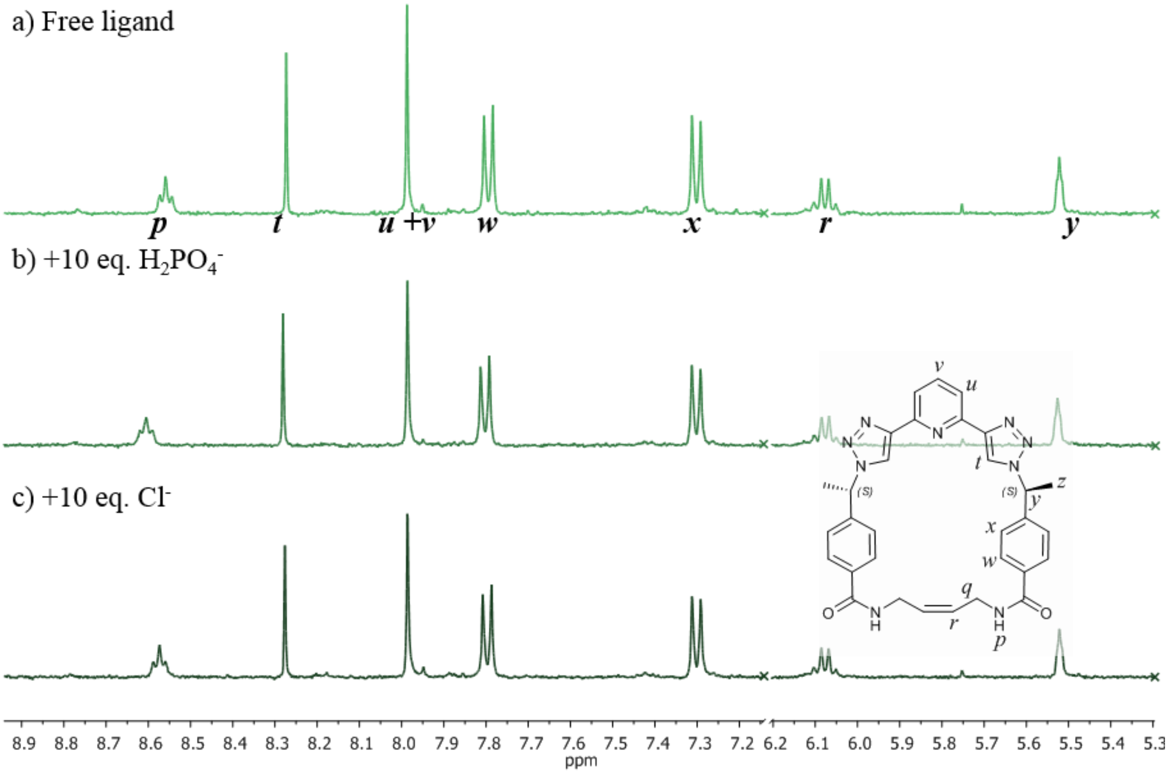

Figure 4.25. Stacked ^{1}H NMR spectra of **95mS**: a) free macrocycle and with the addition of 10 equivalent of b) $H_2PO_4^-$ and c) Cl^-, in DMSO-d_6. [**95mS**] = 1 mM. Featureless regions of spectrum are not shown. This titration is representative of reproducible trends.

with the anions, Figure 4.24 and Figure 4.25. This behaviour was attributed to the presence of the methyl group, which generated steric hindrance and reduced the accessibility to the anion binding sites in the catenane. The absence of any interaction within the macrocycle was more surprising, as the binding sites should be more accessible than in the catenane cavity. However, it is likely that the presence of the methyl group, causes steric hindrance, reducing the flexibility of the macrocycle. From the studies on the differently sized macrocycle above, it was observed that, the flexibility of the cavity could have played a role in the anion binding process, by allowing a rearrangement of the hydrogen bonding donor moieties. Therefore, these results would be consistent with the need for flexibility of the cage to ensure the binding process, as the less flexible methylated macrocycles and [2]catenanes showed no binding with the anions considered. Following on from this, the last macrocycle studied was the *meta*-substituted benzyl isomer of **91m**: **94m**, which will be discussed in the following section.

4.3.5. ^{1}H NMR anion binding studies of macrocycle 94m

The last macrocycle investigated was **94m** which was also titrated with Cl^- and $H_2PO_4^-$ to compare results with the previous analogues and to investigate whether the different substitution pattern had an effect on its anion binding ability. For this macrocycle, the titration with $H_2PO_4^-$ caused the broadening of both amide (***p***) and triazole (***t***) resonances, concomitantly with a downfield shift of 0.75 ppm for ***p*** and of 0.48 ppm for ***t***. Interestingly, the aromatic proton ***o*** was also deshielded significantly, the resonance moving from 7.92 ppm to 8.45 ppm after the addition of 10 equivalents of the anion. All of these changes indicated the formation of hydrogen bonding between the $H_2PO_4^-$ and the macrocycle. In this case, the 1,3-substitution pattern of the phenyl rings, generated the presence of a more acidic aromatic proton, ***o***, which contributed to the binding. The fitting of these changes to a 1:1 model gave a binding constant of $K_{1:1} = 138\ M^{-1}$, which was the largest value obtained among this family of macrocycles and catenanes.

The interaction of **94m** with Cl^-, as for all the macrocycles, did not cause large changes to the ^1H NMR spectrum of the macrocycle, with only small downfield shifts (0.03 ppm) of the amide (***p***) and triazole (***t***) resonances occurring, Figure 4.27. These changes,

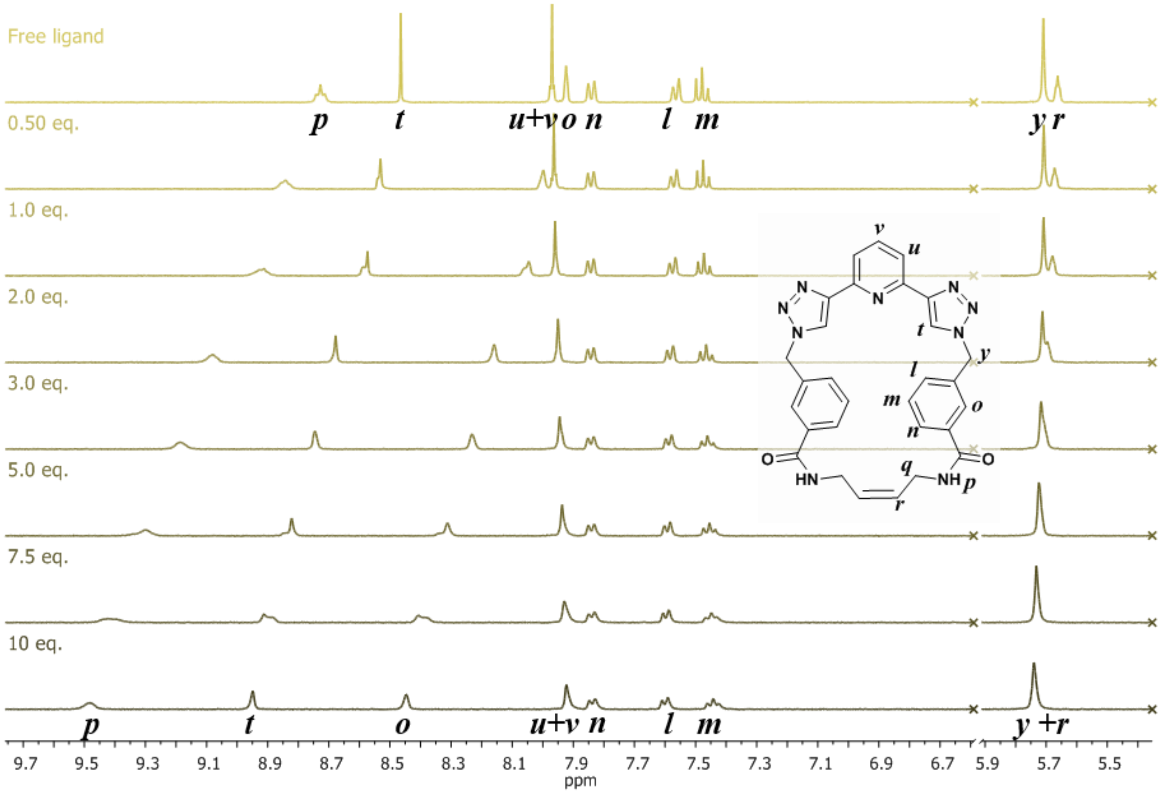

Figure 4.26. ^1H NMR titration profile of **94m** with $H_2PO_4^-$, in DMSO-d_6. [**94m**] = 1 mM. Featureless regions of spectrum are not shown. This titration is representative of reproducible trends.

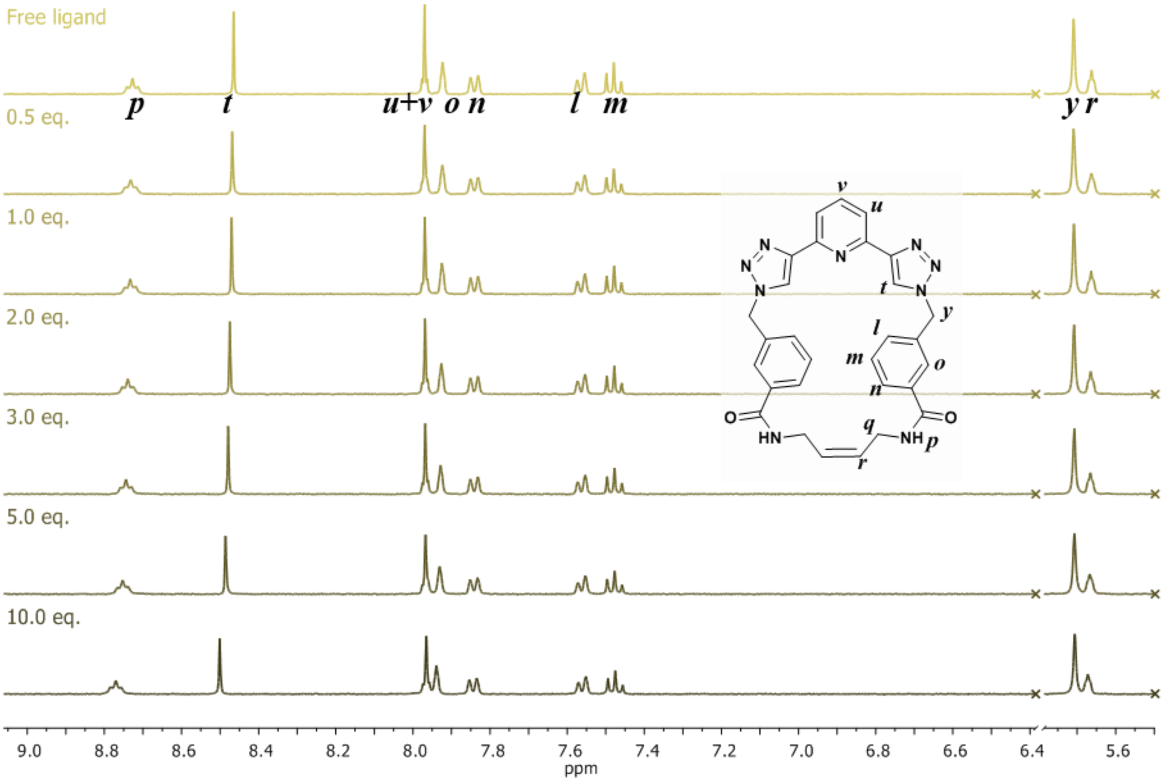

Figure 4.27. ^{1}H NMR titration profile of **94m** with Cl^-, in DMSO-d_6. [**94m**] = 1 mM. Featureless regions of spectrum are not shown. This titration is representative of reproducible trends.

when fitted to a 1:1 binding model, gave a value of $K_{1:1} = 17\ M^{-1}$. This binding constant was the largest observed amongst the family of macrocycles, for the binding of Cl^-.

With both the anions, the macrocycle **94m** displayed better affinity than the other macrocycles of the family. This ligand, as presented above, differed from the others in the family for the *meta*-substitution of the benzyl ring, instead of *para*. In this arrangement, the amidic protons were closer to the triazole acidic protons, which potentially can generate a better hydrogen bonding site. In addition to this, the aromatic proton ***o*** showed significant deshielding while binding with $H_2PO_4^-$, indicating the formation of C–H hydrogen bond with the anion and, therefore, being orientated towards the centre of the cavity. This could be due to the substitution pattern which increased the acidity of this proton, as well as favouring a conformation where this proton is orientated towards the anion.

4.4. Conclusions and future perspective

A family of **btp** based macrocycles and corresponding [2]catenanes were investigated for their binding properties with Cl^- and $H_2PO_4^-$ in highly competitive DMSO-d_6. The most efficient binding with both anions, Table 4.1, was obtained with the *meta*-substituted **94m**, most likely due to the higher preorganisation and proximity of the amides and triazoles within the cavity as well as the presence of an additional C-H hydrogen bond donor. The

Table 4.1. Binding constants as $K_{1:1}$ (M^{-1}) calculated from the non linear regression fitting of the data from reproducible titrations with all of the [2]catenanes and macrocycles in this chapter with $H_2PO_4^-$ and Cl^-.[a] Fitting obtained not considering the amide resonance (***p***) due to deprotonation; [b] fitting obtained considering all resonances; [c] binding not detected. Errors less than 15%.

Catenane (c)			**Macrocycle (m)**		
Compound	**$H_2PO_4^-$**	**Cl^-**	**Compound**	**$H_2PO_4^-$**	**Cl^-**
91c	54[a]	-[c]	**91m**	33[b]	3[b]
92c	112[a]	-[c]	**92m**	15[b]	9[b]
			93m	31[b]	11[b]
95cR	-[c]	-[c]			
95cS	-[c]	-[c]	**95cS**	-[c]	-[c]
			94m	138[b]	17[b]

affinity for Cl^- increased with the size of the macrocycles, indicating that larger flexibility was favouring the rearrangement of the hydrogen bonding donors within the cavity. The affinity for $H_2PO_4^-$ was higher within the smaller macrocycle **91m**, as a result of the smaller cavity size, and with the largest macrocycle **93m**, due to higher flexibility. The chiral macrocycle **95mS** did not show affinity with either of the two anions, probably due to steric hindrance and reduced flexibility of the ligand.

None of the [2]catenanes showed interaction with Cl^-, while the two catenane **91c** and **92c** displayed significant deshielding and broadening of the resonances of protons ***t*** and ***p*** upon addition of $H_2PO_4^-$. In particular the deprotonantion of the amide seemed to occur, which then likely favoured the encapsulation of $H_2PO_4^-$ through the formation of hydrogen bonding from the triazole protons ***t***. DOSY-NMR experiments were consistent with the encapsulation of the anion. The [2]catenanes **91c** and **92c** showed a stronger interaction with the anion compared to their corresponding single macrocycles, with **92c** having the largest binding constant of $K_{1:1} = 112\ M^{-1}$, Table 4.1. The chiral [2]catenanes **95cR/S** did not show any sign of interaction with $H_2PO_4^-$ consistently with their corresponding macrocycles.

The enhanced binding properties of the [2]catenanes towards $H_2PO_4^-$ compared to the respective macrocycles indicate that higher preorganisation and additional hydrogen bonding could favour the binding, similarly to the cryptate effect of a cage. This “catenane effect” did not simply come as a consequence of a template synthesis of the mechanical bond, but was generated by it. This is rarely observed within interlocked molecules.[207,213,214]

The non-chiral molecules from this family showed interesting interaction with $H_2PO_4^-$ and Cl^- due to the presence of hydrogen bonding donor groups such as amides and

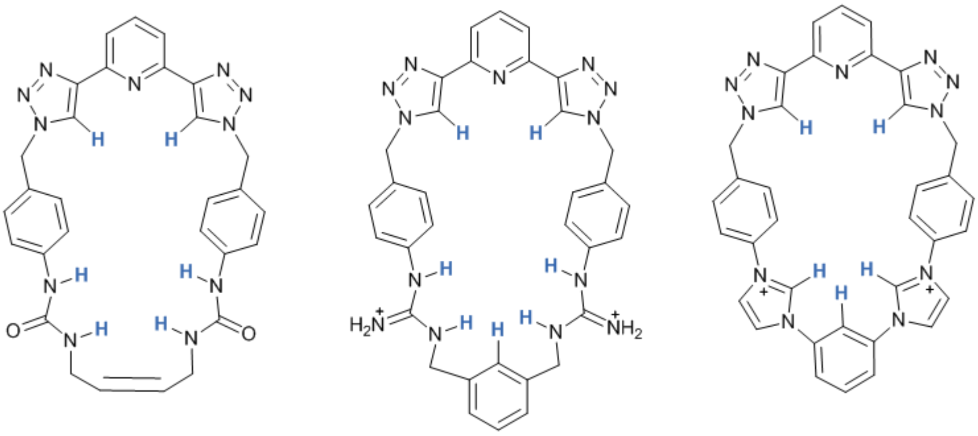

Figure 4.28. Suggested structures for further development of new macrocycles and catenanes.

triazoles. Further development of similar structures, carrying a urea moiety in place of the amide, could potentially increase the hydrogen bonding donors within the cavity of these ligands for higher efficient complexation, Figure 4.28. Including positively charged groups could also improve the binding and retaining the **btp** motif could favour the self-templated synthesis of catenanes or rotaxanes. It would also be interesting to explore the binding abilities of the macrocycles with larger halides such as Br^- and I^-, which could have a stronger binding, because they could take advantage of the macrocycle effect.

5. Tris-imidazolium bis(*tren*) cage for halide encapsulation

5.1. Introduction

This chapter will focus on the research work which was carried out in collaboration with Prof. Valeria Amendola from Università degli Studi di Pavia and considers the anion binding studies of the tris(imidazolium) cage compound **96**, shown in Scheme 5.1. This ligand was designed as a host for the encapsulation of anions through the combination of electrostatic interactions and hydrogen bonding from the imidazolium units. Examples of the use of the imidazolate binding moiety for anion complexation and ATSA were presented in Chapter1 as well as in Chapter 4.

The study of cages for the encapsulation of anions built from tris(2-aminoethyl)amine (***tren***) was developed by Lehn, who also first introduced the concepts of cryptand[215] (from the Greek κρύπτος meaning cavern, cavity) and of 'cascade' reaction.[216,217] This term 'cascade' indicates the complexation of metal ions (*e.g.* Cu^{2+}) or multi-protonation of the amine residues, which triggers the encapsulation of the anion, in a continuous sequence, Figure 5.1. Different examples of such cryptand cages have been developed and studied, with important contribution by Fabbrizzi[38,218] Nelson[219,220] and Bowman-James[2,221,222], among others. Amendola has worked on the studies of bis(***tren***) cages, studying how the presence of different spacers would affect the encapsulation process and anion selectivity.[223] Asymmetric dicopper cryptates **159** and **160**, characterized by alternate furanyl and *p*-xylyl spacers showed binding properties with halides, with

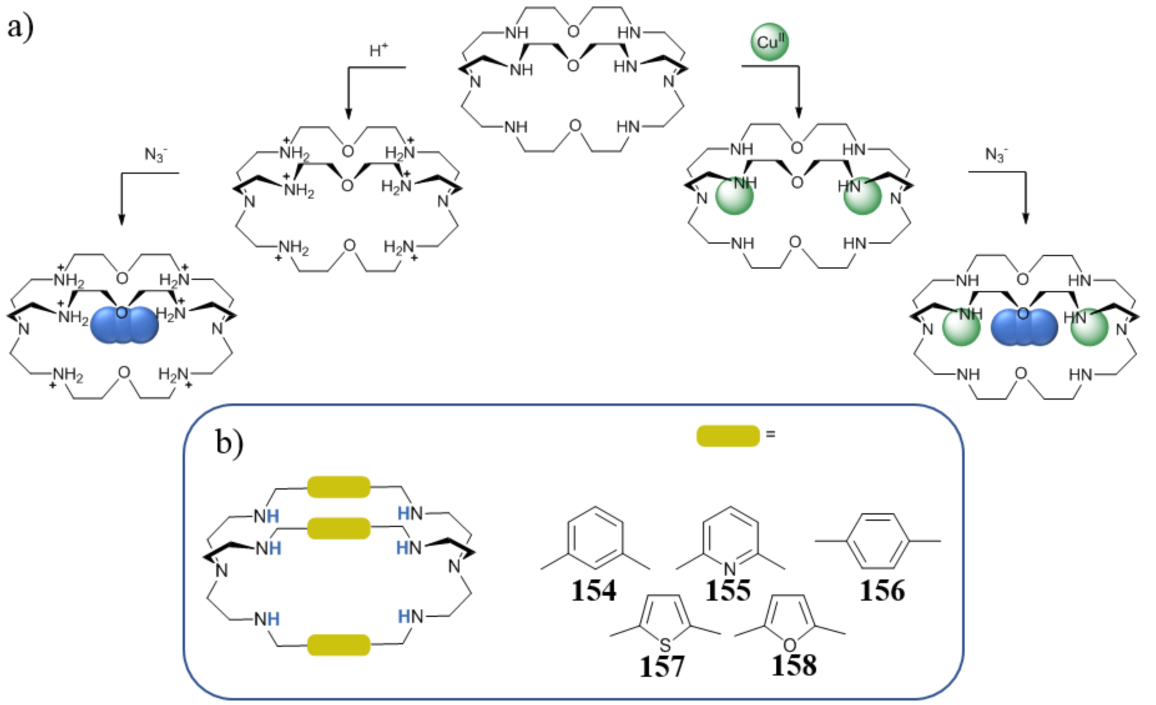

Figure 5.1. a) Example of bis(***tren***) cage developed by Lehn which shows "cascade reactions" with H^+ or Cu^{2+} for the encapsulation of linear anion such as N^{3-}. b) Example s of cages with different spacers.Ref. 223.

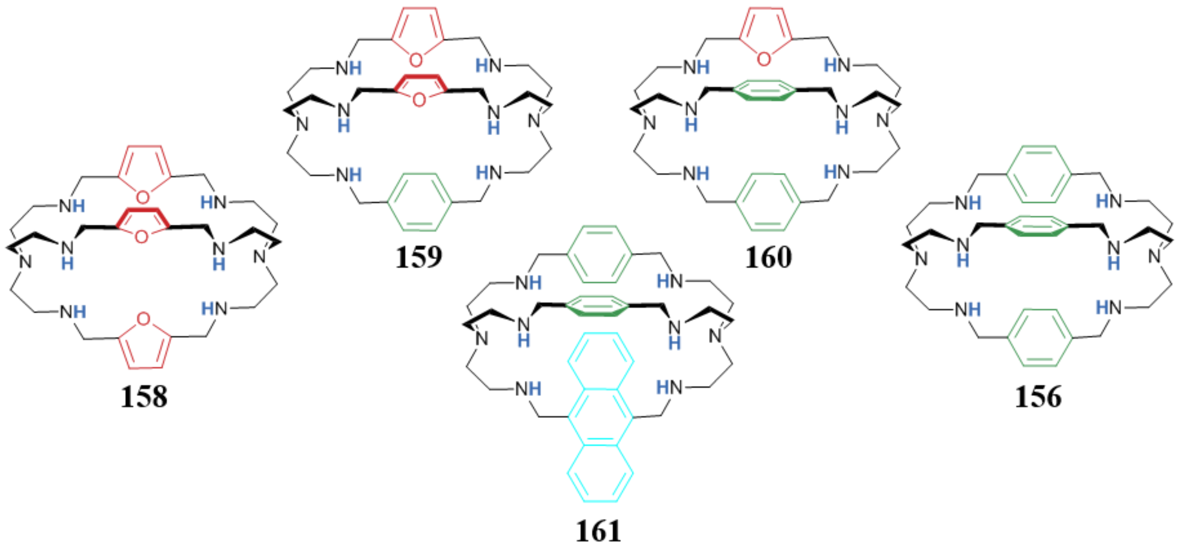

Figure 5.2. Example of symmetric and asymmetric bis(***tren***) cage studied by Amendola for the complexation of halides and other anions. Ref 223.

intermediate values between the symmetrically substituted **156** and **158**, Figure 5.2. While the highest affinity for F^- was observed with the cages with more *p*-xylyl spacers, **156** and **160**, the opposite was observed for the other halide anions.[224] Binding studies of the protonated cage **156** with perrenhate[225] and pertechnetate[173] led to the development of ligand **161** for fluorescent detection and trapping of $^{99}TcO_4^-$ in water.[22]

Imidazolium and benzimidazolium cryptates have also been successfully used by Amendola for the trapping of halides, Figure 5.3.[38] While previous studies on **162** and **163** had shown the impossibility of encapsulating halides, Amendola was able to study and prove the effective inclusion of a F^- atom within the tris(benzimidazolium) cage **164**. The use of a benzimidazolium as a binding unit allowed studies by UV-vis absorption spectroscopy for the anion binding ability, thanks to its improved and more distinctive absorption properties, when compared to the imidazolium chromophore, Figure 5.4a.[38] Significant changes in the UV-vis absorption spectrum of **164** upon addition of F^- were observed, Figure 5.4b, which indicated the formation of the 1:1 complex, Figure 5.4c. The same experiment observed through ^{1}H NMR spectroscopy revealed a slow exchange process, with the broadening and

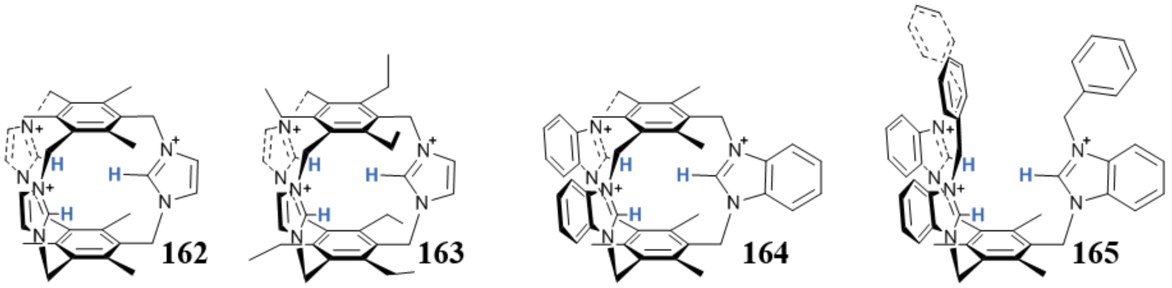

Figure 5.3. Examples of cages containing imidazolium or benzimidazolium binding units studied by Amendola.

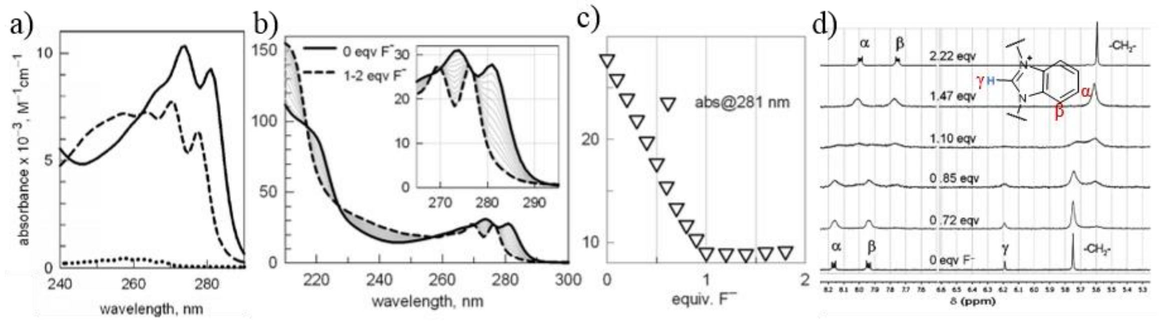

Figure 5.4. a) UV-vis absorption spectra of *N*,*N*’-diphenylimidazolium (dotted line), *N*,*N′*-diphenylbenzimidazolium (dashed line) and **164** (solid line, normalised to the number of benzimidazolium subunits); b) UV-vis absorption titration of [**164**] (2.00 × 10^{-4} M) with F^- in CH_3CN; (c) Titration profile at 281 nm, which indicates the 1:1 stoichiometry of the interaction; d) ^1H NMR titration of [**164**] (2.10 × 10^{-4} M) with F^- in CD_3CN. Reproduced from ref. 38.

disappearance of proton Hγ after the addition of one equivalent of F^-, Figure 5.4d. Due to the cavity size restriction, F^- was the only halide which showed interaction with cage **164**. However, interaction with Cl^- ($K_{1:1}$ = 7.95 × 10^3 M^{-1}, in CH_3CN) was observed for the benzimidazolium tripodal **165** by UV-vis spectroscopy studies, as well as with F^- and the HF_2^-, which formed due to the deprotonation of one of the benzimidazolium proton Hγ ($K_{1:1}$ = 5.62 × 10^5 M^{-1}, $K_{1:2}$ = 1.02 × 10^4 M^{-1}, in CH_3CN). Interaction of tripodal **165** with Br^- was also observed, but low solubility of the complex did not allow the calculation of the binding constant. However, the crystal structure revealed the formation of the 1:1 complex, with the anion lying in the cavity just below the plane of the three benzimidazolium units, receiving hydrogen bonds with length between 2.72-2.75 Å.[38] Interactions with non-spherical anions such as NO_3^- and CH_3COO^- were also observed for the tripodal ligand **165**, while no interaction was observed with I^-. Cage **96**, which is presented in this chapter possesses three imidazolium moieties, which carry three positive charges and, as in the examples discussed above, make it a ligand suitable for anion binding without the need of further dynamic protonation. The binding studies of cage **96** with Cl^-, Br^-, I^- and F^- will be discussed in the next sections.

5.2. Synthesis and characterisation of 96

The synthesis of cage **96**, Scheme 5.1, was carried out by Dr Greta Bergamaschi and Dr Ana Miljkovic in Pavia by reaction of a tripodal imidazole precursor, **166**, with tris(3-(bromomethyl)benzyl)amine, **167**, in a 1:1 mixture of $CHCl_3$:acetone at reflux for 72 hrs. Ligand **96** precipitated as a white solid and was obtained in 45% yield as the hexafluorophosphate salt from hot water, by reaction with NH_4PF_6. The product was used as received from Italy and characterized by NMR (600 MHz, CD_3CN, 298K).

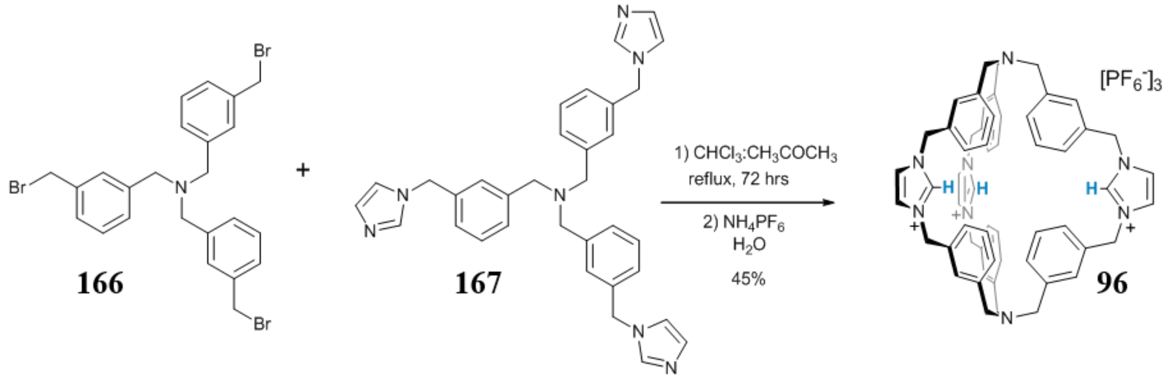

Scheme 5.1. Synthesis of cage **96**.

The ^{1}H NMR spectrum, Figure 5.5, displayed two singlets resonances at 3.27 ppm and 5.30 ppm, which corresponded to the resonances of H1 and H2, respectively. The imidazolium moiety showed two resonances, one doublet ($J_{4\text{-}4'}$ = 1 Hz) in the aromatic region at 7.50 ppm for H4-4′ and the most deshielded resonance as a broad singlet at 8.65 ppm for H3. Protons H6 and H8 had their resonances in the aromatic region (7.07-7.15 ppm) with partially unresolved peaks, while H7 appeared as a doublet at 7.23 ppm. Proton H5, being assigned to the benzoyl moiety, resonated as a broad singlet at 6.95 ppm. MALDI HRMS analysis confirmed the presence of a peak at *m/z* = 851.4568 assigned to the $[M\text{-}2H]^+$ ion with chemical formula $C_{57}H_{55}N_8$. Having elucidated the solution structure of **96**, we next carried

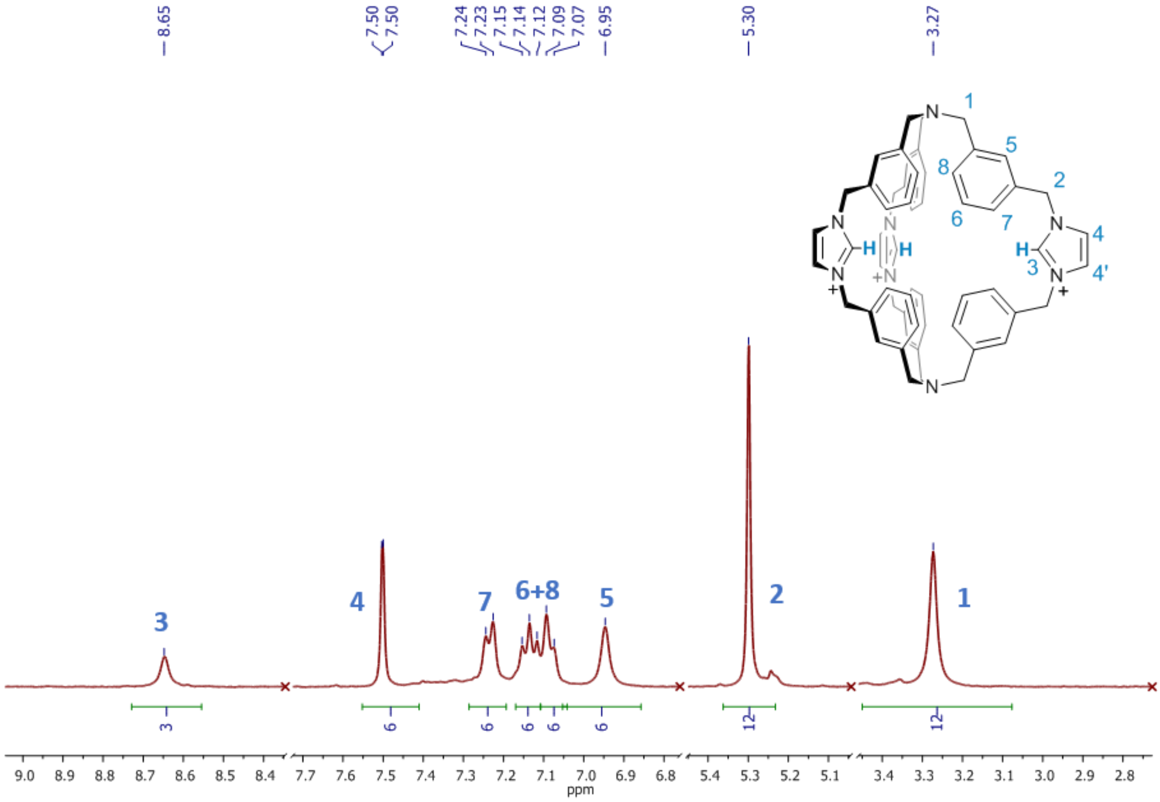

Figure 5.5. ^{1}H NMR spectrum of cage **96** (600 MHz, CD_3CN) with assignment of protons.

out the in-depth analysis of its binding affinity for anions, focusing in particular on Cl^- and F^-.

5.3. Anion binding studies in the solid state

Crystals of both the free ligand and of its Cl^- complex **96**·Cl^- were obtained by researchers in Pavia from diffusion of Et_2O in a solution of **96** in CH_3CN. These crystals were suitable for X-ray diffraction studies to be carried out and were collected and resolved by Prof. Donatella Armentano at Università della Calabria. The solid-state structures showed significant changes in the conformation between the free cage and **96**·Cl^-. The crystal of the free cage was resolved in the trigonal space group P_{-3} with an asymmetric unit containing 1/3 of cage **96** and 5/3 of PF_6^- counterions. In this crystal structure the cage showed an elongated conformation, with the shorter axis passing through the tertiary amines ($N_{tert}\cdots N_{tert}$ distance of 5.65 Å, Figure 5.6a), and the three 'arms' extended symmetrically such that the imidazole was the most external moiety of the cage ($C\text{-}H_{im}\cdots C\text{-}H_{im}$ distance of 11.01 Å, Figure 5.6c).

The crystal structure of the complex **96**·Cl^- was resolved in the triclinic P_{-1} space group, with the asymmetric unit containing one molecule of **96**, one Cl^- anion, one solvent molecule (CH_3CN) and two counter ions, Figure 5.7a-c. The position of the imidazolium groups in **96**·Cl^-, with their most acidic proton pointing towards the central Cl^- ($C\text{-}H\cdots Cl$ angles 112-157°), would suggest a hydrogen bonding interaction with the $C\text{-}H\cdots Cl$ distance of 3.15-3.28 Å, Figure 5.7a. In the crystal structure of the complex, the cage assumed a twisted conformation with the tertiary amines lying on the longer axis ($N_{tert}\cdots N_{tert}$ distance of 9.54 Å, Figure 5.7b) and the imidazolyl moieties closer together ($C\text{-}H_{im}\cdots C\text{-}H_{im}$ distance range 5.30-6.00 Å, Figure 5.7c). The hydrogen bond distances, while being longer than the average distance in the solid state, are within the range of hydrogen bonds distances for this range of

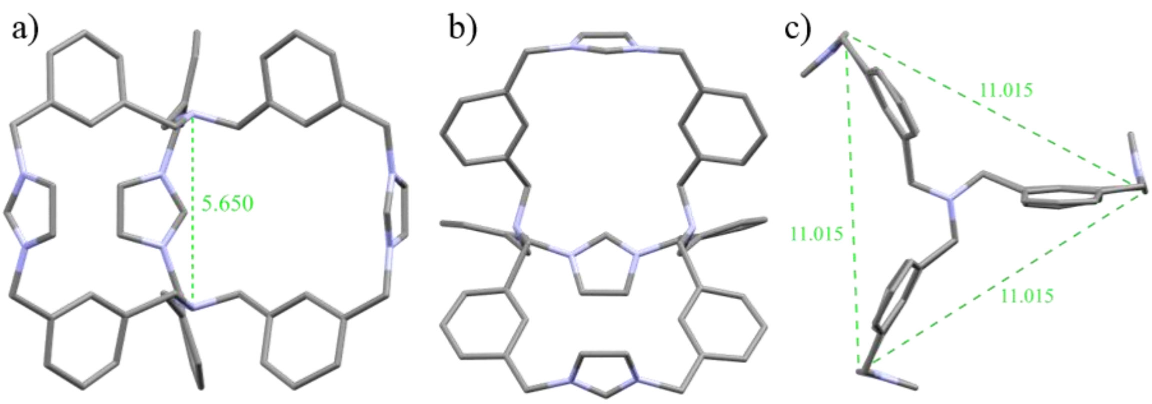

Figure 5.6. Crystal structure of **96**.$(PF_6^-)_4$, view down: a) axis *a*, b) axis *b*, c) axis *c*. Hydrogens, counterions and solvent molecules omitted for clarity. Interaction distances shown in Å.

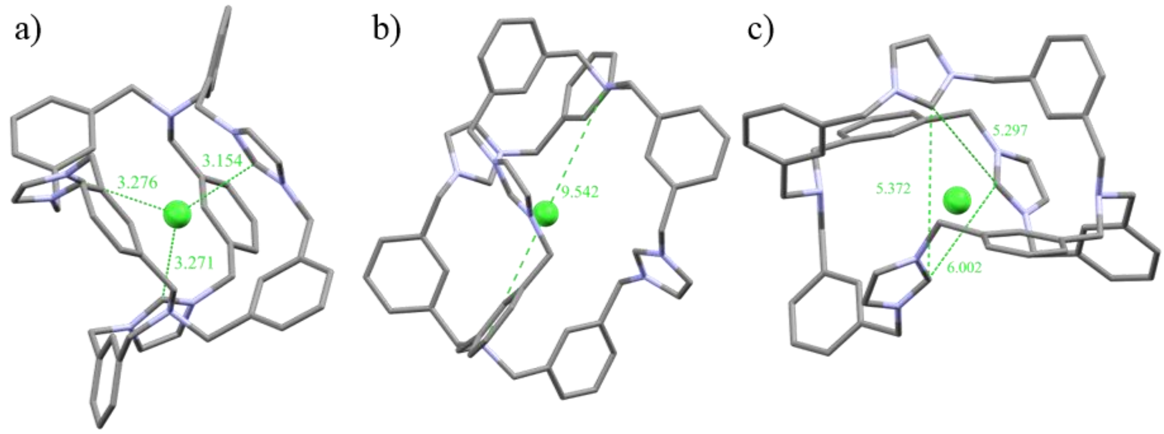

Figure 5.7. Crystal structure of **96**$\cdot(\mathrm{PF_6^-})_2$ $\mathrm{Cl^-\cdot CH_3CN}$, view down: a) axis *a*, b) axis *b*, c) axis *c*. Hydrogens, counterions and solvent molecules omitted for clarity. Interaction distances shown in Å.

H-bond donor.[226] In addition to this, thanks to the positive charge of the imidazolium moieties, we could expect that the attraction to the central anion is balanced by the repulsion between the three sides of the cage, which could force the hydrogen bonds to lengthen and weaken. However, this solid-state analysis could not alone fully describe the binding abilities of the cage and it could not be considered necessarily the exact picture of the dynamic binding occurring in solution. There are a number of techniques available to elucidate the solution behaviour, Isothermal Titration Calorimetry (ITC) is commonly used to determine thermodynamic contribution to measure the binding. However, this was beyond the initial scope of the studies and solution studies of the anion binding process with halides were carried out using spectroscopic techniques and are presented in the following sections.

5.4. Anion binding studies in solution - UV-vis absorption spectroscopy

Similarly to the case of **162**,[38] cage **96** was weakly absorbing in the UV-vis region and its study with this technique could not be carried out. The UV-vis absorption spectrum of **96** in $\mathrm{CH_3CN}$ showed one band at 271 nm and a shoulder at 263 nm, which were partially overlaid with the solvent absorbance bands (both in $\mathrm{CH_3CN}$ and in a mixture of $\mathrm{CH_3CN{:}H_2O}$,98:2) and have a very low extinction coefficient for the band at around 270 nm (< 5000 $\mathrm{M^{-1}cm^{-1}}$, Appendix A5, Figure A5.6) assigned to the π-π* transition of the phenylene moieties. To

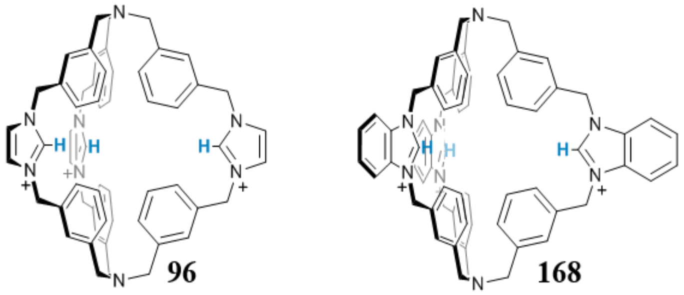

Scheme 5.2. Structures of imidazolium cage **96** and benzimidazolium cage **168**.

have a model for comparison studies of cage compound **96** by UV-vis absorption spectroscopy, a benzimidazole analogue, **168**, was synthesised with a similar procedure as outlined for **96**, for studying the binding ability. The UV-vis absorption spectroscopy studies of the benzimidazole analogue cage **168** were carried out by Amendola and are presented here as a comparison for the studies on cage **96**. The UV-vis absorption spectrum of the benzimidazolium cage **168** showed a broad absorption band with 5 maxima between 255 and 280 nm, with extinction coefficients 5-fold larger than the imidazolium cage **96**, Figure 5.8. This allowed the study of the binding property of **168** with Br^- and Cl^-, which were carried out in CH_3CN and CH_3CN:H_2O (98:2) solutions using the aforementioned anions as their TBA solutions. The overlapping of the absorption bands of TBA^+I^- and cage **168** prevented the study of this interaction by UV-vis absorption spectroscopy and, as such, was omitted from this study.

The addition of Cl^- to a solution of **168** in CH_3CN caused an increase of absorbance in correspondence of the λ_{max}, with the formation of five isosbestic points, Figure 5.8a. The isotherm plots (at 277 nm and 283 nm, respectively, Figure 5.8a-inset) showed a curve with a sharp change that corresponded to the addition of 1 equivalent of Cl^-. This indicated the interaction between the ligand and the anion, with the formation of a 1:1 complex. However, it prevented the calculation of a binding constant by non-linear regression, as it required the presence of a less sharp curve for that the changes to be fitted. For this reason, the binding studies were carried out also in a mixture of CH_3CN:H_2O (98:2), with the presence of a highly protic and polar H_2O, in order to weaken the host-guest interaction making it more competitive. Similar changes were observed as before, with a less sharp change in slope in the isotherm at 277 nm, Figure 5.8b, which allowed to calculation of the binding constant of $K_{1:1} = 1.26 \times 10^6$ M^{-1}. Similar behaviour was observed in the binding with Br^-, with a smaller formation constant for the complex than that calculated for the complex with Cl^-, with a calculated constant of $K_{1:1} = 1.26 \times 10^5$ M^{-1}.

A titration with TBAF was also carried out on **168** in CH_3CN which showed similar changes in the UV-vis absorption spectrum as the other halides, however the isotherm plots showed that a plateau was reached only after the addition of two equivalents, suggesting a different binding mode as the other anions (Appendix A5, Figure A5.9). Considering the binding with F^- of ligand **165**, described above, it is possible that a similar behaviour was occurring.

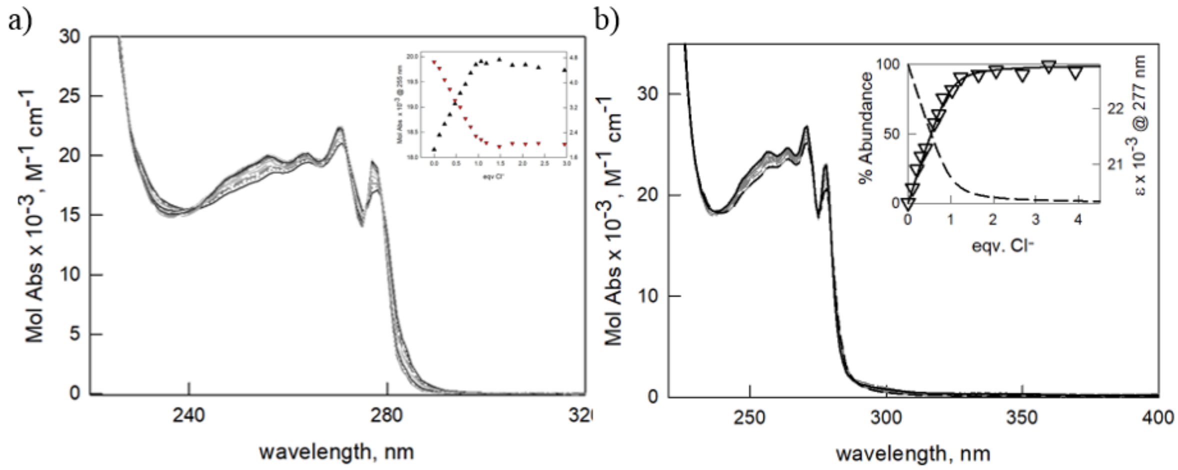

Figure 5.8. UV-vis absorption titration profile of **168** with Cl^- in a) CH_3CN and b) CH_3CN:H_2O (98:2) and isotherm plot and fitting curve. Studies carried out by Amendola and co-workers and reproduced from their report.

While the UV-vis absorption studies on cage **168** provided useful information about the host-guest stoichiometry and allowed the calculation of binding constants, they could not be used to give a full explanation of the binding event and affinity of the cage in solution. In particular, they could not clearly show whether the binding of the cage in solution was accompanied by any conformation changes consistent with the ones observed in the solid-state analysis for cage **96** interacting with Cl^-. Therefore, NMR studies of the binding of **96** with various halides were carried out in CD_3CN, as this would allow us to draw a more accurate comparison between the solid-state results and would allow us to understand better the sensing behaviour of the cage in solution. In particular, the formation of H-bonds through the acidic proton of the imidazole could be followed and verified (for full assignment of proton resonances refer to Figure 5.5). Furthermore, by carrying out NOESY experiments, we anticipated that it would be possible to identify any important through-space interaction among the protons of the structure that would signal conformational change of the ligand in the binding process. Changes in the conformation and size of cage **96** upon binding of the anion were also detected and analysed through DOSY NMR and calculation of the diffusion coefficients. Therefore, we studied the anion binding properties of cage **96** by NMR, and the results will be presented in the next section.

5.5. Anion binding studies in solution using NMR spectroscopy

The choice of the solvent for titrations of ligand **96** by NMR was dictated by the solubility of the ligand and was limited to DMSO-d_6 and CD_3CN. The use of a highly polar and competitive solvent like DMSO-d_6 was desirable, as the binding in this solvent is more challenging, and would test the system more rigorously, like for the systems discussed in the previous chapters. Preliminary studies were carried out in a DMSO-d_6 with phosphate and pyrophosphate anions envisaging a good potential for binding of such anions, because of the flexibility and symmetry of the ligand. However, the interactions observed were shown to be in slow exchange at RT. The resonances were split in many parts, resulting in an overcomplicated spectrum which prevented the possibility of fitting. In addition to this, upon the addition of 1→2 equivalents of the anion, a precipitate would form, which was then found to be re-dissolved upon addition of higher concentrations of the anions. This demonstrated poor solubility of the ligand or its complexes in this media and, furthermore, analysis of the precipitate by mass spectrometry (MALDI) did not show the presence of any host-guest complex, but only the free ligand. For these reasons, despite an interest in studying the binding in more competitive solvents, CD_3CN, was chosen as a working media, given the good solubility of **96**. After confirmation of hydrogen bonding interactions occurring in the solid-state between **96** and Cl^-, the focus moved towards other halides. A dilution study in CD_3CN was initially undertaken to determine a suitable working concentration range. Aggregation of the ligand was not observed and, due to the high symmetry of the ligand which gives high integration for each equivalent proton resonance, it was possible to work at a rather low concentrations of *ca.* 1-1.5 mM in this solvent (Appendix A5, Figure A5.11).

5.5.1. Binding with Cl^-

The reproducible titration of cage **96** with Cl^-, Figure 5.9, displayed significant changes in the ^1H NMR upon interaction of the anion with the cage. These changes were attributed to anion binding to the cage receptor. The most evident effects were an initial broadening, alongside a deshielding and final sharpening of the resonances of protons H3 and H5, respectively. Both resonances were absent in the NMR spectrum between the addition of 0→1 equivalent of Cl^- due to considerable broadening effect. However, sharpening of the peaks became apparent between 1→6.4 equivalents of Cl^- added, when the resonances of these two protons moved to 11.91 ppm, for H3, and 8.35 ppm, for H5. The binding event resulted in the resolution of the aromatic protons. The spectrum of the free ligand, in fact, was not of first order and the peaks not finely resolved, while the spectrum of **96**·Cl^- shows relatively resolved peaks with fine coupling associated with them. This was a first indication that the host-guest **96**·Cl^- complex was a more rigid system than in the free cage. The aromatic proton resonances were deshielded, with no further change being observed, and a plateau reached after the addition of 1 equivalent of Cl^-, as seen in Figure 5.11. Only the imidazole H4 protons seemed to be shielded at the start of the titration and remained so up

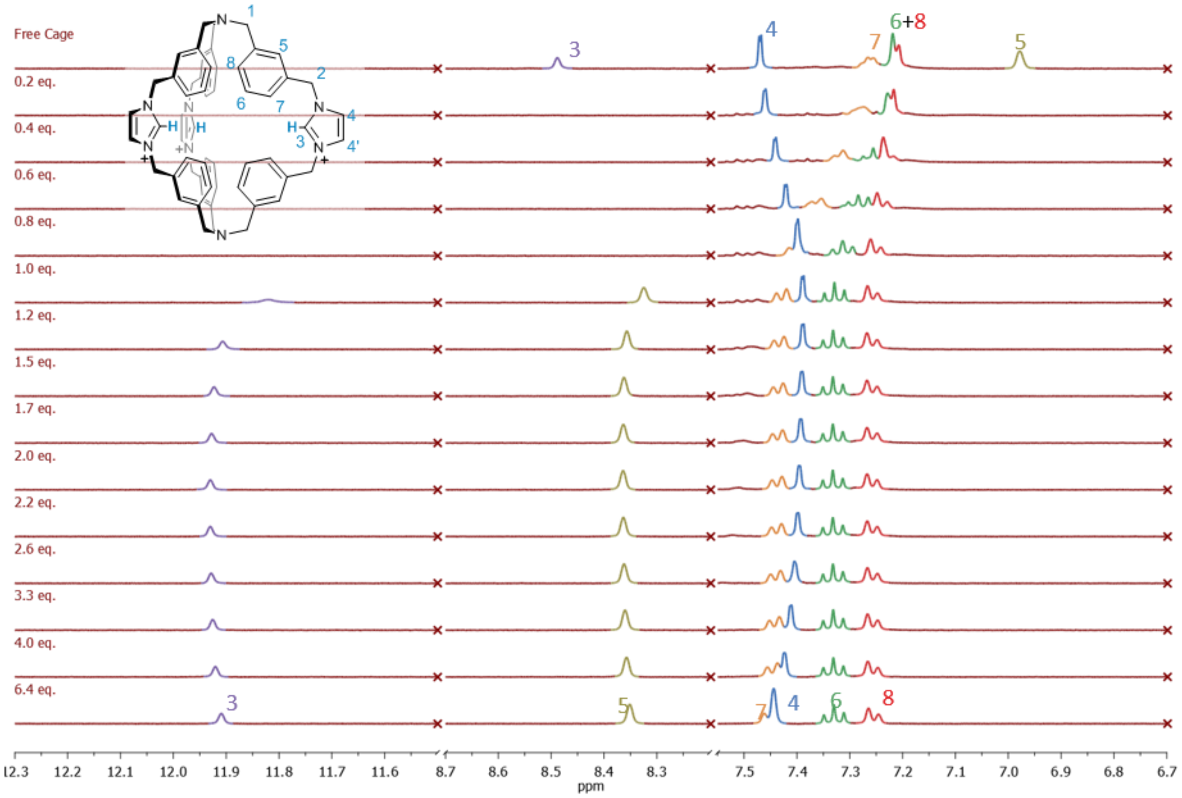

Figure 5.9. Stacked plot of the ^{1}H NMR of the changes observed upon titration of **96** with Cl^- in CD_3CN. [**96**] = 1.5 mM. Featureless regions omitted for clarity, full spectrum can be found in the Appendix A5 (Figure A5.12). This titration is representative of reproducible trends. Proton resonances are numbered according to Figure 5.5.

to the addition of 1 equivalent of anion. After the addition of 1 equivalent and up to 6 equivalents, H4 was, in fact, deshielded and returned to a similar chemical shift as in the free cage. This effect, is potentially due to an ion pairing effect between the cage and the excess anions in solution, which increase the local ionic strength, following to the encapsulation of the first equivalent of anion. The interest of this study was, however, mainly focussed on the understanding of the encapsulation. The resonances shifts seemed to reflect the 'capture' of the Cl^- anion within the cavity of the cage, consistent with that observed in the X-ray diffraction studies. The significant deshielding of protons H3 and H5 would be signs of hydrogen bond interaction, which also agrees with what was observed in the crystal structure of the **96**·Cl^- complex. In particular the deshielding of the aromatic proton H5, is an evidence for a significant change in the electronic environment of the cage, possibly due to conformational changes occurring upon binding to Cl^-. To investigate the Host-Guest interaction further, MS analysis of the NMR solution was undertaken. The analysis by MALDI-TOF of the solution at the end of the titration showed a peak for *m/z* = 887.4358 which was assigned to $C_{57}H_{56}N_8Cl$ (*m/z* = 887.4316), which corresponds to $[M^{3+}-H^{+}+Cl^{-}]$, showing high stability of the **96**·Cl^- complex.

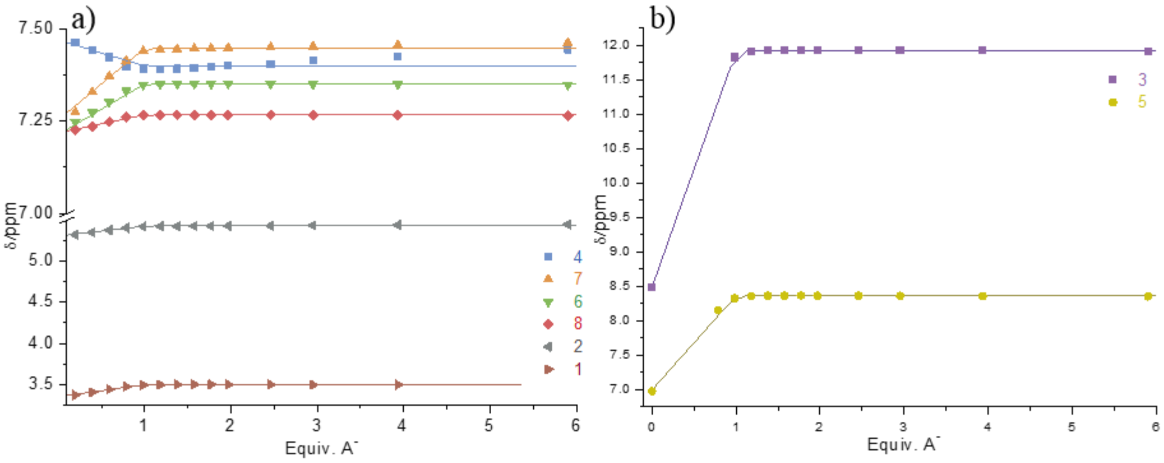

Figure 5.11. a-b) Plots of binding isotherms with the relative fitting curve of ^{1}H NMR titration of **96** with Cl^-. a) Protons H1, H2, H4, H6, H7, H8 and b) protons H3 and H5.

Similarly to what was observed in the UV-vis titrations of benzimidazolium cage **168** with Cl^- in CH_3CN, the isotherm plot, Figure 5.11, displayed a sharp slope change in correspondence of the addition of 1 equivalent of anion. As in the UV-vis absorption study, this indicated a very strong binding, which was not within the measurable range of the technique ($K_{1:1} < 10^6$ M^{-1}).[164] A model with a single host-guest species and a value of $K_{1:1} > 10^6$ M^{-1} would fit the changes as shown in Figure 5.11. However, a precise value could not be obtained. Nevertheless, this change was consistent to the UV-vis absorption studies on the benzimidazolium cage, and indicated a strong binding of **96** to Cl^- through hydrogen bonds in a 1:1 stoichiometry. To gain greater insight into the behaviour and conformational arrangement of the **96**·Cl^- complex in solution, and to understand how this compared to the crystallographic structure, NOE spectroscopy studies were then carried out on the free ligand **96** and the complex **96**·Cl^-.

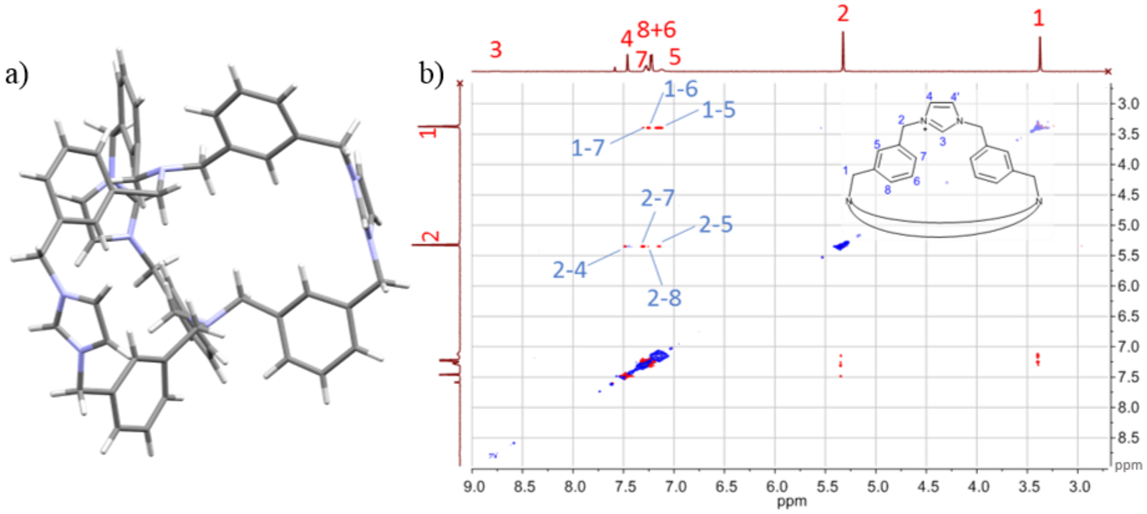

Figure 5.10. a) Crystal structure of structure of free cage **96**; b) NOE spectra of free cage **96** collected in CD_3CN on a 400 MHz spectrometer at 25°C.

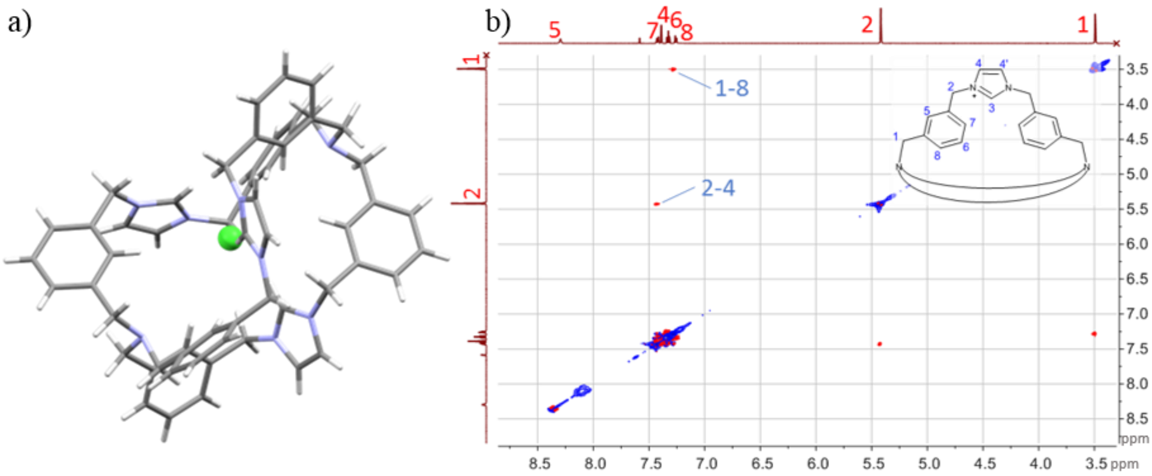

Figure 5.12. a) Crystal structure of structure of **96**·Cl$^-$; b) NOE spectra of **96**·Cl$^-$ collected in CD_3CN on a 400 MHz spectrometer at 25°C.

From the crystal structure of the free cage, Figure 5.10a, it could be noted that the conformation of the tertiary amine found the free electron pair pointing outside of the cage cavity. In such a conformation, the methylenic protons H1 were closer to the aromatic proton H5. In the NOE spectrum, Figure 5.10b, this interaction between, H1 and H5, was indeed clearly visible, suggesting that the conformation of the free cage in solution resembles that seen in the solid state. In addition, other through-space interactions of the aliphatic protons H1 and H2 with the aromatic ones, indicated a certain flexibility of the free cage.

In the crystal structure of **96**·Cl$^-$, Figure 5.12a, it could be noted that, upon binding of Cl$^-$, the tertiary amine inverted its configuration, arranging the free electron pair towards the cavity of the cage. In this conformation the methylenic protons H1 were pointing towards the outside of the cavity, they were then closer to the aromatic protons H8 than H5. This proximity was maintained in solution, according to the NOESY spectrum, Figure 5.12b, as the H1-H8 interaction is clearly visible. This suggested that in solution, like in the solid state, the cage underwent a ‘twist’ and a conformational rearrangement, upon binding to Cl$^-$.

The changes in the shape and size of **96** upon binding of Cl$^-$ can have some effect on the diffusion of the molecule in the solvent. To measure the diffusion coefficient D, DOSY NMR experiment for the free cage **96** as well as for the **96**·Cl$^-$ complex were carried out. The two experiments showed an appreciable difference in the diffusion coefficient which was calculated by global analysis of the DOSY signals for each proton, to be $D = 9.4(1)\times10^{-10}$ m^2s^{-1} for the complex and $D = 8.6(2)\times10^{-10}$ m^2s^{-1} for the free cage. From this small, but significant difference, it was possible to calculate the hydrodynamic radius (through equation 4.1) of the $[Cage]^{3+}$ $r_{FC} = 7.5$ Å and for the $[Cage+Cl^-]^{2+}$ $r_{CC} = 6.8$ Å (considering a value of 0.339 cP[227] for the viscosity (η) in CD_3CN at 298 K). The binding event, therefore,

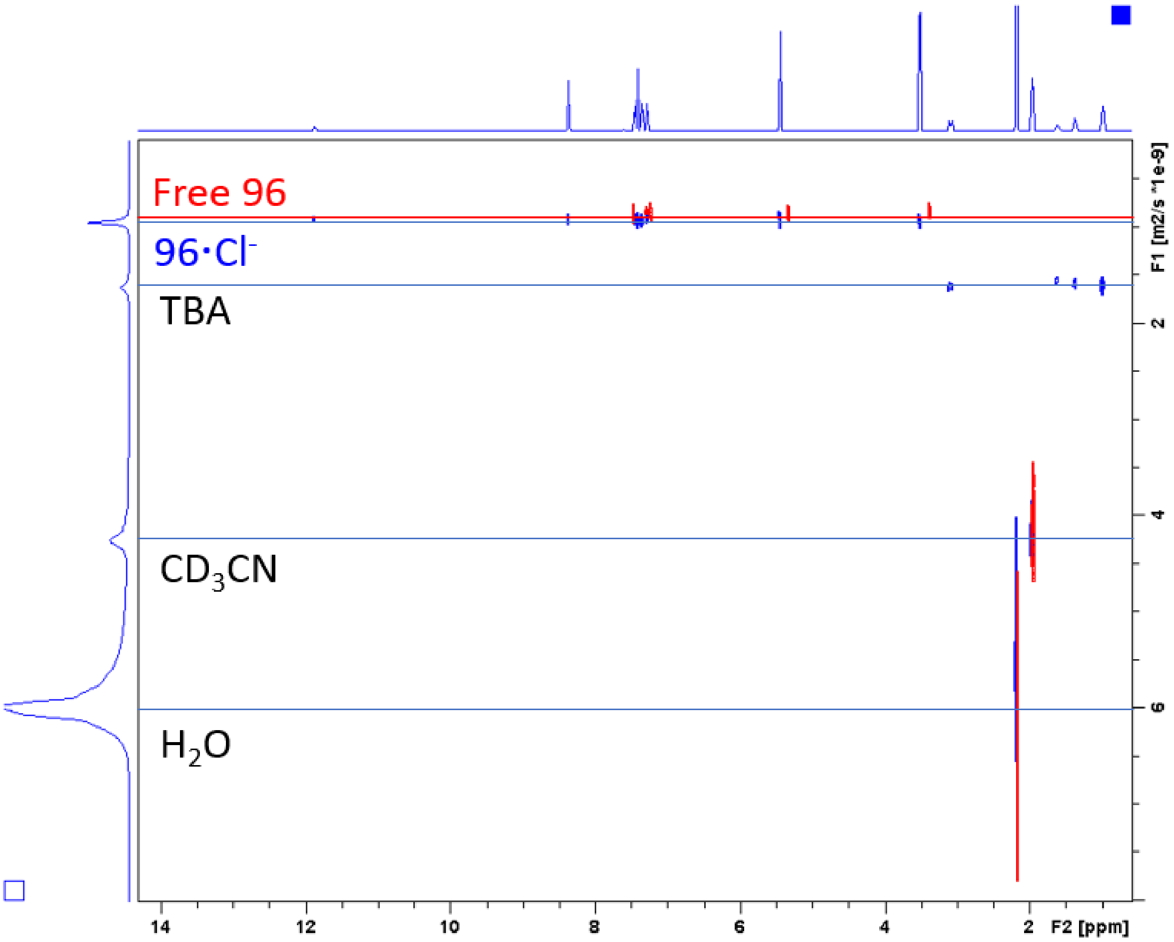

Figure 5.13. Superimposed DOSY experiments of the free cage (red) and **96**·Cl$^-$ (blue) at 25°C in CD_3CN.

caused a change in the hydrodynamic radius of the cage, which got smaller upon encapsulation of Cl$^-$. The hydrodynamic radius of the molecule is dependent, both on the size of the molecule itself, but it is affected also by the electrostatic charge which in the binding event changes from +3 of the free cage to +2, *i.e.* [Cage]$^{3+}$ and [Cage+Cl$^-$]$^{2+}$, respectively.

From the spectroscopic analysis with ^{1}H NMR of **96** and **96**·Cl$^-$ it is possible to understand better their behaviour in solution and confirm the formation of hydrogen bonding between the **96** and Cl$^-$. In addition, by means of NOESY studies comparison of the solid state and solution behaviour of **96** and **96**·Cl$^-$ could be made and it was observed that the conformation of **96**·Cl$^-$ in solution is somewhat similar to the one in the solid state. The reversibility of the complex in solution was also studied by ^{1}H NMR. To a CD_3CN solution of **96** one equivalent of TBACl was added and the formation of the **96**·Cl$^-$ complexed was confirmed by the shifts in the ^{1}H NMR resonances, as described above. To this solution 1 equivalent of $AgNO_3$ was added, which removed the encapsulated Cl$^-$ anion through the precipitation of AgCl, which was then removed from the solution by centrifugation. Analysis

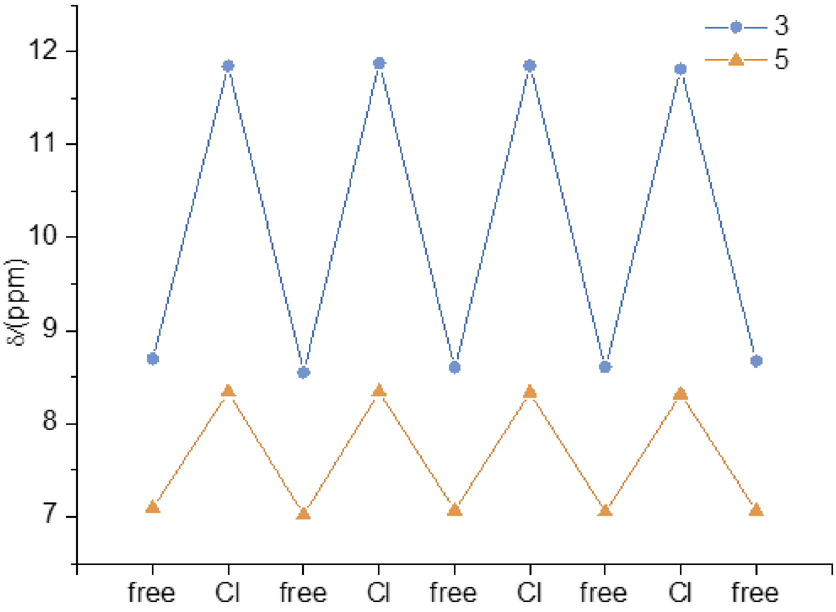

Figure 5.14. Reversibility test: plot of the chemical shifts of protons H3 and H5 over the “breathing” cycles.

of the supernatant solution by ^{1}H NMR showed the resonances shifts corresponding to the free cage, confirming the reversibility of the complex formation. These results demonstrated full reversibility of the binding was observed: in Figure 5.14 the chemical shifts of H3 and H5 upon addition of Cl^- and after the removal of the anion from the cage for up to 4 cycles are reported, showing complete recovery of the free cage state (see full spectra in Appendix A5, Figure A5.15). This behavior was similar to the examples which have been reported by Heitz and co-workers,[228,229] wherein conformational changes could be induced into flexible porphyrinic cages by Ag coordination, and was described as a “breathing” motion. Therefore, considering the conformational changes that the complexation can cause in the cage, this could be described as a Cl^--triggered “breathing motion” of the cage.

As introduced in Chapter 1, the halide anions are monoatomic and all spherically shaped. This makes them fit in the same binding pocket, with the main discriminant being their size and charge density distribution. This can affect their solvation and, as a consequence, the difficulty of a host to overcome this barrier for recognition and binding. Therefore, the binding abilities of cage **96** with Br^- and I^- were next investigated, to elucidate how the recognition was affected by the size of anions, and the results are presented in the following two sections.

5.5.2. Binding with Br$^-$

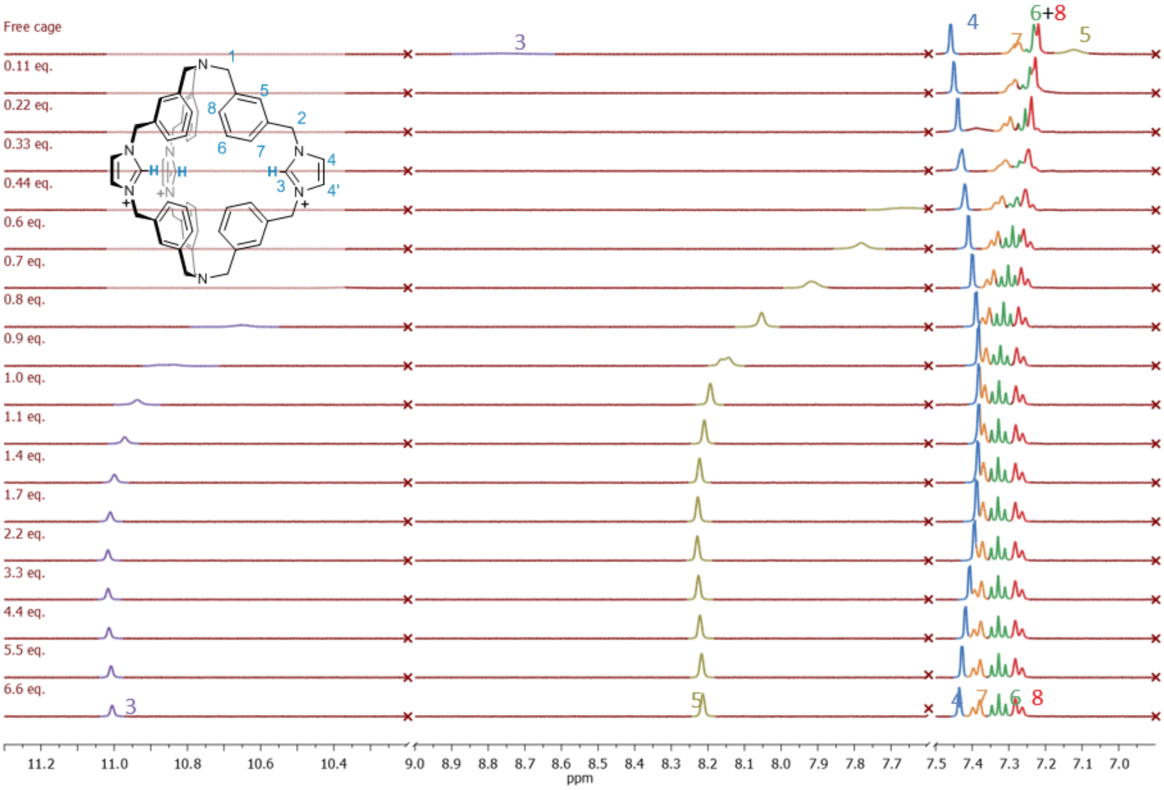

Figure 5.15. Stacked plot of the ^{1}H NMR of the changes observed upon titration of **96** with Br$^-$, in CD$_3$CN. [**96**] = 1 mM. Featureless regions omitted for clarity, full spectrum can be find in the Appendix A5 (Figure A5.17). This titration is representative of reproducible trends. Proton resonances are numbered according to Figure 5.5.

The successive addition of Br$^-$ (TBA$^+$) to a solution of **96** caused significant shifts to occur in all characteristic proton resonances, in a similar manner to that seen for Cl$^-$. This indicated that a similar binding mode was occurring here as seen with Cl$^-$, which included broadening in the H3 and H5 resonances, with deshielding and sharpening of these same resonances after the addition of 1 equivalent of Br$^-$. The aromatic peaks also shifted downfield, as well as becoming more resolved, showing typical aromatic coupling. Furthermore, the interaction with Br$^-$ caused an initial shielding for the H4 protons, followed by a deshielding upon the presence of 1 equivalent of Br$^-$ (and above). This common pattern with Cl$^-$ was indicative of the encapsulation of the Br$^-$ within the cavity of **96** in a similar way as seen and discussed above, indicating the formation of hydrogen bonding between **96** and Br$^-$, as well as a concomitant conformational rearrangement of the cage. However, compared to Cl$^-$, one key difference could be noted: while the binding with Cl$^-$ resulted in the shifting of the resonance up to 11.9 ppm, the same H3 resonance was shifted by Br$^-$ to 11.0 ppm, which could be an indication of weaker binding interaction. As above, the confirmation of the formation of a stable complex was also proven by investigating the interaction using HRMS (MALDI).

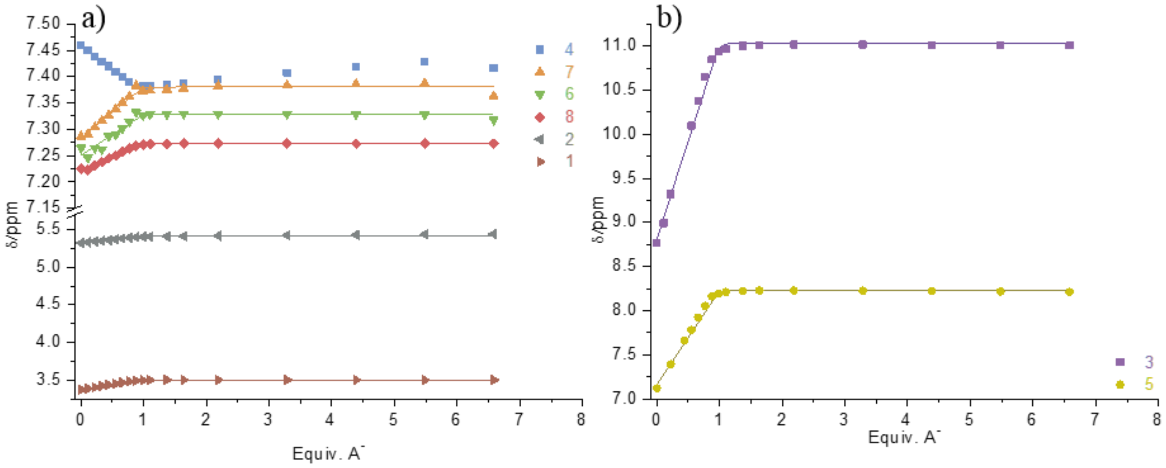

Figure 5.16. a-b) Plots of binding isotherms with the relative fitting curve of **96** with Br^-. a) Protons H1, H2, H4, H6, H7, H8 and b) protons H3 and H5.

This showed a peak at *m/z* = 931.3799 assigned to be a species with the chemical formula $C_{57}H_{56}N_8Br$ (*m/z* = 931.3811), corresponding to $[M^{3+}-H^{+}+Br^{-}]$.

Similarly to the binding with Cl^-, a reliable non-linear regression fitting of the data could not be obtained, due to the sharp plateau after the addition of 1 equivalent of anion. However, a model with a single host-guest species and a value of $K_{1:1} > 10^6$ M^{-1} would fit the changes, Figure 5.16. The changes in the chemical shifts were similar to those observed with Cl^-, indicating that the encapsulation would induce similar conformational changes. Furthermore, this is consistent with the results from the UV titrations on the benzimidazole analogue **168**.

5.5.3. Binding with I^-

The formation of a complex between **96** and I^- was investigated. The increasing addition of TBAI to a solution of **96** in CD_3CN caused significant shifts in the resonances of the ^1H NMR spectrum, as shown in Figure 5.17. The changes in chemical shifts of cage **96** with I^-, however, did not correspond entirely to the ones seen previously for Cl^- and Br^-. The resonances assigned to H5 and H3 were significantly deshielded, similar to the other anions. However, the same extensive broadening was not observed, making it possible to follow these resonances over the entire titration. Imidazole protons H4 showed a similar behaviour to that seen for the Cl^- and Br^-, as did aromatic protons H6 and H8 which once again became deshielded. However, the spectrum of **96**·I^- did not show well resolved aromatic peaks, while also showing, unlike the other complexes, H7 protons resonances at higher chemical shift than that of the free cage. In general, the changes in the chemical shifts were smaller for I^- than Cl^- and Br^-, suggesting that a binding event was happening, but with less strength, therefore reflecting the effect of increasing radius of the ions, Figure 5.18. In this case, the

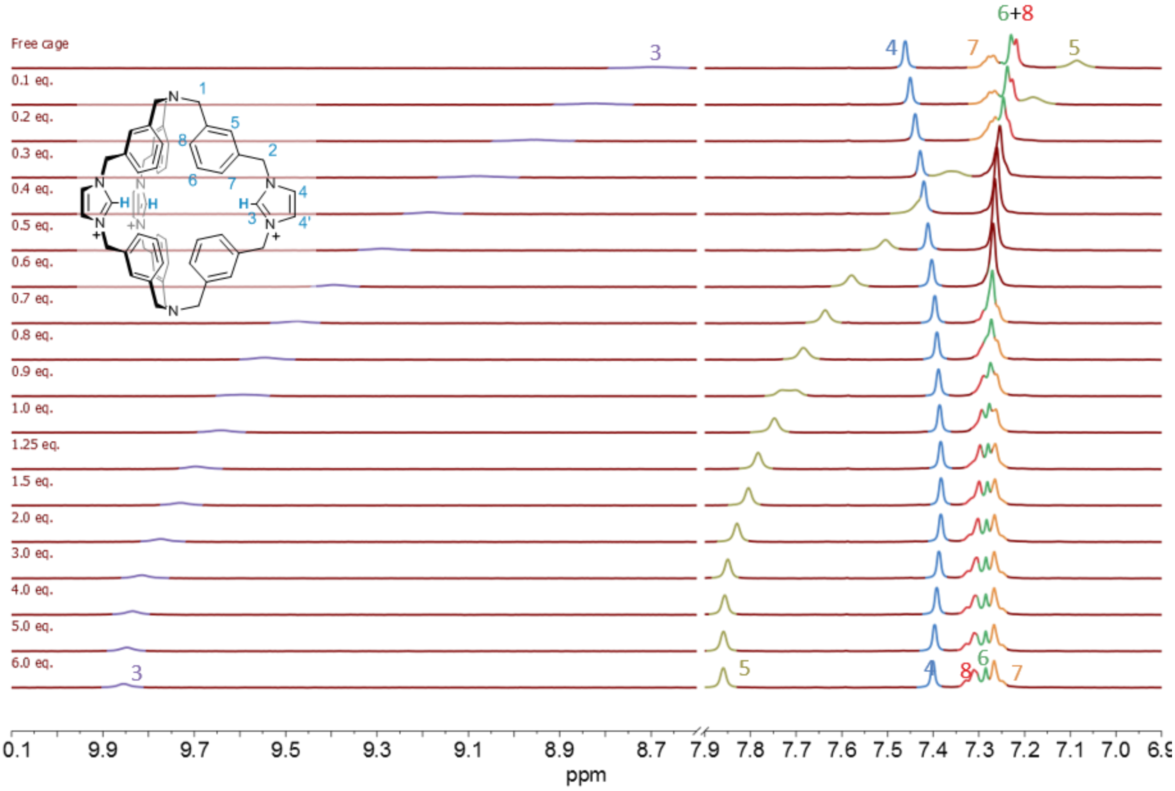

Figure 5.17. Stacked plot of the ^{1}H NMR of the changes observed upon titration of **96** with I$^-$, in CD$_3$CN. [**96**] = 1 mM. Featureless region omitted for clarity, full spectrum can be find in the Appendix A5 (Figure A5.19). This titration is representative of reproducible trends. Proton resonances are numbered according to Figure 5.5

fitting by non-linear regression analysis indicated a binding constant for the interaction of **96** with I$^-$ of $K_{1:1} > 10^4$ M^{-1}. This reflected a weaker binding than that with Cl$^-$ and Br$^-$, while being reasonably strong for this anion.

As before, it was possible to further characterise the solution structure of the **96**·I$^-$ complex by using HRMS. The **96**·I$^-$ complex was observed by MALDI-TOF: *m/z* = 979.3785 for $C_{57}H_{56}N_8I$ (*m/z* calc = 979.3672), corresponding to [M^{3+}-H^++I^-].

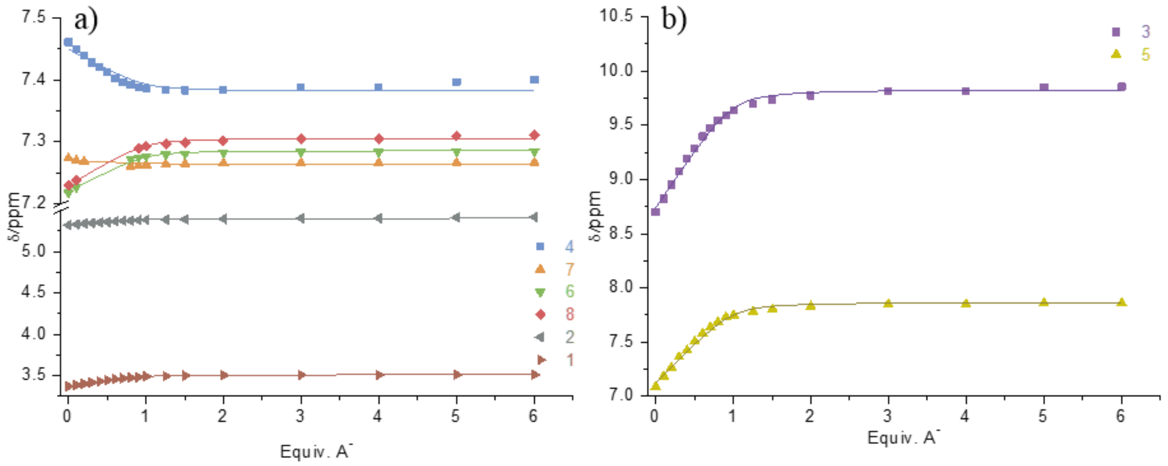

Figure 5.18. a-b) Plots of binding isotherms with the relative fitting curve of **96** with I$^-$. a) Protons H1, H2, H4, H6, H7, H8 and b) protons H3 and H5.

The encapsulation ability of cage **96** seemed to reflect, as expected, the size of the halides, with a stronger binding observed for Cl$^-$ and a lower binding for Br$^-$ and I$^-$. As observed in the literature for similar polymacrocyclic cages, this reflected a therefore a usual trend. To complete the series of halides and make a full comparison, NMR titrations were carried out also with F$^-$ which posseses some peculiar characteristic that make it an exceptional case within the halide series. In fact, with an ionic radius of 1.30 Å it is the smallest of the group and of the entire periodic table, and its charge is less delocalised, making it very basic and highly hydrated.

5.5.4. Binding with F$^-$

To complete the study of the behaviour of cage **96** with halides titration experiment with F$^-$ was carried out. Unlike the halides tested above, F$^-$ is known to not only form host-guest complexes with hydrogen bonding donors, but also, due to its basicity, the deprotonation of acidic protons. From the UV-vis absorption titration of **168** it was also clear that the binding would show a different stoichiometry.

The titration profile of cage **96** with F$^-$, Figure 5.19, showed that the interaction caused a significant downfield shift of H3 from 8.7 to 14.0 ppm. This also showed with a plateau of the isotherm, which was reached only after the addition of 2 equivalents of F$^-$ and,

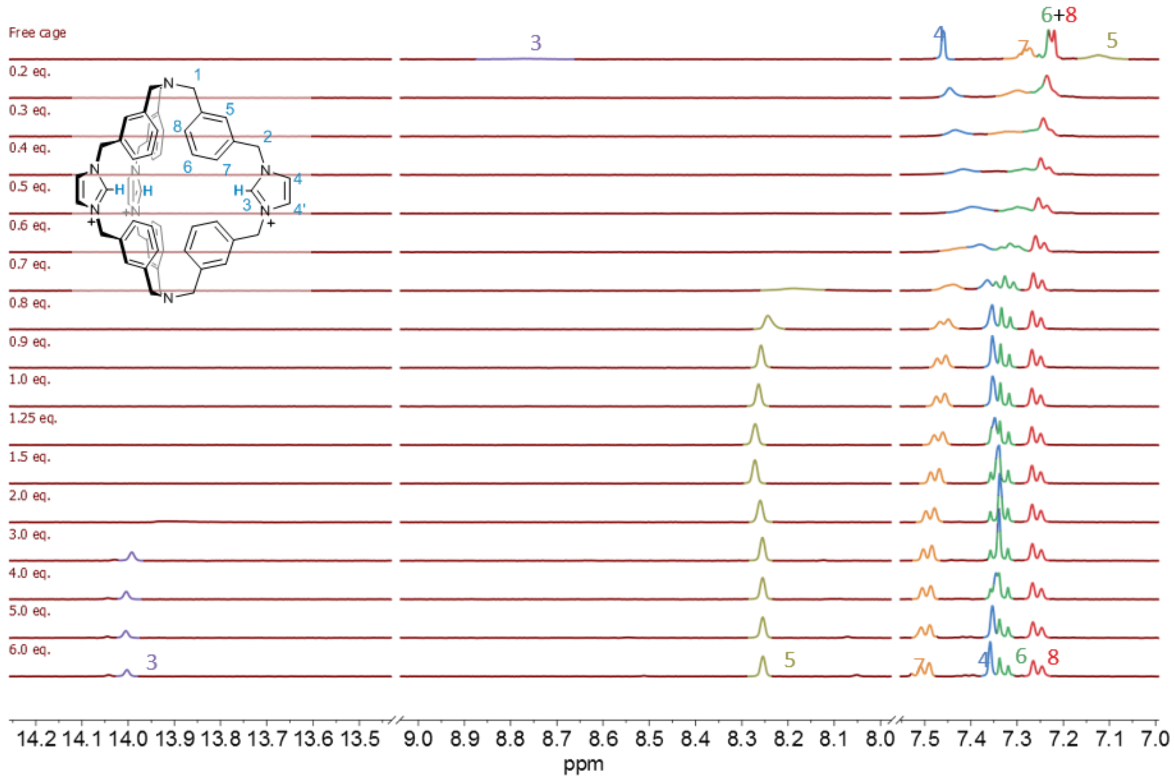

Figure 5.19. Stacked plot of the ^{1}H NMR of the changes observed upon titration of **96** with F$^-$, in CD$_3$CN. [**96**] = 1 mM. Featureless region omitted for clarity, full spectrum can be find in the Appendix A5 (Figure A5.22). This titration is representative of reproducible trends. Proton resonances are numbered according to Figure 5.5.

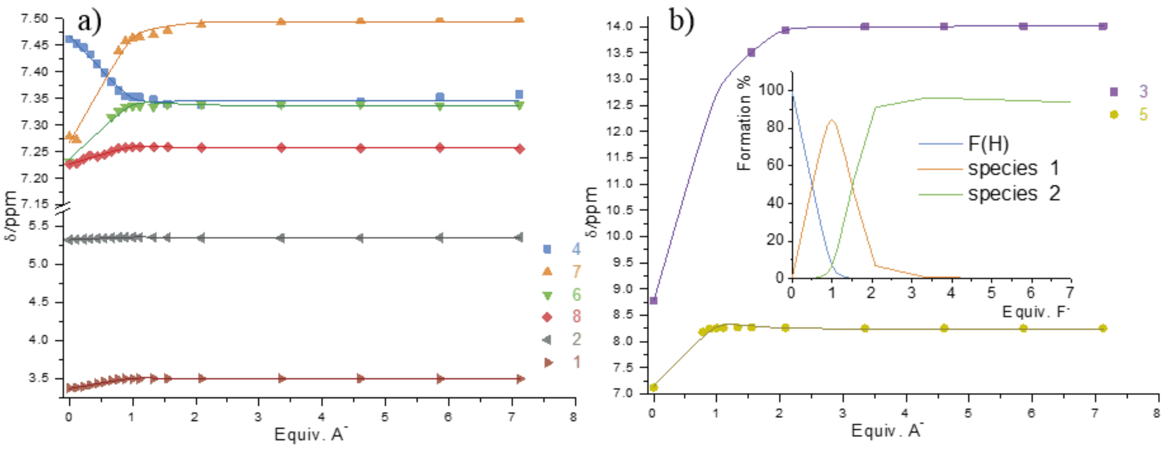

Figure 5.20. a-b) Plots of binding isotherms with the relative fitting curve of **96** with F$^-$. a) Protons H1, H2, H4, H6, H7, H8 and b) protons H3 and H5.

importantly, broadening to disappearance of the resonance in the intermediate steps, Figure 5.20. This was a difference compared to the binding with the other halides and required deeper investigation for its elucidation. Interestingly, the titration pattern, of the other proton resonances was similar to that observed with Cl$^-$ and Br$^-$, with a sharp change of slope after one equivalent, which was in contrast to the plateau after 2 equivalents of H3. In the studies of **164** with F$^-$ presented earlier (Section 5.1), the encapsulation of a single F$^-$ ion was accompanied by a plateau in the isotherm after the addition of 1 equivalent of the anion (by UV-vis absorption analysis, Figure 5.4c). Moreover, in both the ^{1}H NMR and ^{19}F NMR spectra a coupling between the acidic proton of the imidazolium (Hγ) and the fluoride ion of $J_{\text{H-F}}$ = 84Hz was observed.[38] The same coupling in the presence of one equivalent of F$^-$ could not be observed, due to the extreme broadeining of the H3 resonance. Although, even at

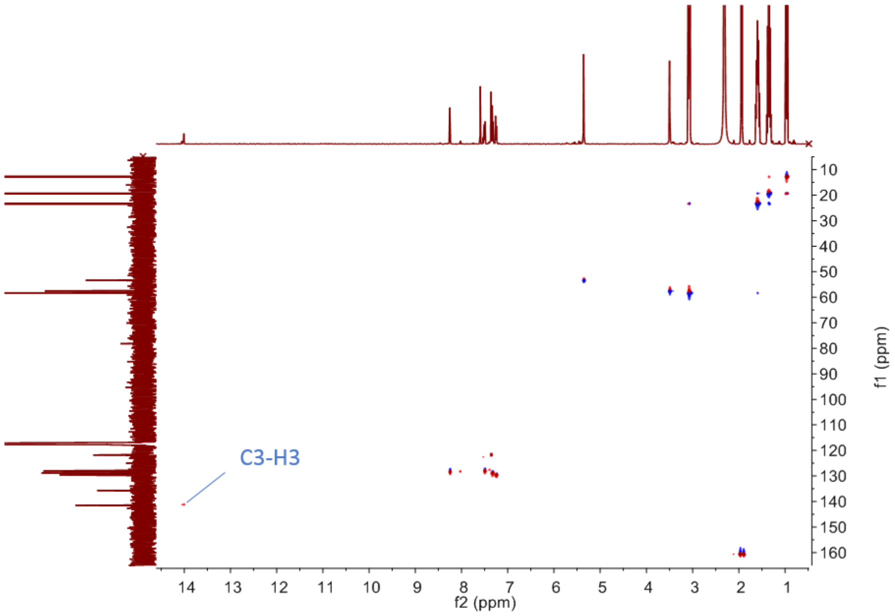

Figure 5.21. ^{1}H – ^{13}C HSQC NMR spectrum of **96**·F$^-$ spectrum to evidence the correlation between the proton shift H3 (14.00ppm) and a carbon resonance at 141.5 ppm.

higher equivalents no coupling was observed in either of the spectra. This difference between the two systems could be attributied to size and flexibility of the host. The smaller cavity of **164**, which can only fit the smallest halide F^-, can provide a tighter cavity a the anion is trapped and locked in the centre of the cavity. On the other hand, the larger cavity of **96**, which can fit larger halides, and has higher flexibility, could not block the anion in the same way.

A behaviour more similar to the case of tripodal ligand **165** was considered.[38] As discussed earlier, this ligand would first bind to one F^- ion between 0→1 equivalents, while the formation of HF_2^- ion would occur at higher equivalents by deprotonation of one of the binding moiety in the ligand and encapsulation of a second F^- ion, according to equations 5.1 and 5.2.

Equation 5.1 $MH_3^{3+} + F^- \rightleftharpoons [MH_3\cdots F]^{2+}$ $K_{1:1}$

Equation 5.2 $[MH_3\cdots F]^{2+} + F^- \rightleftharpoons MH_2^{2+} + HF_2^-$ $K_{1:2}$

This behaviour involves the formation of two species and the formation of bifluoride ion. The initial binding of one F^- anion within the cavity, would justify the changes observed in the resonances upon the binding of the first equivalent, with the rearrangement of the cage, in a similar manner as with the other halides. The flexibility of the cage and the larger cavity could cause a fast exchange and a 'delocalisation' of the anion which results in the broadening and subsequent absence of the H3 resonances in the ^1H NMR spectrum. The addition of a second equivalent of F^- caused the reappearance of H3 at very low fields (14 ppm). The formation of the HF_2^- ion is usually characterised by the appearance of a resonance at *ca*. 16 ppm, which was not observed in this case, excluding the presence of free HF_2^- in solution. This resonance could be consistent with the formation of HF_2^- in a more shielded environment, *i.e.* inside the cage. Moreover, in ^1H-^{13}C HSQC NMR, Figure 5.21, a crosspeak between resonance at 14.0 ppm on the ^1H NMR spectrum and a carbon resonance at 141.5 ppm was observed, meaning the direct connectivity between the ligand carbon network and H3. This confirmed that the resonance was not that of free HF_2^-, however it could not be excluded that it belonged to the same ion encapsulated within the cage.

The solution of **96** and 3 equivalents of F^- was analysed by DOSY NMR, and revealed that the diffusion coefficient (D) of the species in solution was $D = 2.13 \times 10^{-9}\ m^2s^{-1}$, which was larger than that observed for the free cage and for the **96**·Cl^- complex (full spectrum in Appendix A5, Figure A5.23). The hydrodynamic radius of the species calculated from this diffusion coefficient corresponded to 3.02 Å, which indicated a stronger compression of the cage, than that observed in the binding with Cl^- (Section 5.5.1). Analysis of the same solution by ^{19}F NMR did not show the presence of either free F^- or HF_2^-, which was surprising, considering that even if one or two equivalents of anions were bound to cage, the third equivalent should be visible as a free F^- in solution. However, only the resonances of PF_6^- counterions were visible in the ^{19}F NMR spectra (spectrum in Appendix A5, Figure A5.24).

It could not be confirmed yet, on the basis of these studies, whether the binding is occurring through a similar mechanism as the one observed for the tripodal ligand **165**. However, the data could not be fitted to a 1:1 model, while a 1:1 and 1:2 model could better fit the data, Figure 5.20, even if the large binding constants did not allow the determination of precise values ($K_{1:1} > 10^7\ M^{-1}$, $K_{1:2} > 10^4\ M^{-1}$). The speciation diagram, Figure 5.20b-inset, shows the presence of the 1:1 species in over 80% in the presence of one equivalent of F^-, while the 1:2 species would be formed in over 90% at two equivalents, reaching 100% within the addition of three equivalents of anion. Even the values of the binding constants were comparable to those observed for the tripodal benzimidazole compound **165**. The binding to two F^- ions would also agree with the studies in the UV-vis absorption spectroscopy carried out by Amendola (Section 5.4) which showed the isotherm reaching a plateau after the addition of two equivalents of anion. In this case, the HRMS analysis did not provide evidence for the formation of a complex with either F^- or HF_2^-, however did not exclude the possibility of their formation. Additional NMR studies, combining ^{19}F and ^1H are being considered to try and confirm the nature of the complex formation with F^- and HF_2^-.

A strong binding of the cage with F^- was indicated by both ^1H NMR and 2D NMR, as well as DOSY NMR analysis, indicating the formation of a complex, potentially with the formation of two species, 1:1 and 1:2. The 1:2 species is more likely to be the complex of **96** with HF_2^- rather than two discrete F^- ions being encapsulated.[38] The formation of HF_2^- within the cage, with the contribution of the proton from one of the acidic imdiazolium CHs, indicated that an intermediate situation between hydrogen bonding and full deprotonation is occurring, which is favoured by the 'trapping' of the anions within the cage cavity.

5.6. Conclusions

^1H NMR binding studies were carried out on the tris(imidazolium) cage **96** with halides and were able to confirm binding abilities of **96** highlighted by the studies carried out in Italy. Furthermore, these studies provided additional information and created a more complete picture of the binding ability. All the halides interactions with cage **96** caused a significant

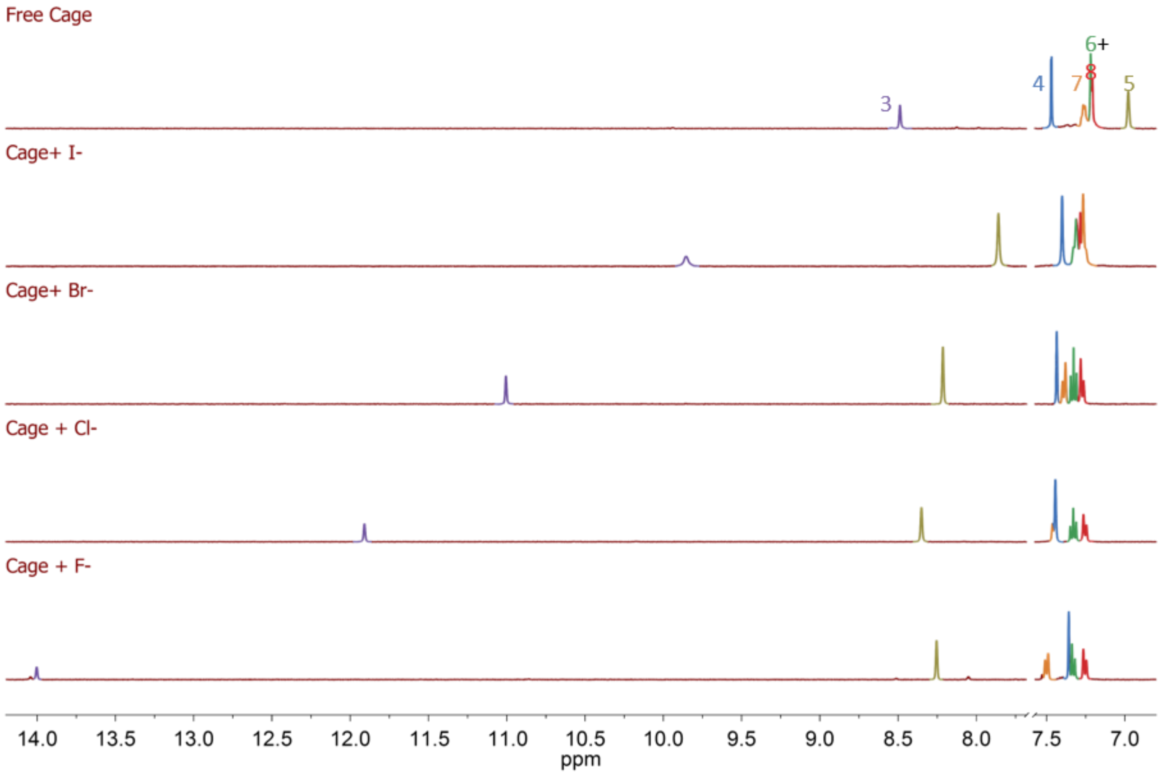

Figure 5.22. Stacked spectra of free cage **96** and complex with the different halides (6 equivalents of anion), full spectrum in Appendix, Figure A5.25.

deshielding of the imidazolate proton H3 and in the aromatic H5 proton, as well as a deshielding of the other aromatic protons which would result in a finer resolution of the resonances in the host-guest complex of the cage with the anion than in the free cage. In most cases, the shift of the resonances would reach a plateau after the addition of 2 equivalent of the corresponding anion. The only exception was that of proton H3 in the presence of F^- which only reached the plateau after the addition of 2 equivalents, suggesting a different binding was occurring, possibly involving the formation of the HF_2^- ion within the cage cavity.

The changes observed in the ^1H NMR of cage **96** proton resonances were consistent within the different anions and showed a size-dependence trend, Figure 5.22, were of reduced intensity as the size if the anion increased, showing a size and a charge-distribution dependence of the binding. The binding constants were in all cases too large to be calculated reliably with this technique, however, they were consistent with the UV-vis absorption spectroscopy studies carried out by collaborators in Italy.

Additional NMR studies on **96**·Cl^- allowed comparison of the solid-state and solution structures. By NOESY, similarities were determined between the conformation of the free cage and the complex **96**·Cl^- in the solid-state and in CD_3CN solution, while by DOSY NMR the formation of a new species was proven through different diffusion coefficient for **96**·Cl^-, D = 9.4×10^{-10} m^2/s, and for the free cage, D = 8.6×10^{-10} m^2/s. Therefore, thanks to these analyses it was possible to demonstrate that cage **96** was indeed able to bind all halides by encapsulation, with a size selection towards the anions with smaller ionic radius.

Additional experiments, such as DOSY NMR on complexes with Br^-, I^- and F^-, which have not been carried out on cage **96** due to time and material availability restriction, could be an interesting follow up of the research carried out to date, to study how the change in the hydrodynamic radius is affected by the size of the anion captured. Furthermore, it would be interesting to study the binding of the cage with oxyanion with geometries different from the spherical one, such as phosphates and sulfate, but solubility issues will need to be addressed in this case. As was briefly mentioned in section 5.5, preliminary tests in DMSO-d_6 showed poor solubility of the ligand, however, other solvents, such as CD_3CN or mixture of CD_3CN:H_2O could be used to test the binding with such anions.

Overall, the studies presented in this chapter were able to highlight the strong binding abilities of the tris(imidazolium) cage **96** which showed the strongest binding with halides among the structures discussed in the previous chapters. The studies were carried out in CD_3CN, a less competitive solvent than DMSO-d_6, used for other structures (tripodal tris(urea)in Chapter 2, catenane and macrocycles in Chapter 4), which favoured the formation of hydrogen bonding interactions. However, the presence of hydrogen bonding moiety with an additional positive charge, evidently introduced a favourable factor to improve the binding affinity by adding a strong electrostatic component. The future developments of this structure will include in-depth studies for the understanding of the F^- complexes, as well as studies of the binding with more complex anions, such as trigonal or tetrahedral oxyanions. There will be interest to understand the influence of the preorganisation of the hydrogen donor moieties on the binding of more complex structures, similarly to the studies carried out in the previous chapters, which highlighted a preference for oxyanions over spherical halide anions.

6. Experimental Details

6.1. General Experimental Details

6.1.1. Materials and Methods

All solvents and chemicals were purchased from commercial sources and used without further purification. Deuterated solvents used for NMR analysis (CD_3CN, DMSO-d_6) were purchased and used as received. Silica chromatography was carried out on a Teledyne Isco CombiFlash automated machine using pre-packed RediSep® cartridges. Infrared spectra were recorded on a Perkin Elmer Spectrum One FT-IR spectrometer fitted with a universal ATR sampling accessory. Melting points were determined using an Electrothermal IA9100 digital melting point apparatus. Where applicable, elemental analysis (CHN) was carried out by the School of Chemistry, University College Dublin.

6.1.2. Mass Spectroscopy

Mass spectrometry was completed in the departmental mass spectrometery service of the School of Chemistry, Trinity College Dublin. Electrospray mass spectra were measured on a Micromass LCT spectrometer calibrated against a leucine enkephaline standard. MALDI Q-ToF mass spectra were recorded on a MALDI Q-TOF Premier (Waters Corporation, Micromass MS Technologies, Manchester, UK) and high-resolution mass spectrometer was performed using Glu-Fib as an internal reference (m/z = 1570.677).

6.1.3. Dynamic light scattering

DLS measurements were made from back scatter in using Malvern Instrument Zetasizer Nano Series at 25° C in quartz cuvette with a path length of 10 mm. Statistical distribution by intensity were determined using the instrument software with standard deviations determined from triple replicate measurements. Samples were prepared using HPLC grade CH_3OH and H_2O filtered six times through a 0.45 μm syringe filters (Acrodisk®, PTFE).

6.2. UV-vis absorption studies

UV-visible absorption spectra were recorded using a Varian Cary 50 spectrophotometer, a spectroscopic window of 450 – 200 nm was used for all spectra with applied baseline correction from blank solvent. All UV-vis measurements were performed at 298 K in CH_3CN or DMSO:CH_3CN (spectroscopic grade) solutions. UV-vis absorption spectra were measured in 1 cm quartz cuvettes, except for the aggregation measurements for which 0.2 cm quartz cuvette was used. Baseline correction was applied for all spectra. Spectroscopic solutions were prepared from stock solutions using Pipetman® Classic micropipettes (Gilson, Inc).

6.2.1. Preparation of solutions for UV-vis titrations with anions

The TBA salts of the anions used in the titrations were of spectroscopic grade and were purchased from Sigma Aldrich. All TBA salts were dried over P_2O_5 at room temperature under vacuum. Solutions of these salts were prepared at varying concentrations of *ca*. 0.1 M, 5×10^{-2} M, 1×10^{-2} M and 1×10^{-3} M. Host solutions of *ca*. 1×10^{-3} M were prepared and then diluted before titration (*ca*. 1×10^{-5} M).

6.2.2. UV-vis titration data fitting

The data obtained were fitted using a non-linear regression analysis software (SPECFIT)[162] a software that employs global analysis to fit each individual wavelength isotherm simultaneously and, therefore, reflects the overall changes in the spectrum. An estimation of the species and the relative formation constant was input into the software, guided by previous results. The fitting algorithm then refined these values to provide the closest model (*i.e.* a weighted average of model components with the smallest overall residual error) that reflected the data. The choice of binding models and constants was made initially trying initial values that were similar to those obtained for similar systems (*i.e. para*-substituted family) for the binding of the same anions. When convergence of the data could be obtained, an evaluation of the resulting fitting was made based on the chemical and physical rationalisation of the binding model as well as the statistical parameter and overall residual error. When multiple binding models met these requirements, without additional evidence for specific species, the simplest model, with the lowest number of species was considered as preferred, in line accepted practice in supramolecular titration,[164] to avoid overfitting of the data.

6.3. ^{1}H NMR studies

The ^{1}H NMR spectra were recorded at either 400 MHz or 600 MHz on Bruker instruments (AV3-400 or AV2-600). ^{13}C NMR spectra were recorded, on the same instruments, at either 150.9 MHz or 100.6 MHz, while ^{19}F NMR spectra were recorded at 376.5 MHz. All ^{13}C NMR spectra were decoupled from ^{1}H, couplings to other nuclei are specified where appropriate. All spectra were recorded in commercially sourced per-deuterated solvents and referenced to residual proton signals of those solvents. Recorded free-induction decay signals were Fourier-transformed and processed using MestreNova v.6 without apodization and chemical shifts expressed in parts per million (ppm / δ) and coupling constants (J) in Hz. Residual solvent resonances were used as the internal reference, while 2D spectra were graphically referenced. All NMR spectra were carried out at 298 K.

6.3.1. Preparation of solutions for ^{1}H NMR titrations with anions

Spectroscopic solutions were prepared from stock solutions using Pipetman® Classic micropipettes (Gilson, Inc). The concentrations of these solutions were prepared in deuterated solvent such that 2 μL would give *ca*. 0.1 molar equivalents of the anion. Host solutions of 7×10^{-3} M were prepared by dissolving a known amount of host in 0.7 mL of deuterated solvent All measurements were performed at 25° C in CD_3CN. Receptors was titrated with a 100-fold more concentrate solution of the anion, as TBA^+ salt. After each addition of the titrant solution, the ^{1}H-NMR spectrum was recorded. TBA salts were dried in vacuum over P_2O_5. The ^{1}H NMR spectra were recorded at 400 MHz on Bruker instruments AV3-400.

6.3.2. ^{1}H NMR titration data fitting

The data obtained were fitted using a non-linear regression analysis software HypNMR[211,212] a software that employs global analysis to fit each resonance simultaneously, reflecting, therefore the overall changes in the spectrum. Additionally, the program is able to perform the simultaneous fitting of multiple repetitions of the same titration, in order to give a robust evaluation of the constant and the corresponding error. An estimation of the species and the relative formation constant was input into the software, guided by previous results. The fitting algorithm then refined these values to provide the closest model (*i.e.* a weighted average of model components with the smallest overall residual error) that reflected the data. The choice of binding models and constants was made initially trying initial values that were similar to those obtained for similar systems (*i.e. para*-substituted family) for the binding of the same anions. When convergence of the data could be obtained, an evaluation of the resulting fitting was made based on the chemical and physical rationalisation of the binding model as well as the statistical parameter and overall residual error. When multiple binding models met these requirements, without additional evidence for specific species, the simplest model, with the lowest number of species was considered as preferred, in line accepted practice in supramolecular titration,[164] to avoid overfitting of the data.

6.4. Scanning electron microscopy

Microscopy analysis of gel-aggregate samples by Scanning Electron Microscopy (SEM) was carried out under collaboration with Mr. Savyasachi A Jayanth and Ms. Amy D. Lynes from the Gunnlaugsson group and using the facilities of the Advanced Microscopy Laboratory (AML) in Trinity College Dublin. Samples were prepared by a drop-casting methodology onto clean silicon wafers (cleaned by sonication in HPLC-grade acetone followed by HPLC-grade propan-2-ol) from glass Pasteur pipettes.[147] The manually drop cast samples were dried overnight in ambient conditions (a week in the case of DMSO solutions) and under high vacuum for 2 hours prior immediately to their imaging. Samples were coated with a conductive Au layer, by sputtering, in order to improve contrast where static charging interfered with the imaging. Low kV SEM was carried out using the Zeiss ULTRA Plus using an SE2 detector.

6.5. Synthetic Procedures

6.5.1. Synthesis of ligands discussed in Chapter 2

N^1,N^3,N^5-trimethyl-N^1,N^3,N^5-tris(3-nitrophenyl)benzene-1,3,5-tricarboxamide (99)

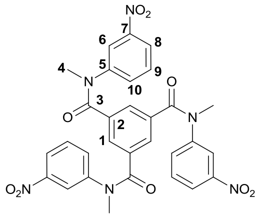

1,3,5-Benzenetricabonyl trichloride (0.250 g, 0.94 mmol, 1 eq.) was taken with N-methyl-3-nitroaniline (0.471 g, 3.10 mmol, 3.3 eq.) in CH_3CN (30 ml) and set at reflux for 48 hours. The reaction mixture was then cooled and solvent concentrated *in vacuo*, obtaining a honey coloured oil. The oil was dissolved in $CHCl_3$ and precipitated by addition of Et_2O. After a trituration in CH_3OH, **99** was obtained as a pale-yellow powder (0.547 g, 0.89 mmol, 95%). ^{1}H NMR (600 MHz, DMSO-d_6, δ) 8.14 (3H, t, J = 2.1 Hz, 6-H), 8.06 (3H, ddd, J = 8.2, 2.1, 0.8 Hz, 8-H), 7.49 (3H, t, J = 8.2 Hz, 9-H), 7.34 (3H, s, 10-H), 7.32 (3H, s, 1-H), 3.23 (9H, s, 4-H). ^{13}C NMR δ_C (151 MHz, DMSO-d_6) 167.9, 148.0, 144.7, 135.7, 133.5, 130.1, 128.7, 121.5, 121.2, 37.7. HRMS (m/z) (ES$^+$) Calculated for $C_{30}H_{24}N_6O_9Na^+$ m/z=635.1502 [M+Na]$^+$. Found m/z=635.1508 [M+Na]$^+$; FT-IR ν_{max} (ATR, cm^{-1}): 3457, 1650, 1610, 1525, 1440, 1350, 687. m.p.: 124-125° C.

N^1,N^3,N^5-tris(3-aminophenyl)-N^1,N^3,N^5-trimethylbenzene-1,3,5-tricarboxamide (100)

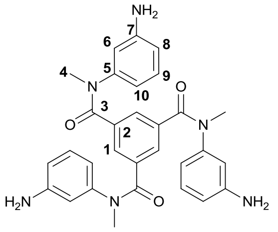

Compound **99** (0.147 g, 0.24 mmol, 1 eq.) was suspended in EtOH (15 ml) together with 10%Pd/C (0.030 g, 20% w/w) and hydrazine monohydrate (15 µL, 0.31 mmol, 1.3 eq.) was added, ensuring that the catalyst was fully suspended. The reaction was conducted under microwave irradiation for 50 minutes, at 95° C. The reaction mixture was filtered through a pad of celite and washed with a hot mixture of MeOH:CH_3CN in 1:1 ratio (250 ml). The solvent was dried and a brown oil obtained, which was dissolved in a 1:1 mixture of $CHCl_3$:MeOH. Upon addition of Et_2O to the solution, an off-white powder precipitated and was filtered under vacuum and washed with additional Et_2O to give **100** (0.104 g, 0.199 mmol, 82%). ^{1}H NMR (600 MHz, DMSO-d_6, δ) 7.06 (3H, s, 1-H), 6.88 (3H, t, J = 7.9 Hz, 9-H), 6.41 (3H, d, J = 7.9 Hz, 8-H), 6.33 (3H, s, 6-H), 5.71 (3H, br, 10-H), 5.28 (6H, s, NH_2), 3.16 (9H, s, 4-H). ^{13}C NMR (151 MHz, DMSO-d_6, δ) 167.7, 149.3, 144.7, 135.3, 129.4, 128.5, 114.8, 112.2, 111.2, 37.7. HRMS (m/z) (ES$^+$) Calculated for

$C_{30}H_{31}N_6O_3^+$ m/z=523.2458 [M+H]$^+$. Found m/z=523.2465 [M+H]$^+$; FT-IR ν_{max} (ATR, cm^{-1}): 3351, 2707, 1630, 1582, 1488, 1365, 1318, 700. m.p.: decomposed over 210°C

General procedure A for 86, 87, 88 and 89

The relevant tripodal aniline (1 eq.) was suspended in CH_3CN (40 mL) together with the relevant isocyanate (3.4 eq.) in a flask and stirred at reflux for 36 hours. The solvent was removed in vacuo and the product purified by flash column chromatography over silica in a gradient of CH_2Cl_2:CH_3OH.

N^1,*N*^{3},*N*^{5}-trimethyl- *N*^{1},*N*^{3},*N*^{5}-tris(3-(3-(4-(trifluoromethyl)phenyl)ureido)phenyl)benzene-1,3,5-tricarboxamide (86)

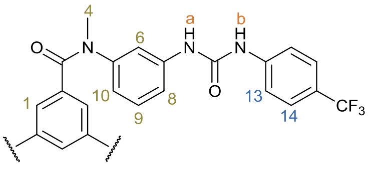

General procedure A. Compound **100** (0.062 g, 0.118 mmol, 1 eq.) was suspended in CH_3CN (40 ml) together with 4-(trifluoro-methyl)phenyl isocyanate (0.0883 g, 0.472 mmol, 4 eq.) in a microwave reactor and reacted at 100°C for 80 minutes. The reaction mixture was dried, redissolved in a EtOAc solution, then the crude product was precipitated upon addition of Et_2O and filtered. The pure receptor was obtained after silica automated chromatographic column, eluting with $CHCl_3$:CH_3OH increasing the gradient from 2% to 10%, yielding **86** as a white powder (0.101 g, 0.093 mmol, 79%). ^{1}H NMR (600 MHz, DMSO-*d*$_6$, δ) 9.17 (3H, s, NHa), 8.94 (3H, s, NHb), 7.64 (6H, d, *J* = 8.8 Hz, 13-H), 7.61 (6H, d, *J* = 8.8 Hz, 14-H), 7.46 (3H, s, 6-H), 7.25 (3H, d, *J* = 8.1 Hz, 8-H), 7.20 – 7.02 (6H, m, 1-H + 9-H), 6.22 (3H, br, 10-H), 3.18 (9H, s, 4-H). ^{13}C NMR (151 MHz, DMSO-*d*$_6$, δ): 167.9, 152.2, 144.3, 143.3, 140.2, 135.6, 129.3, 128.4, 126.0, 124.5 (q, $J_{C\text{-}F}$ = 271 Hz, C-16), 121.9 (q, $J_{C\text{-}F}$ = 32 Hz, C-15), 121.0, 117.9, 116.5, 116.2, 37.8. ^{19}F NMR δ_F (376 MHz, DMSO-*d*$_6$) -60.1 (CF_3). HRMS (m/z) (MALDI$^-$) Calculated for $C_{54}H_{41}F_9N_9O_6^-$ m/z=1082.3036 [M-H]$^-$. Found m/z=1082.2952 [M-H]; FT-IR ν_{max} (ATR, cm^{-1}): 3458, 3323, 1595, 1542, 1365, 1330, 1217. Elemental Analysis: calculated for $C_{54}H_{42}F_9N_9O_6\cdot 2H_2O$, %C = 57.9, %H = 4.1, %N = 11.3. Found %C = 57.6, %H = 3.7, %N = 11.2. m.p.: 201-204°C

N^1,*N*^{3},*N*^{5}-tris(3-(3-(2,4-difluorophenyl)ureido)phenyl)-*N*^{1},*N*^{3},*N*^{5}-trimethylbenzene-1,3,5-tricarboxamide (87)

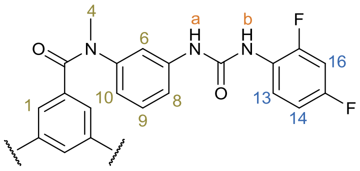

General procedure C. Compound **100** (0.190 g, 0.364 mmol, 1 eq.) was suspended in CH_3CN (40 ml) together with 2,4-difluorophenyl isocyanate (0.186 g, 1.19 mmol, 3.3 eq.) and stirred under reflux for 5 days. The reaction mixture was dried, redissolved into CH_3OH:$CHCl_3$ (1:1), then the crude compound was precipitated upon addition of Et_2O and filtered. Compound **87** was obtained pure as a white powder (0.097 g, 0.098 mmol, 27%). ^{1}H NMR (600 MHz, DMSO-d_6, δ) 9.09 (3H, s, NHa), 8.50 (3H, s, NHb), 8.04 (3H, dd, *J* = 15.3, 9.1 Hz, 13-H), 7.42 (1H, s, 6-H), 7.29 (3H, dd, *J* = 9.1, 8.1 Hz, 16-H), 7.23 (3H, d, *J* = 8.1 Hz, 8-H), 7.13 – 7.09 (6H, m, 1-H + 9-H), 7.02 (3H, dd, *J* = 15.3 Hz, 9.1 Hz, 14-H), 6.22 (3H, br, 10-H), 3.17 (9H, s, 4-H). ^{13}C NMR (150 MHz, DMSO-d_6, δ) 167.8, 156.9 (dd, $J_{C\text{-}F}$ = 242, 12 Hz), 152.3 (dd, $J_{C\text{-}F}$ = 245, 12 Hz), 152.2, 144.3, 140.2, 135.6, 129.3, 128.4, 123.8 (d, $J_{C\text{-}F}$ = 11 Hz), 122.2 (d, $J_{C\text{-}F}$ = 9 Hz), 120.8, 111.0 (d, $J_{C\text{-}F}$ = 22 Hz), 103.9 – 103.6 (m), 37.8. ^{19}F NMR (376 MHz, DMSO-d_6, δ): -118.4, -125.0. HRMS (m/z) (MALDI$^-$) Calculated for $C_{51}H_{38}F_6N_9O_6^-$ m/z=986.2850 [M-H]$^-$. Found m/z=986.2567 [M-H]$^-$. FT-IR ν_{max} (ATR, cm^{-1}): 3326, 3087, 2974, 1712, 1599, 1543, 1487, 1431, 1360, 1304, 1184, 1134, 1099, 958. Elemental Analysis: calculated for $C_{51}H_{39}F_6N_9O_6 \cdot 1.5H_2O$, %C = 60.4, %H = 4.2, %N = 12.4. Found %C = 60.3, %H = 3.6, %N = 12.8. m.p.: 195-197°C

N^1,*N*^{3},*N*^{5}-trimethyl-*N*^{1},*N*^{3},*N*^{5}-tris(3-(3-(2-nitrophenyl)ureido)phenyl)benzene-1,3,5-tricarboxamide (88)

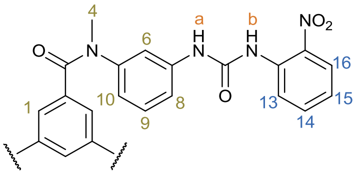

General procedure C. Compound **100** (0.149 g, 0.285 mmol, 1 eq.) was suspended in CH_3CN (40 ml) together with 3-nitrophenyl isocyanate (0.190 g, 1.158 mmol, 4 eq.) and reacted at reflux temperature for 6 days. The reaction mixture was cooled to RT, solvent dried and **88** was obtained as yellow powder through precipitation from CH_3OH. (0.090 g, 0.087 mmol, 31%). ^{1}H NMR (600 MHz, DMSO-d_6, δ) 9.93 (3H, s, NHa), 9.58 (3H, s, NHb), 8.29 (3H, d, *J* = 8.2 Hz, 13-H), 8.08 (3H, d, *J* = 8.2 Hz, 16-H), 7.68 (3H, t, *J* = 7.6 Hz, 15-H), 7.44 (3H, s, 6-H), 7.27 (3H, d, *J* = 7.8 Hz, 8-H), 7.20 (3H, t, *J* = 7.6 Hz, 14-H), 7.13 (6H, m, 1-H + 9-H), 6.26 (3H, s, 10-H), 3.18 (9H, s, 4-H). ^{13}C NMR (150 MHz, DMSO-d_6, δ) 167.8, 151.7, 144.3, 140.0, 137.6, 135.6, 135.0, 134.7, 129.3, 128.4, 125.4, 122.6, 122.4, 121.2, 116.6, 116.4, 37.8. HRMS (m/z) (ESI$^+$) Calculated for $C_{51}H_{42}N_{12}O_{12}Na^+$ m/z=1037.2943 [M+Na]$^+$. Found m/z=1037.2920 [M+Na]$^+$; FT-IR ν_{max} (ATR, cm^{-1}): 3458, 3331, 1628, 1599, 1550, 1367, 1269.Elemental Analysis: calculated for $C_{51}H_{42}N_{12}O_{12}Na_{0.6}Cl_{0.6} \cdot CH_3CN$, %C = 58.3, %H = 4.2, %N = 16.7. Found %C = 58.2, %H = 3.9, %N = 16.4. mp 183-184°C.

N^1,*N*^{3},*N*^{5}-trimethyl-*N*^{1},*N*^{3},*N*^{5}-tris(3-(3-(3-nitrophenyl)ureido)phenyl)benzene-1,3,5-tricarboxamide (89)

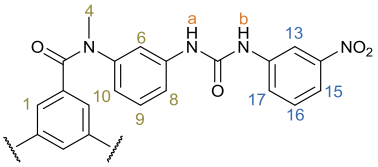

General procedure C. Compound **100** (0.200 g, 0.38 mmol) was suspended in CH_3CN (40 ml) together with 3-nitrophenyl isocyanate (0.216 g, 1.32 mmol) and stirred at reflux for 5 days. Compound **89** was obtained pure by filtration from the reaction mixture as a yellow powder (0.241 g, 0.238 mmol, 62%). ^{1}H NMR (600 MHz, DMSO-d_6, δ): 9.23 (3H, s, NHa), 8.93 (3H, s, NHb), 8.53 (3H, s, 13-H), 7.81 (3H, d, J = 8.1 Hz, 15-H), 7.70 (3H, d, J = 8.1 Hz, 17-H), 7.55 (3H, t, J = 8.1 Hz, 16-H), 7.47 (3H, s, 6-H), 7.27 (3H, d, J = 8.1 Hz, 8-H), 7.15 – 7.11 (6H, m, 1-H + 9-H), 6.24 (3H, br, 10-H), 3.20 (9H, s, 4-H). ^{13}C NMR (151 MHz, DMSO-d_6, δ) 167.9, 152.3, 148.1, 144.3, 140.8, 140.1, 135.6, 130.0, 129.3, 128.4, 124.4, 121.1, 116.7, 116.4, 116.4, 112.2, 37.8. HRMS (m/z) (MALDI$^-$) Calculated for $C_{51}H_{41}N_{12}O_{12}^-$ m/z=1013.2967 [M-H]$^-$. Found m/z=1013.2899 [M-H]$^-$. FT-IR ν_{max} (ATR, cm^{-1}): 3382, 3283, 3255, 3144, 2988, 1719, 1655, 1627, 1592, 1543, 1472, 1430, 1338, 1303, 1240, 1191, 1113, 888. Elemental Analysis: calculated for $C_{51}H_{42}N_{12}O_{12}\cdot0.4H_2O$, %C = 59.9, %H = 4.2, %N = 16.4. Found %C = 59.8, %H = 3.9, %N = 16.2. m.p.: decomposed over 250° C.

6.5.2. Synthesis of ligands discussed in Chapter 3

4-(*Tert*-butoxycarbonyl(methyl)amino)benzoic acid (114)

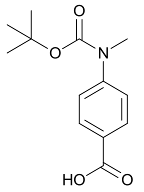

Ligand **114** was synthesised according with literature procedures[230]. A solution of di-tert-butyl dicarbonate (3.20 g) in dioxane (6 mL) was added, via an addition funnel, to a solution of 4-methylamino-benzoic acid (2.0 g, 0.013 mol) in 1 N aqueous sodium hydroxide (14 mL, 0.014 mol) and stirred at ambient temperature for 6 hours. Di-tert-butyl dicarbonate (1.1 g, 0.012 mol) in dioxane (2 ml) was added and stirring was continued for an additional 18 hours. After monitoring by TLC, which showed incomplete reaction, di-tert-butyl dicarbonate (0.5 g) in dioxane (1 ml) was added and stirring was continued an additional day. The solution was diluted with water (60 mL) and cooled on an ice bath. The solution was neutralized with 1 N hydrochloric acid, and the resultant precipitate was collected by filtration, washed with water and dried on the filter funnel, to give the product as a beige solid (2.8 g, 0.011 mol, 87%). ^{1}H NMR (400 MHz, DMSO-d_6, δ): 1.41 (s, 9 H), 3.22 (s, 3 H), 7.41 (d, 2 H), 7.89 (d, 2 H), 12.78 (br s, 1 H). ^{13}C NMR (100 MHz, DMSO-d_6, δ): 166.9, 153.3, 147.3, 129.7, 129.6, 126.8, 124.5, 124.3, 80.3, 36.6, 27.9. FT-IR υ_{max} (ATR, cm^{-1}): 2984, 2672, 2551, 1700, 1674, 1604, 1570, 1517, 1476, 1460, 1426, 1413, 1368, 1338, 1319, 1307, 1289, 1267, 1252, 1192, 1143, 1099, 950. HRMS-ESI (m/z): calculated for $C_{13}H_{17}NO_4^-$, m/z = 250.1079 [M-H]$^-$; found m/z = 250.1080. m.p.: 135-137 °C

Tert-butyl 4-(3-(4-(hexyloxy)phenyl)ureido)phenyl(methyl)carbamate (118)

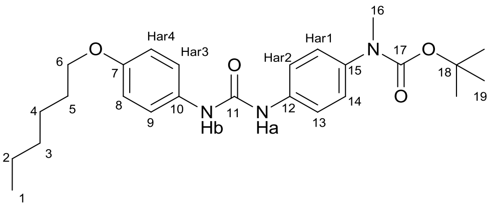

114 (0.411g, 1.6 mmol) was dissolved in CH_3CN and to it TEA (1.7 mmol) and DPPA (1.6 mmol) were added from a syringe stirring. The reaction was stirred at 41° C for one hour, then the reaction mixture was monitored with TLC (5% MeOH/DCM) against **114**. 4-Hexyloxy aniline (0.347 g, 1.7 mmol) was dissolved in 3 mL of CH_3CN and added to the reaction, which was then refluxed for 4 hrs. After cooling down to RT, water (10 ml) was added and the organic solvent was concentrated in vacuo. The aqueous solution was then extracted with EtOAc and dried by rotary evaporation. Flash column was run (increasing gradient of EtOAc in hexanes) on column machine. Compound **118** recrystallized from CH_3CN yielding the product as a white powder (0.642 g, 1.5 mmol, 91%). ^{1}H NMR (600 MHz, DMSO-d_6, δ): 8.57 (s, 1H), 8.42 (s, 1H), 7.39 (d, J = 8.2 Hz, 2H), 7.32 (d, J = 8.4 Hz, 2H), 7.14 (d, J = 8.3 Hz, 2H), 6.85 (d, J = 8.5 Hz, 2H), 3.90 (t, J = 6.4 Hz, 2H), 3.13 (s, 3H), 1.76 – 1.59 (m, 2H), 1.48 – 1.23 (m, 15H), 0.87 (d, J = 6.9 Hz, 3H). ^{13}C NMR (151 MHz, DMSO-d_6, δ): 153.95(17), 153.88(7), 152.71(11), 137.33(15), 137.24(12), 132.58(10), 125.91(14), 120.01(9), 118.09(13), 114.59(8), 79.21(18), 67.58(6), 37.20(16), 31.00(3), 28.72(5), 27.97(19), 25.20(4), 22.06(2), 13.90(1). FT-IR υ_{max} (ATR, cm^{-1}): 3298, 2958, 2925, 2868, 1706, 1634, 1606, 1554, 1509, 1478, 1432, 1391, 1355, 1301, 1242, 1150, 1108, 1052, 1025, 980, 932, 857, 836. HRMS-ESI (*m*/*z*): calculated for $C_{25}H_{35}N_3O_4Na^+$, *m/z* = 464.2525 [M+Na]$^+$; found *m/z* =464.2523. mp 104.1-106.1 °C.

1-(4-(hexyloxy)phenyl)-3-(4-(methylamino)phenyl)urea (113)

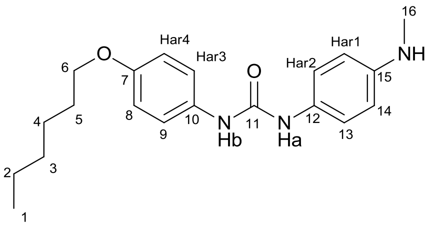

To a solution of **118** (0.578 g, 1.3 mmol) in CH_2Cl_2 (30 mL), TFA (5eq) was added and stirred for 24h at rt. The formation of product was followed by TLC, stained with ninhydrin. At the completion of the reaction, the solution was cooled down and $NaHCO_3$ sat solution was used to neutralise the acid, while stirring. When the acid was neutralised, the product precipitated in the organic phase. The layers were separated, and the product filtered. The remaining organic phase was dried with $MgSO_4$ and solvent removed under vacuum. The product was obtained by trituration with CH_3CN. Compound **113** was obtained as a white powder (0.204 g, 0.598 mmol, 46%). ^{1}H NMR (600 MHz, DMSO-d_6, δ): 8.24 (s, 1H), 8.05 (s, 1H), 7.29 (d, J = 8.9 Hz, 2H), 7.13 (d, J = 8.7 Hz, 2H), 6.82 (d, J = 8.9 Hz, 2H), 6.47 (d, J = 8.7 Hz, 2H), 5.29 (q, J = 5.0 Hz, 1H), 3.89 (t, J = 6.5 Hz, 2H), 2.63 (t, J = 8.2 Hz, 3H), 1.77 – 1.60 (m, 2H), 1.39 (dd, *J* = 14.4, 6.9 Hz, 2H), 1.34 – 1.19 (m, 4H), 0.88 (t, *J* = 6.8 Hz, 3H). ^{13}C NMR (100 MHz, DMSO-*d*$_6$, δ): 153.6, 153.2, 145.6, 133.1, 128.7, 120.7, 119.7, 114.6, 111.8, 67.6, 31.0, 30.2, 28.8, 25.2, 22.1, 13.9. FT-IR υ_{max} (ATR, cm^{-1}): 3342, 2933, 2864, 1706, 1674, 1609, 1549, 1507, 1412, 1309, 1218, 1035, 919, 830.

HRMS-ESI (*m*/*z*): calculated for $C_{20}H_{28}N_3O_2$, *m/z* = 342.2182 [M+H]$^+$; found *m/z* = 342.2177. m.p.: 186.6-187.6°C.

Dibenzyl 5-(methyl(4-nitrophenyl)carbamoyl)isophthalate (121)

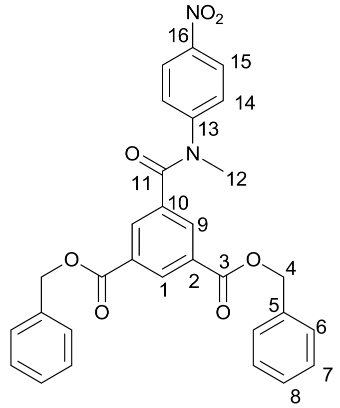

To a solution of 1,3,5-benzenetricarbonyl trichloride (3 g, 11.3 mmol) in dry dichloromethane/THF (90 mL, 8:1) mixture at −20 °C (ice and NaCl) were slowly [for about 1 h (syringe pump)] added benzyl alcohol (2.4 g, 2.3 mL, 22.6 mmol, 2 eq.) and triethylamine (4.7 mL, 33.9 mmol, 3 eq.) in dry CH_2Cl_2/THF (3 mL, 8:1) solution, and the resulting mixture was stirred for an additional 1 h, at −20 °C, then for the next 1h at rt.[179] After N-methyl-4-nitroaniline was added and the reaction refluxed overnight at 50°C. (N.B.: the reaction must be kept under Ar or some crystalline compound sublimes). The solution was cooled down and a white crystalline was separated. Additional compound was precipitated by addition of THF and filtered. NMR showed the peaks of TEA·HCl, and THF. The yellow filtered solution was dried with rotary evaporator, then dissolved in CH_2Cl_2 and loaded onto silica for solid loading and separated by flash chromatography, hexane/EtOAc with increasing gradient. **121** was obtained pure as a pale yellow powder (1.6 g, 3.0 mmol, 27%). ^{1}H NMR (400 MHz, DMSO-*d*$_6$, δ): 8.67 (s, 1H, H-1), 8.17 (s, 2H, H-9), 8.03 (d, *J*=8.6, 2H, H-15), 7.38 (s, 10H, H-6 + H-7 + H-8), 7.16 (d, *J*=8.6, 2H, H-14), 5.31 (s, 4H, H-4), 3.54 (s, 3H, H-12). ^{13}C NMR (100 MHz, DMSO-*d*$_6$, δ): 168.6(C-11), 164.6(C-3), 149.9(C-13), 145.7(C-16), 135.9(C-2), 135.4(C-5), 134.0(C-9), 132.7(C-1), 131.1(C-10), 128.8(C-Ph), 128.8(C- Ph), 128.6(C- Ph), 127.1(C-14), 125.0(C-15), 67.6(C-4), 38.5(C-12). FT-IR υ_{max} (ATR, cm^{-1}): 3117, 3067, 3034, 2951, 1714, 1641, 1591, 1515, 1497, 1451, 1377, 1342, 1300, 1229, 1195, 1105, 993, 949, 920, 856, 737, 692.

HRMS-ESI (*m*/*z*): calculated for $C_{30}H_{24}N_2O_7Na^+$, *m/z* = 547.1481 [M+Na]$^+$; found *m/z* = 547.1485. m.p. 113-115 °C.

5-((4-aminophenyl)(methyl)carbamoyl)isophthalic acid (123)

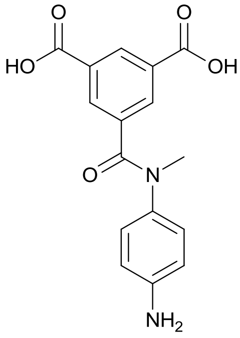

Pd/C (10 wt%) (0.075g, 20%wt) was taken in a three-necked flask filled with inert gas, to it CH_2Cl_2 was added and after CH_3OH was added carefully along the walls of the flask. Compound **121** (0.370 g, 0.705 mmol) was then added to the flask in a CH_2Cl_2 solution, then the flask was evacuated and filled with inert gas and stirred. Following, a hydrogen balloon was fitted with a tap to the flask, and, after evacuation of the flask, the tap was opened, and reaction started. After two hours the reaction was concluded according to TLC, the hydrogen balloon was disconnected, the flask backfilled with inert gas, then the solution filtered through a celite pad. Product obtained pure by evaporation of the solvent, under reduced pressure, as a beige solid (0.220 g, 0.700 mmol, 99%). ^{1}H NMR (400 MHz, DMSO-d_6, δ): 8.64 (s, 1H), 8.30 (s, 1H), 7.98 (s, 2H), 6.82 (d, J = 8.3 Hz, 2H), 6.38 (d, J = 8.3 Hz, 2H), 3.30 (s, 3H), 3.17 (s, 2H). ^{13}C NMR (100 MHz, DMSO-d_6, δ): 167.8, 166.0, 145.2, 137.8, 132.8, 130.8, 130.2, 128.0, 115.3, 48.6, 38.1. FT-IR υ_{max} (ATR, cm^{-1}): 3358, 2922, 2852, 2567, 1707, 1613, 1538, 1513, 1443, 1374, 1263, 1233, 1190, 1134, 1108, 1016, 918. HRMS-ESI (*m/z*): calculated for $C_{16}H_{15}N_2O_5$, *m/z* = 315.0975 [M+H]$^+$; found *m/z* = 315.0978. m.p.: 190-191 °C.

5-((4-(*tert*-butoxycarbonylamino)phenyl)(methyl)carbamoyl)isophthalic acid (124)

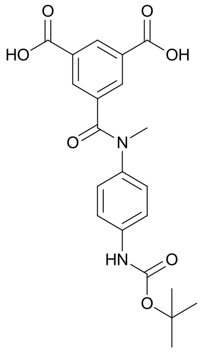

A solution of **123** (0.080 g, 0.25 mmol) was taken in dry THF and to it Boc_2O (0.5 mmol, 2 equiv) was added as crystals. The solution was stirred overnight and gently heated at 40ºC. After completion, the solvent was dried and the mixture was dissolved with EtOAc (30 mL) and washed with brine (2 x 20 mL). the organic phase was dried over anhydrous $MgSO_4$ then the solvent removed, yielding the Boc-protected compound as a beige solid (0.031 g, 0.015 mmol, 30%). The product was used without further purification. ^{1}H NMR (400 MHz, DMSO-d_6, δ): 13.34 (br s, 1H), 9.35 (s, 1H), 8.31 (s, 1H), 7.99 (s, 1H), 7.32 (d, J = 8.3 Hz, 1H), 7.10 (d, J = 8.3 Hz, 1H), 1.44 (s, 5H). ^{13}C NMR (151 MHz, DMSO-d_6, δ): 206.5, 167.8, 165.9, 162.3, 152.6, 138.1, 137.9, 137.4, 132.8, 131.0, 130.4, 127.5, 118.3, 110.9, 79.2, 66.9, 48.6, 31.3, 30.7, 28.1.FT-IR υ_{max} (ATR, cm^{-1}): 3318, 2973, 2931, 2568, 1703, 1630, 1518, 1435, 1412, 1367, 1314, 1234, 1159, 1055, 1025, 948. HRMS-ESI (*m/z*): calculated for $C_{21}H_{22}N_2O_7Na^+$, *m/z* = 437.1319 [M+Na]$^+$; found *m/z* = 437.1309. m.p.: decomposed over 220 °C.

Boc-protected bis(4-hexyloxyphenylurea) dipodal (112)

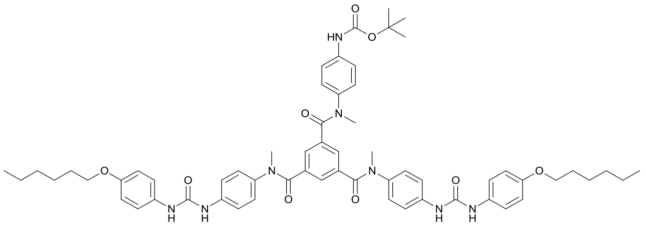

Compound **124** (0.121 g, 0.29 mmol, 1 equiv) was suspended in DCM and cooled to 0° C. To the solution TEA (0.58 mmol, 2 equiv) was added then EDC HCl (0.58 mmol, 2 equiv) and DMAP (0.58 mmol, 2 equiv) while stirring, the solution became clear. Then a suspension of **113** (0.200 g, 0.58 mmol, 2 equiv) was added carefully to it, still at 0° C, and the solid dissolved. The mixture was stirred at 0° C for 1 hr, then at RT over the weekend. The solution was then washed with (2×10ml) of $NaHCO_3$ sat. solution, (2×10ml, 0.5M) citric acid, and (10 ml) deionised water. The organic layer was dried over $MgSO_4$ and evaporated by rotary evaporation. Compound **124** was recovered crude as a glassy solid and was further purified by column chromatography (gradient of CH_3OH in $CHCl_3$) obtaining the desired product as an off-white powder (0.015 g, 0.014 mmol, 5%). HRMS-ESI (*m*/*z*): calculated for $C_{61}H_{72}N_8O_9Na^+$, *m/z* = 1083.5320 $[M+Na]^+$; found *m/z* = 1083.5336. ^1H NMR (400 MHz, DMSO-*d*$_6$, δ): 9.33 (s, 1H), 8.60 (s, 2H), 8.49 (s, 2H), 7.37 (m, 6H), 7.31 (m 6H), 6.96 (s, 2H), 6.80 (m, 5H), 6.75 (s, 2H), 3.86 (m, 5H), 3.27 – 3.14 (m, 7H), 1.78 – 1.53 (m, 5H), 1.41 (m, 12H), 1.41 – 1.35 (m, 4H), 1.35 – 1.24 (m, 11H), 0.87 (m, 6H). ^{13}C NMR (151 MHz, DMSO-*d*$_6$, δ): 154.0, 153.9, 153.5, 153.2, 152.8, 137.3, 132.7, 128.7, 127.0, 125.9, 120.7, 120.1, 120.0, 119.7, 119.5, 118.1, 114.6, 111.8, 79.2, 67.6, 37.2, 31.0, 30.2, 28.8, 28.0, 25.2, 25.2, 22.1, 22.1, 13.9, 13.9.

Bis(4-hexiloxyphenylurea) dipodal (85)

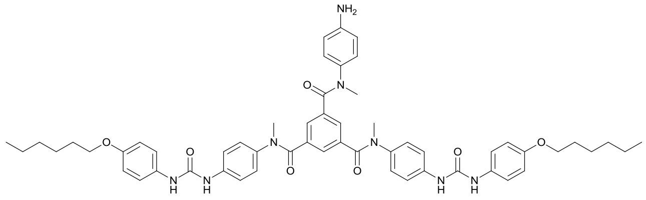

To a solution of **112** in CH_2Cl_2 (30 mL), TFA (5 eq) was added and stirred for 24h at rt. The formation of product was followed by TLC, stained with ninhydrin. At the completion of the reaction, the solution was cooled down and a solution of $NaHCO_3$ (saturated) was used to neutralise the acid, while stirring. When the acid was neutralised, the product precipitated in the organic phase. The layers were separated, and the product filtered. The remaining organic phase was dried with $MgSO_4$ and solvent removed under vacuum yielding **85** (0.0028 g, 0.003 mmol, 20%). HRMS-ESI (*m*/*z*): calculated for $C_{56}H_{64}N_8O_7Na^+$, *m/z* = 983.4796 $[M+Na]^+$; found *m/z* = 983.4801. ^1H NMR (600 MHz, DMSO-*d*$_6$, δ): 8.60 (s, 1H), 8.49 (s, 1H), 7.40 (d, *J* = 7.4 Hz, 2H), 7.37 – 7.27 (m, 3H), 6.91 (s, 1H), 6.86 – 6.75 (m, 2H), 6.69

(d, *J* = 7.4 Hz, 1H), 6.47 (m, 2H), 5.06 (s, 1H), 3.88 – 3.77 (m, 2H), 3.29 – 3.22 (m, 2H), 3.21 – 2.98 (m, 3H), 1.76 – 1.59 (m, 3H), 1.48 – 1.34 (m, 3H), 1.34 – 1.24 (m, 6H), 0.87 (m, 4H). ^{13}C NMR (151 MHz, DMSO-d_6, δ): 168.0, 153.9, 152.7, 132.4, 127.6, 127.2, 120.7, 120.2, 119.7, 118.6, 114.5, 114.0, 111.8, 67.5, 31.0, 28.7, 25.2, 22.1, 13.9.

Bis(4-CF_3phenylthiourea) dipodal (90)

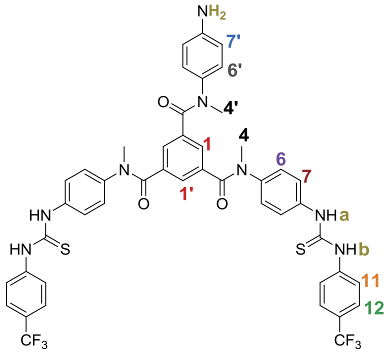

Compound **84** (0.030 g, 0.057 mmol, 1 eq.) was suspended in CH_3CN (40 mL) together with the 4-trifluoromethylphenyl isothiocyanate (2.2 eq.) in a flask and stirred at 60 °C for 36 hours. The dipodal **90** precipitated in the reaction flask as a white powder from which it was filtered. Trituration with CH_3CN gave **90** as an off-white powder (0.024 g, 0.028 mmol, 45%).^{1}H NMR (400 MHz, DMSO-d_6, δ 10.09 (s, 2H, urea NH), 10.00 (s, 2H, urea NH), 7.72 (d, *J* = 8.7 Hz, 4H, ArH), 7.68 (d, *J* = 8.7 Hz, 2H, ArH), 7.62 (d, *J* = 8.7 Hz, 4H, ArH), 7.58 (d, *J* = 8.7 Hz, 2H, ArH), 7.46 (d, *J* = 8.6 Hz, 6H, ArH), 7.00- 6.85(m, 4H, ArH) 6.52,(br s 1H, 1') 6.46 ,(m, 2H, 1), 5.08 (s, 2H, NH_2), 3.20 (m, 9H, 4+4'). ^{13}C NMR (151 MHz, DMSO-d_6, δ): 179.6, 167.8, 155.9 147.2, 143.2, 140.3, 137.7, 137.4, 127.9, 126.9, 125.5, 124.3, 122.8, 113.8, 37. 8, 37.6. FT-IR υ_{max} (ATR, cm^{-1}): 3318, 3231, 3033, 1626, 1509, 1448, 1369, 1332, 1284, 1248, 1165, 1110, 1066, 1015, 904, 840, 720, 670. HRMS-ESI (*m*/*z*): calculated for $C_{46}H_{37}F_6N_8O_3S_2$, *m/z* = 927.2340 $[M-H]^-$; found *m/z* = 927.2344. m.p.: decomposed over 230 °C.

6.5.3. Synthesis of ligands discussed in Chapter 4

General procedure B for Open ligands 149, 149 and 149

Compound **127** (0.20 g, 0.42 mmol) was suspended in 4 mL of $SOCl_2$ and heated to 80 °C for 18 hours under a $CaCl_2$ guard tube. $SOCl_2$ was removed by vacuum distillation and the acid chloride suspended in dry CH_2Cl_2 (10 mL) and used without further purification. An excess of the relevant α-amino-ω-alkene (1 mL) was added and the reaction stirred at room temperature for 18 hours under a $CaCl_2$ guard tube. The reaction mixture was concentrated under reduced pressure and triturated with CH_3OH.

Open ligand 149[a]

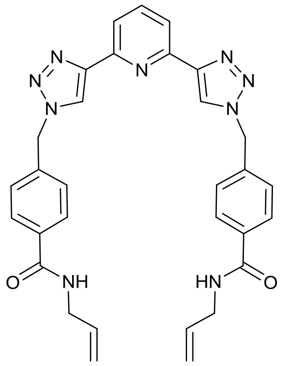

Ligand **149** was synthesized according to the general procedure B from 2,6-Bis(1-(4-(carboxy)benzyl)-1,2,3-triazol-4-yl)pyridine and allyl amine. The product was collected as a white solid upon filtration (0.143 g, 0.26 mmol, 61%). HRMS (*m/z*) (ESI$^+$): Calculated for $C_{31}H_{30}N_9O_2^+$ *m/z* = 560.2522 [M+H]$^+$. Found *m/z* = 560.2547; Calculated for $C_{31}H_{29}N_9O_2Na^+$ *m/z* = 582.2342 [M+Na]$^+$. Found *m/z* = 582.2375; Calculated for $C_{62}H_{58}N_{18}O_4Na^+$ *m/z* = 1141.4785 [2M+Na]$^+$. Found *m/z* = 1141.4424; Calculated for $C_{31}H_{29}N_9O_2\cdot0.5H_2O$, C = 61.98, H = 5.03, N = 20.99. Found C = 61.84, H = 4.70, N = 20.58; ^{1}H NMR (600 MHz, DMSO-*d*$_6$, δ): 3.90 (app t, 4H, NHCH$_2$), 5.05–5.19 (m, 4H, terminal olefin CH$_2$), 5.77 (s, 4H, CH$_2$), 5.84–5.93 (m, 2H, olefin CH), 7.43 (d, 4H, *J* = 8.2 Hz, Ph CH), 7.88 (d, 4H, *J* = 8.2 Hz, Ph CH), 7.98 (m, 3H, pyr CH), 8.66 (br t, 2H, *J* = 5.5 Hz, NH, assigned by NH COSY), 8.71 (s, 2H, triazolyl CH); ^{13}C NMR (150 MHz, DMSO-*d*$_6$, δ): 41.8 (NHCH$_2$), 53.0 (methylene CH$_2$), 115.4 (terminal olefin CH$_2$), 118.9 (pyr CH), 124.1 (triazolyl CH), 128.0 (Ph CH), 128.1 (Ph CH), 134.6 (Ph qt), 135.7 (olefin CH), 138.7 (pyr CH), 139.2 (Ph qt), 147.7 (triazolyl qt), 150.1 (pyr qt), 165.9 (C=O qt); FT-IR υ_{max} (ATR, cm^{-1}): 3314 (N–H, s), 3116, 3078, 2913, 1642 (s, amide C=O), 1575, 1545, 1505, 1454, 1448, 1418, 1340, 1324, 1307, 1235, 1198, 1139, 1055, 1013, 999, 933, 842, 843, 806, 768, 725, 692, 671. m.p.: 225–227 °C.

Open ligand 150[a]

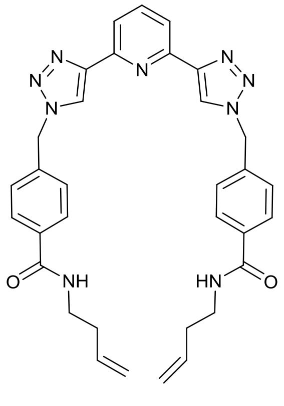

Ligand **150** was synthesized according to the general procedure B from from 2,6-Bis(1-(4-(carboxy)benzyl)-1,2,3-triazol-4-yl)pyridine and but-3-en-1-amine. The product was collected as a white solid upon filtration (0.045 g, 0.08 mmol, 18%). HRMS (*m/z*) (ESI$^+$): Calculated for $C_{33}H_{34}N_9O_2^+$ *m/z* = 588.2835 [M+H]$^+$. Found *m/z* = 588.2825; Calculated for $C_{33}H_{33}N_9O_2Na^+$ *m/z* = 610.2655 [M+Na]$^+$. Found *m/z* = 610.2689; Calculated for $C_{66}H_{66}N_{18}O_4Na^+$ *m/z* = 1197.5412 [2M+Na]$^+$. Found *m/z* = 1197.5414; Calculated for $C_{33}H_{33}N_9O_2\cdot0.5H_2O$, C = 66.43, H = 5.74, N = 21.13. Found C = 66.06, H = 5.51. N = 20.79; ^{1}H NMR (600 MHz, DMSO-*d*$_6$, δ): 2.28 (app q, 4H, butenyl CH$_2$), 3.32 (4H, butenyl CH$_2$ [overlaps with H$_2$O peak; assigned by 2D experiments]), 4.99–5.10 (m, 4H, terminal olefin CH$_2$), 5.77 (s, 4H, CH$_2$), 5.78–5.86 (m, 2H, olefin CH), 7.43 (d, 4H, *J* = 8.3 Hz, Ph CH), 7.84 (d, 4H, *J* = 8.3 Hz, Ph CH), 7.95–8.03 (m, 3H, pyr CH), 8.48 (t, 2H, *J* = 5.6 Hz, NH, assigned by NH COSY), 8.70 (s, 2H, triazolyl CH); ^{13}C NMR (150 MHz, DMSO-*d*$_6$, δ): 33.4

(butenyl CH_2), 38.6 (butenyl CH_2), 52.7 (methylene CH_2), 116.2 (terminal olefin CH_2), 118.5 (pyr CH), 123.7 (triazolyl CH), 127.6 (Ph CH), 127.7 (Ph CH), 134.5 (Ph qt), 136.0 (olefin CH), 138.3 (Ph qt), 138.7 (pyr CH), 147.4 (triazolyl qt), 149.8 (pyr qt), 165.6 (C=O qt); FT-IR υ_{max} (ATR, cm^{-1}): 3331 (br), 3175, 3080, 2935, 1635 (s, amide C=O), 1609, 1575, 1538, 1507, 1462, 1438, 1426 (s), 1315, 1238, 1212, 1198, 1151, 1080, 1045, 1021, 993, 980, 907, 862, 843, 800, 788 (s), 756, 740. m.p.: 223–229 °C.

Open ligand 151[a]

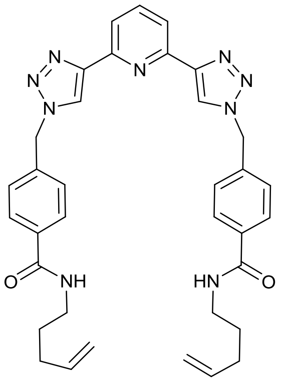

Ligand **151** was synthesized according to the general procedure B from from 2,6-Bis(1-(4-(carboxy)benzyl)-1,2,3-triazol-4-yl)pyridine and pent-4-en-1-amine The product was collected upon filtration as a white, or off-white solid. Quantitative yield. HRMS (*m/z*) (ESI^+): Calculated for $C_{35}H_{38}N_9O_2Na^+$ *m/z* = 638.2974 $[M+Na]^+$. Found *m/z*= 638.2962; Calculated for $C_{70}H_{74}N_{18}O_4Na^+$ *m/z* = 1253.6056 $[2M+Na]^+$. Found *m/z* = 1253.6032; Calculated for $C_{35}H_{37}N_9O_2\cdot0.5H_2O$, C = 67.29, H = 6.13, N = 20.18. Found C = 66.90, H = 5.87, N = 19.86; ^1H NMR (600 MHz, DMSO-d_6, δ): 1.60 (dt, 4H, *J*=14.5, 7.2 Hz, pentenyl CH_2), 2.06 (dd, 4H, *J*=14.5, 7.0 Hz, pentenyl CH_2), 3.26 (dd, 4H, *J*=13.1, 7.0 Hz, pentenyl CH_2), 4.93–5.08 (m, 4H, terminal olefin CH_2), 5.77 (s, 4H, methylene CH_2), 5.78–5.90 (m, 2H, olefin CH), 7.43 (d, 4H, *J*=8.2 Hz, Ph CH), 7.85 (d, 4H, *J*=8.2 Hz, Ph CH), 7.95–8.05 (m, 3H, pyr CH), 8.46 (br t, 2H NH, assigned by NH COSY), 8.70 (s, 2H, triazolyl CH); ^{13}C NMR (150 MHz, DMSO-d_6, δ): 28.6 (2-pentenyl CH_2), 31.0 (3-pentenyl CH_2), 39.1 ($NHCH_2$), 53.0 (methylene CH_2), 115.3 (5-pentenyl CH_2), 118.9 (pyr CH), 124.0 (triazolyl CH), 128.0 (Ph CH adjacent amide), 128.1 (Ph CH adjacent methylene), 134.9 (Ph qt), 138.5 (4-pentenyl CH), 138.6 (pyr CH), 139.0 (Ph qt), 147.7 (triazolyl qt), 150.1 (pyr CH), 166.0 (C=O qt); FT-IR υ_{max} (ATR, cm^{-1}): 3343 (br), 3167, 3075, 2922 (s), 2851 (s), 1632 (s, amide C=O), 1607, 1575, 1534 (s), 1507, 1474, 1463, 1437, 1425, 1357, 1338, 1316,1282, 1265, 1238, 1211, 1198, 1171, 1152, 1120, 1098, 1079, 1045, 1020, 992, 979, 934, 910, 867, 842, 800, 788, 756, 739 (s), 723, 659. m.p.: 221–224 °C.

Open ligand 152[b]

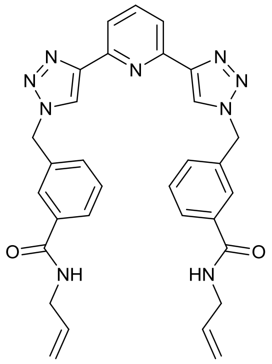

2,6-Bis(1-(3-(carboxy)benzyl)-1,2,3-triazol-4-yl)pyridine (0.500 g, 1.04 mmol), HOBt (0.29 g, 2.18 mmol), DMAP (0.133 g; 1.09 mmol) TEA (0.304 ml, 2.18 mmol) and allylamine (2.28 mmol) were dissolved in CH_2Cl_2: DMF (4:1, 70 mL) and stirred at 0°C for 30 mins. EDCI·HCl (0.597 g; 3.12 mmol) was added and the reaction mixture stirred for a further 30 mins at 0°C, under argon. The reaction mixture was then allowed to reach room temperature and stirred for 66 hours. The reaction mixture was diluted with CH_2Cl_2 and washed with $HCl_{(aq)}$ (1 M), saturated $NaHCO_{3(aq)}$ and H_2O. The organic layer was washed with brine and dried over $MgSO_4$. The crude product was triturated with cold methanol, yielding a white solid (0.355 g; 0.634 mmol; 61%). HRMS (*m/z*) (ESI^+): Calculated for $C_{31}H_{29}N_9O_2Na^+$ *m/z* = 582.2342 $[M+Na]^+$. Found *m/z* = 582.2318; Elemental Analysis: Calculated for $C_{31}H_{29}N_9O_2$, C = 66.53, H = 5.22, N = 22.53. Found, C = 66.38, H = 5.12, N = 22.40.; ^1H NMR (400MHz, DMSO-d_6, δ): 8.70 (s (sh), 4H, triazolyl CH and NH), 7.98 (app t, 3H, 3-, 4- and 5-pyridyl CH), 7.87 (s, 2H, phenyl CH), 7.84 (d, *J* = 5Hz, 2H, phenyl CH), 7.84-7.52 (m, 4H, phenyl CH), 5.86 (m, 2H, alkene CH), 5.75 (s, 4H, CH_2), 5.15 (s, 2H, terminal alkene CH_2), 5.07 (s, 2H, terminal alkene CH_2), 3.88 (app t, 4H, allyl CH_2); ^{13}C NMR (151 MHz, DMSO-d_6, δ): 165.1 (C=O), 150.3 (qt, 2,6-pyridyl), 147.9 (qt, 4-triazolyl), 138.8 (4-pyridyl), 136.6 (3-aryl), 135.8 (2-olefin), 135.4 (1-aryl), 131.2 (6-aryl), 129.3 (5-aryl), 127.5 (4-aryl), 127.3 (2-aryl), 124.1 (5-triazolyl), 119.0 (3,5-pyridyl), 115.7 (1-olefin), 53.3 (CH_2), 42.0 (allyl CH_2).; FT-IR υ_{max} (ATR, cm^{-1}): 3262, 3072, 1637 (C=O), 1604, 1579, 1542, 1450, 1347, 1309, 1215, 1164, 1072, 1042, 992, 910, 800, 785, 705. m.p.: 198.6-201.3°C.

General procedure C for open ligand 153R/S

A solution of the relevant **btp** acid (300 mg, 0.59 mmol), DMAP (75 mg, 0.62 mmol), allylamine (132 μL, 1.78 mmol), TEA (173 μL, 1.24 mmol) in anhydrous DCM:DMF (4:1, 150 mL) was degassed with Argon and cooled to 0 °C for 30 minutes. EDCI·HCl (353 mg, 1.78 mmol) was added and the reaction mixture was allowed to warm to rt and stirred 66 hours. The solvent was removed under reduced pressure and the oil residue was dissolved in a minimum amount of DCM and product was purified by flash chromatography (gradient DCM: CH_3OH (95:5)).

Open ligand 153R[c]

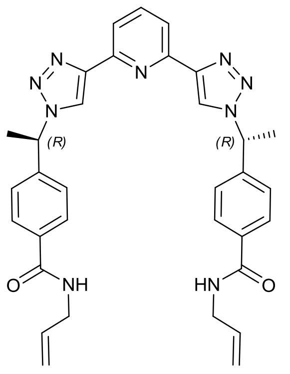

Ligand **153R** was synthesized according to the general procedure C from 2,6-Bis(1-(4'-(carboxy)-*R*-1,1-ethylidenyl)-1,2,3-triazol-4-yl) yielding a white powder (131 mg, 0.224 mmol, 38%).

HRMS- MALDI+ (*m*/*z*): calculated for $C_{33}H_{34}N_9O_2$, *m/z* = 588.2835 $[M+H]^+$; found *m/z* = 588.2853. Elemental analysis for $C_{33}H_{33}N_9O_2 \cdot 0.25CH_2Cl_2 \cdot 0.04CH_3OH$, C = 65.51, H =5.56, N = 20.65. Found C = 65.52, H = 5.53, N = 20.62. ^{1}H NMR (400 MHz, CDCl3) δ 8.22 (s, 2H, triazole), 8.13 (d, *J* = 7.8 Hz, 2H, pyridyl), 7.96 (t, *J* = 7.8 Hz, 1H, pyridyl), 7.49 (d, *J* = 8.1 Hz, 4H, 2,6-aryl), 6.92 (d, *J* = 7.8 Hz, 4H, 3,5-aryl), 6.80 (s,2H, NH), 6.03 (ddd, *J* = 17.2, 10.2, 5.6 Hz, 2H, 2-olefin), 5.74 (q, *J* = 7.0 Hz, 2H, methine), 5.37 (dd, *J* = 17.2, 1.4 Hz, 2H, 1-olefin), 5.26 (dd, *J* = 10.2, 1.4 Hz, 2H, 1-olefin), 4.15 (t, *J* = 5.7 Hz, 4H, methylene), 1.63 (d, *J* = 7.0 Hz, 6H, methyl).^{13}C NMR (101 MHz, CDCl3) δ 167.1 (2C, carbonyl), 149.8 (2C, 2,6-pyridyl), 148.4 (2C, 4-triazolyl), 141.9 (2C, 4-aryl), 138.5 (1C, 4-pyridyl), 135.2 (2C, 1-aryl), 134.1 (2C, 2-olefin), 127.7 (4C, 2,6-aryl), 126.1(4C, 3,5-aryl), 120.6 (2C, 5-triazolyl), 119.4 (2C, 3,5-pyridyl), 116.9 (2C, 1-olefin), 59.6 (2C, methine), 42.6 (2C, methylene), 20.3 (2C, methyl). FT-IR (cm-1), 3302, 3083, 2983, 1638, 1610, 1572, 1535, 1501, 1450, 1429, 1381, 1345, 1301, 1260, 1221, 1164, 1089, 1036, 1018, 993, 918, 854, 813, 788, 766, 719, 669, 615, 572. m.p. 110.1-113.9°C.

Open ligand 153S[c]

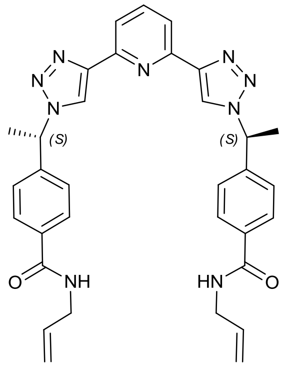

Ligand **153S** was synthesized according to the general procedure C from 2,6-Bis(1-(4'-(carboxy)-*S*-1,1-ethylidenyl)-1,2,3-triazol-4-yl) yielding a white powder (169 mg, 0.28 mmol, 48%). HRMS-MALDI+ (*m*/*z*): calculated for $C_{33}H_{34}N_9O_2$, *m/z* = 588.2835 $[M+H]^+$; found *m/z* = 588.2850. Elemental analysis calculated for $C_{33}H_{33}N_9O_2 \cdot 0.22CH_2Cl_2 \cdot 0.16CH_3OH$, C = 65.55, H = 5.62, N = 20.61. Found C = 65.56, H = 5.59, N = 20.58. ^{1}H NMR (400 MHz, $CDCl_3$) δ 8.14 (s, 2H, triazole), 8.10 (d, *J* = 7.8 Hz, 2H, pyridyl), 7.92 (t, *J* = 7.8 Hz, 2H, pyridyl), 7.56 (d, *J* = 8.0 Hz, 4H, 2,6-aryl), 7.04 (d, *J* = 8.0 Hz, 4H, 3,5-aryl), 6.66 (s (br), 2H, NH), 5.99 (ddd, *J* = 7.2, 10.4, 6.4 Hz, 2H, 2-olefin), 5.77 (q, *J* = 5.7 Hz, 2H, methine), 5.32 (dd, *J* = 17.2, 1.4 Hz, 2H, 1-olefin), 5.22 (dd, *J* = 10.3, 1.4 Hz, 4H, 1-olefin), 4.12 (t, *J* = 5.7 Hz, 4H, methylene), 1.72 (d, *J* = 6.7 Hz, 6H, CHmethyl). ^{13}C NMR (101 MHz, CDCl3) δ 167.1 (2C, carbonyl), 149.8 (2C, 2,6-pyridyl), 148.1 (2C, 4-triazolyl), 141.9 (2C, 4-aryl), 138.5 (1C, 4-pyridyl), 135.2 (2C, 1-aryl), 134.1 (2C, 2-olefin), 127.7 (4C, 2,6-aryl), 126.1

(4C, 3,5-aryl), 120.6 (2C, 5-triazolyl), 119.4 (2C, 3,5-pyridyl), 116.8 (2C, 1-olefin), 59.6 (2C, methine), 42.6 (2C, methylene), 20.3 (2C, methyl). UV-vis (CH$_3$CN) λmax / nm (εmax /dm^3 mol^{-1} cm^{-1}): 236 (43,000), 301 (8,800). FT-IR (cm-1), 3302, 3081, 2985, 2937, 1638, 1611, 1572, 1535, 1501, 1450, 1429, 1381, 1345, 1301, 1260, 1221, 1166, 1090, 1036, 1018, 993, 919, 854, 813, 788, 766, 719, 676, 626, 583. m.p. 110.3-114.1 °C.

General procedure D for Catenanes and Macrocycles RCM synthesis

A solution of the relevant olefin (169 mg, 0.288 mmol) in anhydrous DCM (40 mL) was degassed with argon. A solution of Hoveyda–Grubbs 2nd generation catalyst (90 mg, 0.144 mmol, 50 mol%) in anhydrous DCM (20 mL) was added under inert conditions and after further degassing, the solution was stirred at rt in darkness for 7 days. The reaction mixture was concentrated under reduced pressure and purified by flash chromatography.

[2]Catenane 91c[a]

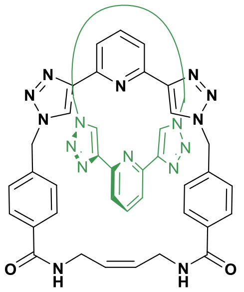

Ligand **91c** was synthesised following procedure D. After 4 days, the reaction mixture was filtered to remove unreacted starting material and then concentrated under reduced pressure. Trituration with CH$_3$OH followed by filtration yielded **91c** as a white solid. Yield: 53. HRMS (*m/z*) (MALDI$^+$): Calculated for $C_{58}H_{51}N_{18}O_4^+$ *m/z* = 1063.4341 [M+H]$^+$. Found *m/z* = 1063.4346; Calculated for $C_{58}H_{50}N_{18}O_4Na^+$ *m/z* = 1085.4159 [M+Na]$^+$. Found *m/z* = 1085.4147; ^{1}H NMR (600 MHz, DMSO-*d*$_6$, δ): 4.02 (br s, 8H, NHCH$_2$), 5.15 (s, 8H, CH$_2$), 6.12 (br s, 4H, olefin CH), 6.42 (d, 8H, *J* = 8.2 Hz, Ph CH), 7.27 (d, 8H, *J* = 8.2 Hz, Ph CH), 7.78 (d, 4H, *J* = 8.0 Hz, 3- and 5-pyr CH), 7.92 (s, 4H, triazolyl CH), 7.99 (t, 2H, *J* = 8.0 Hz, 4-pyr CH), 8.22 (br s, 4H, NH, assigned by NH COSY); ^{13}C NMR (150 MHz, DMSO-*d*$_6$, δ): 40.1 (NHCH$_2$, overlaps with solvent peak, assigned by HSQC), 52.5 (CH$_2$), 118.7 (3- and 5-pyr CH), 121.2 (triazolyl CH), 126.2 (Ph CH), 127.2 (Ph CH), 128.2 (olefin CH), 134.0 (Ph qt), 136.9 (Ph qt), 137.9 (4-pyr CH), 147.3 (triazolyl qt), 148.7 (pyr qt), 165.4 (C=O qt); FT-IR υ_{max} (ATR, cm^{-1}): 3748, 3262 (br), 3106, 2962, 1638 (s, amide C=O), 1611, 1572, 1534, 1503, 1460, 1428, 1350, 1296, 1261, 1232, 1200, 1153,1084, 1045, 1021, 993, 969, 861, 817 (s), 797, 761, 731, 705, 670, 663. %. m.p.: Product decomposed over 348 °C.

Macrocycle 91m[a]

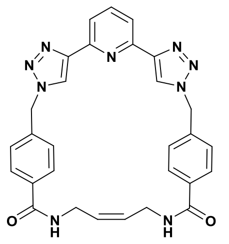

Ligand **91m** was synthesised following procedure D. After 4 days, the reaction mixture was filtered to remove unreacted starting material and then concentrated under reduced pressure. Trituration with CH_3OH followed by filtration and column chromatography (ethyl acetate–methanol gradient) yielded **91m** as a white solid. Yield: 18 HRMS (*m/z*) (MALDI$^+$): Calculated for $C_{29}H_{26}N_9O_2^+$ *m/z* = 532.2209 [M+H]$^+$. Found *m/z* = 532.2225; ^{1}H NMR (400 MHz, DMSO-d_6, δ): 3.80–3.85 (br m, 4H, $NHCH_2$), 5.46–5.51 (br s, 2H, olefin CH), 5.71 (s, 4H, CH_2), 7.28 (d, 4H, J = 8.2 Hz, Ph CH), 7.78 (d, 4H, J = 8.2 Hz, Ph CH), 7.94–7.97 (m, 3H, pyr CH), 8.25 (s, 2H, triazolyl CH), 8.54 (t, 2H, J = 4.5 Hz, NH, assigned by NH COSY); ^{13}C NMR (150 MHz, DMSO-d_6, determined from 2D NMR experiments): δ = 39.4 ($NHCH_2$), 53.1 (methylene CH_2), 118.9 (pyr CH), 122.8 (triazolyl CH), 128.3 (Ph CH), 128.5 (Ph CH), 134.2 (Ph qt) , 138.0 (Ph qt), 138.7 (pyr CH), 147.8 (triazolyl qt), 149.3 (pyr qt), 165.0 (C=O qt); FT-IR υ_{max} (ATR, cm^{-1}): 3304 (br), 2918, 1639 (s, amide C=O), 1574, 1545 (s), 1508, 1463, 1427, 1348, 1316, 1229, 1198, 1154, 1112, 1085, 1044 (s), 1020, 993, 975, 862, 842, 795, 766, 744, 699, 664, 633. %. m.p.: Product decomposed over 355 °C.

[2]catenane 92c[a]

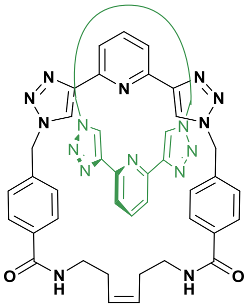

Ligand **92c** was synthesised following procedure D. After 7days the reaction mixture was concentrated under reduced pressure. Column chromatography (ethyl acetate–methanol gradient) yielded. Yield: 36%. HRMS (*m/z*) (ESI$^+$): Calculated for $C_{62}H_{58}N_{18}O_4Na^+$ *m/z* = 1141.4786 [M+Na]$^+$. Found *m/z* =1141.4777; (MALDI$^+$): Calculated for $C_{62}H_{59}N_{18}O_4^+$ *m/z* = 1119.4967 [M+H]$^+$. Found *m/z* = 1119.4996; ^{1}H NMR (400 MHz, DMSO-d_6, δ): 2.36–2.48 (m, 8H, alkyl CH_2, overlaps with solvent peak), 3.35 (alkyl CH, overlaps with solvent peak), 5.12 (s, 8H, methylene CH_2), 5.84–5.96 (m, 4H, olefin CH), 6.45 (d, 8H, J = 8.3 Hz, Ph CH), 7.25 (d, 8H, J = 8.3 Hz, Ph CH), 7.78 (d, 4H, J= 7.9 Hz, 3- and 5-pyr CH), 7.85–7.95 (m, 6H, 4-pyr CH and triazolyl CH), 8.14–8.20 (app t, 4H, NH, assigned by NH COSY); ^{13}C NMR (150 MHz, DMSO-d_6, determined by 2D NMR experiments, δ): 20.1 (alkyl CH_2), 39.0 (alkyl CH_2), 52.7 (methylene CH_2), 118.8 (2- and 5-pyr CH), 121.3 (triazolyl CH), 126.7 (Ph CH), 127.5 (Ph CH), 129.9 (olefin CH), 134.1 (Ph qt), 136.4 (Ph qt), 138.4 (4-pyr CH), 147.5 (triazolyl qt), 149.2 (pyr qt), 165.4 (C=O qt); FT-IR υ_{max} (ATR, cm^{-1}): 3323 (br), 3110, 2927 (br), 1655 (s, amide C=O), 1611, 1573, 1530 (s), 1502, 1466, 1427 (s), 1355, 1305 (br, s), 1258, 1232, 1200, 1152, 1084, 1044, 1019, 993, 968, 855, 817 (s), 797, 760, 733, 707, 662, 647, 631, 620, 611, 603. m.p.: 305–312 °C.

Macrocycle 92m[a]

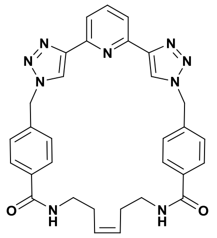

Ligand **92m** was synthesised following procedure D. Trituration with CH_3OH followed by filtration and column chromatography (ethyl acetate–methanol gradient) was used for purification. Yield: 11%. HRMS (*m/z*) (MALDI$^+$): Calculated for $C_{31}H_{30}N_9O_2^+$ *m/z* = 560.2522 [M+H]$^+$. Found *m/z* = 560.2516; ^{1}H NMR (400 MHz, DMSO-d_6, δ): 2.13–2.18 (m, 4H, alkyl CH_2), 3.3 (alkyl CH_2, overlaps with residual H_2O resonance, determined by CH COSY), 5.38–5.45 (m, 2H, olefin CH), 5.70 (s, 4H, methylene CH_2), 7.30 (d, 4H, *J* = 8.3 Hz, Ph CH), 7.77 (d, 4H, *J* = 8.3 Hz, Ph CH), 7.92–7.98 (m, 3H, pyr CH), 8.30 (s, 2H, triazolyl CH), 8.32–8.38 (br m, 2H, NH); ^{13}C NMR (150 MHz, DMSO-d_6, determined from 2D NMR experiments, δ): 32.9 (alkyl CH_2), 39.0 (alkyl CH_2), 52.1 (methylene CH_2), 118.9 (pyr CH), 123.0 (triazolyl CH), 128.2 (Ph CH), 128.6 (Ph CH), 129.8 (olefin CH), 134.6 (Ph qt), 138.3 (Ph qt), 138.8 (pyr CH), 147.7 (triazolyl qt), 149.6 (pyr qt), 165.7 (C=O qt); FT-IR υ_{max} (ATR, cm^{-1}): 3325 (br), 2927, 2851, 1631 (s, amide C=O), 1574, 1535 (s), 1503, 1466, 1428, 1296 (s), 1260, 1231, 1197, 1154, 1082, 1042 (s), 1020, 992, 971, 862, 834, 803 (s), 763, 740, 699, 671, 660, 632, 620. m.p.: Product decomposed over 325 °C.

[2]catenane 93c[a]

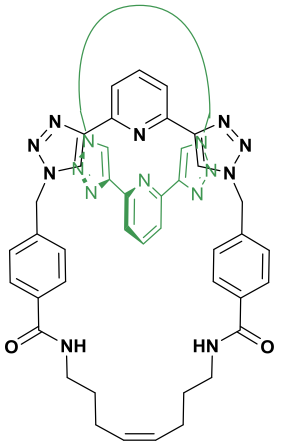

Ligand **93c** was synthesised following procedure D. After 4 days the reaction mixture was filtered to remove unreacted starting material and then concentrated under reduced pressure. Trituration with CH_3OH followed by filtration yielded [2]catenanes **93c** as an off-white solid. Yield: Trace (<1%). HRMS (*m/z*) (MALDI$^+$): Calculated for $C_{66}H_{66}N_{18}O_4Na^+$ *m/z* = 1197.5412 [M+Na]$^+$. Found *m/z* = 1197.5438; FT-IR υ_{max} (ATR, cm^{-1}): 3300 (br, s), 3081, 2933, 1638 (s, amide C=O), 1573, 1552 (s), 1508, 1462, 1433, 1302 (s), 1260, 1234, 1200, 1156, 1084, 1044 (s), 1020, 993, 973, 946, 845, 816, 798 (s), 762, 731, 666. Insufficient compound was isolated to characterise this product fully, however HRMS clearly confirms the formation of the [2]catenane; synthesis and isolation of [2]catenane products clearly becomes much more challenging with increasing chain length in these systems. m.p.: 305–315 °C.

Macrocycle 93m[a]

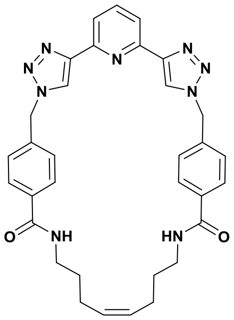

Ligand **93m** was synthesised following procedure D. Trituration with CH_3OH followed by filtration and column chromatography (ethyl acetate–methanol gradient) was used for purification. Yield: 39%. HRMS (*m/z*) (MALDI$^+$): Calculated for $C_{33}H_{34}N_9O_2^+$ *m/z* = 588.2835 $[M+H]^+$. Found *m/z* = 588.2852; ^1H NMR (600 MHz, DMSO-d_6, δ): 1.50–1.57 (m, 4H, alkyl CH), 1.93–2.00 (m, 4H, alkyl CH), 3.18–3.25 (m, 4H, alkyl CH, overlaps with residual H_2O resonance), 5.35–5.42 (m, 2H, olefin CH), 5.77 (s, 4H, methylene CH_2), 7.35 (d, 4H, Ph CH, *J* = 8.0 Hz), 7.81 (d, 4H, Ph CH, *J* = 8.0 Hz), 7.97–8.02 (app s, 3H, pyr CH), 8.31–8.38 (app t, 2H, amide NH, assigned by NH COSY), 8.45 (s, 2H, triazolyl CH); ^{13}C NMR (150 MHz, DMSO-d_6, δ): 28.8, 29.1, 38.2 (alkyl CH_2 resonances), 52.8 (methylene CH_2), 118.5 (pyr CH), 123.0 (triazolyl CH), 127.6 (Ph CH), 127.7 (Ph CH), 130.0 (olefin CH), 134.7 (Ph qt), 138.3 (pyr CH), 138.6 (Ph qt) 147.9 (triazolyl qt), 149.7 (pyr qt), 165.7 (C=O qt); FT-IR υ_{max} (ATR, cm^{-1}): 3333 (br), 3075, 2925 (br), 2852, 1636 (s, amide C=O), 1574, 1541 (s), 1504 (s), 1428, 1302 (br), 1233, 1198, 1154, 1117, 1083, 1044, 1020, 992, 975, 912, 842, 802 (s), 761, 732. m.p.: 248–258 °C.

Macrocycle 94m[b]

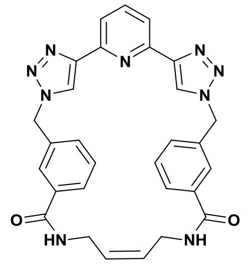

Ligand **152** (0.053 g; 0.065 mmol) and Hoveyda-Grubbs II catalyst (0.028 g; 0. 035 mmol) were added to a round bottom flask which was then degassed with argon. A CH_3NO_2:CH_2Cl_2 (1:9, 40 mL) solvent system was degassed by bubbling with argon and added to the reagents *via* cannula. The round bottom flask was covered in aluminium foil and the reaction mixture stirred under argon at 60°C for 24 hours in darkness. The reaction mixture was cooled to cool and stirred at rt for 3 days. The reaction mixture was concentrated under reduced pressure and the crude product was purified by flash chromatography (gradient CH_2Cl_2/ CH_3OH). The pure product was obtained as a light brown solid (0.029 g; 0.038 mmol; 58%). HRMS (*m/z*) (ESI$^-$): Calculated for $C_{45}H_{56}N_9O_2^-$ *m/z* = 754.4557 $[M-H]^-$. Found *m/z* = 754.4568. ^1H NMR (600 MHz, DMSO-d_6, δ): 8.68 (s, 2H, triazolyl), 8.49 (t, *J* = 5.2 Hz, 2H, NH), 8.00 (app s, 3H, pyridyl), 7.85 (s, 2H, 2-aryl), 7.81 (d, *J* = 7.6 Hz, 2H, 4-aryl), 7.53 (d, *J* = 7.6 Hz, 2H, 6-aryl), 7.49 (t, *J* = 7.6 Hz, 2H, 5-aryl), 5.76 (s, 4H, methylene), 5.32 (s, 2H, olefin), 3.24 (d, *J* = 6.0 Hz, 4H, methylene), 1.94 (d, *J* = 4.7 Hz, 4H, methylene), 1.50 (d, *J* = 6.4 Hz, 4H, methylene), 1.26 (m, *J* = 24.3 Hz, 24H, methylene). ^{13}C NMR (151 MHz, DMSO-d_6, δ): 166.1 (carbonyl), 150.3 (2,6-pyridyl), 147.9 (5-

triazolyl), 138.8 (4-pyridyl), 136.5 (1-aryl), 135.8 (3-aryl), 131.2 (6-aryl), 130.7 (olefin), 129.3 (5-aryl), 127.5 (2-aryl), 127.3 (4-aryl), 124.1 (5-triazolyl), 119.0 (3,5-pyridyl), 53.4 (methylene), 39.6 (9-methylene overlap with solvent peak assigned by HSQC) 32.1 (2-methylene), 29.5 (8-methylene), 29.3 - 26.9 (alkyl chain methylenes). m.p.: 260.1-261.2°C.

[2]catenane 95cR[c]

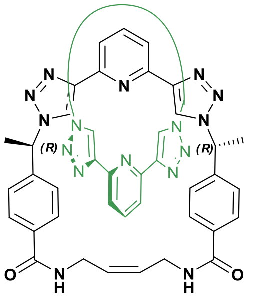

[2]catenane **95cR**was synthesized according to the general procedure D from **153R.** The reaction mixture was concentrated under reduced pressure and purified by flash chromatography (gradient CH_2Cl_2:CH_3OH (95:5)) yielding a beige powder (67 mg, 0.061 mmol, 42%). HRMS (*m/z*) (MALDI$^+$): Calculated for $C_{62}H_{58}N_{18}O_4Na^+$ *m/z* = 1141.4786 [M+Na]$^+$. Found *m/z* = 1141.4824. ^{1}H NMR (400 MHz, DMSO-*d*$_6$, δ): 8.16 (t, *J* = 5.5 Hz, 2H, NH), 8.04 (t, *J* = 7.8 Hz, 1H, pyridyl), 7.89 (s, 2H, triazolyl), 7.81 (d, *J* = 7.8 Hz, 2H, pyridyl), 7.26 (d, *J* = 8.3 Hz, 4H, 2,6-aryl), 6.32 (d, *J* = 8.3 Hz, 4H, 3,5-aryl), 6.13 (s, 2H, olefin), 5.47 (q, *J* = 6.9 Hz, 2H, methine), 4.00 (s, 4H, methylene), 1.33 (d, *J* = 6.9 Hz, 6H, methyl). ^{13}C NMR (151 MHz, DMSO-*d*$_6$, δ): 165.9 (carbonyl), 149.3 (2,6- pyridyl), 147.6 (4-triazolyl), 142.5 (1-aryl), 138.5 (4-pyridyl), 134.3 (4-aryl), 128.7 (olefin), 127.6 (2,6-aryl), 125.0 (3,5-aryl), 121.4 (5-triazolyl), 119.2 (3,5-pyridyl), 58.8 (methine), 40.3 (methylene), 20.3 (methyl). FT-IR υ_{max} (ATR, cm^{-1}) 3366, 2922, 1646, 1610, 1572, 1532, 1504, 1434, 1296, 1261, 1220, 1087, 1036, 1019, 966, 854, 815, 767, 717, 582, 563. m.p.: Product decomposed over 238°C.

[2]catenane 95cS[c]

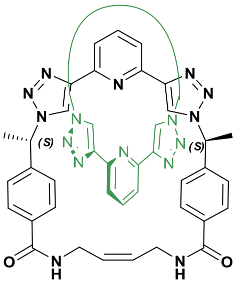

[2]catenane **95cS** was synthesized according to the general procedure D from **153S**. The reaction mixture was concentrated under reduced pressure and purified by flash chromatography (gradient CH_2Cl_2:CH_3OH (95:5)) yielding a beige powder (69 mg, 0.062 mmol, 43%). HRMS (*m/z*) (MALDI$^+$): Calculated for $C_{62}H_{58}N_{18}O_4Na^+$ *m/z* = 1141.4786 [M+Na]$^+$. Found *m/z* = 1141.4813. ^{1}H NMR (400 MHz, DMSO-*d*$_6$, δ): 8.16 (t, *J* = 5.5 Hz, 2H, NH), 8.04 (t, *J* = 7.8 Hz, 1H, pyridyl), 7.89 (s, 2H, triazolyl), 7.81 (d, *J* = 7.8 Hz, 2H, pyridyl), 7.26 (d, *J* = 8.3 Hz, 4H, 2,6-aryl), 6.32 (d, *J* = 8.3 Hz, 4H, 3,5-aryl), 6.14 (s, 2H, olefin), 5.47 (q, *J* = 6.9 Hz, 2H, methine), 4.00 (s, 4H, methylene), 1.33 (d, *J* = 6.9 Hz, 6H, methyl). ^{13}C NMR (151 MHz, DMSO-*d*$_6$, δ): 165.9 (carbonyl), 149.3 (2,6-pyridyl), 147.6 (4-triazolyl), 142.5 (1-aryl), 138.5 (4-pyridyl), 134.3 (4-aryl), 128.7 (olefin), 127.6 (2,6-aryl), 125.0 (3,5-aryl), 121.4 (5-triazolyl), 119.2 (3,5-pyridyl), 58.8 (methine), 40.3 (methylene), 20.3 (methyl). FT-IR υ_{max} (cm^{-1}), 3360, 3103,

2924, 1646, 1610, 1571, 1534, 1502, 1432, 1379, 1348, 1296, 1261, 1220, 1180, 1152, 1088, 1036, 1019, 969, 854, 815, 767, 746, 717, 650, 599, 569, 558. m.p.: Product decomposed over 238°C.

Macrocycle 95mR[c]

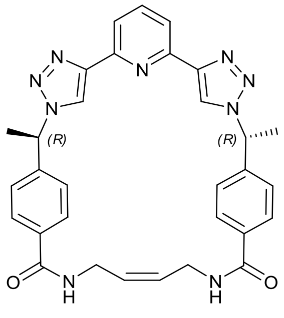

Macrocycle **95mR** was synthesized according to the general procedure D from **153R**. The reaction mixture was concentrated under reduced pressure and purified by flash chromatography (gradient CH_2Cl_2:CH_3OH (95:5)) yielding a beige powder (12 mg, 0.022 mmol, 8%). HRMS (*m/z*) (MALDI$^+$): Calculated for $C_{31}H_{30}N_9O_2^+$ *m/z* = 560.2522 [M+H]$^+$. Found *m/z* = 560.2548. ^{1}H NMR (400 MHz, DMSO-*d*$_6$, δ): 8.54 (t, *J* = 5.7 Hz, 2 NH), 8.26 (s, 2H, triazole), 7.97 (s, 3H, pyridyl), 7.78 (d, *J* = 8.4 Hz, 4H, aryl), 7.28 (d, *J* = 8.4 Hz, 4H, aryl), 6.06 (q, *J* = 7.1 Hz, 2H, methine), 5.50 (app t, *J* = 2.4 Hz, 2H, olefin), 3.84 (ddd, *J* = 17, 15, 5.7 Hz, 4H), 1.95 (d, *J* = 7.0 Hz, 6H, methyl). ^{13}C NMR (151 MHz, DMSO-*d*$_6$, δ): 165.7 (carbonyl), 150.3 (2,6-pyridyl), 148.3 (4-triazolyl), 144.1 (1-aryl), 134.8 (4-aryl), 128.3 (2,6-aryl), 128.3 (olefin), 127.0 (3,5-aryl), 122.5 (5-triazolyl), 119.2 (3,5-pyridyl), 59.7 (methine), 39.7 (methylene, overlaps with solvent peak, assigned by HSQC), 20.8 (methyl).

Macrocycle 95mS[c]

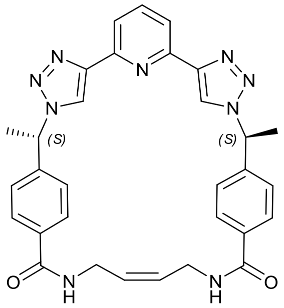

Macrocycle **95mS** was synthesized according to the general procedure D from **153S**. The reaction mixture was concentrated under reduced pressure and purified by flash chromatography (gradient CH_2Cl_2: CH_3OH (95:5)) yielding a beige powder (22 mg, 0.039 mmol, 14%). HRMS (*m/z*) (MALDI$^+$): Calculated for $C_{31}H_{30}N_9O_2^+$ *m/z* = 560.2522 [M+H]$^+$. Found *m/z* = 560.2553. ^{1}H NMR (600 MHz, DMSO-*d*$_6$, δ): 8.56 (t, *J* = 5.8 Hz, 2H, NH), 8.28 (s, 2H, triazolyl), 7.99 (s, 3H, pyridyl), 7.80 (d, *J* = 8.4 Hz, 4H, aryl), 7.31 (d, *J* = 8.4 Hz, 4H, aryl), 6.08 (q, *J* = 7.0 Hz, 2H, methine), 5.53 (app t, *J* = 2.4 Hz, 2H, olefin), 3.86 (ddd, *J* = 19.9, 15.2, 5.7 Hz, 4H, methylene), 1.97 (d, *J* = 7.0 Hz, 6H, methyl). ^{13}C NMR (151 MHz, DMSO-*d*$_6$, δ): 165.7 (carbonyl), 150.3 (2,6-pyridyl), 148.3 (4-triazolyl), 144.1 (1-aryl), 134.8 (4-aryl), 128.3 (2,6-aryl), 128.3 (olefin), 127.0 (3,5-aryl), 122.5 (5-triazolyl), 119.2 (3,5-pyridyl), 59.7 (methine), 39.9 (methylene, overlaps with solvent peak, assigned by HSQC), 20.8 (methyl).

[a] The synthesis of this compound was carried out by Dr Joseph Byrne.

[b] The synthesis of this compound was carried out by Mr William McCarthy.

[c] The synthesis of this compound was carried out by Dr Eoin McCarney.

6.5.4. Synthesis of ligands discussed in Chapter 5

Tris(imidazolium)-bis(tren) cage 96[a]

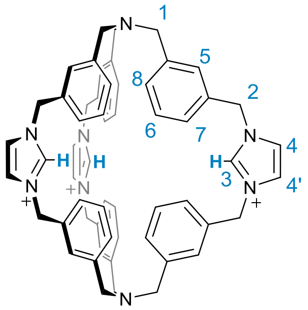

Compound **166** (0.095 mmol), containing imidazole units appended to the tris-(3-methylbenzyl)-amine platform, was dissolved in 30 mL of 1:1 $CHCl_3$:acetone mixture. The obtained solution was added dropwise to a solution of **167** (0.095 mmol) in 60 mL acetone. The reaction mixture was then refluxed for 72 hrs. The product, precipitated as a white solid, was filtered and dissolved hot water. The final receptor was recovered as hexafluorophosphate salt, using NH_4PF_6 for the anion metathesis. Yield = 48% ^{1}H NMR (400 MHz, CD_3CN, δ): 8.65 (s, 1H, H3), 7.50 (d, J = 1.3 Hz, 6H, H4), 7.23 (m, 6H, H7), 7.18 – 7.06 (m, 12H, H6+H8), 6.95 (s, 6H, H5), 5.30 (s, 12H, H2), 3.27 (s, 12H, H1). ^{13}C NMR (101 MHz, CD_3CN, δ): 140.4 (C3), 136.0 (q), 134.4 (q), 129.6 (H6), 129.5 (C8), 127.9 (C5), 127.5 (C7), 123.6 (C4), 57.2(C1), 53.1(C2). IR (cm-1): 3664, 3167, 1611, 1561, 1492, 1448, 1348, 1238, 1147, 1109, 1027, 1004, 828, 741, 700, 621, 556. HRMS-MALDI (*m/z*): calculated for $C_{57}H_{55}N_8$, *m/z* = 851.4550 $[M-2H]^+$; found *m/z* = 851.4568. mp 144-145°C.

[a] The synthesis of this compound was carried out by researchers in Amendola group.

7. References

(1) Park, C. H.; Simmons, H. E. *J. Am. Chem. Soc.* **1968**, *90*, 2431.
(2) Bowman-James, K. *Acc. Chem. Res.* **2005**, *38*, 671.
(3) Shannon, R. D. *Acta Crystallogr., Sect. A: Found. Adv.* **1976**, *32*, 751.
(4) Beer, P. D.; Gale, P. A.; Smith, D. K. *Supramolecular Chemistry*; Oxford University Press, 1999.
(5) Brunetti, E.; Picron, J. F.; Flidrova, K.; Bruylants, G.; Bartik, K.; Jabin, I. *J. Org. Chem.* **2014**, *79*, 6179.
(6) Brooks, S. J.; Edwards, P. R.; Gale, P. A.; Light, M. E. *New J. Chem.* **2006**, *30*, 65.
(7) Park, Y. S.; Bang, S.-H.; Choi, H.-J. *Tetrahedron Lett.* **2013**, *54*, 6708.
(8) Zhang, R.; Zhao, Y. X.; Wang, J. M.; Ji, L. G.; Yang, X. J.; Wu, B. *Cryst. Growth Des.* **2014**, *14*, 544.
(9) Langton, M. J.; Serpell, C. J.; Beer, P. D. *Angew. Chem., Int. Ed.* **2016**, *55*, 1974.
(10) Hunter, C. A. *Angew. Chem., Int. Ed.* **2004**, *43*, 5310.
(11) Sessler, J. L.; Gale, P. A.; Cho, W. S. *Anion Receptor Chemistry*; Royal Society of Chemistry, 2006.
(12) Hofmeister, F. *Arch. Exp. Pathol. Pharmacol.* **1888**, *24*, 247.
(13) Zhao, J.; Yang, D.; Yang, X.-J.; Wu, B. *Coord. Chem. Rev.* **2018**, *10.1016/j.ccr.2018.01.002*.
(14) Yang, D.; Zhao, J.; Yang, X. J.; Wu, B. *Org. Chem. Front.* **2018**, *5*, 662.
(15) Gale, P. A.; Howe, E. N. W.; Wu, X.; Spooner, M. J. *Coord. Chem. Rev.* **2018**, *375*, 333.
(16) Liu, Y.; Sengupta, A.; Raghavachari, K.; Flood, A. H. *Chem* **2017**, *3*, 411.
(17) Gale, P. A.; Davis, J. T.; Quesada, R. *Chem. Soc. Rev.* **2017**, *46*, 2497.
(18) Busschaert, N.; Caltagirone, C.; Van Rossom, W.; Gale, P. A. *Chem. Rev.* **2015**, *115*, 8038.
(19) Carreira-Barral, I.; Rodriguez-Blas, T.; Platas-Iglesias, C.; de Blas, A.; Esteban-Gomez, D. *Inorg. Chem.* **2014**, *53*, 2554.
(20) Aletti, A. B.; Gillen, D. M.; Gunnlaugsson, T. *Coord. Chem. Rev.* **2018**, *354*, 98.
(21) Seipp, C. A.; Williams, N. J.; Bryantsev, V. S.; Custelcean, R.; Moyer, B. A. *RSC Adv.* **2015**, *5*, 107266.
(22) Amendola, V.; Bergamaschi, G.; Boiocchi, M.; Alberto, R.; Braband, H. *Chem. Sci.* **2014**, *5*, 1820.
(23) Hoque, M. N.; Gogoi, A.; Das, G. *Dalton Trans.* **2015**, *44*, 15220.
(24) Saha, I.; Lee, J. T.; Lee, C. H. *Eur. J. Org. Chem.* **2015**, *2015*, 3859.
(25) Amendola, V.; Fabbrizzi, L.; Mosca, L. *Chem. Soc. Rev.* **2010**, *39*, 3889.
(26) Blažek Bregović, V.; Basarić, N.; Mlinarić-Majerski, K. *Coord. Chem. Rev.* **2015**, *295*, 80.
(27) Casula, A.; Begines, P.; Bettoschi, A.; Fernandez-Bolanos, J. G.; Isaia, F.; Lippolis, V.; Lopez, O.; Picci, G.; Andrea Scorciapino, M.; Caltagirone, C. *Chem. Commun.* **2017**, *53*, 11869.
(28) Casula, A.; Llopis-Lorente, A.; Garau, A.; Isaia, F.; Kubicki, M.; Lippolis, V.; Sancenon, F.; Martinez-Manez, R.; Owczarzak, A.; Santi, C.; Andrea Scorciapino, M.; Caltagirone, C. *Chem. Commun.* **2017**, *53*, 3729.
(29) Busschaert, N.; Elmes, R. B.; Czech, D. D.; Wu, X.; Kirby, I. L.; Peck, E. M.; Hendzel, K. D.; Shaw, S. K.; Chan, B.; Smith, B. D.; Jolliffe, K. A.; Gale, P. A. *Chem. Sci.* **2014**, *5*, 3617.
(30) Elmes, R. B.; Jolliffe, K. A. *Chem. Commun.* **2015**, *51*, 4951.
(31) Zwicker, V. E.; Yuen, K. K. Y.; Smith, D. G.; Ho, J.; Qin, L.; Turner, P.; Jolliffe, K. A. *Chem. Eur. J.* **2018**, *24*, 1140.
(32) Ho, J.; Zwicker, V. E.; Yuen, K. K. Y.; Jolliffe, K. A. *J. Org. Chem.* **2017**, *82*, 10732.

(33) Cai, J.; Sessler, J. L. *Chem. Soc. Rev.* **2014**, *43*, 6198.

(34) Pandurangan, K.; Kitchen, J. A.; Gunnlaugsson, T. *Tetrahedron Lett.* **2013**, *54*, 2770.

(35) Tepper, R.; Schubert, U. S. *Angew. Chem., Int. Ed.* **2018**, *57*, 6004.

(36) Cavallo, G.; Metrangolo, P.; Milani, R.; Pilati, T.; Priimagi, A.; Resnati, G.; Terraneo, G. *Chem. Rev.* **2016**, *116*, 2478.

(37) Wu, X.; Judd, Luke W.; Howe, Ethan N. W.; Withecombe, Anne M.; Soto-Cerrato, V.; Li, H.; Busschaert, N.; Valkenier, H.; Pérez-Tomás, R.; Sheppard, David N.; Jiang, Y.-B.; Davis, Anthony P.; Gale, Philip A. *Chem* **2016**, *1*, 127.

(38) Amendola, V.; Boiocchi, M.; Fabbrizzi, L.; Fusco, N. *Eur. J. Org. Chem.* **2011**, *2011*, 6434.

(39) Kang, S. O.; Powell, D.; Day, V. W.; Bowman-James, K. *Angew. Chem., Int. Ed.* **2006**, *45*, 1921.

(40) Kang, S. O.; VanderVelde, D.; Powell, D.; Bowman-James, K. *J. Am. Chem. Soc.* **2004**, *126*, 12272.

(41) Kang, S. O.; Llinares, J. M.; Powell, D.; VanderVelde, D.; Bowman-James, K. *J. Am. Chem. Soc.* **2003**, *125*, 10152.

(42) Curiel, D.; Más-Montoya, M.; Sánchez, G. *Coord. Chem. Rev.* **2015**, *284*, 19.

(43) Wezenberg, S. J.; Vlatkovic, M.; Kistemaker, J. C.; Feringa, B. L. *J. Am. Chem. Soc.* **2014**, *136*, 16784.

(44) Juwarker, H.; Suk, J. M.; Jeong, K. S. *Chem. Soc. Rev.* **2009**, *38*, 3316.

(45) Wu, B.; Jia, C.; Wang, X.; Li, S.; Huang, X.; Yang, X. J. *Org. Lett.* **2012**, *14*, 684.

(46) Wang, X. L.; Jia, C. D.; Huang, X. J.; Wu, B. *Inorg. Chem. Commun.* **2011**, *14*, 1508.

(47) Olivari, M.; Montis, R.; Berry, S. N.; Karagiannidis, L. E.; Coles, S. J.; Horton, P. N.; Mapp, L. K.; Gale, P. A.; Caltagirone, C. *Dalton Trans.* **2016**, *45*, 11892.

(48) Jeon, H. G.; Jang, H. B.; Kang, P.; Choi, Y. R.; Kim, J.; Lee, J. H.; Choi, M. G.; Jeong, K. S. *Org. Lett.* **2016**, *18*, 4404.

(49) Borissov, A.; Lim, J. Y. C.; Brown, A.; Christensen, K. E.; Thompson, A. L.; Smith, M. D.; Beer, P. D. *Chem. Commun.* **2017**, *53*, 2483.

(50) Juwarker, H.; Lenhardt, J. M.; Pham, D. M.; Craig, S. L. *Angew. Chem., Int. Ed.* **2008**, *47*, 3740.

(51) Meudtner, R. M.; Hecht, S. *Angew. Chem., Int. Ed.* **2008**, *47*, 4926.

(52) Jia, C.; Wang, Q. Q.; Begum, R. A.; Day, V. W.; Bowman-James, K. *Org. Biomol. Chem.* **2015**, *13*, 6953.

(53) Robson, R. N.; Hay, B. P.; Pfeffer, F. M. *ChemistrySelect* **2017**, *2*, 4605.

(54) Li, H.; Valkenier, H.; Judd, L. W.; Brotherhood, P. R.; Hussain, S.; Cooper, J. A.; Jurcek, O.; Sparkes, H. A.; Sheppard, D. N.; Davis, A. P. *Nat. Chem.* **2016**, *8*, 24.

(55) Elmes, R. B.; Yuen, K. K.; Jolliffe, K. A. *Chem. Eur. J.* **2014**, *20*, 7373.

(56) Jowett, L. A.; Howe, E. N. W.; Wu, X.; Busschaert, N.; Gale, P. A. *Chem. Eur. J.* **2018**, *24*, 10475.

(57) Rajbanshi, A.; Moyer, B. A.; Custelcean, R. *Cryst. Growth Des.* **2011**, *11*, 2702.

(58) Moyer, B. A.; Custelcean, R.; Hay, B. P.; Sessler, J. L.; Bowman-James, K.; Day, V. W.; Kang, S. O. *Inorg. Chem.* **2013**, *52*, 3473.

(59) Amendola, V.; Bergamaschi, G.; Boiocchi, M.; Legnani, L.; Presti, E. L.; Miljkovic, A.; Monzani, E.; Pancotti, F. *Chem. Commun.* **2016**, *52*, 10910.

(60) Valkenier, H.; Dias, C. M.; Porter Goff, K. L.; Jurcek, O.; Puttreddy, R.; Rissanen, K.; Davis, A. P. *Chem. Commun.* **2015**, *51*, 14235.

(61) Portis, B.; Mirchi, A.; Emami Khansari, M.; Pramanik, A.; Johnson, C. R.; Powell, D. R.; Leszczynski, J.; Hossain, M. A. *ACS Omega* **2017**, *2*, 5840.

(62) Constable, E. C. In *Metals and Ligand Reactivity* 2005, p 135.

(63) Li, Y.; Flood, A. H. *J. Am. Chem. Soc.* **2008**, *130*, 12111.

(64) Qin, L.; Hartley, A.; Turner, P.; Elmes, R. B. P.; Jolliffe, K. A. *Chem. Sci.* **2016**, *7*, 4563.

(65) Leczycka-Wilk, K.; Dabrowa, K.; Cmoch, P.; Jarosz, S. *Org. Lett.* **2017**, *19*, 4596.

(66) Young, P. G.; Jolliffe, K. A. *Org. Biomol. Chem.* **2012**, *10*, 2664.

(67) Dungan, V. J.; Ngo, H. T.; Young, P. G.; Jolliffe, K. A. *Chem. Commun.* **2013**, *49*, 264.

(68) Butler, S. J.; Jolliffe, K. A. *Org. Biomol. Chem.* **2011**, *9*, 3471.

(69) Butler, S. J.; Jolliffe, K. A.; Lee, W. Y. G.; McDonough, M. J.; Reynolds, A. J. *Tetrahedron* **2011**, *67*, 1019.

(70) Butler, S. J.; Jolliffe, K. A. *Chem Asian J* **2012**, *7*, 2621.

(71) Young, P. G.; Clegg, J. K.; Bhadbhade, M.; Jolliffe, K. A. *Chem. Commun.* **2011**, *47*, 463.

(72) Yoon, D. W.; Gross, D. E.; Lynch, V. M.; Sessler, J. L.; Hay, B. P.; Lee, C. H. *Angew. Chem., Int. Ed.* **2008**, *47*, 5038.

(73) Ayme, J. F.; Beves, J. E.; Campbell, C. J.; Gil-Ramirez, G.; Leigh, D. A.; Stephens, A. J. *J. Am. Chem. Soc.* **2015**, *137*, 9812.

(74) Hasenknopf, B.; Lehn, J. M.; Kneisel, B. O.; Baum, G.; Fenske, D. *Angew Chem Int Edit* **1996**, *35*, 1838.

(75) Jowett, L. A.; Howe, E. N. W.; Soto-Cerrato, V.; Van Rossom, W.; Perez-Tomas, R.; Gale, P. A. *Sci Rep* **2017**, *7*, 9397.

(76) Bak, K. M.; Chmielewski, M. J. *Eur. J. Org. Chem.* **2015**, *2015*, 4077.

(77) Zahran, E. M.; Fatila, E. M.; Chen, C. H.; Flood, A. H.; Bachas, L. G. *Anal. Chem.* **2018**, *90*, 1925.

(78) Fatila, E. M.; Twum, E. B.; Sengupta, A.; Pink, M.; Karty, J. A.; Raghavachari, K.; Flood, A. H. *Angew. Chem., Int. Ed.* **2016**, *55*, 14057.

(79) Fatila, E. M.; Twum, E. B.; Karty, J. A.; Flood, A. H. *Chem. Eur. J.* **2017**, *23*, 10652.

(80) Fatila, E. M.; Pink, M.; Twum, E. B.; Karty, J. A.; Flood, A. H. *Chem. Sci.* **2018**, *9*, 2863.

(81) Ji, L.; Yang, Z.; Zhao, Y.; Sun, M.; Cao, L.; Yang, X. J.; Wang, Y. Y.; Wu, B. *Chem. Commun.* **2016**, *52*, 7310.

(82) Dey, S. K.; Basu, A.; Chutia, R.; Das, G. *RSC Adv.* **2016**, *6*, 26568.

(83) Rice, C. R.; Slater, C.; Faulkner, R. A.; Allan, R. L. *Angew. Chem., Int. Ed.* **2018**, *57*, 13071.

(84) Zhao, J.; Yang, D.; Zhao, Y.; Cao, L.; Zhang, Z.; Yang, X. J.; Wu, B. *Dalton Trans.* **2016**, *45*, 7360.

(85) Dutta, R.; Chakraborty, S.; Bose, P.; Ghosh, P. *Eur. J. Inorg. Chem.* **2014**, *2014*, 4134.

(86) Basu, A.; Chutia, R.; Das, G. *CrystEngComm* **2014**, *16*, 4886.

(87) Custelcean, R.; Remy, P. *Cryst. Growth Des.* **2009**, *9*, 1985.

(88) Custelcean, R.; Sloop, F. V.; Rajbanshi, A.; Wan, S.; Moyer, B. A. *Cryst. Growth Des.* **2014**, *15*, 517.

(89) Caballero, A.; Zapata, F.; Beer, P. D. *Coord. Chem. Rev.* **2013**, *257*, 2434.

(90) Mercurio, J. M.; Knighton, R. C.; Cookson, J.; Beer, P. D. *Chem. Eur. J.* **2014**, *20*, 11740.

(91) Mullen, K. M.; Mercurio, J.; Serpell, C. J.; Beer, P. D. *Angew. Chem., Int. Ed.* **2009**, *48*, 4781.

(92) White, N. G.; Costa, P. J.; Carvalho, S.; Felix, V.; Beer, P. D. *Chem. Eur. J.* **2013**, *19*, 17751.

(93) White, N. G.; Beer, P. D. *Chem. Commun.* **2012**, *48*, 8499.

(94) Robinson, S. W.; Mustoe, C. L.; White, N. G.; Brown, A.; Thompson, A. L.; Kennepohl, P.; Beer, P. D. *J. Am. Chem. Soc.* **2015**, *137*, 499.

(95) Langton, M. J.; Beer, P. D. *Chem. Commun.* **2014**, *50*, 8124.

(96) Barendt, T. A.; Rasovic, I.; Lebedeva, M. A.; Farrow, G. A.; Auty, A.; Chekulaev, D.; Sazanovich, I. V.; Weinstein, J. A.; Porfyrakis, K.; Beer, P. D. *J. Am. Chem. Soc.* **2018**, *140*, 1924.

(97) Barendt, T. A.; Ferreira, L.; Marques, I.; Felix, V.; Beer, P. D. *J. Am. Chem. Soc.* **2017**, *139*, 9026.

(98) Manna, U.; Nayak, B.; Das, G. *Cryst. Growth Des.* **2016**, *16*, 7163.

(99) Manna, U.; Chutia, R.; Das, G. *Cryst. Growth Des.* **2016**, *16*, 2893.

(100) Manna, U.; Kayal, S.; Samanta, S.; Das, G. *Dalton Trans.* **2017**, *46*, 10374.

(101) Wu, B.; Li, S.; Lei, Y.; Hu, H.; de Sousa Amadeu, N.; Janiak, C.; Mathieson, J. S.; Long, D. L.; Cronin, L.; Yang, X. J. *Chem. Eur. J.* **2015**, *21*, 2588.

(102) He, Q.; Tu, P.; Sessler, J. L. *Chem* **2018**, *4*, 46.

(103) Chutia, R.; Dey, S. K.; Das, G. *Cryst. Growth Des.* **2015**, *15*, 4993.

(104) Blazek, V.; Molcanov, K.; Mlinaric-Majerski, K.; Kojic-Prodic, B.; Basaric, N. *Tetrahedron* **2013**, *69*, 517.

(105) Zhang, D.; Ronson, T. K.; Mosquera, J.; Martinez, A.; Guy, L.; Nitschke, J. R. *J. Am. Chem. Soc.* **2017**, *139*, 6574.

(106) Zhang, D.; Ronson, T. K.; Mosquera, J.; Martinez, A.; Nitschke, J. R. *Angew. Chem., Int. Ed.* **2018**, *57*, 3717.

(107) Zhang, W.; Yang, D.; Zhao, J.; Hou, L.; Sessler, J. L.; Yang, X. J.; Wu, B. *J. Am. Chem. Soc.* **2018**, *140*, 5248.

(108) Yang, D.; Zhao, J.; Yu, L.; Lin, X.; Zhang, W.; Ma, H.; Gogoll, A.; Zhang, Z.; Wang, Y.; Yang, X. J.; Wu, B. *J. Am. Chem. Soc.* **2017**, *139*, 5946.

(109) Wu, B.; Cui, F.; Lei, Y.; Li, S.; Amadeu Nde, S.; Janiak, C.; Lin, Y. J.; Weng, L. H.; Wang, Y. Y.; Yang, X. J. *Angew. Chem., Int. Ed.* **2013**, *52*, 5096.

(110) Jia, C.; Wu, B.; Li, S.; Huang, X.; Zhao, Q.; Li, Q. S.; Yang, X. J. *Angew. Chem., Int. Ed.* **2011**, *50*, 486.

(111) Marcos, V.; Stephens, A. J.; Jaramillo-Garcia, J.; Nussbaumer, A. L.; Woltering, S. L.; Valero, A.; Lemonnier, J. F.; Vitorica-Yrezabal, I. J.; Leigh, D. A. *Science* **2016**, *352*, 1555.

(112) Leigh, D. A.; Pritchard, R. G.; Stephens, A. J. *Nat. Chem.* **2014**, *6*, 978.

(113) Ayme, J. F.; Beves, J. E.; Leigh, D. A.; McBurney, R. T.; Rissanen, K.; Schultz, D. *J. Am. Chem. Soc.* **2012**, *134*, 9488.

(114) Ayme, J. F.; Beves, J. E.; Leigh, D. A.; McBurney, R. T.; Rissanen, K.; Schultz, D. *Nat. Chem.* **2011**, *4*, 15.

(115) Lee, S.; Chen, C. H.; Flood, A. H. *Nat. Chem.* **2013**, *5*, 704.

(116) Qiao, B.; Liu, Y.; Lee, S.; Pink, M.; Flood, A. H. *Chem. Commun.* **2016**, *52*, 13675.

(117) Savyasachi, A. J.; Kotova, O.; Shanmugaraju, S.; Bradberry, S. J.; O'Maille, G. M.; Gunnlaugsson, T. *Chem* **2017**, *3*, 764.

(118) Winter, A.; Schubert, U. S. *Chem. Soc. Rev.* **2016**, *45*, 5311.

(119) Ding, X. H.; Wang, S.; Li, Y. H.; Huang, W. *J. Mol. Struct.* **2015**, *1079*, 266.

(120) Ding, X. H.; Wang, S.; Li, Y. H.; Huang, W. *Inorg. Chem. Front.* **2015**, *2*, 263.

(121) White, N. G.; Carta, V.; MacLachlan, M. J. *Cryst. Growth Des.* **2015**, *15*, 1540.

(122) White, N. G.; MacLachlan, M. J. *Cryst. Growth Des.* **2015**, *15*, 5629.

(123) White, N. G.; MacLachlan, M. J. *Chem. Sci.* **2015**, *6*, 6245.

(124) Custelcean, R.; Williams, N. J.; Seipp, C. A. *Angew. Chem., Int. Ed.* **2015**, *54*, 10525.

(125) Basu, A.; Das, G. *J. Org. Chem.* **2014**, *79*, 2647.

(126) Zapata, F.; Gonzalez, L.; Caballero, A.; Bastida, A.; Bautista, D.; Molina, P. *J. Am. Chem. Soc.* **2018**, *140*, 2041.

(127) Piepenbrock, M. O.; Lloyd, G. O.; Clarke, N.; Steed, J. W. *Chem. Commun.* **2008**, 2644.

(128) Stanley, C. E.; Clarke, N.; Anderson, K. M.; Elder, J. A.; Lenthall, J. T.; Steed, J. W. *Chem. Commun.* **2006**, 3199.

(129) Yamanaka, M. *Chem. Rec.* **2016**, *16*, 768.

(130) Offiler, C. A.; Jones, C. D.; Steed, J. W. *Chem. Commun.* **2017**, *53*, 2024.

(131) James, S. J.; Perrin, A.; Jones, C. D.; Yufit, D. S.; Steed, J. W. *Chem. Commun.* **2014**, *50*, 12851.

(132) Garcia, F.; Torres, M. R.; Matesanz, E.; Sanchez, L. *Chem. Commun.* **2011**, *47*, 5016.

(133) Garcia, F.; Arago, J.; Viruela, R.; Orti, E.; Sanchez, L. *Org. Biomol. Chem.* **2013**, *11*, 765.

(134) Bhardwaj, I.; Haridas, V. *Tetrahedron* **2016**, *72*, 2900.

(135) Ghosh, A.; Das, P.; Kaushik, R.; Damodaran, K. K.; Jose, D. A. *RSC Adv.* **2016**, *6*, 83303.

(136) dos Santos, C. M. G.; Fernández, P. B.; Plush, S. E.; Leonard, J. P.; Gunnlaugsson, T. *Chem. Commun.* **2007**, 3389.

(137) Duke, R. M.; Gunnlaugsson, T. *Tetrahedron Lett.* **2011**, *52*, 1503.

(138) Pandurangan, K.; Aletti, A. B.; Montroni, D.; Kitchen, J. A.; Martinez-Calvo, M.; Blasco, S.; Gunnlaugsson, T.; Scanlan, E. M. *Org. Lett.* **2017**, *19*, 1068.

(139) Klein-Hitpaß, M.; Lynes, A. D.; Hawes, C. S.; Byrne, K.; Schmitt, W.; Gunnlaugsson, T. *Supramol. Chem.* **2017**, *30*, 93.

(140) McCarney, E. P.; Hawes, C. S.; Kitchen, J. A.; Byrne, K.; Schmitt, W.; Gunnlaugsson, T. *Inorg. Chem.* **2018**, *57*, 3920.

(141) Shanmugaraju, S.; Hawes, C. S.; Savyasachi, A. J.; Blasco, S.; Kitchen, J. A.; Gunnlaugsson, T. *Chem. Commun.* **2017**, *53*, 12512.

(142) Barry, D. E.; Hawes, C. S.; Blasco, S.; Gunnlaugsson, T. *Cryst. Growth Des.* **2016**, *16*, 5194.

(143) Gillen, D. M.; Hawes, C. S.; Gunnlaugsson, T. *J. Org. Chem.* **2018**, *83*, 10398.

(144) Lynes, A. D.; Hawes, C. S.; Byrne, K.; Schmitt, W.; Gunnlaugsson, T. *Dalton Trans.* **2018**, *47*, 5259.

(145) Shanmugaraju, S.; Umadevi, D.; Savyasachi, A. J.; Byrne, K.; Ruether, M.; Schmitt, W.; Watson, G. W.; Gunnlaugsson, T. *J. Mater. Chem. A* **2017**, *5*, 25014.

(146) Lynes, A. D.; Hawes, C. S.; Ward, E. N.; Haffner, B.; Mobius, M. E.; Byrne, K.; Schmitt, W.; Pal, R.; Gunnlaugsson, T. *CrystEngComm* **2017**, *19*, 1427.

(147) Martinez-Calvo, M.; Kotova, O.; Mobius, M. E.; Bell, A. P.; McCabe, T.; Boland, J. J.; Gunnlaugsson, T. *J. Am. Chem. Soc.* **2015**, *137*, 1983.

(148) Kotova, O.; Daly, R.; dos Santos, C. M.; Kruger, P. E.; Boland, J. J.; Gunnlaugsson, T. *Inorg. Chem.* **2015**, *54*, 7735.

(149) Daly, R.; Kotova, O.; Boese, M.; Gunnlaugsson, T.; Boland, J. J. *ACS Nano* **2013**, *7*, 4838.

(150) Kotova, O.; Daly, R.; dos Santos, C. M.; Boese, M.; Kruger, P. E.; Boland, J. J.; Gunnlaugsson, T. *Angew. Chem., Int. Ed.* **2012**, *51*, 7208.

(151) dos Santos, C. M.; Boyle, E. M.; De Solis, S.; Kruger, P. E.; Gunnlaugsson, T. *Chem. Commun.* **2011**, *47*, 12176.

(152) Pandurangan, K.; Kitchen, J. A.; Blasco, S.; Boyle, E. M.; Fitzpatrick, B.; Feeney, M.; Kruger, P. E.; Gunnlaugsson, T. *Angew. Chem., Int. Ed.* **2015**, *54*, 4566.

(153) dos Santos, C. M.; McCabe, T.; Watson, G. W.; Kruger, P. E.; Gunnlaugsson, T. *J. Org. Chem.* **2008**, *73*, 9235.

(154) Jørgensen, M.; Krebs, F. C. *Tetrahedron Lett.* **2001**, *42*, 4717.
(155) Byrne, J. P.; Blasco, S.; Aletti, A. B.; Hessman, G.; Gunnlaugsson, T. *Angew. Chem., Int. Ed.* **2016**, *55*, 8938.
(156) Aletti, A., Synthesis of Heterocycles assisted by Urea:Anion complexes, Università degli Studi di Pavia and Trinity College, Dublin, 2014.
(157) Schneider, H. J. *Angew. Chem., Int. Ed.* **2009**, *48*, 3924.
(158) Biedermann, F.; Schneider, H. J. *Chem. Rev.* **2016**, *116*, 5216.
(159) Pandurangan, K.; Kitchen, J. A.; Blasco, S.; Paradisi, F.; Gunnlaugsson, T. *Chem. Commun.* **2014**, *50*, 10819.
(160) Solomos, M. A.; Watts, T. A.; Swift, J. A. *Cryst. Growth Des.* **2017**, *17*, 5065.
(161) Watt, M. M.; Zakharov, L. N.; Haley, M. M.; Johnson, D. W. *Angew. Chem., Int. Ed.* **2013**, *52*, 10275.
(162) Gampp, H.; Maeder, M.; Meyer, C. J.; Zuberbuhler, A. D. *Talanta* **1985**, *32*, 95.
(163) Sessler, J. L.; Gale, P.; Cho, W.-S. *Anion Receptor Chemistry*; Royal Society of Chemistry, Cambridge, 2006.
(164) Thordarson, P. *Chem. Soc. Rev.* **2011**, *40*, 1305.
(165) Blažek, V.; Bregović, N.; Mlinarić-Majerski, K.; Basarić, N. *Tetrahedron* **2011**, *67*, 3846.
(166) Arunachalam, M.; Ghosh, P. *Chem. Commun.* **2011**, *47*, 8477.
(167) Honglawan, A.; Yang, S. *Soft Matter* **2012**, *8*, 11897.
(168) Decato, S.; Mecozzi, S. In *Colloid and Interface Science in Pharmaceutical Research and Development*; Makino, K., Ed.; Elsevier: Amsterdam, 2014, p 319.
(169) Ji, X.; Wu, R. T.; Long, L.; Guo, C.; Khashab, N. M.; Huang, F.; Sessler, J. L. *J. Am. Chem. Soc.* **2018**, *140*, 2777.
(170) Shen, J.; Chai, W.; Wang, K.; Zhang, F. *ACS Appl Mater Interfaces* **2017**, *9*, 22440.
(171) Lito, P. F.; Aniceto, J. P. S.; Silva, C. M. *Water Air and Soil Pollution* **2012**, *223*, 6133.
(172) Ravikumar, I.; Ghosh, P. *Chem. Soc. Rev.* **2012**, *41*, 3077.
(173) Alberto, R.; Bergamaschi, G.; Braband, H.; Fox, T.; Amendola, V. *Angew. Chem., Int. Ed.* **2012**, *51*, 9772.
(174) Alberti, G.; Amendola, V.; Bergamaschi, G.; Colleoni, R.; Milanese, C.; Biesuz, R. *Dalton Trans.* **2013**, *42*, 6227.
(175) Zdanowski, S.; Romanski, J. *New J. Chem.* **2015**, *39*, 6216.
(176) Romanski, J.; Piatek, P. *Chem. Commun.* **2012**, *48*, 11346.
(177) Stals, P. J.; Korevaar, P. A.; Gillissen, M. A.; de Greef, T. F.; Fitie, C. F.; Sijbesma, R. P.; Palmans, A. R.; Meijer, E. W. *Angew. Chem., Int. Ed.* **2012**, *51*, 11297.
(178) Salamończyk, G. M. *Tetrahedron Lett.* **2011**, *52*, 155.
(179) Salamończyk, G. M. *Tetrahedron* **2012**, *68*, 10209.
(180) Ghosez, L.; Marchand-Brynaert, J. In *Encyclopedia of Reagents for Organic Synthesis* 2001.
(181) McCoy, C. P.; Brady, C.; Cowley, J. F.; McGlinchey, S. M.; McGoldrick, N.; Kinnear, D. J.; Andrews, G. P.; Jones, D. S. *Expert Opin Drug Deliv* **2010**, *7*, 605.
(182) Liu, Z. M.; Li, N. K.; Huang, X. F.; Wu, B.; Li, N.; Kwok, C. Y.; Wang, Y.; Wang, X. W. *Tetrahedron* **2014**, *70*, 2406.
(183) Shang, J.; Zhao, W.; Li, X.; Wang, Y.; Jiang, H. *Chem. Commun.* **2016**, *52*, 4505.
(184) Zurro, M.; Asmus, S.; Beckendorf, S.; Muck-Lichtenfeld, C.; Mancheno, O. G. *J. Am. Chem. Soc.* **2014**, *136*, 13999.
(185) Wang, Y.; Xiang, J.; Jiang, H. *Chem. Eur. J.* **2011**, *17*, 613.
(186) Schulze, B.; Schubert, U. S. *Chem. Soc. Rev.* **2014**, *43*, 2522.
(187) Haridas, V.; Sahu, S.; Kumar, P. P. P.; Sapala, A. R. *RSC Adv.* **2012**, *2*, 12594.

(188) Byrne, J. P.; Kitchen, J. A.; Gunnlaugsson, T. *Chem. Soc. Rev.* **2014**, *43*, 5302.

(189) Byrne, J. P.; Kitchen, J. A.; Kotova, O.; Leigh, V.; Bell, A. P.; Boland, J. J.; Albrecht, M.; Gunnlaugsson, T. *Dalton Trans.* **2014**, *43*, 196.

(190) Byrne, J. P.; Martinez-Calvo, M.; Peacock, R. D.; Gunnlaugsson, T. *Chem. Eur. J.* **2016**, *22*, 486.

(191) Li, Y.; Flood, A. H. *Angew. Chem., Int. Ed.* **2008**, *47*, 2649.

(192) Li, Y.; Pink, M.; Karty, J. A.; Flood, A. H. *J. Am. Chem. Soc.* **2008**, *130*, 17293.

(193) Bandyopadhyay, I.; Raghavachari, K.; Flood, A. H. *ChemPhysChem* **2009**, *10*, 2535.

(194) Bruns, C. J.; Stoddart, J. F. *The Nature of the Mechanical Bond: From Molecules to Machines*; Wiley, 2016.

(195) Gong, H. Y.; Rambo, B. M.; Karnas, E.; Lynch, V. M.; Sessler, J. L. *Nat. Chem.* **2010**, *2*, 406.

(196) Asakawa, M.; Dehaen, W.; Labbe, G.; Menzer, S.; Nouwen, J.; Raymo, F. M.; Stoddart, J. F.; Williams, D. J. *J. Org. Chem.* **1996**, *61*, 9591.

(197) Nielsen, M. B.; Jeppesen, J. O.; Lau, J.; Lomholt, C.; Damgaard, D.; Jacobsen, J. P.; Becher, J.; Stoddart, J. F. *J. Org. Chem.* **2001**, *66*, 3559.

(198) Yang, Y. D.; Sessler, J. L.; Gong, H. Y. *Chem. Commun.* **2017**, *53*, 9684.

(199) Wang, C. L.; Zhou, L.; Zhang, L.; Xiang, J. F.; Rambo, B. M.; Sessler, J. L.; Gong, H. Y. *Chem. Commun.* **2017**, *53*, 3669.

(200) Sessler, J. L.; Cai, J.; Gong, H. Y.; Yang, X.; Arambula, J. F.; Hay, B. P. *J. Am. Chem. Soc.* **2010**, *132*, 14058.

(201) Mungalpara, D.; Stegmuller, S.; Kubik, S. *Chem. Commun.* **2017**, *53*, 5095.

(202) Mungalpara, D.; Kelm, H.; Valkonen, A.; Rissanen, K.; Keller, S.; Kubik, S. *Org. Biomol. Chem.* **2016**, *15*, 102.

(203) Hancock, L. M.; Gilday, L. C.; Carvalho, S.; Costa, P. J.; Felix, V.; Serpell, C. J.; Kilah, N. L.; Beer, P. D. *Chem. Eur. J.* **2010**, *16*, 13082.

(204) Langton, M. J.; Robinson, S. W.; Marques, I.; Felix, V.; Beer, P. D. *Nat. Chem.* **2014**, *6*, 1039.

(205) Sambrook, M. R.; Beer, P. D.; Wisner, J. A.; Paul, R. L.; Cowley, A. R. *J. Am. Chem. Soc.* **2004**, *126*, 15364.

(206) Zheng, H.; Zhou, W.; Lv, J.; Yin, X.; Li, Y.; Liu, H.; Li, Y. *Chem. Eur. J.* **2009**, *15*, 13253.

(207) Denis, M.; Qin, L.; Turner, P.; Jolliffe, K. A.; Goldup, S. M. *Angew. Chem., Int. Ed.* **2018**, *57*, 5315.

(208) Marrs, C. N.; Evans, N. H. *Org. Biomol. Chem.* **2015**, *13*, 11021.

(209) Dietrich-Buchecker, C. O.; Sauvage, J. P.; Kern, J. M. *J. Am. Chem. Soc.* **1984**, *106*, 3043.

(210) McCarney, E. P., Templated synthesis of novel molecules and materials using 1,4-disubstituted-1,2,3-triazole supramolecular building blocks, Trinity College Dublin, 2017.

(211) Frassineti, C.; Ghelli, S.; Gans, P.; Sabatini, A.; Moruzzi, M. S.; Vacca, A. *Anal. Biochem.* **1995**, *231*, 374.

(212) Frassineti, C.; Alderighi, L.; Gans, P.; Sabatini, A.; Vacca, A.; Ghelli, S. *Anal. Bioanal. Chem.* **2003**, *376*, 1041.

(213) Collins, C. G.; Peck, E. M.; Kramer, P. J.; Smith, B. D. *Chem. Sci.* **2013**, *4*, 2557.

(214) Brown, A.; Lang, T.; Mullen, K. M.; Beer, P. D. *Org. Biomol. Chem.* **2017**, *15*, 4587.

(215) Dietrich, B.; Lehn, J. M.; Sauvage, J. P. *Tetrahedron Lett.* **1969**, *10*, 2889.

(216) Lehn, J. M.; Pine, S. H.; Watanabe, E.; Willard, A. K. *J. Am. Chem. Soc.* **1977**, *99*, 6766.

(217) Lehn, J. M. *Pure Appl. Chem.* **1977**, *49*, 857.

(218) Amendola, V.; Bergamaschi, G.; Buttafava, A.; Fabbrizzi, L.; Monzani, E. *J. Am. Chem. Soc.* **2010**, *132*, 147.
(219) Bond, A. D.; Derossi, S.; Jensen, F.; Larsen, F. B.; McKenzie, C. J.; Nelson, J. *Inorg. Chem.* **2005**, *44*, 5987.
(220) Arnaud-Neu, F.; Fuangswasdi, S.; Maubert, B.; Nelson, J.; McKee, V. *Inorg. Chem.* **2000**, *39*, 573.
(221) Wang, Q. Q.; Day, V. W.; Bowman-James, K. *Chem. Sci.* **2011**, *2*, 1735.
(222) Kang, S. O.; Llinares, J. M.; Day, V. W.; Bowman-James, K. *Chem. Soc. Rev.* **2010**, *39*, 3980.
(223) Alibrandi, G.; Amendola, V.; Bergamaschi, G.; Fabbrizzi, L.; Licchelli, M. *Org. Biomol. Chem.* **2015**, *13*, 3510.
(224) Bergamaschi, G.; Boiocchi, M.; Perrone, M. L.; Poggi, A.; Viviani, I.; Amendola, V. *Dalton Trans.* **2014**, *43*, 11352.
(225) Amendola, V.; Alberti, G.; Bergamaschi, G.; Biesuz, R.; Boiocchi, M.; Ferrito, S.; Schmidtchen, F. P. *Eur. J. Inorg. Chem.* **2012**, *2012*, 3410.
(226) Steiner, T. *Angew. Chem., Int. Ed.* **2002**, *41*, 49.
(227) Loughnane, B. J.; Scodinu, A.; Farrer, R. A.; Fourkas, J. T.; Mohanty, U. *J. Chem. Phys.* **1999**, *111*, 2686.
(228) Schoepff, L.; Kocher, L.; Durot, S.; Heitz, V. *J. Org. Chem.* **2017**, *82*, 5845.
(229) Kocher, L.; Durot, S.; Heitz, V. *Chem. Commun.* **2015**, *51*, 13181.
(230) Janssen Pharmaceutica N.V., Belg. Quinoline-derived amide modulators of vanilloid VR1 receptor, and their preparation, pharmaceutical compositions, and methods of use in the treatment of pain, inflammatory, and pulmonary conditions. WO2004069792A2, 2004

A2. Appendix Chapter 2

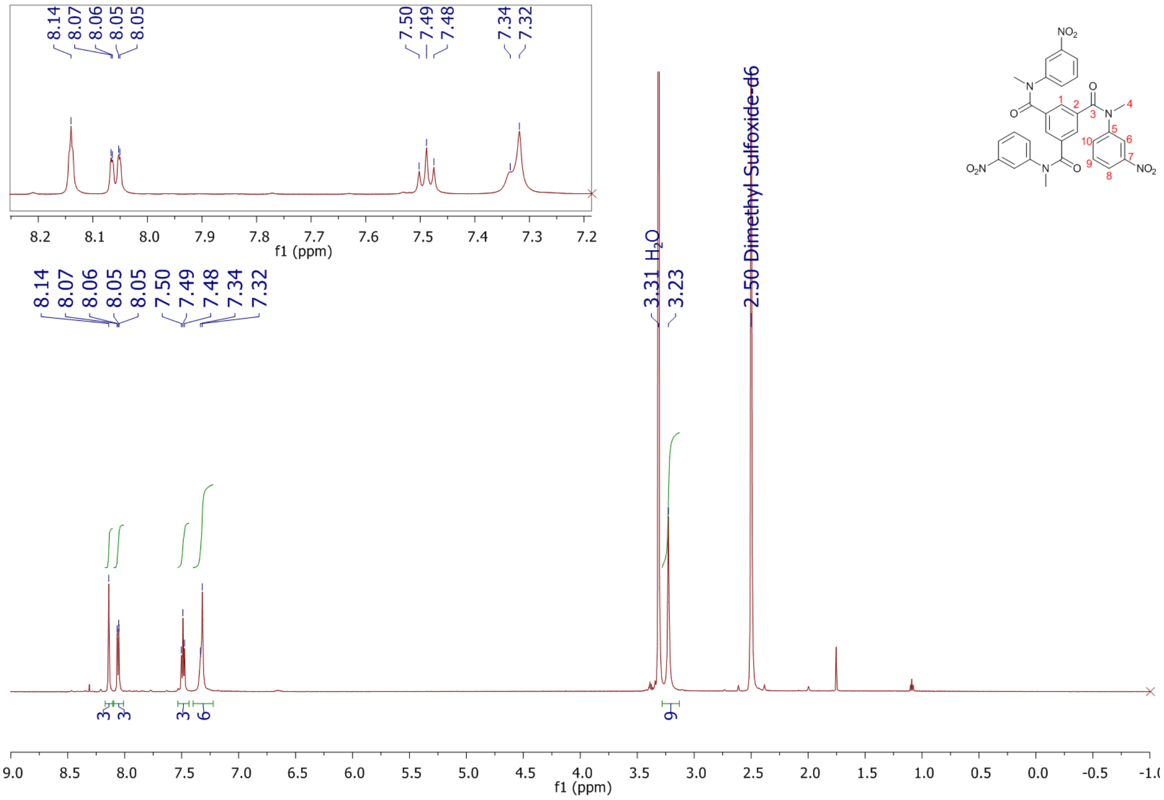

Figure A2. 1. 1^{1}H NMR (600 MHz) spectrum of **99** in DMSO-d_6.

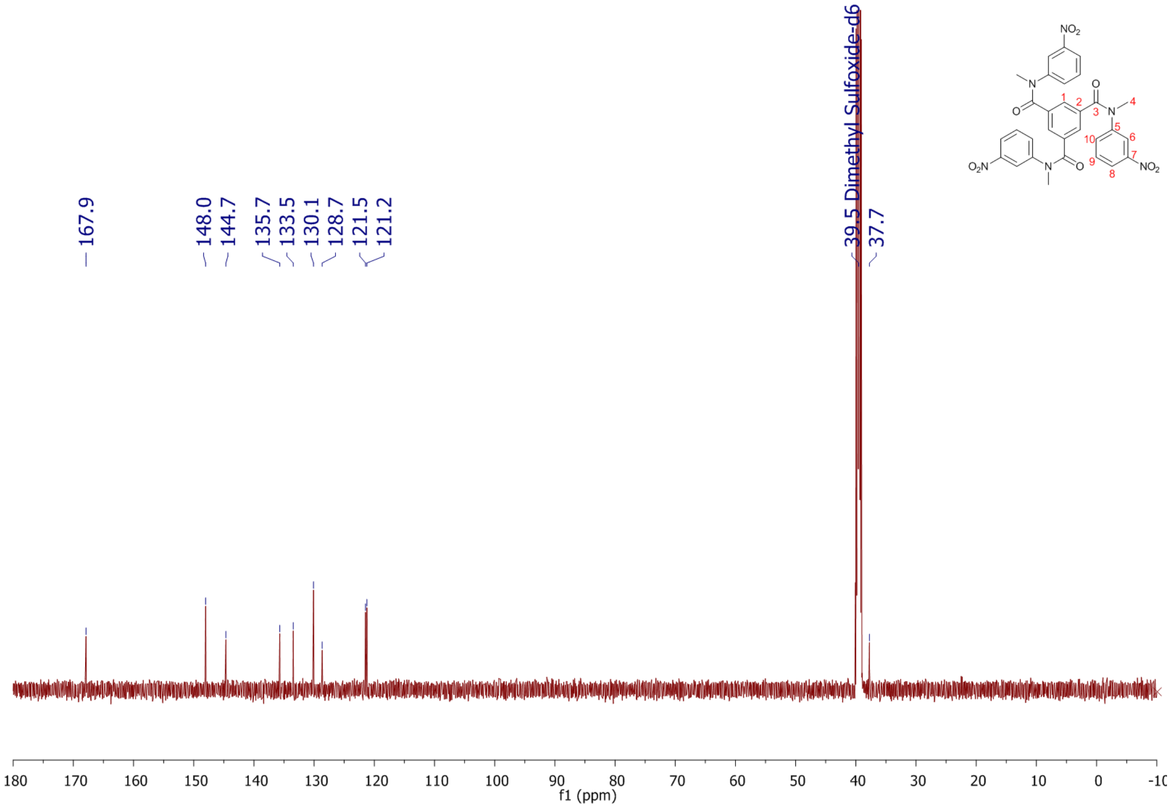

Figure A2. 2. ^{13}C NMR (151 MHz) spectrum of **99** in DMSO-d_6.

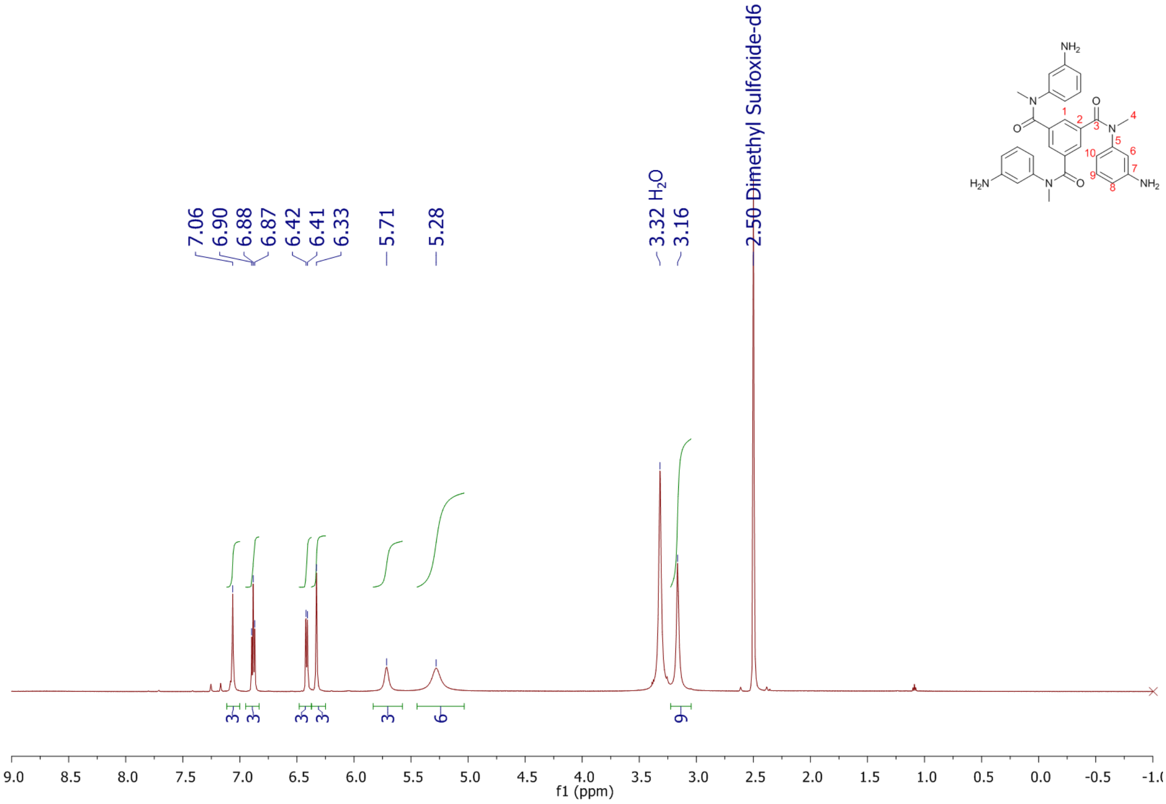

Figure A2. 3. ^{1}H NMR (600 MHz) spectrum of **100** in DMSO-d_6.

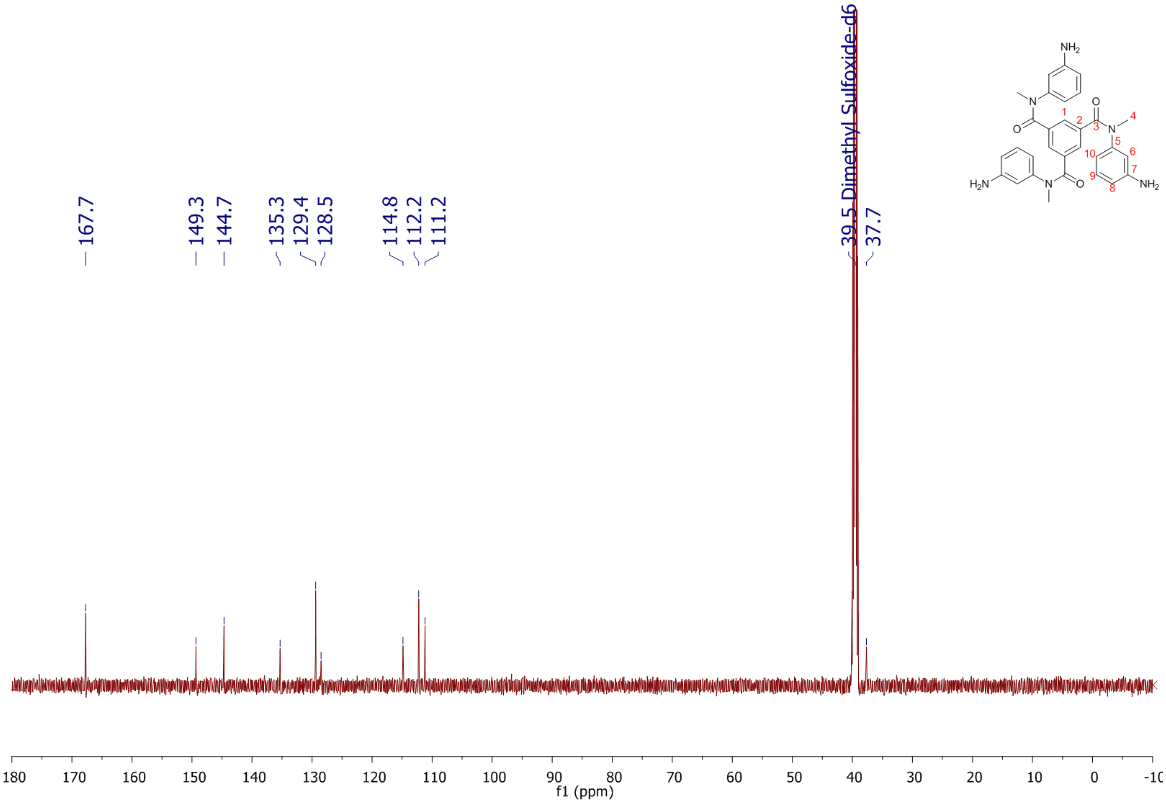

Figure A2. 4. ^{13}C NMR (151 MHz) spectrum of **100** in DMSO-d_6.

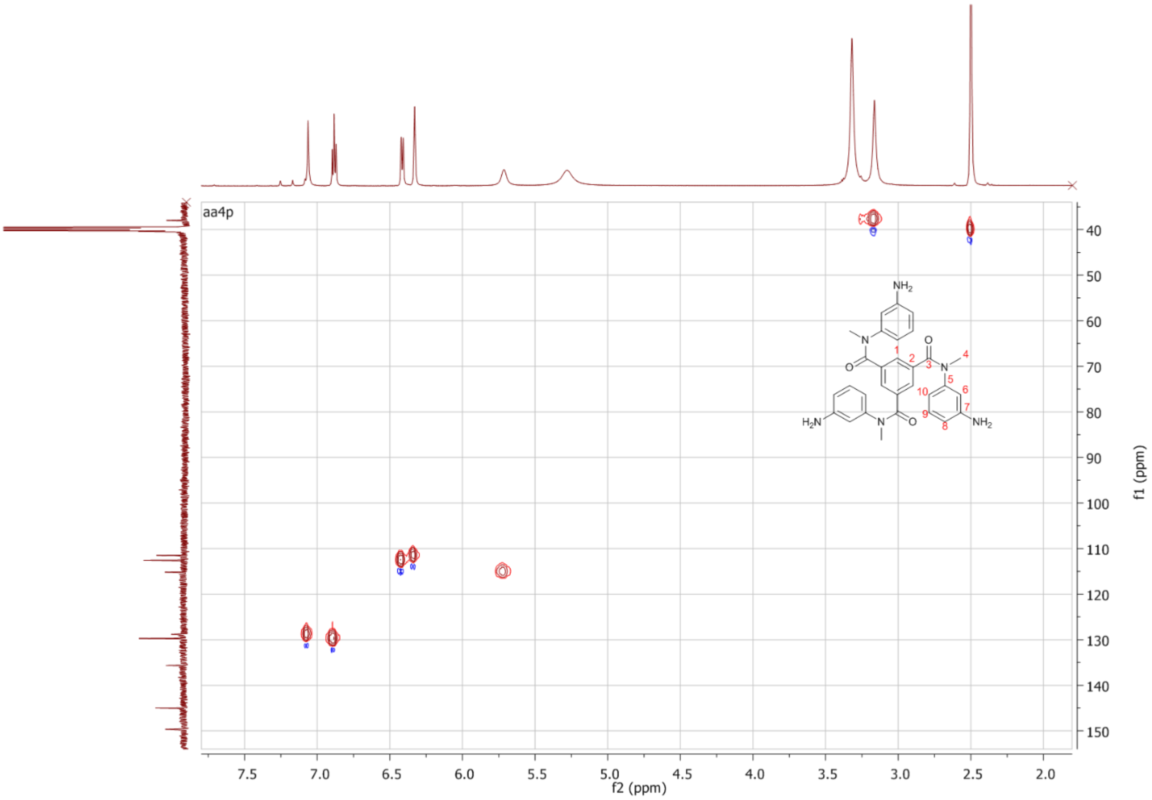

Figure A2. 5. . ^{13}C-^{1}H HSQC NMR spectrum of **100** in DMSO-d_6.

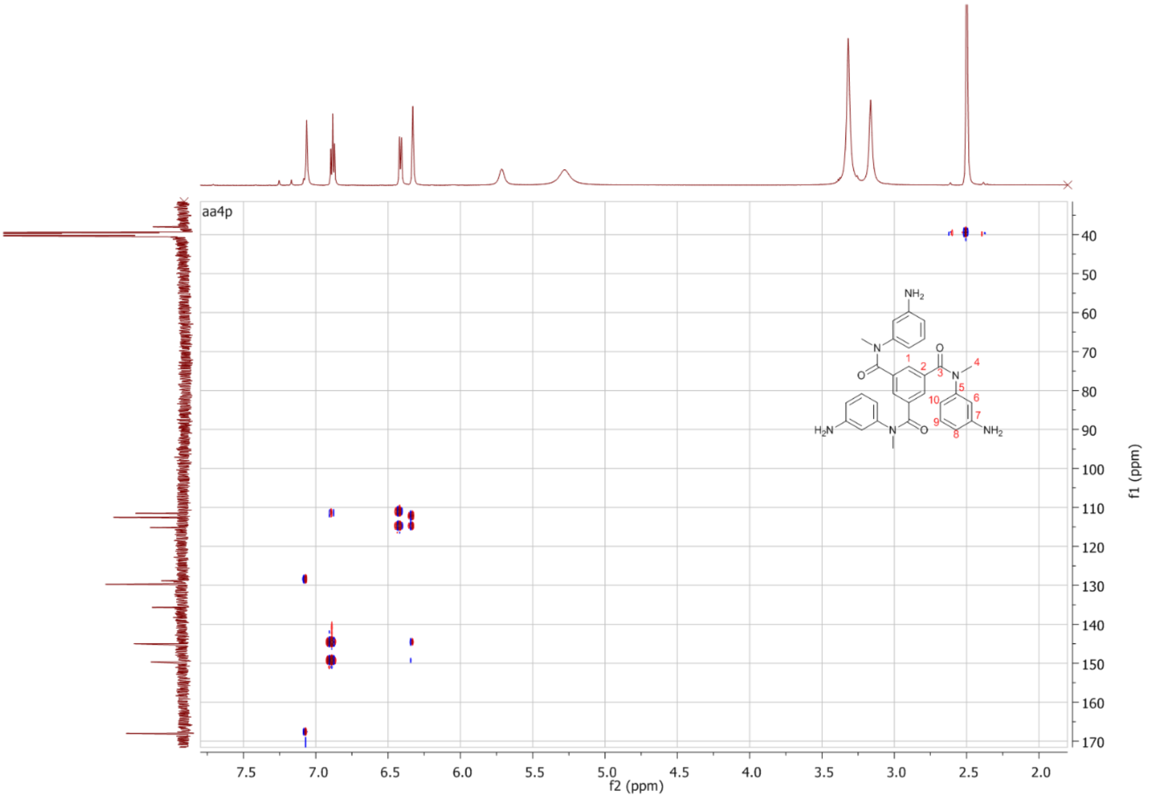

Figure A2. 6. ^{13}C-^{1}H HMBC NM R spectrum of **100** in DMSO-d_6.

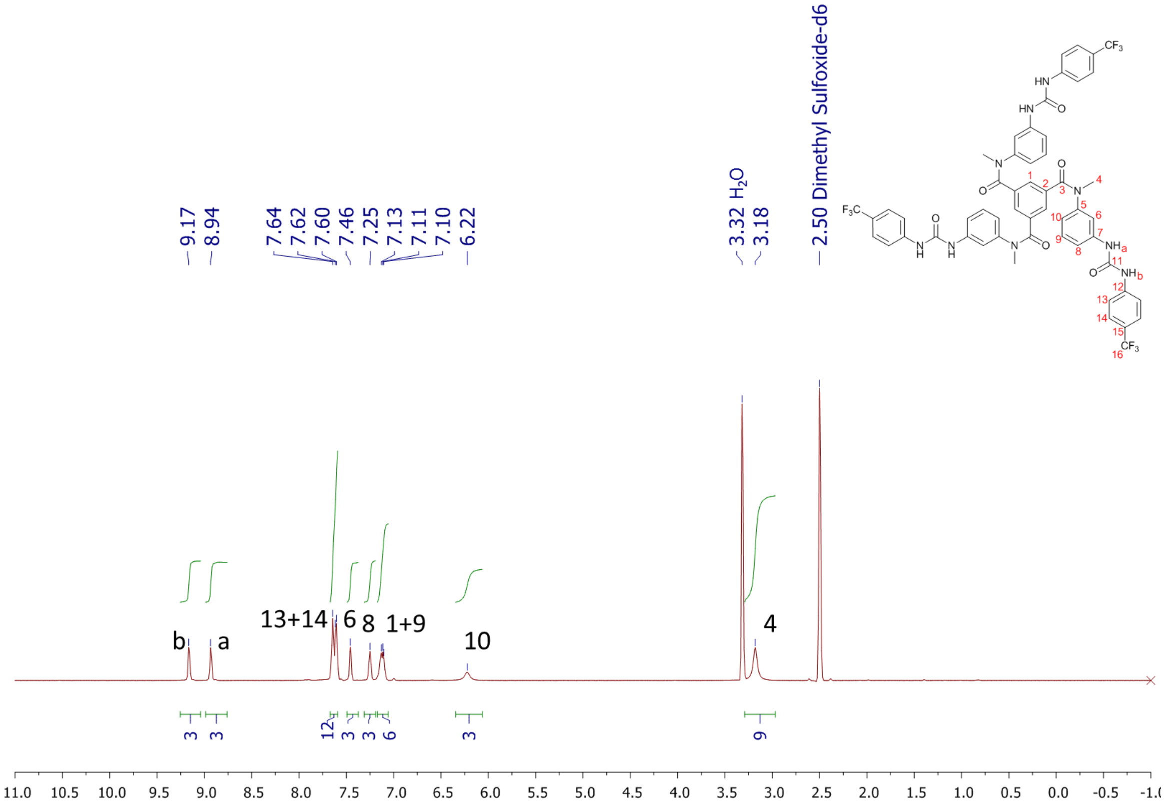

Figure A2. 7. ^{1}H NMR (600 MHz) of **86** in DMSO-d_6

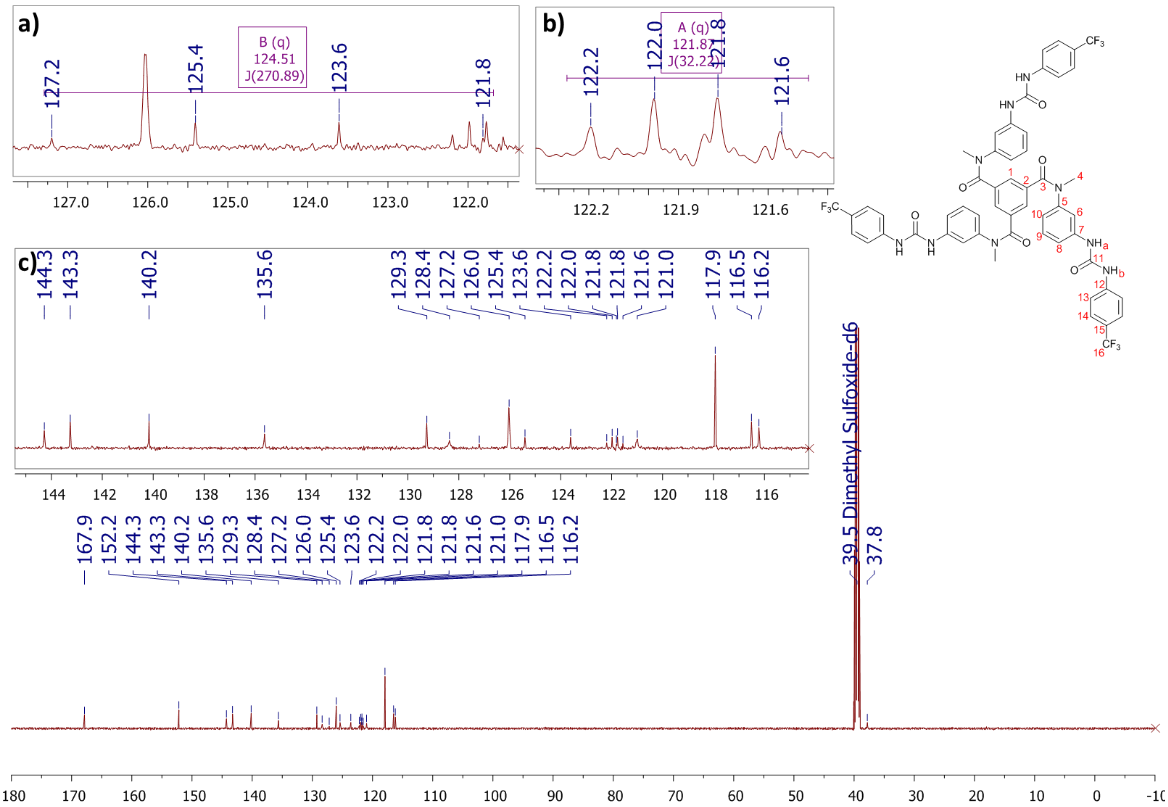

Figure A2. 8. ^{13}C NMR (151 MHz) of **86** in DMSO-d_6. a) Expansion in the quartet relative to C-16; b) Expansion on quartet relative to C-15.

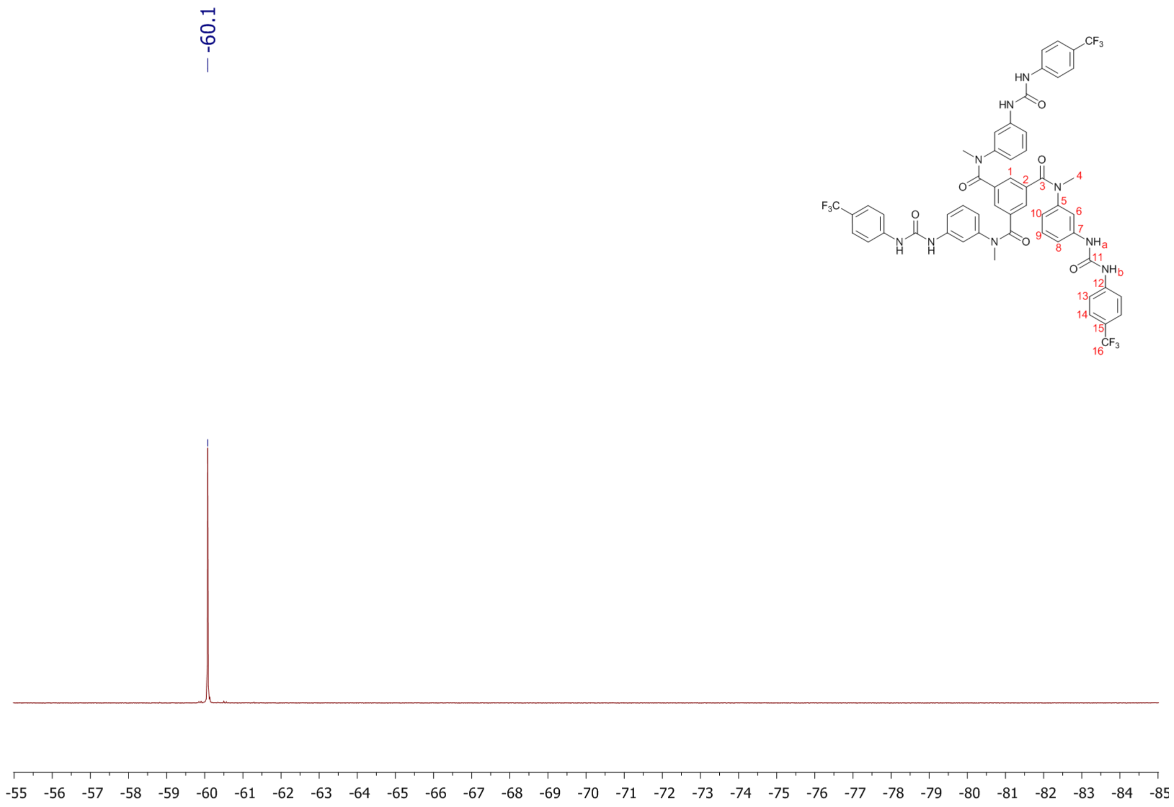

Figure A2. 10. ^{19}F NMR (376 MHz) spectrum of **86** in DMSO-*d*$_6$.

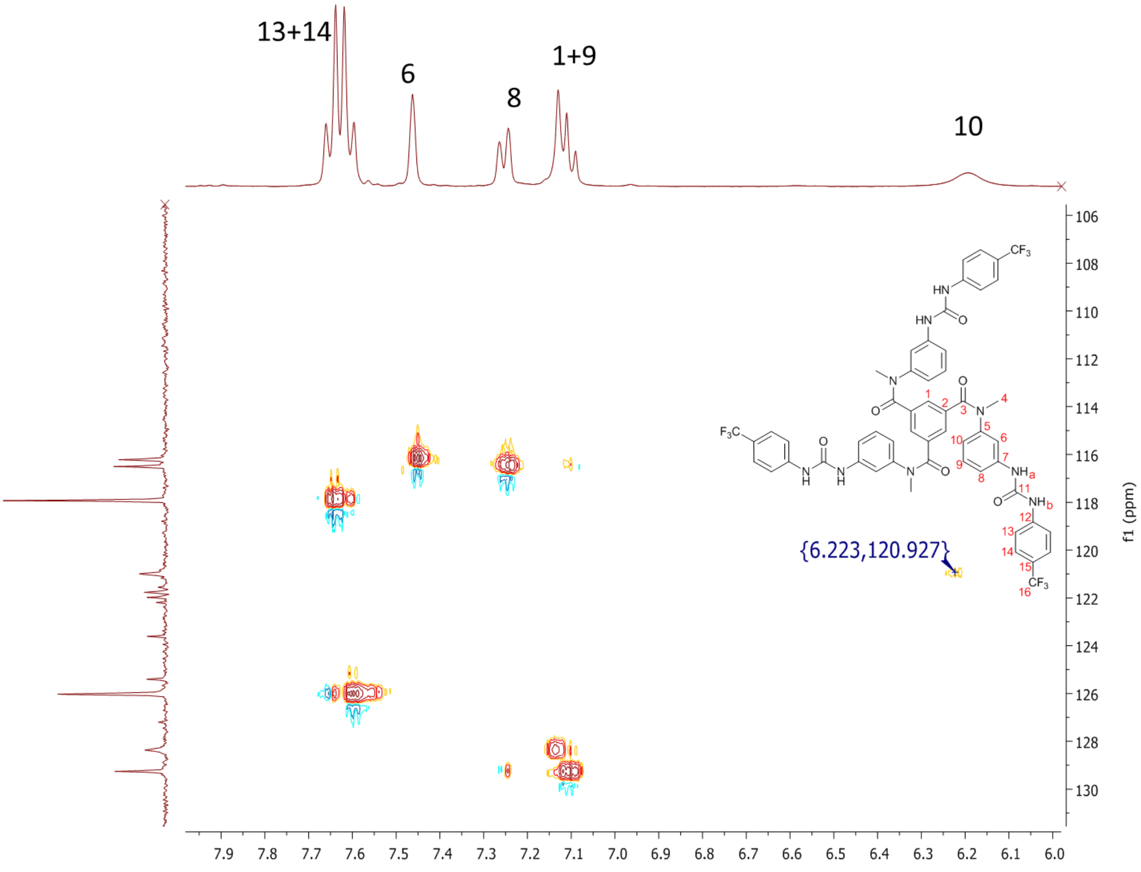

Figure A2. 9. ^{13}C-^{1}H HSQC NMR spectrum of **86** in DMSO-*d*$_6$.

Appendix A2

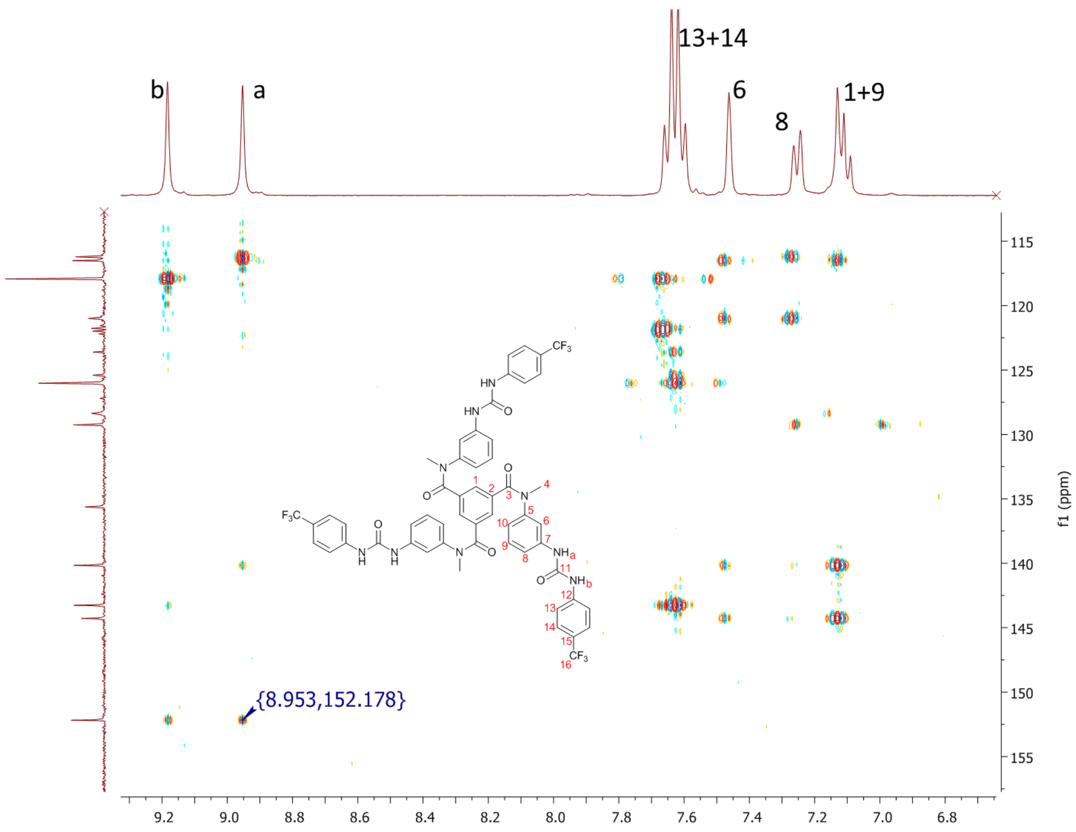

Figure A2. 11. ^{13}C-^{1}H HMBC NM R spectrum of **86** in DMSO-*d*$_6$.

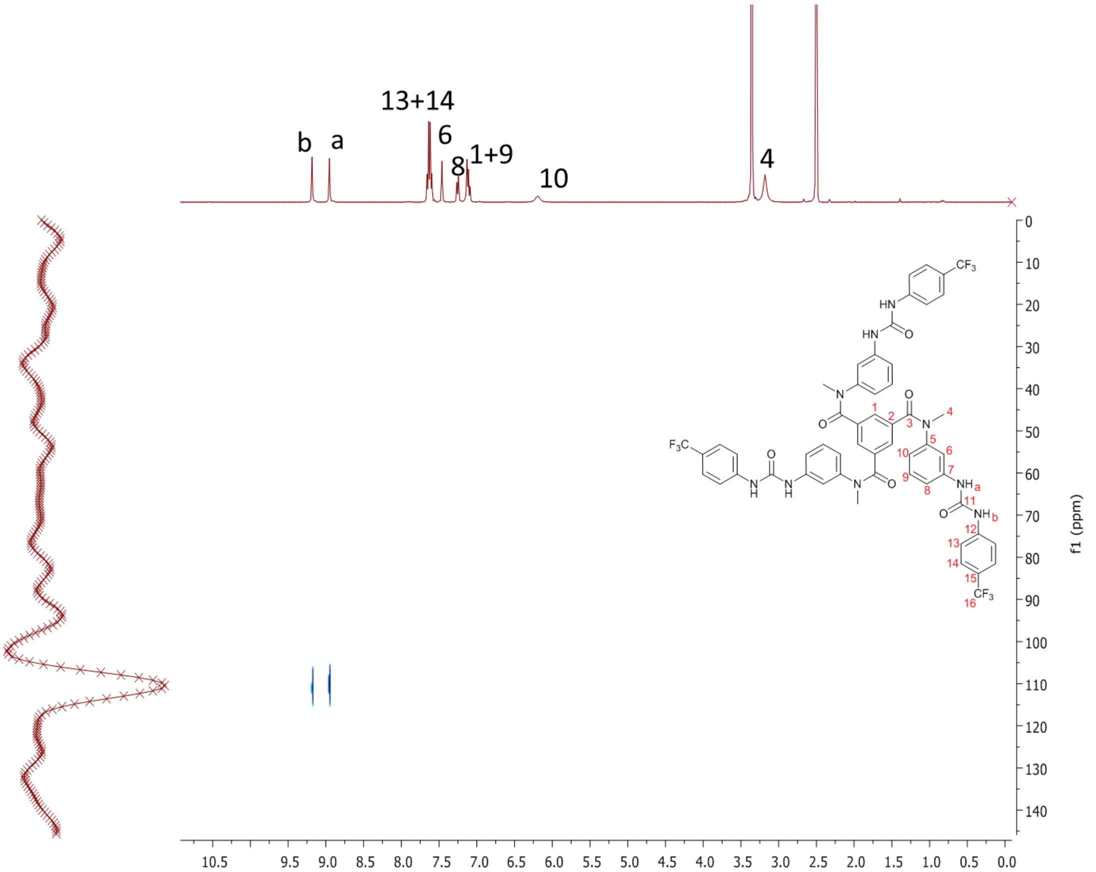

Figure A2. 12. ^{15}N-^{1}H HSQC NMR spectrum of **86** in DMSO-*d*$_6$.

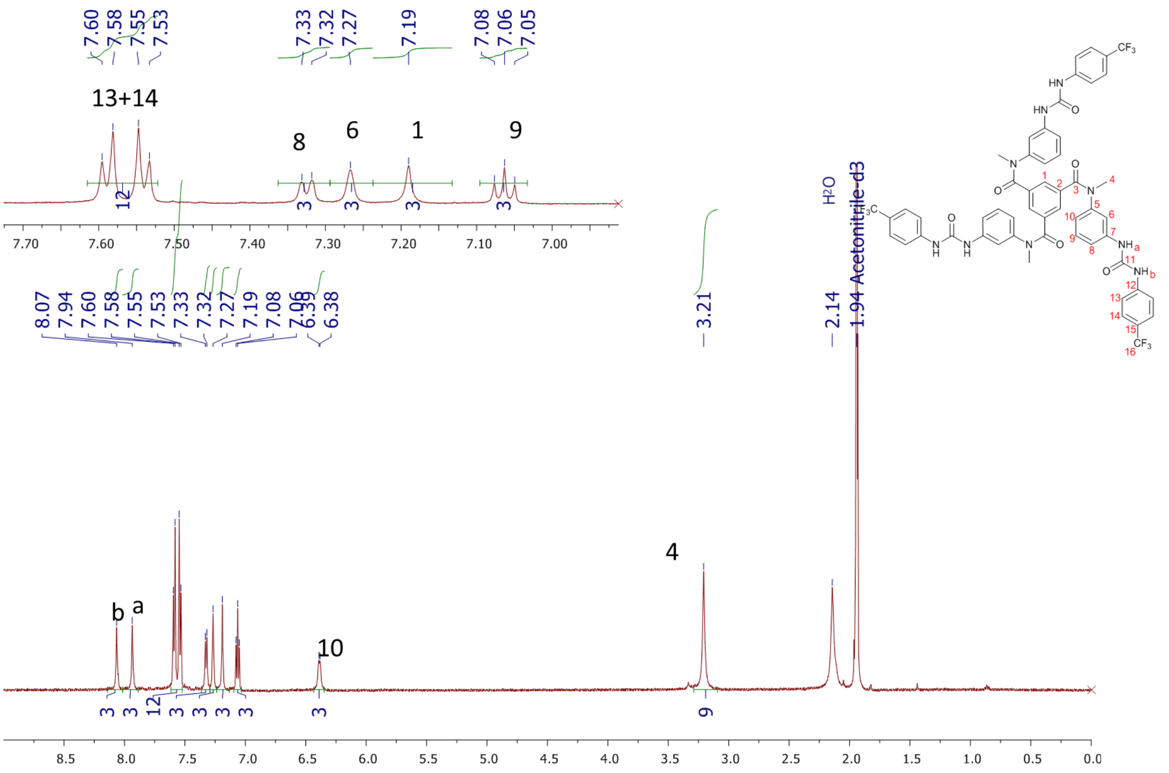

Figure A2. 13. ^{1}H NMR (600 MHz) spectrum of **86** in CD_3CN.

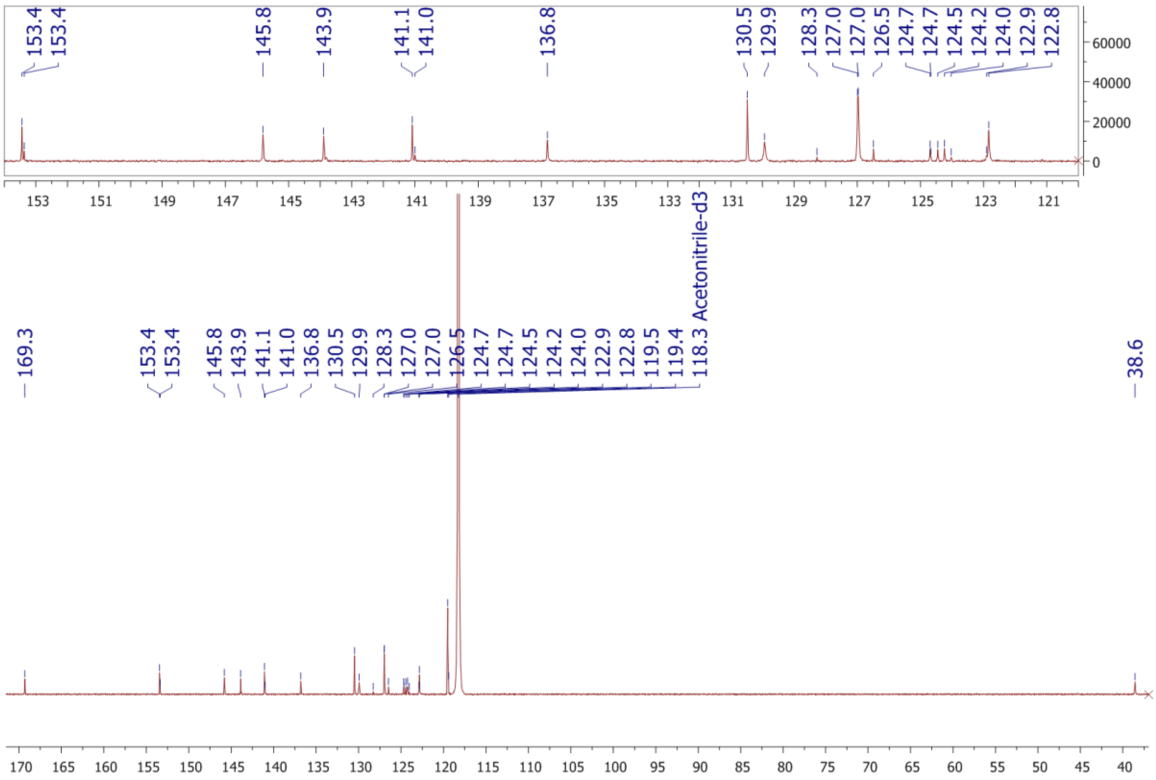

Figure A2. 14. ^{13}C NMR (151 MHz) spectrum of **86** in CD_3CN.

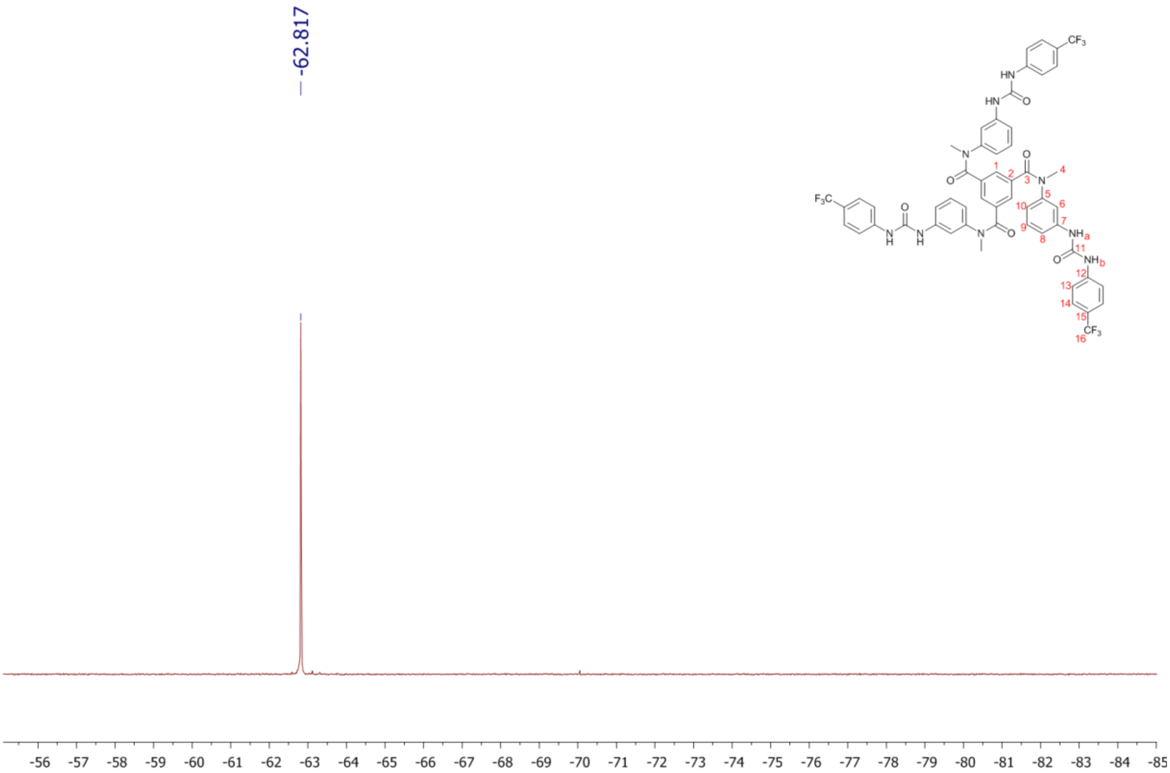

Figure A2. 15. ^{19}F NMR (376 MHz) spectrum of **86** in CD$_3$CN.

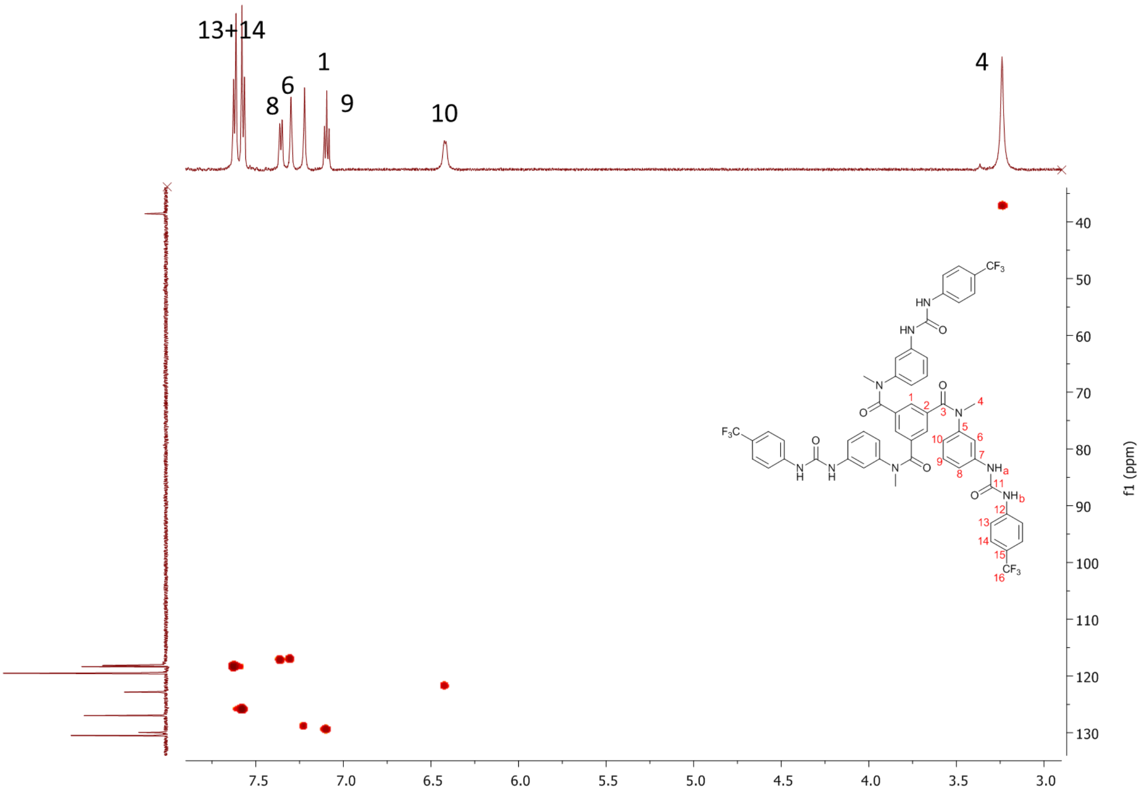

Figure A2. 16. ^{13}C-^{1}H HSQC NMR spectrum of **86** in CD$_3$CN.

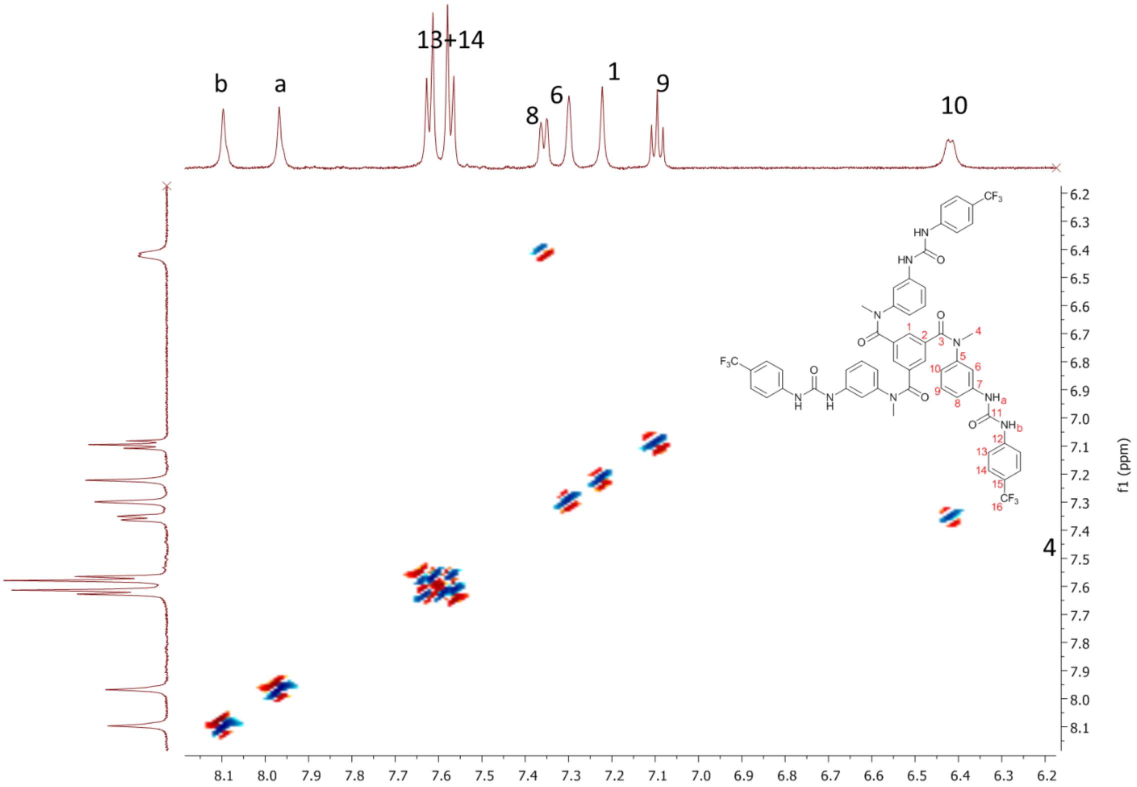

Figure A2. 17. ^{1}H-^{1}H COSY NMR spectrum of **86** in CD_3CN.

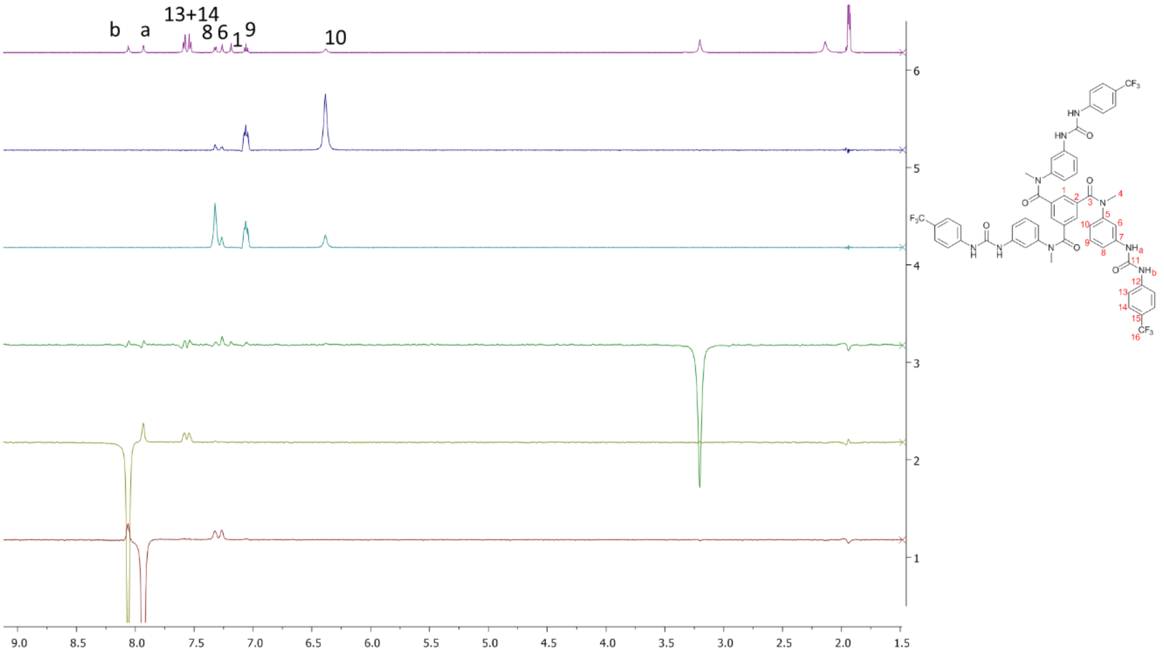

Figure A2. 18. Selective ^{1}H ROESY NMR spectra of **86** in CD_3CN.

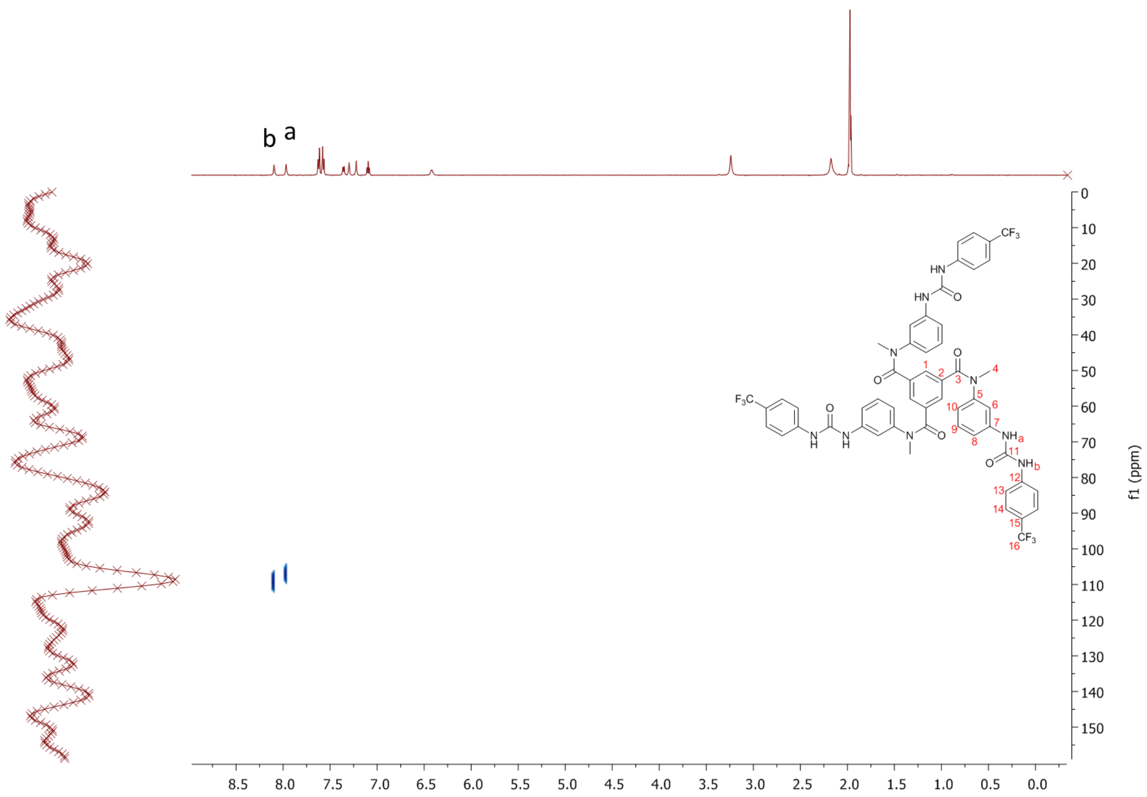

Figure A2. 20. ^{15}N-^{1}H HSQC NMR spectrum of 1 in CD$_3$CN.

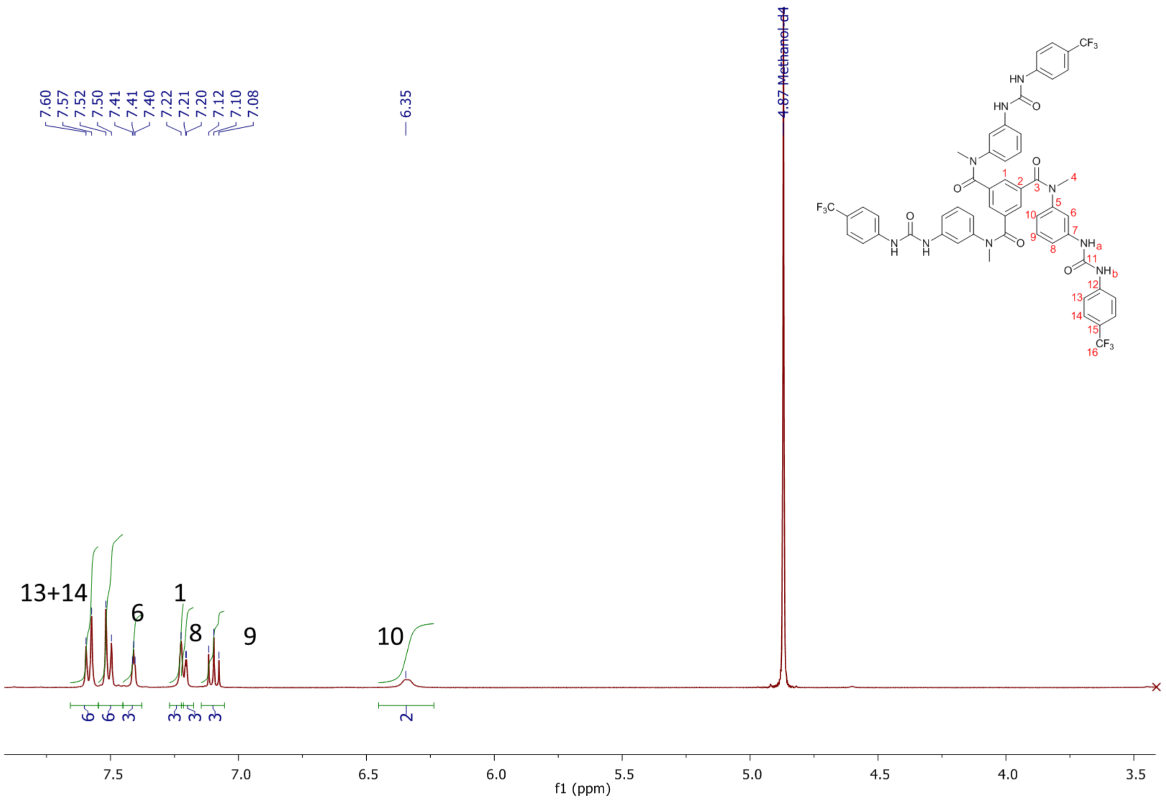

Figure A2. 19. ^{1}H NMR (600 MHz) spectrum of **86** in CD$_3$OD.

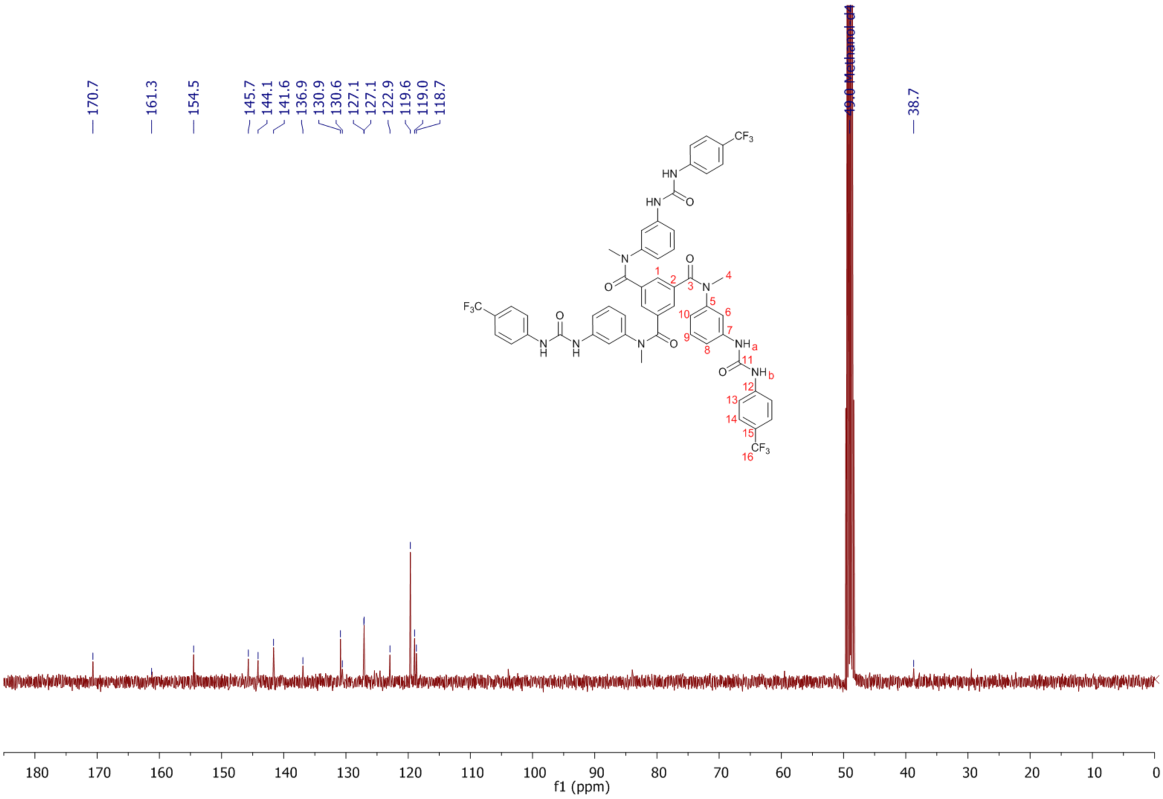

Figure A2. 22. ^{13}C NMR (151 MHz) spectrum of **86** in CD$_3$OD.

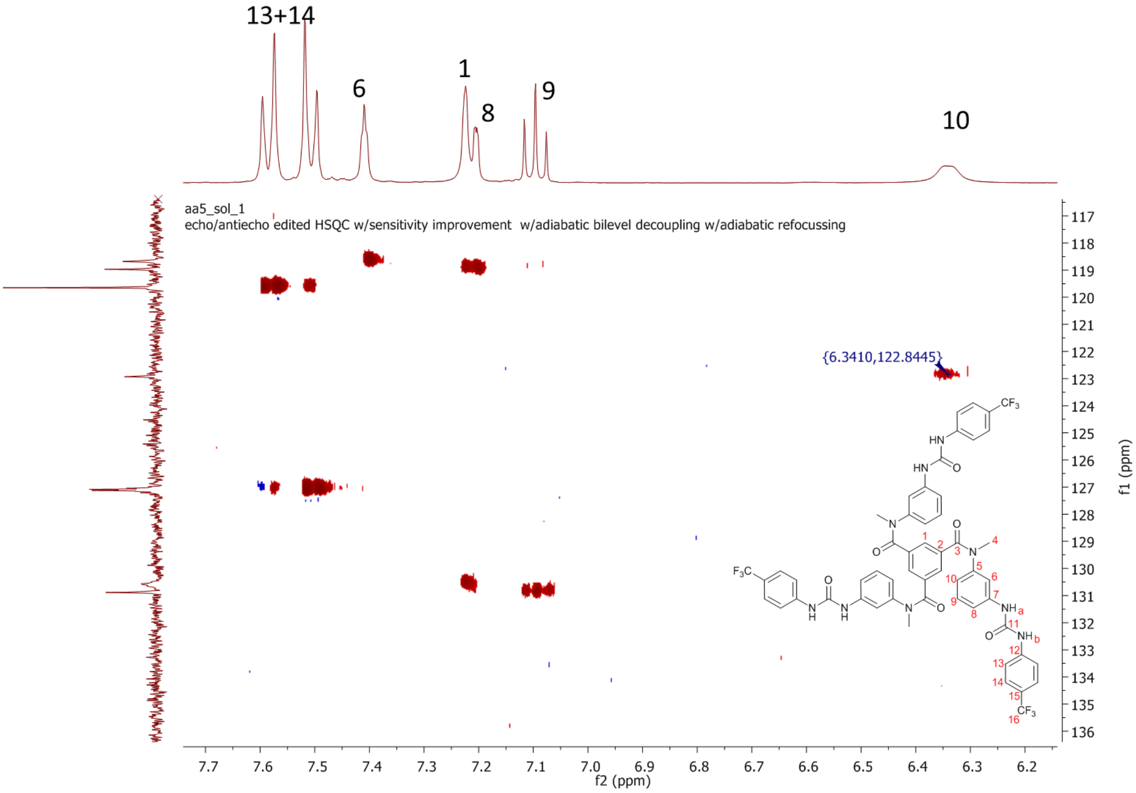

Figure A2. 21. ^{13}C-^{1}H HSQC NMR spectrum of 1 in CD$_3$OD.

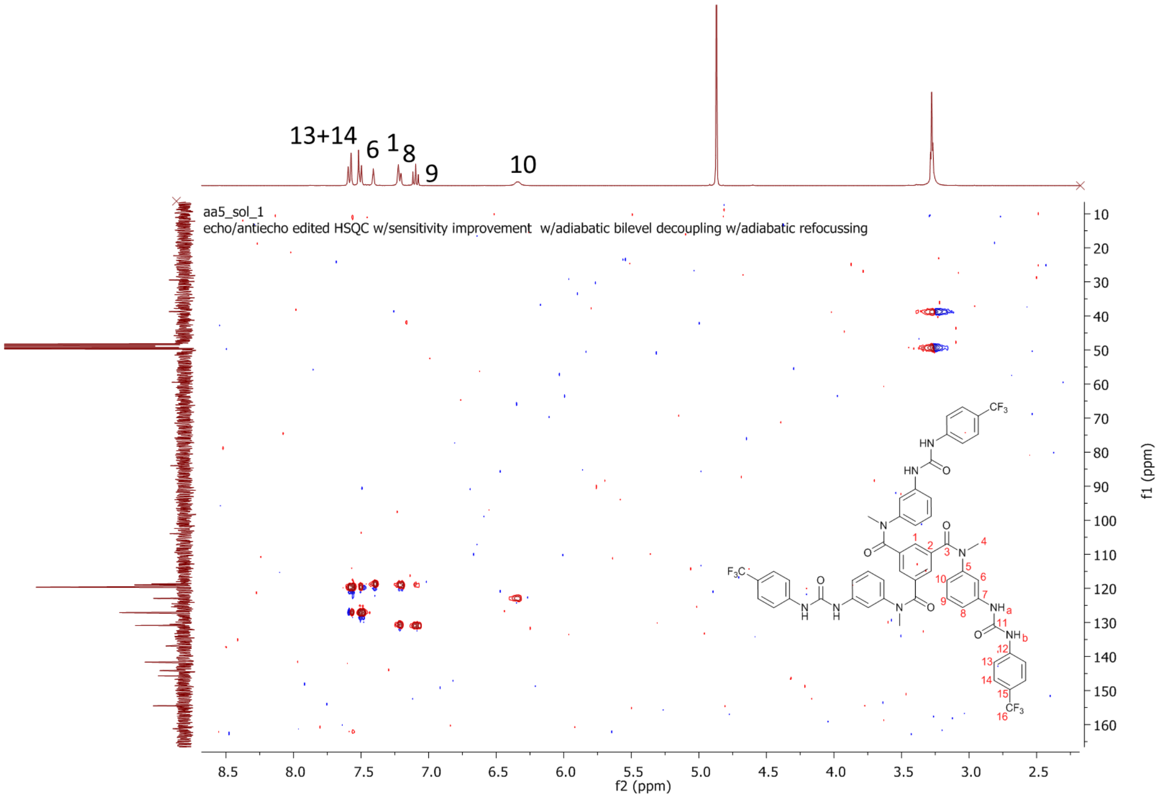

Figure A2. 23. ^{13}C-^{1}H HSQC NMR spectrum of **86** in CD$_3$OD.

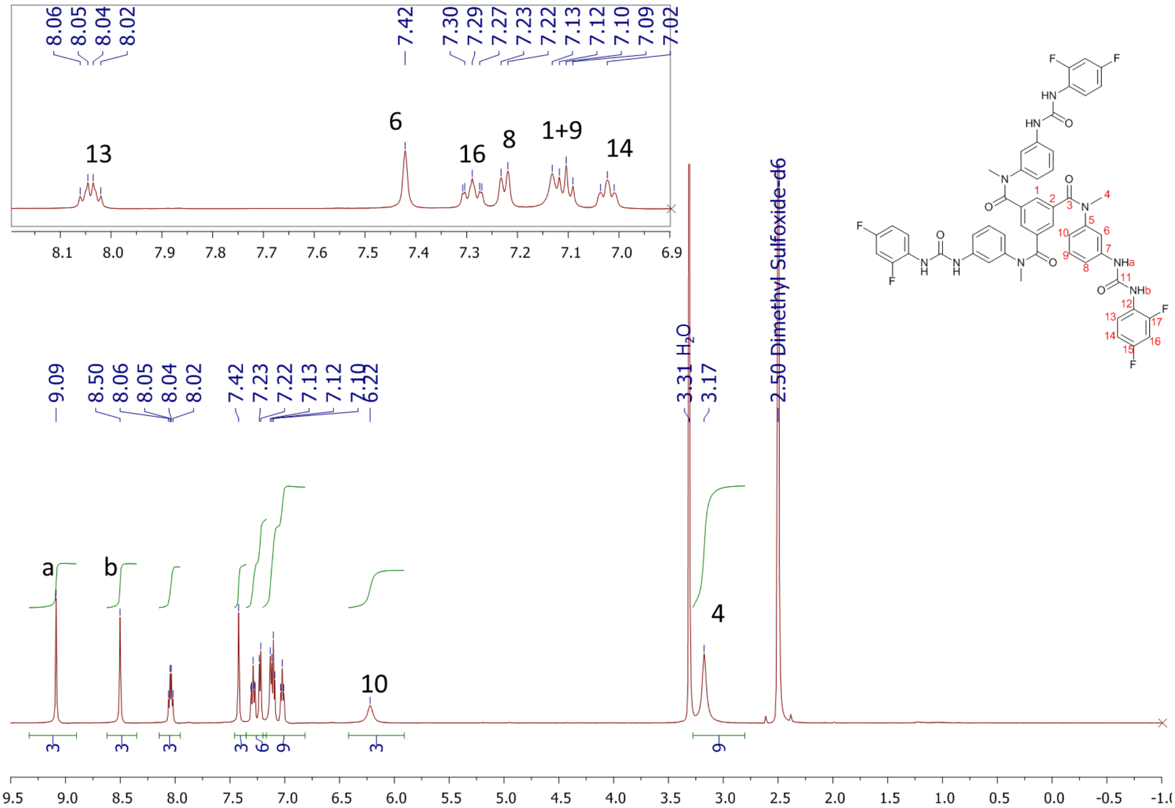

Figure A2. 24. ^{1}H NMR (600 MHz) spectrum of **87** in DMSO-d_6.

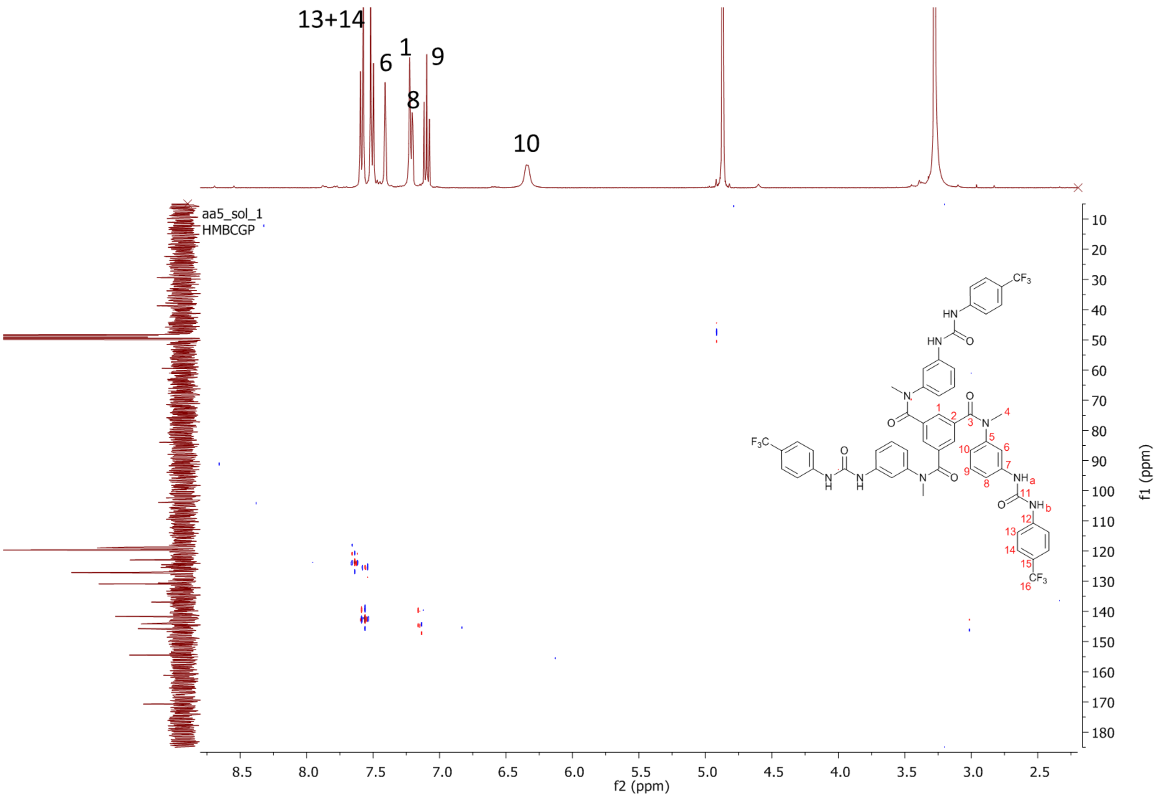

Figure A2. 25. ^{13}C-^{1}H HMBC NMR spectrum of **86** in CD_3OD.

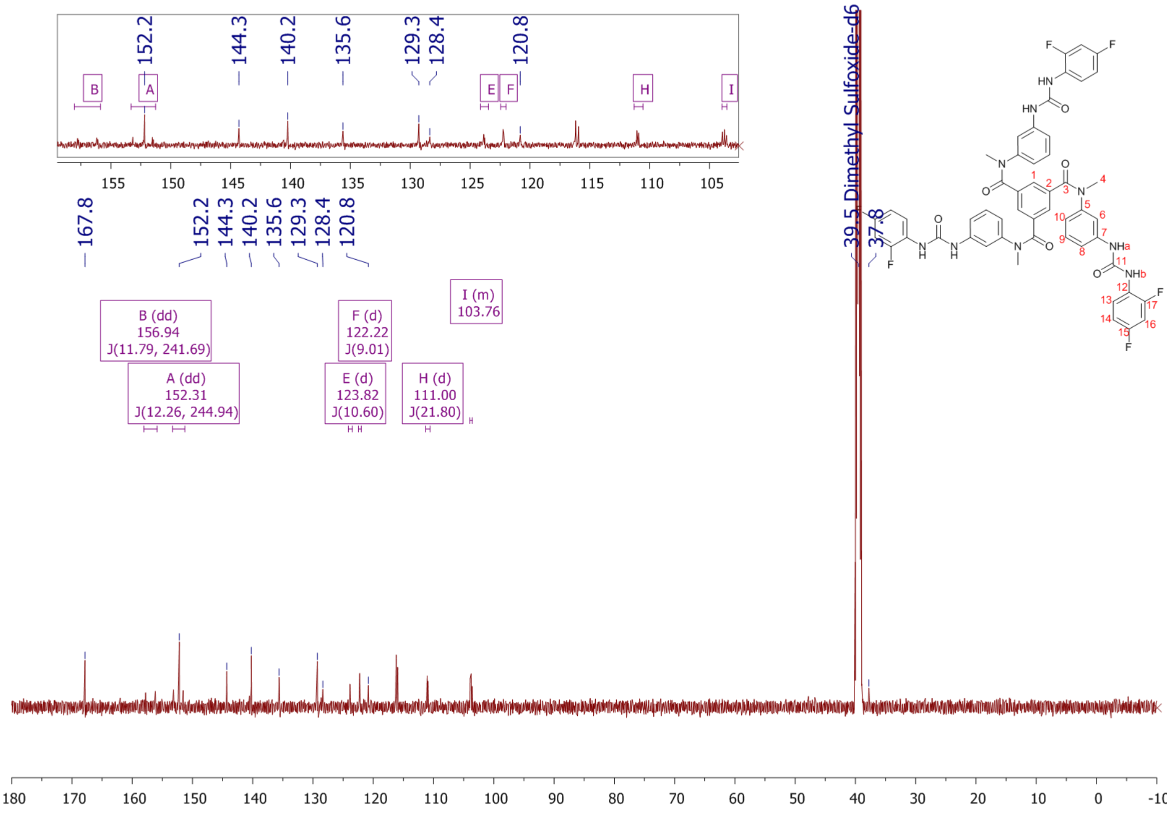

Figure A2. 26. ^{13}C NMR (151 MHz) spectrum of **87** in DMSO-d_6.

Appendix A2

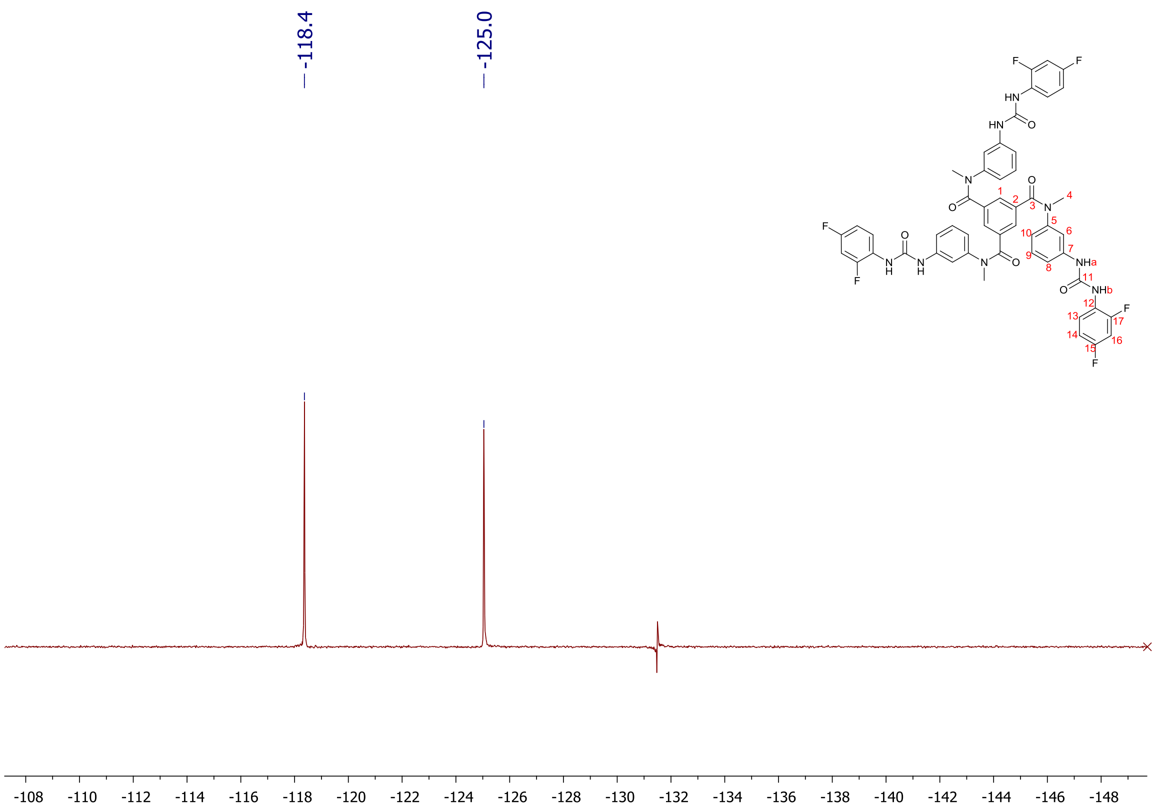

Figure A2. 27. ^{19}F NMR (376 MHz) spectrum of **87** in DMSO-*d*$_6$.

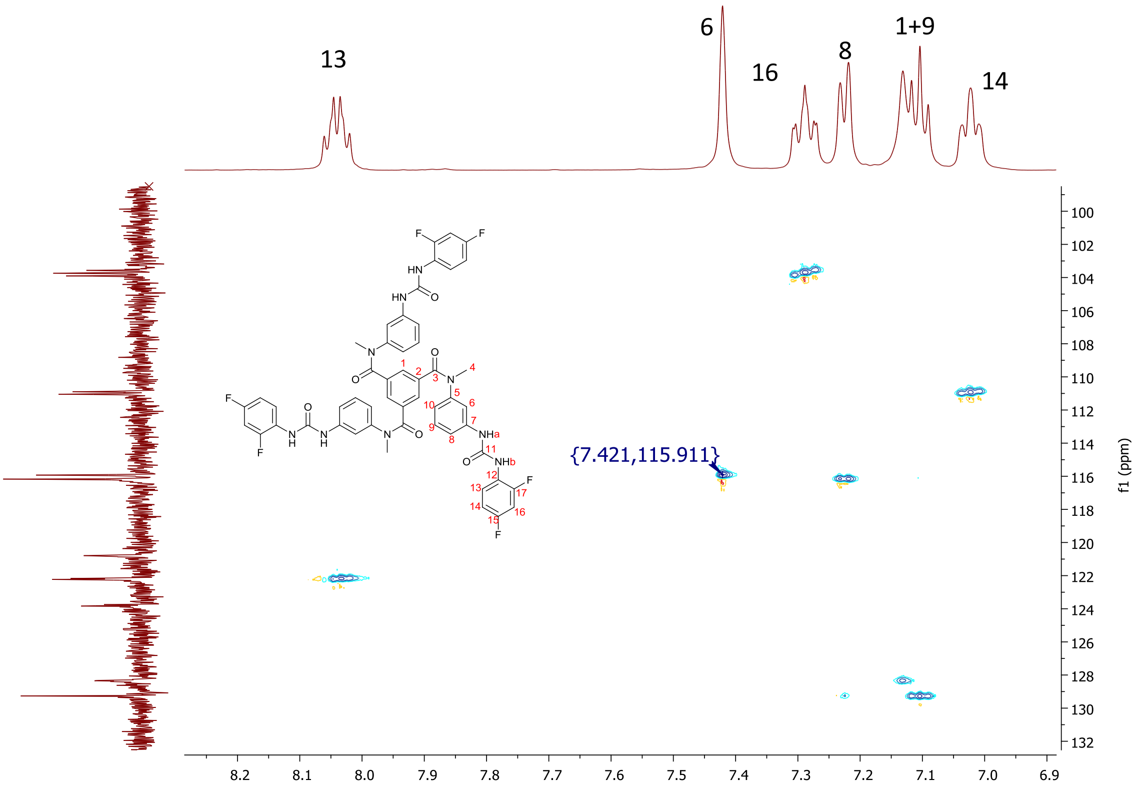

Figure A2. 28. ^{13}C-^{1}H HSQC NMR spectrum of **87** in DMSO-*d*$_6$

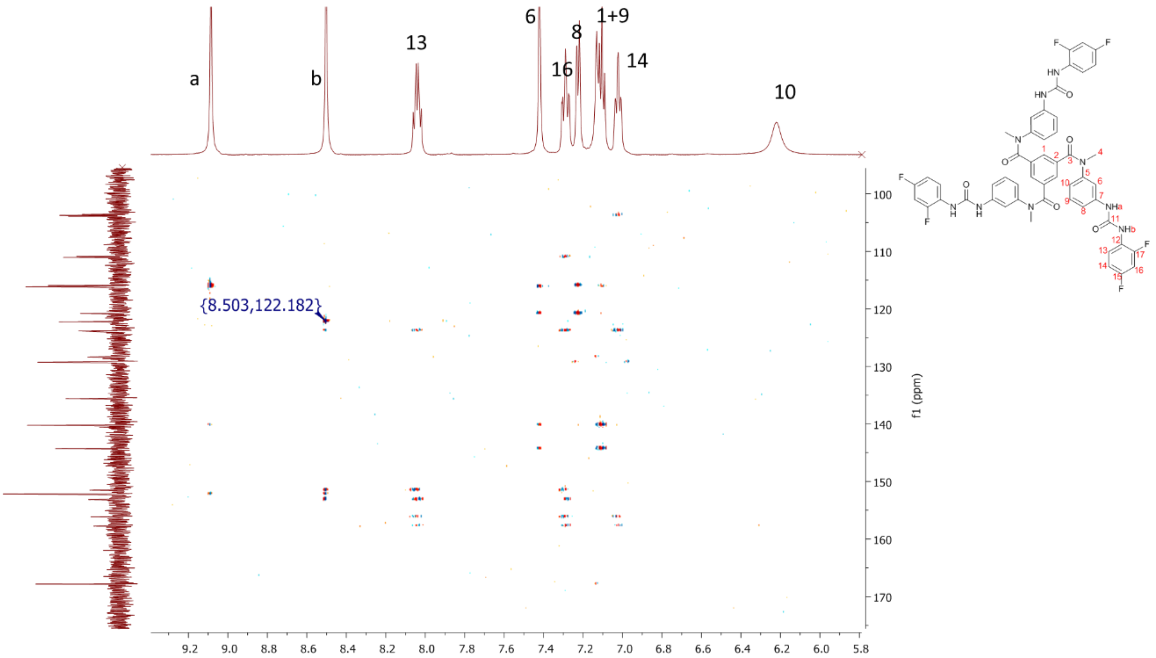

Figure A2. 29. ^{13}C-^{1}H HMBC NMR spectrum of **87** in DMSO-*d*$_6$.

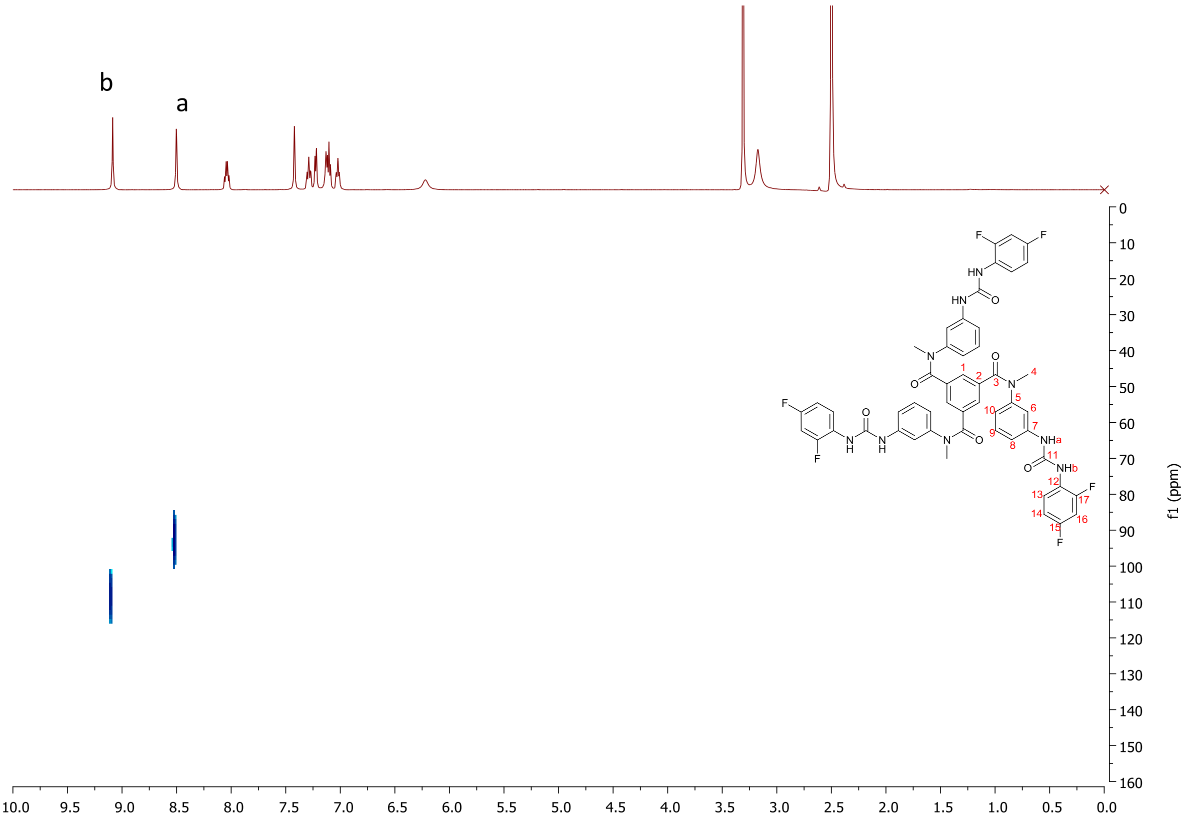

Figure A2. 30. ^{15}N-^{1}H HSQC NMR spectrum of **87** in DMSO-*d*$_6$.

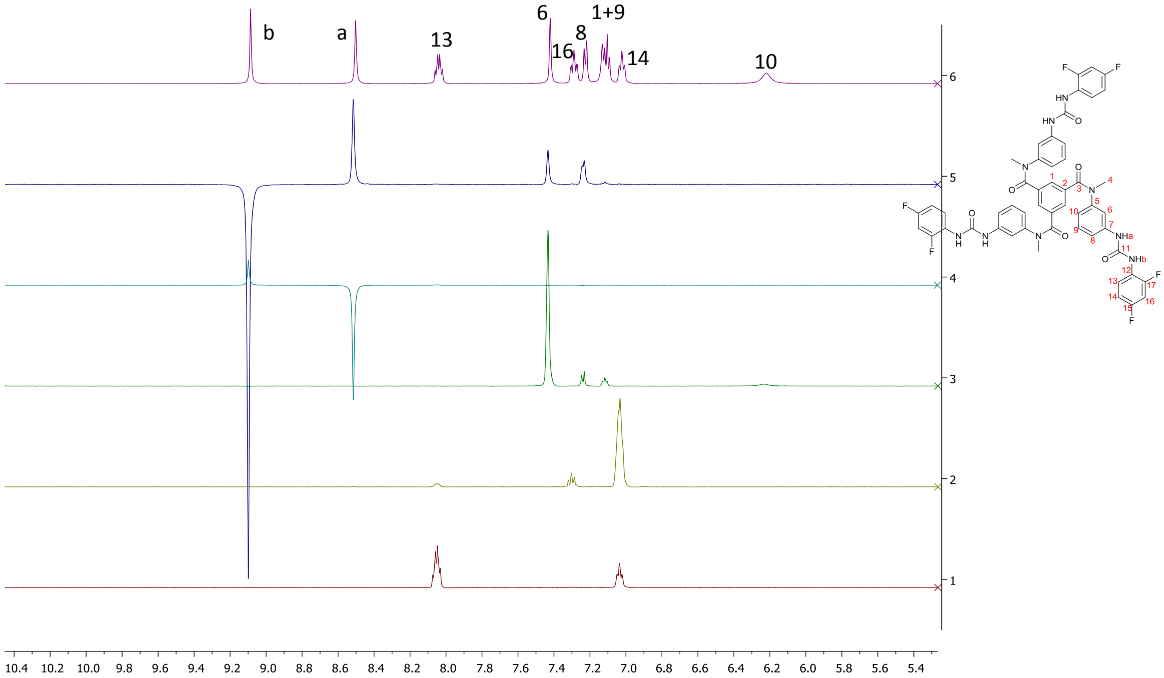

Figure A2. 31. Selective ^{1}H ROESY NMR spectra of 2 in DMSO-d_6.

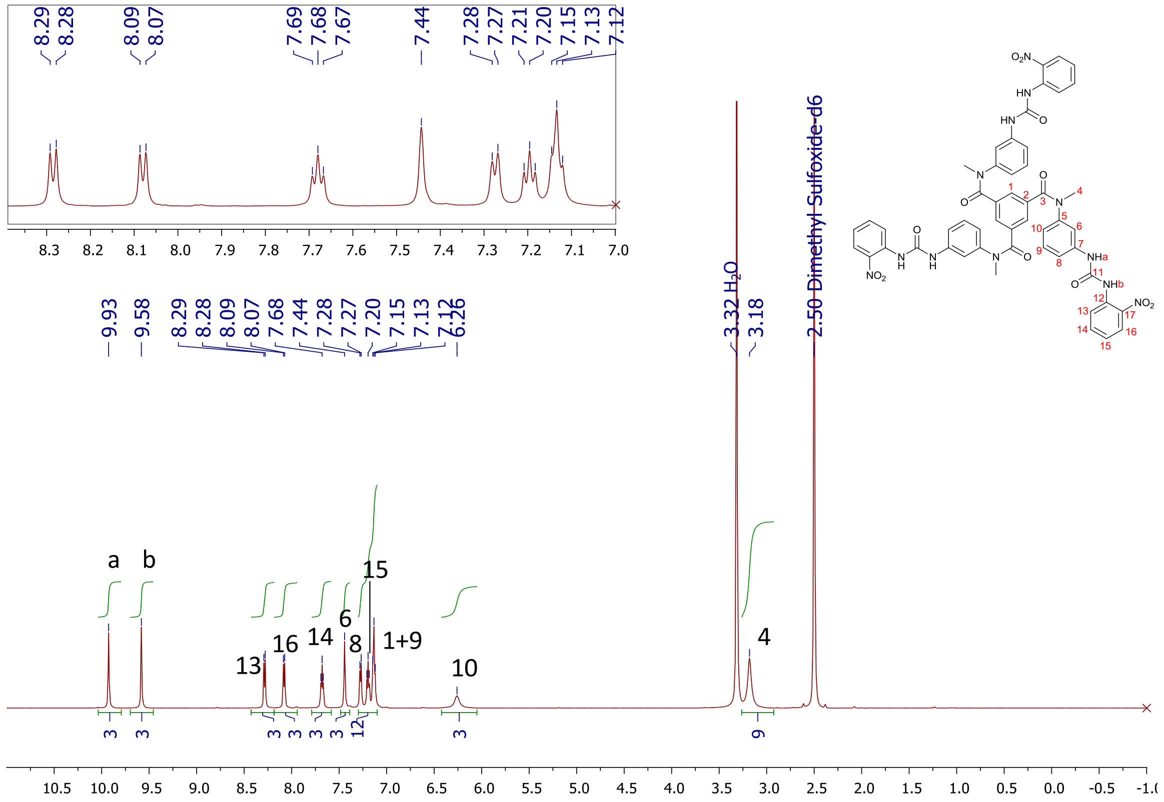

Figure A2. 32. ^{1}H NMR (600 MHz) spectrum of **88** in DMSO-d_6.

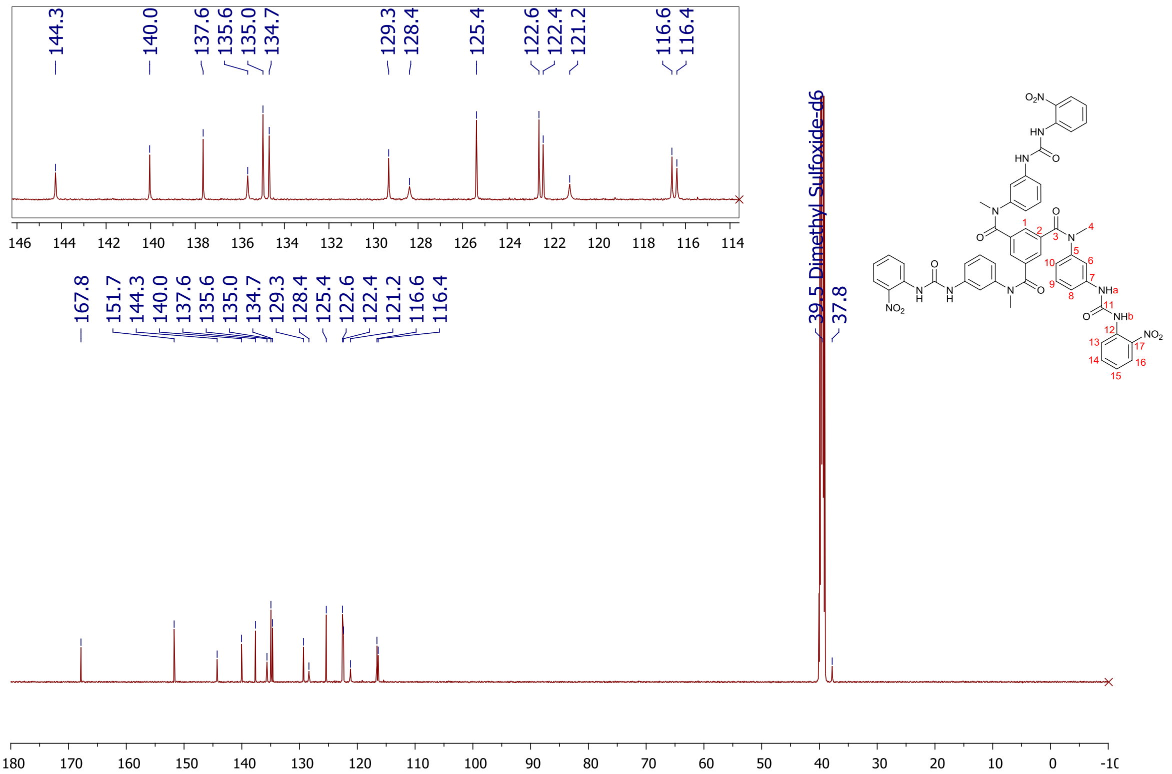

Figure A2. 33. ^{13}C NMR (151 MHz) spectrum of **88** in DMSO-*d*$_6$.

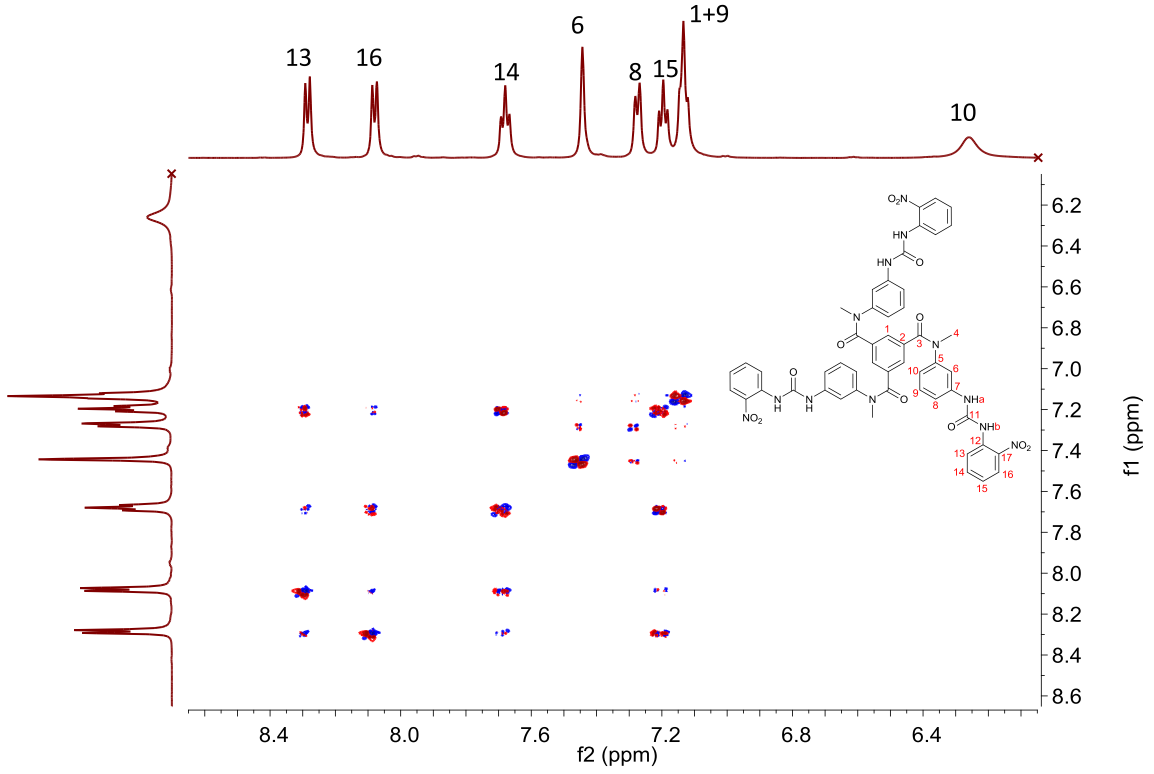

Figure A2. 34. ^{1}H-^{1}H COSY NMR spectrum of **88** in DMSO-*d*$_6$.

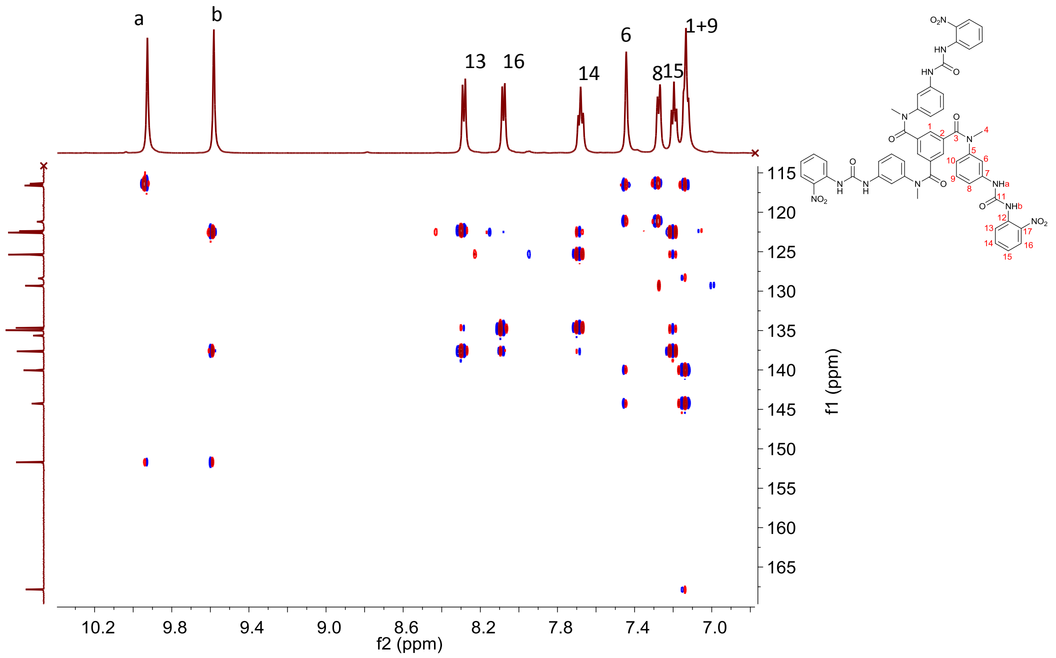

Figure A2. 35. ^{13}C-^{1}H HMBC NMR spectrum of **88** in DMSO-d_6.

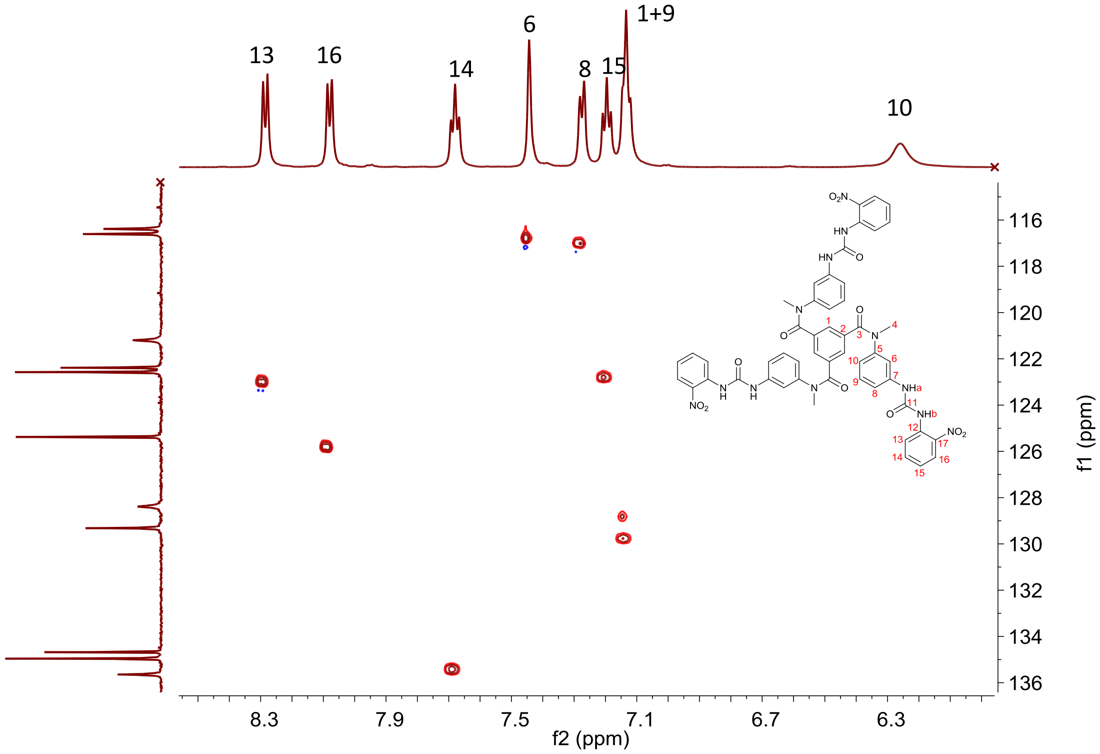

Figure A2. 36. ^{13}C-^{1}H HSQC NMR spectrum of **88** in DMSO-d_6.

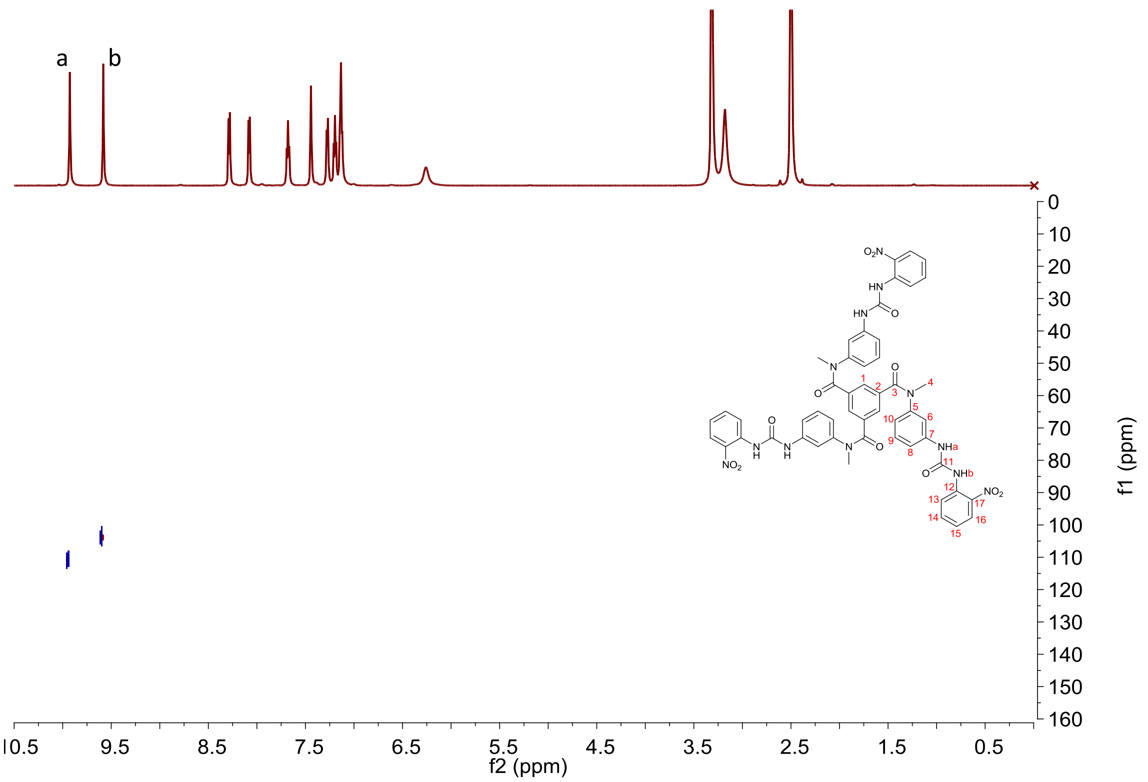

Figure A2. 38. ^{15}N-^{1}H HSQC NMR spectrum of **88** in DMSO-*d*$_6$.

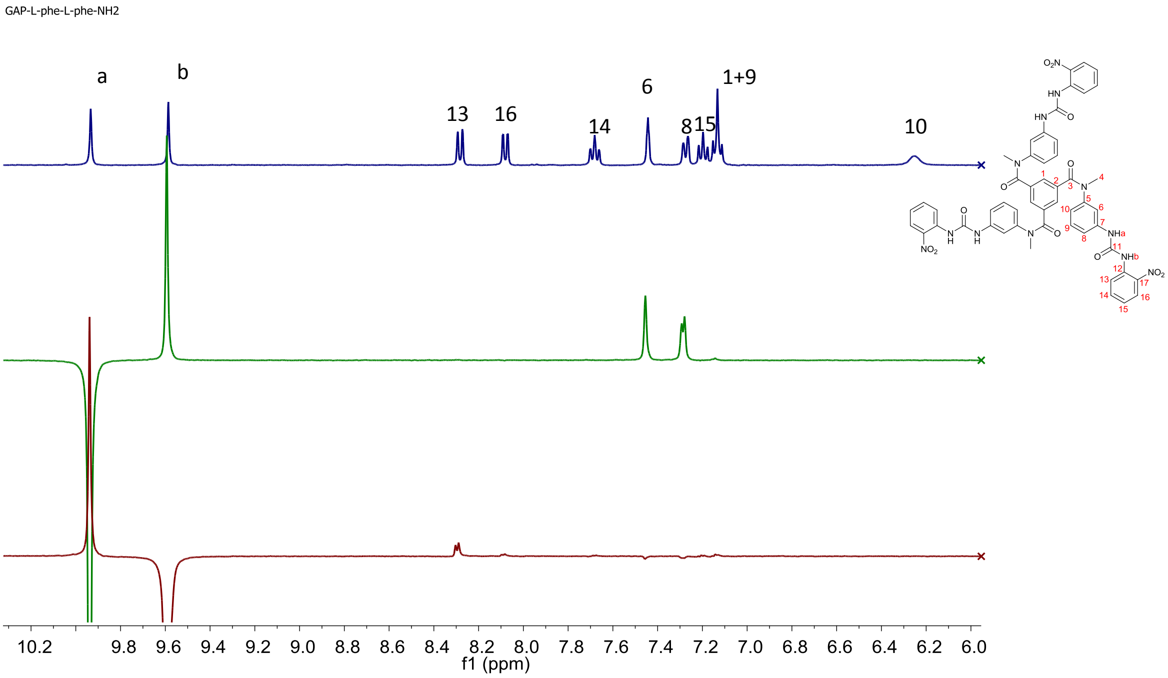

Figure A2. 37. Selective ^{1}H ROESY NMR spectra of **88** in DMSO-*d*$_6$.

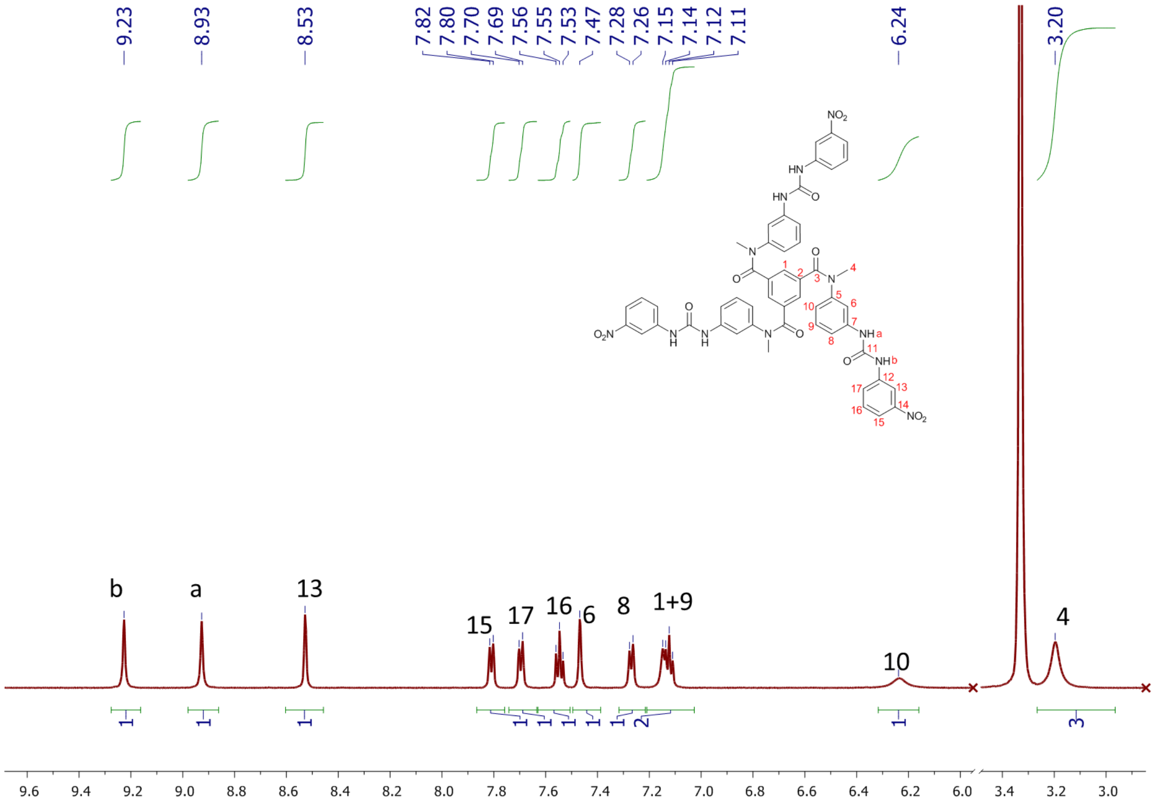

Figure A2. 39. ^{1}H NMR (600 MHz) spectrum of **89** in DMSO-d_6.

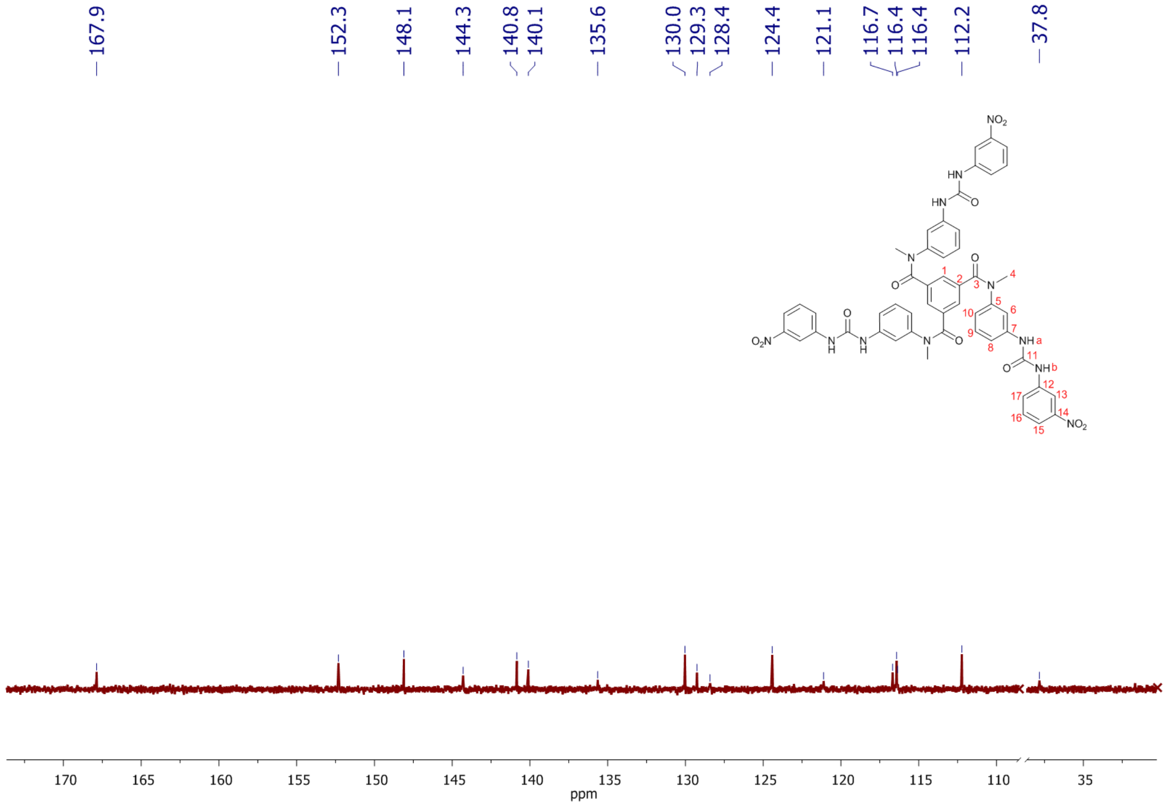

Figure A2. 40. ^{13}C NMR (151 MHz) spectrum of **89** in DMSO-d_6.

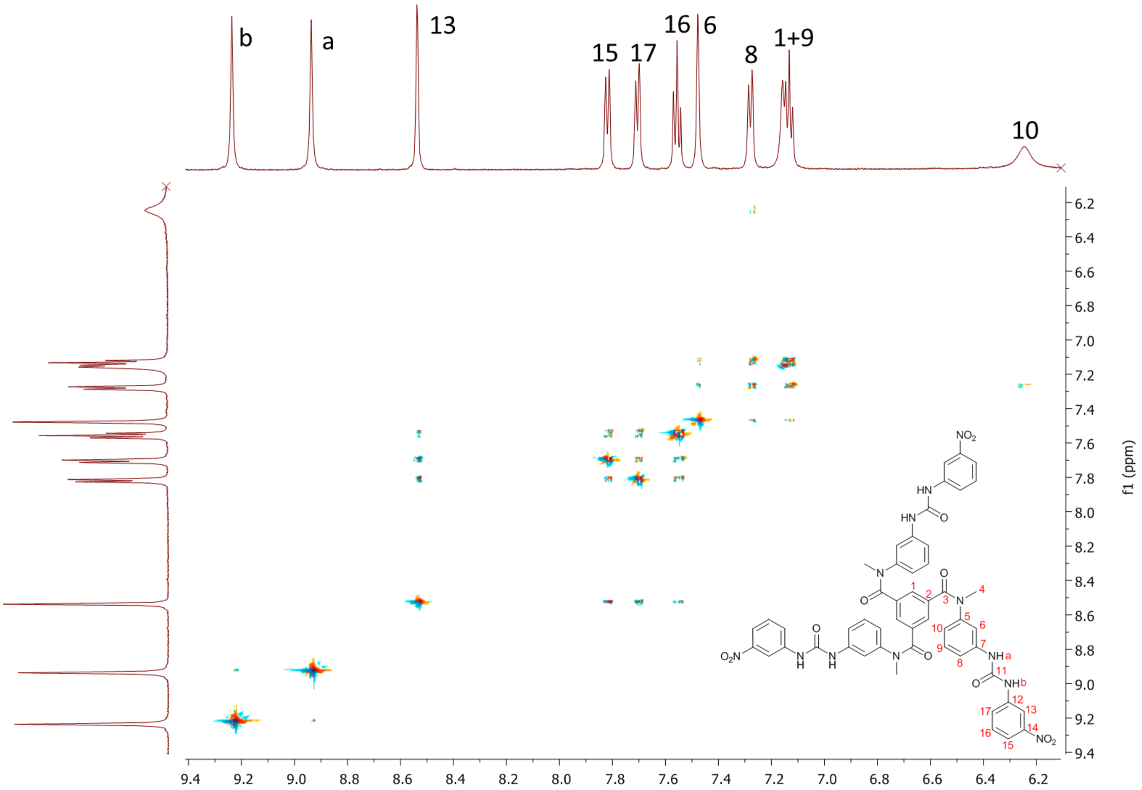

Figure A2. 41. ^{1}H-^{1}H COSY NMR spectrum of **89** in DMSO-d_6.

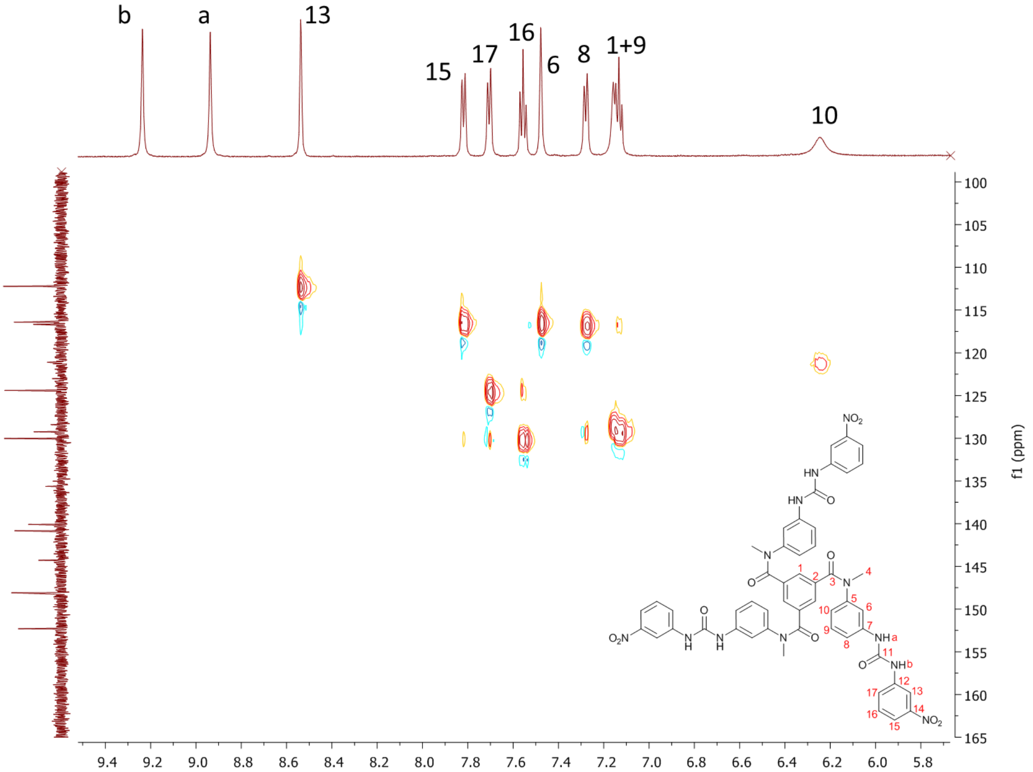

Figure A2. 42. ^{13}C-^{1}H HSQC NMR spectrum of **89** in DMSO-d_6.

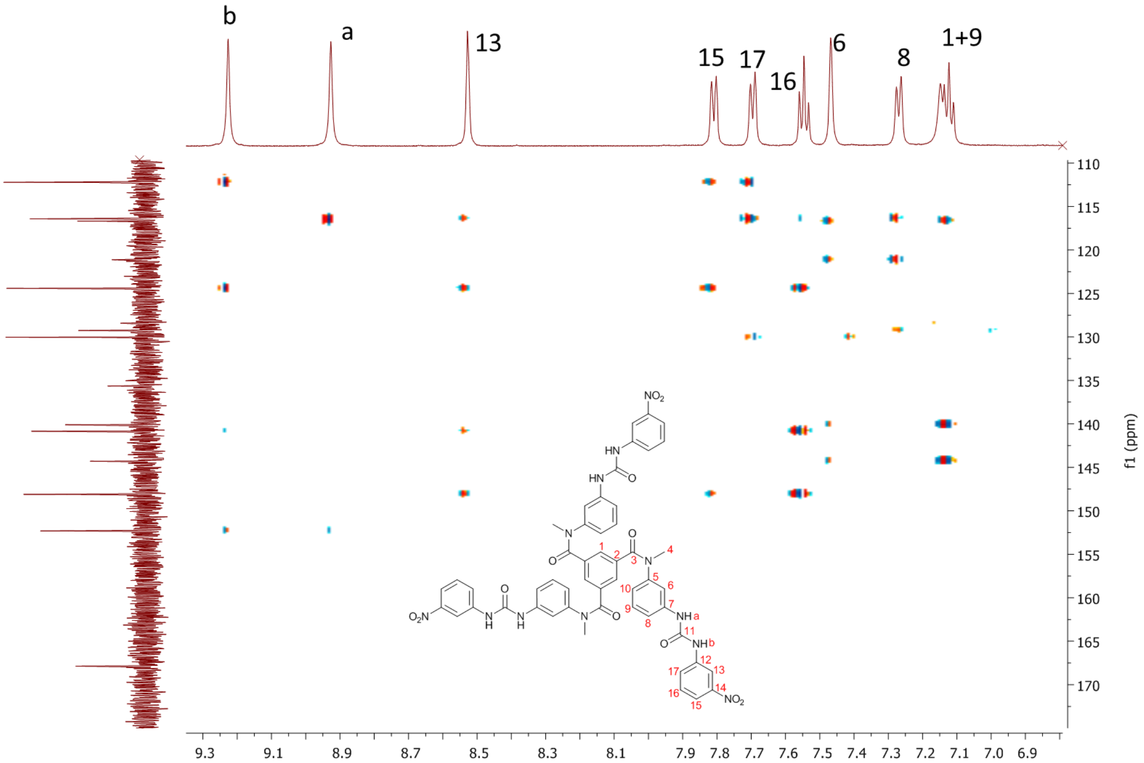

Figure A2. 43. ^{13}C-^{1}H HMBC NMR spectrum of **89** in DMSO-d_6.

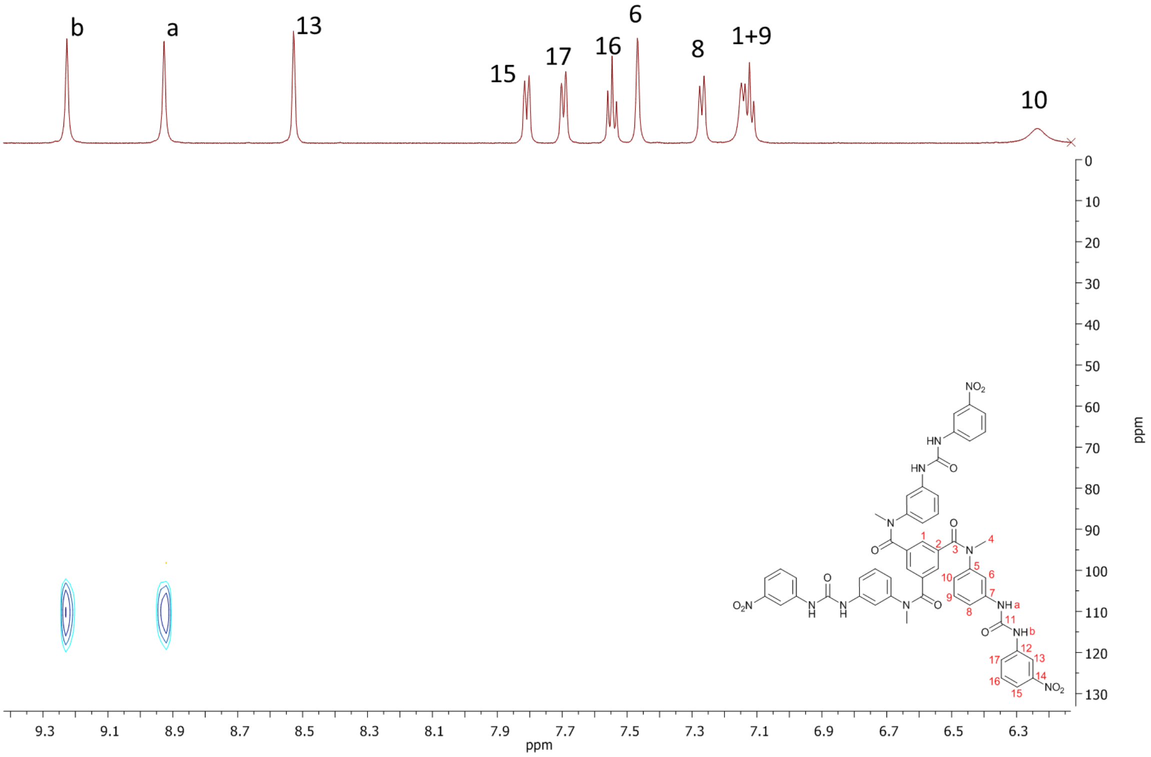

Figure A2. 44. ^{15}N-^{1}H HSQC NMR spectrum of **89** in DMSO-d_6.

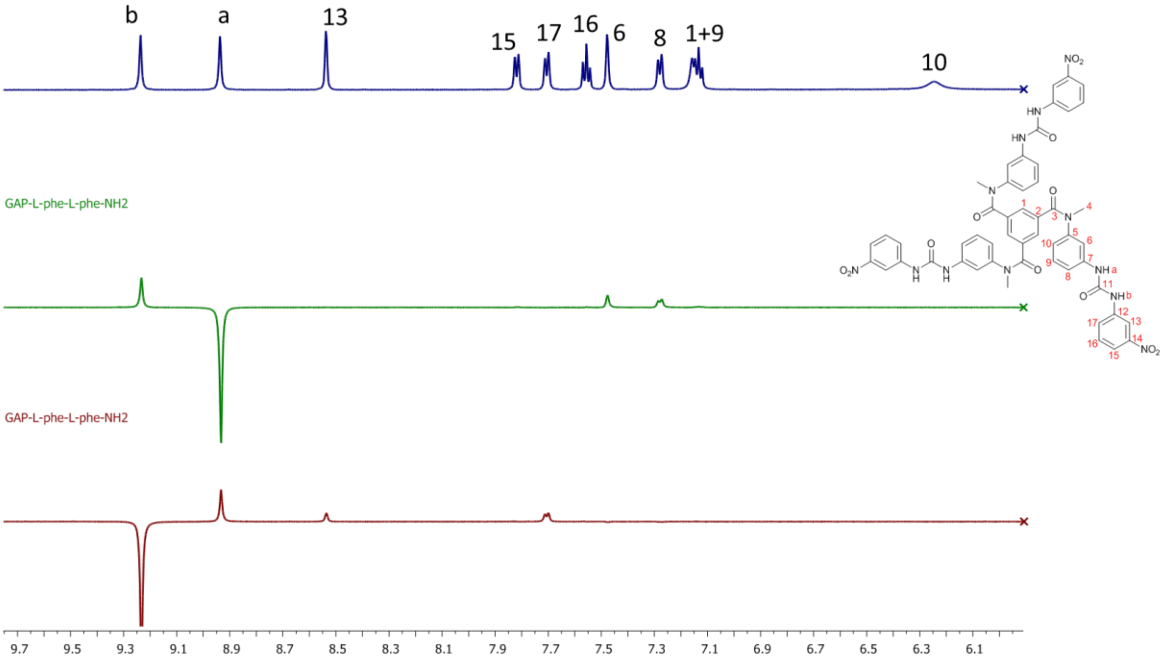

Figure A2. 45. Selective ^{1}H ROESY NMR spectra of **89** in DMSO-d_6.

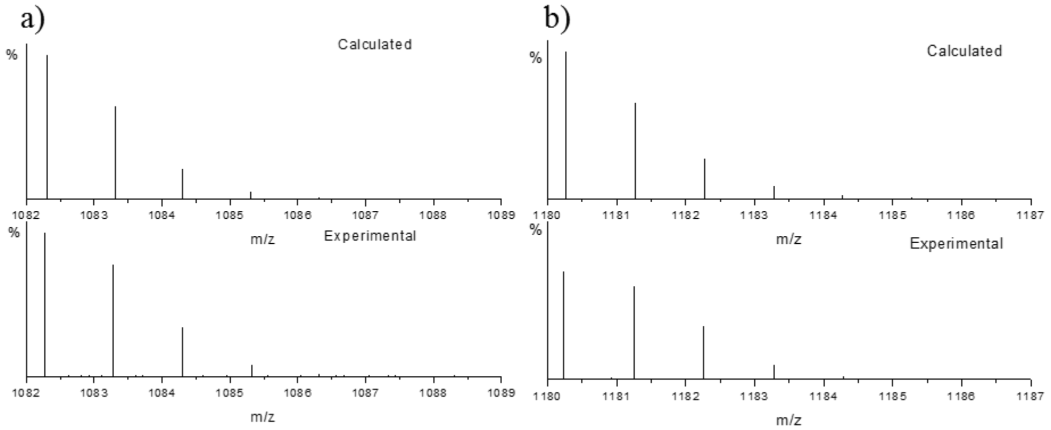

Figure A2. 46. Mass spectra of receptor **86** a) **86** Calcd. mass for $C_{54}H_{41}N_9O_6F_9$: 1082.3036, Found mass: 1082.2952; b) **86**. SO_4^{2-} complex. Calcd. mass for $C_{54}H_{43}N_9O_{10}F_9S$: 1180.2721, Found mass: 1180.2635.

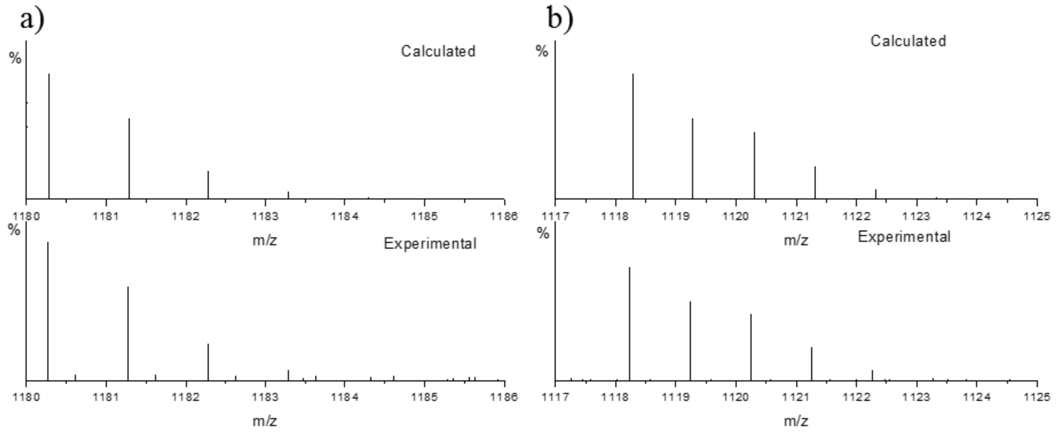

Figure A2. 47. Mass spectra of receptor **86** a) **86**.$H_2PO_4^-$ complex. Calcd. mass for $C_{54}H_{44}N_9O_{10}F_9P$: 1180.2811, Found mass: 1180.2640; b) **86**. Cl^- complex. Calcd. mass for $C_{54}H_{42}N_9O_6F_9Cl$: 1118.2808, Found mass: 1118.2367

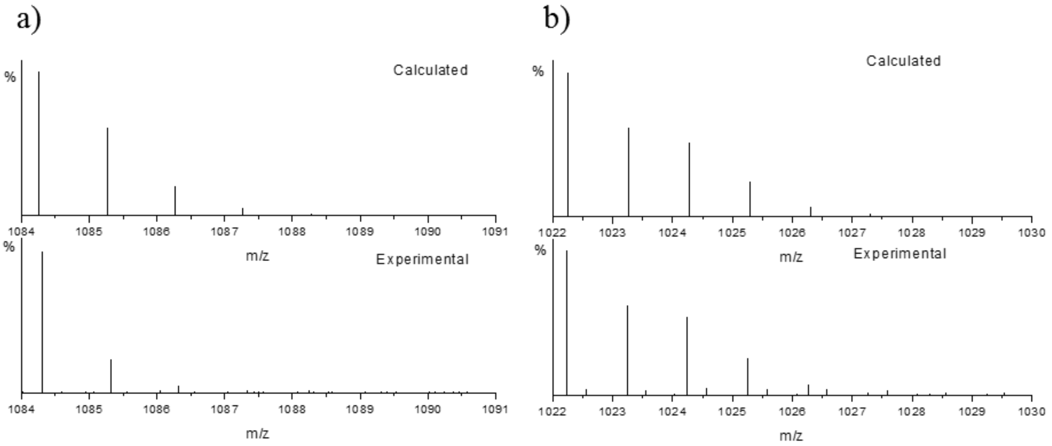

Figure A2. 48. Mass spectra of receptor **87** a) **87**.$H_2PO_4^-$ complex. Calcd. mass for $C_{51}H_{41}N_9O_{10}F_6P$: 1084.2624, Found mass: 1084.1840; b) **87**.Cl^- complex. Calcd. mass for $C_{51}H_{39}N_9O_6F_6Cl$: 1022.2622, Found mass: 1022.2443.

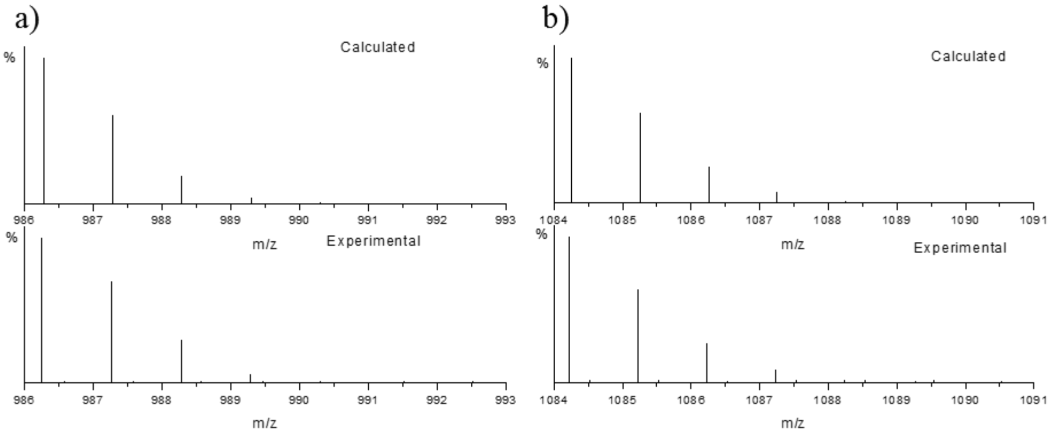

Figure A2. 49. Mass spectra of receptor **87** a) **87** Calcd. mass for $C_{51}H_{38}N_9O_6F_6$: 986.2850, Found mass: 986.2567; b) **87**.SO_4^{2-} -complex. Calcd. mass for $C_{51}H_{40}N_9O_{10}F_6S$: 1084.2534, Found mass: 1084.2198

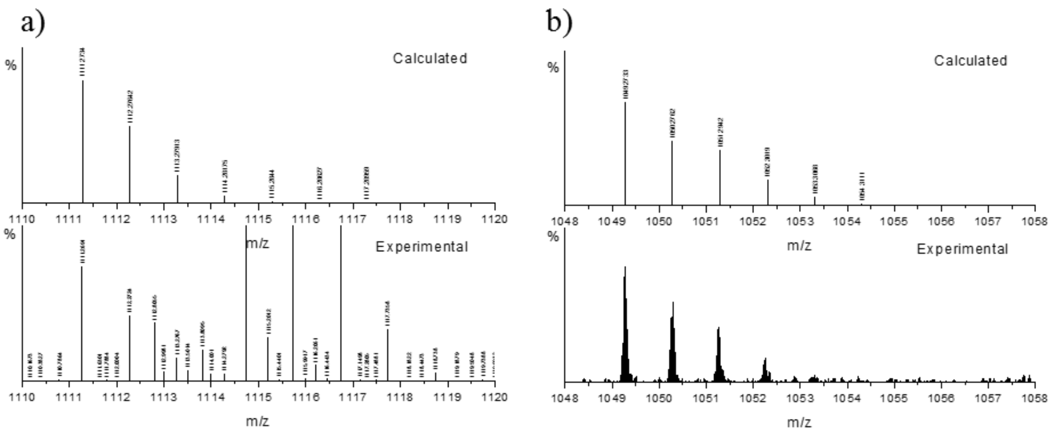

Figure A2. 50. Mass spectra of receptor **88** a) **88**.$H_2PO_4^-$ complex. Calcd. mass for $C_{51}H_{44}N_{12}O_{16}P$: 1111.2741, Found mass: 1111.2691; b) **88**.Cl^- complex. Calcd. mass for $C_{51}H_{42}N_{12}O_{12}Cl$: 1049.2739, Found mass: 1049.2748

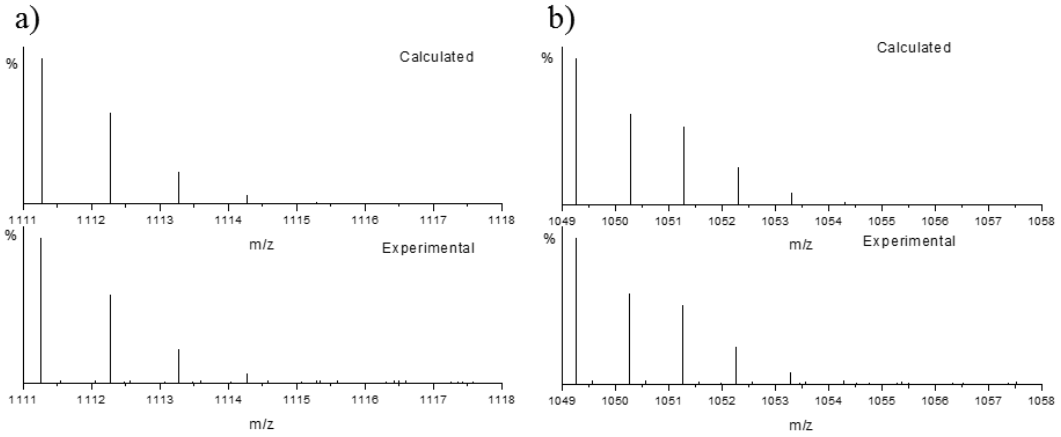

Figure A2. 51. Mass spectra of receptor **89** a) **89**.$H_2PO_4^-$ complex. Calcd. mass for $C_{51}H_{44}N_{12}O_{16}P$: 1111.2741, Found mass: 1111.2673; b) **89**.Cl^- complex. Calcd. mass for $C_{51}H_{42}N_{12}O_{12}Cl$: 1049.2739, Found mass: 1049.2670

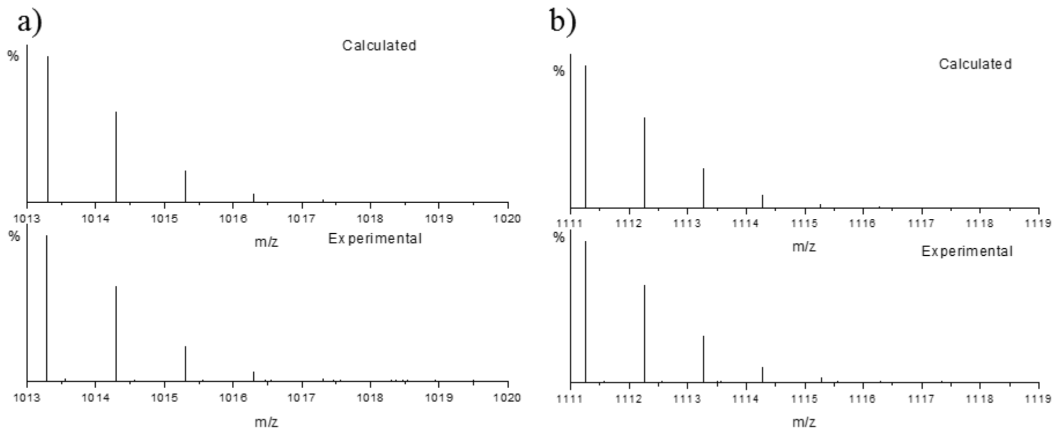

Figure A2. 52. Mass spectra of receptor **89** a): **89** Calcd. mass for $C_{51}H_{41}N_{12}O_{12}$: 1013.2967, Found mass: 1013.2899; b) **89**.SO_4^{2-} complex. Calcd. mass for $C_{51}H_{43}N_{12}O_{16}S$: 1111.2652, Found mass: 1111.2523.

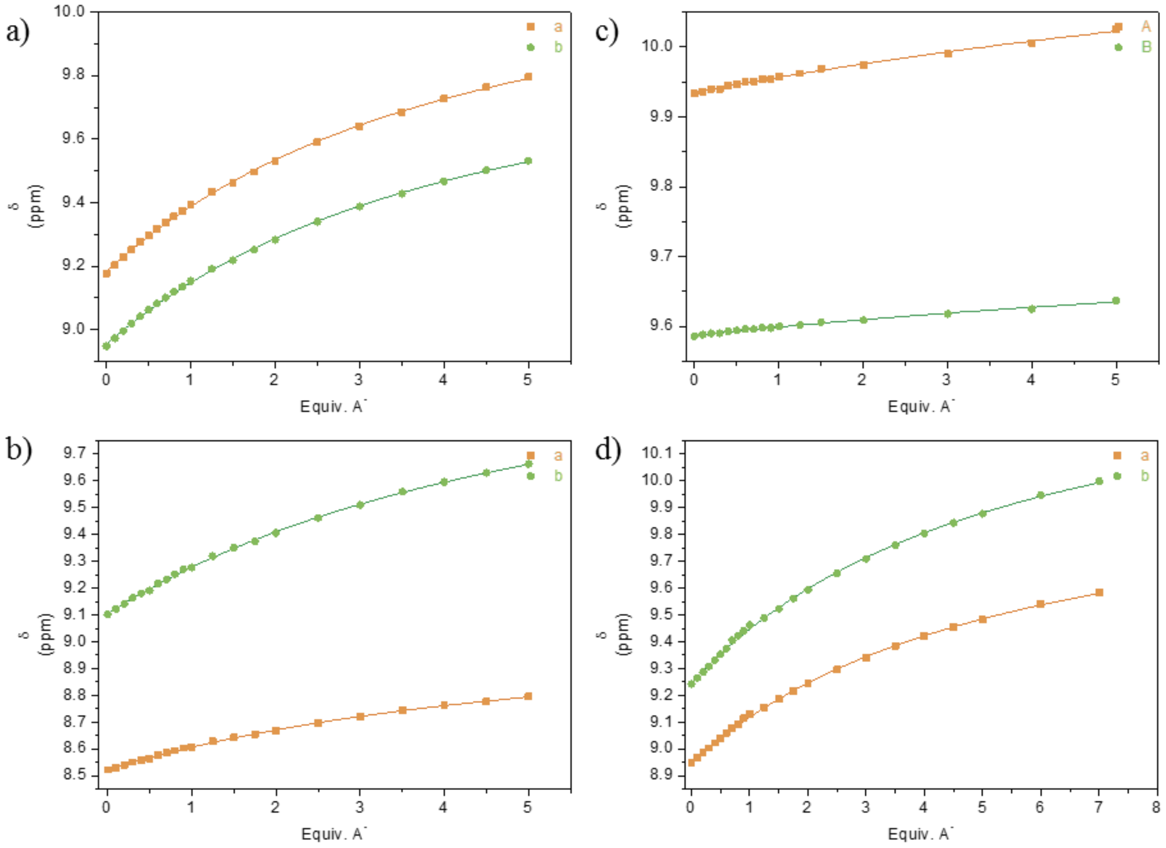

Figure A2. 53. Binding isotherms and fitting curve relative to the urea Ha and Hb resonances upon titrations of tripodal ligands **86-89** with Cl^- in DMSO-d_6. a) **86**, b) **87**, c) **88** and d) **89**.

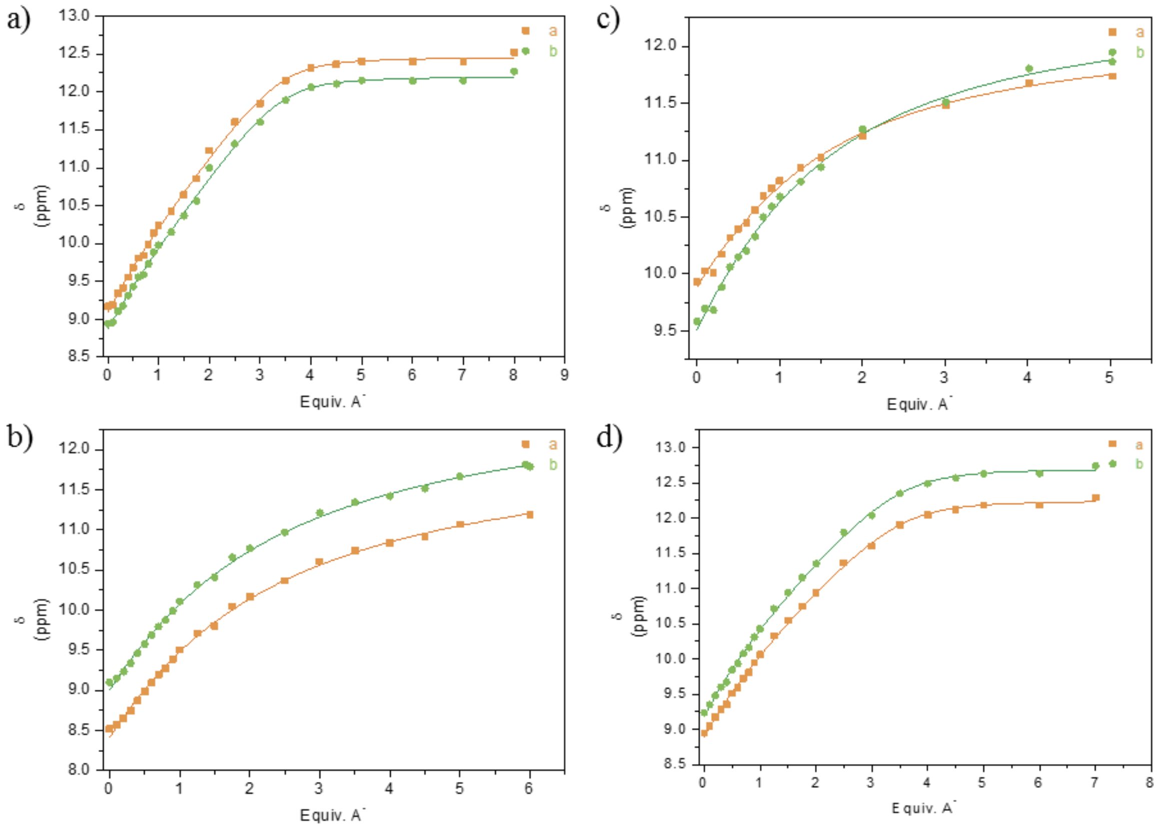

Figure A2. 54. Binding isotherms and fitting curve relative to the urea Ha and Hb resonances for titrations of tripodal ligands **86-89** with CH_3COO^- in DMSO-d_6. a) **86**, b) **87**, c) **88** and d) **89**.

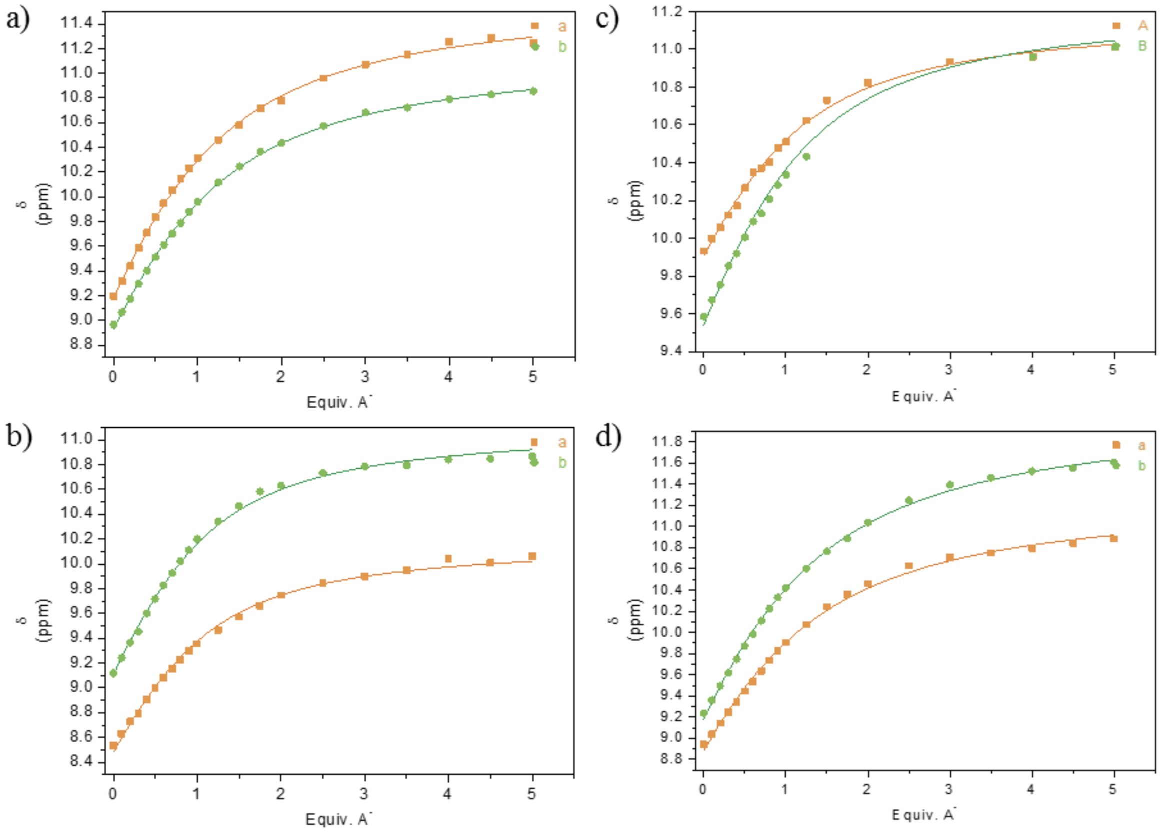

Figure A2. 56. Binding isotherms and fitting curve relative to the urea Ha and Hb resonances for titrations of tripodal ligands **86-89** with $H_2PO_4^-$ in DMSO-d_6. a) **86**, b) **87**, c) **88** and d) **89**.

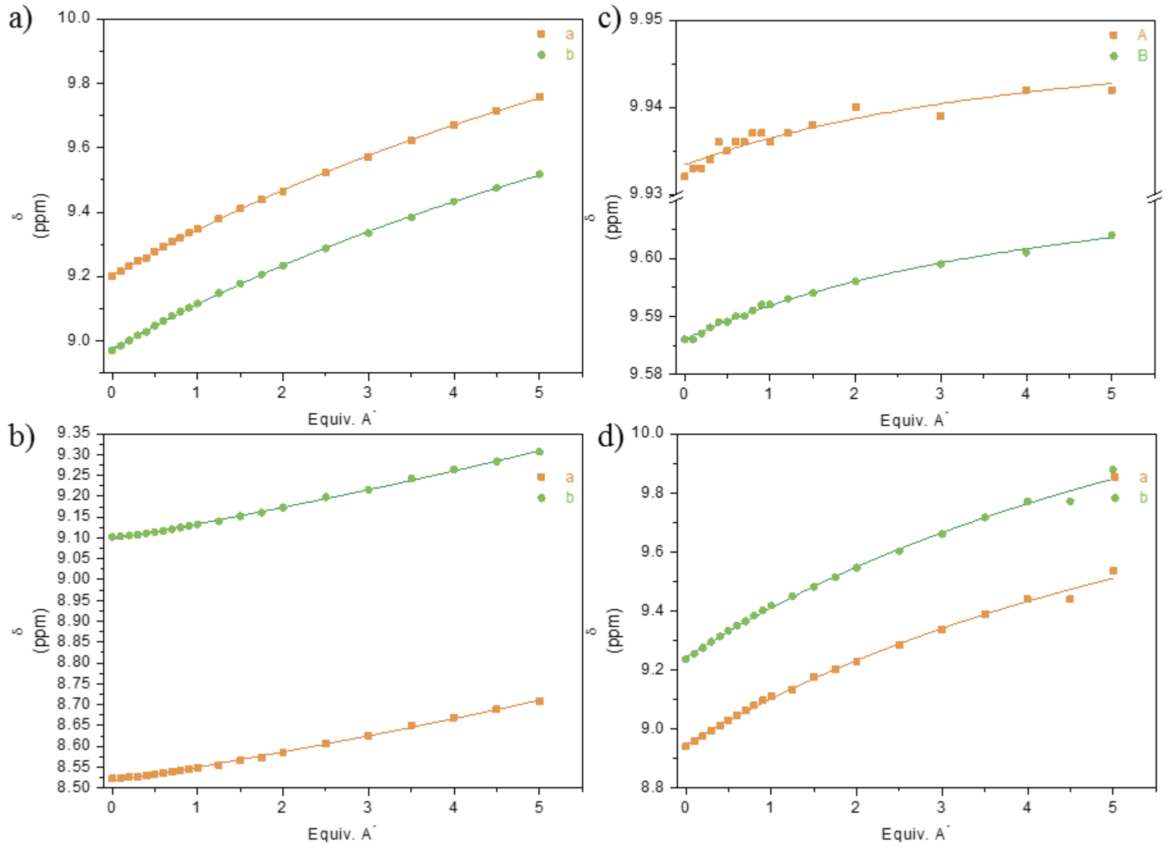

Figure A2. 55. Binding isotherms and fitting curve relative to the urea Ha and Hb resonances for titrations of tripodal ligands **86-89** with SO_4^{2-} in DMSO-d_6. a) **86**, b) **87**, c) **88** and d) **89**.

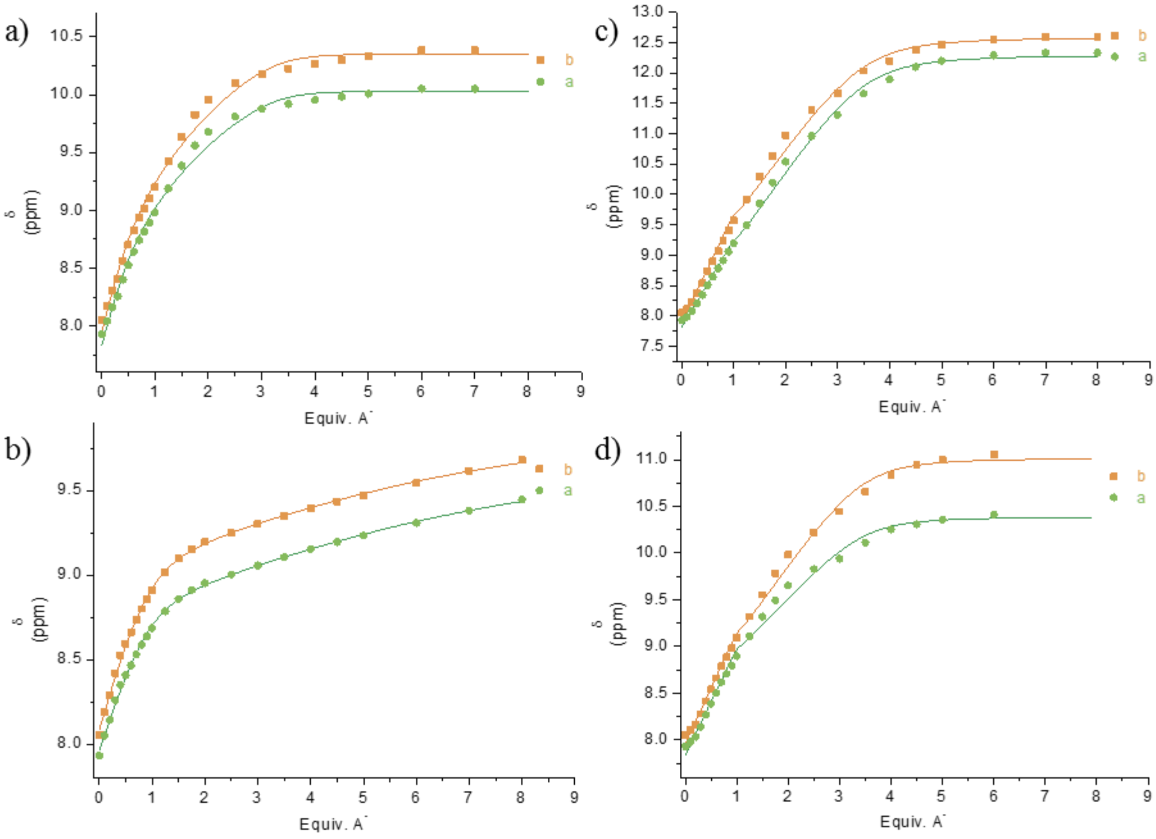

Figure A2. 58. Binding isotherms and fitting curve relative to the urea Ha and Hb resonances for titrations of tripodal ligand **86** with different anions in CD$_3$CN. a) Cl$^-$, b) SO$_4^{2-}$ c) CH$_3$COO$^-$ and d) H$_2$PO$_4^-$.

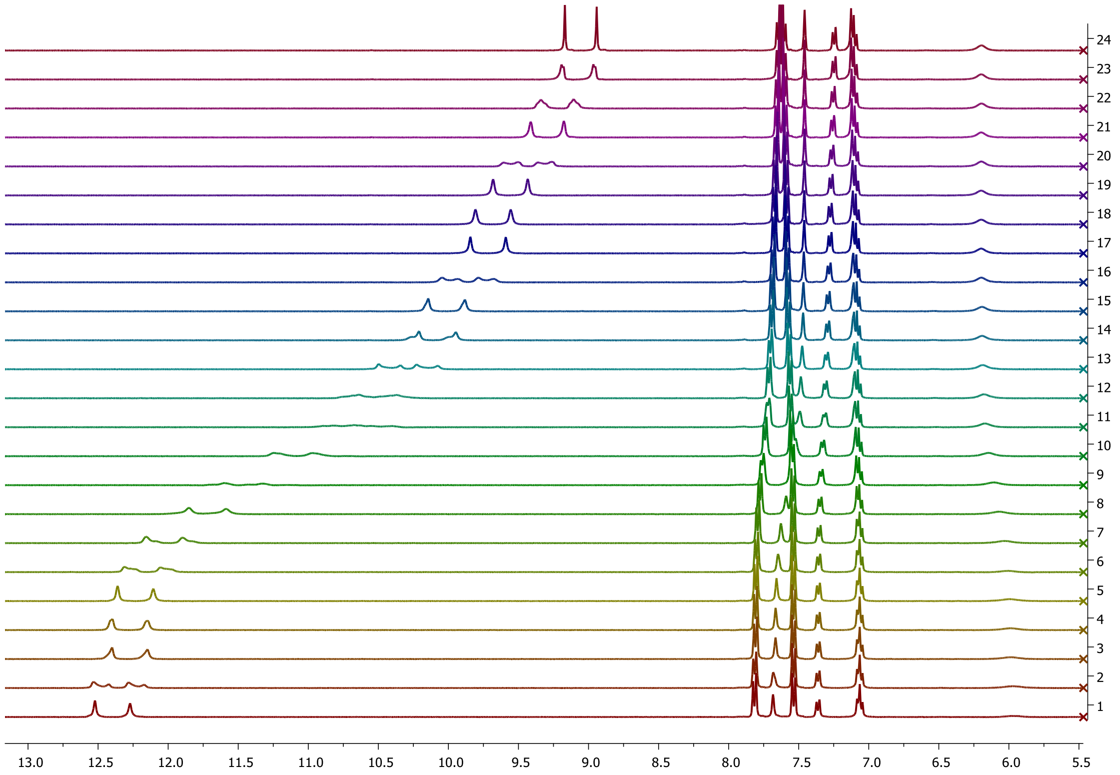

Figure A2. 57. ^{1}H NMR titration profile of **86** with CH$_3$COO$^-$, in DMSO-d_6. [**86**] = 7 mM, showing the splitting of the urea resonances.

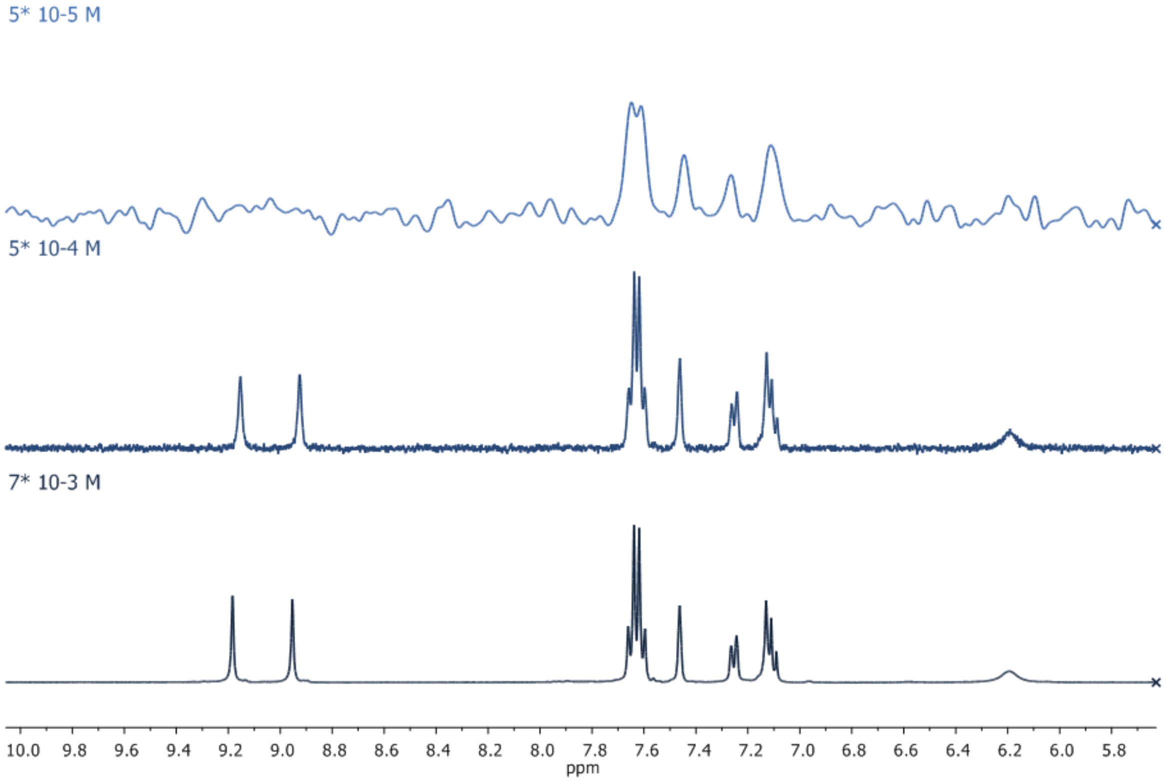

Figure A2. 59. ^{1}H NMR of **86** in DMSO-d_6 at different concentrations.

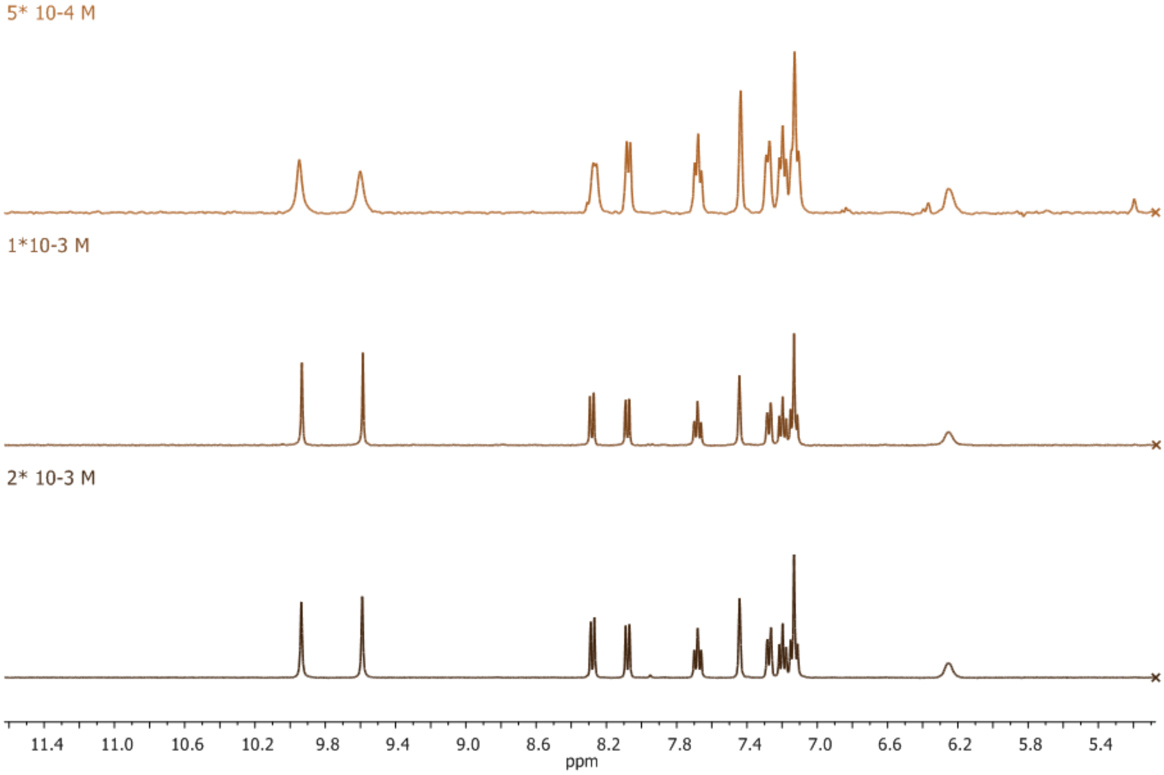

Figure A2. 60. ^{1}H NMR of **88** in DMSO-d_6 at different concentrations.

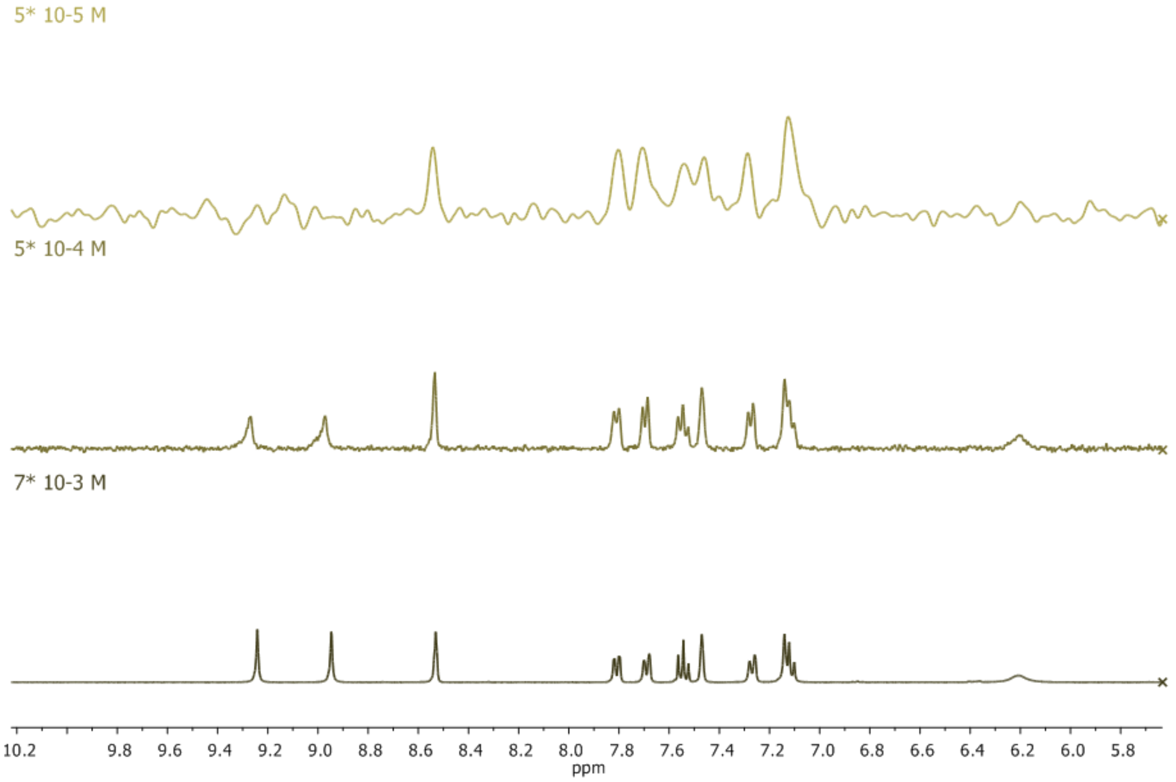

Figure A2. 61. ^{1}H NMR of **89** in DMSO-d_6 at different concentrations.

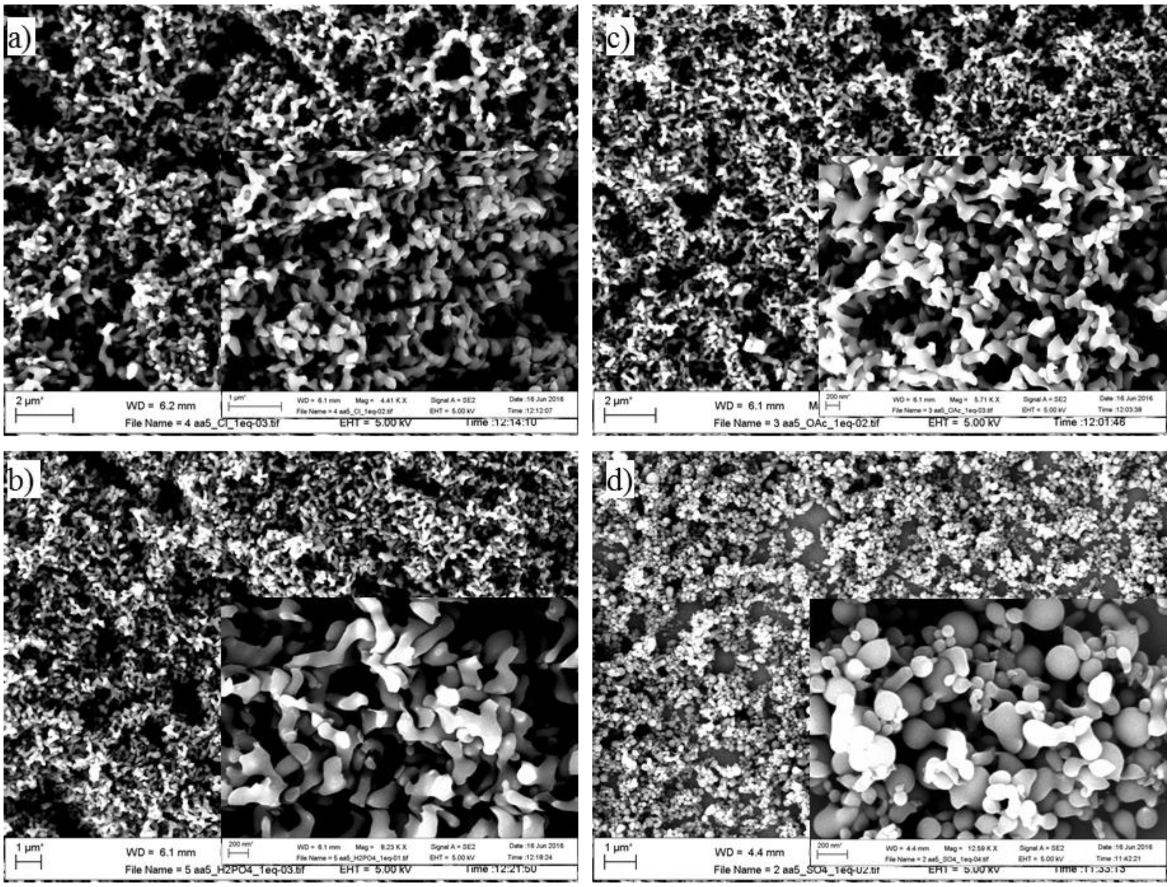

Figure A2. 62. SEM images of AA5 self-assembled spheres with the addition of 1 equivalent of a) Cl^-, b) CH_3COO^-, c) $H_2PO_4^-$ and d) SO_4^{2-}.

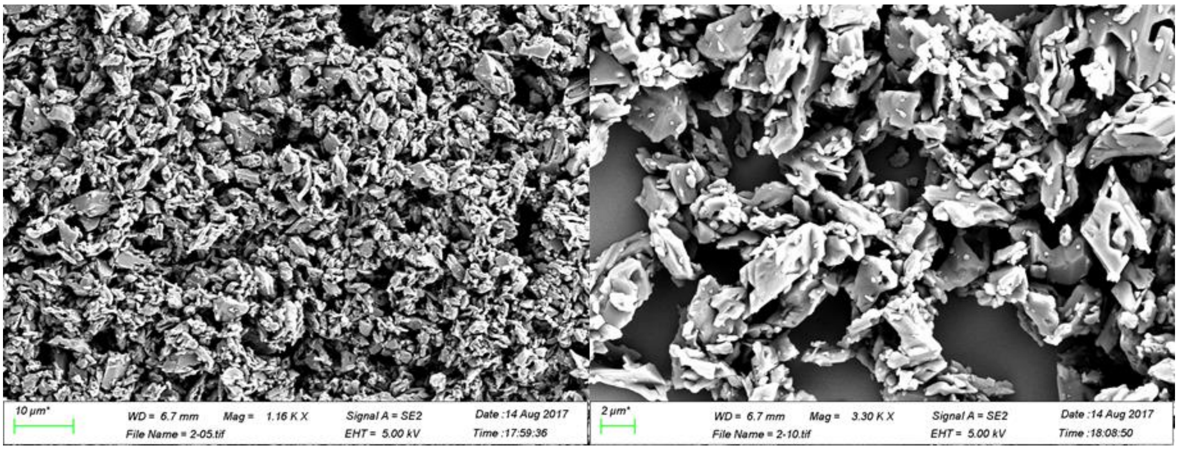

Figure A2. 63. SEM images of a deposited solution of **81** in CH_3OH:H_2O.

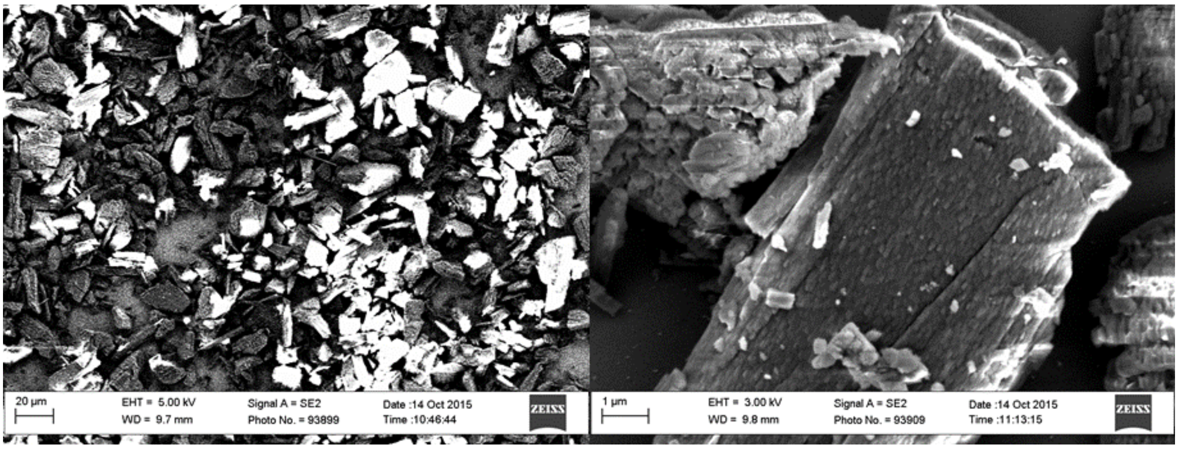

Figure A2. 64. SEM images of a deposited solution of **87** in CH_3OH:H_2O.

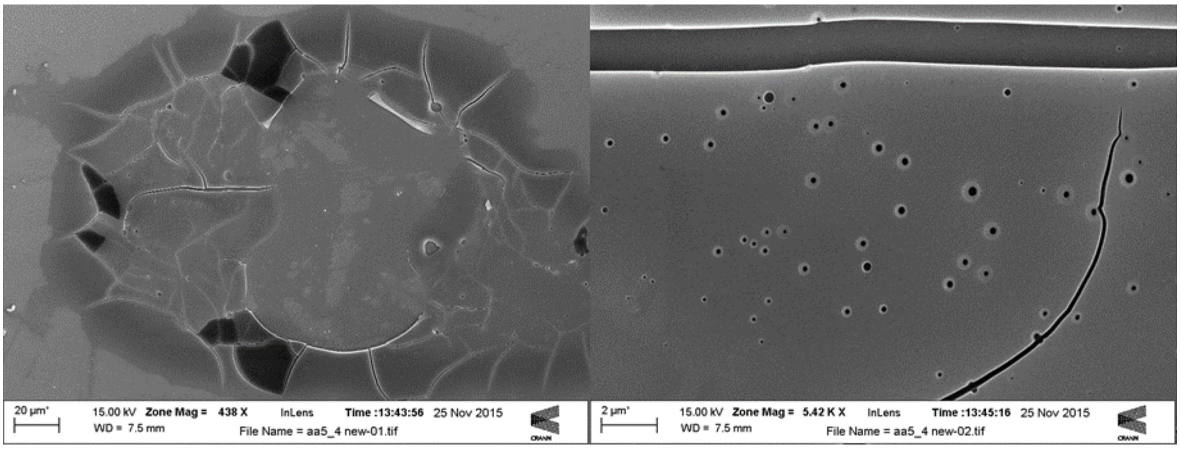

Figure A2. 65. SEM images of a deposited solution of **86**·SO_4^{2-} in CH_3OH to which H_2O was added, no spherical self-assembly of the particles was observed.

Table A2. 1. Selected crystallographic data and structure refinements for the structures in Section 2.2.1.

Compound	**100**	**87**(CH$_3$OH)	**87**(DMSO)	**88**
Chemical formula	$C_{18}H_{30}N_9O_3$	$C_{51}H_{39}F_6N_9O_6 \cdot 2(CH_4O)$	$C_{51}H_{39}F_6N_9O_6 \cdot 2(C_2H_6OS)$	$C_{51}H_{42}N_{12}O_{12} \cdot 2.584(C_2H_3$
M_r (g·mol^{-1})	420.51	1051.99	1144.16	1121.05
Crystal size (mm)	× ×	0.19 × 0.06 × 0.02	0.34 × 0.21 × 0.09	0.19 × 0.17 × 0.08
Crystal system	Monoclinic	Triclinic	Triclinic	Triclinic
Space group	$P2_1/c$	$P\bar{1}$	$P\bar{1}$	$P\bar{1}$
T(K)	293	100	100	100
a(Å)	9.5615 (5)	9.0643 (5)	8.320 (11)	8.817 (6)
b(Å)	37.1334 (19)	13.0734 (7)	17.18 (2)	12.915 (8)
c (Å)	7.8168 (4)	21.9995 (11)	23.64 (3)	23.844 (15)
α(°)	90	94.699 (2)	77.62 (3)	92.432 (17)
β(°)	95.418 (2)	101.707 (2)	88.26 (2)	98.11 (2)
γ (°)	90	102.535 (2)	82.572 (17)	99.519 (17)
V (Å^3)	2763.0 (2)	2470.2 (2)	3273 (7)	2645 (3)
Z	4	2	2	2
F(000)	900	1092	1188	1170
D_x (Mg m^{-3})	1.011	1.414	1.161	1.408
Radiation type	Mo $K\alpha$	Mo $K\alpha$	Mo $K\alpha$	Cu $K\alpha$
μ (mm^{-1})	0.07	0.11	0.15	0.85
$R[F^2 > 2\sigma(F^2)]$	0.073	0.064	0.087	0.051
$wR(F2)$	0.187	0.161	0.266	0.137
S	1.13	0.93	1.05	1.04

Table A2. 2. Selected crystallographic data and structure refinements for the structures in Section2.3.3.

Compound	**87·SO$_4^{2-}$ (DMSO)**	**87·SO$_4^{2-}$ (CH$_3$CN)**
Chemical formula	$C_{51}H_{39}F_6N_9O_6 \cdot 0.5(O_8S)$	$0.5(O_8S) \cdot C_{51}H_{42}F_6N_9O_6$
M_r (g·mol^{-1})	1067.94	1070.96
Crystal size (mm)	0.07 × 0.05 × 0.02	0.07 × 0.05 × 0.02
Crystal system	Trigonal	Trigonal
Space group	$R\bar{3}$	$R\bar{3}$
T(K)	100	100
a(Å)	16.3374 (12)	16.311 (5)
b(Å)	16.3374 (12)	16.311 (5)
c (Å)	50.401 (4)	50.261 (18)
α(°)	90	90
β(°)	90	90
γ (°)	120	120
V (Å^3)	11650 (2)	11580 (8)
Z	6	6
F(000)	3300	3318
D_x (Mg m^{-3})	0.913	0.921
Radiation type	Cu $K\alpha$	Cu $K\alpha$
μ (mm^{-1})	0.76	0.76
$R[F^2 > 2\sigma(F^2)]$	0.095	0.089
wR(F2)	0.295	0.283
S	1.14	1.1

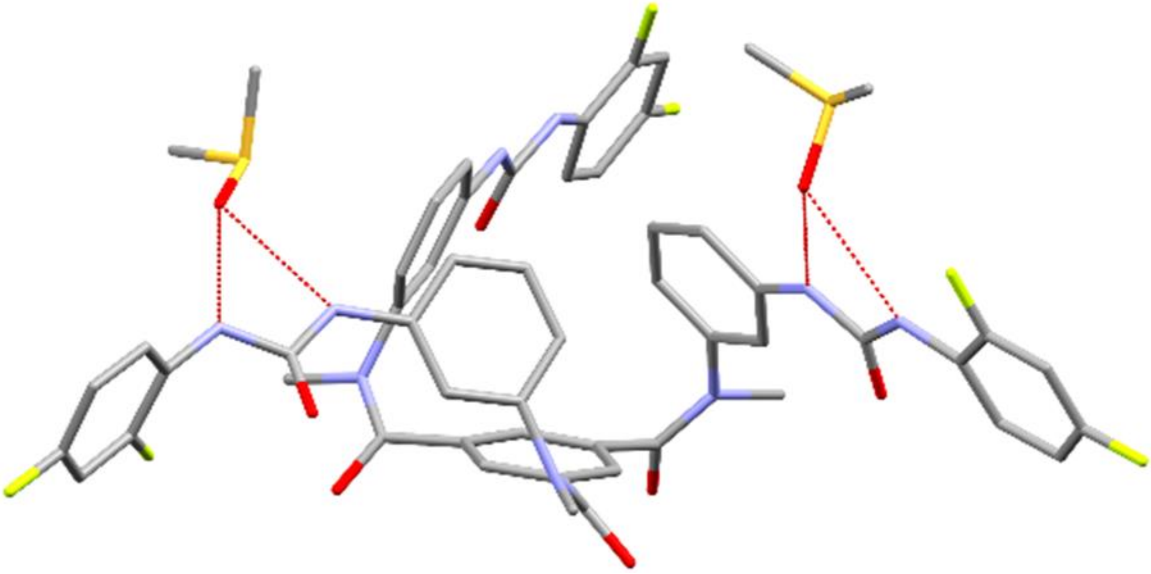

Figure A2. 66. Capped stick structure of compound 2 showing the interaction with molecules of DMSO (hydrogens are not shown).

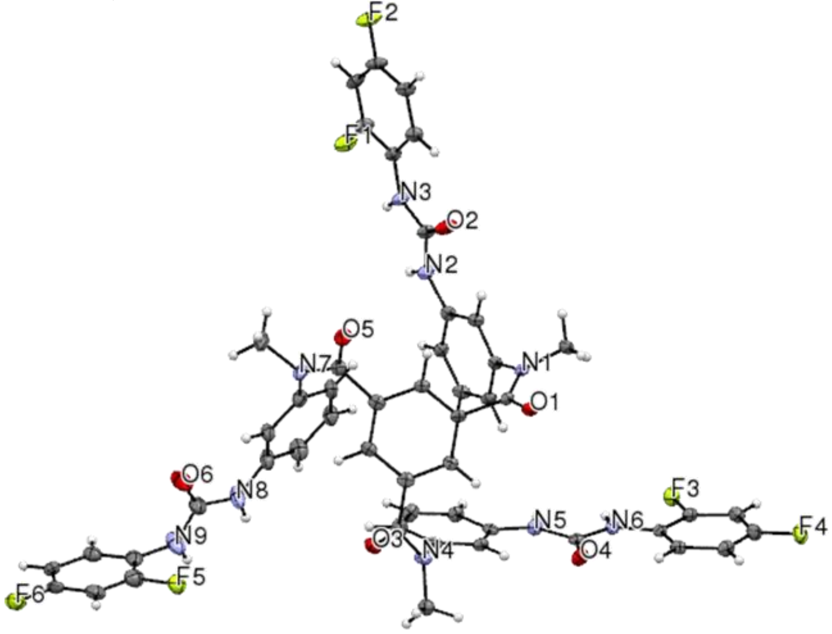

Figure A2. 67. ORTEP representation of **87**. Solvent molecules omitted.

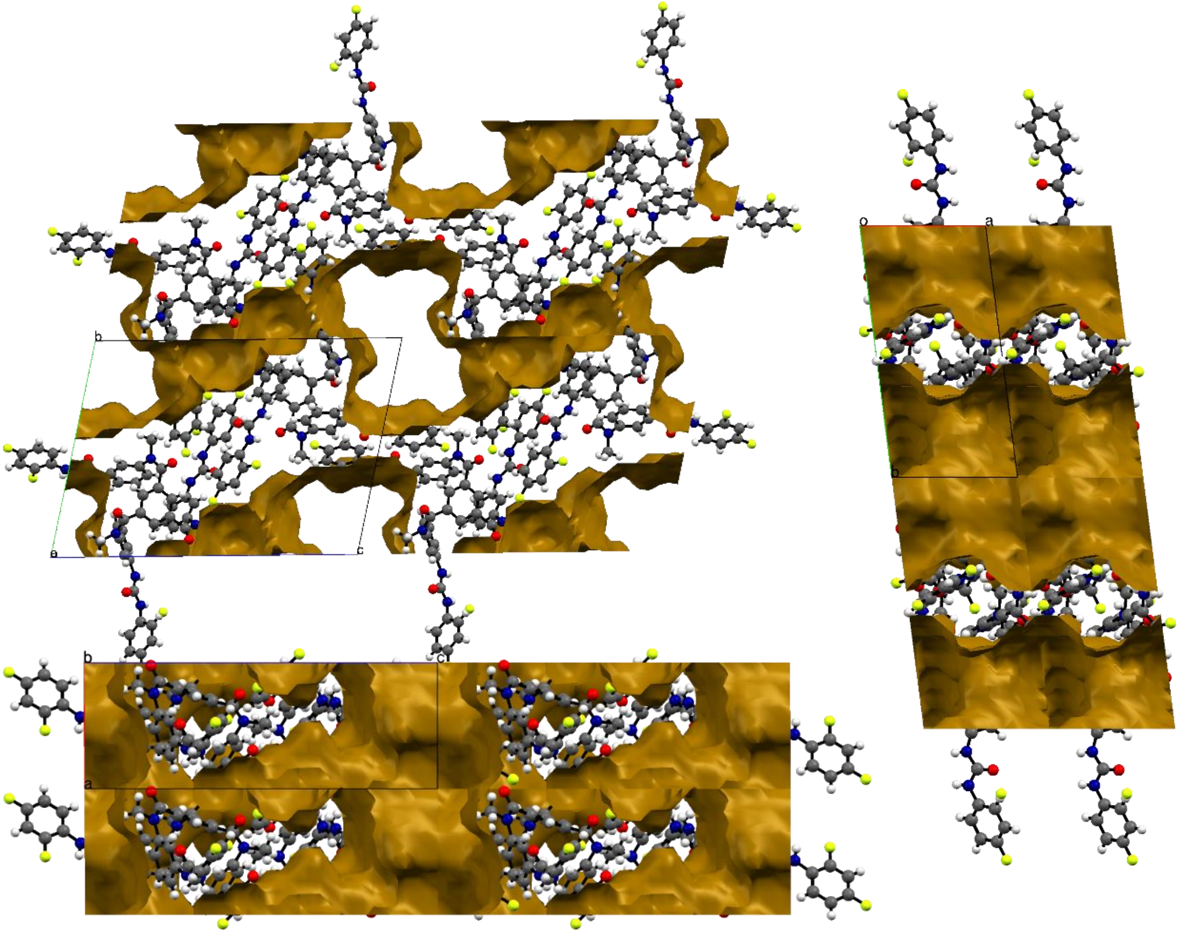

Figure A2. 68. Crystal of 2 :representation of contact surface for the voids found in the crystal structure as

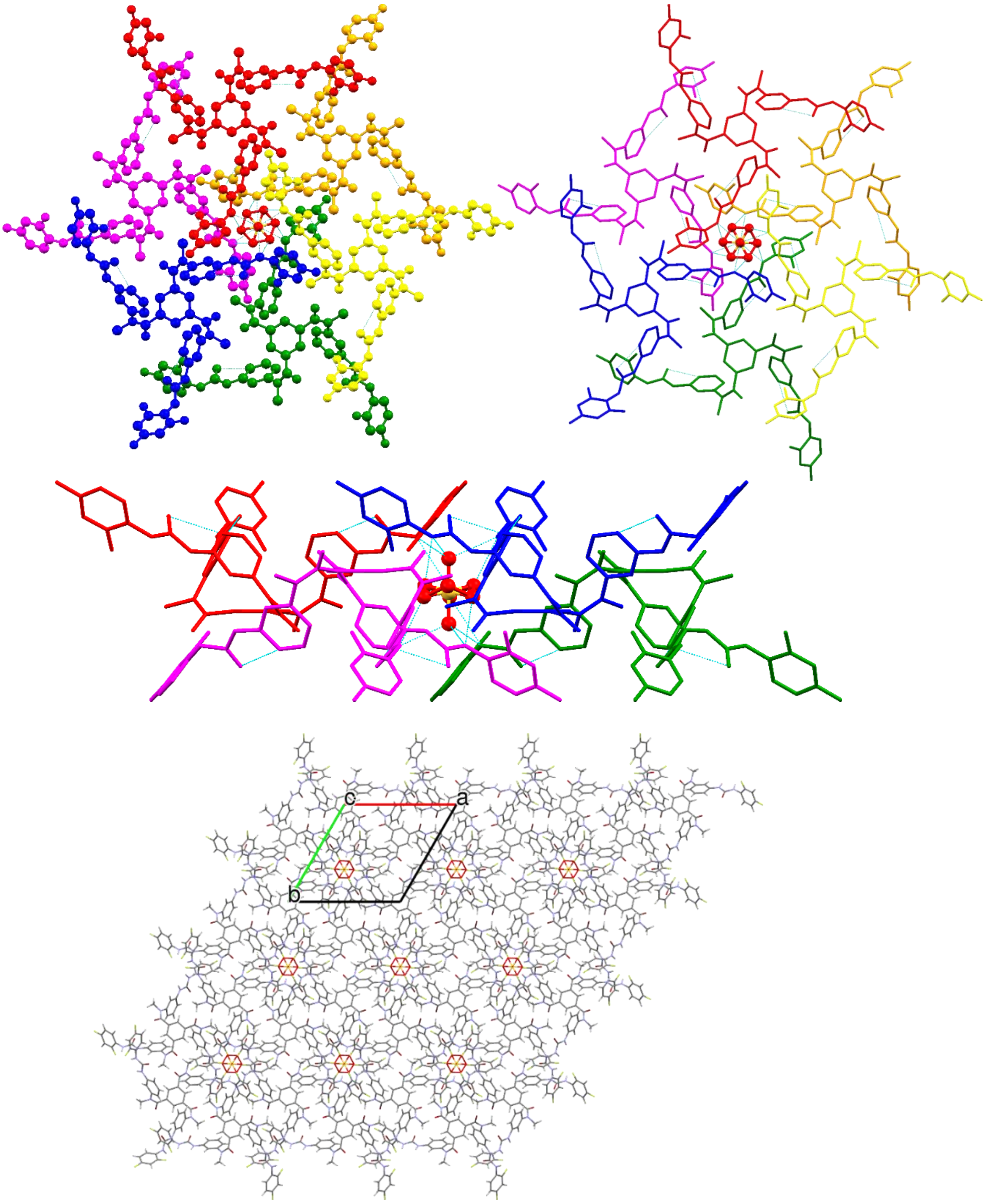

Figure A2. 69. Different views of the interaction between **87** and the sulphate anion.

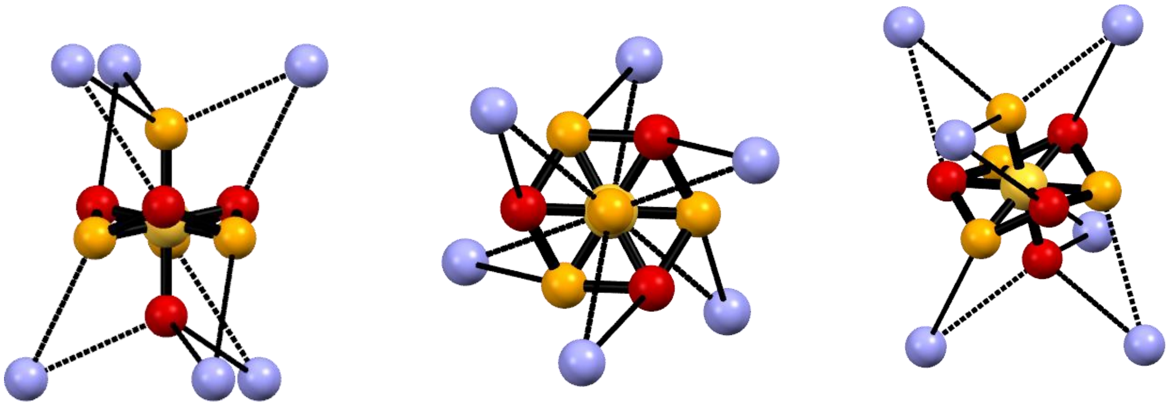

Figure A2. 70. Detail on hydrogen bonding on sulphate moiety. Red and orange atoms represent two possible orientations for the sulphate.

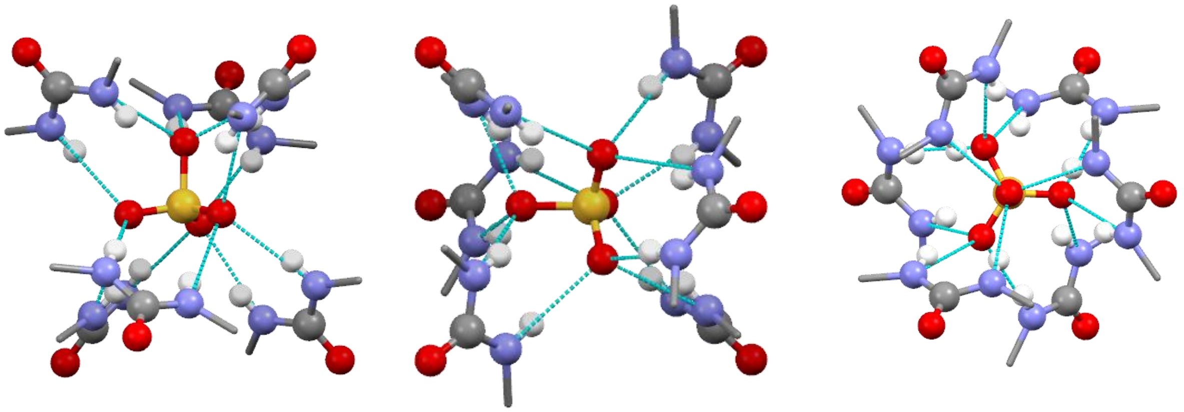

Figure A2. 71. Perspective and detail of the sulfate hydrogen bonding. Each oxygen receives three hydrogen bonds. Sequentially shown view down *a*; view down *b*; view down *c*.

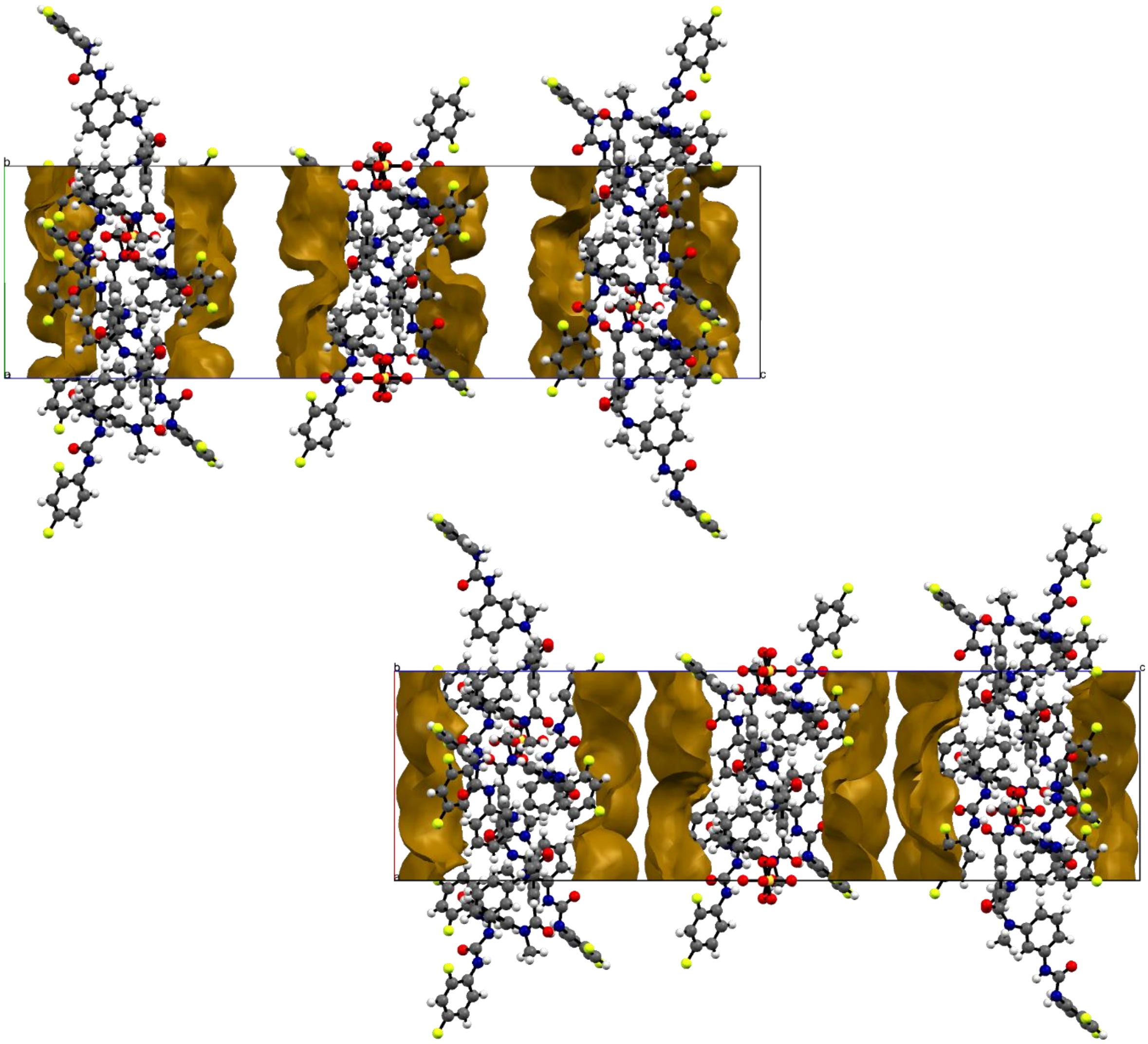

Figure A2. 72. Representation of the voids found in the crystal structure as calculated by Mercury 3.5 viewed down the *a* axes. (1) is the contact surface for the voids while (2) is the volume accessible by the solvent.

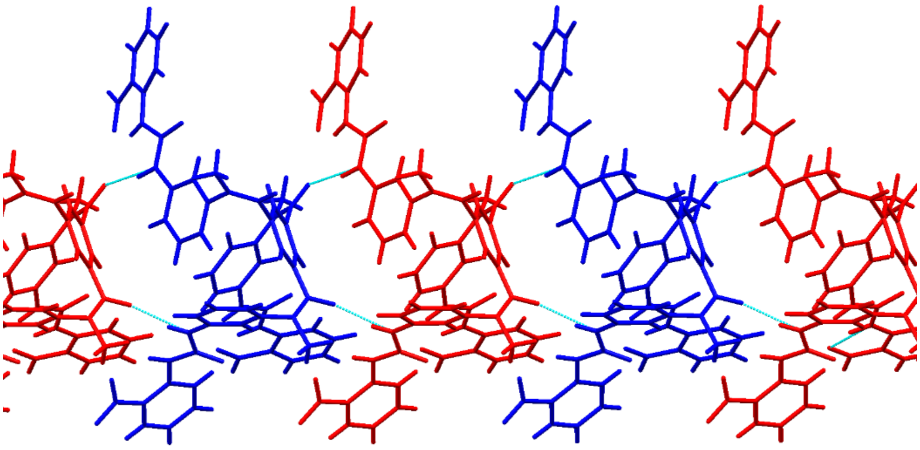

Figure A2. 73. Intermolecular H-bonding between molecules of compound **88** forming a twisted 1D networks in the crystallography *a* axis.

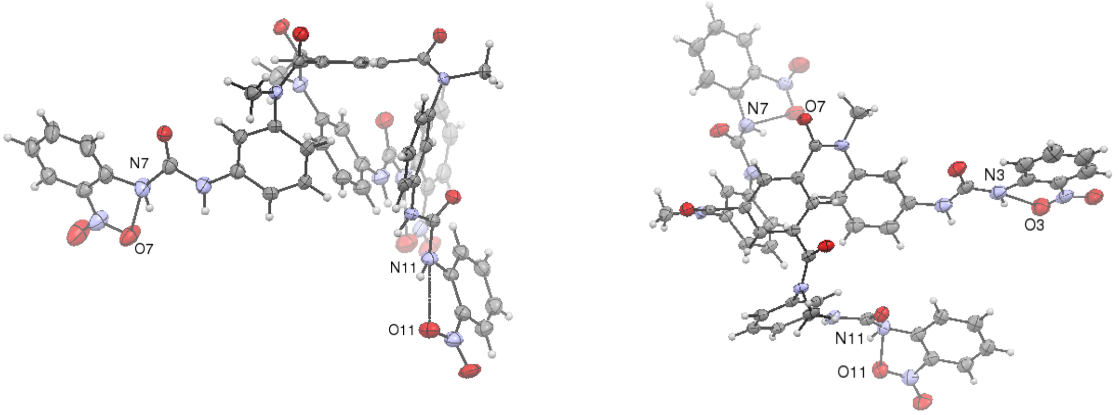

Figure A2. 75 ORTEP representation of **88**. Solvent molecules omitted.

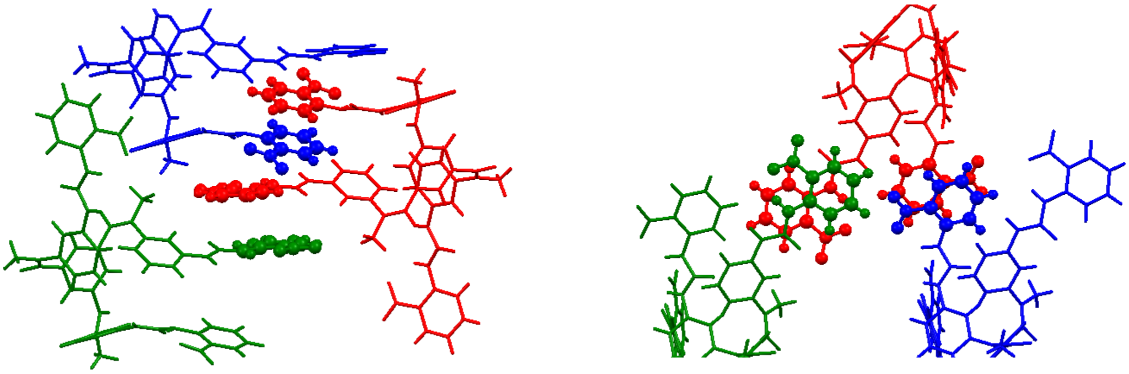

Figure A2. 74. π-π stacking interactions between the *o*-nitro phenyl moieties from different molecules of **88**.

Table A2. 3. Examples of variation in the DLS aggregation studies with **86** in $CH_3OH:H_2O$ (1:1)

Sample #	**Initial conc. CH_3OH solution\M**	**Final concentration\M**	**Speed rate syringe pump\ml/h**	**z-Average**	**pdI**	**%Intensity**
1	1.6 10^{-5}	8 10^{-6}	120	334.0	0.197	100
2	1.6 10^{-5}	8 10^{-6}	60	332.6	0.063	100
3	8 10^{-6}	4 10^{-6}	120	224.0	0.057	98.4

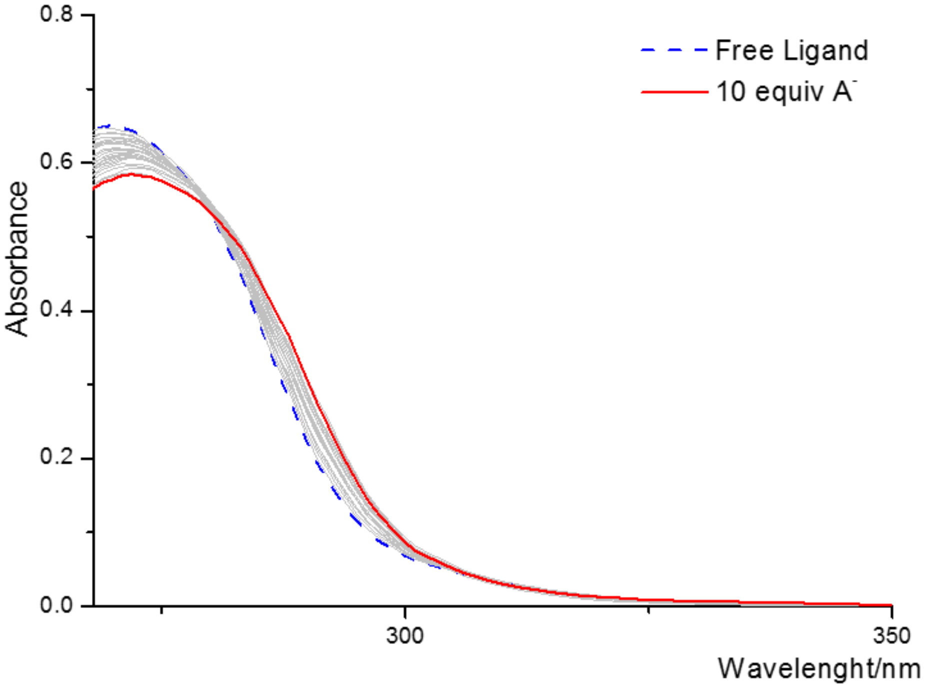

Figure A2. 76. Changes in the absorption spectra of ligand **86** in DMSO during the titration up to addition of 10 equiv. of $H_2PO_4^-$.

A3. Appendix Chapter 3

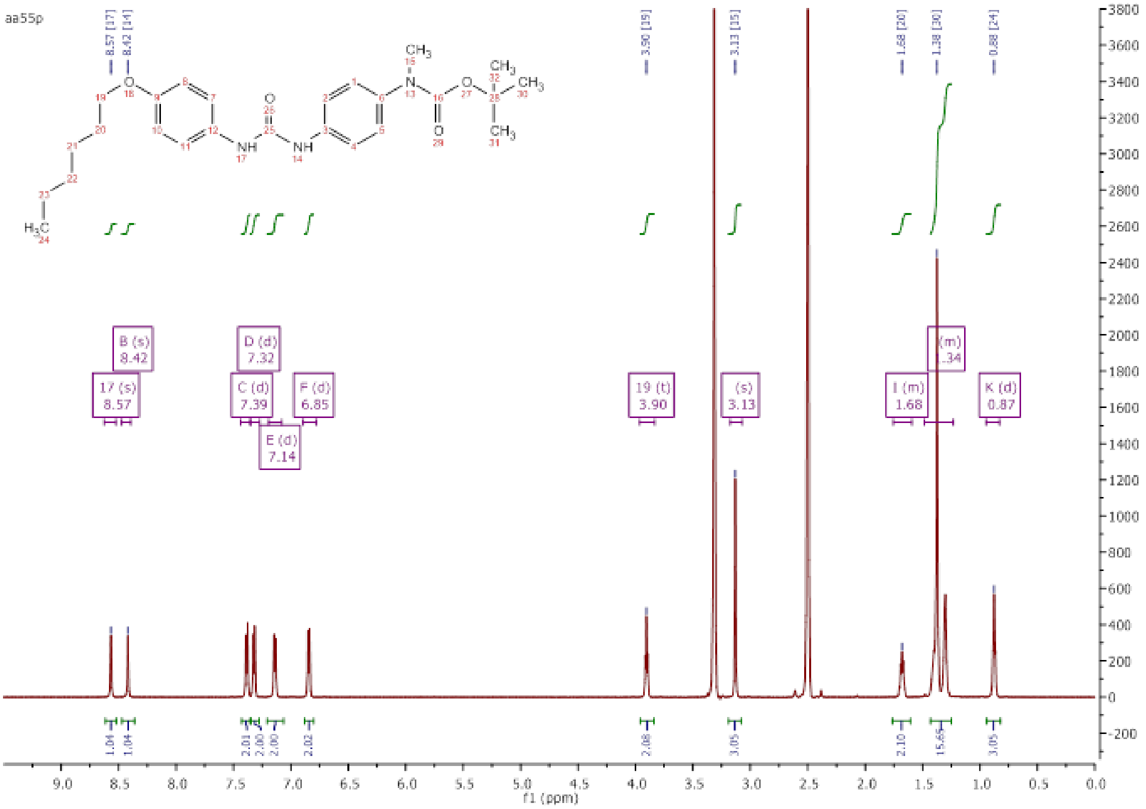

Figure A3. 1. ^{1}H NMR (400 MHz) spectrum of **118** in DMSO-d_6.

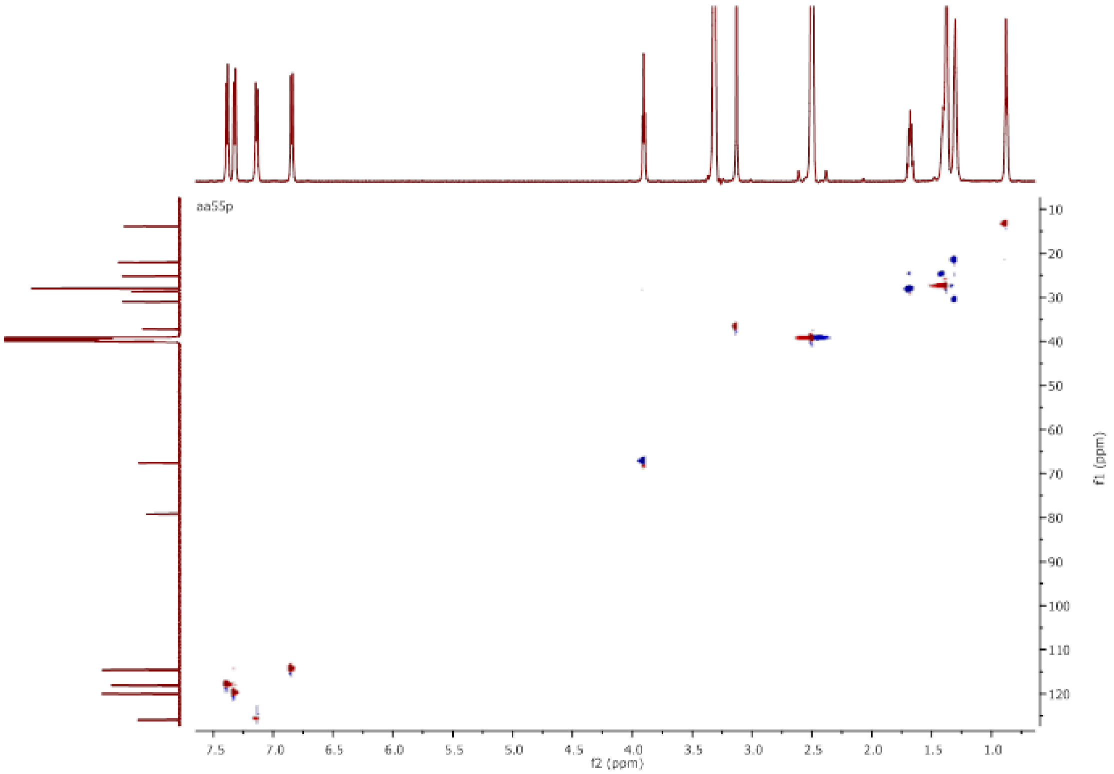

Figure A3. 3. ^{13}C-^{1}H HSQC NMR spectrum of **118** in DMSO-*d*$_6$.

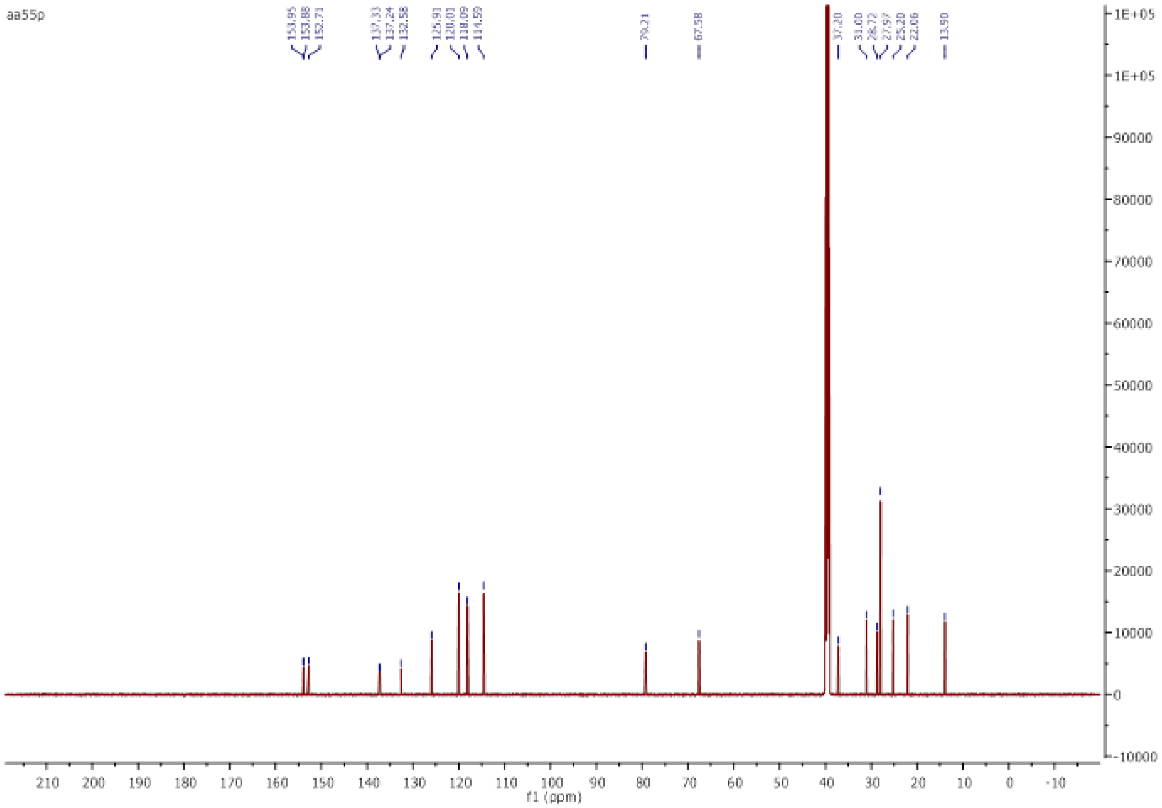

Figure A3. 2. ^{13}C NMR (100 MHz) spectrum of **118** in DMSO-*d*$_6$.

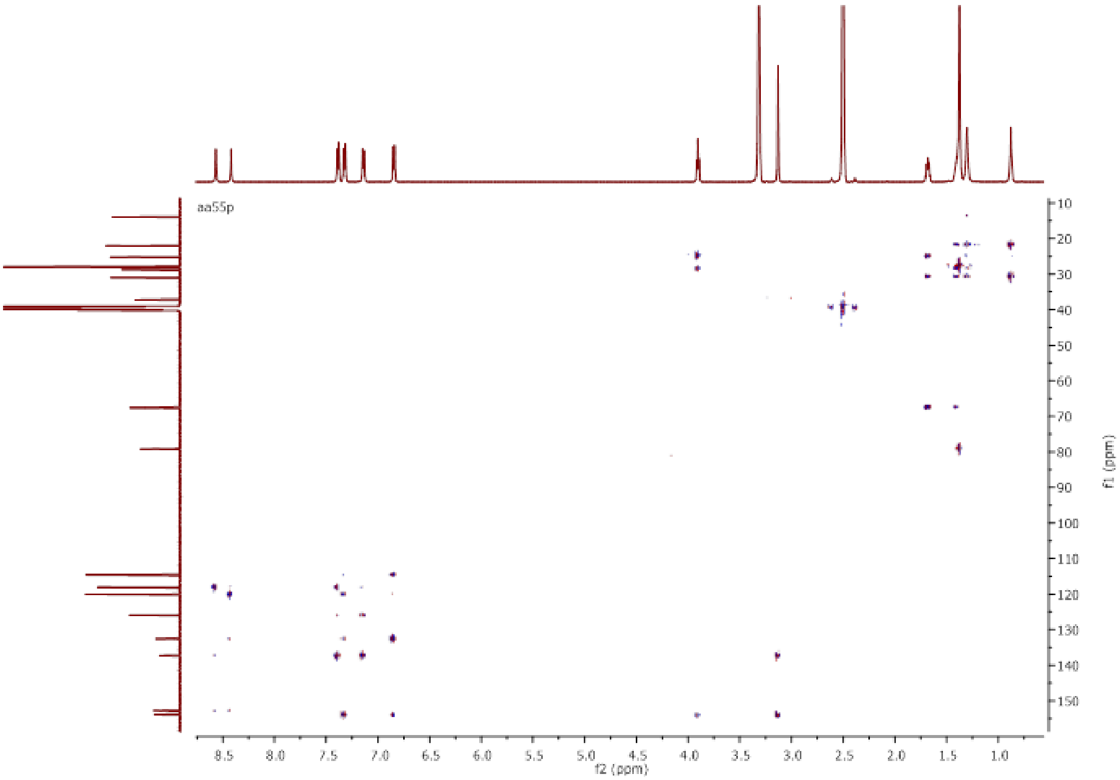

Figure A3. 5. ^{13}C-^{1}H HMBC NMR spectrum of **118** in DMSO-d_6.

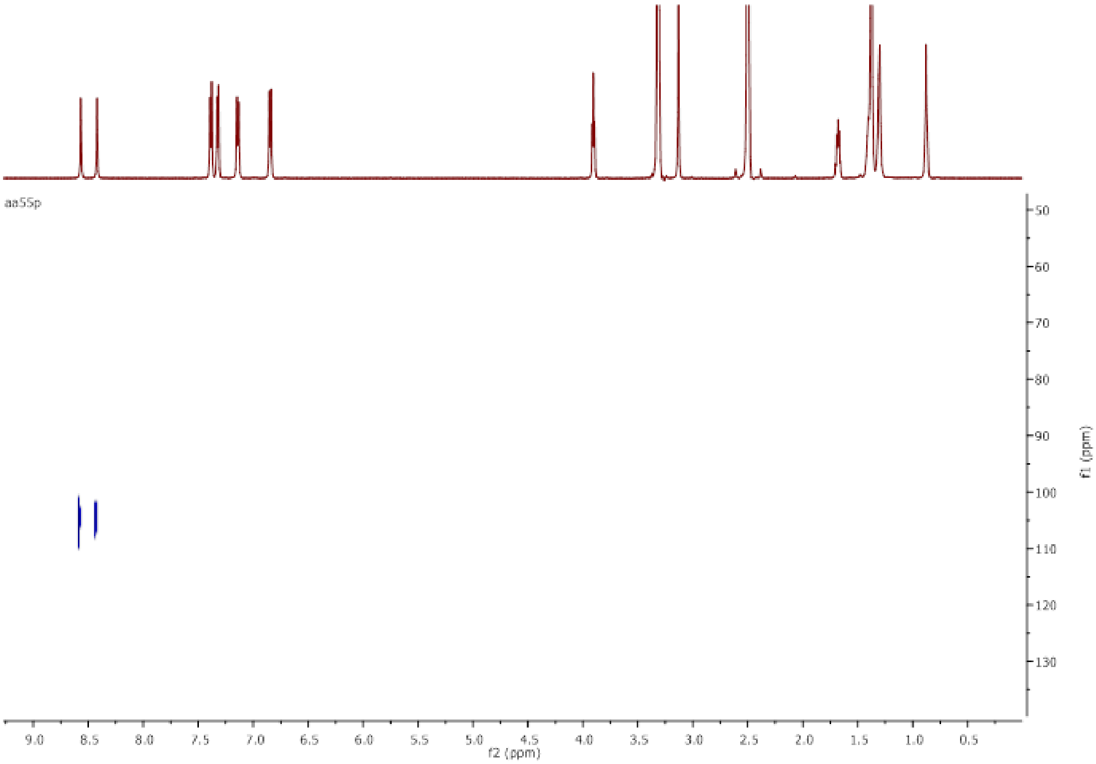

Figure A3. 4. ^{15}N-^{1}H HSQC NMR spectrum of **118** in DMSO-d_6.

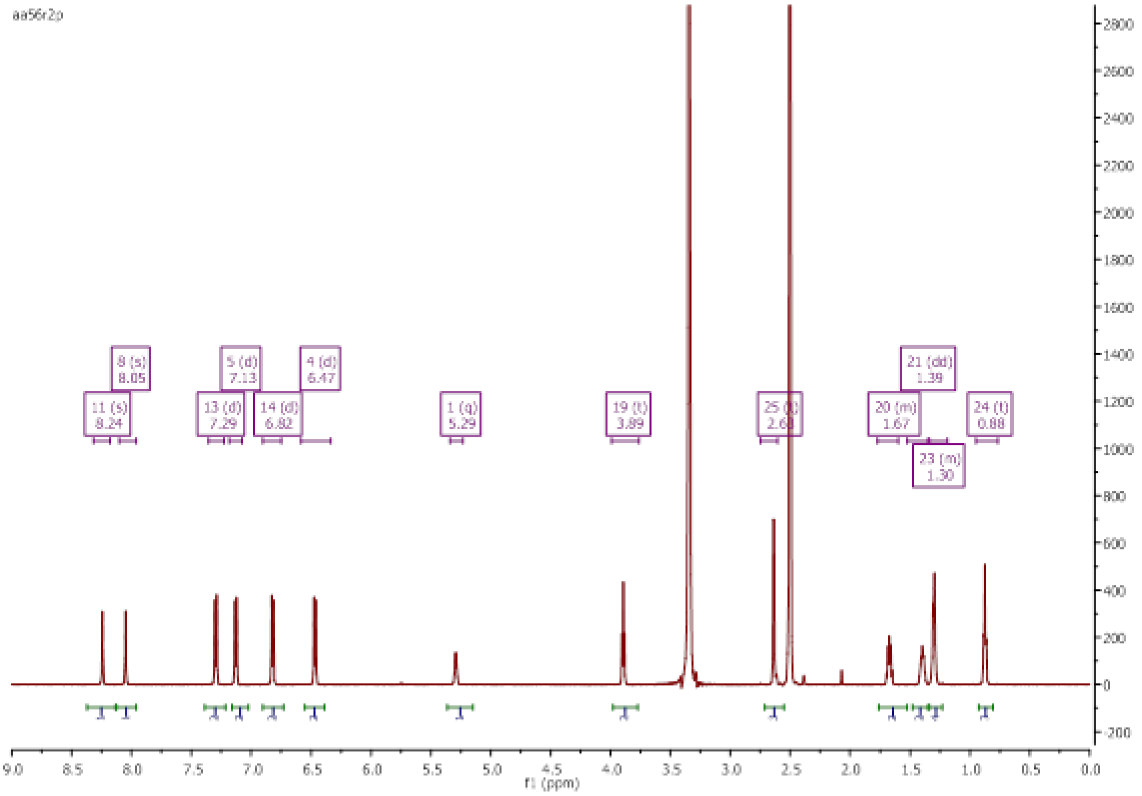

Figure A3. 7. ^{1}H NMR (400 MHz) spectrum of **113** in DMSO-d_6.

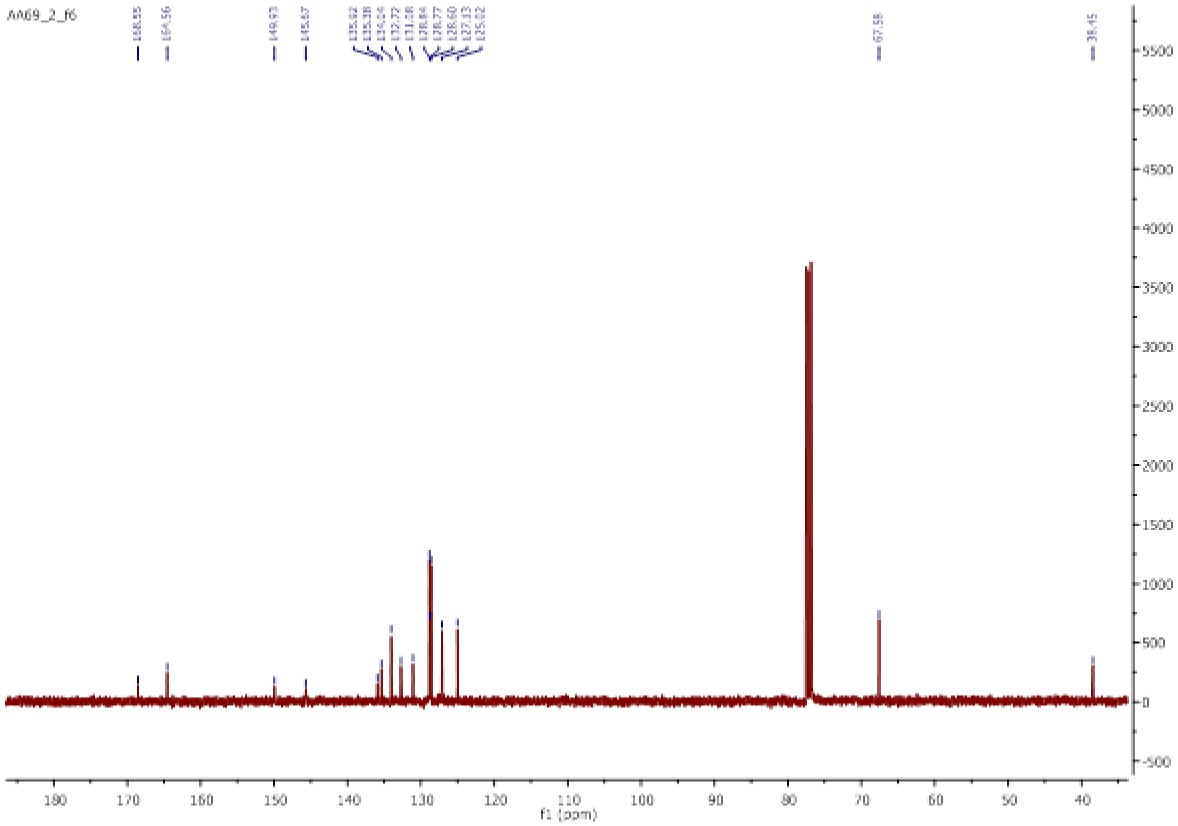

Figure A3. 6. ^{13}C NMR (100 MHz) spectrum of **121** in DMSO-d_6.

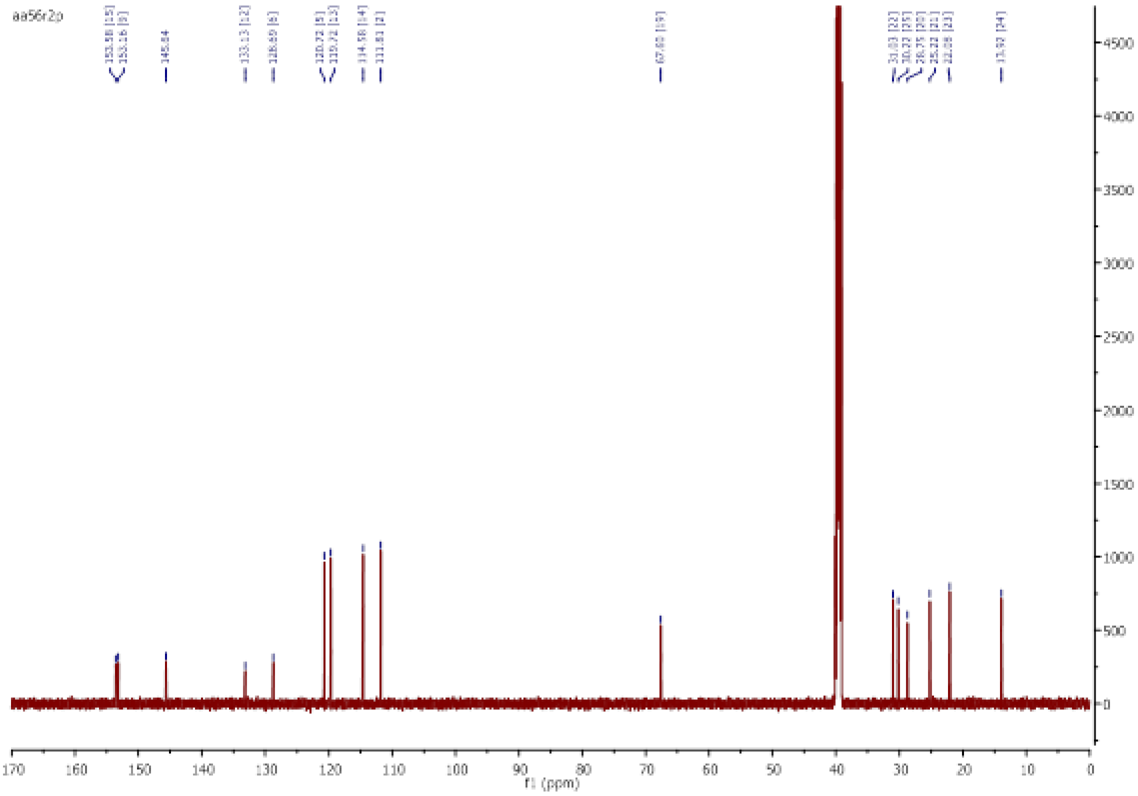

Figure A3. 8. ^{13}C NMR (100 MHz) spectrum of **113** in DMSO-*d*$_6$.

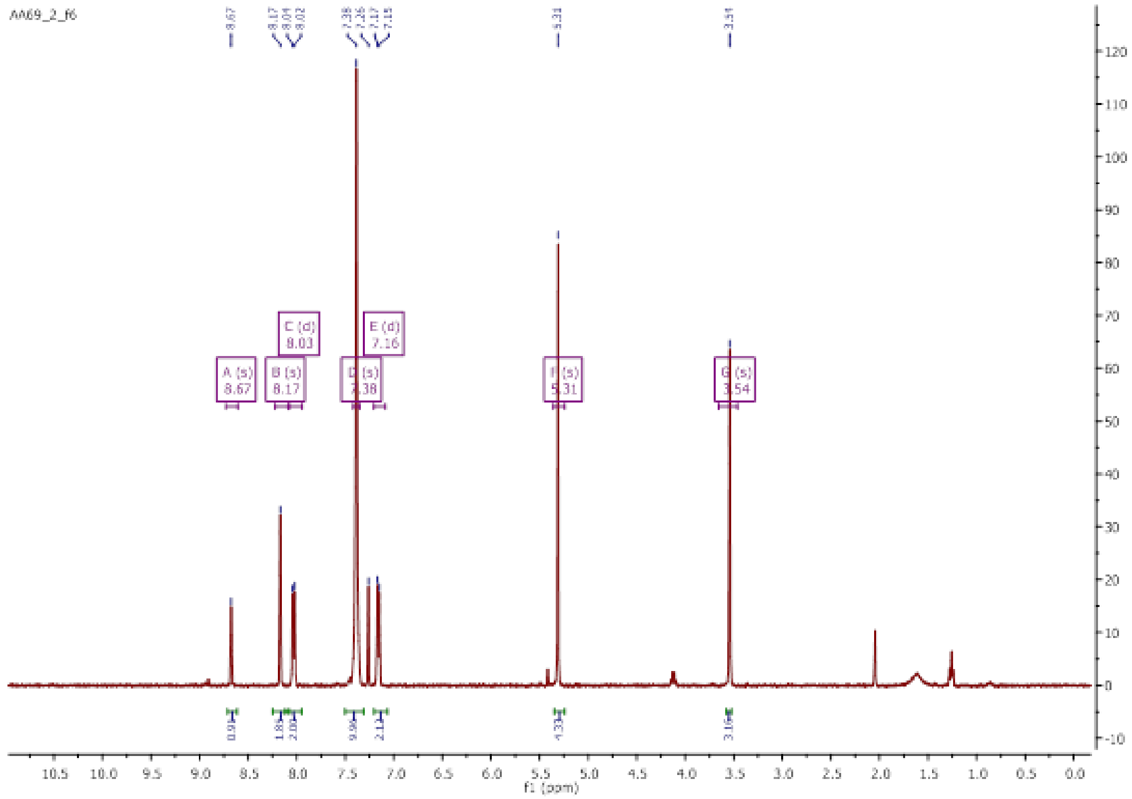

Figure A3. 9. ^{1}H NMR (400 MHz) spectrum of **121** in DMSO-*d*$_6$.

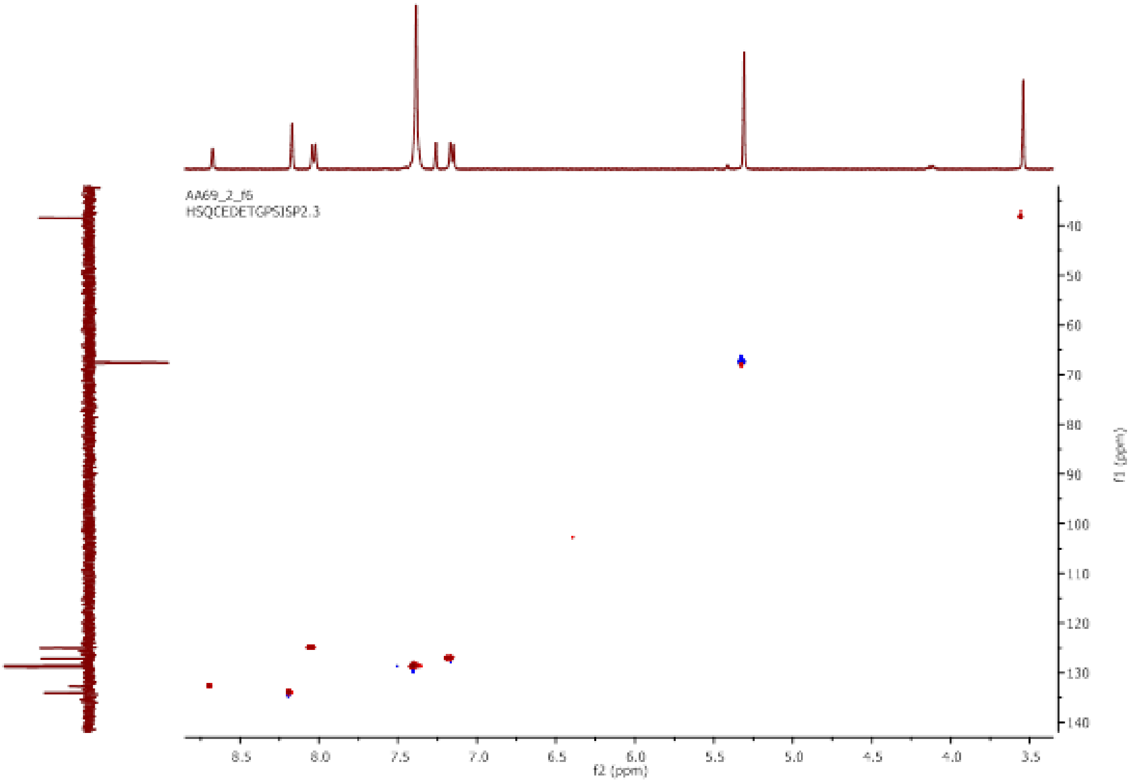

Figure A3. 10. ^{13}C-^{1}H HSQC NMR spectrum of **121** in DMSO-*d*$_6$.

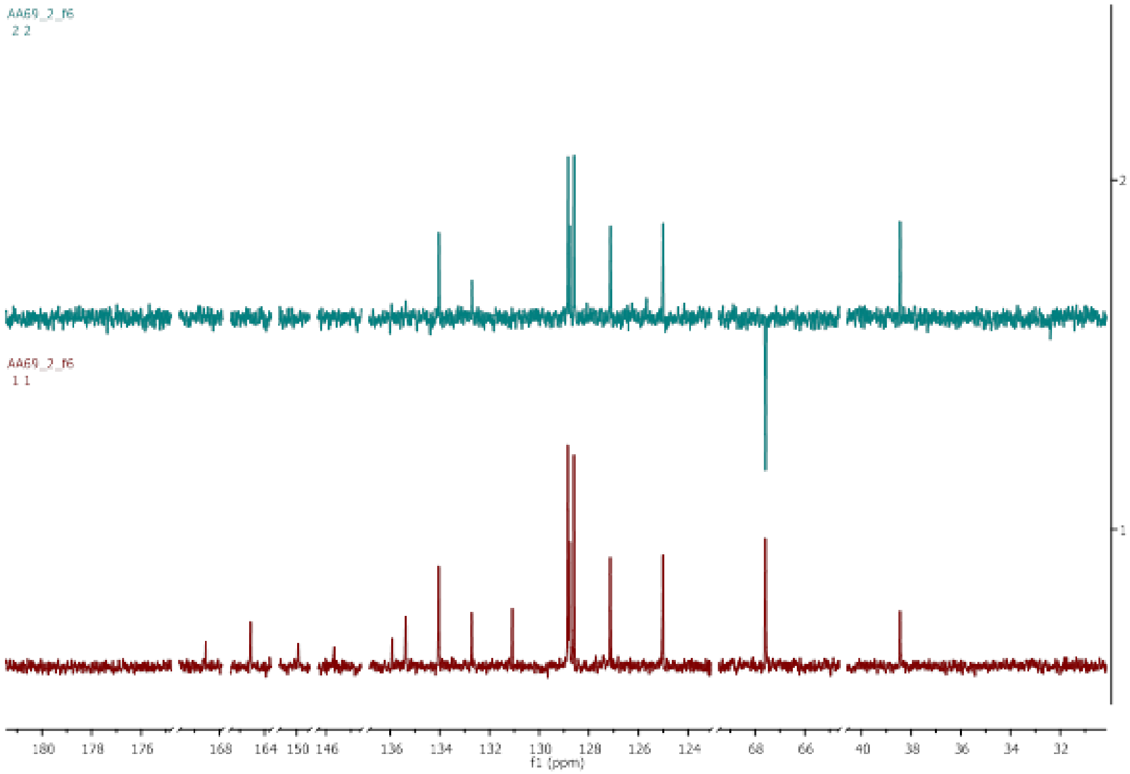

Figure A3. 11. Stacked ^{13}C NMR and DEPT-135 spectra of **121** in DMSO-d_6.

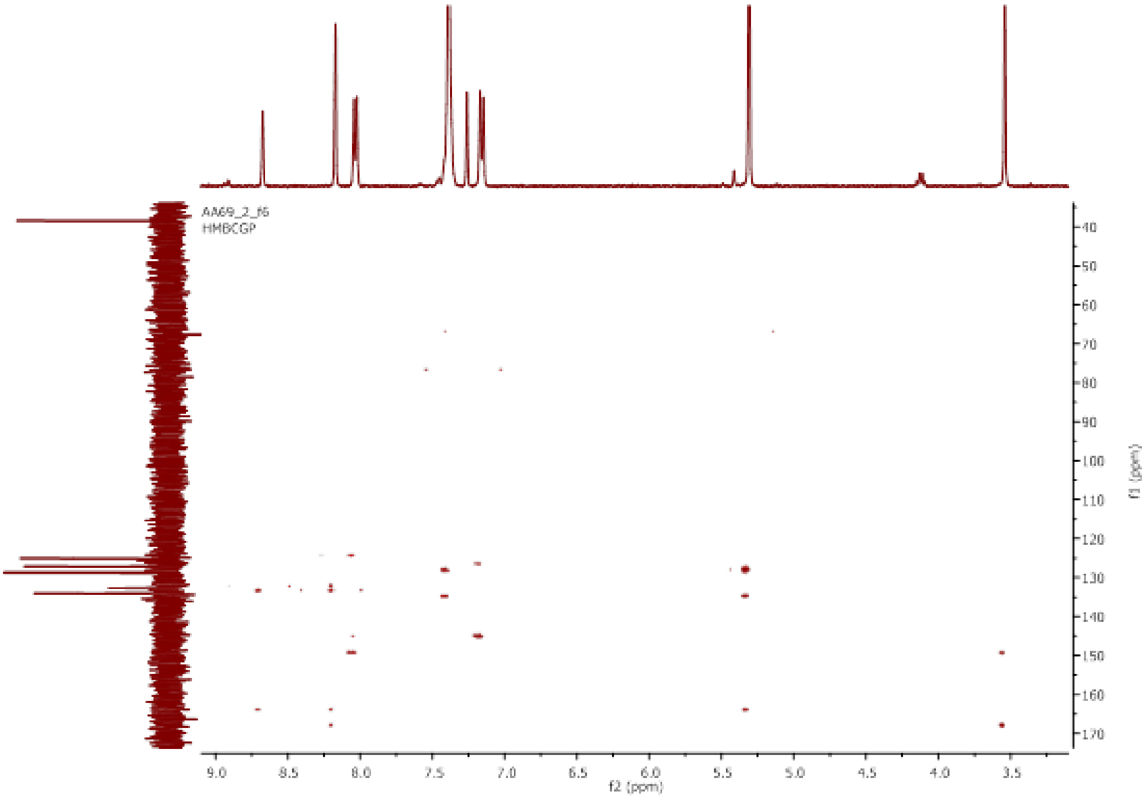

Figure A3. 12. ^{13}C-^{1}H HMBC NMR spectrum of **121** in DMSO-d_6.

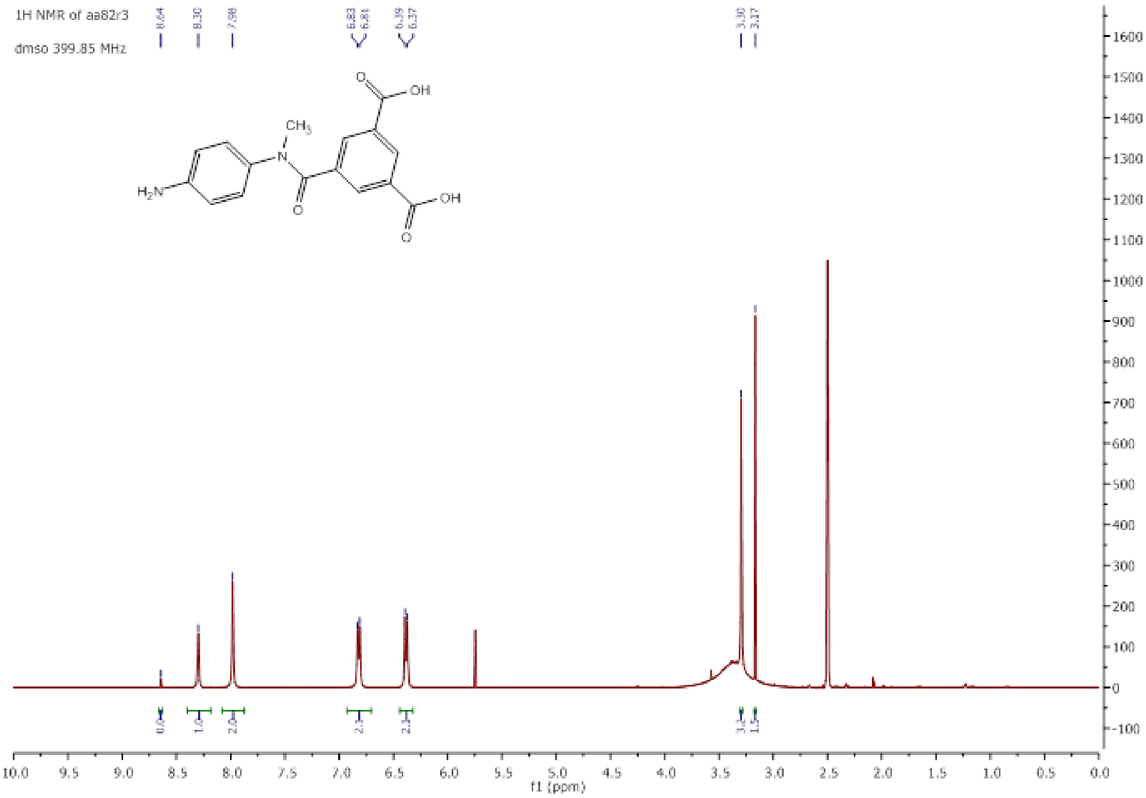

Figure A3. 13. ^{1}H NMR (400 MHz) spectrum of **123** in DMSO-d_6.

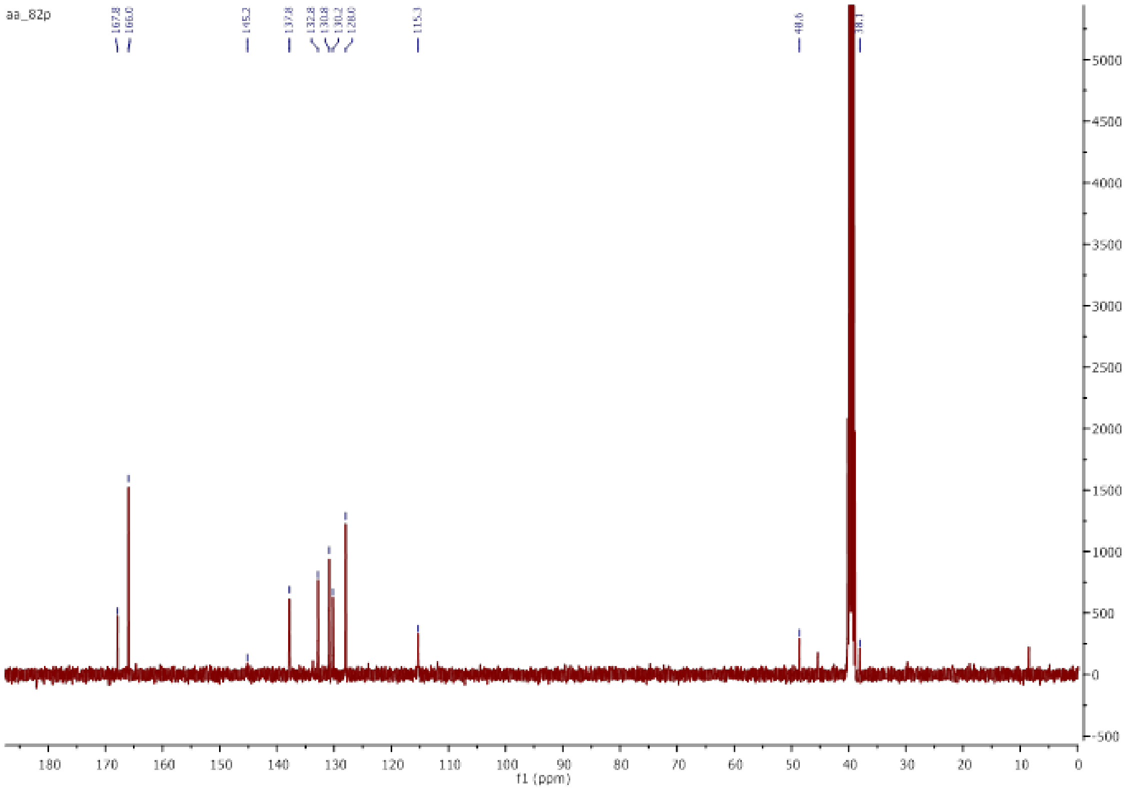

Figure A3. 14. ^{13}C NMR (100 MHz) spectrum of **123** in DMSO-d_6.

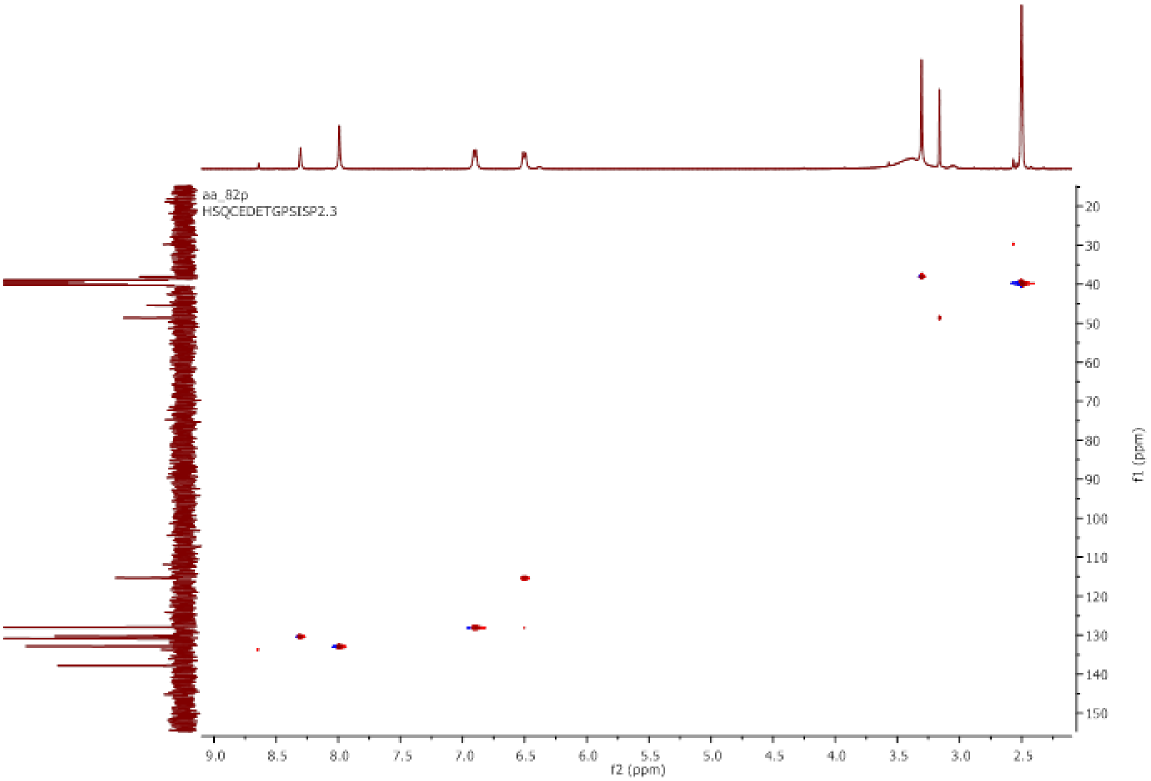

Figure A3. 15. ^{13}C-^{1}H HSQC NMR spectrum of **123** in DMSO-d_6.

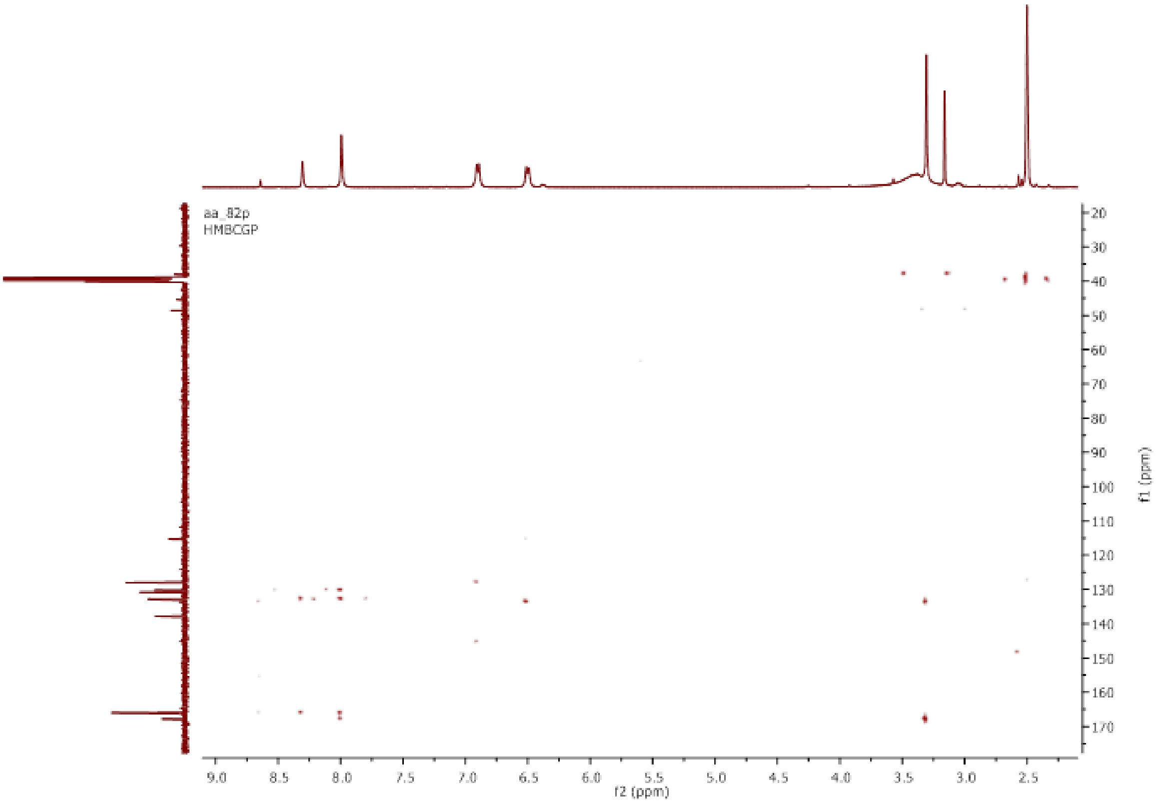

Figure A3. 16. ^{13}C-^{1}H HMBC NMR spectrum of **123** in DMSO-d_6.

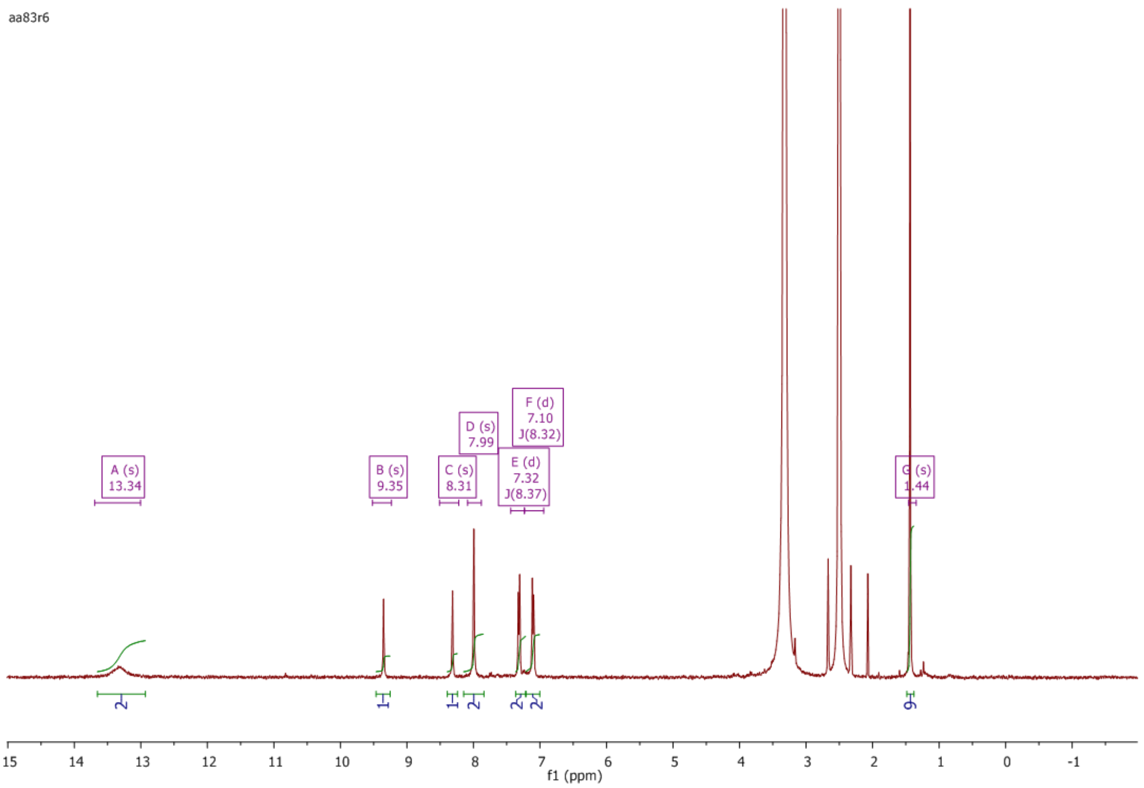

Figure A3. 17. ^{1}H NMR (400 MHz) spectrum of **124** in DMSO-d_6.

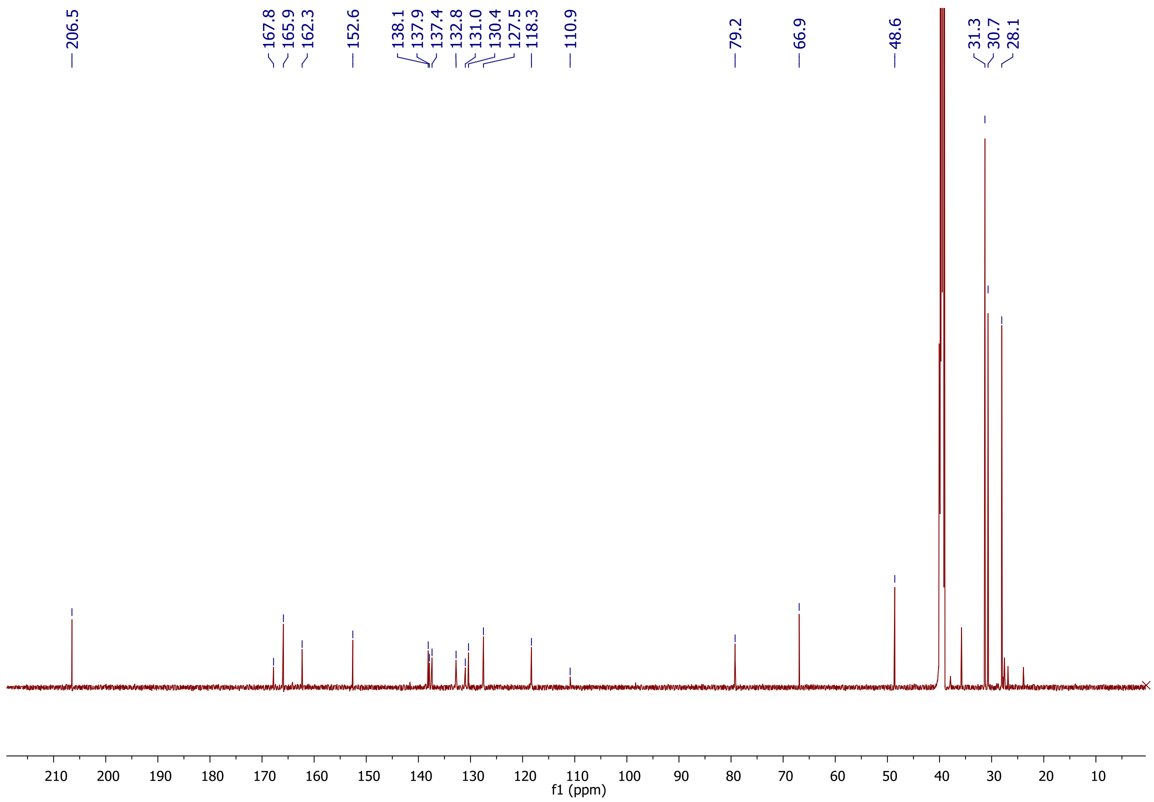

Figure A3. 18. ^{13}C NMR (100 MHz) spectrum of **124** in DMSO-d_6.

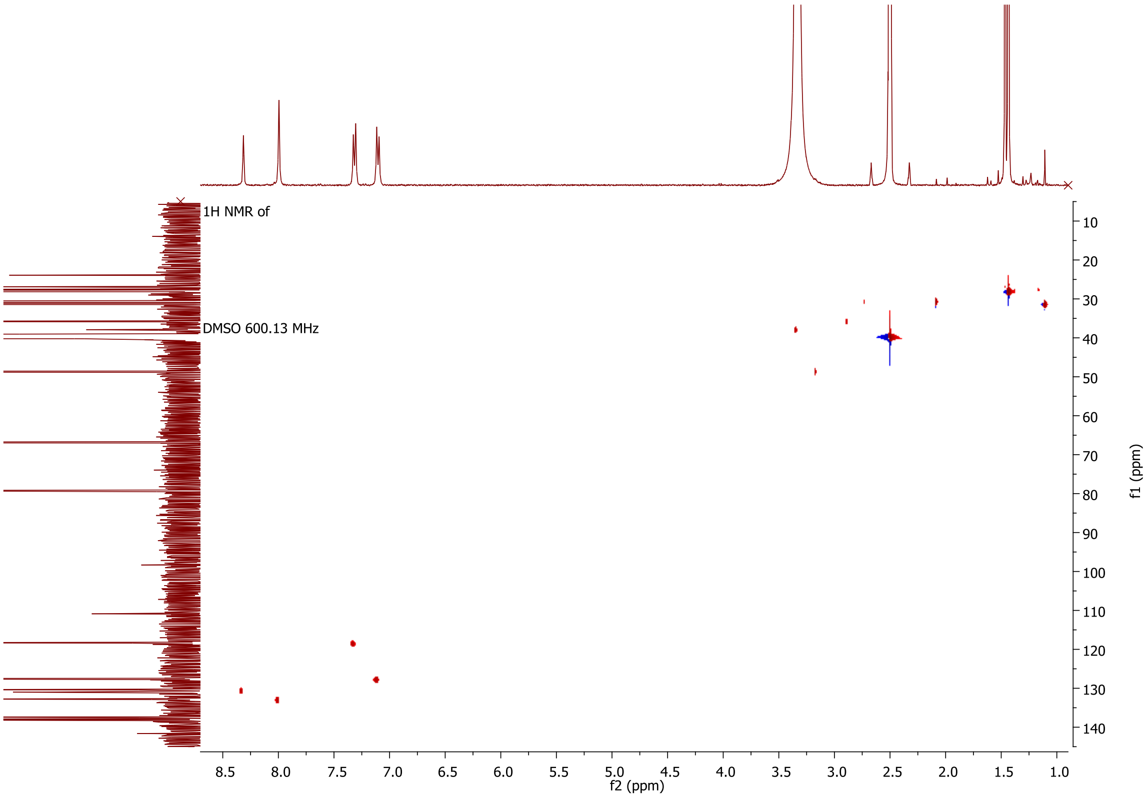

Figure A3. 19. ^{13}C-^{1}H HSQC NMR spectrum of **124** in DMSO-*d*$_6$.

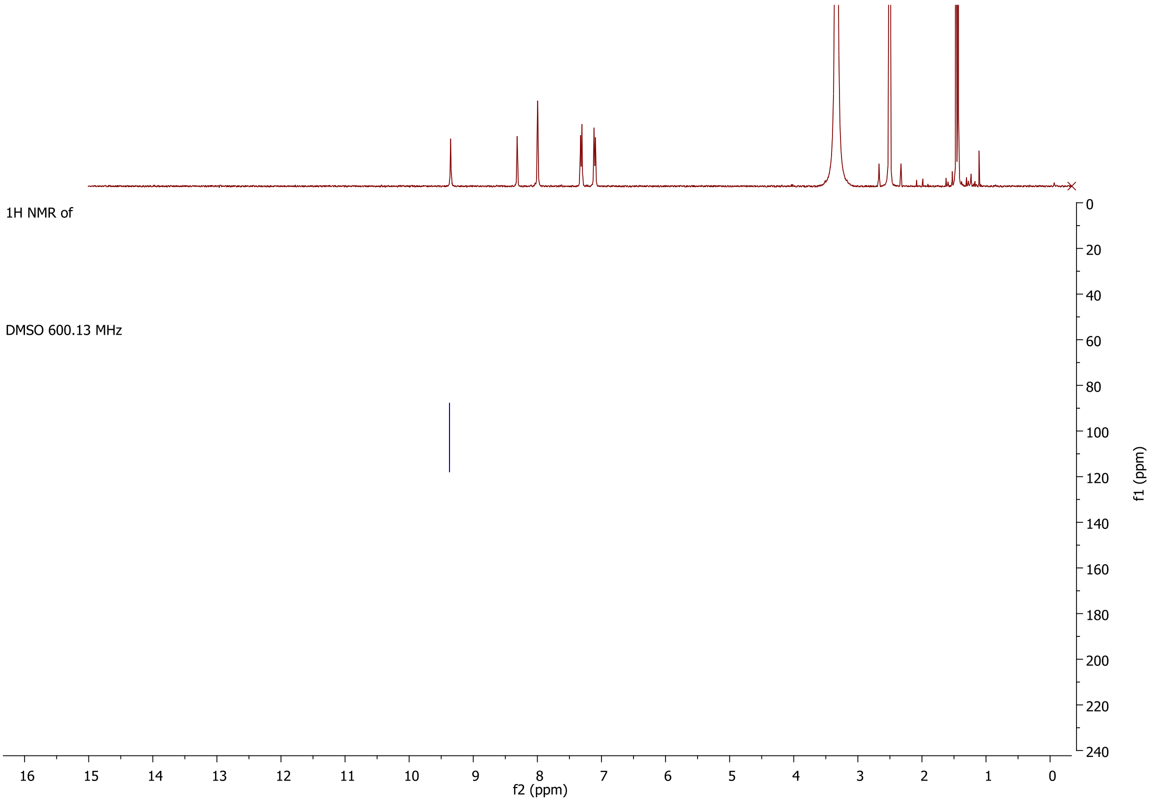

Figure A3. 20. ^{15}N-^{1}H HSQC NMR spectrum of **124** in DMSO-*d*$_6$.

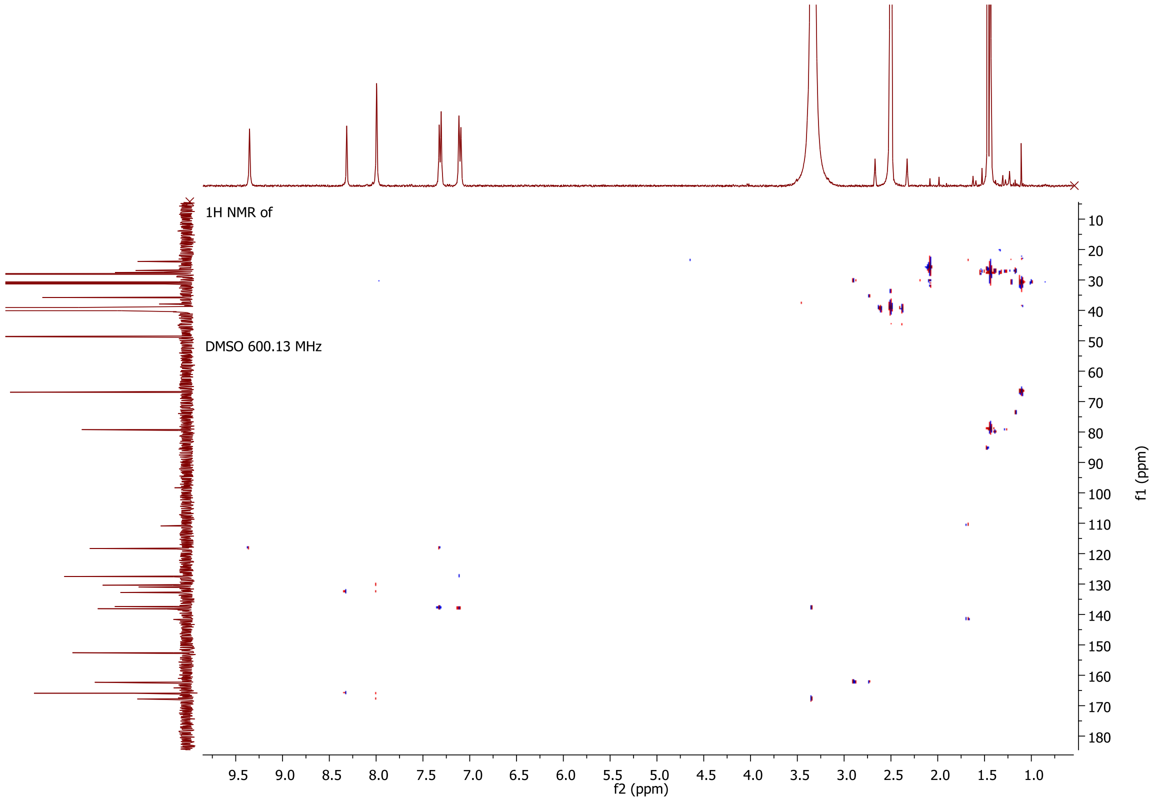

Figure A3. 21. ^{13}C-^{1}H HMBC NMR spectrum of **124** in DMSO-d_6.

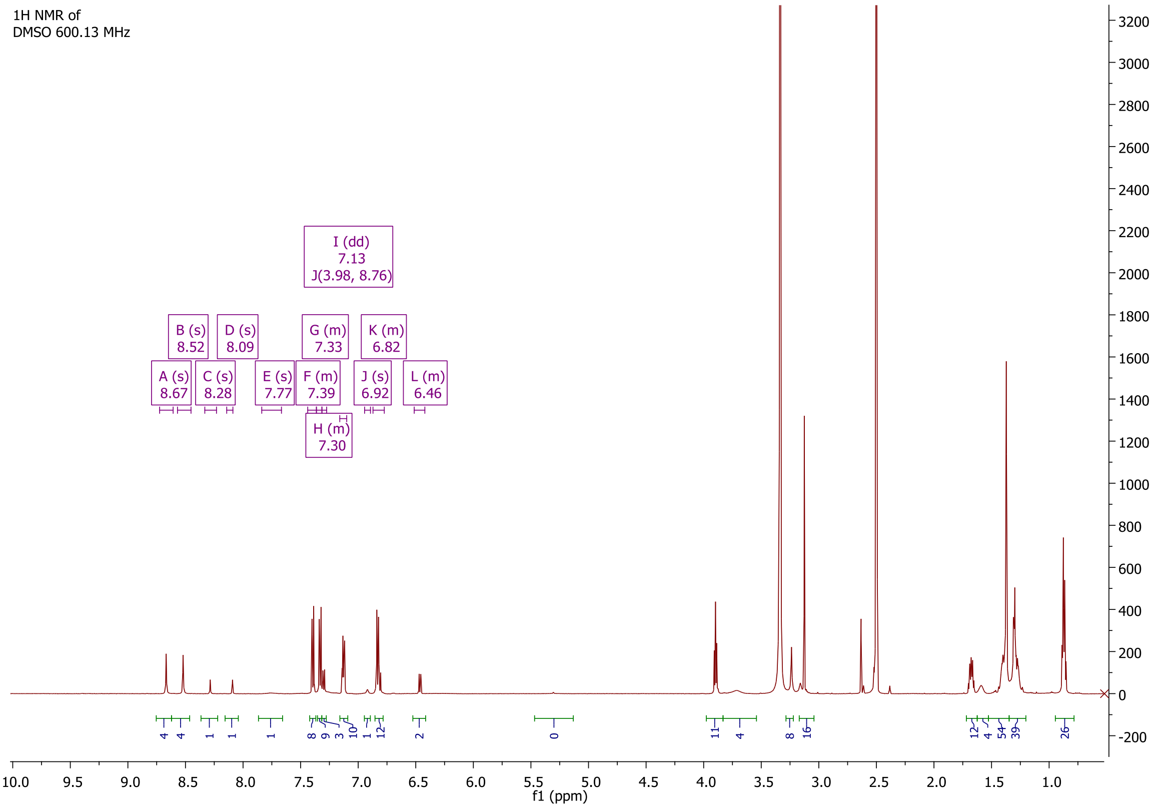

Figure A3. 22. ^{1}H NMR (600 MHz) spectrum of **112** in DMSO-d_6.

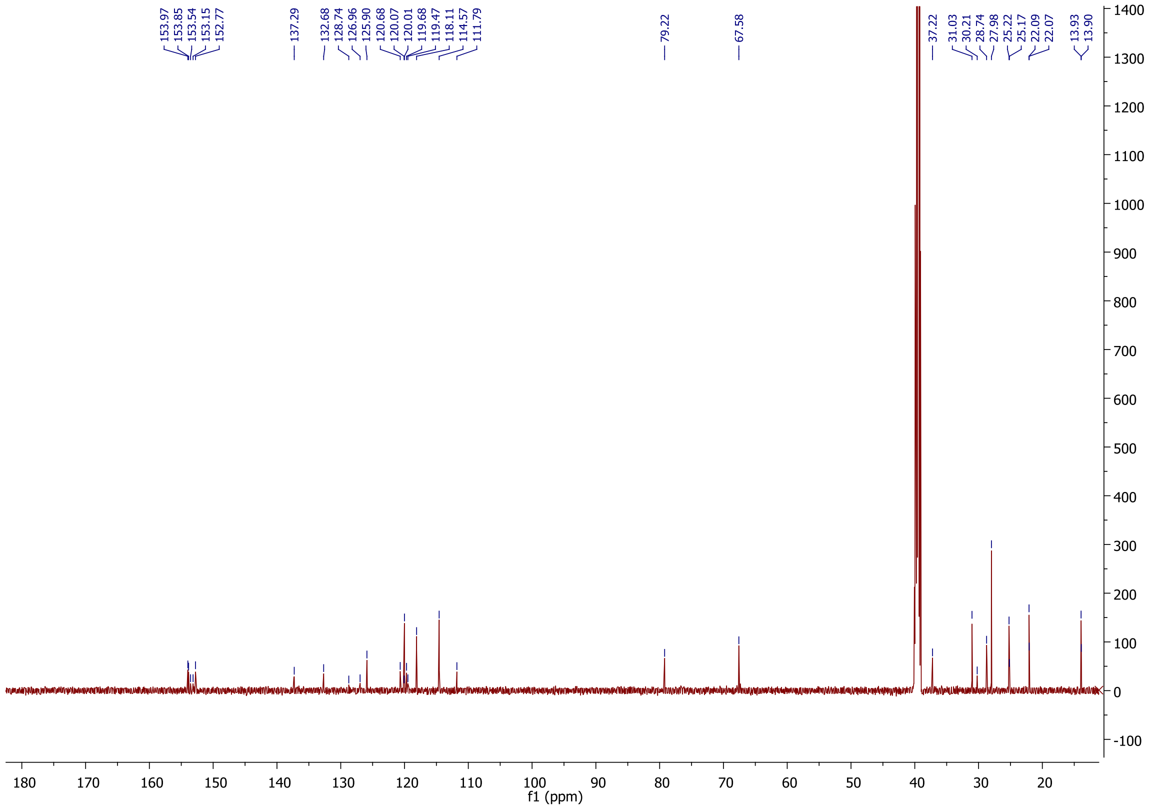

Figure A3. 23. ^{13}C NMR (151 MHz) spectrum of **112** in DMSO-*d*$_6$.

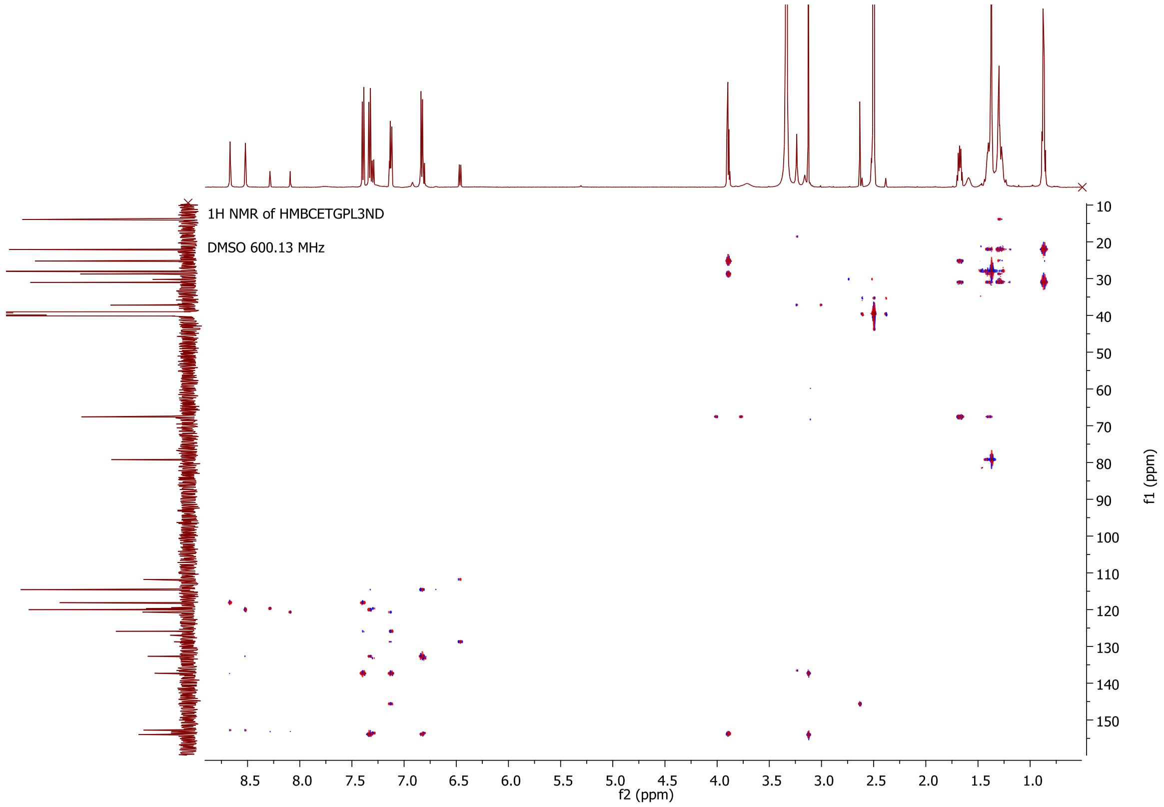

Figure A3. 24. ^{13}C-^{1}H HMBC NMR spectrum of **112** in DMSO-*d*$_6$.

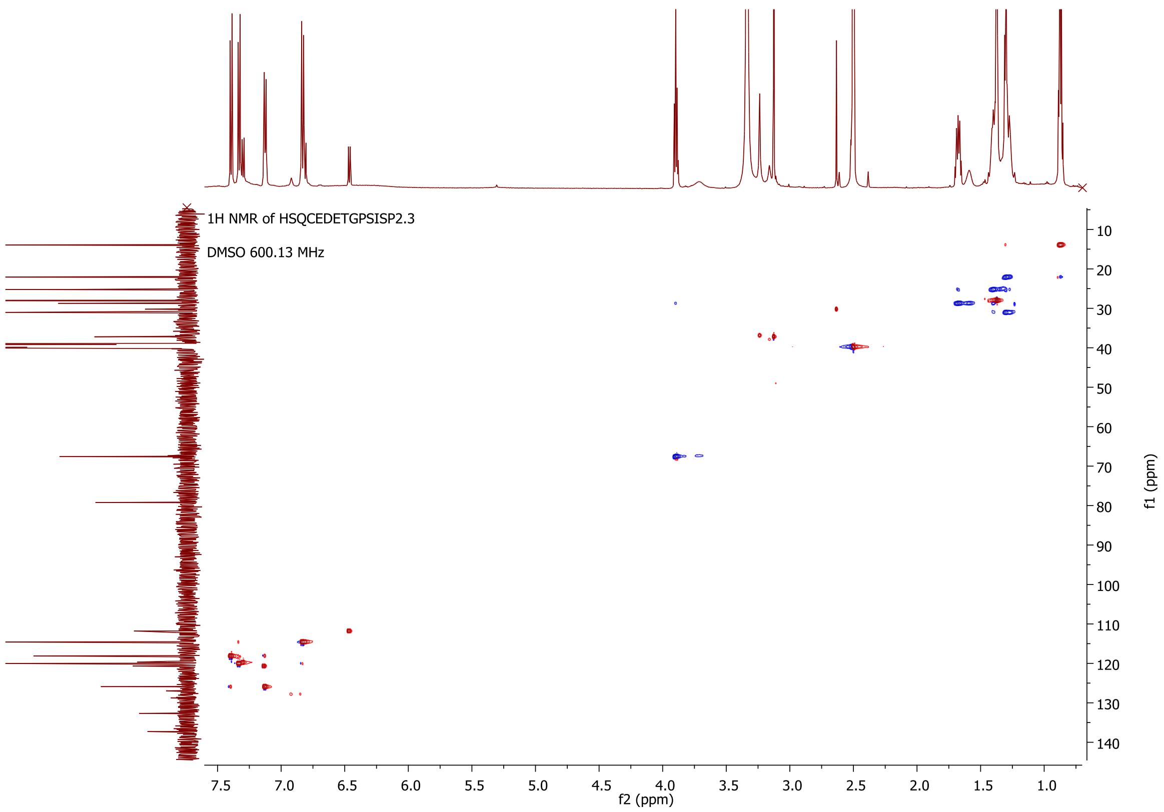

Figure A3. 25. ^{13}C-^{1}H HSQC NMR spectrum of **112** in DMSO-d_6.

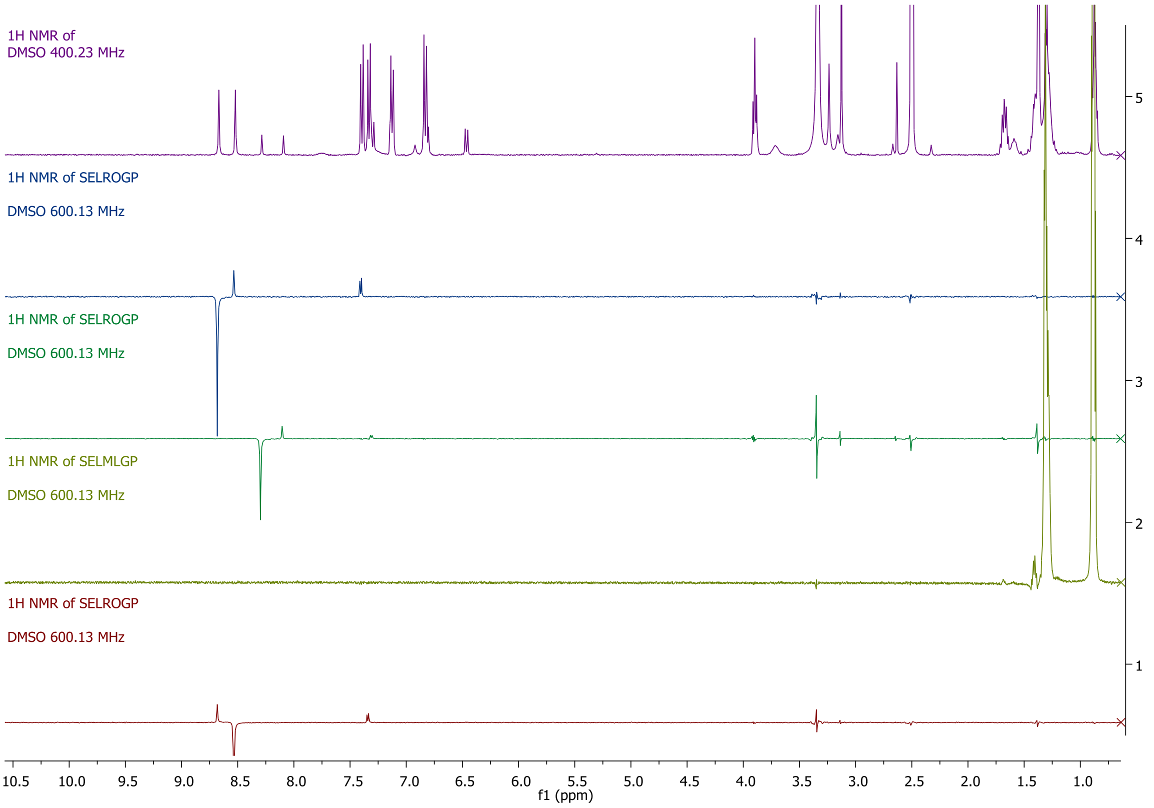

Figure A3. 26. Selective ^{1}H ROESY NMR spectra of **112** in DMSO-d_6.

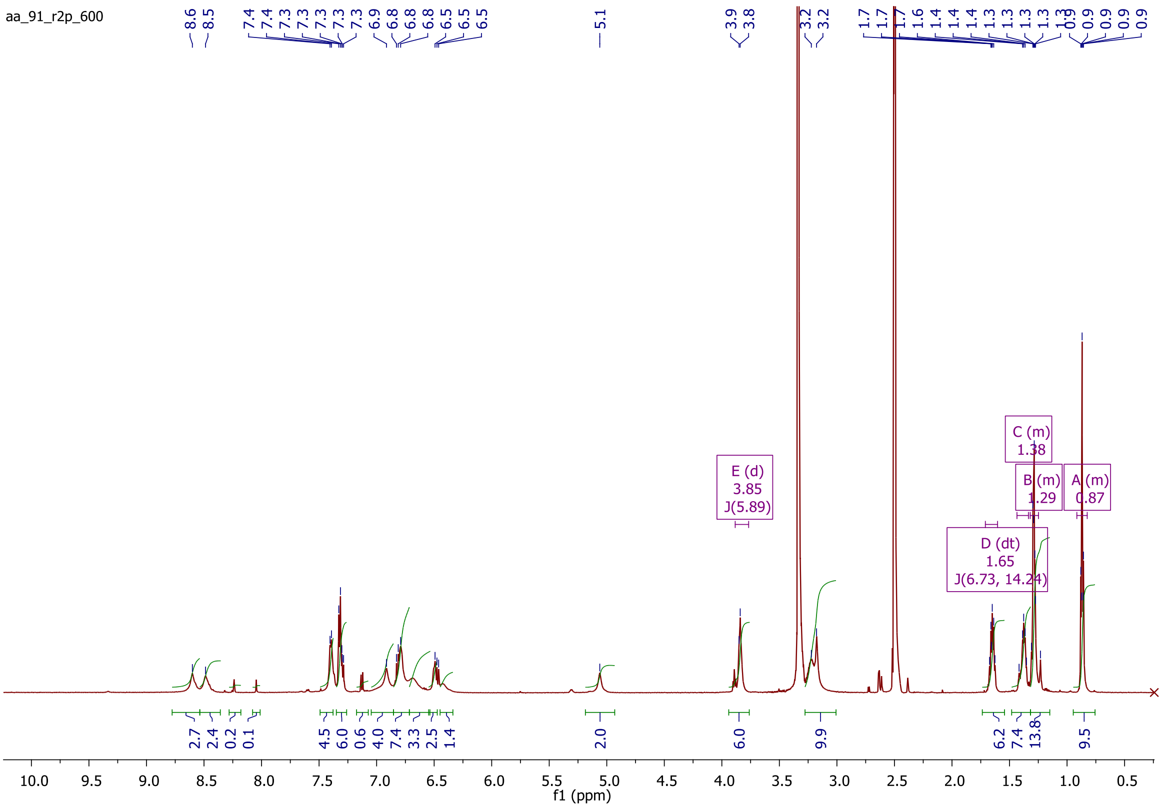

Figure A3. 27. ^{1}H NMR (600 MHz) spectrum of **85** in DMSO-d_6.

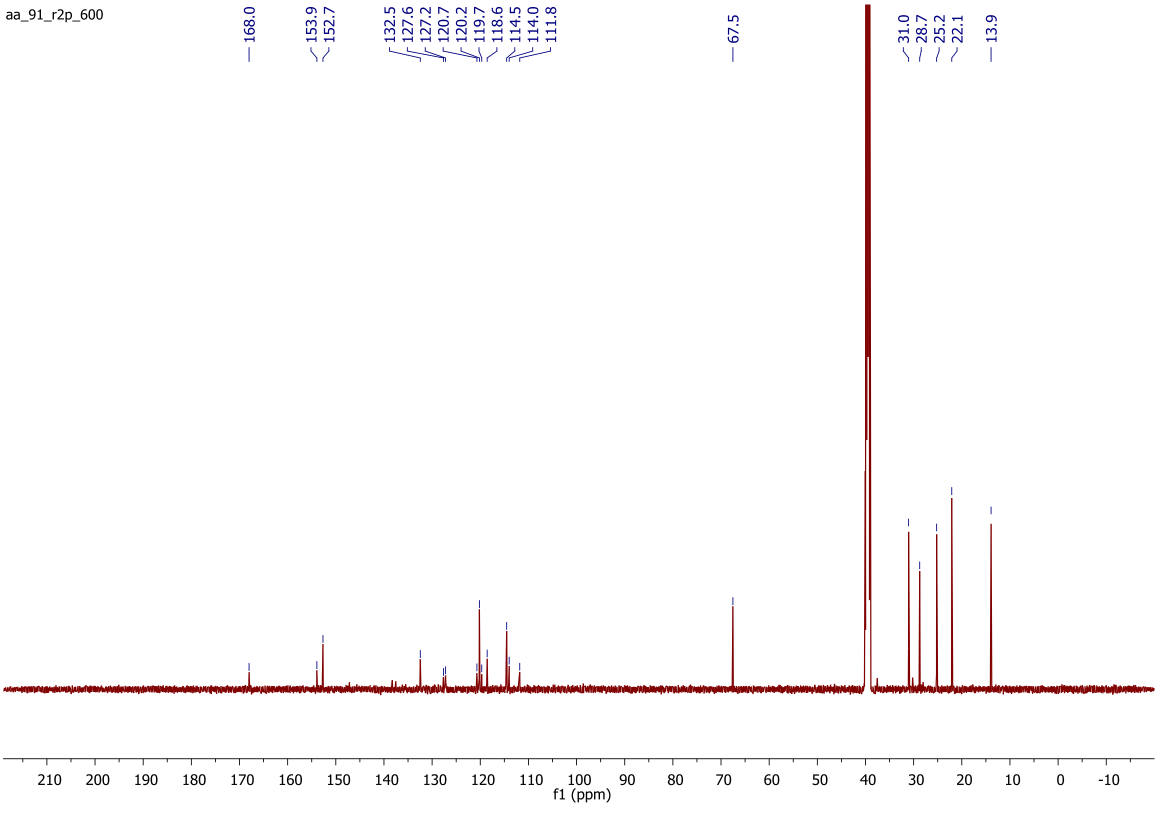

Figure A3. 28. ^{13}C NMR (151 MHz) spectrum of **85** in DMSO-d_6.

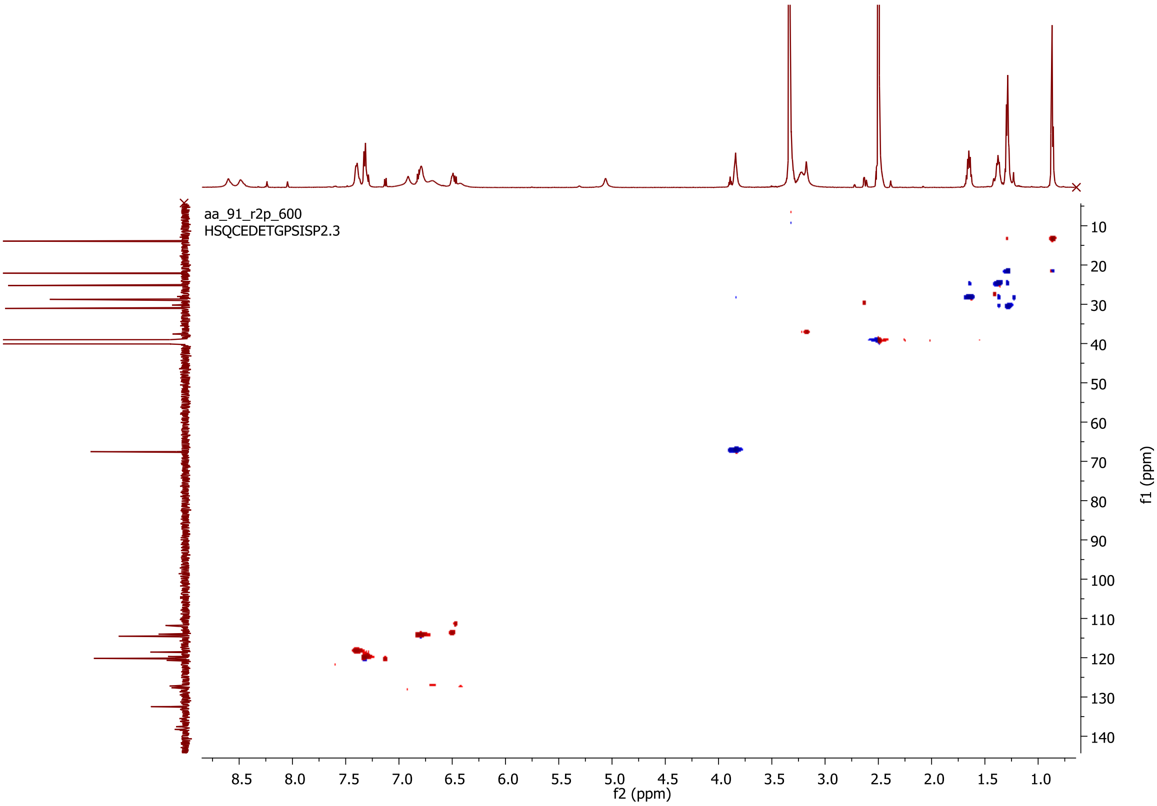

Figure A3. 29. ^{13}C-^{1}H HSQC NMR spectrum of **85** in DMSO-*d*$_6$.

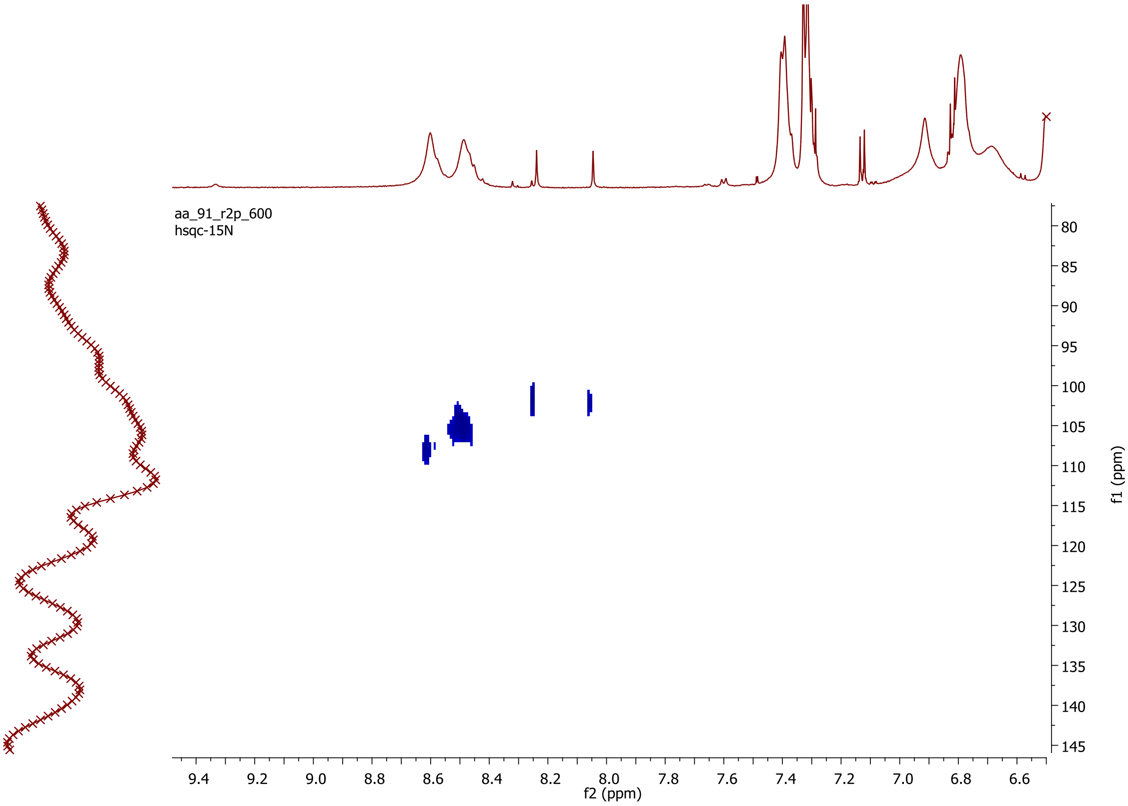

Figure A3. 30. ^{15}N-^{1}H HSQC NMR spectrum of **85** in DMSO-*d*$_6$.

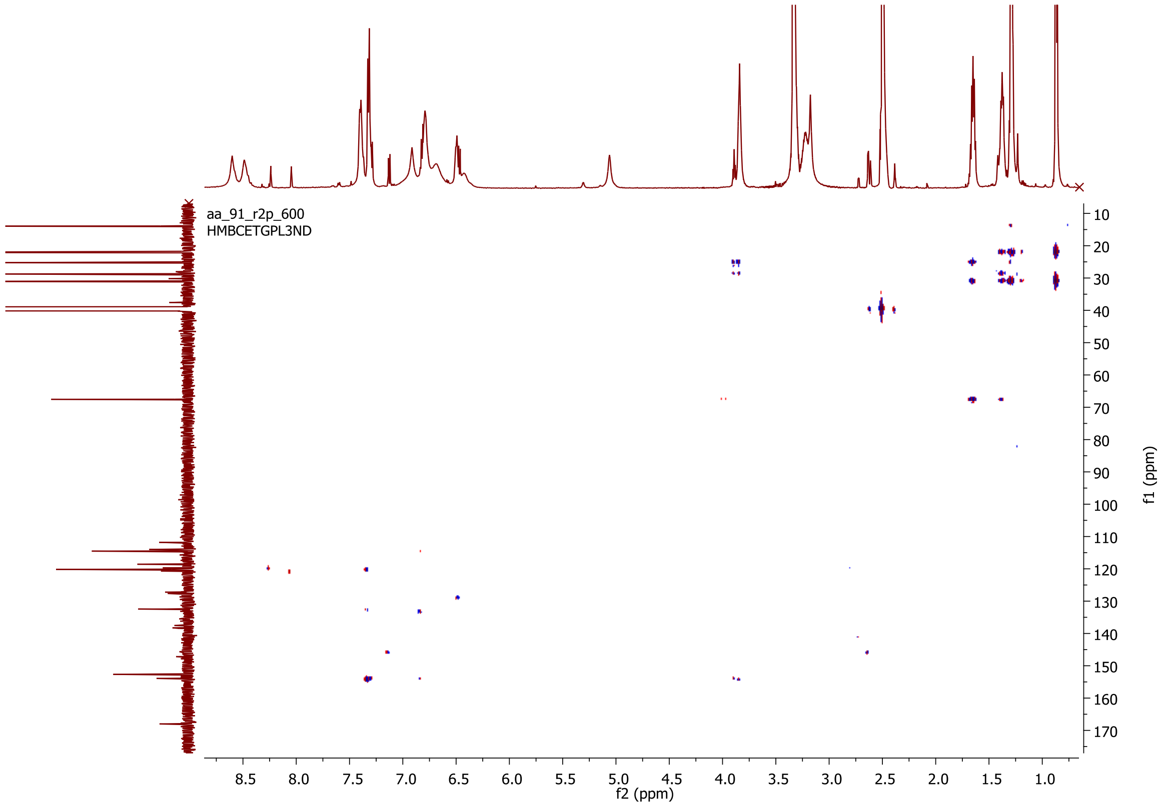

Figure A3. 31. ^{13}C-^{1}H HMBC NMR spectrum of **85** in DMSO-d_6.

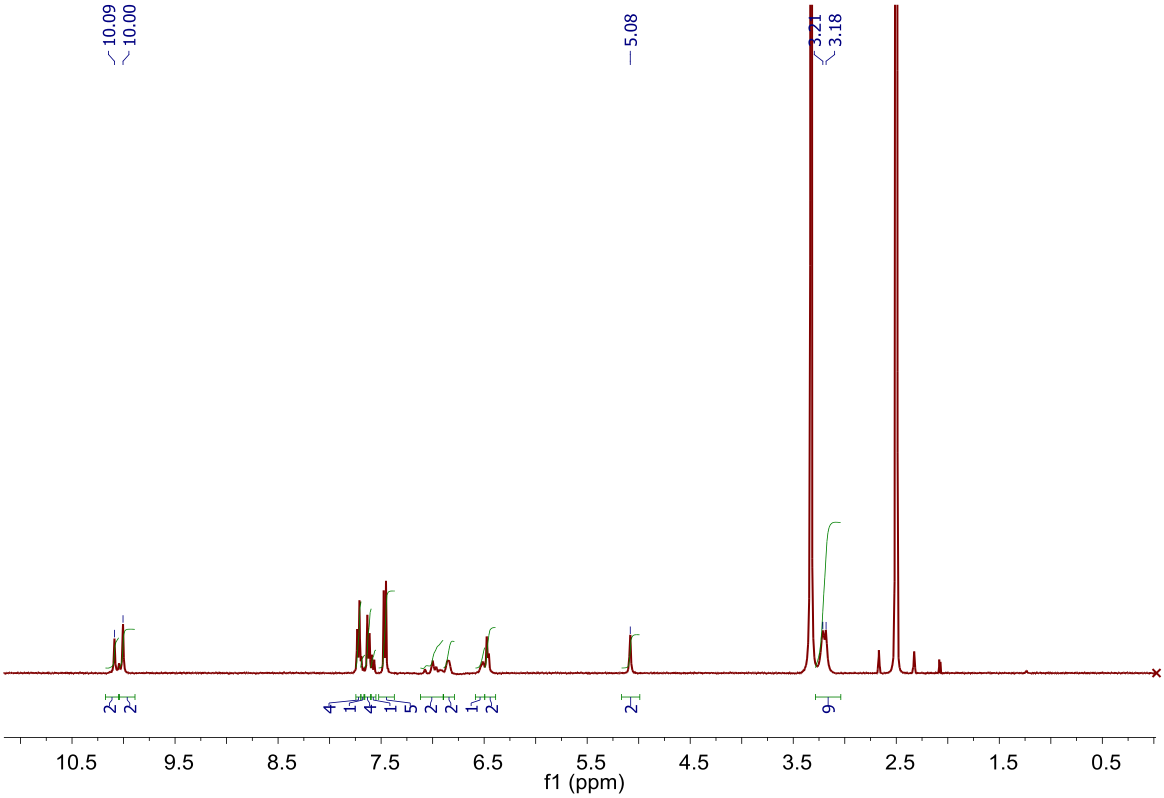

Figure A3. 32. ^{1}H NMR (600 MHz) spectrum of **90** in DMSO-d_6.

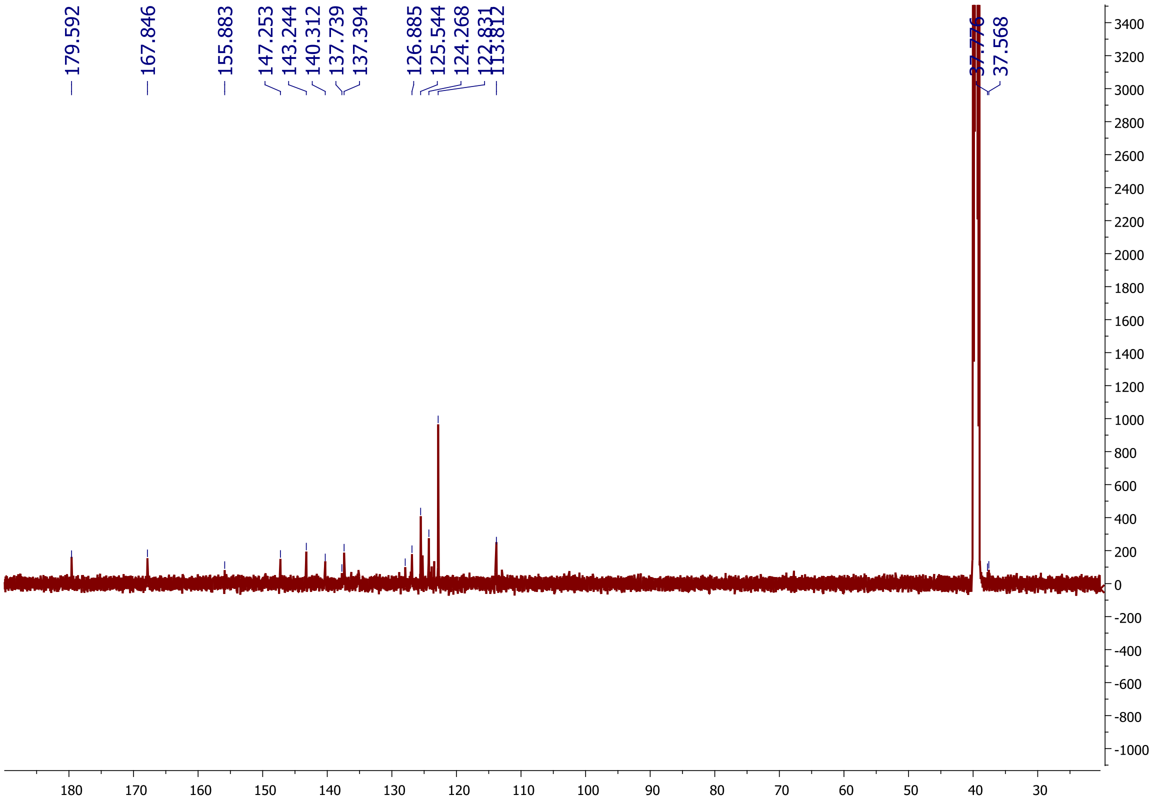

Figure A3. 33. ^{13}C NMR (151 MHz) spectrum of **90** in DMSO-d_6.

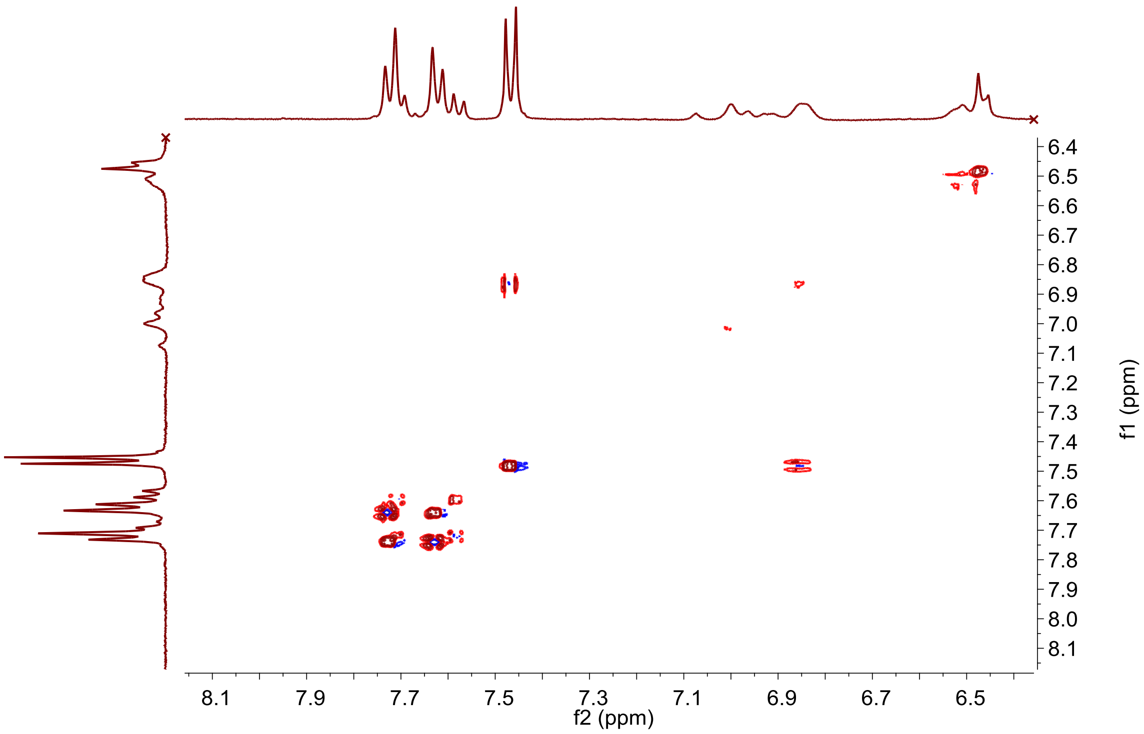

Figure A3. 34. ^{1}H-^{1}H COSY NMR spectrum of **90** in DMSO-d_6.

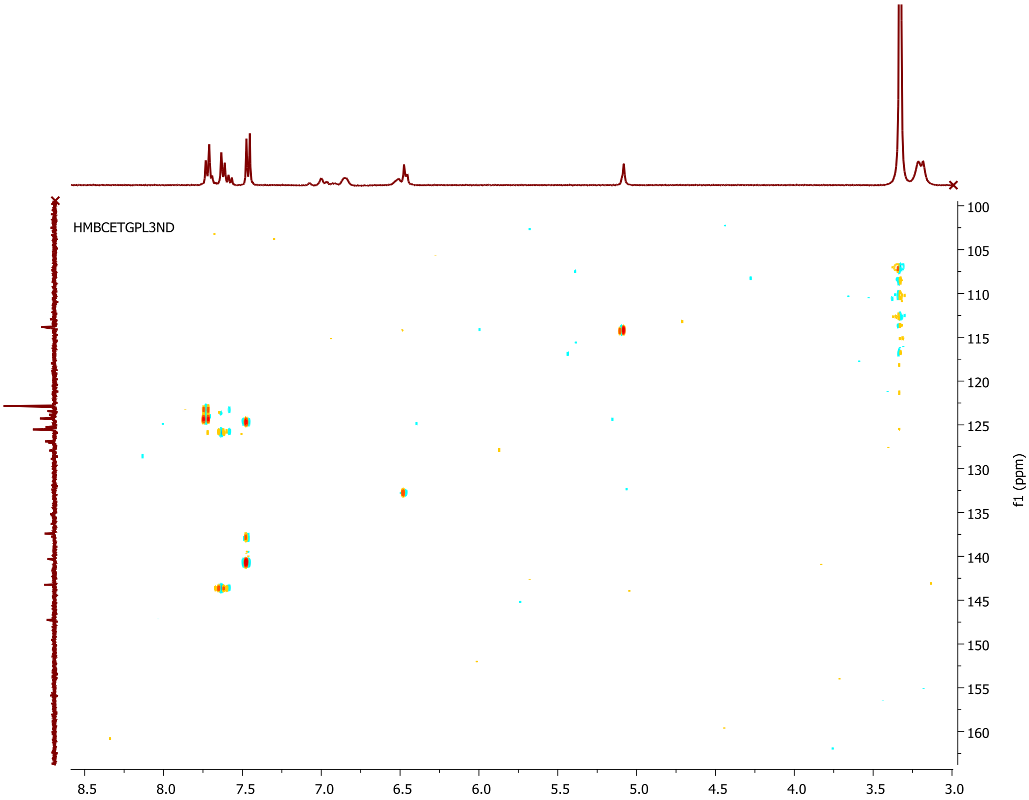

Figure A3. 35. ^{13}C-^{1}H HMBC NMR spectrum of of **90** in DMSO-d_6.

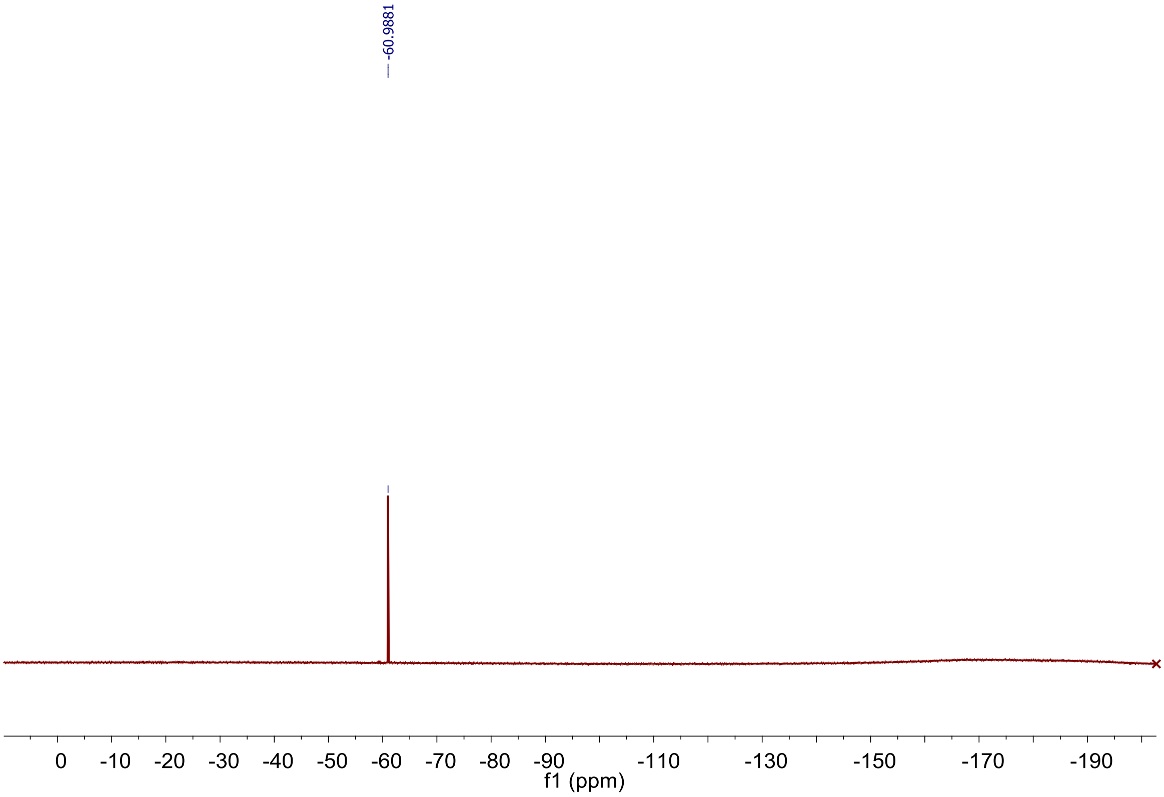

Figure A3. 36. ^{19}F NMR (376 MHz) spectrum of **90** in DMSO-d_6.

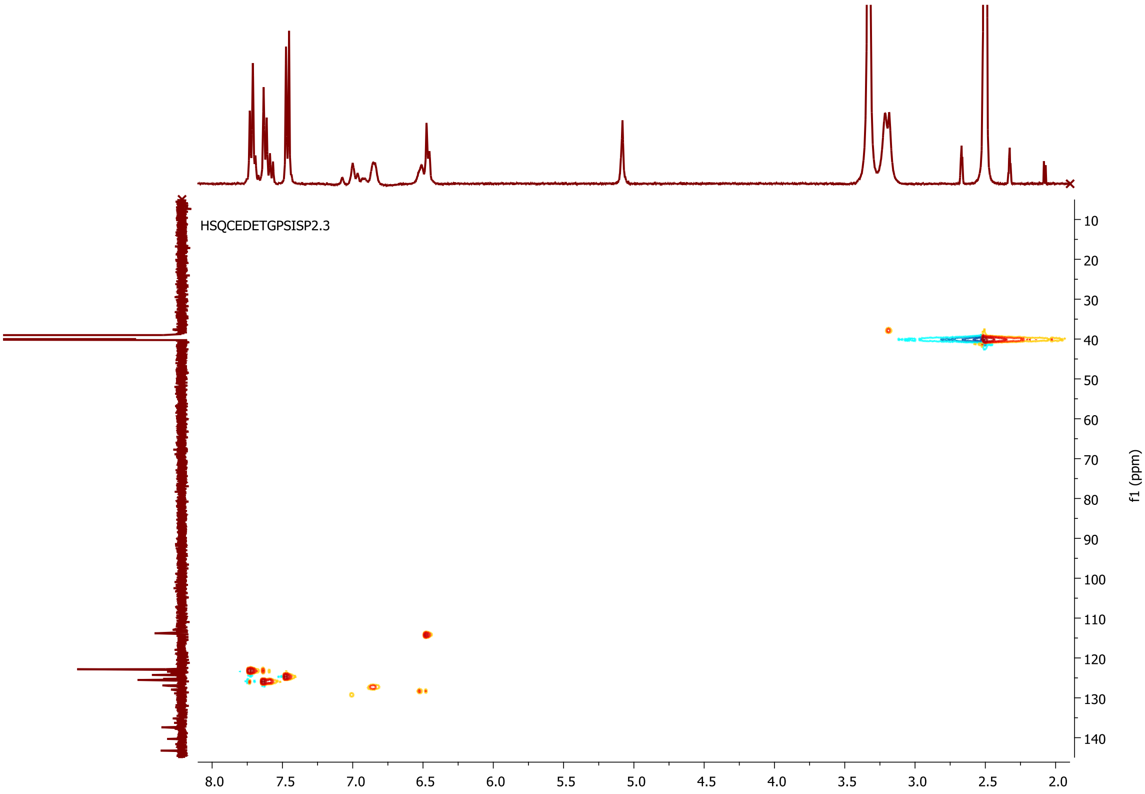

Figure A3. 37. ^{13}C-^{1}H HSQC NMR spectrum of **90** in DMSO-d_6.

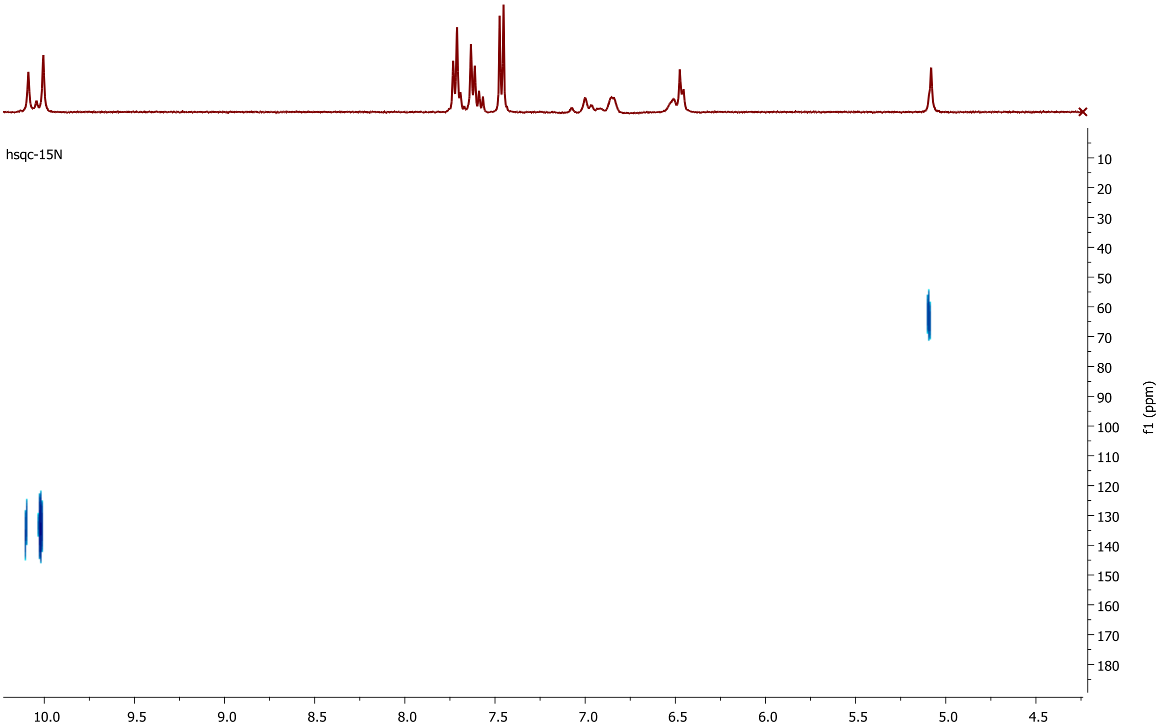

Figure A3. 38. ^{15}N-^{1}H HSQC NMR spectrum of **90** in DMSO-d_6.

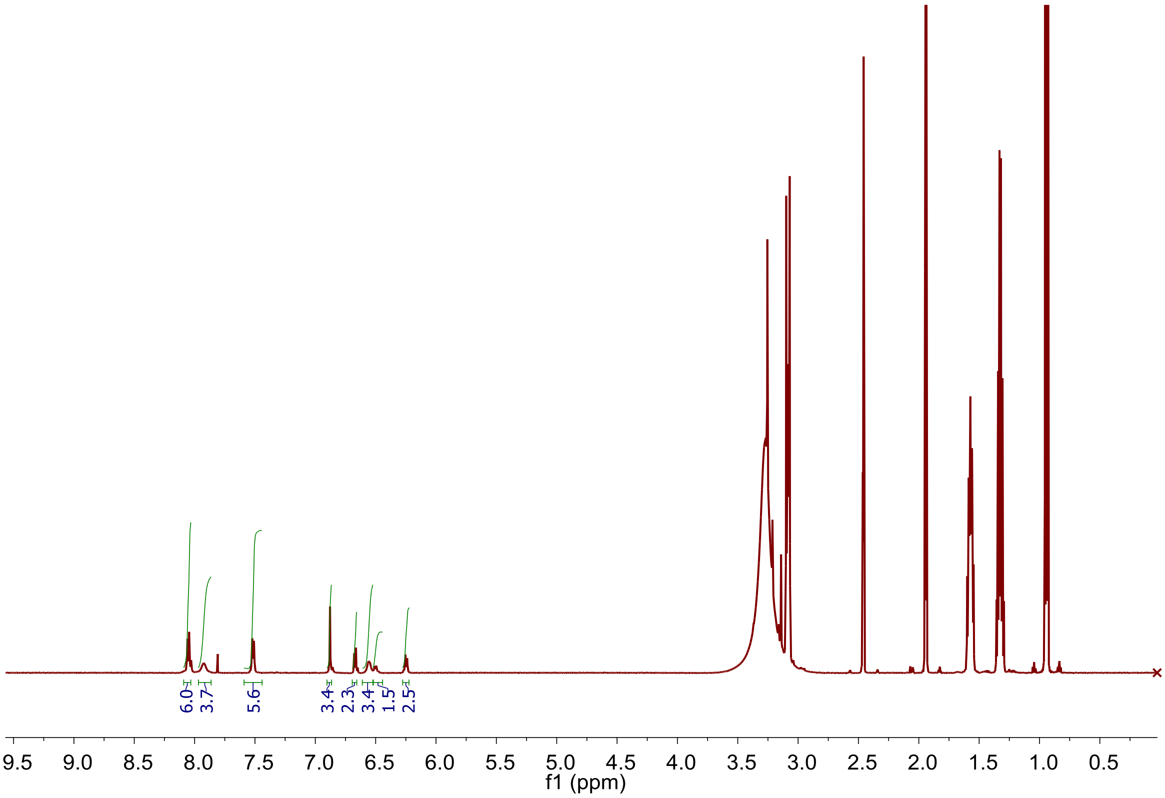

Figure A3. 39. ^1H NMR (600 MHz) spectrum of **90**·$H_2PO_4^-$ in CD_3CN:DMSO-d_6 (5:1).

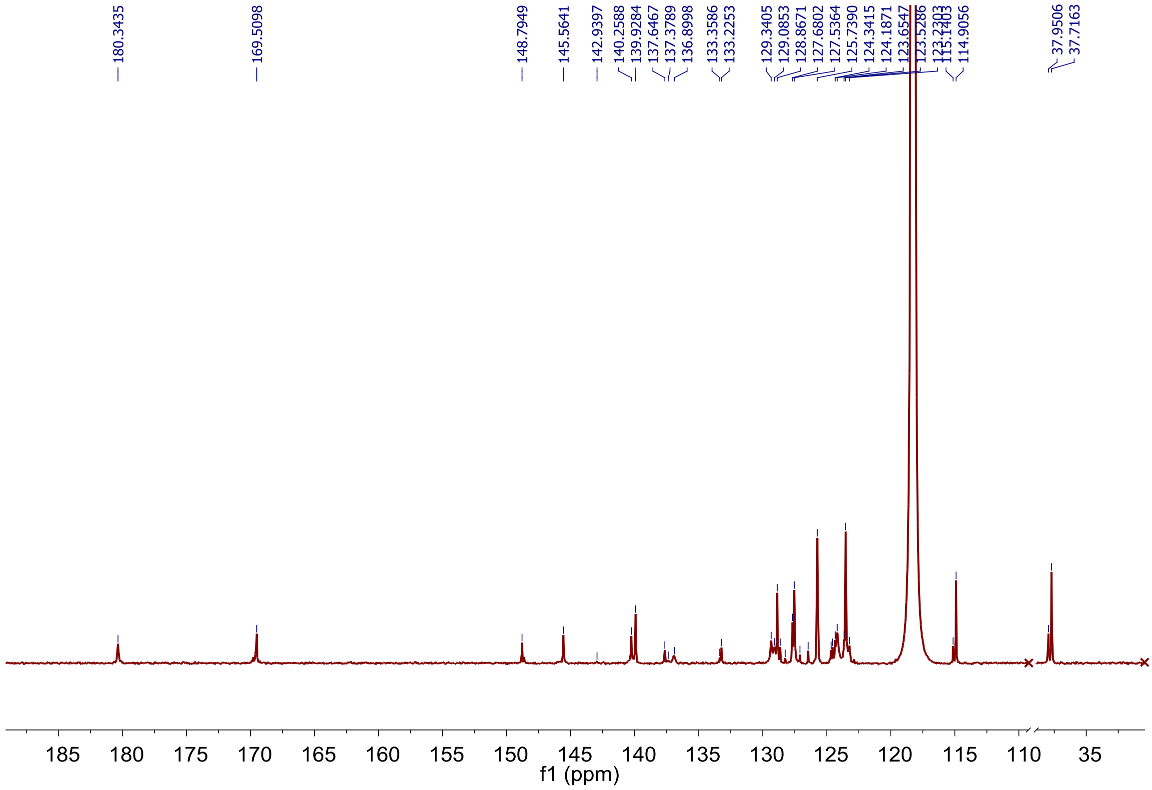

Figure A3. 40. ^{13}C NMR (151 MHz) spectrum of **90**·$H_2PO_4^-$ in CD_3CN:DMSO-d_6 (5:1).

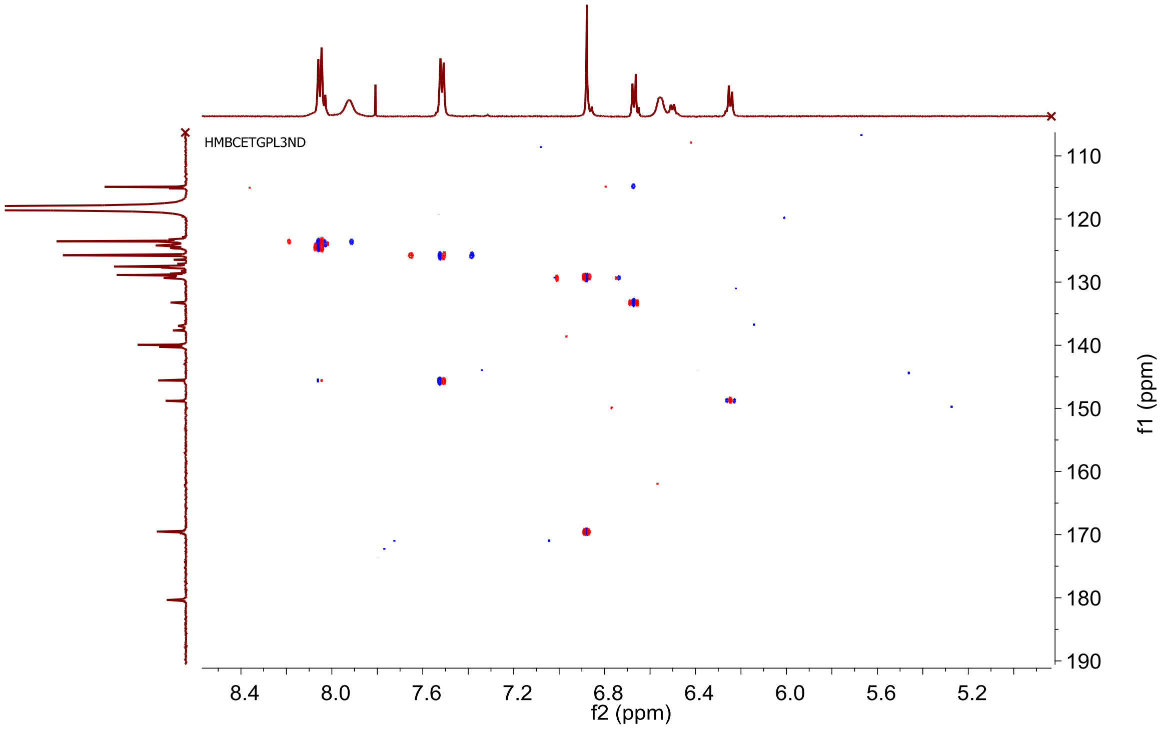

Figure A3. 41. ^{13}C-^{1}H HMBC NMR spectrum of **90**·$H_2PO_4^-$ in CD_3CN:DMSO-*d*$_6$ (5:1).

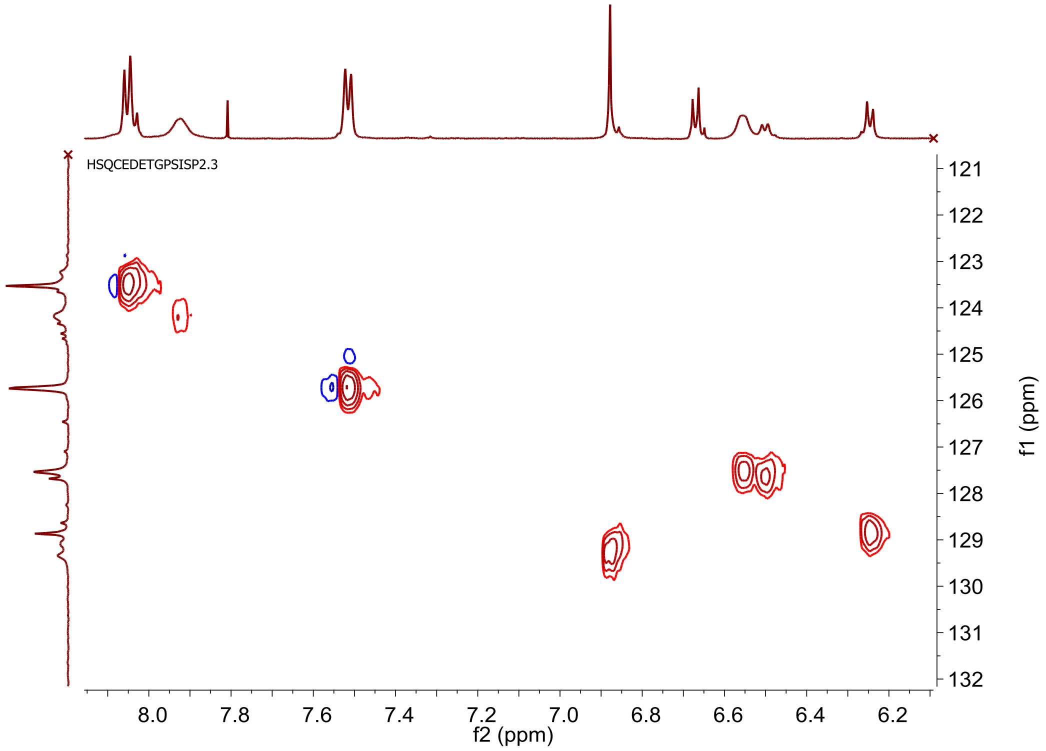

Figure A3. 42. ^{13}C-^{1}H HSQC NMR spectrum of **90**·$H_2PO_4^-$ in CD_3CN:DMSO-*d*$_6$ (5:1).

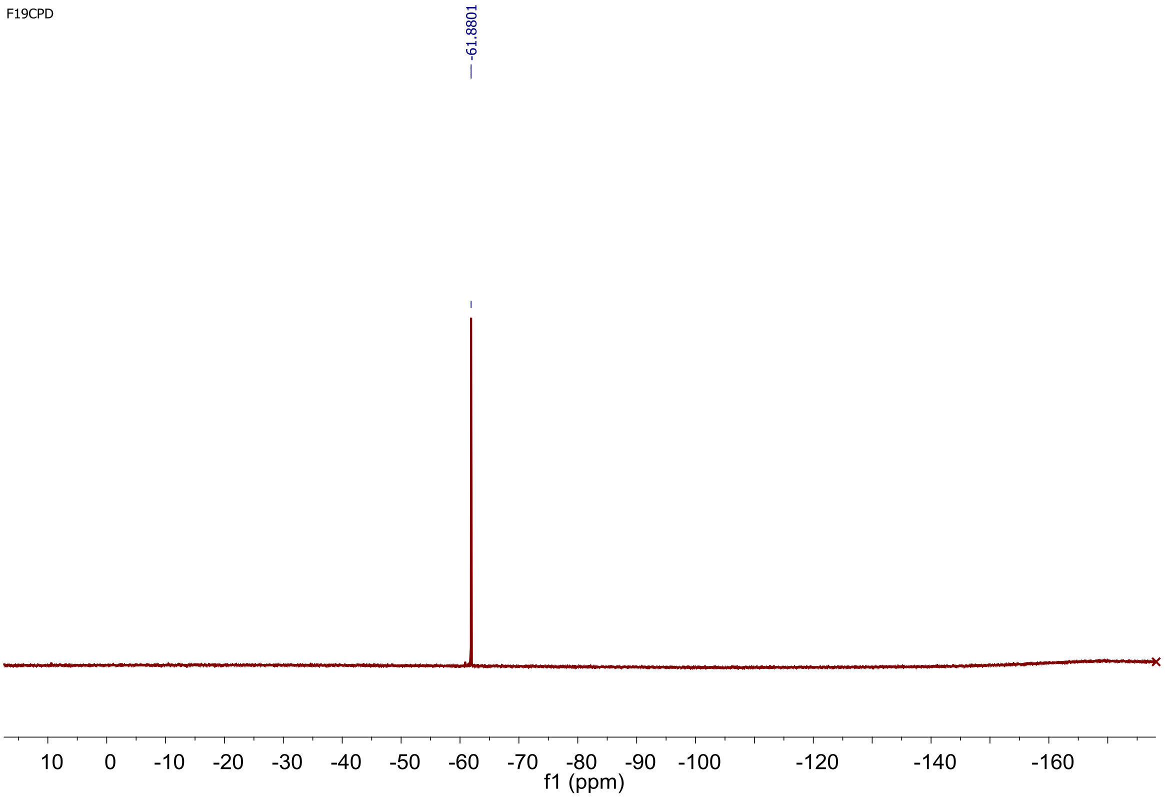

Figure A3. 43. ^{19}F NMR (376 MHz) spectrum of **90**·$H_2PO_4^-$ in CD_3CN:DMSO-d_6 (5:1).

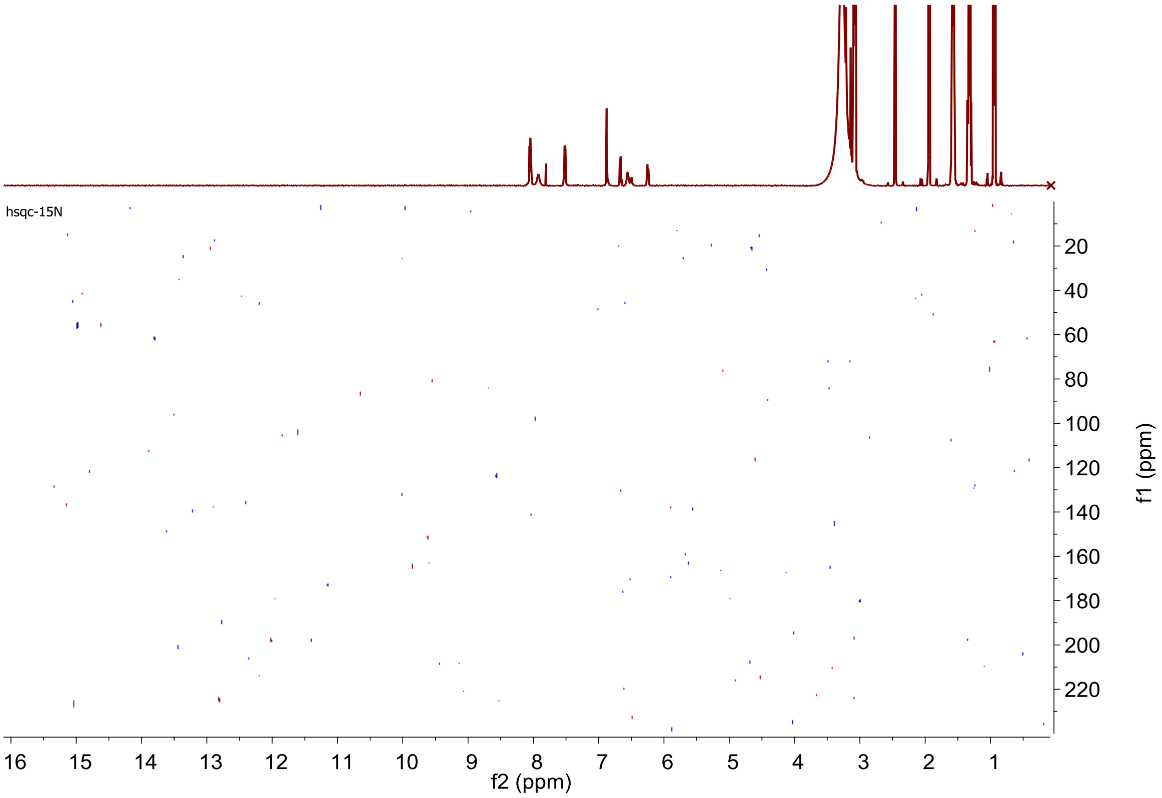

Figure A3. 44. ^{15}N-^{1}H HSQC NMR spectrum of **90**·$H_2PO_4^-$ in CD_3CN:DMSO-d_6 (5:1).

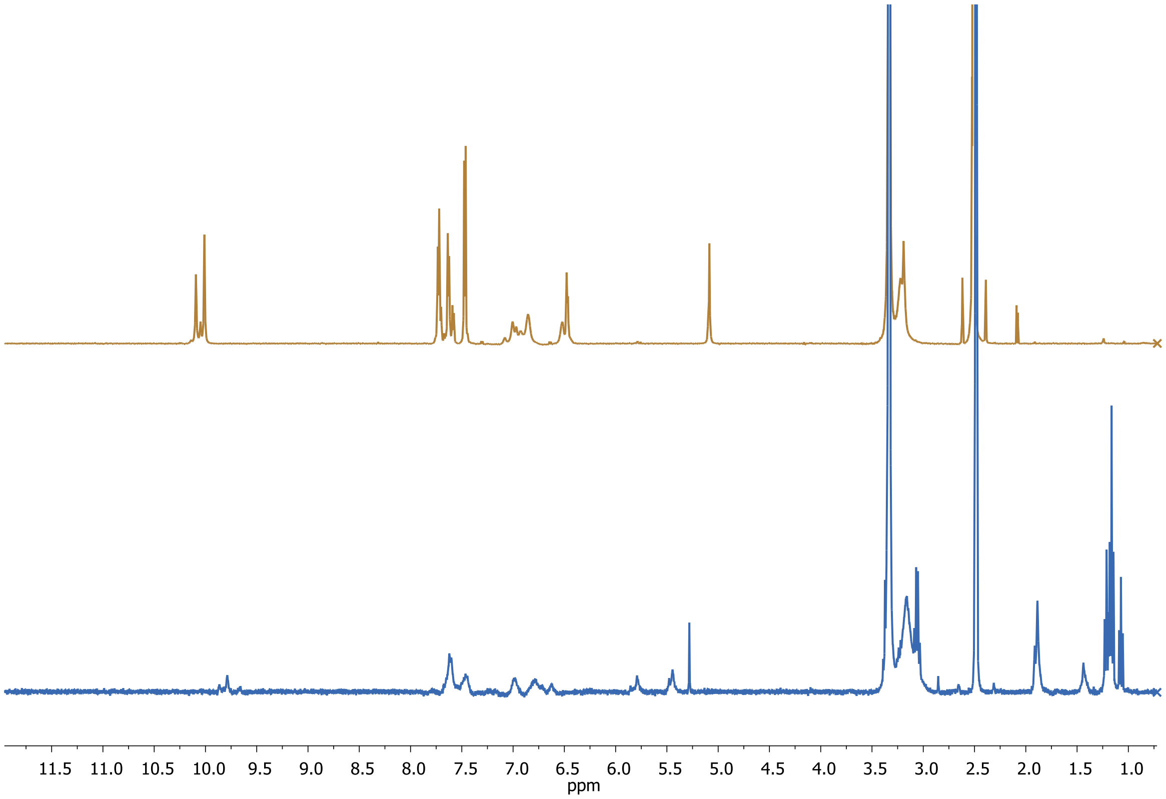

Figure A3. 45. Stacked ^{1}H NMR (400 MHz) spectrum of **90** (top) and **126** in DMSO-d_6. Doublets at 5.4 ppm and 5.7 ppm belong to the olefin, indicating the success of the reaction.

Table A0.1. Selected crystallographic data and structure refinements for the structures in Section 3.2.1.

Compound	**118**	**113**
Chemical formula	$C_{25}H_{35}N_3O_4$	$C_{20}H_{27}N_3O_2$
M_r (g·mol^{-1})	441.56	341.44
Crystal size (mm)	0.34 × 0.11 × 0.01	0.13 × 0.05 × 0.03
Crystal system	Orthorhombic	Monoclinic
Space group	*Pbca*	*C*2
T(K)	100	100
a(Å)	9.1397 (19)	68.769 (4)
b(Å)	13.920 (3)	4.6494 (3)
c (Å)	37.859 (8)	31.1760 (19)
α (°)	90	90
β (°)	90	114.086 (5)
γ (°)	90	90
V (Å^3)	4816.6 (17)	9100.1 (10)
Z	8	20
F(000)	1904	3680
D_x (Mg m^{-3})	1.218	1.246
Radiation type	Mo Kα	Cu Kα
μ (mm^{-1})	0.08	0.65
$R[F^2 > 2\sigma(F^2)]$	0.09	0.082
wR(F2)	0.236	0.23
S	1.11	0.99

A4. Appendix Chapter 4

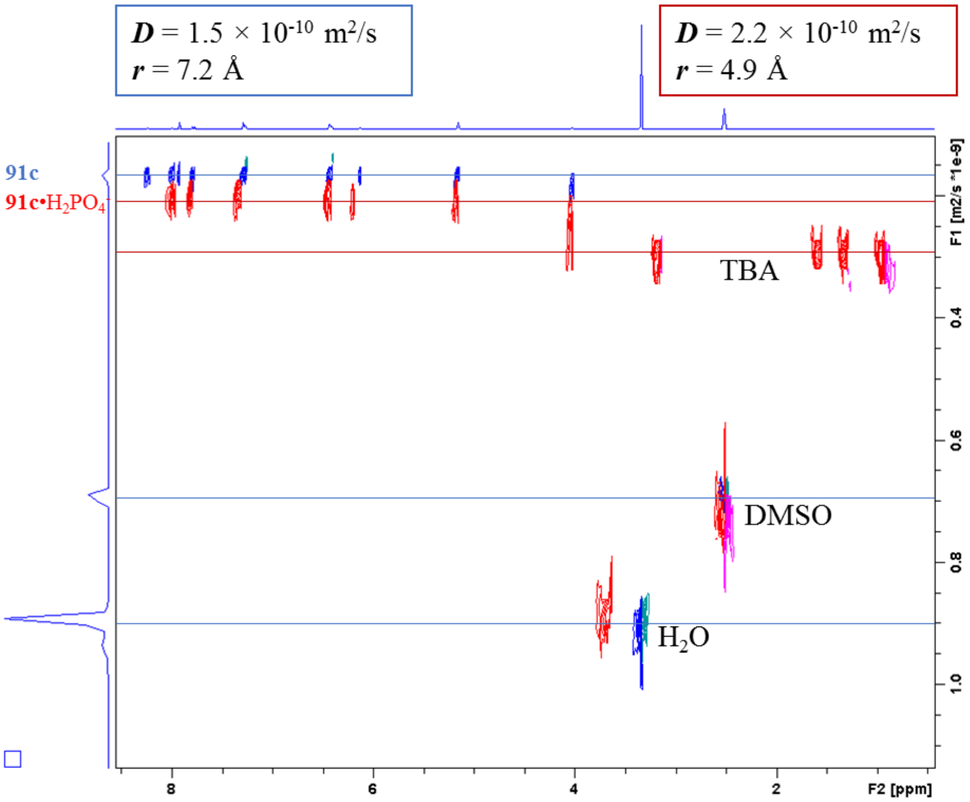

Figure A4. 1. Superimposed DOSY NMR experiments of free **91c** (blue) and complex **91c**·$H_2PO_4^-$ (red) at 25 °C in DMSO-d_6.

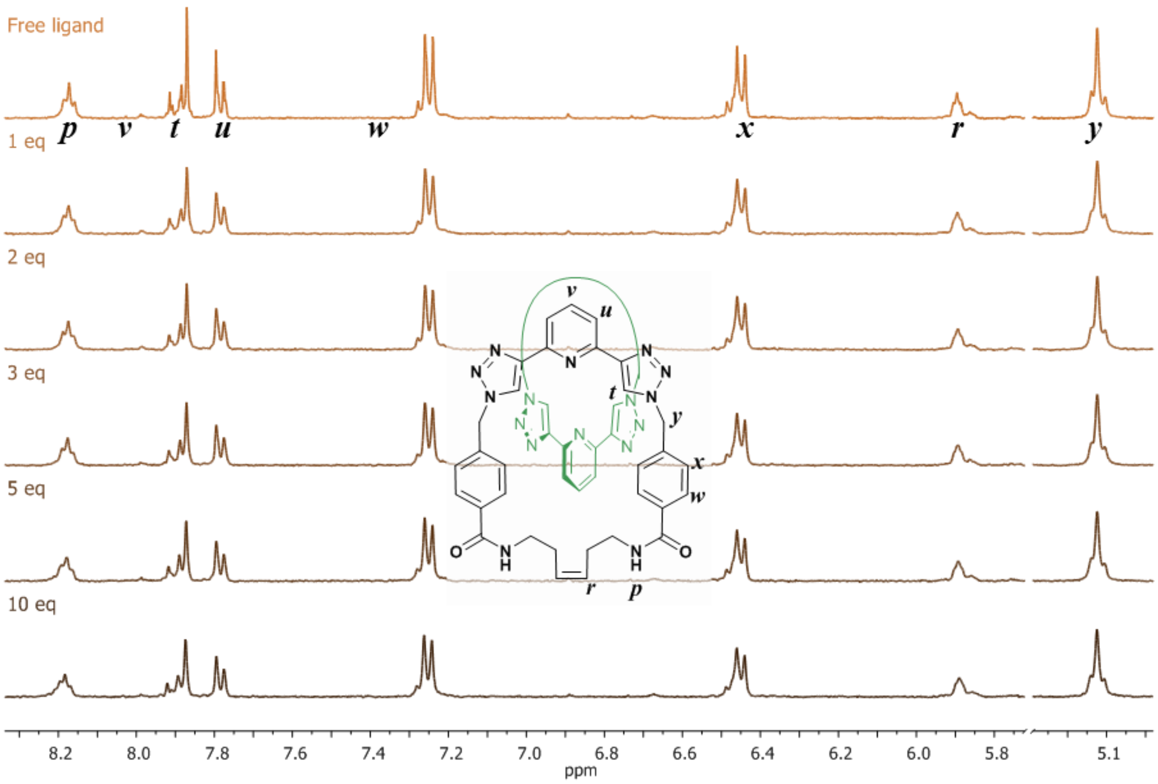

Figure A4. 2. ^{1}H NMR titration profile of **92c** with Cl$^-$, in DMSO-d_6. [**92c**] = 1 mM. Featureless regions of spectrum are not shown. This titration is representative of reproducible trends.

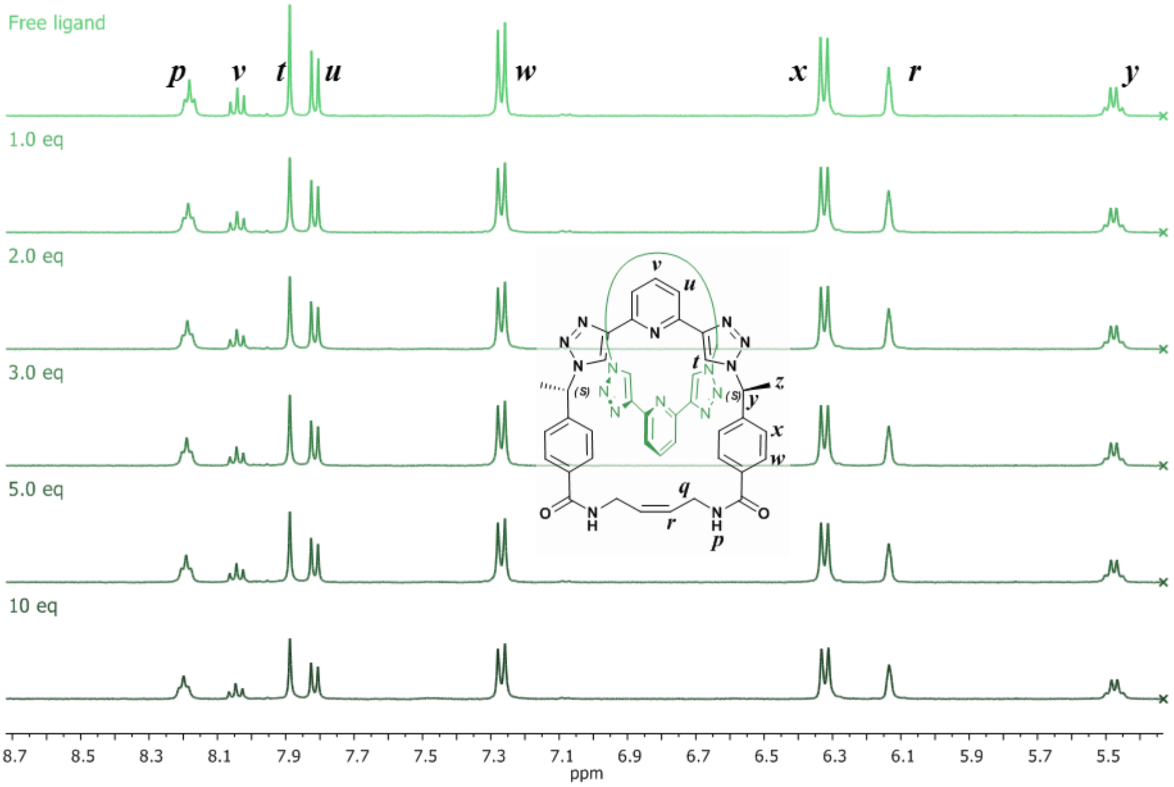

Figure A4. 4. ^{1}H NMR titration profile of **95cS** with $H_2PO_4^-$, in DMSO-d_6. [**95cS**] = 1 mM. Featureless regions of spectrum are not shown. This titration is representative of reproducible trends.

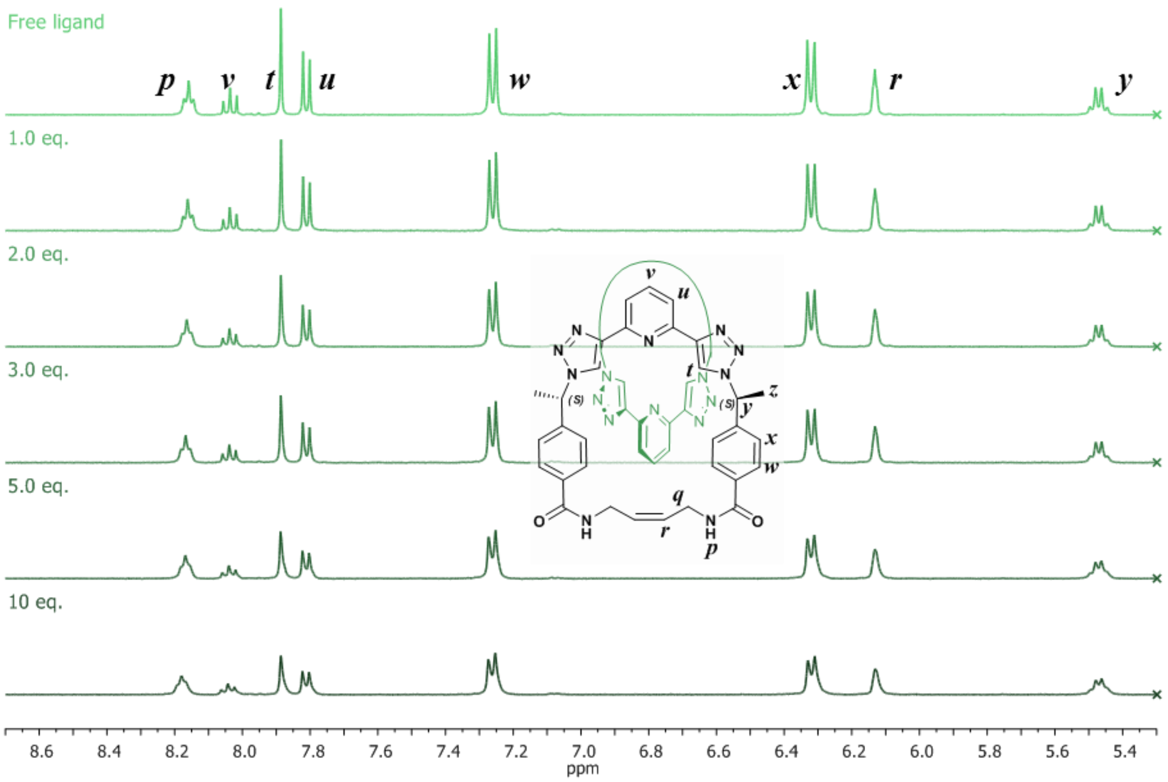

Figure A4. 3. ^{1}H NMR titration profile of **95cS** with Cl^-, in DMSO-d_6. [**95cS**] = 1 mM. Featureless regions of spectrum are not shown. This titration is representative of reproducible trends.

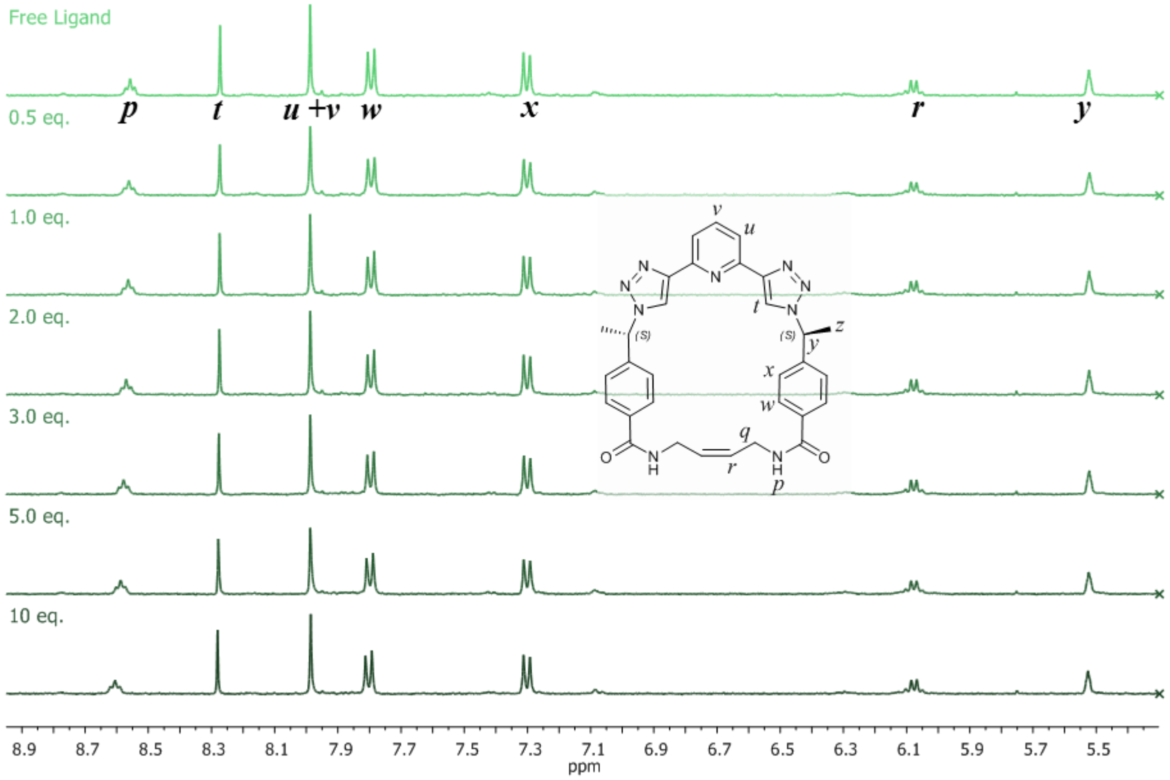

Figure A4. 6. ^{1}H NMR titration profile of **95mS** with $H_2PO_4^-$, in DMSO-d_6. [**95mS**] = 1 mM. Featureless regions of spectrum are not shown. This titration is representative of reproducible trends.

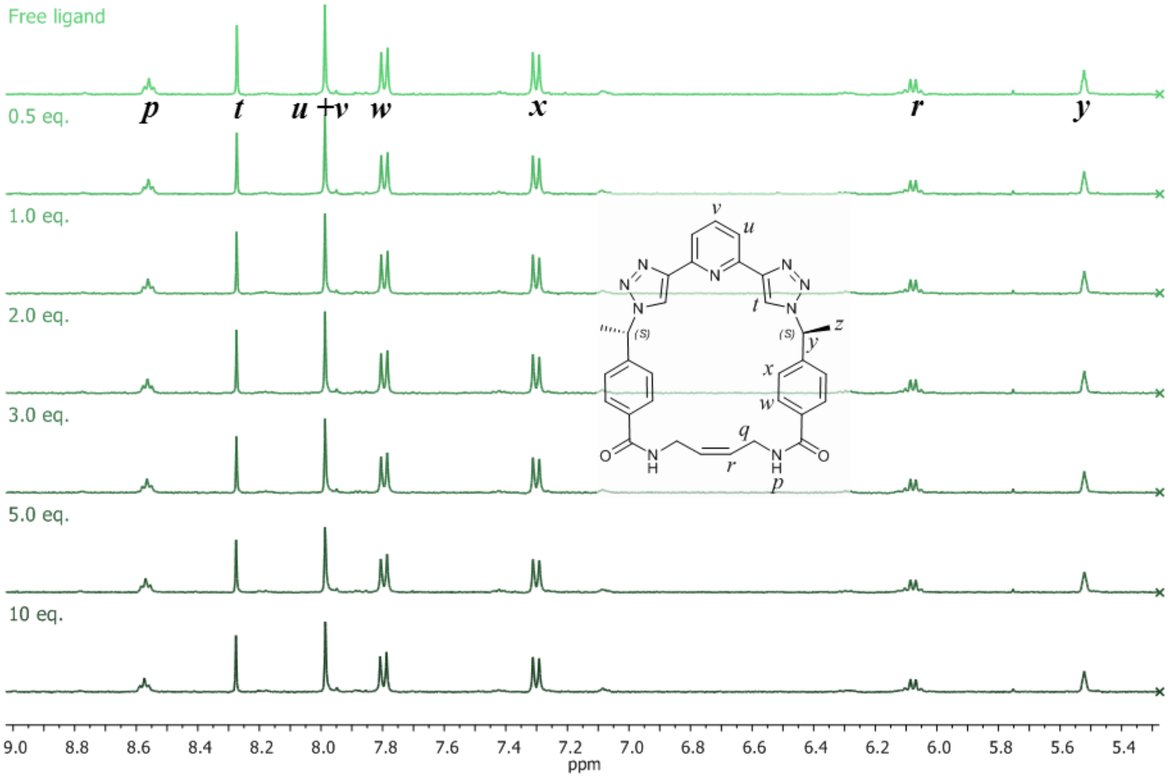

Figure A4. 5. ^{1}H NMR titration profile of **95mS** with Cl^-, in DMSO-d_6. [**95mS**] = 1 mM. Featureless regions of spectrum are not shown. This titration is representative of reproducible trends.

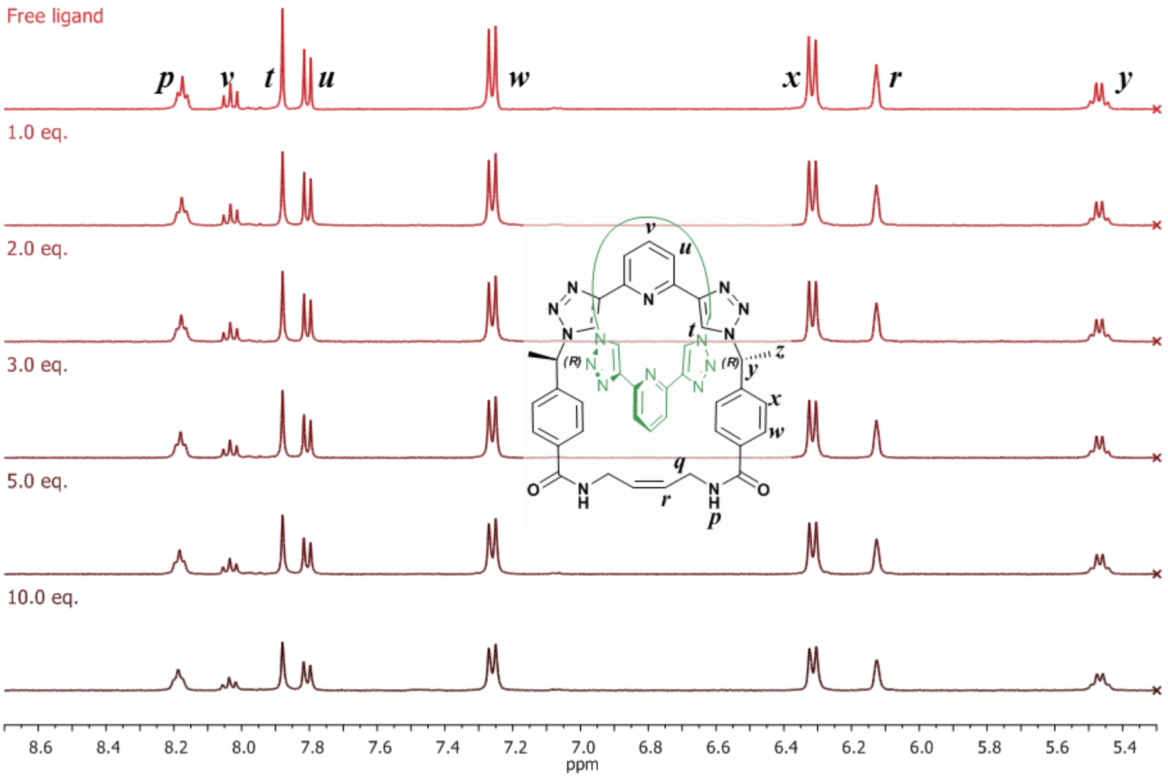

Figure A4. 8. ^{1}H NMR titration profile of **95cR** with $H_2PO_4^-$, in DMSO-d_6. [**95cR**] = 1 mM. Featureless regions of spectrum are not shown. This titration is representative of reproducible trends.

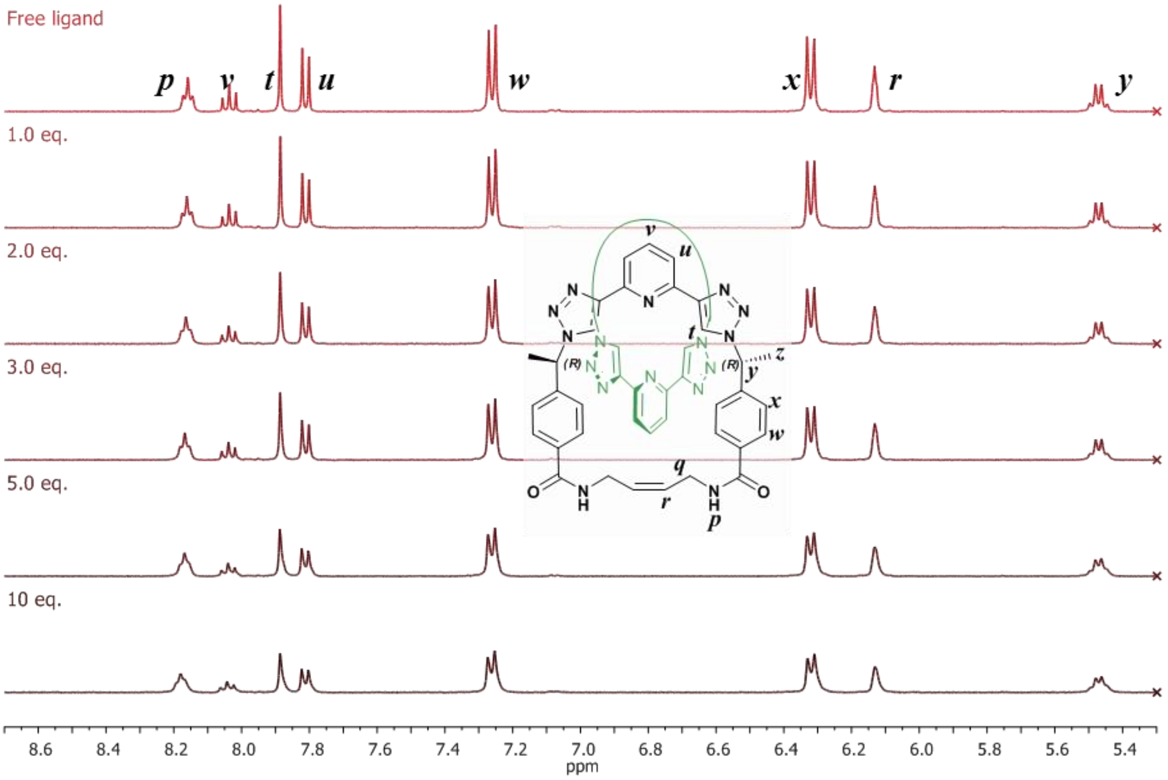

Figure A4. 7. ^{1}H NMR titration profile of **95cR** with Cl^-, in DMSO-d_6. [**95cR**] = 1 mM. Featureless regions of spectrum are not shown. This titration is representative of reproducible trends.

A5. Appendix Chapter 5

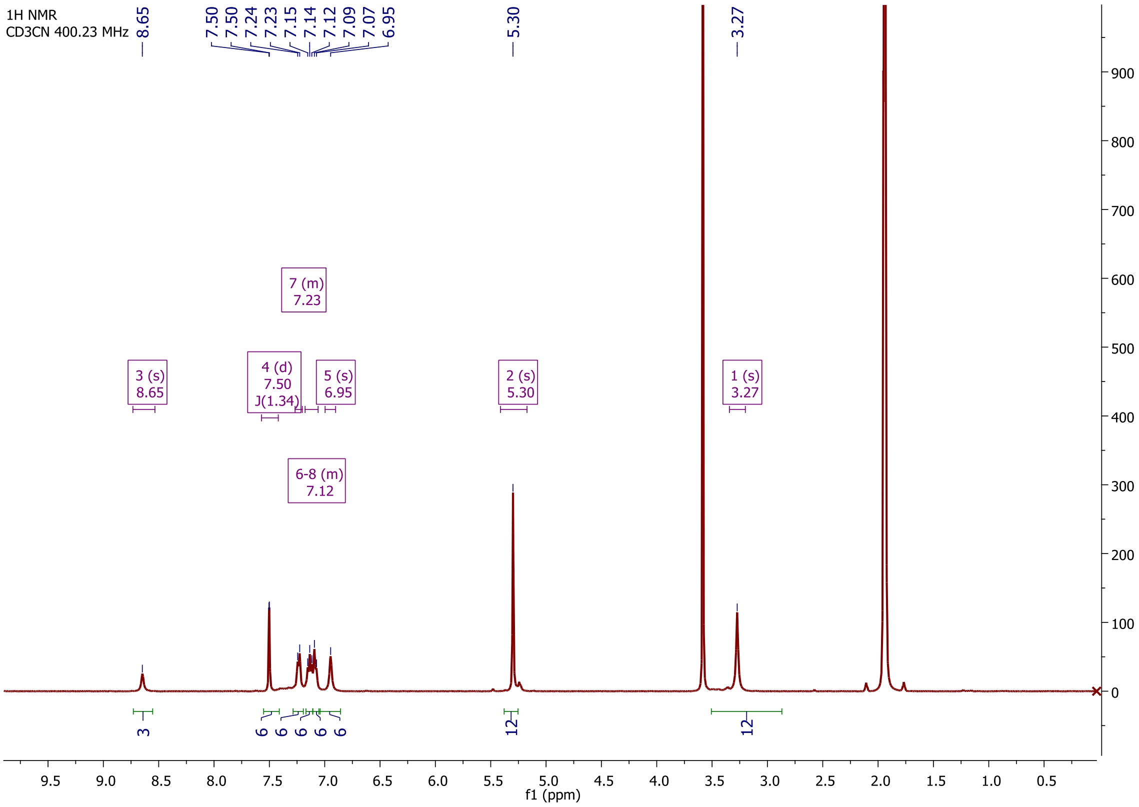

Figure A5. 1. ^{1}H NMR (400 MHz) spectrum of **96** in CD_3CN.

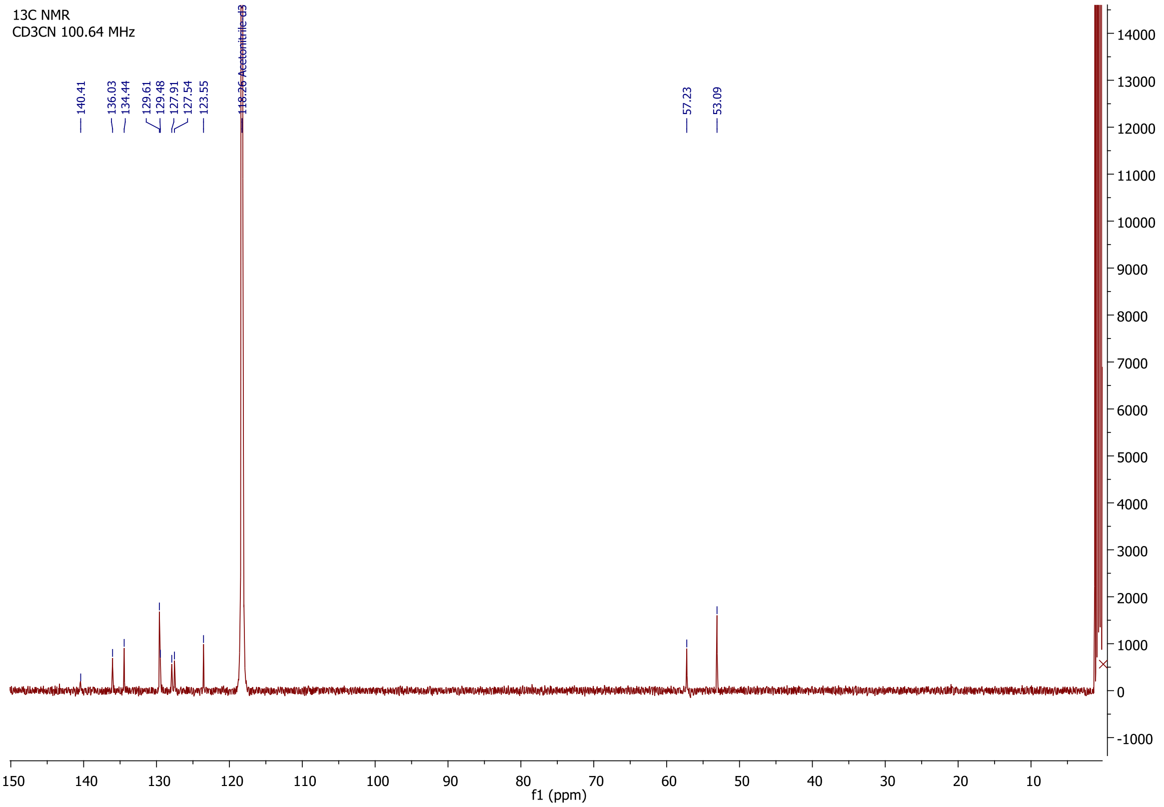

Figure A5. 2. ^{13}C NMR (151 MHz) spectrum of **96** in CD$_3$CN.

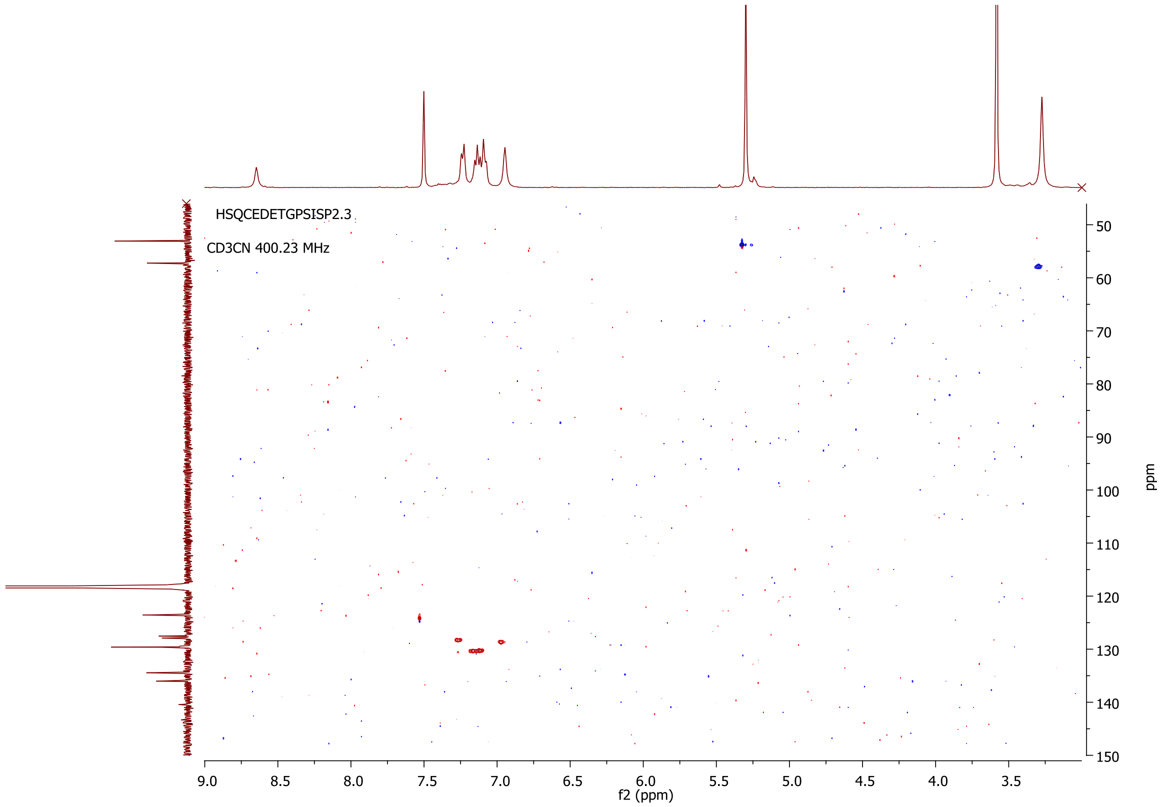

Figure A5. 3. ^{13}C-^{1}H HSQC NMR spectrum of **96** in CD$_3$CN.

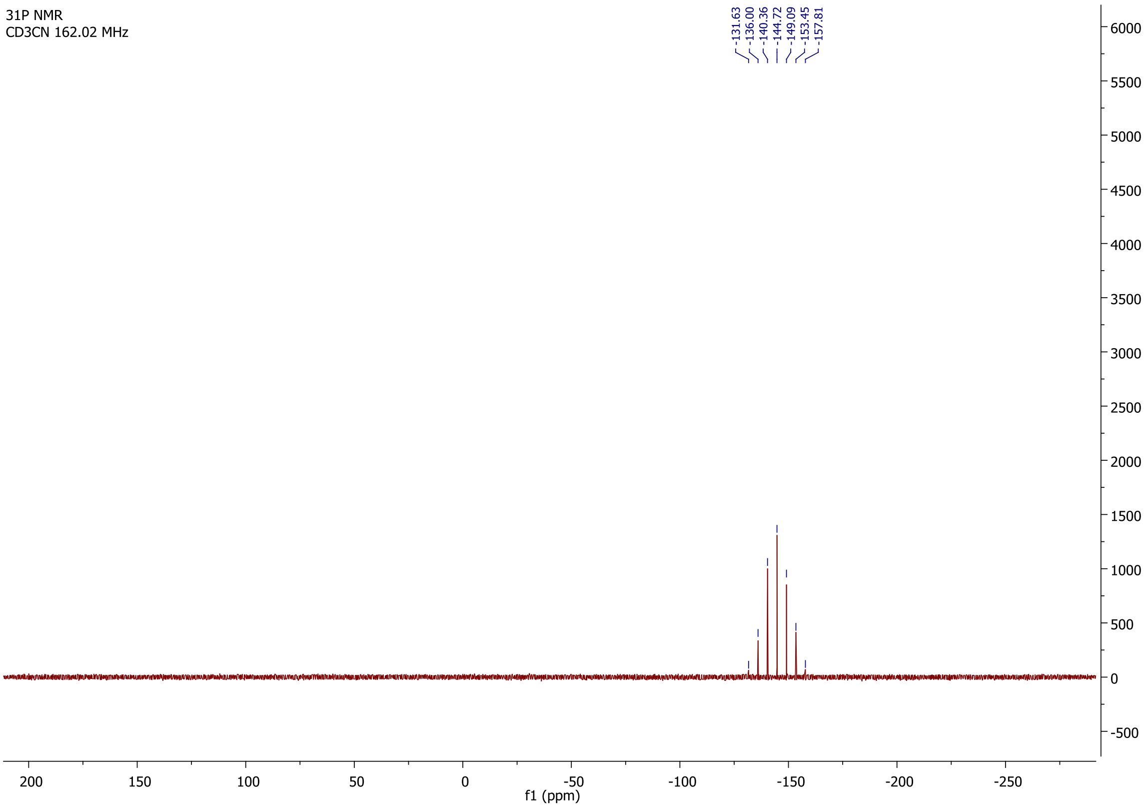

Figure A5. 4. ^{31}P NMR spectrum of **96** in CD_3CN.

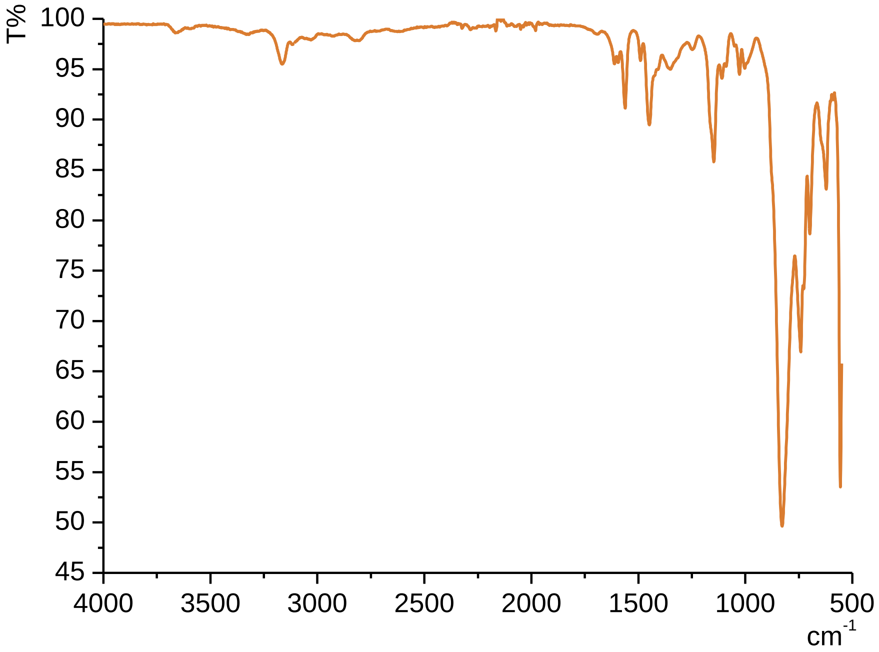

Figure A5. 5. FT IR spectrum of **96**.

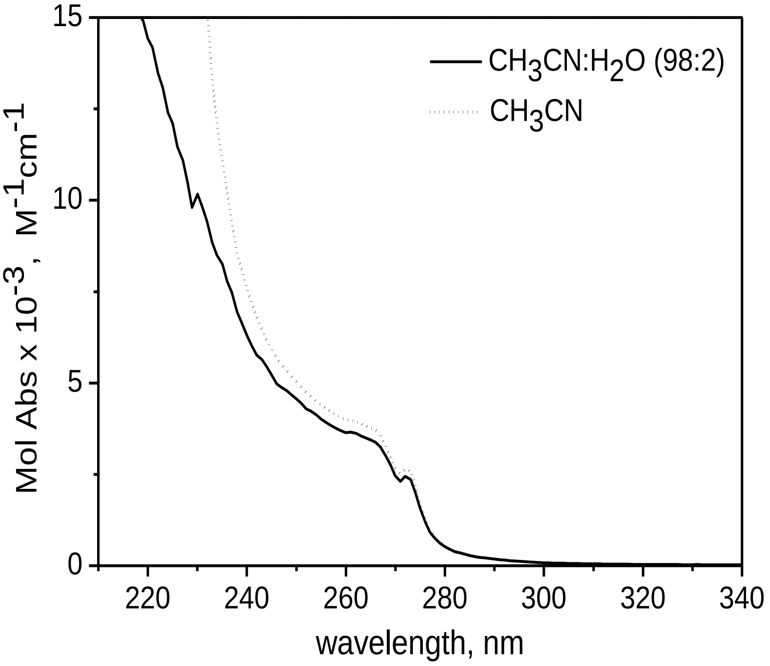

Figure A5. 6. UV-vis absorption spectrum of **96** in CH_3CN and CH_3CN:H_2O (98:2).

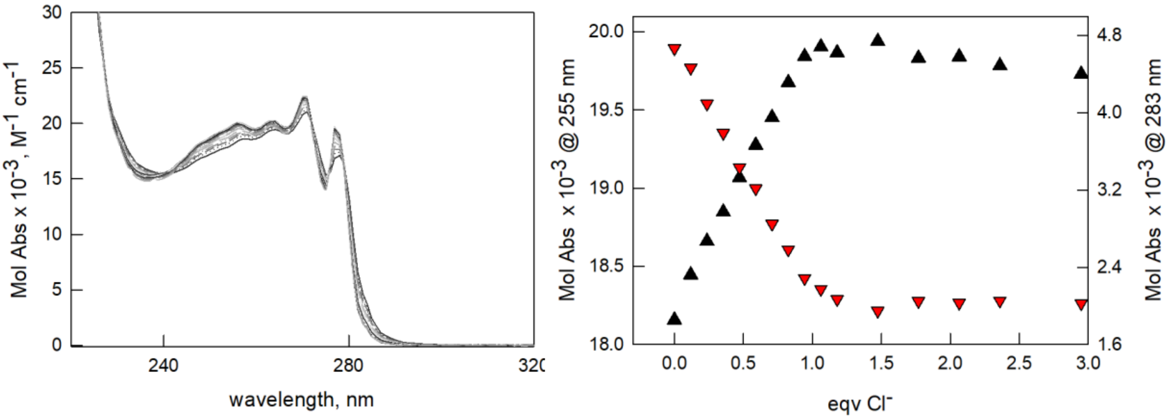

Figure A5. 7. UV-vis. titration of **168**$(PF_6)_3$ (0.2 mM) with TBACl in pure MeCN (T = 25°C, l = 0.1 cm). Left: family of UV-vis spectra; right: titration profiles of Mol Abs x 10^{-3} at 255 and 283 nm (black and red symbols, respectively).

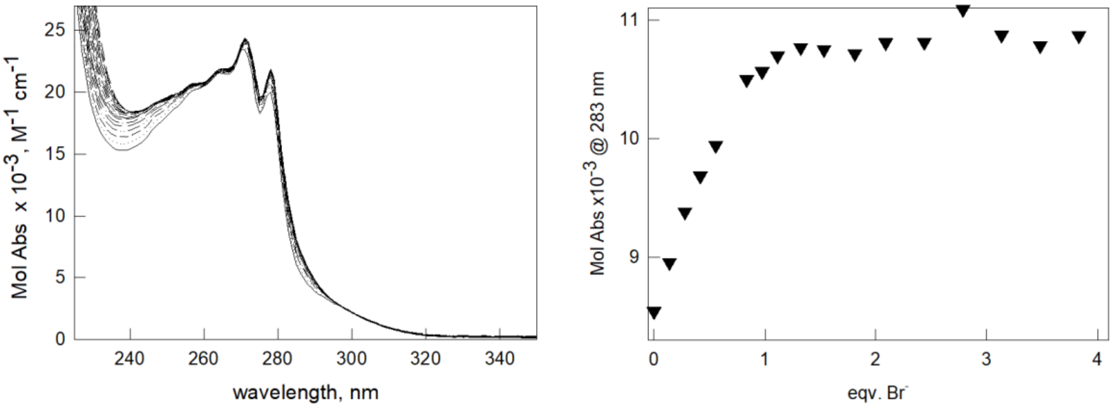

Figure A5. 8. UV-vis. titration of **168**(PF$_6$)$_3$ (0.2 mM) with TBABr in pure MeCN (T = 25°C, l = 0.1 cm). Left: family of UV-vis spectra; right: titration profiles of Mol Abs x 10^{-3} at 283 nm.

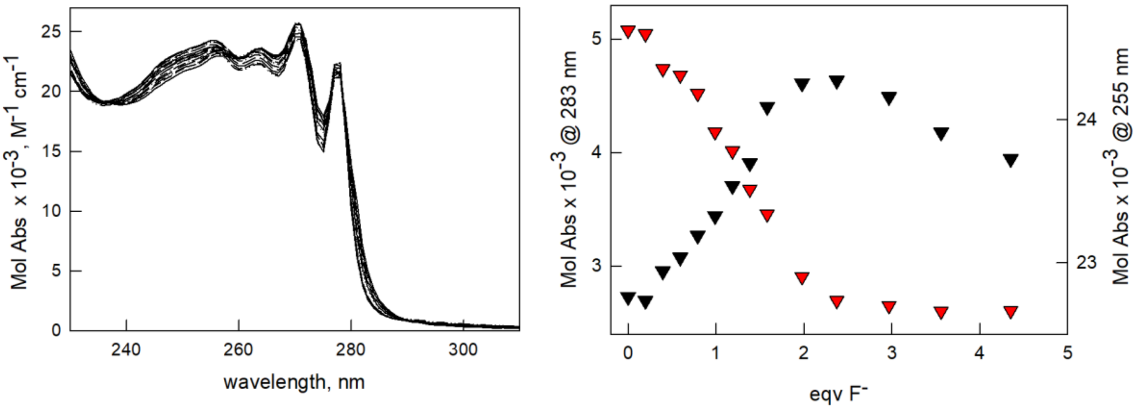

Figure A5. 9. UV-vis. titration of **168**(PF$_6$)$_3$ (20 μM) with TBAF in pure MeCN (T = 25°C, l = 1 cm). Left: family of UV-vis spectra; right: titration profiles of Mol Abs x 10^{-3} at 255 and 283 nm (black and red symbols, respectively).

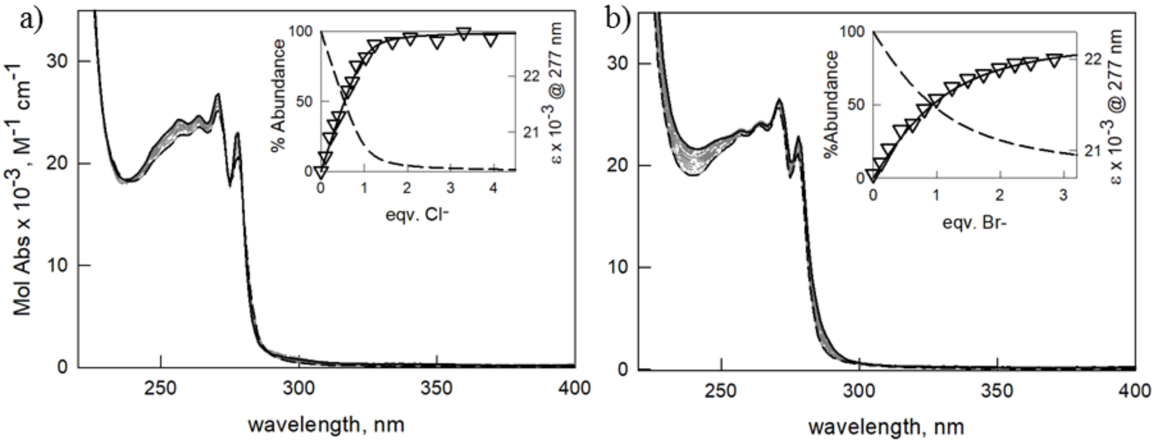

Figure A5. 10. UV-vis. titration of **168**(PF_6)$_3$ (20 μM) with a) TBACl and b) TBABr in MeCN:H_2O 98:2 (v:v) mixture (T = 25°C, l = 1 cm). Inset: titration profile of ε (i.e. Mol Abs) x 10^{-3} at 277 nm (triangles), superimposed to the distribution diagram of the species (**168**$^{3+}$: dashed line; [**168**(X)]$^{2+}$: solid line). Calculated a) LogK_{11} = 6.1, b) LogK_{11} = 5.1.

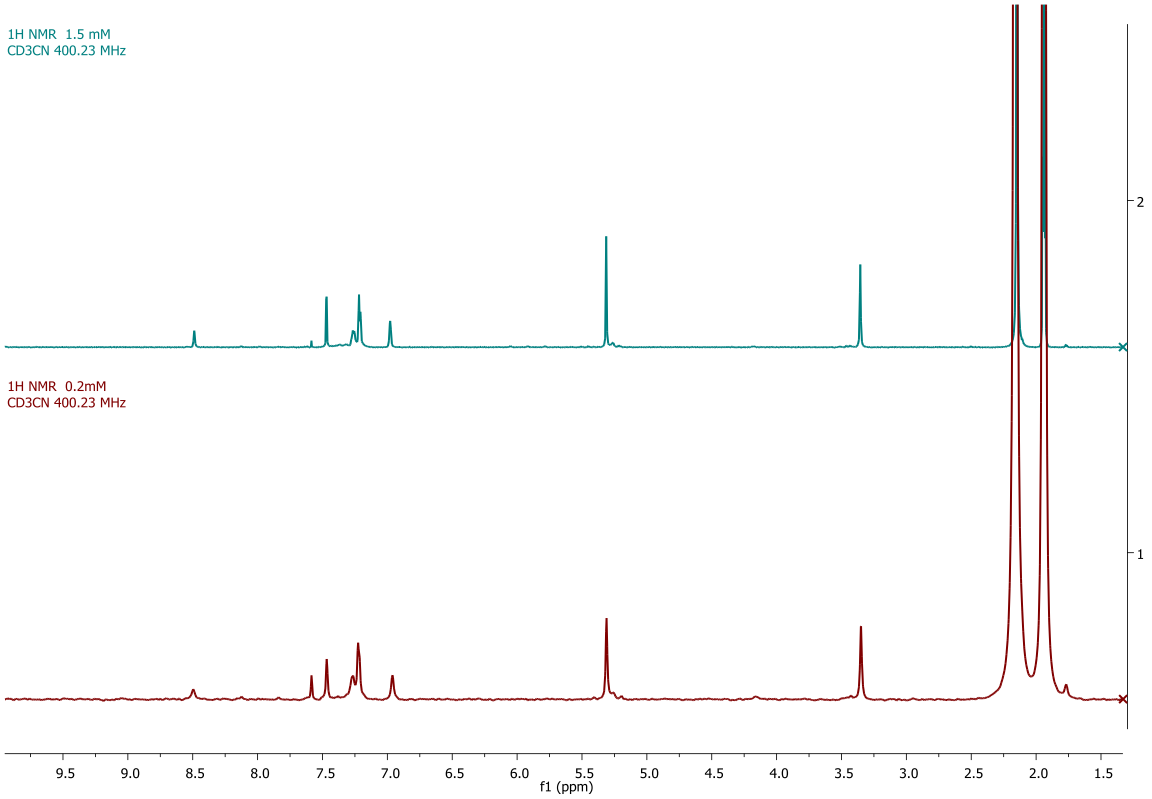

Figure A5. 11 Dilution study: comparison of ^{1}H NMR (400 MHz) spectra of **96** in CD_3CN, at 0.2 mM and 1.5mM.

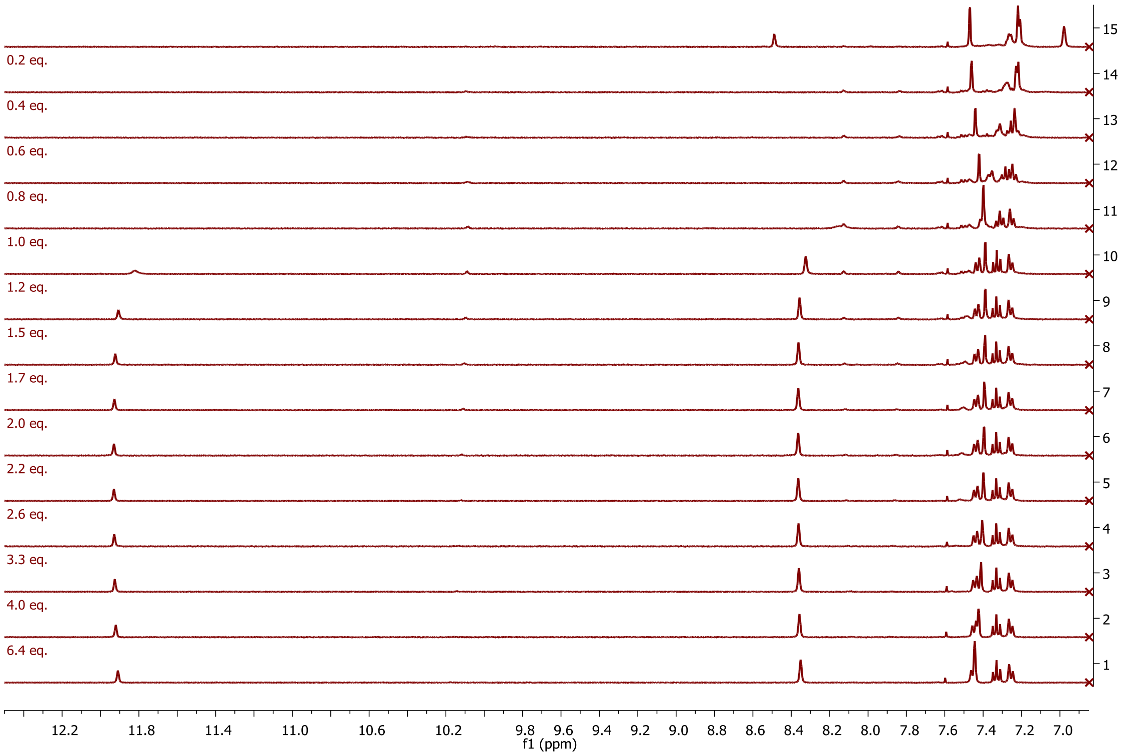

Figure A5. 12. ^{1}H NMR titration profile of **96** with Cl$^-$, in CD$_3$CN. [Cage]$_{in}$=1.5 mM.

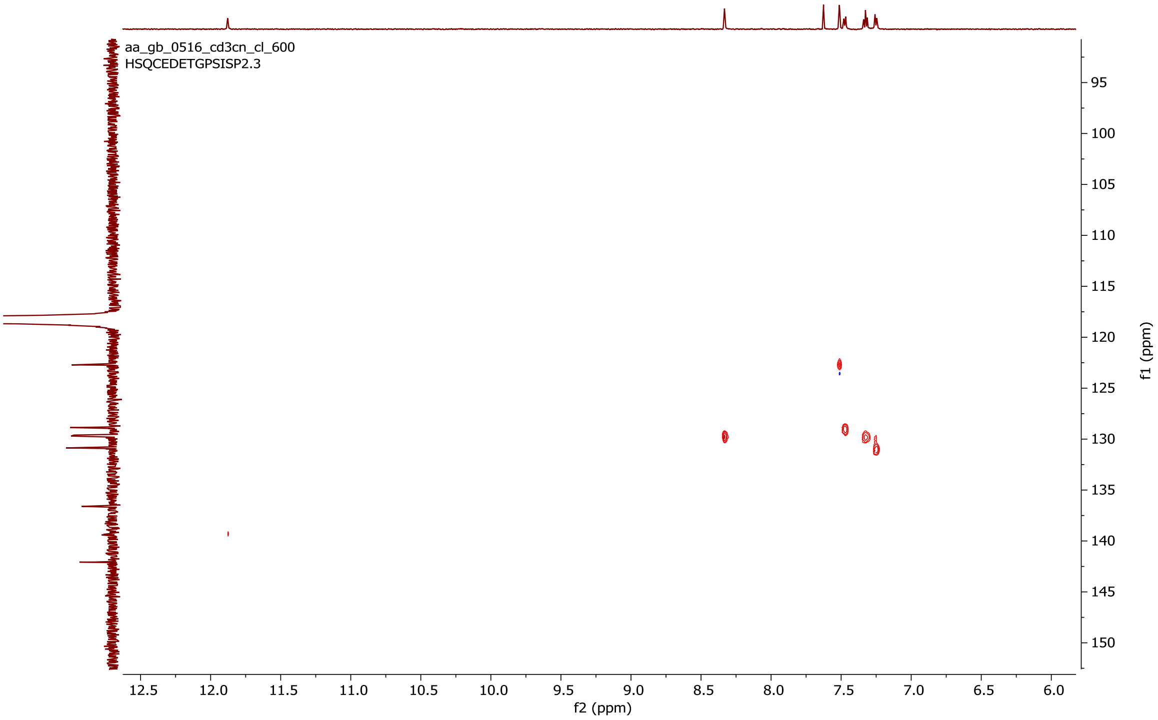

Figure A5. 13. ^{1}H – ^{13}C HSQC NMR spectrum of **96**·Cl$^-$.

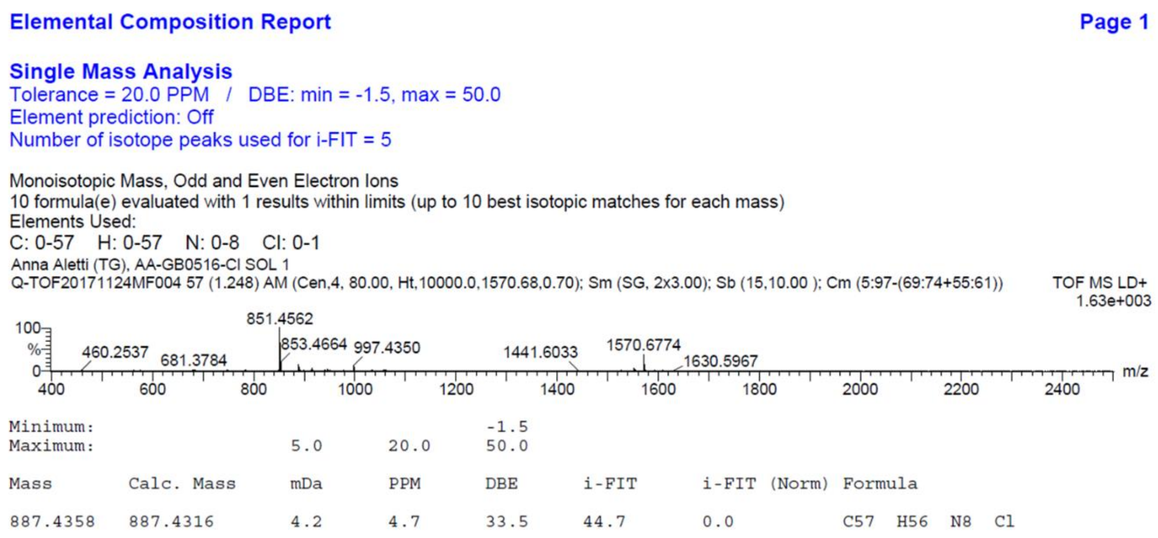

Elemental Composition Report **Page 1**

Single Mass Analysis
Tolerance = 20.0 PPM / DBE: min = -1.5, max = 50.0
Element prediction: Off
Number of isotope peaks used for i-FIT = 5

Monoisotopic Mass, Odd and Even Electron Ions
10 formula(e) evaluated with 1 results within limits (up to 10 best isotopic matches for each mass)
Elements Used:
C: 0-57 H: 0-57 N: 0-8 Cl: 0-1
Anna Aletti (TG), AA-GB0516-Cl SOL 1
Q-TOF20171124MF004 57 (1.248) AM (Cen,4, 80.00, Ht,10000.0,1570.68,0.70); Sm (SG, 2x3.00); Sb (15,10.00); Cm (5:97-(69:74+55:61)) TOF MS LD+ 1.63e+003

```
Minimum:                                        -1.5
Maximum:                        5.0      20.0   50.0

Mass       Calc. Mass   mDa      PPM      DBE     i-FIT     i-FIT (Norm) Formula

887.4358   887.4316     4.2      4.7      33.5    44.7      0.0          C57  H56  N8  Cl
```

Figure A5. 14. MALDI-TOF of **96**·Cl^{-}.

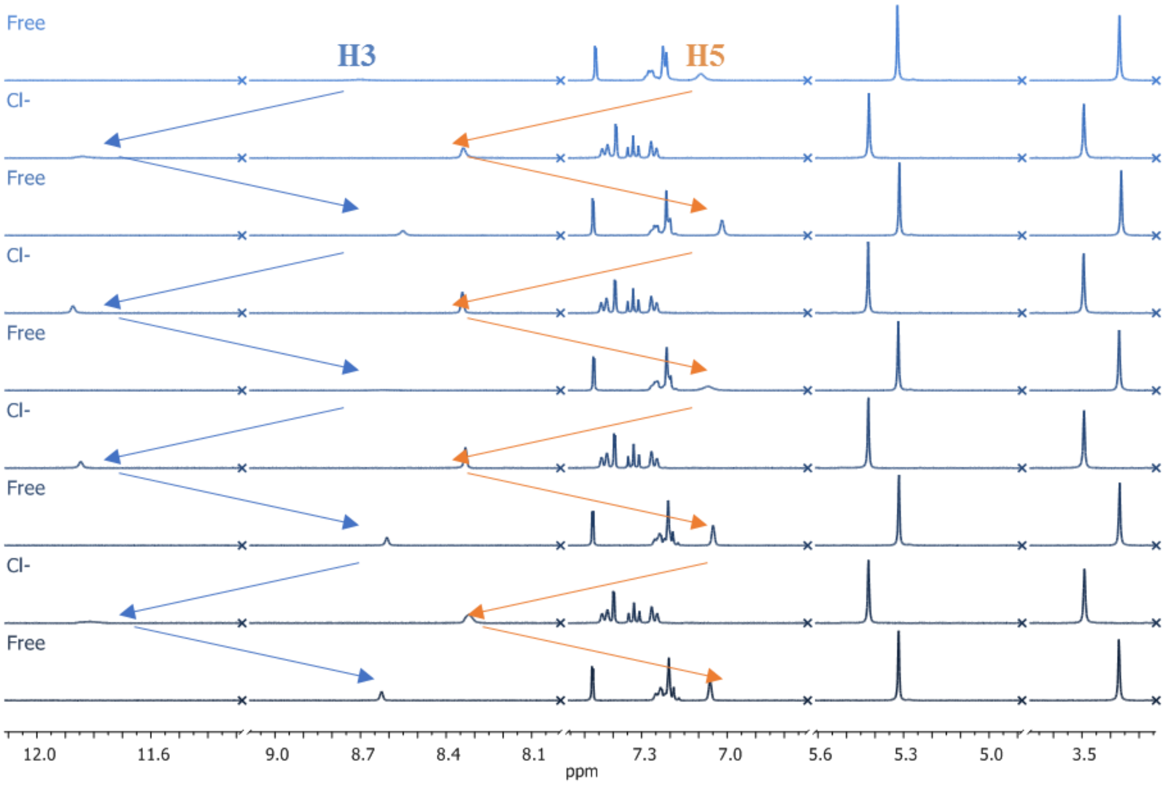

Figure A5. 15. ^{1}H–NMR spectra recorded under the subsequent additions of TBACl and $AgNO_3$ to a solution of **96**$^{3+}$ (1 mM) in CD_3CN, T = 25°C. Cycle 0: upon addition of TBACl (1 eqv.) to **96**$^{3+}$, relevant changes in the ^{1}H–NMR spectrum of the free cage were found, consistent with the formation of the chloride complex (Free → Cl^{-}). The free cage was then recovered by addition of $AgNO_3$ (1 eqv.) to the solution (see Cycle 1, Free).The cycle of chemical stimuli was repeated four times (Cycle 0 → 4).

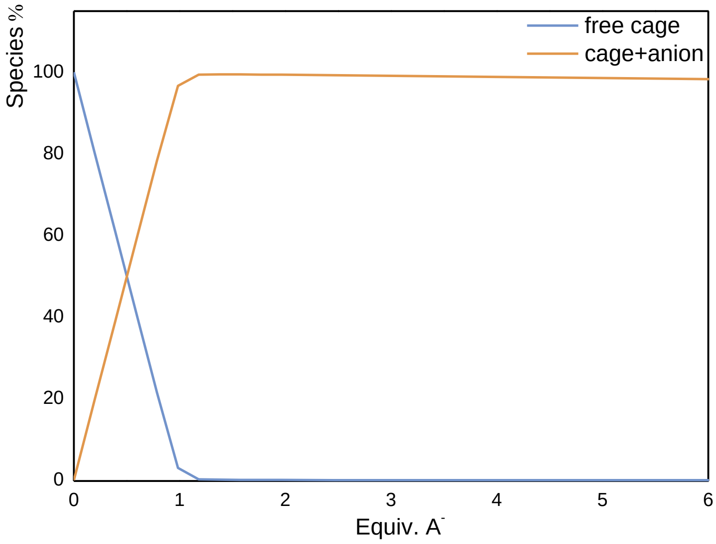

Figure A5. 16 Speciation diagram obtained from fitting of ^{1}H NMR titration of **96** with Cl$^-$.

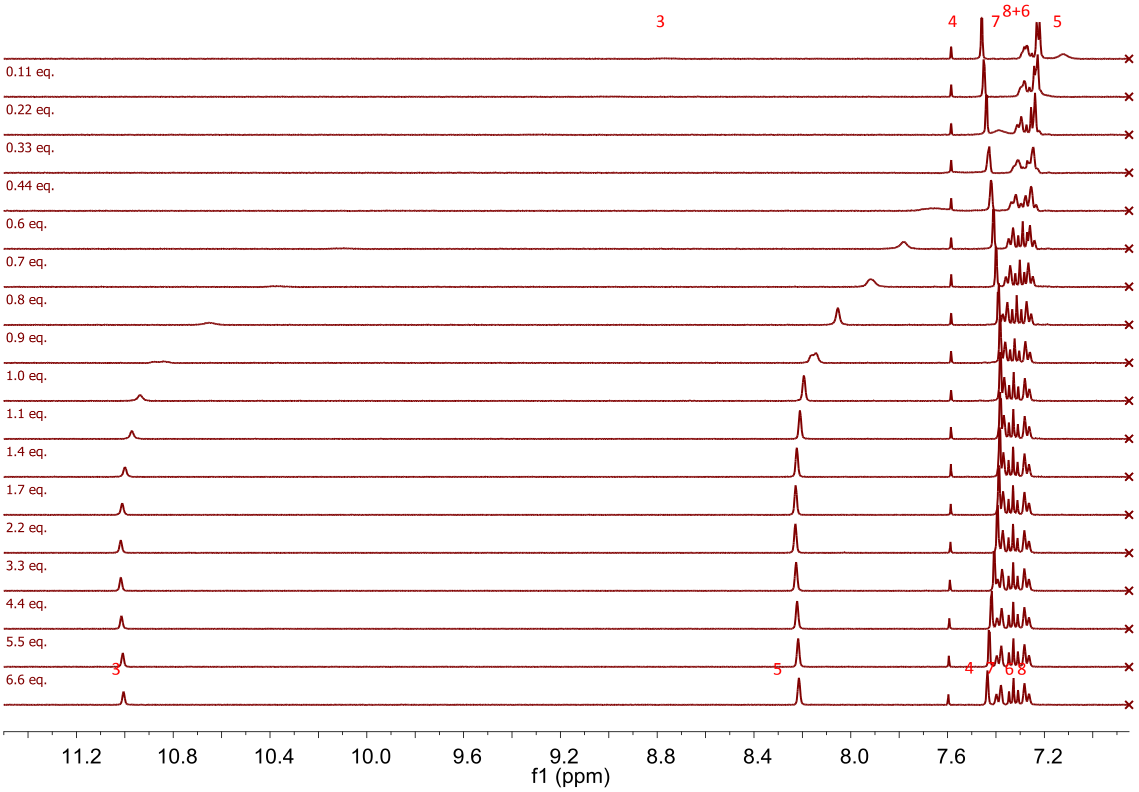

Figure A5. 17. ^{1}H NMR titration profile of **96** with Br$^-$, in CD$_3$CN. [Cage]$_{in}$=1 mM.

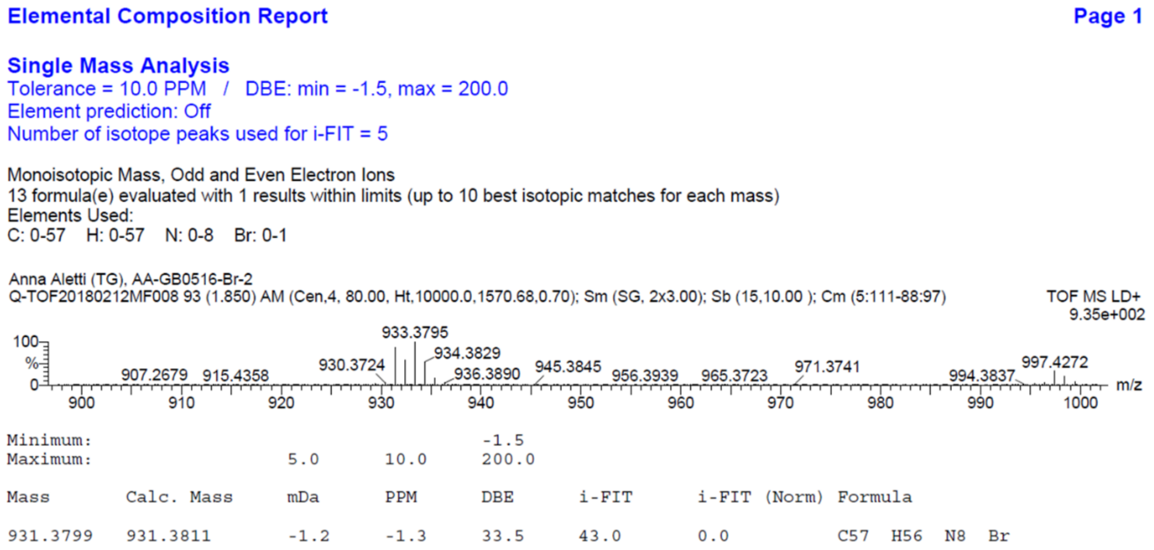

Elemental Composition Report **Page 1**

Single Mass Analysis
Tolerance = 10.0 PPM / DBE: min = -1.5, max = 200.0
Element prediction: Off
Number of isotope peaks used for i-FIT = 5

Monoisotopic Mass, Odd and Even Electron Ions
13 formula(e) evaluated with 1 results within limits (up to 10 best isotopic matches for each mass)
Elements Used:
C: 0-57 H: 0-57 N: 0-8 Br: 0-1

Anna Aletti (TG), AA-GB0516-Br-2
Q-TOF20180212MF008 93 (1.850) AM (Cen,4, 80.00, Ht,10000.0,1570.68,0.70); Sm (SG, 2x3.00); Sb (15,10.00); Cm (5:111-88:97)
TOF MS LD+
9.35e+002

```
Minimum:                                  -1.5
Maximum:                  5.0      10.0   200.0

Mass      Calc. Mass     mDa      PPM     DBE      i-FIT     i-FIT (Norm) Formula

931.3799  931.3811       -1.2     -1.3    33.5     43.0      0.0          C57  H56  N8  Br
```

Figure A5. 18. MALDI-TOF of **96**·Br$^-$.

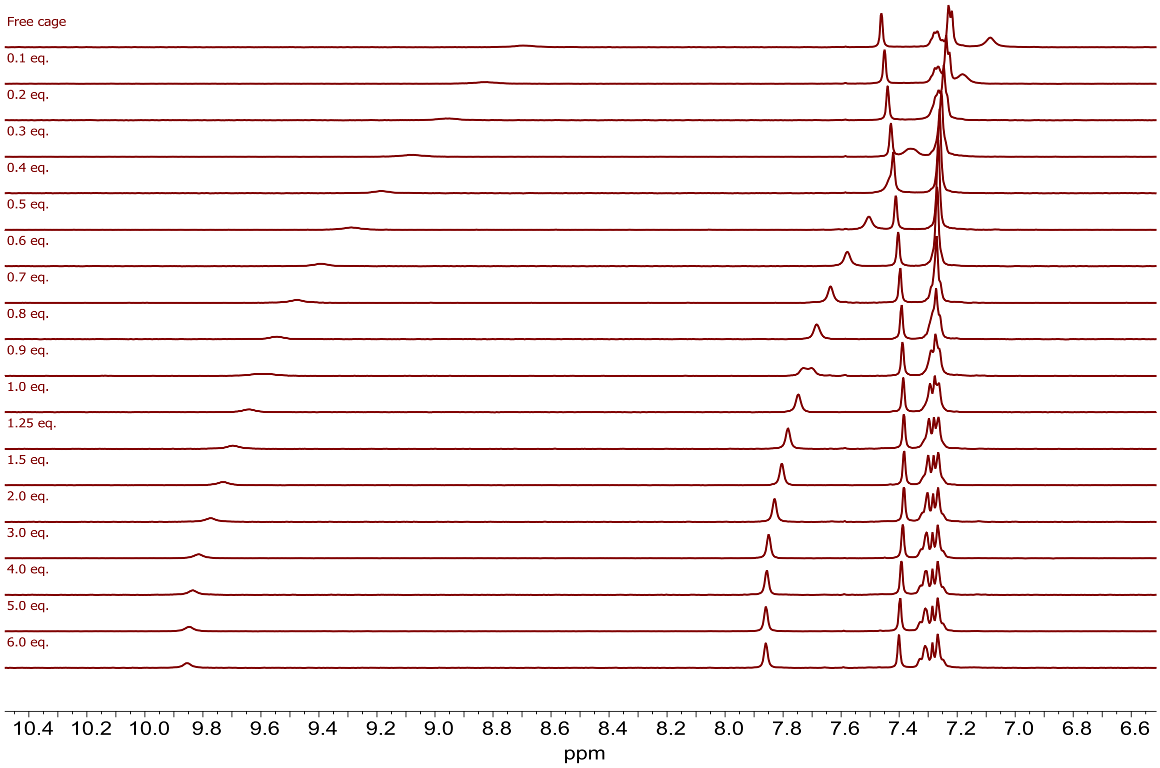

Figure A5. 19. ^{1}H NMR titration profile of **96** with I$^-$, in CD_3CN. $[Cage]_{in}$=1 mM.

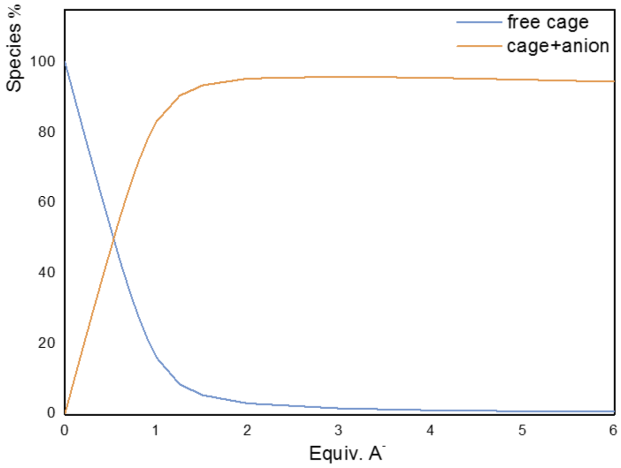

Figure A5. 20. Speciation diagram obtained from fitting of ^{1}H NMR titration of **96** with I$^-$.

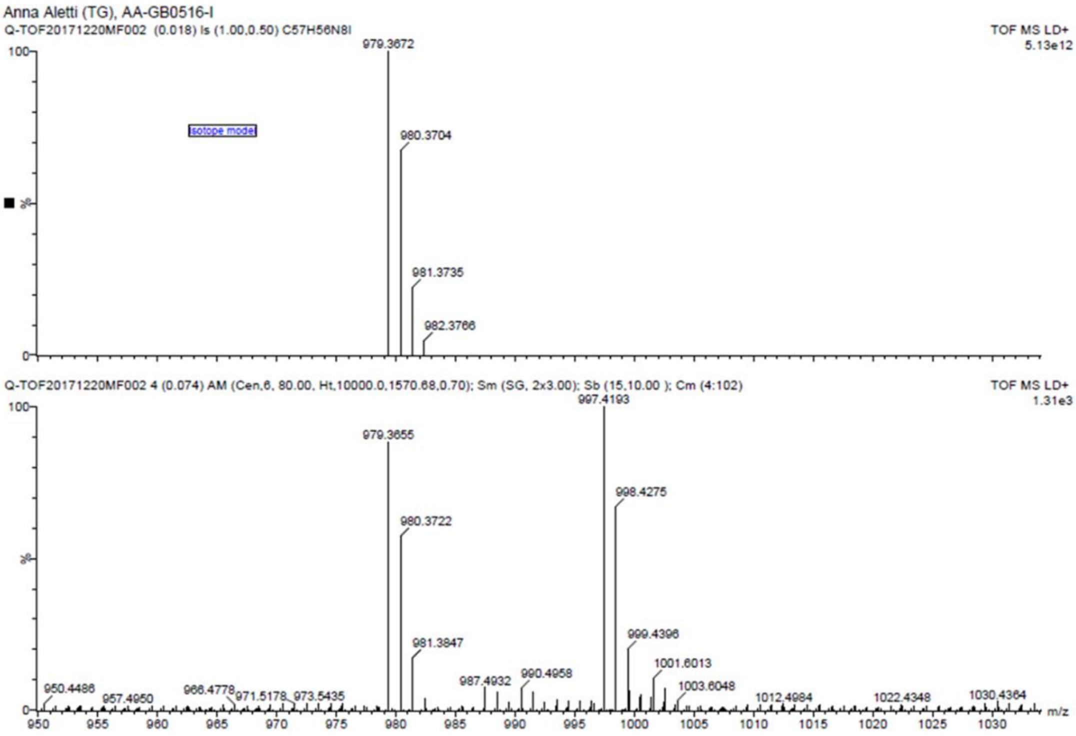

Figure A5. 21. MALDI-TOF of **96**·I$^-$.

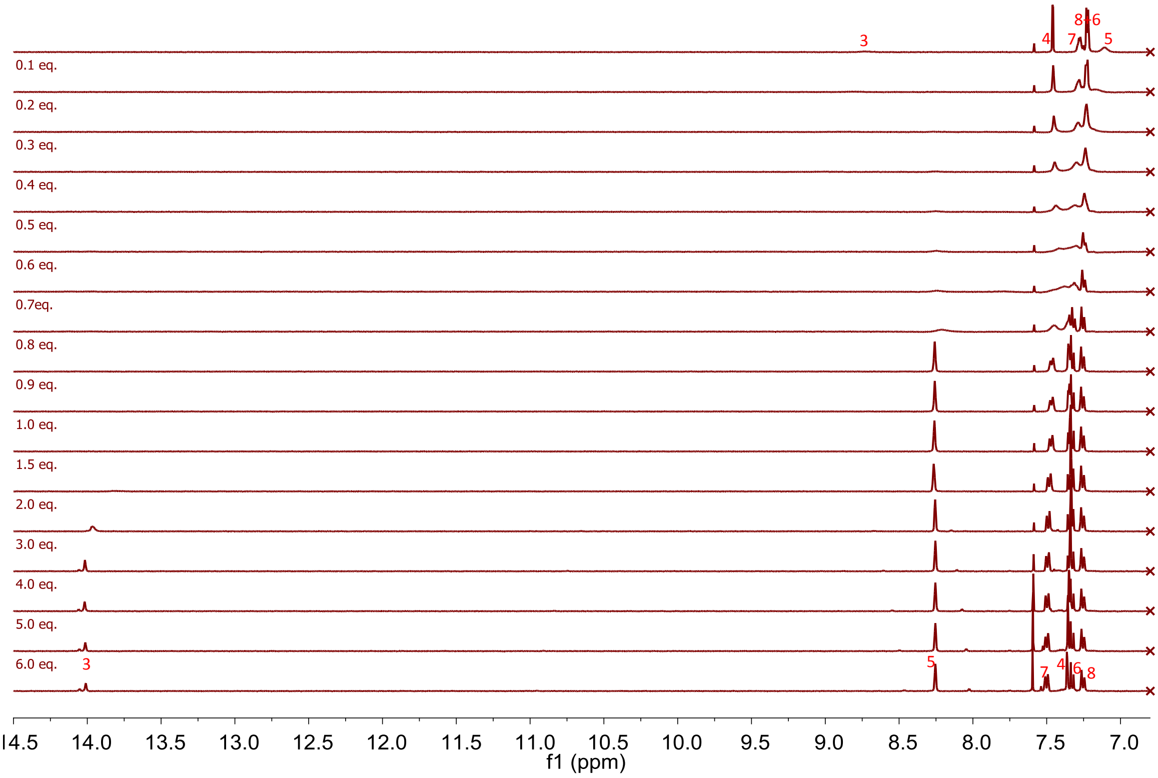

Figure A5. 22. ^{1}H NMR titration profile of **96** with F$^-$, in CD_3CN. [Cage]$_{in}$=1 mM.

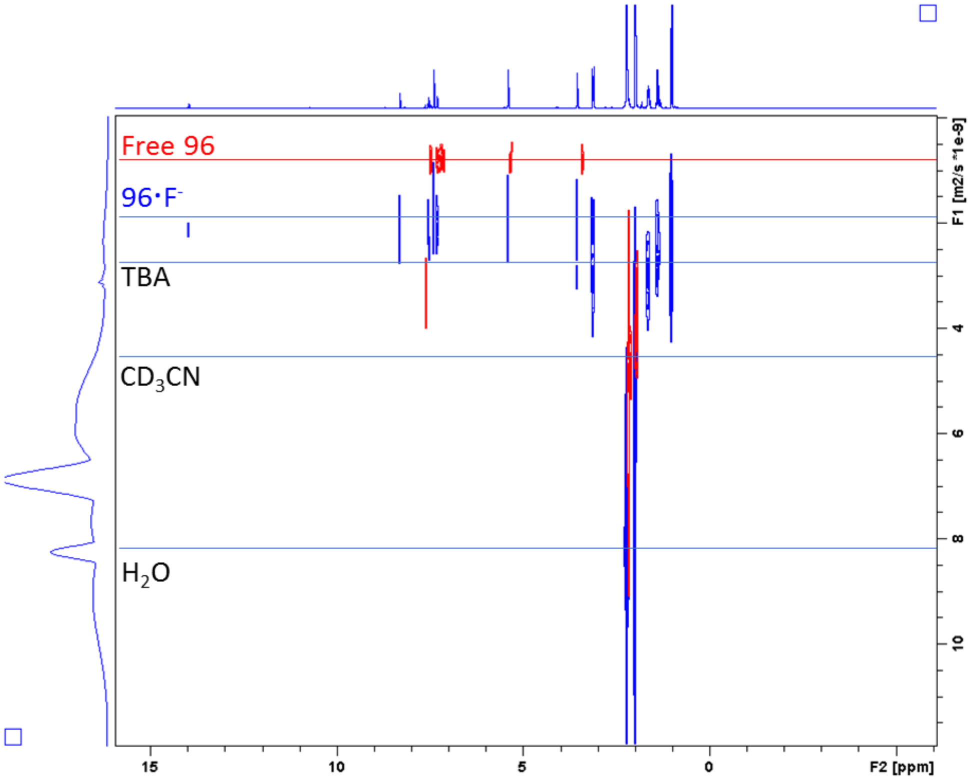

Figure A5. 23. Superimposed DOSY experiments of the free cage **96**$(PF_6)_3$ (red) and **96**$(PF_6)_3$with excess (3 equiv. of TBAF (blue) at 25°C in CD_3CN.

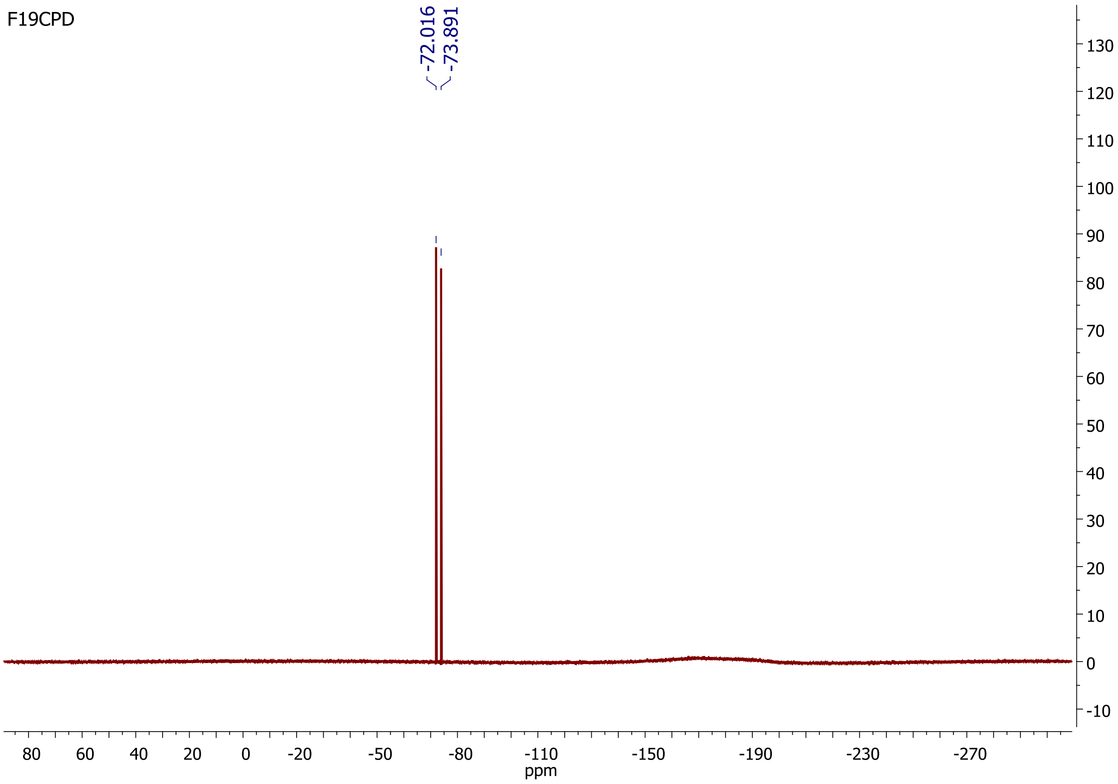

Figure A5. 24. ^{19}F NMR spectrum of **96**·F^{-} in CD$_3$CN.

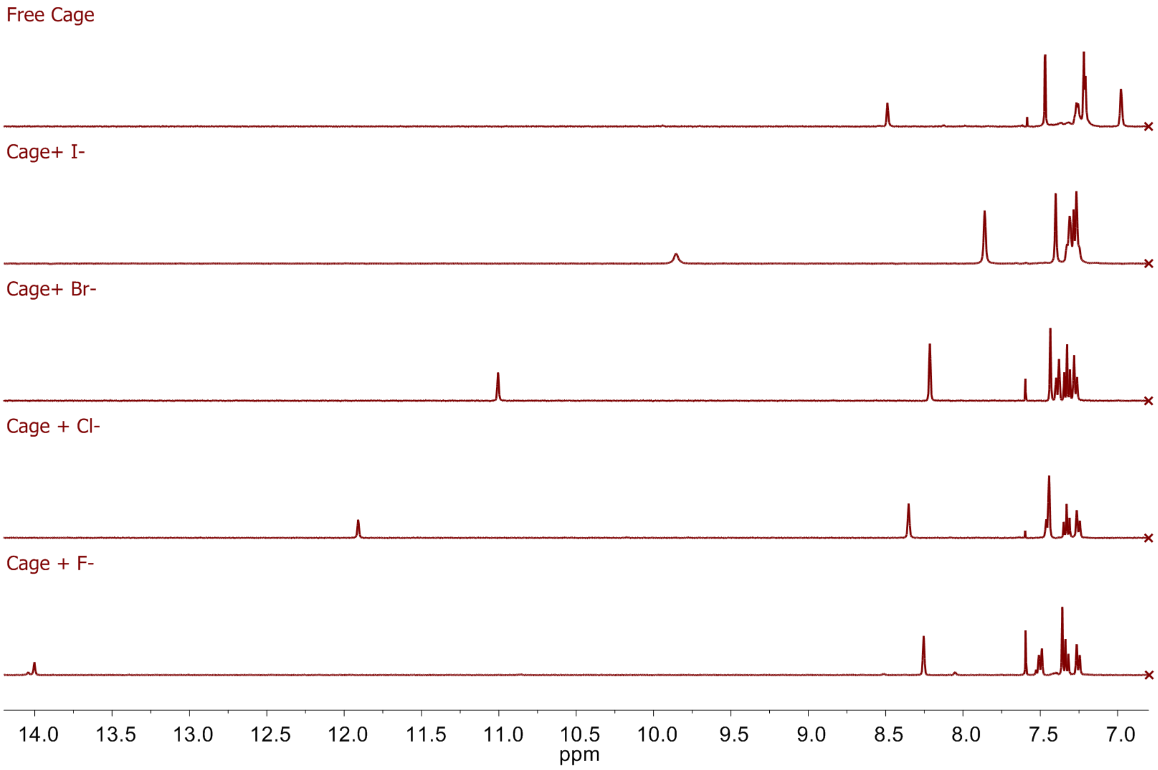

Figure A5. 25. Stacked spectra of free cage **96** and adduct with the different halides (6 equivalents of anion).